A Multi-Sensor Approach to the Retrieval and Model Validation of Global Cloudiness

By
Steven D. Miller and Graeme L. Stephens

Department of Atmospheric Science
Colorado State University
Fort Collins, Colorado

Research supported by NASA Student Fellowship NGT5-50007-0002, NASA grant NAG5-6637-0001, DOE/ARM grant DE-FG03-94ER61748, and NASA/FIRE grant NAG-1-2062

Colorado State University

Department of Atmospheric Science

Paper No. 692

A MULTI-SENSOR APPROACH TO THE RETRIEVAL AND MODEL VALIDATION OF GLOBAL CLOUDINESS

Steven D. Miller and Graeme L. Stephens

Research supported by NASA Student Fellowship NGT5-50007-0002, NASA grant NAG5-6637 0001, DOE/ARM grant DE-FG03-94ER61748, and NASA/FIRE grant NAG-1-2062

Principal Investigator: Graeme L. Stephens

Department of Atmospheric Science

Colorado State University

Fort Collins, Colorado

March, 2000

Atmospheric Science Paper No. 692

ABSTRACT

A MULTI-SENSOR APPROACH TO THE RETRIEVAL AND MODEL VALIDATION OF GLOBAL CLOUDINESS

The ephemeral clouds have represented a daunting challenge to the atmospheric modeling community from the very beginning. Namely, their far-reaching importance to the energy balance and hydrological cycle of our planet is eclipsed only by the level of complexity at which they are nested within the non-linear climate feedback system. Too often are clouds oversimplified in atmospheric models simply for lack of a sound physical understanding of their integral role in the system. Historically, our knowledge of atmospheric variables has been steeped in a tradition of observations, and clouds are no exception. Hence, the onus falls squarely upon atmospheric remote sensing to provide this burden of truth through detailed, accurate observations of the physical system. Our inability to resolve by means of traditional passive sensors the detail of information required to characterize clouds has challenged us to explore other resources at our disposal. In this spirit, this research seeks to illustrate and, where applicable, quantify the ways in which active (e.g., radar and lidar) remote sensing devices on existing and proposed platforms can serve to improve our current understanding of cloud and cloud processes. Two perspectives are emphasized: 1) the role of active sensors in the improvement of cloud property retrievals and 2) their application to the validation/development of clouds in numerical weather prediction models.

First, a new retrieval technique which employs active sensors (e.g., lidar and cloud radar) to constrain cloud boundaries in the vertical is shown to decrease significantly the errors incurred by traditional passive satellite retrievals (which approximate cloud heights

by various emission or shadow-geometry techniques), and those of night-time cirrus in particular. Based on results from twelve independent single-layer cloud case studies using reflected radiance/brightness-temperature information from GOES, the CSU SSP, and MAS, the *a priori* data were shown to improve the retrieval uncertainty of night-time cirrus optical properties in excess of 20% for effective particle radius, and 10-20% for optical depth. Uncertainties associated with solar reflection based single-layer retrievals showed improvements typically less than 5% (however, the unexplored benefits of active cloud profile information in the case of day-time multi-layered clouds remain significant).

The retrieval results are brought together with detailed cloud profile sampling from the Lidar In-space Technology Experiment (LITE) to conduct the first global-scale active sensor validation of the ECMWF prognostic cloud scheme. Short-range (20-30 hr) forecasts matched to 66 night-time LITE orbits display remarkable agreement in cloud spatial distribution both in the horizontal and vertical. A weighted statistical analysis revealed hit rates between 75-90%, threat scores 45-75%, probabilities of detection $\approx$ 80%, and false alarm rates 10-45%. Retrieved cloud properties were converted to equivalent cloud liquid/ice water paths and compared against model forecasts. The findings of these comparisons reveal that while there is obvious room for improvement, the level of realism displayed currently by the ECMWF prognostic cloud scheme forecasts suggest that the reanalysis data may be considered as a new resource for global cloud information. A practical application of these findings has been outlined in the context of defining CloudSat instrument requirements based on virtual orbital observations created from ECMWF global cloud distributions of liquid and ice water contents.

The outcomes of the research are a near-operational GOES retrieval scheme with performance diagnostics, an quantified assessment of the benefits provided to cloud property retrievals using a multi-sensor observing system that includes active components, and a new perspective on the currently ability of numerical weather prediction models to forecast clouds. This final outcome gives cause for new hope in capturing the complex radiative, convective, and dynamical feedback mechanisms associated with clouds in the climate feedback system. Insodoing, this research appeals to the need for an improved collaborative rapport between the now largely disjoint modeling and measurement communities.

Establishment of this link is argued to be the key step toward realizing the true potential of multi-sensor data in addressing the cloud/climate problem.

Steven D. Miller
Department of Atmospheric Science
Colorado State University
Fort Collins, Colorado 80523
Spring 2000

ACKNOWLEDGEMENTS

We are indebted to the many people who supported this research in a variety of capacities, including Kelly Dean and Nan McClurg of CIRA (satellite data acquisition and processing tools), Ian Wittmeyer of CSU (hardware support), Mark Vaughan of NASA LaRC (assistance with LITE data), Tina Baucom of Swales Aerospace (GOES instrument noise characterization), Greg Sadowy of JPL and Steve Sekelsky of UMass (providing ACR data and guidance), Philip Partain of CSU (assistance with software and conceptual development), and Andy Heidinger of NOAA/NESDIS (development of radiative transfer and retrieval theory). We acknowledge in particular Anton Beljaars and Christian Jakob of ECMWF who provided valuable model data and helpful interpretation in connection to the NWP/observation validation exercises. Financial support for this research was provided by NASA Student Fellowship #NGT5-50007-0002, NASA grant NAG5-6637 0001, DOE/ARM grant DE-FG03-94ER61748, and NASA/FIRE grant NAG-1-2062.

CONTENTS

LIST OF FIGURES

LIST OF TABLES

Chapter 1

INTRODUCTION

Finite to fail, but infinite to venture.
For the one ship that struts the shore
Many's the gallant, overwhelmed creature
Nodding in navies nevermore.

—Emily Dickinson

When one embarks upon the harrowing voyage of composing their Dissertation, the most troublesome leg is often the first. As Shakespeare duly noted, "brevity is the soul of wit," and so in turn do we strive to articulate years of labor, long days and longer nights, triumphs and (primarily) tribulations, into a cohesive description of "what we did," "why we did it," and "what was learned"–hopefully without lulling the reader into a trance of disinterest somewhere *en route*. To what extent Shakespeare's advice applies to Dissertations is debatable, although avoiding this most unenviable of writer's fates in a scientific forum (perhaps the least forgiving of them all) remains a valid concern. One mustn't plunge hurriedly into the grit of the matter without first mentioning the stone which it aims to polish. We must take care to first paint meticulously a clear and motivating picture of what the content is to be. The most obvious means to attaching relevance to a work (or at least suggest a method to the ensuing madness) is to locate and identify concisely where this specific research fits within the greater scope of the *Big Picture* appealing to the interests and concerns of The Many. This development is by no means at odds with the aforementioned appeal to brevity; for without it even the first sentence is a mountain to scale. And so in this spirit, it is here that we shall launch our discussion with the hope that by journey's end the reader has not drowned in the details.

1.1 The Big Picture

We begin by introducing the main focus of this research and where it falls within the context of the greater scheme of things. A unifying goal of the many sub-disciplines in atmospheric science is to understand how all the components of the climate system, great and small, convolve and converse in complex, non-linear ways to manifest the ensemble system as we know it. The differential heating of our planet's atmosphere and surface by solar (shortwave) energy serves as the primary driving mechanism to this system. Radiative equilibrium is achieved by re-emitting thermal (longwave) energy to space and mixing of heat from regions of surplus to deficit. All circulations cascading down to smaller and smaller areas, characterized by the dynamics of a rotating fluid, the thermodynamics and chemistry associated with this fluid, and the radiative properties (absorption, emission, and reflection) of the atmosphere and underlying surface, engage in an incessant attempt to maximize the entropy of the system (i.e., achieve a state of equilibrium). In the highly relevant analogy to system and control theory, we observe the convolution of internal gains and feedbacks of the Earth's *dynamic* transfer function in the form of weather (high frequency) and climate (low frequency) phenomenon.

Clouds are an important and active component of this feedback system. As three-dimensional dynamic manifestations of the hydrological cycle at work, clouds influence the nature of the radiative exchange in terms of how much energy (both shortwave and longwave) enters or exits the system and where (spatially) energy surpluses (heating) and deficits (cooling) occur. This distribution of radiative heating feeds back to modify the synoptic-scale atmospheric circulation, which in turn dictates the incipient formation of cloud, and so assumes a closed-loop feedback element of the climate system. In other words, clouds close their feedback "circuit" by in turn influencing (by virtue of their *optical properties*[1] the very circulations responsible for their formation. The relationship is rendered more complex by the fact that different clouds interact with radiation in

[1]That is, how the cloud interacts with electromagnetic radiation

different ways, depending on their height, thickness, and microphysical properties such as phase, particle shape and size distribution. Further, the optical properties of clouds and the gaseous soup in which they reside are highly variable across the spectrum, owing in large part to complex absorption spectra of water. The simple minded picture of a single feedback gives way to a much more complicated situation of multiple feedbacks intertwined. Being woven so tightly into the fabric of the climate feedback system, clouds remain an unresolved and challenging obstacle to improving of our current understanding of clouds and their role in climate. It is to this challenge that we must rise in undertaking the charge of characterizing the Earth's cloud climatology in a comprehensive manner.

In addition to latent heating processes, clouds affect the Earth's energy budget by interacting with solar and thermal radiation in a complicated way. In most cases, clouds reflect more radiation to space than a clear sky with reflecting lower boundary alone, leading to a cooling effect at the surface. In the thermal part of the electromagnetic spectrum (roughly 3.9-μm and upwards in wavelength), high clouds absorb upwelling radiation from the warmer surface and underlying atmosphere and re-emit this radiation to space at their cooler environmental temperature (and hence trapping energy), leading to a warming effect on the surface and lower atmosphere. Harrison *et al.* (1990) define a radiative forcing parameter exemplifying the insulator-like properties of cloud cover and yielding a globally, annually-averaged longwave and shortwave radiative effect of clouds on the order of +31 and -48 W/m^2, respectively, yielding a net cooling effect by clouds of -17 W/m^2. Regressing Earth Radiation Budget Experiment (ERBE) data with International Satellite Cloud Climatology Project (ISCCP) cloud classification algorithm products, Ockert-Bell and Hartmann (1992) partition cloud forcing effects as a function of cloud type. They find that high clouds contribute most to the longwave (warming) flux effect and optically-thick high clouds in the tropics and lower clouds at mid-to-high latitudes contribute most to the shortwave (cooling) effect.

In order to better acknowledge their role in the global climate system, cloud distributions and optical properties must of course be better understood and quantified on the global scale. The most convenient vehicle to addressing these needs is the environmental

satellite platform. Instruments flown aboard satellites in either geostationary (GEO) or low-earth (LEO) orbits provide a global vantage point from which we can observe cloud formations from scales of hundreds of kilometers down in tens of meters, depending on the instruments used. Environmental satellites historically have carried passive radiometer instruments due primarily to cost and technology constraints. While the ability of passive remote sensing devices to observe many key elements of atmospheric structure, dynamics, and constituents are proven, there remain important shortcomings associated with vertical resolution of profile. Specific examples include the detection of cloud layers residing below upper layers of optically thick clouds, the placement in the vertical of optically thin cirrus, and the physical structures within the clouds themselves.

Many passive sensor techniques taking advantage of spectral-dependence and atmospheric column absorption have been developed to extract information from the integrated scene as observed from the satellite platform. Daytime retrievals, for example, take advantage of solar reflection measurements which help to constrain solutions to optical depth and particle size. Nighttime retrievals (which must rely only upon emission information from the cloud and atmosphere system) can pose larger problems to passive remote sensor retrievals (e.g., cloud location and emissivity become critical players in measurement sensitivity). Uncertainties that can be attached to these retrieval approaches, however, could be reduced considerably by including *a priori* information (e.g., cloud profile information as provided by an active sensor).

Implicit to the term "satellite platform" is the notion that satellites are not limited inherently to accommodating only a single genre of instrument. With advancing technology, new instruments (to space that is, e.g., active sensors such as lidars and radars which have heretofore been confined to terrestrial/aircraft platforms due to size, power consumption, and high data acquisition rates) are now joining passive sensors on satellites. With their ability to penetrate and profile a cloud's internal structure, these instruments will provide literally a new dimension to cloud observations on the global scale. Notable examples of active instruments that have or will soon be included on civilian environmental satellites are the Tropical Rainfall Measuring Mission (TRMM) (precipitation radar; Simpson,

1988), CloudSat (94 GHz cloud profiling radar; Stephens *et al.*, 2000), and the Pathfinder Instruments for Cloud and Aerosol Spaceborne Observations (PICASSO) (532-nm lidar; Winker *et al.*, 1999) programs.

1.2 Our Current Level of Understanding

The lion's share of what we know about clouds in terms of their physical makeup, spatial/temporal distribution, formation and dissipation mechanisms/time-scales, type classification and radiative impacts on Earth's radiative energy budget draws from a wide array of contributions from environmental satellite and Earth-based missions. While much has been accomplished, the scale of the problem demands a great deal more. Included here is a summary of the more notable developments in the area of cloud remote sensing and modeling.

1.2.1 Remote sensing campaigns

The ERBE mission (Barkstrom, 1986), carried on the National Oceanic and Atmospheric Administration (NOAA) 9 and NOAA-10 satellites and the Earth Radiation Budget Satellite (ERBS), have made measurements of the incident/reflected solar and Earth-emitted longwave radiation to compute accurate ($\sim$ 1%) monthly-averaged products at 250-km resolution. These data provide the first global estimates of meridional heat transport and cloud radiative forcing. As the first project of the World Meteorological Organization's (WMO) World Climate Research Program (WCRP), the ISCCP (Rossow *et al.*, 1985) gathered visible and infrared satellite imagery to formulate a cloud climatology with classifications based on cloud type, optical thickness, and cloud top pressure. The Atmospheric Radiation Measurement program (ARM; *ARM Program Plan, 1990*) is an ongoing collaborative effort among many remote sensing groups to investigate continental, tropical, and arctic cloud properties enlisting a suite of sensors and multi-platform observing system. The National Aeronautics and Space Administration's (NASA) Clouds and the Earth's Radiant Energy System (CERES; *NASA Ref., 1995*) program has developed a systematic approach to identifying and retrieving the optical properties of clouds and the

surface from high spatial and spectral resolution satellite observations as part of the theoretical development for the Moderate-Resolution Imaging Spectroradiometer (MODIS) to be flown on the Earth Observing System (EOS)-AM and -PM satellites. In addition to these ventures, many cloud distribution and property retrieval studies have been carried out by a great number of independent researchers using satellite, airborne and land-based narrow-band/broadband radiometers, spectrometers, and active instruments. Several of the established remote sensing techniques from which this research draws are revisited farther along.

1.2.2 Modeling of clouds

Concurrent with the efforts of the remote sensing community to better observe clouds are those of the modelers to represent clouds more realistically in numerical weather prediction (NWP) models for forecasting and general circulation models (GCMs) for climate research. Arakawa (1975) cited succinctly the reasons for parameterizing clouds in GCMs:

> "The importance of clouds in climate modeling cannot be overemphasized. Clouds, and their associated physical processes, influence the climate in the following ways:
>
> 1. By coupling dynamical and hydrological processes in the atmosphere through the heat of condensation and evaporation and redistributions of sensible and latent heat and momentum.
> 2. By coupling radiative and dynamical-hydrological processes in the atmosphere through the reflection, absorption, and emission of radiation.
> 3. By coupling hydrological processes in the atmosphere and in the ground through precipitation; and
> 4. By influencing the couplings between the atmosphere and the ground through modification of the radiation and the turbulent transfers at the surface.

> Although these cloud-dominated processes have long been known to be important in determining climate, clouds have been very poorly formulated in climate models."

Early cloud parameterizations were concerned only with the radiative effects of clouds on the atmosphere and surface (Slingo, 1987). These schemes diagnosed fractional cloud coverage and condensate from large-area conditions such that the important latent heat effects associated with clouds and precipitation had to be handled with separate (and highly simplified schemes). The fundamental problem of these schemes was that the clouds interacting with radiation were not related to the model condensation and evaporation processes (Jakob, 1999). The work of Tiedke (1993) has revolutionized the field by including budget equations for cloud fraction liquid/ice water in a fully-prognostic treatment which is now in use operationally at the European Centre for Medium-Range Weather Forecasts (ECMWF). Instead of computing cloud parameters *ad hoc* (after all physical processes have been computed independently), the new scheme couples these processes to the generation/dissipation of cloud (following in time the evolution of cloud fraction and total condensate by means of advection, source and dissipation terms). Attempts to assess the performance of this scheme using observational data have been performed by Mace (1998) using ground-based cloud radar and Miller *et al.* (1999) using global lidar data from LITE. These developments have rekindled hope that clouds may indeed be representable in global NWP models in a non-statistical, non-diagnostic, and physically intuitive way.

The continued development of model cloud schemes hinges on the ability of atmospheric remote sensing to provide detailed and quality-controlled training and validation data for clouds and other relevant atmospheric parameters on the global scale. The piecemeal quality of our existing data, the inconsistencies among the many approaches, and the amount of uncertainty implicit to each of them paints an indecisive picture of how clouds contribute to global radiative feedback processes. While the ISCCP provides an invaluable service in composing the first ensemble cloud climatology (drawing from an extensive composite of methodologies from the literature in the process), the uncertainties and physical limitations associated with the passive instrument techniques it is forced to

employ leaves a great deal of room for improvement. The refinement of cloud representation in GCMs is limited by our current inability to provide the necessary validation data at the required space/time resolution. As active instruments become operational on the space platform, we are justified in demanding a higher standard by which we define the global cloud climatology.

1.3 Primary Areas of Deficiency

The data accumulated from remote sensing campaigns form collectively a rather porous archive of cloud spatial distributions and certain bulk cloud radiative effects. While important strides have been taken, the current state-of-the-art in remote sensing products still leaves much to be desired. Three principle areas of concern stand out. First and foremost is the pressing need for a more advanced observing system that includes active instrumentation on the space platform to complement the existing array of passive infrared and microwave radiometers. Working together, these instruments will provide crucial three-dimensional information about the altitude, temperature, precipitation processes, water content and microphysics of clouds, never-before obtained on the global scale. Secondly, the methods applied to the retrieval of cloud optical properties must be refined to optimize the utility of the new information provided by active sensors. Information on the true cloud boundaries, for example, eliminates a great deal of the uncertainty associated with the night-time (infrared-only) retrieval of optically-thin cirrus clouds. Lastly, it is imperative that an improved rapport between modelers and measurement groups be established and maintained. In this way free exchange of ideas and needs are communicated and addressed. Materializing any one of the above amendments would, in and of itself, go far to improving our understanding of clouds in the framework of climate feedback.

1.4 Scientific Objectives and Basis

In light of the satellite missions currently underway, the material addressed here in this work is timely. Convincing evidence warranting the ongoing implementation of these expensive payloads in space must be quantified. Proof-of-concept must be demonstrated.

It is anticipated that the new research avenues opened by forthcoming missions will install active remote sensors as a permanent fixture to this observing platform in its own right. Even so, the time to begin paving these avenues is now. It is no longer difficult or even unrealistic at this juncture to envision a "space based ARM-equivalent" observing system in the not-so-distant future, dedicated to global cloud and aerosol detection and retrieval under an armada of passive and active instrumentation operating in concert. These are indeed exciting times for the atmospheric science community!

Before realizing these goals, however, the road-blocks outlined above must first be negotiated. This research addresses the first two points by illustrating the utility of active sensor information when applied the retrieval of cloud optical properties. Emphasized in these case studies is the role of the active sensor in providing the retrieval with *a priori* cloud height data at a resolution unavailable to passive radiometer instruments These data are used in synergy with satellite, surface, and aircraft-based radiometers in conventional retrieval approaches based on established physical relationships between a cloud's spectral reflectance/emittance and its microphysical properties. The third issue is addressed by outlining a collaborative effort carried forth with ECMWF to assess problem areas in the current implementation of the prognostic cloud scheme (Miller *et al.*, 1999). This study, featuring global scale cloud height information from LITE, is the very first of its kind, and speaks to the potential for active sensors on the space platform to provide a paradigm shift in the way we measure, model, and understand cloud processes.

1.5 A Road Map

The plan of attack proposed to address the scientific objectives defining this work is outlined as follows. In Chapter 2, elementary concepts of radiative transfer theory and numerical methods to solving the radiative transfer equation are introduced as a launching point for the ensuing discussion of a doubling and adding radiative transfer model developed for the cloud property retrievals of this work. The model was designed to simulate passive radiometer measurements throughout the visible and infrared spectrum with accommodation for the instrument channel response function and atmospheric gaseous

absorption. The attributes, shortcomings, and sensitivity of this "forward model" are discussed in the context of cloud optical properties. Chapter 3 introduces the general concept of retrieval theory and focuses specifically on the estimation approach of Rodgers (1976); one which provides often overlooked error diagnostics that are essential to characterizing the quality of retrieval. Chapter 4 delves into the topic of model sensitivity, provides a physical basis for what cloud properties are retrievable, and outlines procedures followed in assignment of forward model and measurement uncertainties. Having established this background, Chapter 5 presents a series of retrieval case studies intended to illustrate and quantify the benefits of *a priori* information provided by active sensors in cloud optical depth and effective particle radius retrievals. Chapters 6-7 comprise the heart of this work; exploring the synergy of active instrument cloud height data, cloud property retrievals, and NWP models drawing from the retrieval case studies of Chapter 5. Here, active sensor information is shown to be an indispensable tool in the validation and ongoing development of NWP cloud schemes. Chapter 8 provides a summary of findings, implications of conclusions drawn, and suggestions for relevant future research.

1.6 What Was Found

Through numerous cases spanning a great range of passive/active instrument combinations and cloud types, it was shown quantitatively the extent to which active sensor cloud-height information aids in the retrieval of cloud optical depth and effective particle radius. Ensemble case study results show the most dramatic improvements in retrieval uncertainty for night-time retrievals of optically thin cirrus clouds (where accurate knowledge of cloud location in the vertical is critical). Typical values for these improvements in these cases were 20% for effective particle radius, and 10-20% for optical depth. The uncertainties associated with solar reflection based single cloud layer retrievals showed improvements usually less than 5%. This does not discount the benefits of active sensors to day-time applications, including the collection of detailed cloud profile information as well as retrievals where multi-layered clouds are present.

Active instruments upon the space platform were also shown to be an invaluable resource in the validation of global forecasting models. Focusing on the ECMWF model, which employs the prognostic cloud scheme of Tiedke (1993), short-range (e.g., 24 hr) model forecasts of cloud cover were found to agree remarkably with LITE data binned to model resolution. For the 66 night-time LITE orbits considered, a weighted statistical analysis revealed hit rates between 75-90%, threat scores 45-75%, probabilities of detection $\approx$ 80%, and false alarm rates 10-45%. The level of agreement in these comparisons (a complete qualitative and quantitative analysis is included in Appendix B) far exceeded original expectations at the onset of this research. Combined active+passive cloud property retrievals were used to validate model liquid and ice water contents. The findings indicated that while the ECMWF prognostic cloud scheme forecasts realistic vertical, horizontal and temporal distributions of cloud cover, there remain discrepancies in the liquid/ice contents which define ultimately their radiative forcing effect in the climate system. Nonetheless, the forecasted cloud condensate values were determined to be realistic with respect to observations. The composite result of this study unveil a very significant result: that while there is obvious room for improvement, the current level of realism displayed by the ECMWF prognostic cloud scheme forecasts suggests that the reanalysis data may be considered as a new resource for global cloud information. Practical applications of this result in the context of CloudSat instrument requirement analysis was examined; representing one of many possibilities for a burgeoning area of new research in the coming decade.

With continued improvement of model cloud parameterizations afforded by new validation data, reanalysis products hold promise as a viable means to exploring cloud convective, radiative, and dynamical feedbacks in the controlled model environment. The next logical step would be to explore the ways in which the growing active sensor database could serve NWP in an operational sense (i.e., in terms of data assimilation). The findings of this research contributed in part to the CloudSat mission proposal (now accepted and scheduled for launch in 2003) which may be regarded as a stepping stone toward a network of active sensor data on the space platform. To convey the research embodying

this Dissertation to the greater scientific community, a number of articles have been submitted to the public domain. Included are the materials covered in Chapters 2-5 (Miller *et al.*, 2000; Stephens *et al.*, 1999; and one paper in preparation), Chapter 6 (Miller *et al.*, 1999), and Chapter 7 (in preparation). Perhaps most importantly, this dissertation appeals to the need for a much stronger collaborative relationship between modelers and remote sensing observationalists (with a particular emphasis on the space platform) than what exists currently.

1.7 Summary

A global understanding of cloud distribution and optical properties is of paramount importance in our quest to characterize the role(s) of clouds in climate and climate feedback processes. Today, nearly four decades after the launch of the first environmental satellite, the cloud climatology we have managed to compile remains altogether crude from the perspective of what we really need to know. The long-awaited addition to the space platform of active remote sensing instruments is finally underway. The high resolution profile information that they supply stands to revolutionize the way cloud optical properties are retrieved (especially in cases of multiple cloud layer profiles and night-time retrievals of cirrus), and their ability to penetrate and identify mid- and lower-level cloud layers below cirrus enables the first complete global climatology of all cloud types to be compiled.

While brevity certainly has its appreciated place in scientific writing, here it has been compromised for the sake of a more thorough treatment of the problem at hand. Stated succinctly, this work seeks to exemplify the complementary role of active sensors to passive radiometers (i.e., a multi-sensor approach) in space for the remote sensing of clouds on the global scale, and to numerical weather prediction models in the capacity of model validation and development. Toward this end, a cloud property retrieval scheme was assembled "from the ground up," and applied to several organized cloud remote sensing projects which featured active sensor measurements of cloud profiles. The potential for these measurements to aid in the development of numerical weather prediction models was

addressed in the presentation of an ECMWF/LITE correlative study for global cloud profile validation, and retrieved cloud optical properties were compared to model-equivalent quantities. The results of these comparisons formed a quantitative assessment of the current ability of cloud schemes in numerical weather prediction models and an encouraging commentary on the potential for non-traditional active sensor data to serve as a vehicle in their continued improvement. Between where we stand today and a true understanding of clouds is a sea of challenges. The active instrument is proposed here as the appropriate vessel to navigate it.

Chapter 2

THE FORWARD MODEL

2.1 Introduction

The first step in the development of any physically-based cloud property retrieval is the construction of a model capable of simulating how clouds interact with electromagnetic radiation within an absorbing, emitting and scattering atmosphere. The underlying premise is that if this model can represent faithfully the physics of the system (i.e., reproduce observable radiances, for example), the model parameters characterizing the cloud can be tuned to match observations and thereby arrive at a solution (assuming that conditions for all other parameters affecting these radiances are known *a priori*) representative of the true physical state of the system. This "forward model," as posed, represents our best attempt at characterizing this physical system. A great number of forward models have been constructed for the purposes of cloud retrievals, ranging in complexity from simple parameterizations geared to a specific application to fully 3-dimensional, high spectral resolution models which include all elements of the radiative transfer equation explicitly. Even the most complex and generally-applicable of these models, however, is only as accurate as our ability to specify accurately the many inputs that it requires (how these forward models are applied to retrievals is the subject of the next chapter).

This chapter develops from first principles a discrete ordinates radiative transfer model based on the interaction principle and the methods of doubling and adding (and designed ultimately to serve as the forward model used in a cloud property retrieval). In the development of this model, the plane-parallel assumption is invoked, which ignores the effects of horizontal heterogeneity (and hence, horizontal photon transport) that are known to be prevalent in the real atmosphere. Details of the model/user interface are provided

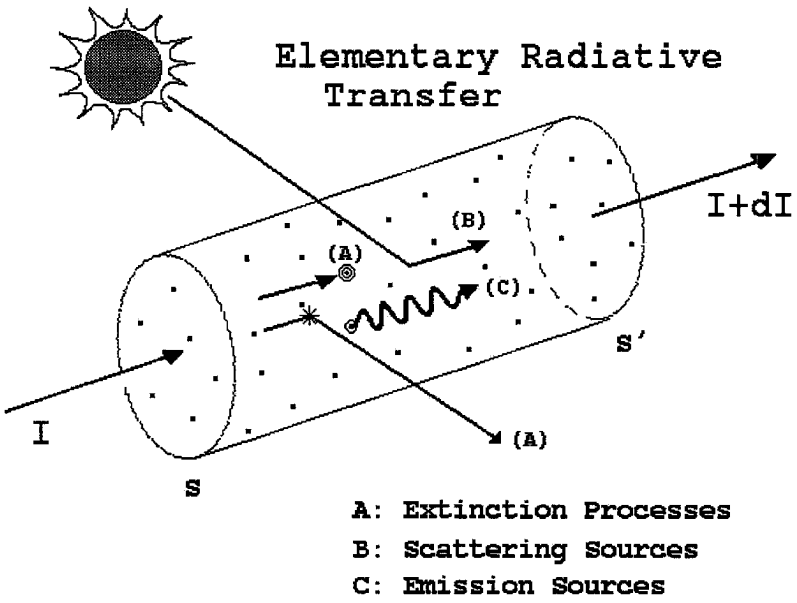

Figure 2.1: Fundamental source and extinction components of radiative transfer theory.

in Appendix A of this dissertation. While more applicable to some clouds/atmospheric-profiles and less-so to others, the uncertainty associated with this constraint to the forward model must be accounted for in the error statistics of the retrieval.

2.2 Radiative Transfer Theory

Plane parallel radiative transfer models are well established in the literature (Twomey *et al.* (1966), Hansen and Travis (1974), Greenwald and Stephens (1988), among many others). Fundamental to all of them are the mechanisms governing the change in spectral intensity I of wavelength λ in direction $\vec{\xi}$ along path s (see Figure 2.1). Within any scattering/absorbing/emitting medium, this be represented simply as an energy balance equation formed by three main terms:

$$\frac{dI_\lambda}{ds} = -\sigma_{ext} I_\lambda + \sigma_{sca} S_\lambda + \sigma_{abs} B_\lambda \tag{2.1}$$

where σ_{ext} is the volume extinction coefficient contributed to by gas, cloud, and aerosol formed by the composite of the volume scattering and absorption coefficients, σ_{sca} and

σ_{abs} (all having units of inverse length). The first term on the right hand side (RHS) of this equation describes loss due to extinction (either absorption of photons or scattering out of direction $\vec{\xi}$), the second is a "virtual source" term accounting for the scattering of photons *into* the direction $\vec{\xi}$, and the final term is a source due to emissions from within the medium itself.

In this system, the vertical coordinate is expressed in terms of the optical depth $\tau(z)$, given by the projection of the optical path

$$\tau(s) = \int_s^{s'} -\sigma_{ext} ds \tag{2.2}$$

onto the local vertical according to

$$\tau(z) = \tau(s) cos(\theta), \tag{2.3}$$

where θ is the angle formed between the path (s, s') and the local vertical. The minus-sign introduced to the definition of optical path follows the conventions of astronomy, where atmospheres of stars and other planets are historically observed from top down. In this way, τ increases *downward* from a value of zero at the top of the atmosphere. It should also be noted that the optical depth is a function of wavelength (the λ subscript will be omitted in the interest avoiding equation clutter, with the dependence regarded as implicit). The relationship between τ at different wavelengths will be shown further along.

Rearrangement of Equation 2.1 yields the monochromatic 1-D radiative transfer equation (RTE), with subscripts denoting wavelength dependence omitted for brevity, is expressed as

$$\begin{aligned} \mu \frac{dI(\tau;\mu,\phi)}{d\tau} &= -I(\tau;\mu,\phi) + \frac{\omega_o}{4\pi} \int_0^{2\pi} \int_{-1}^{1} P(\tau;\mu,\mu',\phi,\phi') I(\tau;\mu',\phi') d\mu' d\phi' \\ &\quad + J(\tau;\mu,\phi), \end{aligned} \tag{2.4}$$

where $\mu = cos(\theta)$, ω_o is the single-scatter albedo given by

$$\omega_o = \frac{\sigma_{sca}}{\sigma_{ext}}. \tag{2.5}$$

The single-scatter phase function for intensity, $(P(\tau;\mu,\mu',\phi,\phi'))$, describes how energy scattered from an incident direction (μ', ϕ') into the direction of observation (μ, ϕ) within

the medium, defining the scattering plane. This describes the behavior for a *single* scattering event, and the global reflectivity and transmission properties of a medium follow accordingly. Reflection from optically thin clouds sometimes retain structural properties of the phase function (e.g., glories upon cloud tops as viewed from aircraft, or halos around the sun and moon), while optically thicker clouds (where multiple scattering reigns) tend to smooth out these properties (and the cloud radiance field becomes less sensitive to details of the phase function shape).

The scattering angle, Θ, expressed mathematically as

$$cos\Theta = \mu\mu' + (1-\mu^2)^{1/2}(1-\mu'^2)^{1/2}cos(\phi'-\phi), \tag{2.6}$$

defines the angle formed between the incident and scattered directions of photon travel as defined by (μ, ϕ, μ', ϕ') (equivalent to the dot product of the incident $(\vec{\xi})$ and scattered $(\vec{\xi'})$ unit vectors). By definition,

$$\int_\Omega P(cos\Theta)d\Omega = 4\pi \tag{2.7}$$

where Ω is the full solid angle of integration. Normalization by 4π results in the integration to unity requisite of all probability density functions.

The structure of the phase function is characterized by the asymmetry parameter

$$g = \frac{1}{2}\int_{-1}^{1} \mu P(\mu)d\mu, \tag{2.8}$$

where $P(\mu)$ is the unpolarized azimuthally-symmetric phase function (ϕ-dependence integrated out). Interpretation of the asymmetry parameter is as follows: $g = 1$ corresponds to complete forward scattering, $g = -1$ corresponds to complete backward scattering, and $g = 0$ corresponds to isotropic scattering. By definition, the asymmetry parameter can be interpreted as the expected value of the scattering angle defining μ.

An approximation used extensively in the literature is that of the double Henyey-Greenstein (DHG) phase function

$$\begin{aligned} P(\Theta) &= bP(g_1, cos(\Theta)) + (1-b)P(g_2, cos(\Theta)) \\ (0 < &\ b\ < 1), \end{aligned} \tag{2.9}$$

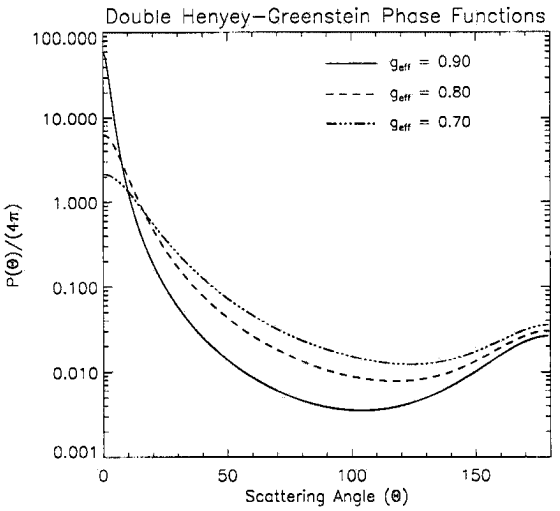

Figure 2.2: Examples of the double Henyey-Greenstein phase function for varying values of effective asymmetry parameter.

which is comprised of two single Henyey-Greenstein phase functions given by

$$P(g_i) = \frac{1 - g_i^2}{(1 + g_i^2 - 2g_i cos(\Theta))^{3/2}} \quad (i = 1, 2) \tag{2.10}$$

The DHG phase function reduces to single Henyey-Greenstein for a weight b of unity. DHG parameters were computed by specifying an "effective" asymmetry parameter, g_{eff}, and computing the according to

$$\begin{aligned} g_1 &= g_{eff} + 0.05 \\ g_2 &= -0.60 \\ b &= \frac{g_{eff} - g_2}{g_1 - g2}. \end{aligned} \tag{2.11}$$

Examples of the DHG phase function for varying g_{eff} are shown in Figure 2.2. Duda (1994) and Stackhouse (1995) use this parameterization to provide a reasonable representation of Mie scattering phase functions, particularly in the backscattering lobe. The errors incurred by approximating real phase functions by DHG are discussed in the following chapter.

Analogous to Equation 2.1, the first term of Equation 2.4 describes extinction according to Beer's law, the second term represents a source of radiation arising from multiple

scattering of diffuse radiation into the (observing) direction of interest, and the last term is a source term (when applicable) owing to single scatter of the direct beam, spectral reflection at the surface, and thermal emission from the surface and atmosphere:

$$\begin{aligned} J(\tau;\mu,\phi) &= \frac{\omega_\circ}{4\pi}F_\circ P(\tau;\mu,\phi,-\mu_\circ,\phi_\circ)e^{-\tau/\mu_\circ} \\ &+ \frac{\omega_\circ}{4\pi}F_\circ \alpha_{sfc} P(\tau;\mu,\phi,-\mu_\circ,\phi_\circ)e^{-(2\tau^*-\tau)/\mu_\circ} \\ &+ \sigma_{abs}B(T), \end{aligned} \tag{2.12}$$

where $F_\circ$, α_{sfc}, and τ^* are terms representing the monochromatic solar flux, surface albedo, and the total integrated optical depth of the atmospheric column, respectively. $B(T)$ is the thermal emission source according to Planckian emission:

$$B_\lambda(T) = \frac{2hc^2}{\lambda^5(e^{hc/K_b\lambda T}-1)} \tag{2.13}$$

where K_b, h, and c are Boltzmann's constant, Planck's constant, and the speed of light, respectively.

2.2.1 Solution to the 1-D RTE

Were it not for the presence of the integral term in Equation 2.4), the RTE reduces to a simple differential equation which is straightforward to solve. The problem is handled generally by representing the continuous radiation field in terms of a finite number of discrete ordinates, or "streams." This results in a partitioning of the energy field in the upward and downward hemispheres into "n" discrete ordinates (a "2n-stream approximation"). The scattering phase function is thereby expressed as a Legendre polynomial expansion (see Chandrasekhar, 1960))

$$P(cos\Theta) = \sum_{l=0}^{N} \chi_l P_l cos(\Theta), \tag{2.14}$$

where P_l are associated Legendre polynomials of order l, χ_l is the l^{th} expansion coefficient given by

$$\chi_l^m = (2-\delta_{0,m})\chi_l \frac{(l-m)!}{(l+m)!}, \tag{2.15}$$

and $\delta_{0,m}$ is the Kronecker delta function (which only "fires" at $m = 0$). The addition theorem for spherical harmonics Equation 2.14 to be expanded as a sum of associated Legendre polynomials in azimuth (ϕ)

$$P(\mu, \phi, \mu', \phi') = \sum_{m=0}^{N} \sum_{l=m}^{N} \chi_l^m P_l^m(\mu) P_l^m(\mu') cosm(\phi' - \phi), \tag{2.16}$$

where P_l^m are associated Legendre polynomials of order l and degree m. Because this expansion becomes numerically unstable for higher-order polynomials, a renormalization following Dave and Armstrong (1970) is applied which involves the rewriting of Equation 2.16 as

$$P(\mu, \phi, \mu', \phi') = \sum_{m=0}^{N} \sum_{l=m}^{N} \chi_l^m Y_l^m(\mu) Y_l^m(\mu') cosm(\phi' - \phi), \tag{2.17}$$

where the expansion coefficients become

$$\chi_l^m = (2 - \delta_{0,m}) \chi_l, \tag{2.18}$$

and the factorial term is distributed within the normalized Legendre polynomials according to

$$Y_l^m(\mu) = \left[\frac{(l-m)!}{(l+m)!} \right]^{\frac{1}{2}} P_l^m(\mu). \tag{2.19}$$

The RTE is converted into a linear system of equations by rewriting the intensity field in terms of a Fourier series expansion

$$I(\tau; \mu, \phi) \;\; = \;\; \sum_{m=0}^{N} I^m(\tau; \mu) cos(m(\phi_\circ - \phi)), \tag{2.20}$$

where $\phi_\circ$ is the solar azimuth angle and $I^m(\tau; \mu)$ is the m^{th} intensity amplitude (Fourier coefficient). This method handles azimuthal structure of the intensity field for horizontally *homogeneous* media. Hence, this applies only to radiation fields assumed symmetric about $\phi_\circ$. The number of expansion terms required to represent this field is dependent on the solar/observer geometry, the optical depth of the layer, and the complexity of the scattering phase functions involved. The Fourier series expansion allows for the rewriting of Equation 2.4 as set of N+1 azimuthally decoupled equations of the form

$$\mu \frac{dI^m(\tau; \mu)}{d\tau} = -I^m(\tau; \mu, \phi) + (1 + \delta_{0,m}) \frac{\omega_\circ}{4\pi} \sum_{l=m}^{N} \chi_l^m Y_l^m(\mu) \int_{-1}^{1} Y_l^m(\mu') I^m(\tau; \mu') d\mu'$$
$$+ \frac{\omega_\circ}{4\pi} F_\circ \sum_{l=m}^{N} \chi_l^m Y_l^m(\mu) Y_l^m(-\mu_\circ) e^{-\tau/\mu_\circ} + \frac{\omega_\circ}{4\pi} \alpha_{sfc} \sum_{l=m}^{N} \chi_l^m Y_l^m(\mu) Y_l^m(\mu_\circ) e^{-(2\tau^* - \tau)/\mu_\circ}. \tag{2.21}$$

The integral term in Equation 2.21 has no closed analytical solution, and therefore must be solved via numerical methods. The interpolatory quadrature approximation (Johnson and Riess, 1982) can be applied do approximate the integral of any function in terms of polynomial interpolation:

$$\int_{x_1}^{x_2} f(x)dx \approx \sum_{i=1}^{n} w_i f(x_i) \tag{2.22}$$

where w_i are quadrature weights computed according to

$$w_i = \int_{x_1}^{x_2} l_{i-1}(x)W(x)dx \tag{2.23}$$

with $W(x)$ a positive weighting function, l_{i-1} a polynomial of order $i-1$, and x_i are the abscissas of the quadrature expansion. Application of this approximation to the integral term of Equation 2.21 results in

$$\int_{-1}^{1} Y_l^m(\mu')I^m(\tau;\mu')d\mu' \approx \sum_{i=1}^{n} w_i Y_l^m(\mu_i')I^m(\tau,\mu_i') + \sum_{i=1}^{n} w_i Y_l^m(-\mu_i')I^m(\tau,-\mu_i'), \tag{2.24}$$

where the originally continuous RTE has been discretized into n streams in each (upwelling and downwelling) hemisphere. Gaussian quadrature methods are often used for this purpose, with conservation of energy (phase function integrals normalize to unity) achieved for polynomials of degree $N \leq 2n-1$. Both the number of Legendre expansion coefficients and the number of Fourier intensity amplitudes (m) have an upper-limit specified by the number of streams n. Hence, accurate representation of complex scattering media (which require a high order Legendre polynomial expansion to capture) demand a correspondingly larger number of streams.

The Fourier-decoupled, discrete-ordinate transfer equations can then be written in matrix form as upward (+) and downward (-) spectral intensity vectors:

$${}^mI^+ = \begin{bmatrix} I^m(\tau,\mu_1) \\ \vdots \\ I^m(\tau,\mu_n \end{bmatrix}, \quad {}^mI^- = \begin{bmatrix} I^m(\tau,-\mu_1) \\ \vdots \\ I^m(\tau,-\mu_n \end{bmatrix}, \tag{2.25}$$

where $\pm\mu$ define stream zenith angles in the upwelling (0 ¡ μ ¡ 1) and downwelling (0 ¿ μ ¿ -1) hemispheres. The scattering phase function is also represented using discrete ordinates in terms of forward scatter P^{++} and backward scatter P^{+-}. For simplicity,

the phase function is assumed to be azimuthally symmetric such that the discrete phase matrices are the same in each hemisphere, yielding

$$ {}^{m}P^{\pm} = \begin{bmatrix} P^{m}(\pm\mu_1,\mu_1) & \cdots & P^{m}(\pm\mu_1,\mu_n) \\ \vdots & \ddots & \vdots \\ P^{m}(\pm\mu_n,\mu_1) & \cdots & P^{m}(\pm\mu_n,\mu_n) \end{bmatrix} \tag{2.26} $$

for diffuse bidirectional phase functions and

$$ {}^{m}P_{\circ}^{\pm} = \begin{bmatrix} P^{m}(\mp\mu_1,-\mu_{\circ}) \\ \vdots \\ P^{m}(\mp\mu_n,-\mu_{\circ}) \end{bmatrix} \tag{2.27} $$

for single scatter of the direct solar beam.

The invocation of discrete ordinates allows for the recasting of Equation 2.21 (the Fourier series decoupling of the RTE) entirely in terms of matrix operations

$$ \pm\frac{d\,{}^{m}I^{\pm}}{d\tau} = -M^{-1}\,{}^{m}I^{\pm} + (1+\delta_{0,m})\frac{\omega_{\circ}}{4\pi}[M^{-1}\,{}^{m}P^{\pm}W\,{}^{m}I^{+} + M^{-1}\,{}^{m}P^{\mp}W\,{}^{m}I^{-}] + \\ \frac{\omega_{\circ}}{4\pi}F_{\circ}M^{-1}\,{}^{m}P_{\circ}^{\mp}e^{-\tau/\mu_{\circ}} + \frac{\omega_{\circ}}{4\pi}F_{\circ}\alpha_{sfc}M^{-1}\,{}^{m}P_{\circ}^{\pm}e^{-(2\tau^{*}-\tau)/\mu_{\circ}}, m = 0,1,2,\ldots,2n-1 \tag{2.28} $$

where M, W are diagonal matrices of quadrature abscissas and weights, respectively, and $2n-1$ defines the maximum degree of Legendre expansion satisfying conservation of energy for Gaussian interpolatory quadrature as described above.

Through a clever definition of terms, equation 2.28 can be massaged into the form

$$ \frac{d}{d\tau}\begin{bmatrix} {}^{m}I^{+} \\ {}^{m}I^{-} \end{bmatrix} = \begin{bmatrix} -t^{m} & r^{m} \\ -r^{m} & t^{m} \end{bmatrix}\begin{bmatrix} {}^{m}I^{+} \\ {}^{m}I^{-} \end{bmatrix} + \begin{bmatrix} {}^{m}S^{+} \\ {}^{m}S^{-} \end{bmatrix}, m = 0,1,2,\ldots,2n-1 \tag{2.29} $$

where the local reflection and transmission matrices for the m^{th} azimuthal mode are given respectively by

$$ r^{m} = (1-\delta_{0,m})\frac{\omega_{\circ}}{4\pi}M^{-1}\,{}^{m}P^{-}W \tag{2.30} $$

and

$$ t^{m} = M^{-1} - (1-\delta_{0,m})\frac{\omega_{\circ}}{4\pi}M^{-1}\,{}^{m}P^{+}W, \tag{2.31} $$

and source terms given by

$$ {}^{m}S^{\pm} = \frac{\omega_{\circ}}{4\pi}F_{\circ}M^{-1}\,{}^{m}P_{\circ}^{\mp}e^{-\tau/\mu_{\circ}} + \frac{\omega_{\circ}}{4\pi}F_{\circ}\alpha_{sfc}M^{-1}\,{}^{m}P_{\circ}^{\pm}e^{-(2\tau^{*}-\tau)/\mu_{\circ}} \tag{2.32} $$

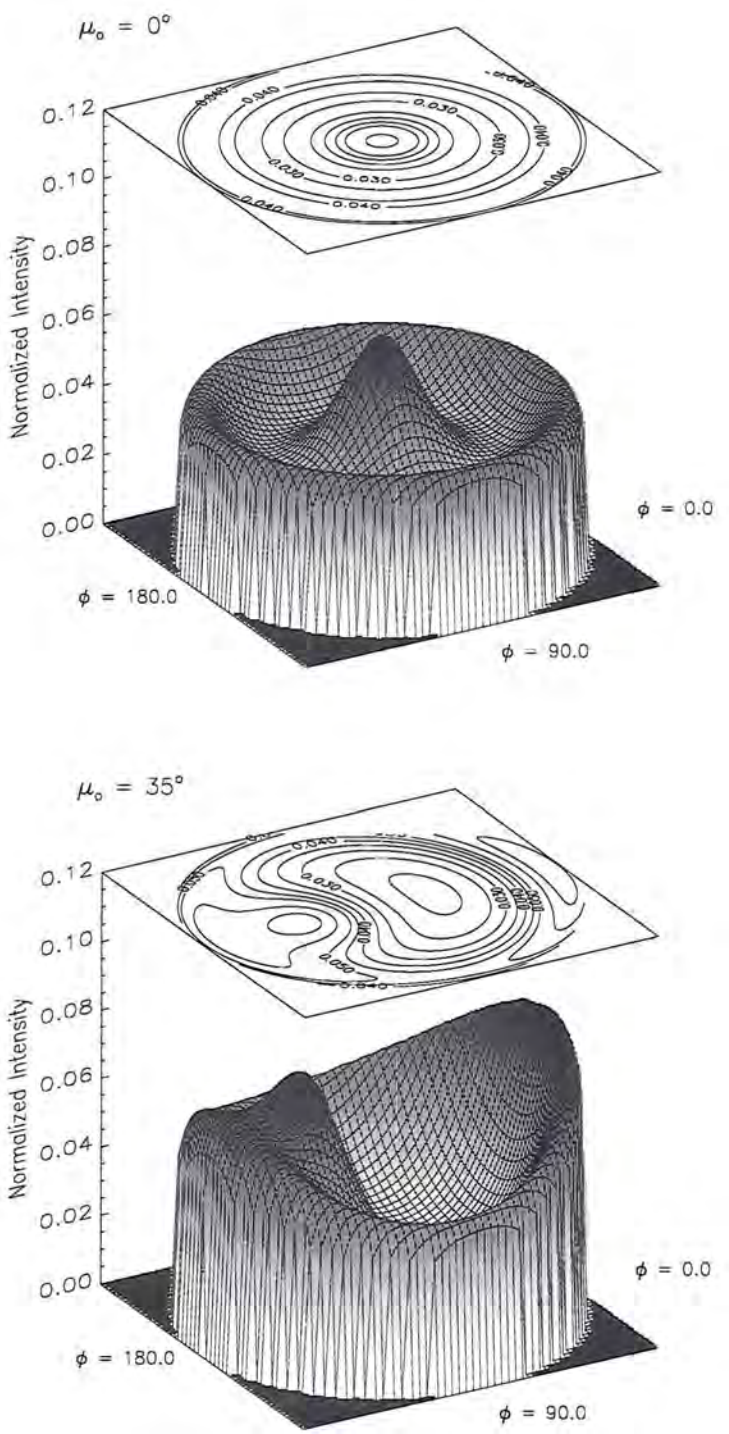

Figure 2.3: Upwelling intensity field with azimuthal structure modeled for a single cloud layer. Top panel: DHG phase function, $\tau = 1.0, g_1 = 0.85, g_2 = -0.6, g_{\text{eff}} = 0.70, \omega_o = 1.0$, and $\theta_o = 0°$ only (equivalent to azimuthally averaged m = 0 structure). Lower panel: same optical properties as above azimuthal expansion $m = 16, \theta_o = 35°$.

For retrievals applying thermal emission measurements only, the azimuthally symmetric term ($m = 0$) suffices. Figure 2.3 demonstrates the model variation in the azimuth for a 128-stream Gaussian quadrature with a 16-term Fourier expansion terms. A small cloud optical depth of $\tau = 1.0$ was chosen to highlight the single scattering behavior of the phase function. of the surface (i.e., as observer zenith angles approach 90°) is due to multiple scattering within the cloud layer (a phenomenon known as limb brightening). The central bump is due to the backscattering peak in the DHG phase function geometry; for the sun directly overhead ($\theta_\circ = 0°$) the 180° backscatter lobe occurs at a viewer zenith angle of $\theta_{obs} = 0°$ (azimuth independent), while a solar geometry of $\theta_\circ = 35°, \phi_\circ = 0°$ requires a viewing geometry of roughly $\theta_{obs} = 35°, \phi_{obs} = 0°$ to observe this same backscattering lobe. While the radiance field remains symmetric about $\phi = 0°$, the Fourier expansion is shown to yield significant structure compared to the azimuthally-averaged case (which holds in general only for infrared radiation fields). Modeling solar reflection at off-nadir observation angles requires a degree m dependent on the solar/observer geometry, the cloud optical depth, and the degree of phase function asymmetry.

2.3 The Macroscopic Radiation Field

Provided now a tractable method of computing the local radiative properties of a medium, the next step is to extrapolate to the macroscopic radiation field. This field is comprised of the ensemble contributions and interactions taking place between the many stacked layers of varying optical properties that comprise our plane-parallel view of the atmosphere. This requires the methods of doubling and adding founded upon the *interaction principle* of radiative transfer (Chandrasekar, 1960) to build "global" reflection and transmission matrices from the local quantities.

2.3.1 The "Adding" method

The adding method is used to combine layers having different optical properties. To illustrate the process, we consider a single atmospheric layer bounded at the top by level "t" and at the base by level "b" (see Figure 2.4). The interaction principle states that for a layer as posed, an exitant photon is accounted by one of three possibilities: (1) originating

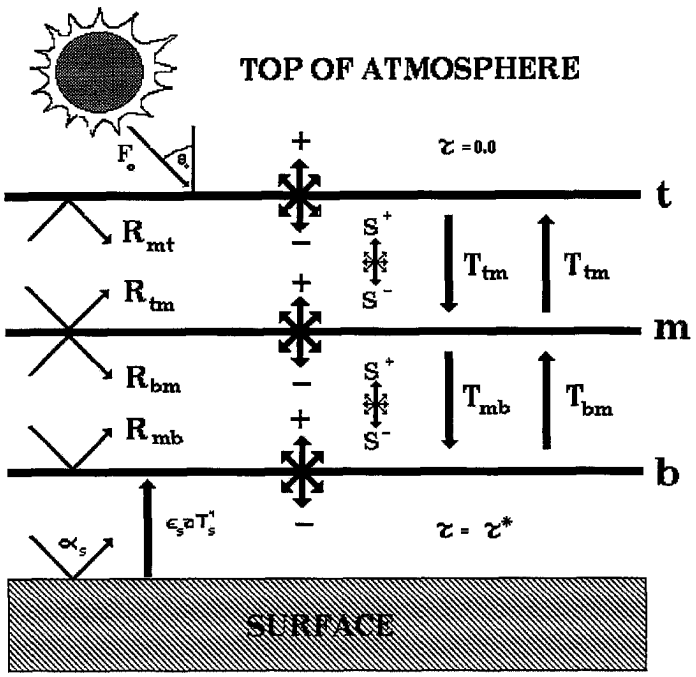

Figure 2.4: Plane-parallel atmosphere transmission, reflection, and source functions considered in discussion of the interaction principle and the doubling and adding methods.

from emission from within the layer, (2) reflection, or (3) transmission from the opposite boundary. If we can assume that the incident boundary radiances (I_t^- and I_b^+) are known, then the energy departing the layer can be written according to the interaction principle as

$$I_t^+ = R_{tb} I_t^- + T_{bt} I_b^+ + S_{tb}^+ \tag{2.33}$$

and

$$I_b^- = R_{bt} I_b^+ + T_{tb} I_t^- + S_{tb}^-, \tag{2.34}$$

where $R_{bt}, R_{tb}, T_{bt}, T_{tb}$ are the global reflection and transmission matrices (noting that for vertically-inhomogeneous atmospheres $(R_{bt}, T_{bt}) \neq (R_{tb}, T_{tb})$), and $S^{\pm}$ are the global source matrices. Considering the case where level "t" represents the top-of-atmosphere (TOA) and level "b" represents the surface, the boundary radiances are written as

$$I_t^- = \frac{\mu_o F_o}{\pi} \tag{2.35}$$

$$I_b^+ = R_b I_b^- + \frac{\sigma T_{sfc}^4}{\pi} \tag{2.36}$$

for TOA downwelling solar flux and a reflecting lower surface with thermal emission included.

Now, consider the insertion of a middle level "m" within this layer. Invoking once more the interaction principle, the unknown exitant radiances for each layer may be written individually as

$$I_t^+ = R_{tm}I_t^- + T_{mt}I_m^+ + S_{tm}^+ \tag{2.37}$$

$$I_m^- = R_{mt}I_m^+ + T_{tm}I_t^- + S_{tm}^- \tag{2.38}$$

$$I_m^+ = R_{mb}I_m^- + T_{bm}I_b^+ + S_{mb}^+ \tag{2.39}$$

$$I_b^- = R_{bm}I_b^+ + T_{mb}I_m^- + S_{mb}^-. \tag{2.40}$$

Elimination of the $I_m^\pm$ terms on the RHS of Equations 2.38-2.39 yields

$$I_m^+ = (1 - R_{mb}R_{mt})^{-1}(R_{mb}T_{tm}I_t^- + R_{mb}S_{tm}^- + T_{bm}I_b^+ + S_{mb}^+) \tag{2.41}$$

$$I_m^- = (1 - R_{mt}R_{mb})^{-1}(R_{mt}T_{bm}I_b^+ + R_{mt}S_{mb}^+ + T_{tm}I_t^- + S_{tm}^-). \tag{2.42}$$

Now, introducing shorthand notation for the propagation terms

$$\Gamma_{mbmt} = (1 - R_{mb}R_{mt})^{-1} \tag{2.43}$$

$$\Gamma_{mtmb} = (1 - R_{mt}R_{mb})^{-1} \tag{2.44}$$

Equations 2.41 and 2.42 are substituted back into Equations 2.37 and 2.40 in order to represent the exitant top and base radiances in terms of the incident boundary radiances alone:

$$\begin{aligned} I_t^+ &= (T_{mt}\Gamma_{mbmt}T_{bm})I_b^+ + (T_{mt}\Gamma_{mbmt}R_{mb}T_{tm} + R_{tm})I_t^- + (T_{mt}\Gamma_{mbmt}R_{mb})S_{tm}^- \\ &+ (T_{mt}\Gamma_{mbmt})S_{mb}^+ + S_{tm}^+ \end{aligned} \tag{2.45}$$

$$\begin{aligned} I_b^- &= (T_{mb}\Gamma_{mtmb}T_{tm})I_t^- + (T_{mb}\Gamma_{mtmb}R_{mt}T_{bm} + R_{bm})I_b^+ + (T_{mb}\Gamma_{mtmb}R_{mt})S_{mb}^+ \\ &+ (T_{mb}\Gamma_{mtmb})S_{tm}^- + S_{mb}^- \end{aligned} \tag{2.46}$$

These equations, when compared to the global boundary radiances as specified by the interaction principle in Equations 2.33-2.34, yield expressions for the global reflection,

transmission, and source terms of the two-layer-added system:

$$R_{tb} = T_{mt}\Gamma_{mbmt}R_{mb}T_{tm} + R_{tm} \quad (2.47)$$

$$R_{bt} = T_{mb}\Gamma_{mtmb}R_{mt}T_{bm} + R_{bm} \quad (2.48)$$

$$T_{tb} = T_{mb}\Gamma_{mtmb}T_{tm} \quad (2.49)$$

$$T_{bt} = T_{mt}\Gamma_{mbmt}T_{bm} \quad (2.50)$$

$$S^{+}_{tb} = T_{mt}\Gamma_{mbmt}(R_{mb}S^{-}_{tm} + S^{+}_{mb}) + S^{+}_{tm} \quad (2.51)$$

$$S^{-}_{tb} = T_{mb}\Gamma_{mtmb}(R_{mt}S^{+}_{mb} + S^{-}_{tm}) + S^{-}_{mb} \quad (2.52)$$

2.3.2 The "Doubling" method

The local reflection and transmission properties of adjacent layers each having optical thickness $\delta\tau$ and identical optical properties (i.e., $(R_{bt}, T_{bt}) = (R_{tb}, T_{tb})$) are combined to yield global radiative properties using the method of doubling. Doubling is in fact a special-case of the more general adding method. Infinitesimal layers of identical optical thickness $\delta\tau$ are combined until the optical thickness of the full homogeneous layer is attained. The layer $\delta\tau$ is chosen sufficiently thin such that its global reflection, transmission, and source properties are inferable directly from the local properties. An infinitesimal generator scheme (see Wiscombe, 1976) is used for this model.

The doubling method follows directly from the adding method with the simplifying assumption of the added layers having identical optical properties. Doubling is accomplished rapidly, with an optical depth $\tau = 2^n\,\delta\tau$ achieved after n doubling steps. Doubling rules for the global reflection and transmission matrices follow from Equation 2.47-2.52 as

$$R_{n+1} = T_n\Gamma_n R_n T_n + R_n \quad (2.53)$$

$$T_{n+1} = T_n\Gamma_n T_n. \quad (2.54)$$

The source terms also fall directly from the adding method. The only modification is that the source terms are attenuated by transmission. In this way, the solar source terms are given by

$$S^{+}_{n+1} = T_n\Gamma_n(R_n S^{-}_n + a_n S^{+}_n) + S^{+}_n \quad (2.55)$$

$$S^{-}_{n+1} = T_n\Gamma_n(R_n a_n S^{+}_n + S^{-}_n) + a_n S^{-}_n \quad (2.56)$$

where

$$a_n = e^{-\frac{2^n \delta\tau}{\mu_0}}. \tag{2.57}$$

In the computation of global properties, doubling through homogeneous layers is followed by the adding of heterogeneous layers. In the plane-parallel approximation, the vertical inhomogeneity of the atmosphere is represented by stacked homogeneous layers of various optical properties. A compromise exists between the number of layers (and hence the ability to capture vertical variability in the profile) and computational cost incurred by increasing the resolution. The trade-offs between computational speed and errors incurred by forward model simplification are the subject of the retrieval discussion forthcoming.

2.4 Model Specifications

The Shortwave/Longwave Adding and Doubling Radiative Transfer model (SLADRT), was developed from the discrete ordinates solution to the RTE as outlined above. While designed to be as application-general as possible, the specific function of this forward model was for simulation of measurements made by satellite radiometers. As such, the inclusion of gaseous absorption and channel band weighting, were essential peripherals to the radiative transfer code (considered now as a "black-box" element in SLADRT).

The model input architecture reflects its format versatility. Written in the C programming language, dynamic memory structures were used throughout to ensure optimal runtime efficiency and freedom of input. The input structure allows for atmospheric layer input parameters to be specified in a number of different formats with varying complexity. Appendix A provides a detailed summary of the forward model input structure. With this amount of freedom comes the danger of incompatibility among the many possible input architecture combinations. Through rigorous testing (and more often, accidental discoveries), the code is now robust. This section outlines features, attributes and shortcomings of the forward model.

2.4.1 Conventions

Fundamental to any physical radiative transfer model is the establishment of a coordinate system. The geometric setting is that of a horizontally homogeneous scattering

and absorbing atmosphere (i.e., the intensity field varies spatially only in the vertical dimension) with a reflecting lower boundary. There are two angular coordinates: the zenith angle (θ) referenced normal to the local vertical, and the azimuthal angle (ϕ) measured with respect to the solar azimuth angle ($\phi_\circ$) in the shortwave cases (azimuthal symmetry of the radiation field has been assumed for the longwave cases). The vertical coordinate is expressed in terms of optical depth, and increases downward from a value of zero at TOA to a value of τ^* as described above.

2.4.2 Model flow

A model run begins by reading and initializing memory structures as required by the user-specified input "card." It is here that the atmospheric profile, containing all the necessary temperature and optical properties are arranged for use by the radiative transfer blackbox (see Appendix A). This profile includes the computation of aerosol effects, cloud layer insertion, and the set-up of profile-dependent gaseous absorption (for the case of instrument/channel calculations). The radiative transfer model is then called once (for monochromatic runs) or several times in succession (for gaseous absorption and channel band-weighted runs) to compute the radiance field at all required model levels, azimuth angles and quadrature nodes. The results are interpolated to user-specified levels and angles (e.g., the observing angle of a satellite to a pixel) using cubic-splining and written to file in selectable format. The program terminates with a cleaning of memory storage and a run-status report. Run-time diagnostics are reported to varying degrees of detail according to switches set at compile-time.

2.4.3 Gaseous absorption

Viewing the world as we do through an atmospheric window, it is sometimes easy to forget that the atmosphere is in fact a sea of gases that is not transparent to all radiation impinging upon it. As indicated by Figure 2.5, absorption across the spectrum (and hence the opacity of the atmosphere) is a strong function of these gases.

For a given gas, absorption takes place at discrete wavelengths (or "lines") along the spectrum according to excitation modes unique to its molecular construct. The mecha-

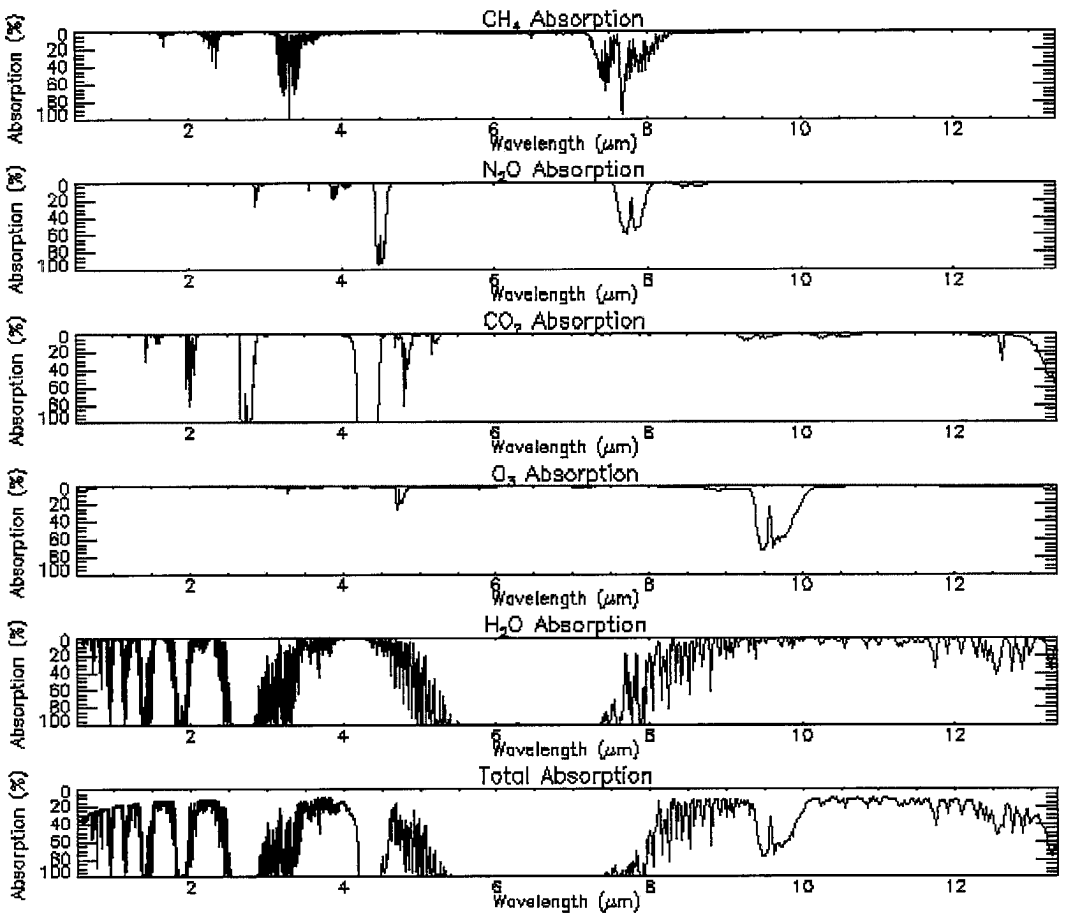

Figure 2.5: Atmospheric absorption spectra for different absorbing gases of the Earth's atmosphere across the measurement bandwidth of interest for this work. Generated from MODTRAN database for a US-Standard Atmosphere.

nisms that give rise to the absorption range from photo-dissociation/ionization at ultraviolet to visible wavelengths (λ typically lower than 1μm) to vibrational modes in the mid- to near-infrared ($1 < \lambda < 20\mu$m) and finally rotational modes at longer wavelengths in the far-infrared and upwards into microwave ($\lambda \sim 1$ cm) radiation. The frequency and spacing of the lines across the spectrum is a function of molecular geometry (symmetric/asymmetric) and the molecule's speed in forming dipoles in response to the incident radiation. The structures range from the neatly spaced P, Q, and R branch absorption of the linear carbon dioxide molecule to the highly irregular behavior of the heteropolar (having a permanent dipole moment owing to unshared electrons) asymmetric-top water molecule which has three different moments of inertia, rotational constants, and quantum number sets. Water vapor, by far the most dominant of the greenhouse gases, has complex absorption features dispersed throughout the electromagnetic spectrum and to a large extent dictates the distribution of atmospheric windows.

While absorption lines are discrete entities, their influence is actually broadened in a neighborhood about their center due to the actions of colliding molecules (pressure broadening) and motion-induced frequency shifts (Doppler broadening), leading to a wide range of influence across a spectral band. The primary line-broadening mechanism in the atmosphere below 50-km is pressure broadening. Further, absorption amount is not a linear function of absorber path, but rather follows a "curve of growth" transitioning from linear to square-root growth rates. Given these considerations, the absorption coefficient for a gas is characterized according to the Lorentz model of pressure broadening as

$$k_\lambda = Sf(\lambda - \lambda_\circ) \tag{2.58}$$

$$f((\lambda - \lambda_\circ) = \frac{\alpha_L/\pi}{(\lambda - \lambda_\circ)^2 + \alpha_L^2} \tag{2.59}$$

$$\alpha_L = \alpha_{L,\circ}(\frac{P}{P_\circ})(\frac{T_\circ}{T})^{1/2} \tag{2.60}$$

where S is the line strength, $f((\lambda - \lambda_\circ)$ is the line shape function at some position in the line wing off the central line at $\lambda_\circ$, α_L is the Lorentz line half-width. The latter is defined for a given gas in terms of a temperature and pressure scaling with respect to the laboratory standard $\alpha_{L,\circ}$ defined at standard $P_\circ$ and $T_\circ$. The absorption coefficient

(m^2/kg) is transformed into an equivalent gas optical depth $\tau_\lambda(u)$ and band-transmission $T_{\delta\lambda}(u)$ by introducing the appropriate path factor

$$du = \rho_g ds, \tag{2.61}$$

(where ρ_g is the gas density) to produce

$$\tau_{g,\lambda}(u) = \int_{z1}^{z2} k_\lambda du \tag{2.62}$$

$$T_{\Delta\lambda}(u) = \frac{1}{\Delta\lambda}\int_{\Delta\lambda} e^{-\tau_{g,\lambda}(u)} d\lambda. \tag{2.63}$$

Account for absorption by atmospheric gases (*e.g.*, H_2O, CO_2, O_3, N_2O, and CH_4) in both the NIR and IR is necessary for modeling the satellite measurements used in this work. Even channels situated within the atmospheric windows are susceptible to some amount of continuum absorption (dependencies that are exploited by Arking and Childs, 1985, and King et al., 1992). Unfortunately, this is not a simple matter of adding up the individual absorption lines and strengths for each gas across a channel bandwidth. Because of the profile-dependent pressure, temperature, absorber-amount dependencies, and shear number of absorption lines contributed by different gases coexisting within a single band, a statistical correlated-K distribution approach must be applied.

The gaseous absorption parameterization used in the model follows the correlated-K approach of Kratz (1995) with revisions by Drummond and Stephens (1998). Stated briefly here, the approach begins with the assertion that for a homogeneous atmosphere transmission across a band is independent of the spectral ordering of the absorption coefficients (k):

$$T(u) = \int_0^\infty e^{-k'u} f(k') dk' \tag{2.64}$$

where $f(k)$ is the probability density function of k across the band

$$\int_0^\infty f(k') dk' = 1.0. \tag{2.65}$$

Introducing the cumulative distribution for $f(k)$

$$g(k) = \int_0^k f(k') dk' \tag{2.66}$$

(a monotonically increasing function k-space) allows for the rewriting of the band transmission as

$$T(u) = \int_0^1 e^{-k(g)u} dg. \tag{2.67}$$

The general condition under which the method holds for non-homogeneous atmospheres and for a group of absorption lines is when the strong and weak lines occur at the same wavelengths at all altitudes in the profile. In this way, the cumulative probability distribution $g(k)$ is independent of temperature and pressure and the transmission is correlated throughout the atmospheric profile.

In terms of runtime cost, the K-distribution approach is far superior to the arduous alternative of stepping through the highly variable line-by-line absorption features encountered across the bandwidths. For bands containing contributions from several gases, the multiplication transmissivity property (which assumes that overlapping absorption features from different gases in the the band are uncorrelated is assumed to hold. For a given instrument and channel combination, a known number of absorbing gases exist, each of which has associated with it a finite number of intervals over the channel bandwidth whose number and spectral widths are determined by the varying absorption behavior of the gas and the response function of the channel (Kratz, personal communication). Assigned to each interval for each gas are weights whose sum across the channel bandwidth is unity (e.g., Figure 2.6). Because each absorber can have a different number of intervals (and hence, weights), SLADRT routines invoke the multiplicative-transmissivity property to build (τ_g) recursively for all possible combinations of absorbers and intervals, calculating the intermediate radiative transfer results and weighting them according to the combinations used. The end result is a final radiance field that accounts for all absorbers over all intervals.

An accurate and computationally more efficient amendment to the correlated-K approach developed by Drummond and Stephens (1998) has improved the original handling of gaseous absorption in the model by effectively reducing the relative absorption and transmission errors (with respect to line-by-line calculations) while maintaining spectral traceability of the absorber gas contributions. These parameters are computed off-line

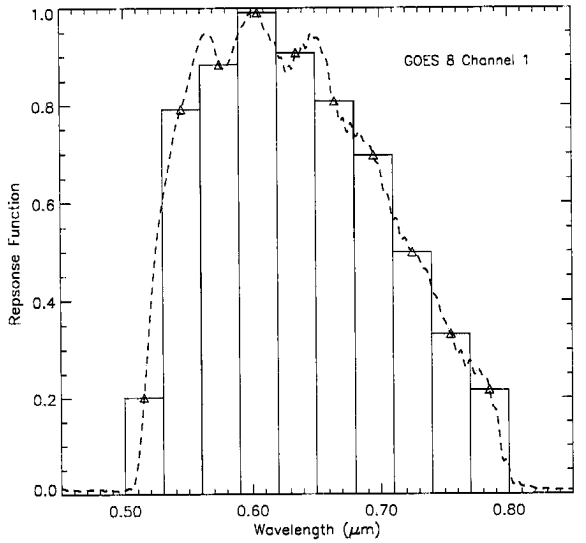

Figure 2.6: Discretization of the instrument response function shown for GOES-8 Channel 1 (0.65μm). (The weights associated with these discrete intervals are normalized such that they integrate to unity over the bandwidth.)

for arbitrary channel bandwidths. Using the new approach, recursive calls (which mingle absorber intervals among the various gases) to the forward model are replaced by a single integration through the band using gaseous optical depths computed for optimized sub-band intervals. The traditional recursion is eliminated by virtue of the method's ability to retain spectral absorber information during the optimization process, such that all gaseous absorber information that goes into producing the subinterval τ_{gas} originates from within the spectral bandwidth in question. Furthermore, because detector response is implicit to the instrument/channel specific parameters, the loop over channel band-weights described above is also eliminated.

2.4.4 Instrument response

Because instrument filter functions are not ideal step-functions of uniform response across their bandwidths, variable instrument response must be accounted for within the satellite radiative transfer calculations. The procedure involves partitioning the detector response function into discrete bins sufficient in spectral resolution to capture the structure. An example is provided for the GOES-8 imager Channel 1 in Figure 2.6. The weights

associated with each subinterval are the normalized filter function response and sum to unity. The forward model is called N-times in succession and the band-weighted intensity field is given by

$$I_{band}(\tau, \mu, \phi) = \sum_{\lambda=1}^{N} I_\lambda(\tau, \mu, \phi) W_\lambda, \tag{2.68}$$

where N is the number of band weights and W_λ are the normalized instrument response weights. Solar spectral flux data (W m^{-2} sr^{-1} μm^{-1}) were also computed as interval-averaged quantities.

2.4.5 Aerosol loading

Aerosol occurs usually at lower levels in the atmosphere (and to a lesser degree in the stratosphere) with visible optical depths typically under 0.1. Because their distribution and shapes/compositions are not well known, this translates to a corresponding ambiguity in their treatment radiatively. Aerosol optical parameters were handled here using selectable turbidity profiles representing a wide variety of boundary-layer, tropospheric, and stratospheric visibility conditions for rural, urban and maritime climatologies. The approach used is to calculate aerosol optical properties for a single wavelength and specified relative humidity profile. For the modeling of satellite channels, the central channel wavelength is selected for this purpose and the aerosol properties are assumed grey across the band. Information from the visible (0.6 μm) standard aerosol profile is rescaled to user-specified (or standard default) total aerosol optical depth and interpolated to the user-input profile. Finally, the computed aerosol optical properties ($\tau_{aer}, \omega_{o,aer}$, and g_{aer}) are rescaled from the standard wavelength to the wavelength of interest for the retrieval. The source for these data is the parameterization outlined in Shettel and Fenn (1979). Appendix A provides additional details on the selectable aerosol turbidity profiles.

2.4.6 Cloud insertion and parameter lookup tables

Ice and water clouds are incorporated into the forward model by inserting additional layers containing the relevant optical properties into the established layered profile. Gas, Rayleigh, and aerosol optical depths in the layers intersected by cloud are recomputed by logarithmic interpolation to the new profile levels. Clouds with variable extinction, phase

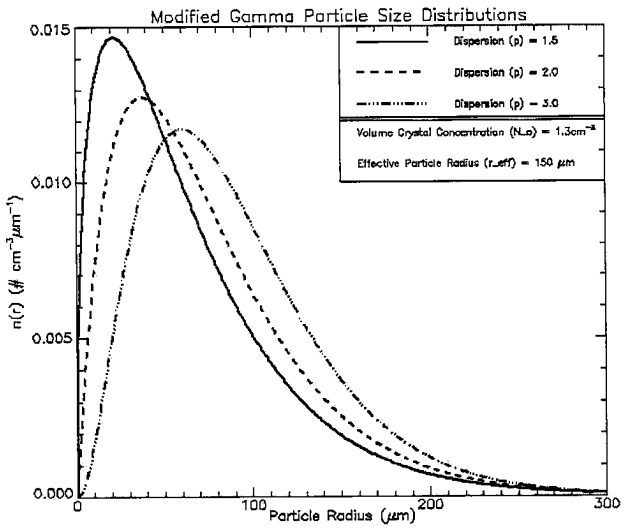

Figure 2.7: Examples of the modified-gamma distribution for different values of dispersion used to approximate cloud droplet distributions in SLADRT.

(ice/water), and scattering behaviors in the vertical are modeled as stacked homogeneous layers. The specifiable cloud properties for each cloud layer are the phase (ice or water), cloud top and base altitude, single scatter albedo, and scattering phase function properties (*e.g.* Henyey-Greenstein parameters or a referenced table of Legendre expansion coefficients representative of a more detailed phase function).

Typical cloud particle size distributions are characterized by a sharp rise to a maximum particle size followed by a gentle decrease toward larger sizes. A modified gamma function is often used as a reasonable approximation to this distribution shape,

$$n(r)dr = ar^{\alpha}exp(-br^{\gamma})dr, \tag{2.69}$$

where $n(r)dr$ is the number of droplets between sizes r and $r + dr$ per unit volume, $0 \leq r < \infty$, a, α, b, and γ are positive, real constants, and α is an integer. An example of modified-gamma distributions is shown in Figure 2.7.

How radiation is scattered/absorbed by a cloud is highly dependent on the distribution of particle shapes and sizes that comprise it. The effective particle radius Hansen and Travis (1974) is given by

$$r_e = \frac{\int_0^{\infty} r^3 n(r)dr}{\int_0^{\infty} r^2 n(r)dr}, \tag{2.70}$$

where $n(r)$ is the particle size distribution and r is the actual particle radius. Lorenz-Mie theory was used to (generated off-line, see Appendix A) construct tables of asymmetry parameter (g) and single-scatter albedo (ω_o) associated with specified r_e for a given wavelength (assuming a modified-gamma distribution as described above). Implicit to Lorenz-Mie theory is the assumption of sphericity for both water *and ice* particles. For ice particles, the radii refer to ice spheres of equivalent volume to the non-spherical ice crystals (the implications of this rather cavalier assumption are discussed below).

2.4.7 Delta-M scaling

Scattering phase functions with strong forward peaks are very difficult to model explicitly with a Legendre polynomial expansion. To represent numerically the strongly asymmetric/forward-peaked phase functions of most clouds found in nature, the Delta-M scaling method of Wiscombe (1976) was applied. A logical extension of the delta-Eddington approximation of Joseph *et al.* (1976), Delta-M scaling assumes a Dirac delta-function representation of forward scattering, considering this fraction of energy as directly-transmitted light:

$$P^*(\Theta) \approx 2f(\delta(1 - cos(\Theta)) + (1 - f) \sum_{l=0}^{2N-1} (2l + 1)\chi_l P_l(cos(\Theta)), \tag{2.71}$$

where the coefficients χ_l are the moments of P with respect to the Legendre polynomials

$$\chi_l = 0.5 \int_{-1}^{1} P(cos(\Theta))P_l(cos(\Theta))dcos(\Theta). \tag{2.72}$$

The coefficients of P^* (the truncated phase function) are matched to those of P according to

$$\chi_l = 0.5 \int_{-1}^{1} P^*(\Theta)P_l(cos(\Theta))dcos(\Theta) \tag{2.73}$$

which yields

$$\begin{array}{ll} f + (1 - f)\chi_l^*, & l \leq 2N - 1 \\ f, & l \geq 2N \end{array} \tag{2.74}$$

This is usually not a bad assumption, since a considerable amount of the scattering integral resides within a degree of the forward scattering direction. The Delta-M method

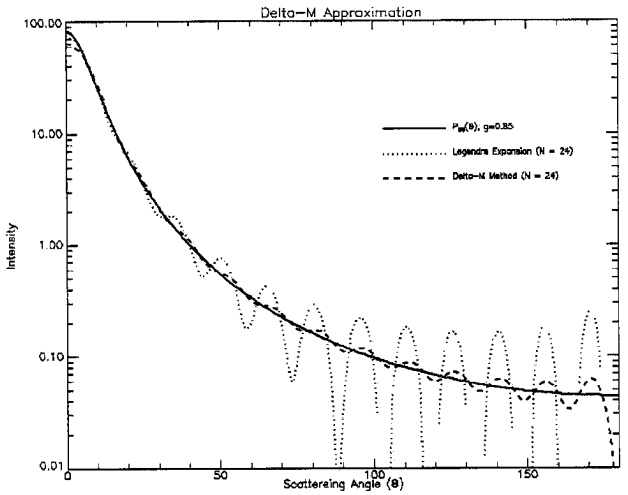

Figure 2.8: Legendre expansion of a Henyey-Greenstein phase function showing Delta-M improvement in approximation for the same order of expansion.

requires a rescaling of the Legendre expansion coefficients and a corresponding rescaling of the optical properties

$$\tau^* = (1 - \omega_o f)\tau\omega_o^* = \frac{\omega_o(1-f)}{1-\omega_o f}, \tag{2.75}$$

since some of the radiation that was actually scattered is now being treated as directly-transmitted energy instead. This rescaling is done to maintain the solution to the original RTE. The method achieves higher accuracy for a given order of expansion (shorter model run times) and flux conservation is automatic. Figure 2.8 shows the improvement afforded by the Delta-M scaling for the simple case of a single Henyey-Greenstein phase function. For the complex ice crystal phase functions considered further along (which have forward scattering peaks with magnitudes on the order of 10^5), the method is essential in making the problem computationally tractable.

2.4.8 Treatment of complex scattering phase functions

The forward model is not restricted to usage of Henyey-Greenstein scattering functions exclusively. The Legendre polynomial expansion can, in principle, be used to represent any realistic scattering phase function provided a sufficient number of terms. The ability to do so in a *reasonable* number (with regards to computational cost) for highly

forward-peaked phase functions is afforded by the Delta-M approximation. Provided tabulated phase function data (at discrete scattering angles between 0 and 180 degrees, and assumed constant in azimuth), the χ terms can be computed, written to file, and read-in at runtime to construct the scattering matrices. This is termed as a χ-expansion of the scattering phase function, and together with the Delta-M method allows for highly variable cirrus phase functions to be represented numerically in a computationally efficient manner.

First, the phase function is truncated within the first degree of forward scattering and the weight associated with this removed energy, f_T is computed according to

$$f_T = 1 - \int_{-1}^{1} P(\mu) d\mu, \tag{2.76}$$

and the truncated phase function integral is renormalized to 2.0. Because the truncated phase function yields a different asymmetry parameter than the original (g_o), a renormalization is computed to provide the correct value of g

$$g_T = f_T + (1 - f_T) * g \tag{2.77}$$

$$f_g = \frac{g_o - g_T}{1 - g_T}, \tag{2.78}$$

and the final, combined weight f associated with the truncated phase function becomes

$$f = 1 - (1 - f_T)(1 - f_g) \tag{2.79}$$

(A. Heidinger, personal communication).

Figure 2.9 illustrates this approach applied to a tabulated ice-crystal phase function ($\lambda = 0.65, g = 0.8045, \omega_o = 0.9999$) obtained from Yang *et al.* (1998). Evident from this figure is the disproportionate amount of energy residing at the forward scattering peak. When the abscissae, expressed here in scattering angle degrees, are plotted in terms of $cos\Theta$, the forward lobe appears even more as a delta-spike (a testament to the validity of the δ-M assumption).

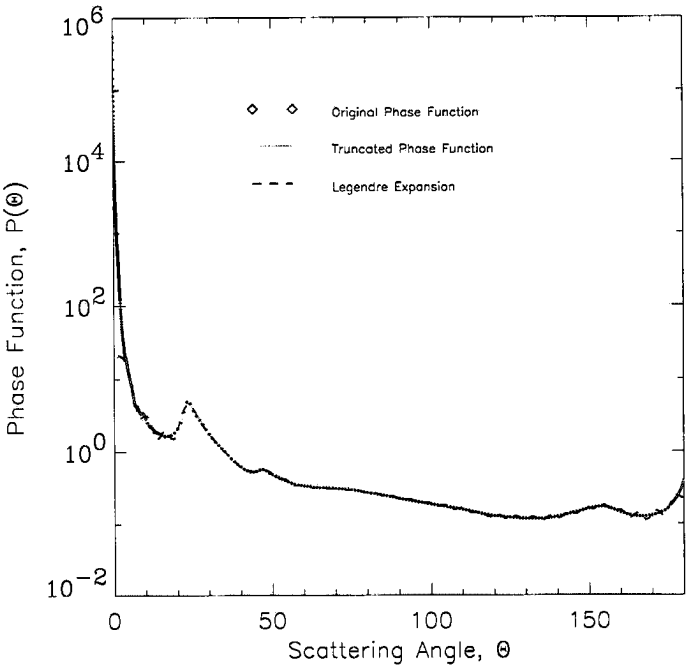

Figure 2.9: Legendre expansion of a tabulated ice crystal phase (Yang *et al.*, 1998) function from which χ-expansion terms are computed.

2.5 Model Shortcomings

Ideally, the "virtual measurement" provided by the forward model would represent exactly the what the satellite instrument measurement (specified by a channel with a characteristic bandwidth and spectral response) observes for a specified atmospheric/surface state and observer/solar geometry. This ideal is compromised in reality by the need to capture the physics in a computationally efficient way and by our inability to specify comprehensively the entire array of unretrievable (and unknown) quantities which contribute to the actual measurement without some attachment of finite uncertainty. These shortcomings must be accounted for in the estimate of errors introduced to the retrieval.

2.5.1 Plane-parallel approximation

An important compromise made by plane-parallel (1-D radiative transfer) modeling to real-world clouds is the approximation of three-dimensional heterogeneous cloud fields as one-dimensional homogeneous slabs. Inhomogeneities in a cloud tend to reduce its

reflectance compared to plane-parallel clouds (see McKee and Cox, 1974). Ignoring the effects of horizontal transport of photons escaping from cloud edges has the effect of modeling brighter clouds for a given (τ, r_{eff}) translating to possible underestimates of these quantities (to reduce the forward model reflection and thereby match the observations) in a retrieval based on solar reflection measurements (Duda *et al.*, 1996). At infrared wavelengths, partial cloud cover in a scene will result in an increased signal contribution from warmer emissions from the surface and atmosphere below the cloud. While the plane-parallel approximation represents a model shortcoming, errors associated with the latter are driven largely by the pixel resolution of the instrument (e.g., GOES-8 infrared channel resolution is on the order of 4 × 4 km at nadir). Errors associated with cloud inhomogeneity can be assessed by using 3-dimensional Monte Carlo modeling (see Heidinger and Stephens, 1998). In general, their magnitudes increase with increasing solar zenith angle (more cloud edge/shadow effects) and smaller pixel areas. To minimize these contributions, then, one might enforce a maximum solar zenith angle threshold (e.g. 60°) on visible retrievals. If the cloud is of sufficient spatial extent, an areal average intensity (and a resultant "smoothed" retrieval) can be used in favor of the pixel-by-pixel quantities. These errors are included in the model/measurement error covariance matrix of the retrieval scheme outlined in Chapter 3.

2.5.2 Spherical geometry approximation

While the concept of the "effective particle radius" has been used to describe the radiative properties of water clouds which are largely insensitive to the shape and width of the particle size distribution (Hansen and Travis, 1974), the same cannot be said for ice clouds. Lorenz-Mie theory represents these particles as being spherical (with refractive properties of ice), whereas ice crystals are composed of columns, bullets, rosettes, plates, and aggregates thereof whose habits, sizes, and growth rates are determined largely by the availability of water vapor and the environmental temperature. Platt *et al.* (1980) find that most high-altitude cirrus clouds were comprised of long columnar and hexagonal ice crystals. Comparing the scattering phase function properties between the ice crystal distributions of Takano and Liou (1995) with typical water phase functions such as

Deirmendjian's C1 (cumulus) cloud reveal marked differences in the scattering behaviors. The disparity is only worsened when comparing simple analytic functions like the double Henyey-Greenstein phase function used often in contemporary retrieval work (Heidinger and Stephens, 1998).

The χ-expansion of complex ice crystal scattering phase functions attempts to remedy in part this error. In the application to retrieval work, however, the discrete nature of the tabulated data from Yang *et al.* poses a problem to the iterative-solution approach (which requires the phase function to be defined in a continuous manner). Yang *et al.* do supply parameterizations for the absorption/extinction efficiencies and the asymmetry parameter such that, provided adequate spectral resolution, the discrete choice of phase function shape will not lead to instability in the retrieval convergence. These data have been implemented in some of the cirrus retrieval case studies presented in Chapter 5.

2.6 Model Validation

Selected cases from the tabulated results of Van de Hulst (1980) and the discrete ordinates model ("DISORT") outlined by Stamnes *et al.* (1988) served as established benchmarks for validation of the SLADRT model. The comparison between the three sets of results is shown in Fig. 2.10 for the simple cases of a single-layer atmosphere with isotropic and Henyey-Greenstein phase functions and two different lower boundary reflection conditions (zero and Lambertian). These results indicated the correct numerical implementation of the RTE outlined above within the SLADRT blackbox.

Azimuthal asymmetry of the model radiance field was also compared with the results of a backward Monte Carlo (a stochastic method to solving the RTE, see Hammersley and Handscomb, 1964, and Marchuk *et al.*, 1980) routine run for identical input conditions for a single cloud layer with $\tau = 1.0$ and $g_{\text{eff}} = 0.85$. Figure 2.11 shows a two-panel comparison for a simple, single layer cloud in a uniform atmosphere with no reflecting surface. An azimuth angle of $\phi = 0°$ in these panels corresponds to the sun being directly behind the observer (at a solar zenith angle of 45°, with the sun in front of the observer for $\phi = 180°$. The structure of the azimuthal field for this case is in agreement with the

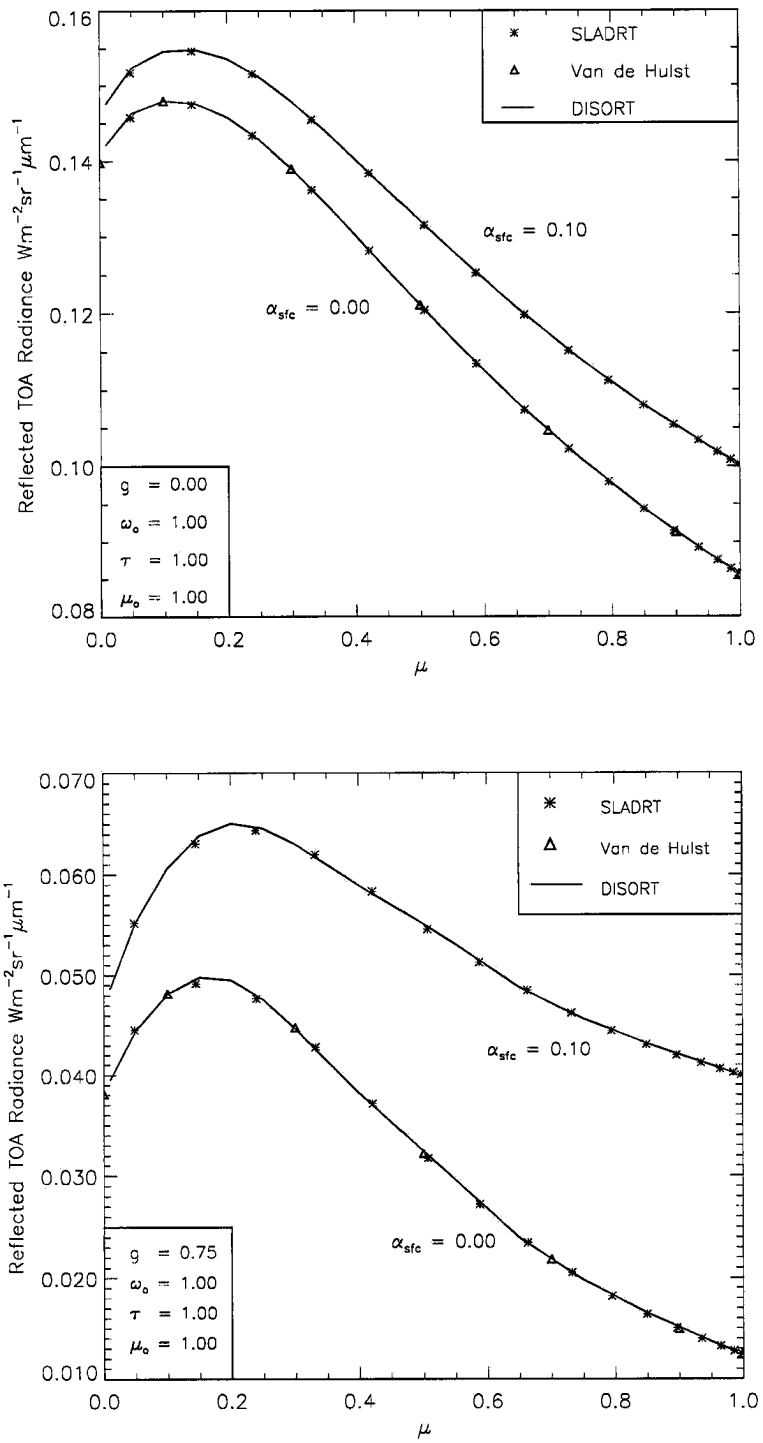

Figure 2.10: Forward model verification for an isotropic scattering medium (top) and a single Henyey-Greenstein scattering medium (bottom).

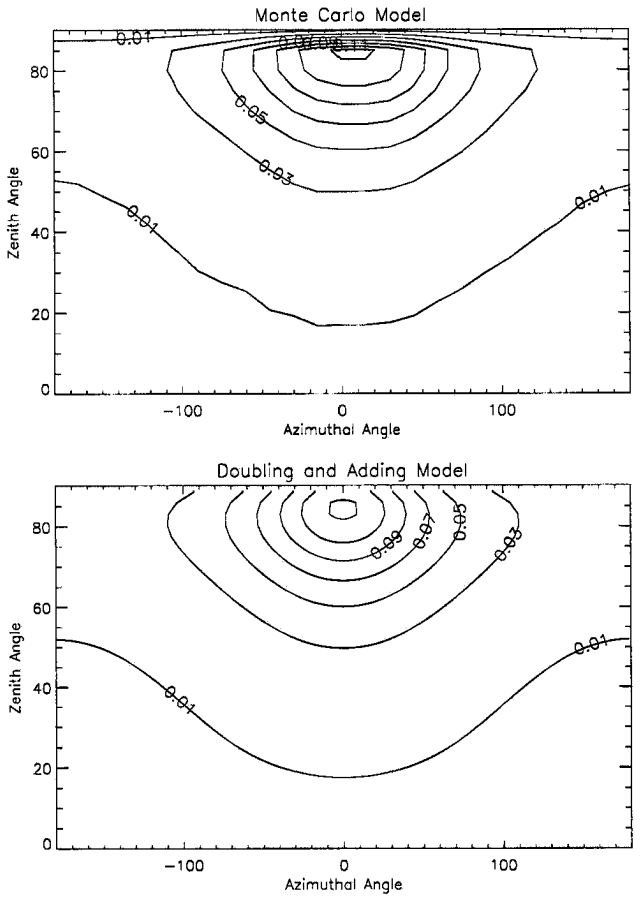

Figure 2.11: Forward model verification for azimuthal varying radiances compared against a Monte Carlo simulation.

independent Monte Carlo run. Some contours do not close in the doubling/adding code due to an under-sampling of quadrature points at these angles.

2.7 Summary

This chapter described a plane-parallel, discrete ordinates doubling and adding code (SLADRT) developed from first principles of radiative transfer theory. It was designed for use as the forward model in satellite retrievals of cloud optical properties. While quite general in applicability, special accommodations were made to the forward model enabling it to simulate narrow-band passive radiometer instrument measurements from satellite and airborne platforms. This model was validated against existing radiative transfer codes and published data. These measurements comprise the forward estimate vector of the retrieval. While simplifying assumptions regarding physical geometry and optical properties of the model medium give rise to uncertainties when comparing results to actual measurements, the *a priori* data needed to eliminate these uncertainties is seldom available to a retrieval. To what extent active sensors, in providing accurate *a priori* information about cloud location in the vertical, aid in improving these retrievals was a fundamental question posed by this dissertation.

Chapter 3

INVERSION THEORY

3.1 Introduction

A suitable method for combining forward model estimates with satellite radiometer measurements to back-out (invert) atmospheric parameters of interest is required. This requires not only a basic understanding of the physics behind the problem but also a keen awareness of the numerics involved. In describing the nature of inversion theory and its inherent numerical caveats, Twomey (1976) recounts

> *For a time it was thought that precision and accuracy in the computer were the core of the problem and more accurate numerical procedures were sought and applied without success. Soon it was realized that the problem was not inaccuracy in calculations, but a fundamental ambiguity in the presence of inevitable experimental inaccuracy – sets of measured quantities differing only minutely from each other could correspond to unknown functions differing very greatly from each other.*

Before proceeding to detail the mathematical constructs of the cloud property retrieval scheme used in this work, it is first worthwhile to step back and look again at the big picture. The ultimate goal of cloud retrievals is to be able to convert radiometer measurements of radiance (a *signature* of the cloud) into physical characteristics relevant to understanding the ways in which clouds affect the energetics of the atmosphere. To do so requires a sense of how the parameters of interest interact with radiation along with all the other contributing elements of the surface and atmosphere to produce the end-product measurement. Our understanding of this physical process is embedded in the forward model presented in the previous chapter. It is now the onus of the estimation problem to begin with these end-product measurements and, using the forward model as a guide, trace back the physical properties of the clouds responsible for them. If this can be

accomplished in a way that affords some sense of the uncertainty assigned to the results, this data can provide information critical to understanding the part clouds play in the climate feedback system.

This chapter introduces the concept of retrieval theory and outlines the estimation method (used in solving the inverse problem) chosen for cloud property retrievals conducted in this paper. Based on the pioneering work of Rodgers (1976) (originally applied to the retrieval of atmospheric profiles of temperature and moisture) this method provides statistical diagnostic variables describing the error associated with the retrieval vector and how reliant the solution is on *a priori* assumptions/constraints applied here to the retrieval of cloud optical depth and effective radius, these diagnostics are not available to most other retrievals of these quantities.

3.2 The Premise of Retrieval Theory

The fundamental goal of any remote sensing measurement is, by definition, to enable the characterization of some property of an object inaccessible to *in situ* sampling. In a simple-minded view of this problem, one might consider the analogy of the impact history of craters on the Moon. Given a knowledge of the number, sizes, density, speeds, trajectories, and times of meteors impacting upon the lunar surface, one could (with appropriate assumptions about the nature of the surface) create a map comprised of the superposition of impacts occurring over some period of time to arrive at a final lunar topography. This exercise embodies the so-called "forward problem." The inverse problem for this example begins with the final topographic map and then attemps to deduce from it the meteorite properties as given above. It is not difficult to conceive of instances where a small crater formed by an earlier impact is completely obliterated by an ensuing large impact. In this way, a component of impact events may be unretrievable. In other cases, a more dense meteorite may leave the same size crater as one of lesser density traveling at a higher speed. This is an example of the ill-posed (underconstrained) problem that arises whenever multiple solutions to the same system of equations exist. If an *a priori* knowledge of the meteorite distribution or lunar surface properties is available (e.g., the Moon is not

made out of Swiss cheese), the solution may be constrained to the more likely scenarios. The determination of the best-possible solution embodies the "estimation approach" used in solving the inverse problem.

In an example more down-to-Earth, consider the problem of measuring the temperature of the ocean surface. In this example, the *in situ* experiment entails the straightforward reading of an immersed liquid-in-glass thermometer. To obtain this same quantity remotely (e.g., using a radiometer instrument on the satellite platform), the infrared/microwave emission from the ocean surface is measured in the form of a spectral radiance and the temperature obtained by inversion of the Planck function. In the former case, uncertainty resides entirely in the calibration of the instrument. The latter case is complicated by several caveats, including attenuation of surface emissions by the atmospheric constituents (even in "window channels" where such extinction is minimized locally), emission contributions from other levels (at different temperatures), and uncertainty in surface spectral emittance (describing how similar a material behaves to a pure blackbody at a given wavelength). Radiometric measurements of the Earth's atmosphere and surface require an ability to deconvolve the many contributions to the measured signal in order to isolate the component of interest. Knowledge of the system components and physics, then, is at the heart of all retrieval problems.

3.3 The Rodgers Estimation Method

This section outlines the constructs of an optimized estimation of cloud optical depth and effective particle size. The approach is first outlined by *Rodgers* [1976, 1990] and *Marks and Rodgers* [1993]. It has been applied to the retrieval of ozone and water vapor by Engelen and Stephens (1997,1998) and to soundings of cloud and aerosol by Heidinger and Stephens (1998). In this work, it has been adapted to the retrieval of cloud optical properties.

To fix ideas, we begin by considering cloud radiance (reflected solar, thermal emission, or both) as measured by a radiometer on the satellite platform. The satellite measurements (brightness temperature and/or radiance at a given channel) $\vec{y}$ are expressed in terms of

the forward model as

$$\vec{y} \;=\; F(\vec{x},\vec{b}) + \epsilon_y, \tag{3.1}$$

where F is the forward model (developed in Chapter 2) describing numerically the physical relationships between the measurements $\vec{y}$ and the retrieved parameters $\vec{x}$. The *a priori* parameters ($\vec{b}$) embody all unretrieved parameters required by the forward model. Specification of these parameters can in some cases drive the solution, and the extent to which this holds is an important diagnostic. The error term ϵ_y provides an estimate of uncertainty in the measurements (e.g., instrument noise) and forward model errors. Nowhere is it implied that a unique $(\vec{x}, b)$ solution pair must exist satisfying Equation 3.1.

Defining estimates for the retrievable ($\vec{x}$) and *a priori* (x_a) quantities, the approach follows from "optimal estimation" theory, in which a scalar *cost function* is minimized:

$$\phi = (\vec{x} - x_a)^T S_a^{-1}(\vec{x} - \vec{x_a}) + (\vec{y} - F(\vec{x}))^T S_y^{-1}(\vec{y} - F(\vec{x})), \tag{3.2}$$

where S_y is the measurement error covariance matrix (those errors defining ϵ_y in 3.1), S_a contains the errors associated with any *a priori* constraints imposed on the retrieved (estimated) parameters, and $\vec{x_a}$ is the *a priori* estimate vector. This development follows directly from Bayes theorem of Gaussian statistics.

We develop the general solution by first examining a specific pair of independent measurements (x_1, x_2) of the quantity x (e.g., cloud optical depth). These measurements can be combined as a weighted-average using the reciprocals of their variances as the weights

$$\hat{x} = \left(\frac{x_1}{\sigma_1^2} + \frac{x_2}{\sigma_2^2}\right) / \left(\frac{1}{\sigma_1^2} + \frac{1}{\sigma_2^2}\right), \tag{3.3}$$

where $\sigma_{1,2}$ are standard deviations and the variance of x based on these two measurements is given by

$$\hat{\sigma_x^2} = \left(\frac{1}{\sigma_1^2} + \frac{1}{\sigma_2^2}\right)^{-1}. \tag{3.4}$$

The generalization of Equation 3.3 to any number of retrieved parameters follows directly as

$$\hat{x} = (S_1^{-1} + S_2^{-1})^{-1}(S_1^{-1}x_1 + S_2^{-1}x_2), \tag{3.5}$$

where x_i now assume vector quantities and $S_{1,2}$ are error covariance matrices given by

$$\hat{S} = (S_1^{-1} + S_2^{-1})^{-1}. \tag{3.6}$$

Now we consider a system having a virtual measurement $\vec{x_a}$ with covariance S_a and a direct measurement $\vec{y} = K\vec{x}$ with covariance S_y. The matrix K is the "Fréchet derivative" (or "kernel matrix") evaluated at $\vec{x}$, specifying the sensitivity of the forward model to a perturbation of the parameters to be retrieved:

$$K = \frac{\partial F}{\partial \vec{x}}. \tag{3.7}$$

This implicit assumption of response linearity in the neighborhood of $\vec{x}$ runs throughout this development. Expressed in terms of m-measurements and n-parameters, the kernel matrix may be written explicitly as

$$K = \begin{bmatrix} \frac{\partial F_1(\vec{x},\vec{b})}{\partial x(1)} & \frac{\partial F_1(\vec{x},\vec{b})}{\partial x(2)} & \cdots & \frac{\partial F_1(\vec{x},\vec{b})}{\partial x(n-1)} & \frac{\partial F_1(\vec{x},\vec{b})}{\partial x(n)} \\ \frac{\partial F_2(\vec{x},\vec{b})}{\partial x(1)} & \frac{\partial F_2(\vec{x},\vec{b})}{\partial x(2)} & \cdots & \frac{\partial F_2(\vec{x},\vec{b})}{\partial x(n-1)} & \frac{\partial F_2(\vec{x},\vec{b})}{\partial x(n)} \\ \vdots & \vdots & \ddots & \vdots & \vdots \\ \frac{\partial F_{m-1}(\vec{x},\vec{b})}{\partial x(1)} & \frac{\partial F_{m-1}(\vec{x},\vec{b})}{\partial x(2)} & \cdots & \frac{\partial F_{m-1}(\vec{x},\vec{b})}{\partial x(n-1)} & \frac{\partial F_{m-1}(\vec{x},\vec{b})}{\partial x(n)} \\ \frac{\partial F_m(\vec{x},\vec{b})}{\partial x(1)} & \frac{\partial F_m(\vec{x},\vec{b})}{\partial x(2)} & \cdots & \frac{\partial F_m(\vec{x},\vec{b})}{\partial x(n-1)} & \frac{\partial F_m(\vec{x},\vec{b})}{\partial x(n)} \end{bmatrix}. \tag{3.8}$$

It should be noted here that the matrices are not always square (e.g., if the number of measurements exceeds the number of retrieved parameters), in which case matrix inversions employ method of singular value decomposition to obtain the generalized inverse.

Following the example above, we seek the minimum in ϕ with respect to the parameter vector $\vec{x}$ by taking its derivative and setting the quantity equal to zero. Working again with scalar quantities for simplicity, Equation 3.2 becomes

$$\begin{aligned} \frac{\partial}{\partial x}\left[\left(\frac{\hat{x}-x_a}{\sigma_a}\right)^2 + \left(\frac{K\hat{x}-y}{\sigma_y}\right)^2\right] &= 0 \\ \frac{\hat{x}-x_a}{\sigma_a^2} + \frac{K^2\hat{x}-Ky}{\sigma_y^2} &= 0 \\ \hat{x} = \left(\frac{1}{\sigma_a^2} + \frac{K^2}{\sigma_y^2}\right)^{-1}\left(\frac{x_a}{\sigma_a^2} + \frac{Ky}{\sigma_y^2}\right) & \end{aligned} \tag{3.9}$$

which is the same form as Equation 3.3. Observing the rules of linear algebra, Equation 3.9 is then rewritten in matrix form as

$$\begin{aligned} \hat{x} &= (S_a^{-1} + K^T S_y^{-1} K)^{-1} (S_a^{-1} \vec{x_a} + K^T S_y^{-1} \vec{y}) \\ &= \hat{S_x} (S_a^{-1} \vec{x_a} + K^T S_y^{-1} \vec{y}) \end{aligned} \tag{3.10}$$

where

$$\hat{S_x} = (S_a^{-1} + K^T S_y^{-1} K)^{-1} \tag{3.11}$$

is the covariance matrix of the estimated parameters. These errors are dependent on the correct assignment of the measurement and forward model uncertainties. To gain an intuitive feel for this important diagnostic, we can rewrite Equation 3.11 in terms of units of the measurements (M) and parameters (P). Recalling the definition of the Kernel matrix and that the diagonal elements of covariance matrices are the squares of the standard deviations (variances), the scalar version of Equation 3.11 is written as

$$\hat{S_x} = \left[\left(\frac{1}{\Delta^2(P)} \right) + \left(\frac{\Delta(M)}{\Delta(P)} \right) \left(\frac{1}{\Delta^2(M)} \right) \left(\frac{\Delta(M)}{\Delta(P)} \right) \right]^{-1} = \Delta^2(P), \tag{3.12}$$

such that the square root of $\hat{S_x}$ yields the standard deviation error for the retrieved parameter. The breakdown of the uncertainties associated with $\hat{S_x}$ in the retrievals work of this dissertation are given in the following chapter.

The Newtonian iterative method involves writing the forward equation as a Taylor series expansion about a guess of the solution vector (x_i):

$$\vec{y} = F(\vec{x_i}) + \frac{\partial F}{\partial \vec{x}} (\vec{x} - \vec{x_i}) + \text{H.O.T.}. \tag{3.13}$$

Invoking the definition for the Fréchet derivative (Equation 3.8) and the forward model approximation to the measurement vector $F(\vec{x_i}) = \vec{y_i}$, this equation can be rewritten as

$$\vec{y} = y_i + K_i(\vec{x} - \vec{x_i}) + \text{H.O.T} \tag{3.14}$$

With the higher order terms omitted, the resultant linear equation set with *a priori* constraint $\vec{x_a}$ is

$$K_i \vec{x} = \vec{y} - \vec{y_i} + K_i \vec{x_i} \tag{3.15}$$

$$\vec{x} = \vec{x_a}. \tag{3.16}$$

Specifying the associated error covariances matrices

$$Cov(K_i\vec{x}) = S_y \tag{3.17}$$

$$Cov(\vec{x}_a) = S_a, \tag{3.18}$$

and following the form of Equation 3.10-3.11, the iterative solution for the "best fit" of $\vec{x}$ to the measurements $\vec{y}$ is given by

$$\begin{aligned}
\vec{x}_{i+1} &= (S_a^{-1} + K_i^T S_y^{-1} K_i)^{-1}[K_i^T S_y^{-1}(\vec{y} - \vec{y}_i + K_i\vec{x}_i) + S_a^{-1}\vec{x}_a] \\
&= (S_a^{-1} + K_i^T S_y^{-1} K_i)^{-1}[K_i^T S_y^{-1}(\vec{y} - \vec{y}_i) + K_i^T S_y^{-1} K_i\vec{x}_i + S_a^{-1}\vec{x}_a] \\
&= (S_a^{-1} + K_i^T S_y^{-1} K_i)^{-1}[K_i^T S_y^{-1}(\vec{y} - \vec{y}_i) + K_i^T S_y^{-1} K_i\vec{x}_i + S_a^{-1}\vec{x}_i - S_a^{-1}\vec{x}_i + S_a^{-1}\vec{x}_a] \\
&= (S_a^{-1} + K_i^T S_y^{-1} K_i)^{-1}[K_i^T S_y^{-1}(\vec{y} - \vec{y}_i) + (S_a^{-1} + K_i^T S_y^{-1} K_i)\vec{x}_i + S_a^{-1}(\vec{x}_a - \vec{x}_i)] \\
&= (S_a^{-1} + K_i^T S_y^{-1} K_i)^{-1}(S_a^{-1} + K_i^T S_y^{-1} K_i)\vec{x}_i \\
&\quad +(S_a^{-1} + K_i^T S_y^{-1} K_i)^{-1}[K_i^T S_y^{-1}(\vec{y} - \vec{y}_i) + S_a^{-1}(\vec{x}_a - \vec{x}_i)] \\
&= \vec{x}_i + (S_a^{-1} + K_i^T S_y^{-1} K_i)^{-1}[K_i^T S_y^{-1}(\vec{y} - \vec{y}_i) + S_a^{-1}(\vec{x}_a - \vec{x}_i)].
\end{aligned} \tag{3.19}$$

Using of Equation 3.11 and rewriting $\vec{y}_i$ in terms of the forward estimate F_i yields the final iterative form of the solution

$$\vec{x}_{i+1} = \vec{x}_i + \frac{K_i^T S_y^{-1}(\vec{y} - F_i) + S_a^{-1}(\vec{x}_a - \vec{x}_i)}{\hat{S}_x^{-1}}. \tag{3.20}$$

A useful retrieval diagnostic is obtained by introducing the following matrix quantity

$$A = \hat{S}_x K_i^T S_y^{-1} K_i \tag{3.21}$$

such that (3.20) may be recast as

$$\vec{x}_{i+1} = \vec{x}_i + AK_i^{-1}(y - F_i) + (I - A)(x_a - \vec{x}_i). \tag{3.22}$$

Equation 3.22 reveals the utility of the "*A Priori* Matrix," A, in ascertaining the dependency of the estimated parameters on the *a priori* constraints imposed on the the retrieval. Recalling the definition of $\hat{S}_x$ (Equation 3.11), when the errors associated with the *a priori* error covariance matrix (S_a) are large, the denominator of Equation 3.21 approaches the numerator (causing the ratio to approach unity), while for small S_a the

denominator exceeds the numerator and the ratio tends toward zero. When forward model sensitivity is small (i.e., small Kernel matrix components) or values of model/measurement uncertainty are high (i.e., S_y components are large) Equation 3.21 becomes increasingly dominated by the nature of the *a priori* covariance matrix. A retrieval that does not rely on *a priori* information will yield an identity matrix for A. This is illustrated further by Equation 3.22; when A is an identity matrix, the third term on the right hand side of Equation 3.22 vanishes, indicating that *a priori* information has not influenced the estimated parameters; a property of any ideal observing system. Departures from the identity matrix indicate either lower sensitivity of the measurements to the retrieved parameters or higher errors in the forward model or measurements, characteristic of real observing systems. The sensitivity of the retrieval to changes in the *a priori* parameters is given by

$$D_a = I - A. \tag{3.23}$$

The ensemble contribution of the Rodgers diagnostic parameters affords a qualified retrieval product of known credibility, inasmuch as the uncertainties associated with the forward model and measurements are known and quantified.

Following Marks and Rodgers (1993), the error in the retrieved parameters may be expressed formally as

$$\hat{x} - \vec{x} = (A - I)(\vec{x} - \vec{x_a}) + D_y(\Delta F - \overline{\Delta F}) + D_y \epsilon_y, \tag{3.24}$$

where $\hat{x}$ comprises the true values of the retrieval parameters and

$$D_y = \frac{K^T S_y^{-1}}{\hat{S}_x^{-1}} \tag{3.25}$$

is the matrix of contribution functions (the sensitivity of the retrieved parameters to changes in the measurements). The first term describes smoothing errors due to the *a priori* constraints, the second term describes forward model errors, and the last term describes measurement errors. The diagonal elements of $\hat{S}_x$ provide error estimates for the retrieved parameters

$$\delta_{\vec{x}}^2 = \frac{\sqrt{\hat{S}_x}}{\vec{x}}, \tag{3.26}$$

and off-diagonal elements are cross-correlations between parameter errors.

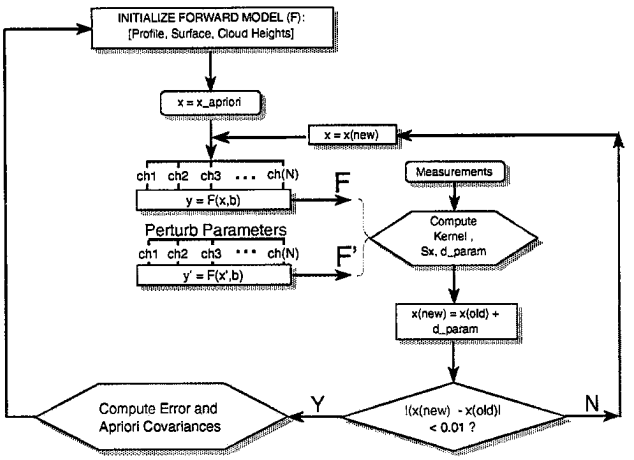

Figure 3.1: A simple schematic of the iterative retrieval flow.

3.3.1 Implementation architecture

The general flow of the retrieval is illustrated in Fig. 3.1. For a single retrieval point (e.g., along a flight track) all information required by the forward model is gathered. An *a priori* guess for τ and r_{eff} is used to begin the convergence loop. After using the forward model to compute virtual measurements for all channels, each cloud parameter to be retrieved is perturbed individually by a small value.

The radiances or brightness temperatures for the perturbed parameters are computed, and the kernel matrix is thereby constructed according to Equation 3.7. In addition to revealing model sensitivity to a change in the retrieved cloud properties, the kernel matrix also tells the retrieval in which direction to "tune" the estimated parameters to approach the observed measurements. The new estimates are computed according to Equation 3.20 and the entire process is repeated until a specified convergence criterion (change in the retrieval parameters from one iteration to the next is much less that solution errors) is achieved. Upon convergence, model performance diagnostic information (Equations 3.26-3.21) is computed and the final results (retrieval vector and accompanying diagnostics) are stored.

The required forward model data includes profiles of temperature, moisture, and gaseous absorbers (as provided from either rawinsonde or ECMWF reanalysis), solar/satellite angles (computed from spherical geometry), surface albedo, and cloud height (either estimated or provided by an active sensor). The number of retrieved parameters (e.g., τ and r_{eff}) are specified (defining the dimensions of the Kernel matrix). Initial guesses are made based on *a priori* knowledge of cloud type, height, and climatology when applicable. These data are used to construct a SLADRT input-card file.The interface to the forward model was coded in the Interactive Data Language (IDL) to handle multiple calls to the forward model, assignment of model/measurement uncertainties, the computation of the Rodgers retrieval parameters and update of the the retrieval vector, and loop termination as defined by the specified convergence criterion.

A sensitivity analysis, performed off-line, determines which channels and multiple-channel products to use in the retrieval. The measurement vector is created from channel-differencing, ratios, or conversions from radiance to brightness temperature as required by this sensitivity analysis. *A priori* forward model uncertainties (also computed off-line) are stored for combination with the measurement errors further along. Quality checks are performed on these data to filter missing/bad data from the retrieval. Given the measurements, noise is computed according to instrument specifications. These data are combined with forward model uncertainty figures to compute diagonal elements of the S_y matrix (errors are assumed to be uncorrelated between channels, and are in units of the measurement).

A "While not converged..." loop, truncated by a maximum allowable number of iterations, is entered. Within each iteration of the retrieval, a series of calls to the forward model are made. In the first loop, the forward model is called for each channel to compute a synthetic measurement vector. To account for the spectral variation of optical depth, it is noted that τ may be written as

$$\tau_\lambda = \int_{z_1}^{z_2} \int_0^\infty Q_{ext,\lambda} \pi r^2 n(r) dr\, dz \tag{3.27}$$

where Q_{ext} is the extinction efficiency (the effective-to-physical cross-sectional area). For the same cloud (i.e., same size distribution $n(r)$ at two different wavelengths), the ratio

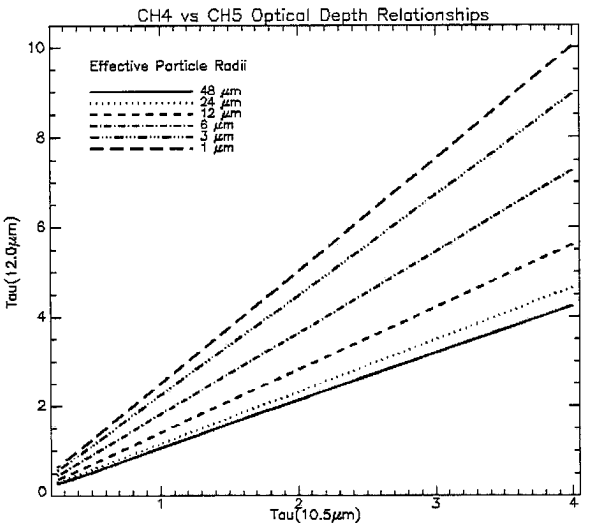

Figure 3.2: Example of relationship between optical depths at two different wavelengths as given by Equation 3.28.

of optical depths reduces to

$$\frac{\tau_{\lambda_1}}{\tau_{\lambda_2}} = \frac{Q_{ext,\lambda_1}}{Q_{ext,\lambda_2}}. \tag{3.28}$$

Figure 3.2 illustrates this simple relationship for two different wavelengths as a function of effective particle radius. Mie theory for water spheres with a modified-gamma droplet distribution was used to compute the extinction efficiencies. Lookup-tables of extinction efficiency were computed as a function of effective radius for all instrument channels used in these retrievals in a similar fashion (see Appendix A).

After computing channel radiances corresponding to the initial-guesses, each parameter in $\vec{x}$ is perturbed by a small amount (typically 1%) and the entire synthetic measurement vector is recomputed. In this way, the Kernel matrix (Equation 3.8) is constructed from the perturbed and unperturbed forward model results. The new retrieval vector is computed according to Equation 3.20 and the associated errors (Δx) are computed by Equation 3.11. Following Marks and Rodgers (1993), the level of solution convergence is given by

$$\epsilon = \Delta\vec{x}^T \hat{S}_x^{-1} \Delta\vec{x} \ll n_x, \tag{3.29}$$

where n_x is the dimension of the retrieval vector, $\vec{x}$. This follows quadratic convergence, such that Δx is much smaller than the expected errors in the solution. The convergence

criterion for these retrievals was specified as

$$\epsilon \leq \frac{n_x}{10}. \tag{3.30}$$

When this criterion is met for all components of the retrieval vector, the master loop over retrieval iterations is terminated, the *a priori* matrix (Equation 3.21) is computed, and results for the single-pixel retrieval are stored. The program then clears memory and resets for the next pixel in the retrieval, or terminates upon completion.

Clearly, this retrieval procedure is computationally intensive at run-time in comparison to those employing a set of look-up tables. The latter applications, which yields batch-results instantaneously via simple interpolation of the measurement data to static grids, are applied most widely in operational settings. The dynamic method used here, which must call the forward model $\#_{iter} \times (\#_{chan} + (\#_{param} \times \#_{chan}))$ times for a single pixel, is tolerable to research applications and provides important retrieval diagnostic products unavailable to look-up table approaches. As this research seeks to assess the benefits of active sensors, the time required to attain these diagnostic parameters far outweighs any appeal to runtime brevity. The Rodgers method itself, however, can be applied in either case.

3.4 Summary

Reiterating the problem of retrieval theory applied here to cloud remote sensing, we seek to infer cloud properties given measurements of the thermal/shortwave radiation emitted/reflected by clouds embedded in the Earth/atmosphere system (the spectral intensity of which depending on the state of the system in a known way). As posed, retrieval theory involves two distinct elements: the "Forward Problem" and the "Inverse Problem." The forward problem uses a forward model (here, SLADRT) to generate virtual measurements that are representative of the physical instrument and are a function of the cloud parameters desired. The inverse problem (which invokes the optimal estimation approach described in this chapter) involves determining the best solution among possibly several that are consistent with the observations and must be chosen according to some

appropriate criteria (usually governed by the physics of the problem and included as *a priori* constraints to the solution). For the retrievals done in this research, the optimal estimation approach of Rodgers (1976) was selected. This method seeks to minimize a scalar cost function with respect to three primary components: (1) measurement error, (2) forward model error, and (3) *a priori* error. Each component is quantifiable–a powerful diagnostic feature of the Rodgers approach.

Chapter 4

CLOUD PROPERTY RETRIEVALS: A PHYSICAL BASIS

4.1 Introduction

While applications of retrieval theory in remote sensing are indeed diverse, all are founded under the same general premise: if the governing physics of the system can be cast into a mathematical system of equations whose unknowns comprise the parameters to be retrieved (i.e., a sound forward model based on all the relevant system variables), then the problem reduces to the ability of remote sensor measurements to span uniquely the column (solution) space of the system. For example, to solve three unknowns requires a system of three *independent* equations (i.e, no equation can be represented as a linear combination of the other two). Insodoing, the appropriate combination of system variables resulting in agreement in all measurements yields the retrieved result. Selection of the appropriate radiometer channels/channel-combinations at which the desired cloud parameters are sensitive is an example of casting the system equations mentioned above.

In addition to developing a physical basis for why certain cloud properties can be retrieved, this chapter introduces the two primary passive remote sensing instruments used in this research to this end: the Geostationary Operational Environmental Satellites (GOES) imager and the Colorado State University (CSU) Scanning Spectral Polarimeter (SSP). These instruments have fixed spectral channels of variable bandwidth spanning the visible (VIS) to infrared (IR) wavelengths (roughly 0.4 to 12.0 μm). Using the governing physics describing the electromagnetic behavior of cloud particles, gases/aerosols, and the surface, the question "what parameters are retrievable from these instruments" is addressed. Those relationships providing parameter sensitivity (and minimal uncertainty contributions from the unretrievable system variables) shall comprise the system equations

Cloud Property Retrievals			
Investigator(s)	Cloud Type	Retrieved	Instruments/Wavelengths Used
Platt et al. [1979]	Cirrus	α, ϵ, τ	SMS-2/GOES VIS, 10-12μm
Szejwach [1982]	Cirrus	T, ϵ	METEOSAT 6.5μm, 11.5μm
Prabhakara et al. [1988]	Cirrus	τ, r_{eff}	IRIS 10.6μm, 12.8μm
Liou et al. [1990]	Cirrus	τ, ϵ	NASA ER-2 Radiometer 6.5μm, 10.5μm
Minnis et al. [1990]	Cirrus	τ, ϵ	GOES/AVHRR 0.65μm, 11.5μm
Stone et al. [1990]	Cirrus	τ, r_{eff}	GOES/AVHRR 3.7μm, 10.9μm, 12.7μm
Wielicki et al. [1990]	Cirrus/Altocumulus	phase, r_{eff}	LANDSAT 0.83μm, 1.65μm, 2.21μm
Minnis et al. [1993]	Cirrus	τ, Z	AVHRR/GOES 0.65μm, 11.5μm
Ou et al. [1993]	Cirrus	τ, T, D_{eff}	AVHRR 3.7μm, 10.9μm
Ou et al. [1995]	Cirrus	T, D_{eff}, τ	AVHRR 3.7μm, 10.9μm
Curran and Wu [1981]	Lee-Wave	τ, phase, r_{eff}	Skylab Radiometer 0.83μm, 1.61μm, 2.125μm, 11.4μm
Kleepsies [1995]	Stratocumulus	r_{eff}	GOES 3.9μm, 11.0μm
Rawlins and Foot [1990]	Stratocumulus	τ, r_{eff}	Multi-Channel Radiometer (7 channels in VIS and NIR)
Nakajima et al. [1991]	Stratocumulus	τ, r_{eff}	NASA ER-2 Radiometer 0.75μm, 1.65μm, 2.16μm
Minnis et al. [1992]	Stratocumulus	τ, Z, T, r_{eff}	GOES 0.65μm, 11.5μm
Nakajima and Nakajima [1995]	Stratocumulus	τ, r_{eff}	AVHRR 0.65μm, 3.7μm, 10.9μm
Platnick and Valero [1995]	Stratocumulus	τ, r_{eff}	AVHRR 0.65μm, 3.7μm
Arking and Childs [1985]	(General)	τ, CF, T, r_{eff}	AVHRR 0.65μm, 3.7μm, 11.0μm
Twomey and Cocks [1989]	(General)	τ, r_{eff}	0.75μm, 1.0μm, 1.2μm, 1.6μm, 2.25μm
King et al. [1992]	(General)	τ, r_{eff}, P_{top}, T	MODIS (36 channels 0.65μm-14.24μm) (proposed)
Smith et al. [1996]	(General)	τ, D_{eff}, Z	GOES 3.9μm, 10.7μm, 12.0μm
Heidinger and Stephens [1998]	(General)	τ, P_{top}, g, δp	0_2 A-Band 0.76-0.77μm, $\delta\lambda \sim 2.0E-04\mu$m

Table 4.1: A selected collection of passive remote sensor cloud optical property retrieval approaches described in the literature. Cloud property symbols are: τ = optical depth, r_{eff} = effective particle radius (water), D_{eff} = effective ice crystal diameter, ϵ = cloud emissivity, α = albedo, P_{top} = cloud top pressure, T = cloud temperature, Z = cloud height, phase = (ice/water), CF = cloud fraction, g = asymmetry parameter, and δp = pressure thickness.

for the retrieval. Additionally, this chapter discusses the uncertainty associated with the instruments and the forward model. This leads to the formulation from components of the Rodgers uncertainty matrices described in Chapter 3.

4.2 Passive Radiometer Instruments

Extensive work has been done in the area of passive-sensor cloud property retrievals. Table 4.1 lists a by no means exhaustive collection of these efforts. The NASA CERES program incorporates many of the algorithms developed in these studies in its operational retrieval package. Daytime retrievals take advantage of solar reflection measurements which help to constrain solutions to optical depth and particle size and night-time retrievals (which rely only upon emission information from the cloud and atmosphere system) can pose comparatively larger problems to passive remote sensor retrievals (e.g., cloud location and emissivity become critical players in measurement sensitivity). Uncertainties attached to these retrieval approaches, however, could be reduced considerably simply by including

cloud level data as provided by an active sensor. It is this point that this work seeks to both show and quantify. Instead of seeking out a novel scheme to add to the list, this research builds upon established passive-only retrieval techniques by including cloud height information provided by active sensors to the *a priori* parameters specified in the forward model.

The retrievals presented in this research center on passive radiometer measurements. These devices are equipped to measure the flux (or *irradiance*, (W m^{-2}) of photons impinging a finite detector surface characterized by a spectral bandwidth and filter response function. The solid angle (Ω) subtended by the remote scene at the detector is given by

$$\Omega = \frac{A}{R^2}, \tag{4.1}$$

where A is the area of the scene projected onto the plane orthogonal to the detector's line-of-site and R is the geometric distance between the detector and scene. With A sufficiently small and R sufficiently large, an approximation to the field-invariant quantity intensity (or *radiance*, W m^{-2} sr^{-1}) is obtained. In practice, calibration coefficients computed pre-launch relate the digitized voltage counts to spectral radiance (W m^{-2} sr^{-1} μm^{-1}). This becomes problemmatic in operation as these coefficients drift with time (e.g., owing to degradation in amplifier gains or contamination of the optical assembly) from their pre-launch values. To produce meaningful quantities, the calibration must be known as accurately as possible, and the remaining uncertainty must be included in the forward estimate of the measurments. Radiometer instruments are termed "passive" because they do not interact physically with the medium they sense (as would a radar or lidar). The measured radiation can be thought of as a convolution of all emitting/reflecting sources and virtual sources in the detector field of view. This section details the two primary passive radiometers used for retrievals of this study: GOES (on the satellite platform) and the SSP (flown upon aircraft and unmanned aerospace vehicle (UAV) platforms).

4.2.1 The GOES Imager

The GOES program, run under the auspices the NOAA, launched the first of its series in 1975. The first satellite busses featured a Visible and Infrared Spin-Scan Radiometer (VISSR) instrument to image the Earth's surface, atmospheric moisture, and

cloud cover. The VISSR Atmospheric Sounder (VAS) instrument was first included on GOES-4 in 1981. Operation was problematic, as the imager and sounder could not be operated simultaneously and the spin-scan stabilization approach offered an Earth-view only 5% of the time (compromising signal-to-noise ratios (SNR) and the quality/resolution of sounding/imager data). Motivated by the desire to eliminate these problems, a next-generation GOES series was implemented (Menzel and Purdom, 1994). The first of the series, GOES-8, featured over 9 year's worth of research and development improvements, including

- Independent imager and sounder operations.
- Earth-oriented, three-axis stabilization design affording for better pixel registration (navigation).
- Improved imager resolution and SNR.
- More accurate temperature and moisture soundings.
- New and more efficient data acquisition protocol.

Patterned after the NOAA AVHRR instruments, the next-generation GOES imager is a filter radiometer (response is dependent on the amount of radiation received within a pass-bands of the filters) which uses a 12.25-in diameter aperture with dichromatic beam splitters to divide the scene radiation into five spectral pass-band channels at 0.55-0.75 (Ch. 1, visible), 3.8-4.0 (Ch 2., shortwave IR), 6.5-7.0 (Ch. 3, water vapor), 10.2-11.2 (Ch. 4, longave IR), and 11.5-12.5 (Ch. 5, water-vapor window) microns across the optical spectrum. A scanning instrument, the GOES imager uses a dual-axis system to perform East-West horizontal scans followed by North-South steps between scan lines. The system completes a full-Earth-disk image in roughly 25 minutes. Smaller area scans (e.g., of the continental United States (CONUS)) which require less time are included in the GOES schedule, and 3-minute "rapid-scan" mode is operated during priority-interrupt periods focusing on a particular mesoscale event. GOES pixel resolution for data used in this study are 1-km for visible imagery and 4 km for IR (4×8 km for the water vapor channel).

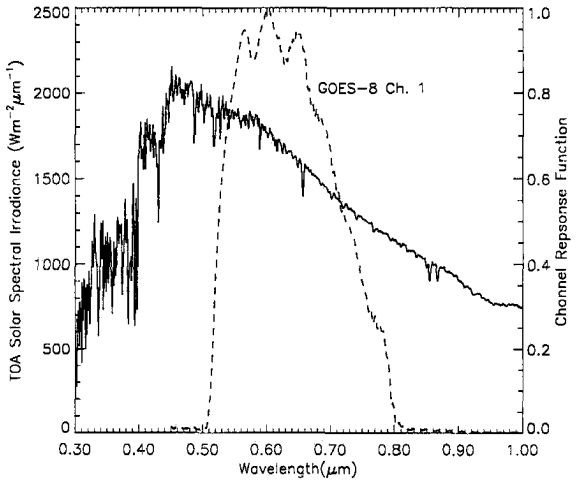

Figure 4.1: GOES-8 Channel 1 (0.65 μm central wavelength) filter response with TOA downwelling Solar Spectral Flux data.

Cloud heterogeneity exists well below these scales, and must be taken into consideration when conducting retrievals these pixel data.

GOES Channel 1

GOES Ch. 1 is situated near the heart of solar emission with the upper-limit of its filter function falling off far short of the near-infrared (NIR) spectral regime where signal contributions from terrestrial/atmospheric emissions become significant. Figure 4.1 shows the positioning of this bandwidth with respect to the TOA downwelling direct solar flux (unattenuated/diffused by the Earth's atmosphere). It is located in an atmospheric window, such that absorption by the main gaseous constituents of the Earth's atmosphere (see Chapter 2) is minimal. Being insensitive to thermal radiative sources, Ch. 1 is used for day-time imaging exclusively. Temporal loops of Ch. 1 imagery on the nightly news weather segments are the most familiar interface of these data to the general public. Because most clouds have higher albedos than the underlying surface (with the exception of snow/ice backgrounds), measurements of solar reflection by clouds is useful in identifying clouds and organized cloud systems at all scales down to the pixel resolution. It will be shown that Ch. 1 reflection can also be used as a proxy to cloud optical depth.

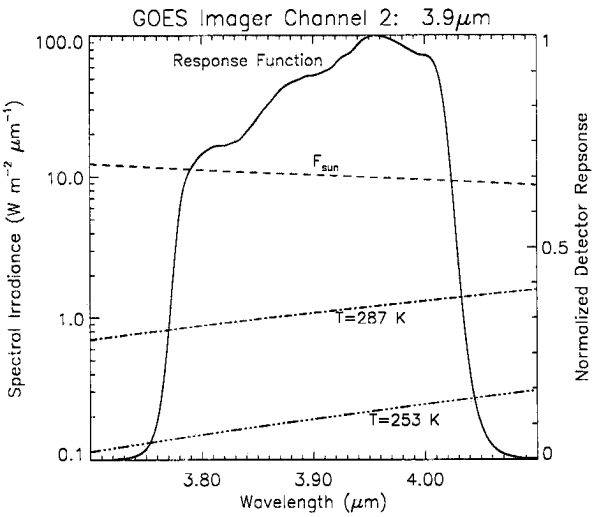

Figure 4.2: GOES-8 Channel 2 (3.9 μm central wavelength) filter response with TOA downwelling Solar Spectral Flux data.

Bandweighting is performed in the forward model simulations of Ch. 1 measurements in order to capture the variability of the solar spectral flux across the filter's pass-band.

GOES Channel 2

The spectra of solar and terrestrial emissions are considered generally as decoupled from one another, such that shortwave (reflection) and longwave (emission) radiative properties as measured by satellite are discussed largely as separate entities. Cursory examination of the Planck emission spectra for blackbodies with temperatures of 5780 °K and 253 °K (approximate figures for the sun and the earth/atmosphere, respectively) reveals the approximation to hold quite well to first order, with only a small region of overlap between the two curves in the region of Ch. 2. For detector channels in spectral bands well outside of this region (e.g., visible imagery at 0.65 μm or IR imagery at 10.7 μm), the concerns for potential contamination by either thermal emission or solar reflection are minimal to negligible. However, an instrument whose detector passband is situated in the region of crossover possesses the inherent capability of detecting both solar reflection and thermal emission simultaneously.

The pass-band of GOES Ch. 2 is located in a special window portion of the spectrum that is sensitive in comparable magnitude to both emissions from the Earth/atmosphere system and reflection of solar radiation. Figure 4.2 indicates that the reflected downwelling (assuming a range of surface/cloud albedos from 0.0 to 0.5 and a solar zenith angle of 0°, for example) spectral solar flux is roughly the same order of magnitude as typical upwelling emissive fluxes (the 287 °K blackbody curve corresponds to a global mean surface temperature, while the 253 °K curve corresponds to the global mean radiating temperature of the Earth/atmosphere system in radiative equilibrium). It is for this reason that clouds in Ch. 2 usually appear brighter (warmer) than the underlying surface during the day and darker (cooler) at night (demonstrating properties of both the visible and IR channels). The interest in this channel arises from the fact that solar reflection in the NIR is a strong function of cloud particle sizes. For this reason, many attempts to decouple the thermal and solar components of the day-time 3.9 μm imagery have been made to variable levels of approximation (e.g., Coakley and Davies (1986), Ou *et al.* (1993), Rao *et al.* (1995), Kleepsies (1995), and Nakajima and Nakajima (1995)). An assessment of this problem using total solar eclipse data as a means to decoupling these radiative components is outlined by Miller (1999).

GOES Channel 3

The bandwidth of GOES Ch. 3 is situated within a strong water vapor absorption region (refer back to Figure 2.5). The water vapor may be used to detect atmospheric motions (e.g., circulations, regions of rising/subsiding air) in cloud-free regions invisible to the other channels (all other GOES imager channels are positioned in atmospheric windows). The channel has also proved useful for the detection of cirrus clouds from space using a bi-spectral approach (the *shape* of cirrus clouds will appear the same in both Ch. 1 and Ch. 2, as these clouds are above the majority of the obscuring water vapor). In this study, this channel was used along with the method of Szejwach (1982) as a passive-only method to determining cirrus cloud heights (Chapter 5 outlines this approach in detail).

GOES Channels 4 and 5

GOES channels 4 and 5 comprise the "split-window," so-called because while both channels exist in an atmospheric window (located between strong water vapor and CO_2 absorption bands), there is an enhanced absorption by liquid and ice at 12.0 μm compared to at 10.7 μm. Sometimes Ch. 5 is referred to as a "dirty window" for this reason (although all window channels are subject to some amount of gaseous absorption). The size parameter, defined as

$$\chi = \frac{2\pi r}{\lambda} \tag{4.2}$$

associated with (upwelling thermal) radiation in Ch. 4 is larger than in Ch. 5, resulting in a slightly higher forward scatter component of the phase function Combining these differential optical effects result in positive Ch. 4 - Ch. 5 brightness temperature difference residuals which can be used for detection of thin cirrus, for example. A bi-spectral method following Prabhakara *et al.* (1988) employing the split-window channels is included in the discussion of optical parameter sensitivities to follow.

4.2.2 The SSP

The scanning spectral polarimeter was designed and built by Graeme Stephens and Bob McCoy at Colorado State University. A detailed discussion of instrument characteristics, calibration procedures, error analysis, and sample results are provided elsewhere by Stephens *et al.* (1999) and Ries and Stephens (1995). Figure 4.3 shows the first-generation SSP instrument outer chassis, with detector head assembly on the right. To perform spectral scanning, it utilizes a rotating optical bandpass filter to measure polarized/unpolarized radiances and fluxes over a spectral region spanning [0.4,1.1 μm] (first and second generations) and [0.4,4.0 μm] (third generation). As such, retrievals involving SSP data are applicable to day-time observations exclusively. The half-bandwidths of the channels are narrow, on the order of 20 nm. In normal operation, light passes through the optics head and is focused onto a rotating circular variable filter and then upon a six detector assembly (flux, unpolarized radiance, and four polarized radiances: parallel,

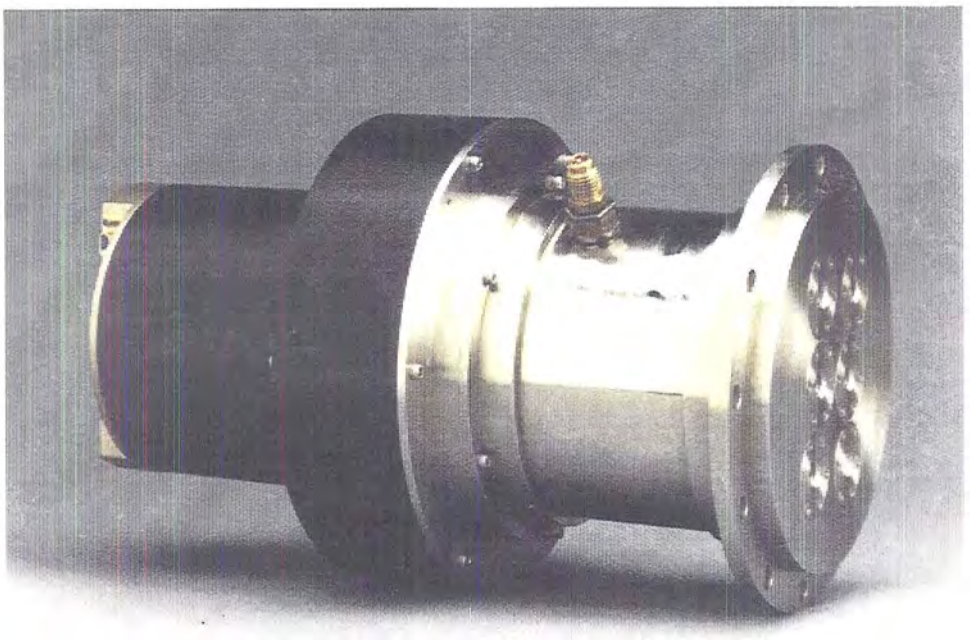

Figure 4.3: The Scanning Spectral Polarimeter (SSP) instrument (first generation) designed and built at Colorado State University.

perpendicular, right-hand circular, and left-hand circular). For this research, only the unpolarized radiance field (detector 3, with measured half-angle field of view of 20 mrad) was used. Unfortunately, the SSP suffers a lack of sensitivity (not enough energy is collected) to solar reflection in the NIR. The first atmospheric window channels that offer sensitivity to cloud particle size are near 1.5 μm and 2.0 μm. This necessitated an assumption on r_{eff} in order to retrieve optical depth (and an error attached to this assignment). Details of retrieval case studies involving the SSP are given in Chapter 5.

4.3 Which Cloud Parameters are Retrievable?

Retrieval of atmospheric properties from multi-spectral passive radiometer data requires a knowledge of their spectral behavior and selection of appropriate channels to exploit regimes of high sensitivity. For the case of clouds, whose optical effects are tied strongly to altitude, the most useful bandwidths to retrievals are those in atmospheric windows or in a region dominated by a well-mixed (quantifiable) absorbing gases like O_2 or CO_2. For the retrievals presented in this work, only atmospheric window channels are

used. In this way, the dominant processes responsible for spectral variation in reflectance or emittance are associated with the optical properties of the cloud and the underlying surface alone. Here we discuss some of these spectral properties in the context of retrieval theory.

4.3.1 The scattering/absorption spectrum

The fact that absorption, scattering, and emission properties of clouds vary with wavelength motivates the use of multi-spectral approaches in retrievals; each channel providing different information about the same cloud. The complex spectral behaviors of water and ice cloud single-scatter albedo and asymmetry parameter (characterizing the absorption and scattering properties of the medium) are illustrated in Figures 4.4-4.5. To produce these figures, Mie theory for spheres was applied to a modified-γ size distribution with a dispersion factor of 2. Revealed in these figures are the subtle differences between the optical properties of water and ice clouds owing to differences in the refractive index which are exploited in cloud detection algorithms. Scattering behavior in the split window channels is a strong function of particle size, and absorption is negligible ($\omega_o = 1.0$) for both cloud phases at visible wavelengths.

Illustrated in Figures 4.6-4.7 are channel cross-sections of Figures 4.4-4.5. The asymmetry parameter is observed to be a strong function of effective radius for all wavelengths as larger particles (with respect to the incident wavelength) scatter energy preferentially in the forward direction. The single-scatter albedo shows more variability with wavelength, ranging from non-absorbing at the visible wavelengths to strong absorption in the NIR and IR. The visible (0.65 μm) reveals only a very small sensitivity to effective radius through the asymmetry parameter. It may be concluded from these figures that reflection of sunlight in a NIR channel (e.g., GOES Ch. 2) is a much stronger function of effective radius than in Ch. 1. In general, the greatest sensitivity of these optical parameters is for effective radii less than 40 μm.

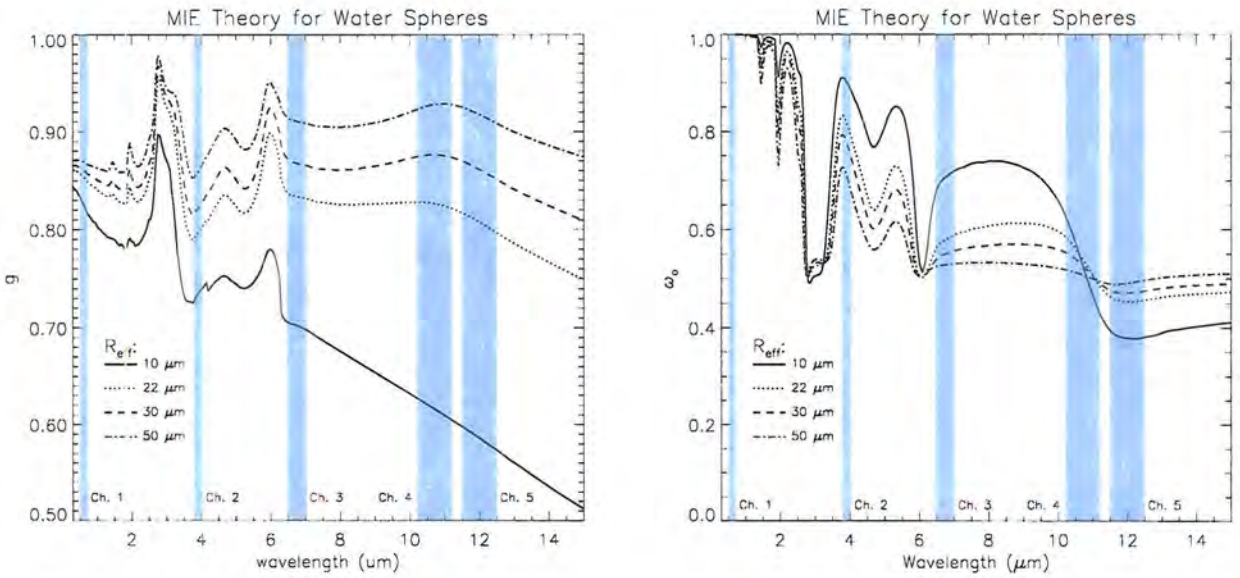

Figure 4.4: Spectral dependency of cloud optical parameters based on Mie theory for water spheres and a modified-γ size distribution. GOES imager channel bandwidths are indicated. Left panel: asymmetry parameter, Right panel: single-scatter albedo.

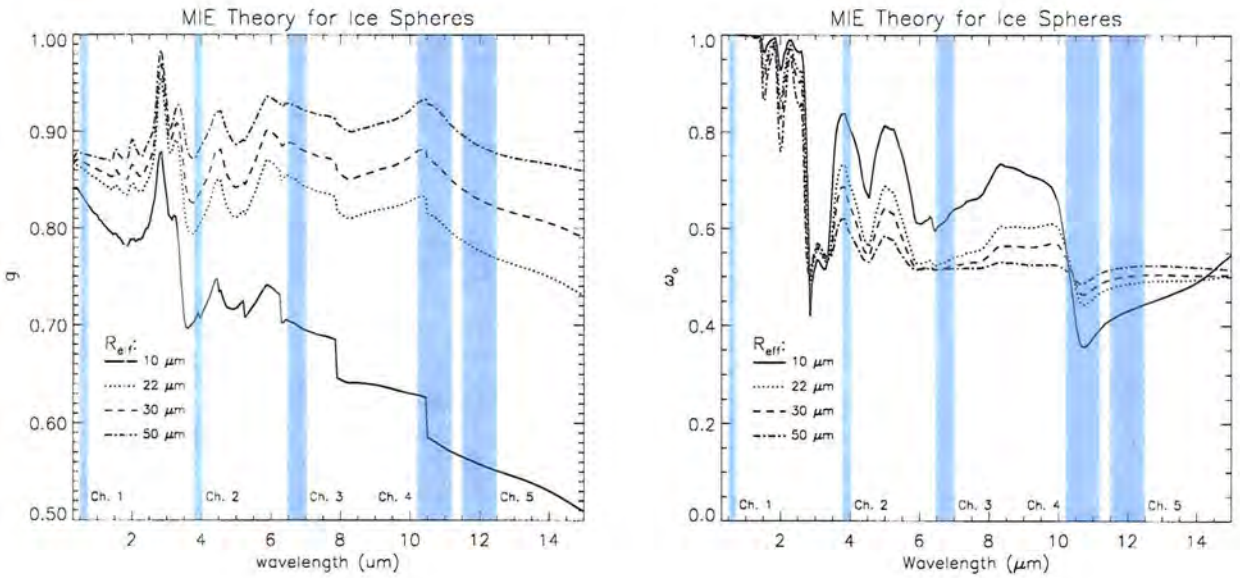

Figure 4.5: Same as above but for ice clouds.

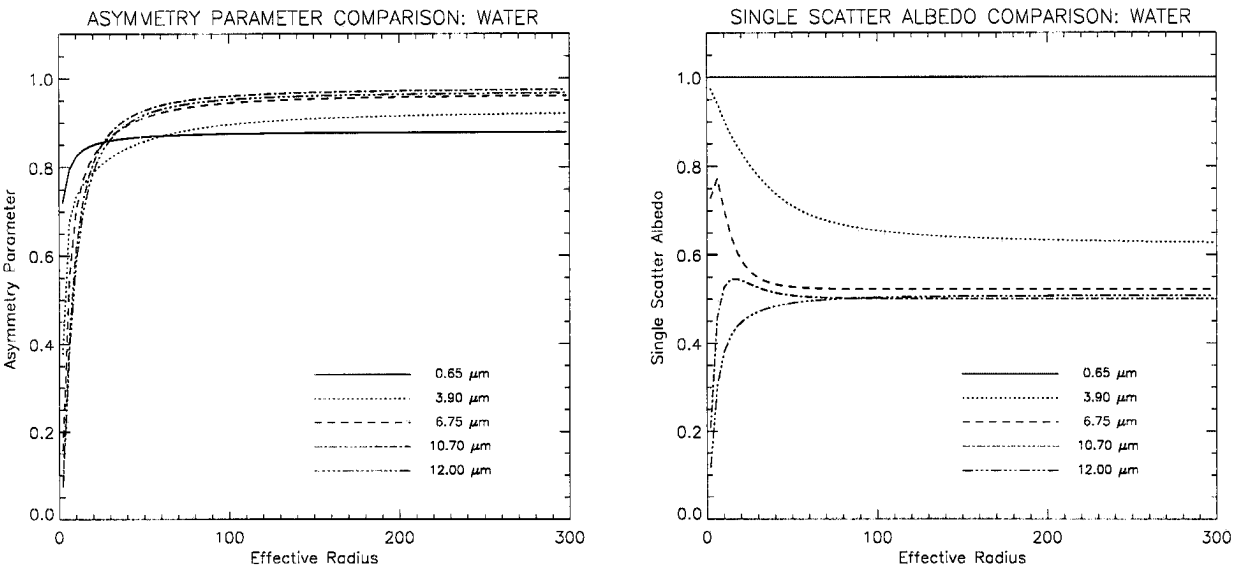

Figure 4.6: Effective-radius-dependent cloud optical properties shown for GOES imager channels based on Mie theory for water spheres in a modified-γ size distribution. Left panel: asymmetry parameter, Right panel: single-scatter albedo.

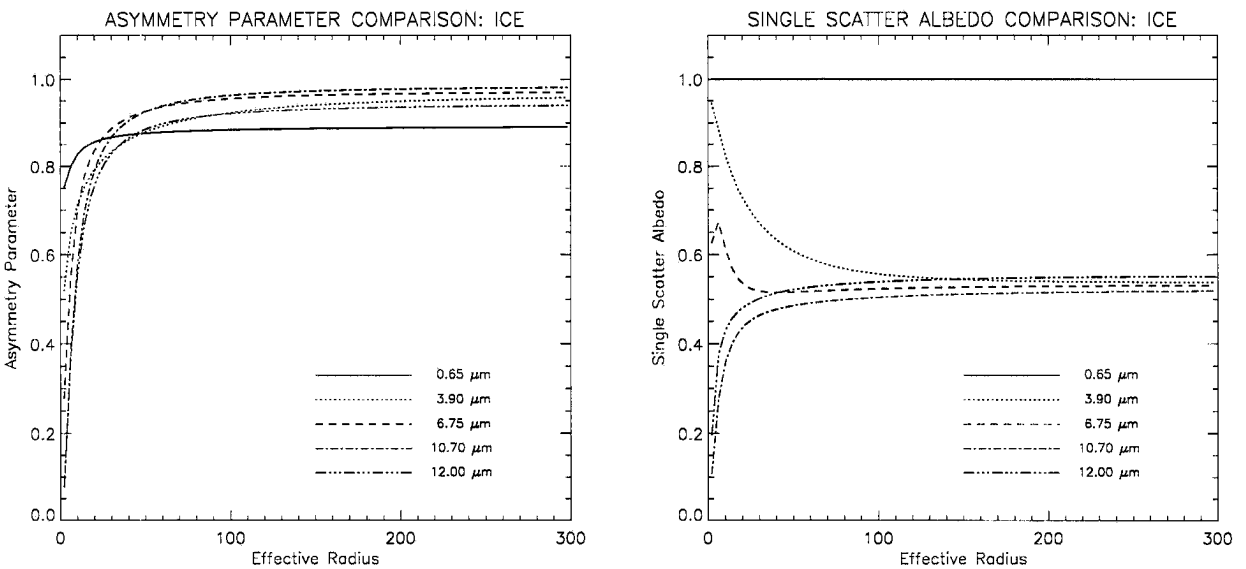

Figure 4.7: Same as above but for ice clouds.

4.3.2 Across-band variability of cloud optical properties

GOES-8 channel sensitivities to asymmetry parameter, single-scatter albedo, and the similarity parameter defined as

$$s = \left[\frac{1-\omega_o}{1-g\omega_o}\right]^{1/2} \tag{4.3}$$

are shown for Mie calculations of water and ice clouds and for a variety of effective radii. The similarity parameter describes the condition under which two clouds of different optical properties (ω_o, g) will produce identical reflection behavior (multiplicity of solution). It is seen that absorption at Ch. 1 is negligible, and the asymmetry parameter (related to the scattering phase function and tied ultimately to the particle size distribution) is not a strong function of effective radius. In stark contrast, the NIR and IR channels all display marked absorption and sensitivity to particle size. Of particular note is the decrease in single-scatter albedo across the Ch. 4 band (as water absorption strengthens toward Ch. 5) as well as the slightly higher asymmetry parameters in Ch. 4 owing to effective size parameter differences as explained above. The between-channel differences of these optical properties forms the basis for bi-spectral retrieval techniques using GOES imager data.

4.3.3 Multi-spectral retrieval approaches

An important determinant in the selection of an appropriate retrieval method is whether or not the sun is illuminating the clouds. The two main paradigms of retrieval problems are those of reflection and those of absorption/emission (with a "grey area" in the day-time NIR band). The methods employed most commonly in retrieval work (and comprising the theoretical basis for the cloud retrievals performed in this research) are demonstrated here for both cases.

Daytime retrieval approaches

In general, the cloudy-sky radiance measured by passive satellite radiometers is a function cloud microphysics, cloud optical depth, the temperature profile, and the solar/observer geometry. Sagan and Pollack (1967) and Hansen and Pollack (1969) are credited with establishing the precedent for using spectral variation of cloud reflectivity as

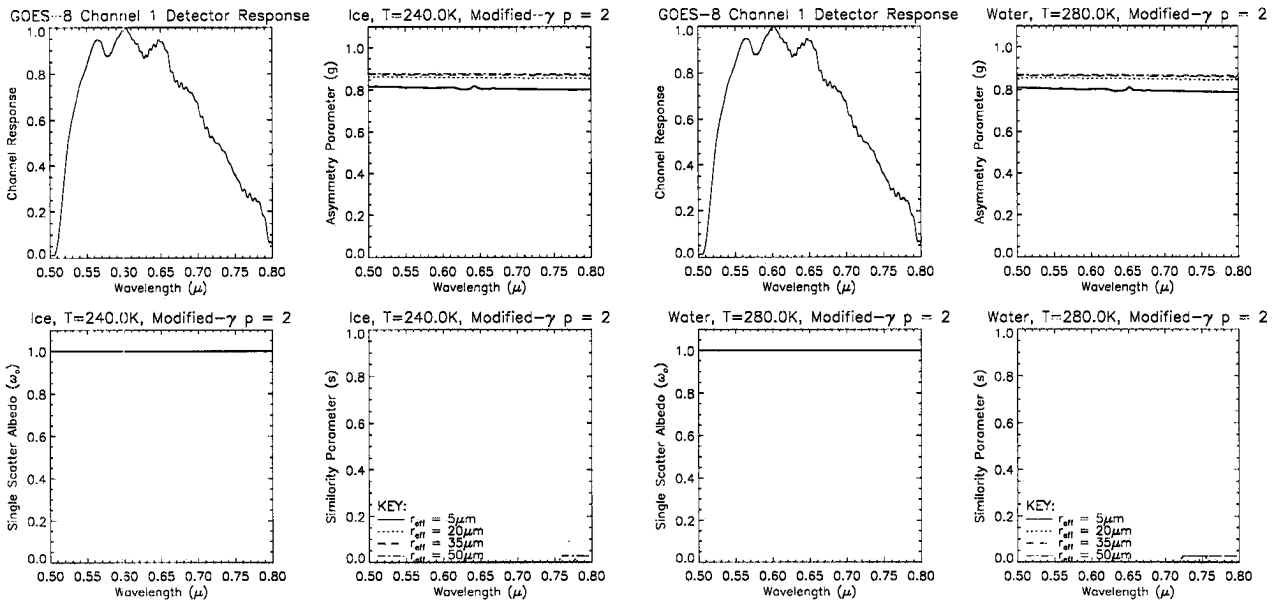

Figure 4.8: GOES-8 Channel 1 (0.65 μm central wavelength) band sensitivity for ice and water clouds according to Mie theory

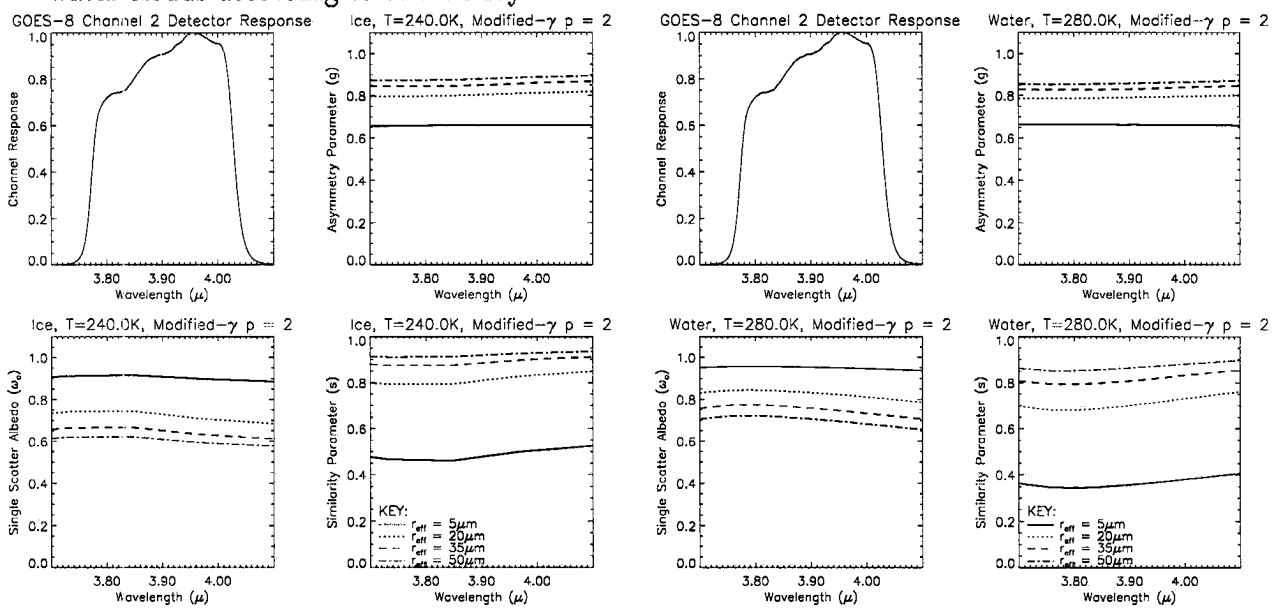

Figure 4.9: GOES-8 Channel 2 (3.90 μm central wavelength) band sensitivity for ice and water clouds according to Mie theory

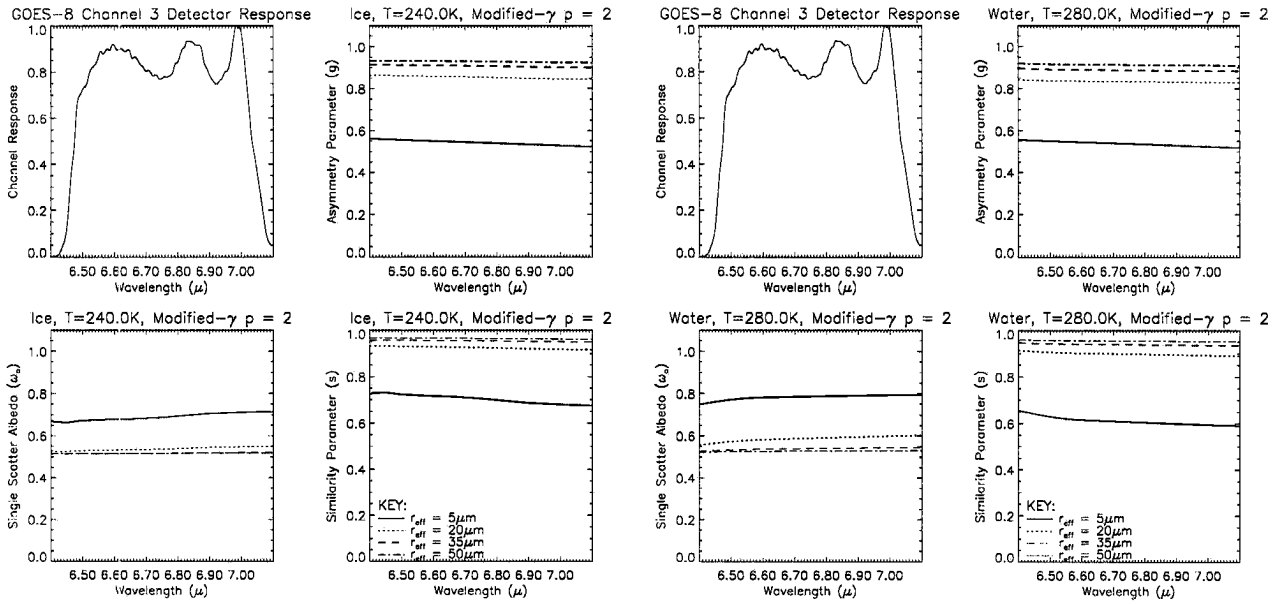

Figure 4.10: GOES-8 Channel 3 (6.7 μm central wavelength) band sensitivity for ice and water clouds according to Mie theory

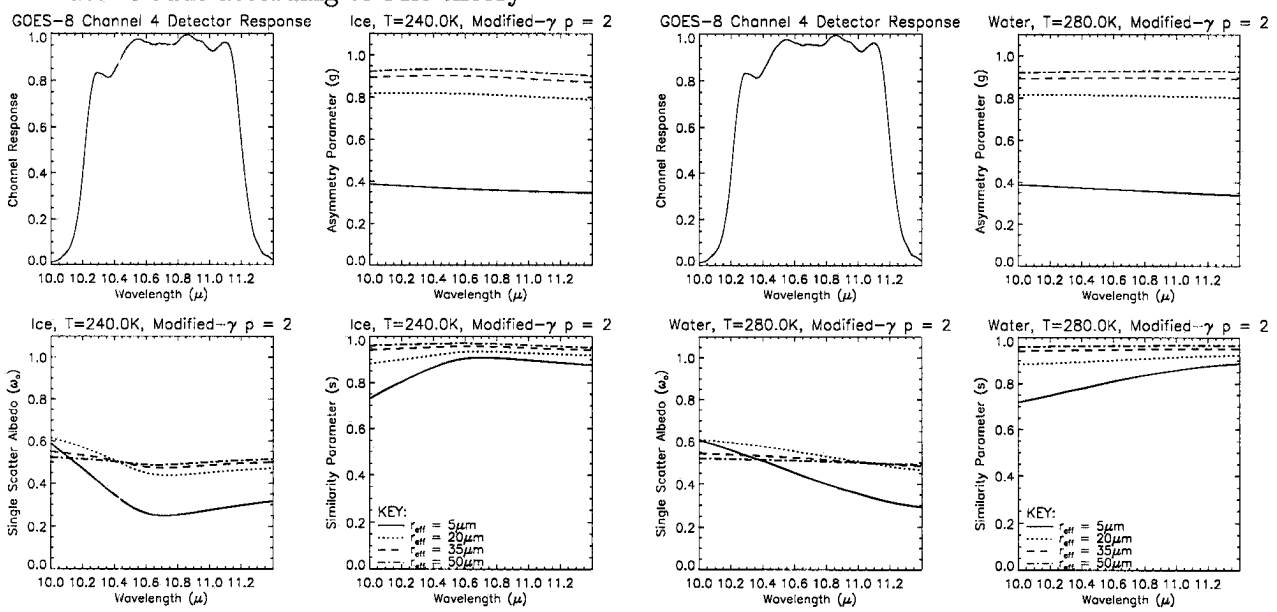

Figure 4.11: GOES-8 Channel 4 (10.7 μm central wavelength) band sensitivity for ice and water clouds according to Mie theory

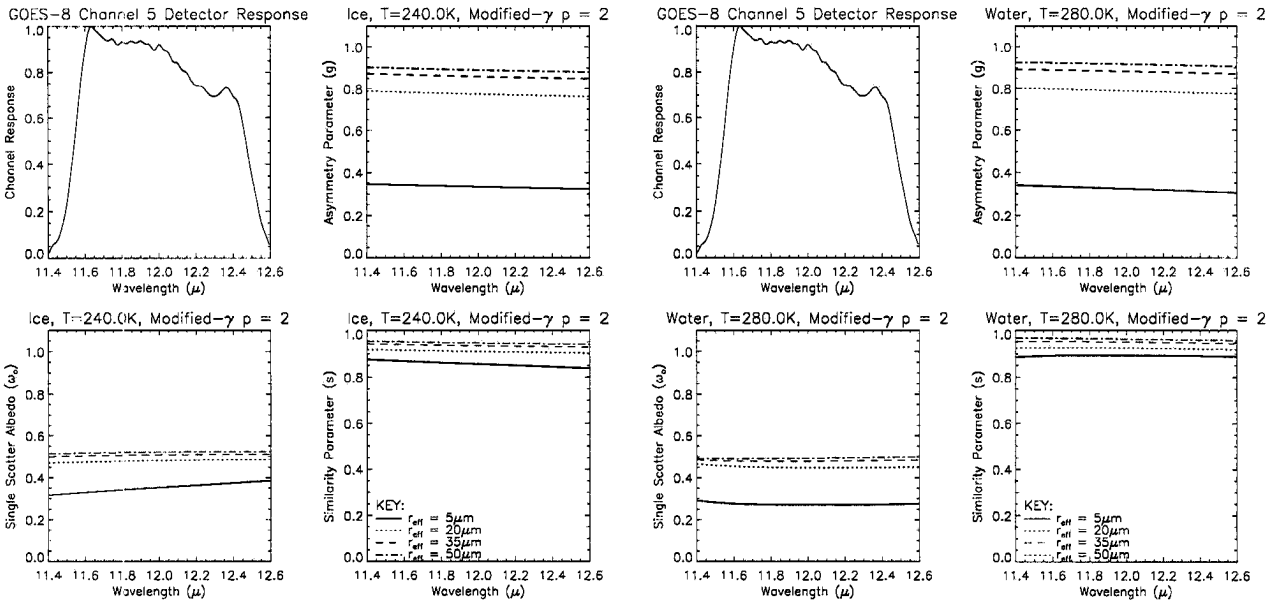

Figure 4.12: GOES-8 Channel 5 (12.0 μm central wavelength) band sensitivity for ice and water clouds according to Mie theory

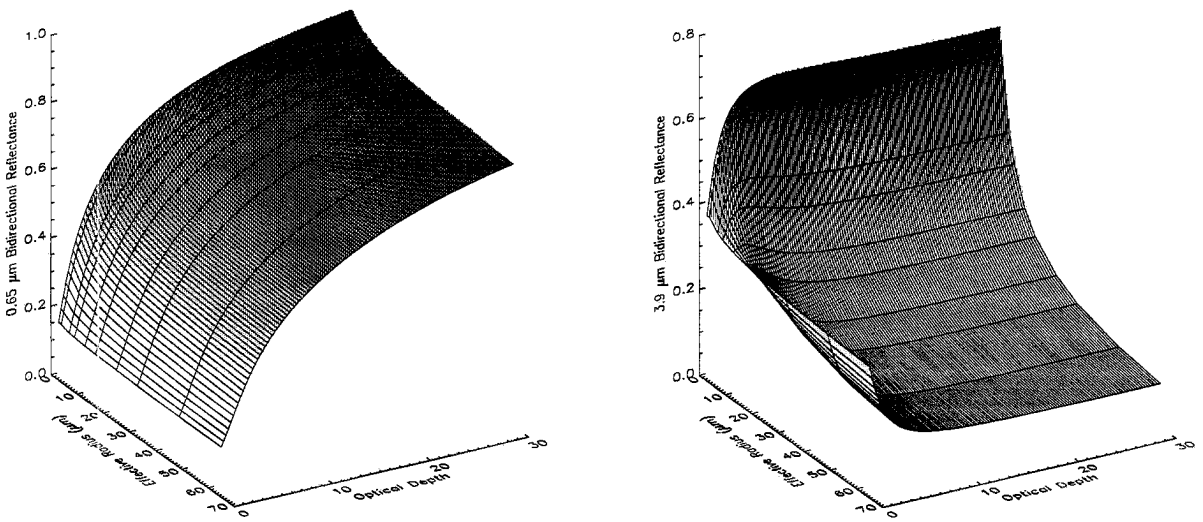

Figure 4.13: GOES Ch1 (0.65 μm) and Ch2 (3.9 μm) cloud parameter sensitivities for a 1km-thick water cloud ($\mu_\circ = 0.6$, $\mu = 0.707$, $\phi - \phi_\circ = 0.0$).

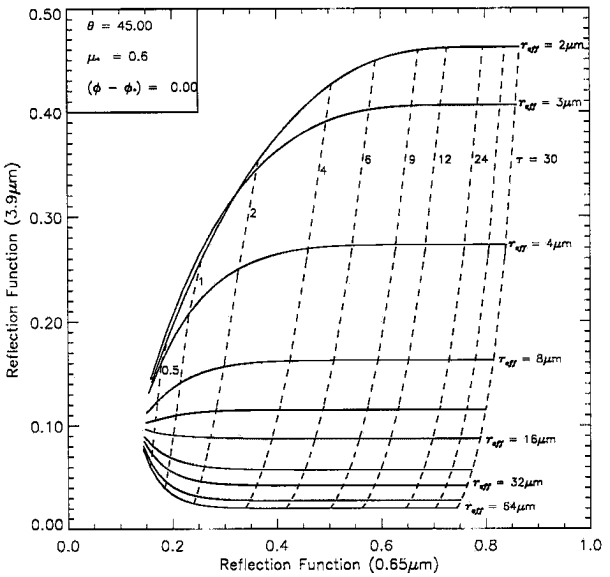

Figure 4.14: The bi-spectral retrieval approach. (Following Nakajima and King, (1990))

a means to infer particle phase, size, and total cloud optical depth. At wavelengths where water absorption is strong, clouds with larger droplet size distributions exhibit greater extinction due to absorption and a stronger tendency for forward scatter; resulting in a reduced reflectivity. Wavelengths at which water absorption is weaker are less sensitive to changes in the droplet size distribution and more sensitive to extinction due to scattering processes (i.e., droplet *number* concentration according to Equation 3.27; recall the relative invariant behavior of g and ω_o as a function of r_{eff} in Figures 4.6-4.7). These relationships are best illustrated by forward model simulations shown in Fig. 4.13. Plotted are iso-surfaces of bidirectional reflectance, given by

$$R(\vec{\xi}, \vec{\xi_o}) = \frac{\pi I(\vec{\xi})}{(F_o \, cos\theta_o)} \tag{4.4}$$

where $\vec{\xi}$ and $\vec{\xi_o}$ define the directions associated with incident (solar) and reflected (observed) radiation, and F_o is the incident solar flux density. A nearly orthogonal relationship is observed between the two surfaces over a large range of the parameter space, with the exception of optically thin and small-particle clouds where sensitivity to both the cloud droplet size distribution and number concentration exist.

These kinds of bi-spectral relationships have been exploited by a handful of researchers in satellite remote sensing. The specific approach taken is determined largely by whether

or not solar reflection information is available in the measurements. The bidirectional reflection function as defined in Equation 4.4 is often used to convert a single satellite radiance to an "equivalent isotropic reflectance" of the scene. This quantity is used by Nakajima and King (1990) to formulate a gridded retrieval approach for τ and r_{eff} as shown by SLADRT forward model simulations in Fig. 4.14. The measurement orthogonality inferred from Fig. 4.13 is clearly evident in these grids. The shape (and hence quality) of this relationship changes with the solar/viewer geometry.

Nighttime retrieval approaches

Nighttime passive-sensor-only retrievals must rely exclusively upon IR measurements of atmospheric thermal emission (the TOA downwelling cosmic term representing deep-space emissions at roughly 2° K is neglected). Spectral absorption by atmospheric gases and aerosol (which are not always uniformly mixed throughout the profile, especially in the case of aerosol) complicates satellite measurements in some channels by absorbing and then re-emitting at their ambient temperatures. In this way, a passive radiometer measurement represents a convolution of all active emitters in the profile. Upwelling emissions from the surface and lower (warmer) atmosphere often transmit through optically thin clouds, resulting in a stronger satellite radiance measurement not representative of the cloud's ambient temperature. In some cases the measured temperature is to be used in conjunction with a temperature profile to place the cloud at a given altitude. Implicit to this assumption is that the cloud's optical thickness is sufficient to extinguish all upwelling emissions, and that the emissivity of the cloud itself is near unity. Of course, neither assumption must necessarily hold, and the credibility of such retrievals must be held in question.

Methods do exist to approximate cloud top altitudes based on departure from the emission profile of a well known atmospheric gas; a prominent example being the CO_2 slicing technique (Menzel *et al.*, 1983; Wylie *et al.*, 1989; Wylie *et al.*, 1994). While useful in many instances, the cost incurred by uncertainty (on the order of kilometers), no indication of cloud physical thickness and the inability to resolve multiple-layered cloud profiles compromises the technique . Clearly, an *a priori* knowledge of the exact location

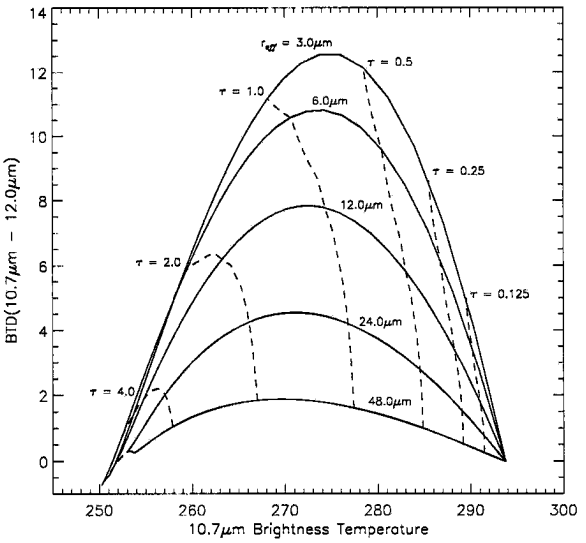

Figure 4.15: Infrared-only measurements can provide limited information on τ and r_{eff} (Following Prabhakara et al., (1988)).

of a cloud in the profile would benefit night-time retrievals immensely and enable an unambiguous estimate of optical depth.

Infrared retrievals employ channel-differencing methods have attempted to circumvent the dilemmas associated with to the night-time retrieval. Prabhakara *et al.* (1988) adapt the findings of Inoue (1985) to investigate the retrievability of optically thin clouds in the IR split window (GOES Ch. 4 and 5) by taking advantage of the differential extinction properties (for small particles, the extinction in Ch. 5 is roughly twice as large as in Ch. 4, see Bohren and Huffman (1983)) at these wavelengths. Figure 4.15 is a forward model-generated example of this technique, which offers sensitivity to cloud optical depth up to about $\tau \approx 4.0$.

In another application of spectral differencing, Stone *et al.* (1990) take advantage of the differential absorption ($\omega_o(\lambda)$) properties of cloud particles at wavelengths equivalent to GOES Ch. 2, 4 and 5. Figure 4.16 is a forward model-generated illustration of the Stone *et al.* (1990) approach. Because Ch. 2 is sensitive to both thermal and solar radiation, their technique is applicable to both day-time and night-time retrievals. The range of retrievable τ in the night-time retrievals is similar to the Prabhakara *et al.* technique,

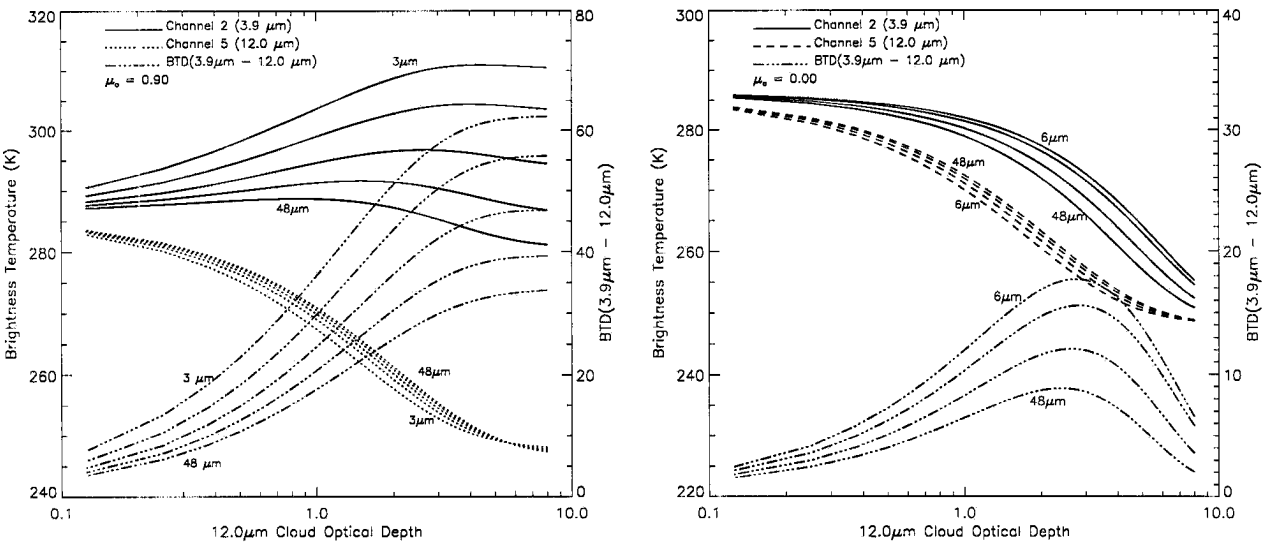

Figure 4.16: Gaining sensitivity to particle size from channel differencing (Following Stone et al., (1990)). Daytime and night-time simulations are shown in the upper and lower panels, respectively.

while the day-time retrievals take advantage of the reflected solar beam to provide additional sensitivity to both τ and r_{eff}. As a technical note to the latter day-time case, the "brightness temperature" shown at 3.9 μm is enhanced by contributions from the reflected solar intensity, and no longer represents an emitting temperature of the cloud particles. In their studies, both Stone *et al.* (1990) and Prabhakara *et al.* (1988) make implicit use of *a priori* cloud height information to supplement the forward models in their retrievals.

4.4 Forward Model Uncertainty and Sensitivity

As discussed, an important product of the Rodgers retrieval is the quantification of errors associated with the forward model, measurements, and the *a priori* constraints. These errors are the fundamental drivers of the retrieval; defining both the quality and physical credibility of the results obtained. The S_y error covariance matrix contains information on the uncertainties associated with both the measurements and the forward model. This section outlines sensitivities of the model observing system to a variety of cloud optical properties, in-cloud distributions, geometric thickness and position in the vertical. In general, the higher the forward model sensitivities are to perturbance of a

cloud parameter, the higher the potential for successful retrieval of that parameter. For simplicity, only single layer clouds are considered for these exercises (with vertical heterogeneity approximated by stacked plane-parallel clouds of varying optical properties).

Forward model uncertainties are associated with several factors, including i) the discretization of the radiance field, ii) vertical variability of gas and cloud extinction, iii) scattering phase function approximation, iv) gaseous absorption approximations, v) the assumptions imposed upon the unretrieved model parameters, and vi) the application of a plane parallel model to a horizontally inhomogeneous cloud field (Heidinger and Stephens, 1998). The errors for (i) and (ii) can be quantified using high resolution forward model simulations. Some estimates of the error of (iii) can be obtained by comparison of the double Henyey-Greenstein phase function to tabulated phase functions (Deirmendjian C1 water and Takano and Liou (1995) hexagonal ice crystal phase functions). To account for uncertainties in gaseous absorption (iv), figures from Kratz (1995) reporting channel radiance errors on the order of 0.2% for the correlated-K method were used. Temperature, water vapor, and gaseous absorber abundances are derived from ECMWF initializations and, whenever possible, rawinsonde observations. A comparison of the observational soundings with co-located ECMWF profiles is used as a measure of the temperature profile uncertainty (v) in regions where only model data are available.

The uncertainty in the approximation of a heterogeneous scene by a plane-parallel model is a quantity dependent on the scene in question. For the case of GOES pixels, clouds often do not fill pixels completely, resulting in a clearsky contamination (warming) of the cloud signal. The active sensor can to some extent ascertain the degree of cloud heterogeneity within the corresponding GOES pixel (albeit a 2 dimension vertical slice view). As this error was common to both the active/passive and passive-only retrievals, this unknown and unquantifiable error component is argued to be tolerable in the context of relative-error comparisons between the two methods operating on the same pixels. This is not a concern to the SSP-based retrievals where detector FOV and range-to-cloud are both sufficiently small as to approximate a point-reflection at cloud top.

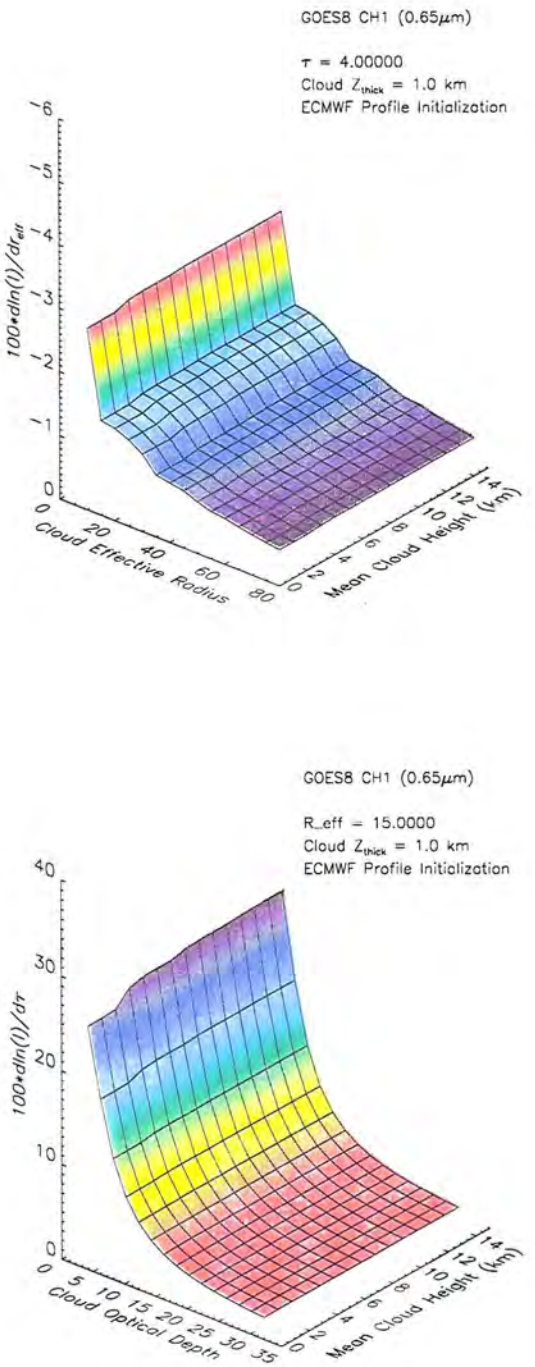

Figure 4.17: GOES Ch. 1 sensitivity to optical property perturbance as a function of cloud height. Top panel: sensitivity to r_{eff}, Bottom Panel: sensitivity to τ.

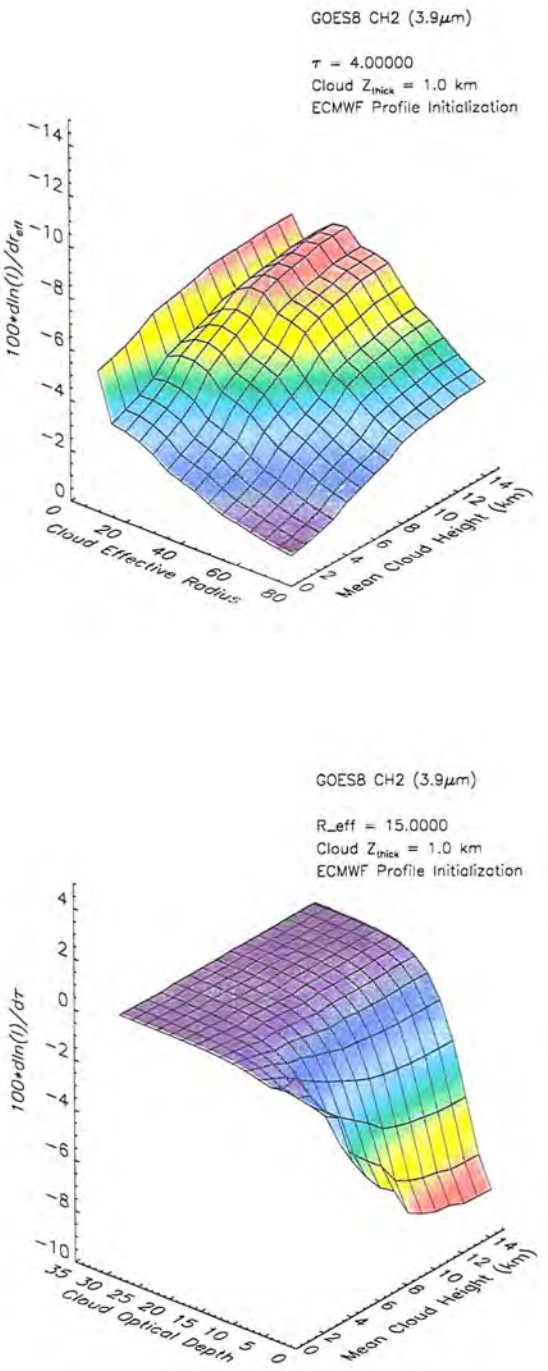

Figure 4.18: GOES Ch. 2 sensitivity to optical property perturbance as a function of cloud height: Daytime case. Top panel: sensitivity to r_{eff}, Bottom Panel: sensitivity to τ.

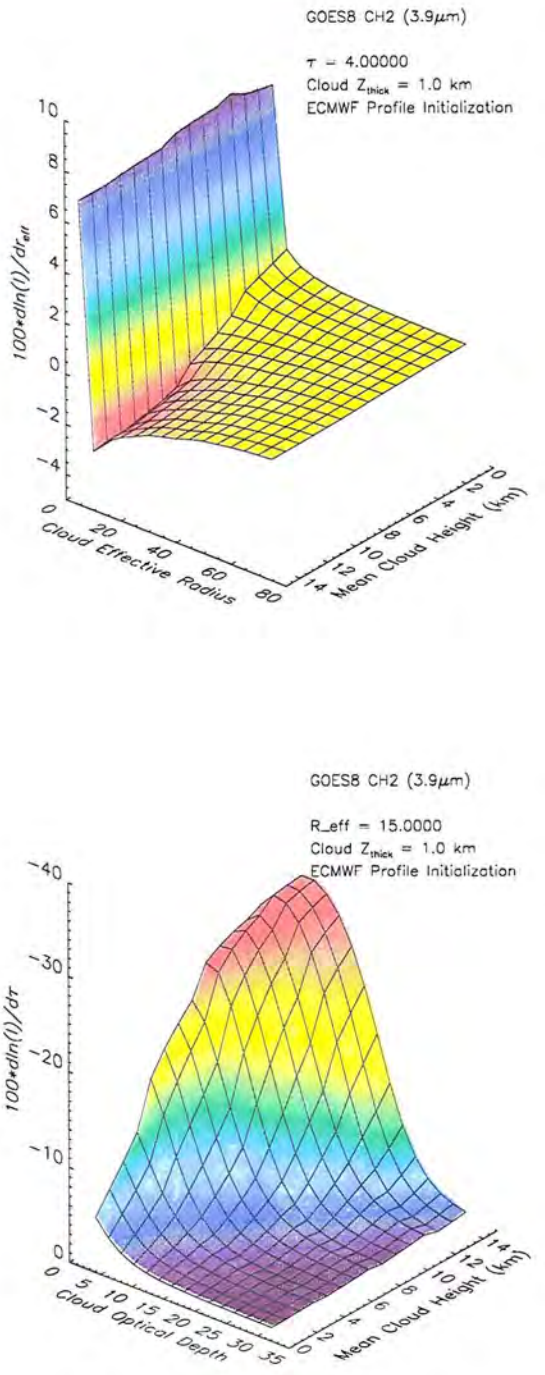

Figure 4.19: GOES Ch. 2 sensitivity to optical property perturbance as a function of cloud height: Nighttime case. Top panel: sensitivity to r_{eff}, Bottom Panel: sensitivity to τ.

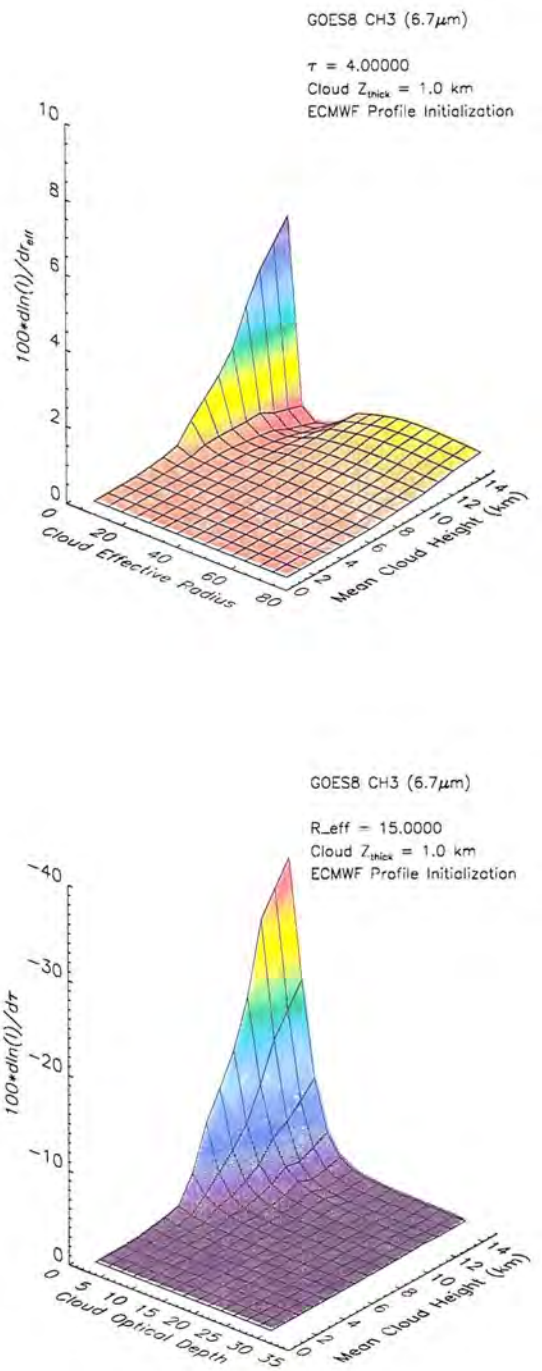

Figure 4.20: GOES Ch. 3 sensitivity to optical property perturbance as a function of cloud height. Top panel: sensitivity to r_{eff}, Bottom Panel: sensitivity to τ.

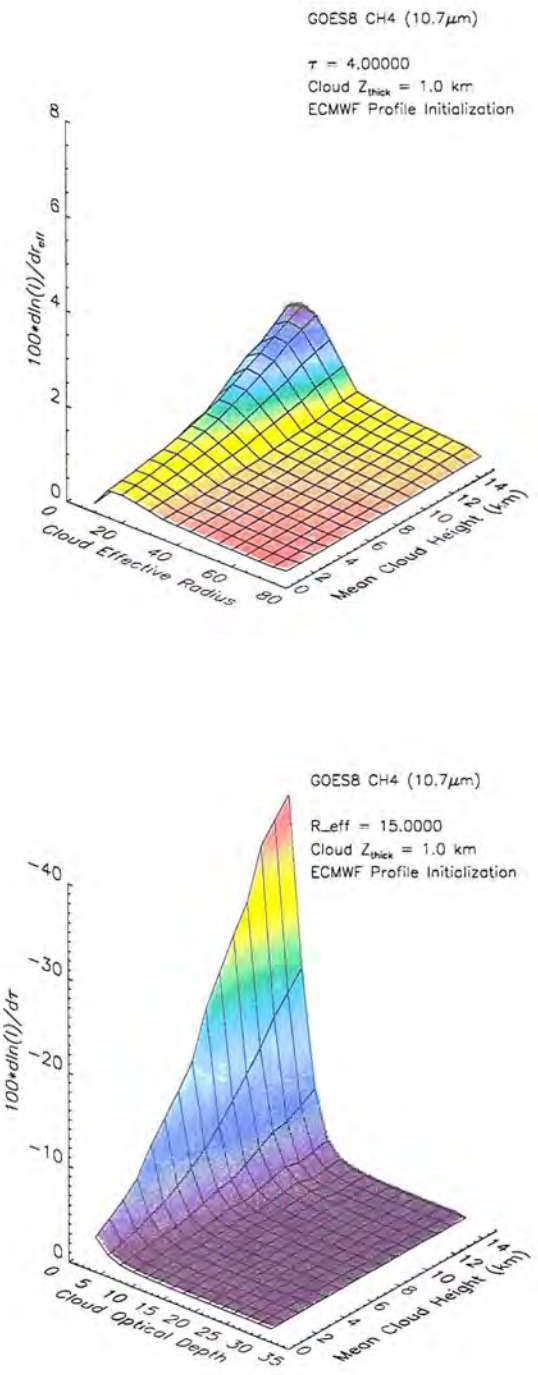

Figure 4.21: GOES Ch. 4 sensitivity to optical property perturbance as a function of cloud height. Top panel: sensitivity to r_{eff}, Bottom Panel: sensitivity to τ.

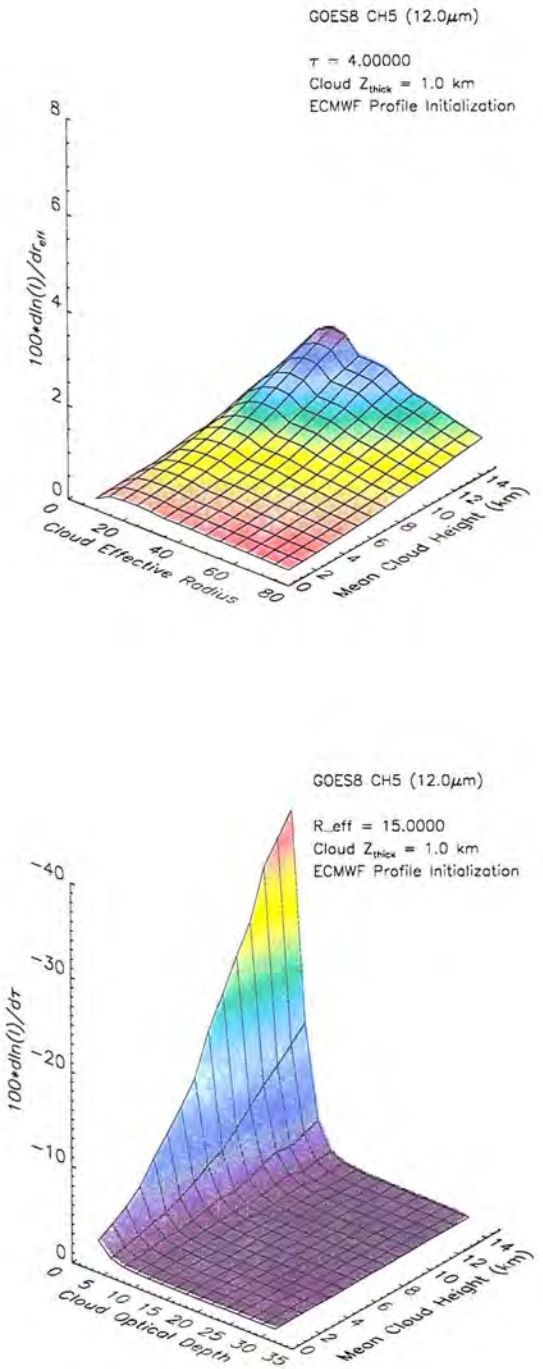

Figure 4.22: GOES Ch. 5 sensitivity to optical property perturbance as a function of cloud height. Top panel: sensitivity to r_{eff}, Bottom Panel: sensitivity to τ.

4.4.1 Sensitivity to retrievable parameters

To determine the sensitivity of spectral radiance to variations of τ and r_{eff} independently and as a function of cloud altitude, a single 1 km cloud layer of uniform optical depth and particle size distribution was incremented through an atmospheric profile inhomogeneous in temperature, molecular scatter, water vapor, and other gaseous absorbers. At each incremental height, the cloud optical properties were perturbed and a differential radiance computed. This was repeated for a wide array of τ and r_{eff} for all five GOES channels. The sensitivity computations were defined as the relative percent-change in the radiance measurement as a function of a differential change in the optical property:

$$\frac{dln(I)}{dp} = 100 \times \frac{(I(p') - I(p))/I(p)}{p' - p}, \tag{4.5}$$

where p is the optical property (τ,r_{eff}) and p' is its perturbed value (increased by 5%). Effective radius sensitivities were computed for fixed optical depths ranging from 1 to 30, and optical depth sensitivities were computed of an effective radii range of 5 to 75 μm. DHG phase functions were used, and the solar and satellite zenith angles were held at $\mu_\circ = 0.80, \mu = 0.94$ and $\phi_\circ - \phi = 0.0$ degrees. For the Ch. 2 simulations, runs with and without the solar source were performed.

Displayed in Figures 4.17-4.22 are sensitivities to the perturbed optical properties as a function of height and GOES Channel. While the examples shown are for a single fixed value of τ or r_{eff}, these were computed for the full range mentioned above. Summarizing the salient features of these plots and companion-plots not shown,

- Channel 1:

    1. Model sensitivity to effective radius at 0.65-μm was tied to a rapid increase in the asymmetry parameter (g)over low values of r_{eff}. As defined, the derivatives are negative since an increase in g results in stronger forward scatter at the expense of backscatter. At lower cloud heights the presence of stronger Rayleigh scatter serves to dampen the sensitivity. The general structure of this sensitivity surface remained intact but increased in magnitude from $\tau = 2.0$ to a maximum

at $\tau = 8.0$; decreasing beyond this value. Below this maximum reflectivity increased rapidly with optical depth, while at higher τ the relationship were observed to asymptote.

2. Sensitivities to optical depth displayed the opposite sign, since in the visible an increase yields invariably a finite increase in cloud reflectance. A small fall-off in sensitivity at lower cloud due to Rayleigh scatter heights was observed, and sensitivity decreases for increasing values of fixed effective radius. As effective radius increases the likelihood of transmission through optically thinner clouds increases in turn. As a result, the maximum sensitivity to optical depth shifted towards higher τ with increasing r_{eff} (corresponding to a shift in where the strongest reflections *and* for an incremental change in τ at a given r_{eff} exist).

- Channel 2 Daytime (Solar+Infrared):

1. The sign of the Ch. 2 day-time sensitivity to effective radius is negative for entirely different reasons physical reasons than in Ch. 1. As discussed, 3.9-μm radiation is very sensitive to particle size (owing high water absorption, see Figure 4.6). Thus, a perturbance to higher effective radii will result in the cloud absorbing a larger amount of solar radiation (as well as the cloud emitting at a lower temperature closer to its ambient temperature). These effects lower the net energy reaching the satellite in the perturbed cloud state. The effects of increasing asymmetry parameter and *decreasing* single-scatter albedo with effective radius interacting with both solar *and* thermal radiation results in a complex sensitivity structure. While both of these trends lead to decreased solar reflection, the thermal emission component of the signal is affected in opposite ways: increasing g enhances forward transmission of lower-level warm emissions (increasing the signal), while decreasing ω_o leads to more absorption and hence a lower signal. While the absorption effects dominate the signal, the structure "riding atop" owes to these competing thermal effects. This structure is observed to weaken in amplitude at lower cloud heights where the differential temperature between the cloud and the lower atmosphere/surface is less.

2. Sensitivity to optical depth exhibited a complex behavior with varying effective radius. Note that the optical depth axis in Figure 4.18 has been reversed in range with respect to the other plots to focus on the region of interest. Over a majority of the optical depth range, sensitivities were negligible. At small r_{eff} and τ, however, the derivative was a positive quantity (an increase of τ results in an enhance cloud reflection). By $r_{\text{eff}} = 15$-μm, the derivative at low τ had begun to reverse sign to negative values as absorption increases dramatically with particle size (again referring to Figure 4.6). Viewed together, these figures highlight model sensitivity of Ch. 2 to r_{eff} and relative insensitivity to τ (with the exception of small τ).

- Channel 2 Nighttime (Infrared-Only):

1. Similar to the its day-time counterpart, the night-time sensitivity of Ch. 2 to effective radius displays a complex structure owing to the behaviors of g and ω_o (or equivalently, r_{eff}). The height axis has been reversed in Figure 4.19 to highlight the region of interest. Due to the rapid decrease from unity of ω_o (i.e., toward more absorption) with increasing r_{eff}, sensitivities are negative for high clouds where differential cloud/surface temperatures are largest. At the smallest effective radius point (5-μm), ω_o is near unity (relatively non-absorbing), and perturbances of this value at all cloud heights are dominated by the increase in g; yielding positive derivatives. The negative "notch" increases in magnitude until $\tau \approx 14.0$, at which point the cloud effectively removes significant upwelling contributions from the signal.
2. Strong sensitivity to Ch. 2 perturbances in optical depth were observed for night-time simulations. The relationship is simple compared to effective radius perturbances: an increased optical depth inhibits upwelling emissions and results in the signal arising from emissions at the ambient cloud temperature. The differential effect is strongest for high clouds. A peak in τ-sensitivity near 5.0 is reached before falling off for larger τ (where a perturbance will not yield as great a change in radiance for an already-dark cloud).

- Channel 3:

  1. Little sensitivity to r_{eff} was observed for the water vapor channel with the exception of very small r_{eff} and τ, in which case the effect of increasing g (and its associated effect of enhanced transmitting upwelling emissions) wins-out over the counteracting effect of decreasing ω_o; leading to a positive derivative. An asymptotic limit for ω_o is reached near $r_{\text{eff}} = 40$-μm, while g continues to increase over this range. This corresponds to a sudden shift in sensitivity toward stronger magnitude positive values as a differential change in r_{eff} results in enhanced forward scatter without further enhanced absorption. As g begins to asymptote at still higher r_{eff}, the "bump" of enhanced sensitivity begins to decay. At low cloud heights the presence of strong water vapor absorption drowns-out any sensitivity here. The sensitivity that is observed decreases rapidly with increasing τ as lesser amounts of upwelling radiation can transmit through the optically thicker cloud regardless of differential changes in g.
  2. The structure of sensitivity to τ in Ch. 3 has the opposite sign to that of r_{eff}, as an incremental increase in τ yields invariably a colder cloud as seen from satellite. Only a slight, uniform decrease in the magnitude of this surface is observed for increasing r_{eff} as the corresponding increase in ω_o serves to nudge the cloud toward its ambient emitting temperature more rapidly and in-turn lower the differential changes for a given perturbance of τ.

- Channel 4:

  1. At small optical depths (i.e., where multiple scattering is minimal), the main cause of radiances differences is due to changes in the single scatter behavior as dictated by the phase function. Because g increases rapidly at lower values of r_{eff} in GOES Ch. 4, the derivatives at low τ are positive (owing to an enhanced transmission of warmer upwelling emissions). At increased optical depths, the sensitivity is determined more by the behavior of ω_o, which for Ch. 4 is observed to increase slightly at low r_{eff} (Figure 4.6). Because absorption

is not as strong when r_{eff} (ω_o) is increased in the optically-thicker clouds, the cloud scatters back down a greater component of the upwelling flux, resulting in a lower upwelling flux at cloud top. This effect vanishes for $r_{\text{eff}} > 15$-μm, when ω_o achieves an asymptotic value.

2. Sensitivity to τ yields negative derivatives (increasing the optical thickness always reduces upwelling transmissions) for all r_{eff}. The magnitude varies only slightly with r_{eff}, reaching a local maximum at $r_{\text{eff}} = 15$-μm following the structure of the ω_o variation. A strong sensitivity dependence on cloud height is observed.

- Channel 5: The behaviors of both sensitivity plots are very similar to those of GOES Ch. 4 and warrant no further notes other than that there is a slightly broader sensitivity to r_{eff} in Ch. 5 owing to a monotonically increasing ω_o over the range of r_{eff} shown, and a slight decrease in Ch. 5 τ sensitivity magnitude owing to a smaller Ch. 5 ω_o at all r_{eff}.

Gathering together the information from Figures 4.17-4.22 allows one to gain a general feel for what limits exist on the retrievability of τ and r_{eff} using this observing system. If a criterion (based on instrument noise specifications, for example) of 1% is established as a sensitivity threshold (i.e., a change in the optical property resulting in a value less than 1 on any of the z-axes in any of the plots above), then day-time retrievals are seen to be sensitive to $\tau < 30.0$ and $\tau < 10.0$ for night-time retrievals. Based on Ch. 2, Ch. 4 and Ch. 5 data, the observing system is most sensitive to effective radii over the range of 10 to about 60 μm. The figures also indicate that sensitivity increases with increasing cloud height, especially for IR channels where the ambient cloud temperature determines emission strength. These rough figures are useful in red-flagging retrieval results in weak sensitivity regimes. As will be demonstrated in the retrieval case studies of Chapter 5, this information is embedded within the Rodgers retrieval diagnostics.

4.4.2 In-cloud vertical sensitivity to retrieved parameters

Real clouds seldom adhere to the simple constructs of horizontally-homogeneous plane-parallel theory. In their examination of a variety of stratocumulus cloud fields (perhaps the cloud for which plane-parallel assumptions best apply), for example, Stephens and Platt (1987) find a large vertical variation in the extinction coefficient. It is also not difficult to conceive of multiple size distributions over the vertical extent of both ice and liquid water clouds owing to variations in the profile of cloud/ice condensation nuclei (CCN/ICN), temperature, and hence supersaturation with respect to ice/water which dictate the distributions and growth-rates. Analyses of modeled satellite measurement sensitivity to cloud vertical inhomogeneity help to assess what the plane-parallel retrieved parameters represent in the context of a vertically-variable cloud.

The procedure followed was to begin with a homogeneous, 2 km thick ice cloud placed in an gaseous absorbing, emitting, and aerosol/molecular scattering atmosphere with a Lambertian reflecting lower boundary. TOA radiances were computed for this homogeneous base-case, I_{hom}. The cloud was then split vertically into 10 equally-spaced sublayers of identical optical properties (optical depth of a sublayer is $\frac{1}{10}$ that of the total 2 km cloud optical depth). Looping over the sublayers, one of the retrieved optical properties (τ or r_{eff}) was perturbed by 5% with the other held fixed, and a new perturbed-radiance field was computed, I_{pert}. In this way, each sublayer was perturbed for each optical parameter, P, individually, and derivatives between the perturbed radiance and base-case with respect to a logarithmic change in the optical parameters were computed as

$$I' = P \times \frac{I_{\text{hom}} - I_{\text{pert}}}{P - 1.05P}, \tag{4.6}$$

since

$$d\,ln(P) = \frac{1}{P} dP. \tag{4.7}$$

This exercise was repeated for fixed values of $\tau = (1, 2, 4, 8, 16)$ (when perturbing r_{eff}) and $r_{\text{eff}} = (10, 20, 40, 80, 160)$ (when perturbing τ) and derivative results plotted as a function of perturbation position within the cloud profile. A DHG phase function was used with the weighting scheme of Equation 2.11.

The complete analysis for τ and r_{eff} and all GOES channels are presented in Figures 4.23-4.27.

- Channel 1:

  1. As expected, sensitivity to optical depth perturbations is positive for all values of effective radius (i.e., increasing the optical depth at any position in the cloud for a fixed effective radius leads to an increase in cloud reflectance and hence a positive differential result in Equation 4.6). Stronger sensitivities occur for larger optical depths. Little sensitivity is observed to perturbation position in the vertical or as a function of increasing effective radius.

  2. Ch. 1 sensitivity to effective radius perturbances increase with increasing cloud optical depth and are strongest at smaller r_{eff} near cloud top. At higher optical depths, in-cloud multiple-scattering effects play an increasing role in the top-of-cloud upwelling radiance field. The forward and backward scattering lobes of the DHG phase function increase with increasing r_{eff} (referring to Figure 4.7, the parameterization yields a higher DHG forward and backward scattering peak for an increase in g_{eff}). At smaller r_{eff} the the phase function properties change most rapidly from more to less isotropic with increasing r_{eff}, resulting in negative derivatives for the topmost perturbed sublayers (i.e., the unperturbed cloud reflectance is greater than the perturbed). At higher values of r_{eff}, the DHG phase function produces less energy in side-lobe scattering in favor of the forward and backward lobes. For increasing r_{eff} in this case, the enhanced forward lobe allows for a greater penetration of downwelling direct/diffuse flux into the cloud sublayers below it, and the enhanced backscatter lobe of the perturbed sublayer serves to reflect direct/diffuse flux into the observer direction at TOA.

- Channel 2:

  1. In contrast to Ch. 1, increasing cloud optical depth in Ch. 2 results in negative derivatives owing to the strong water absorption in this band. Sensitivity

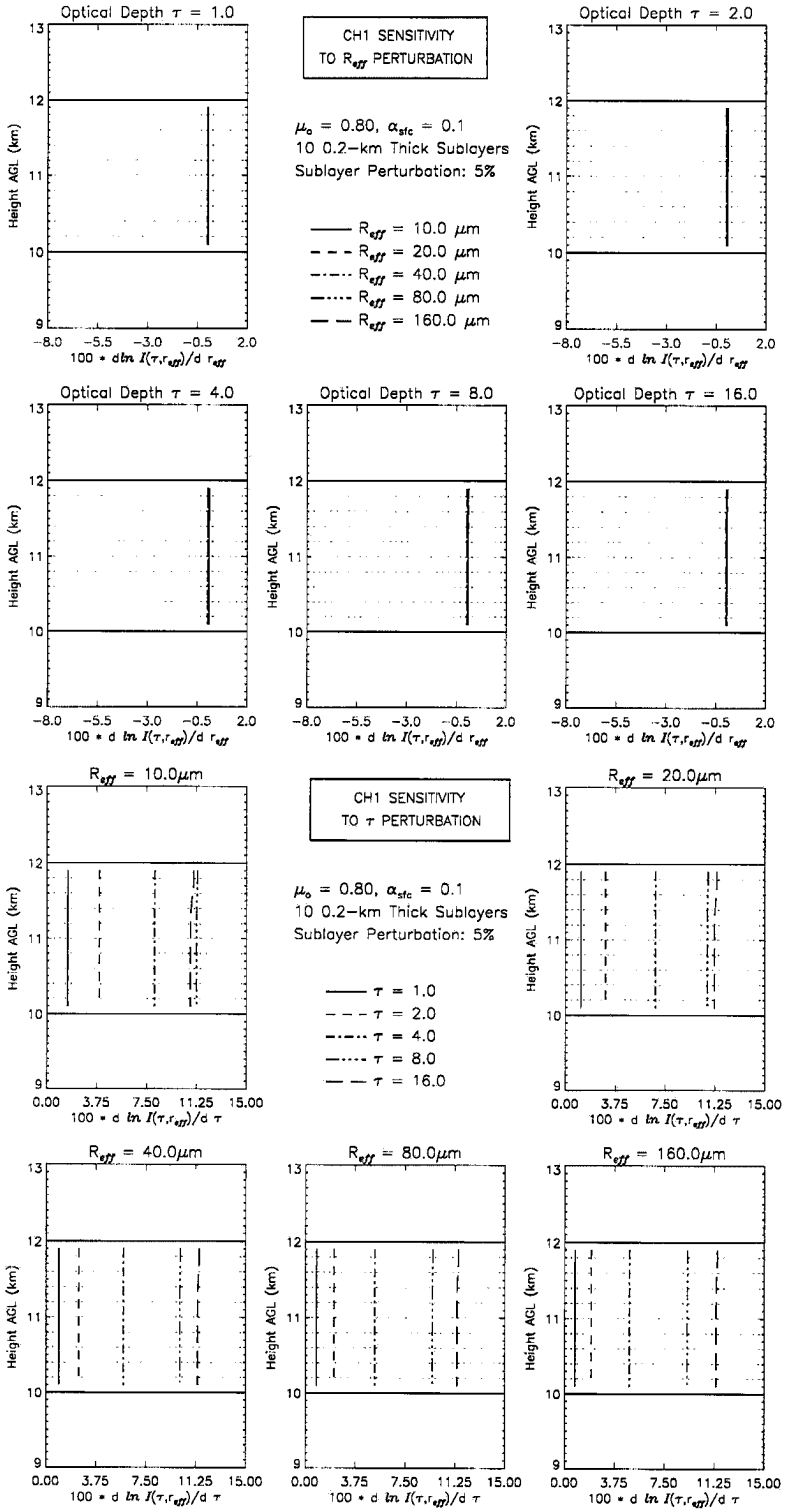

Figure 4.23: Sensitivity to cloud vertical inhomogeneity for a 2-km thick cirrus cloud: GOES Ch. 1

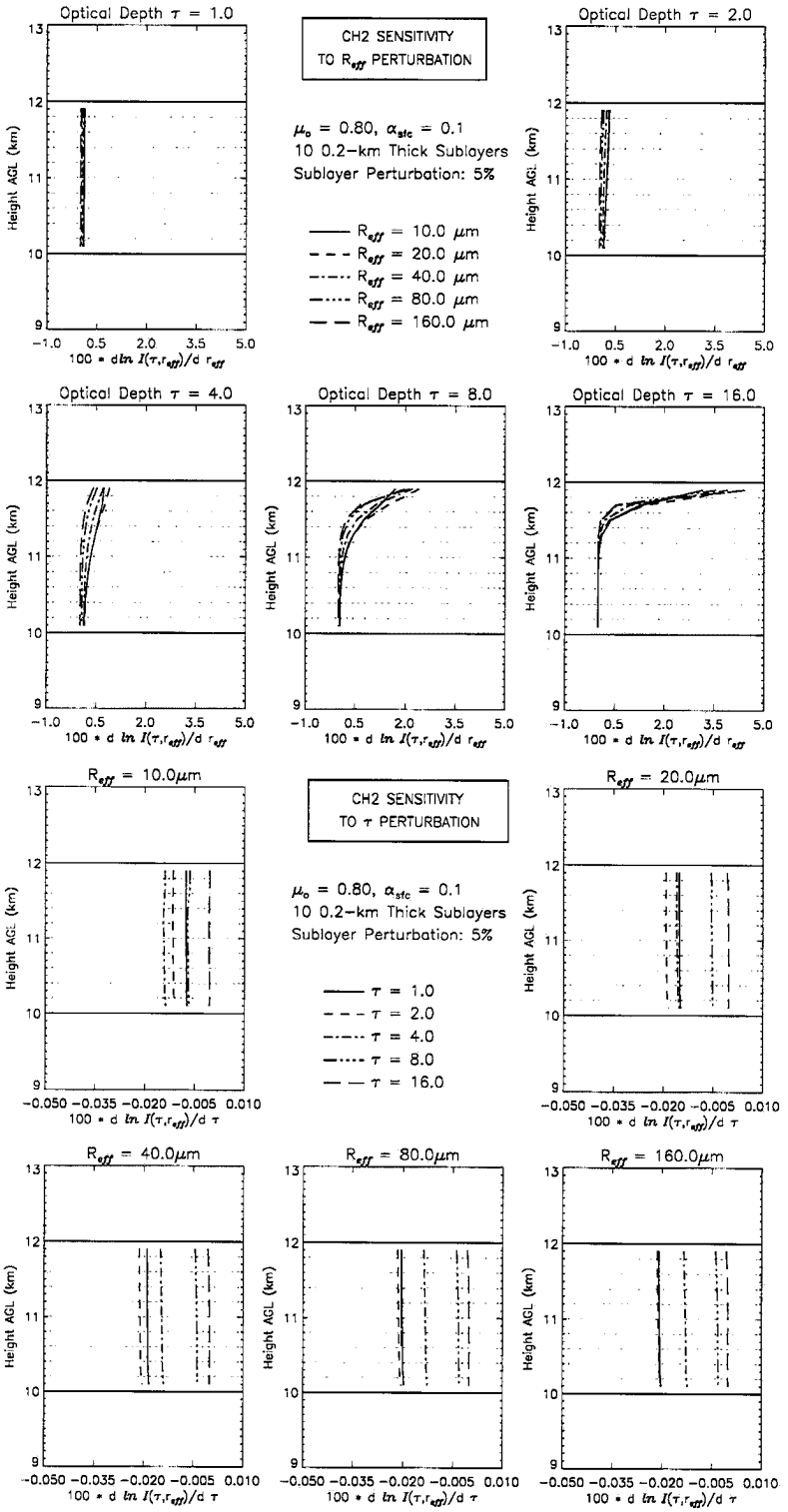

Figure 4.24: Sensitivity to cloud vertical inhomogeneity for a 2-km thick cirrus cloud: GOES Ch. 2

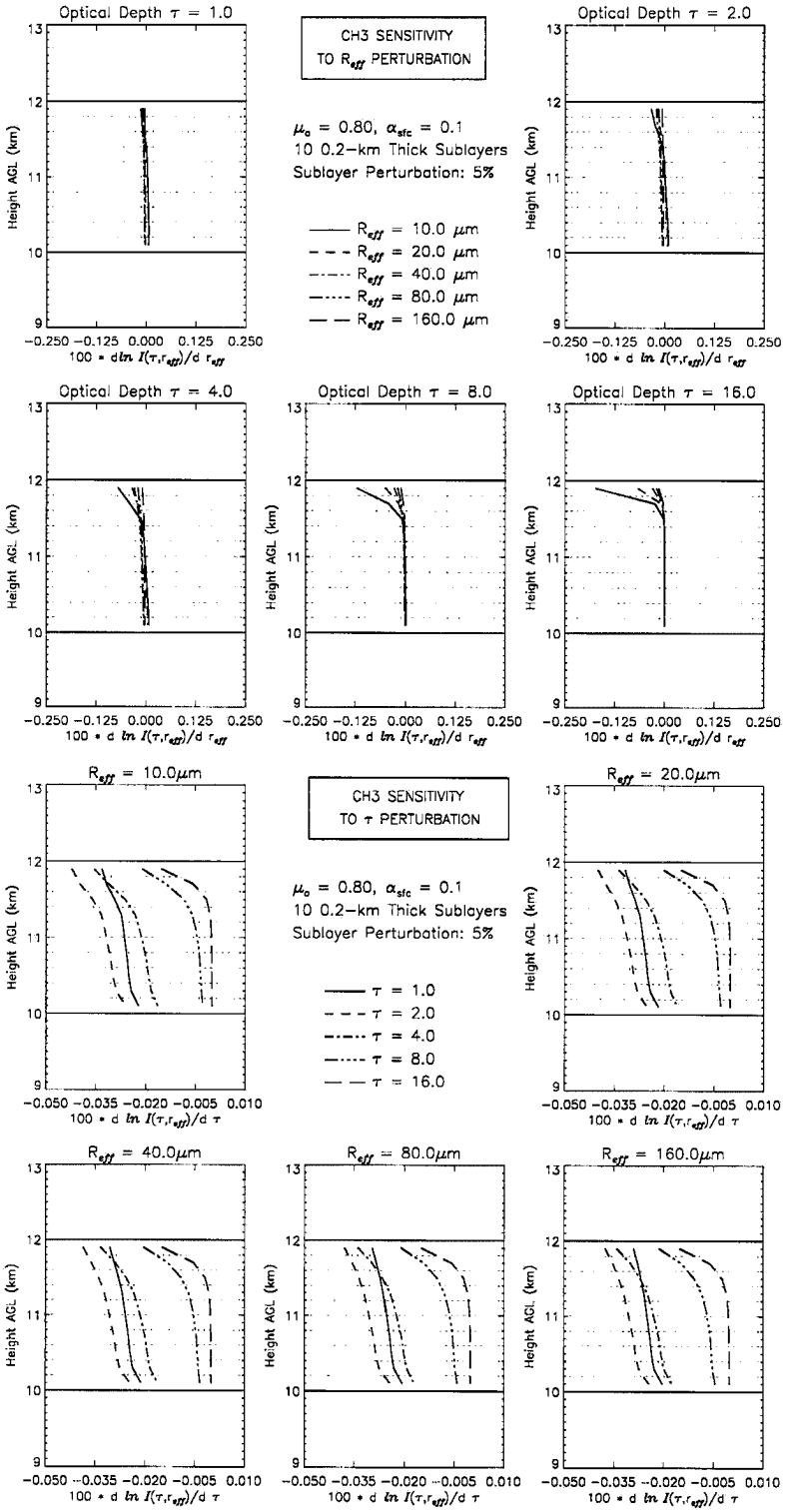

Figure 4.25: Sensitivity to cloud vertical inhomogeneity for a 2-km thick cirrus cloud: GOES Ch. 3

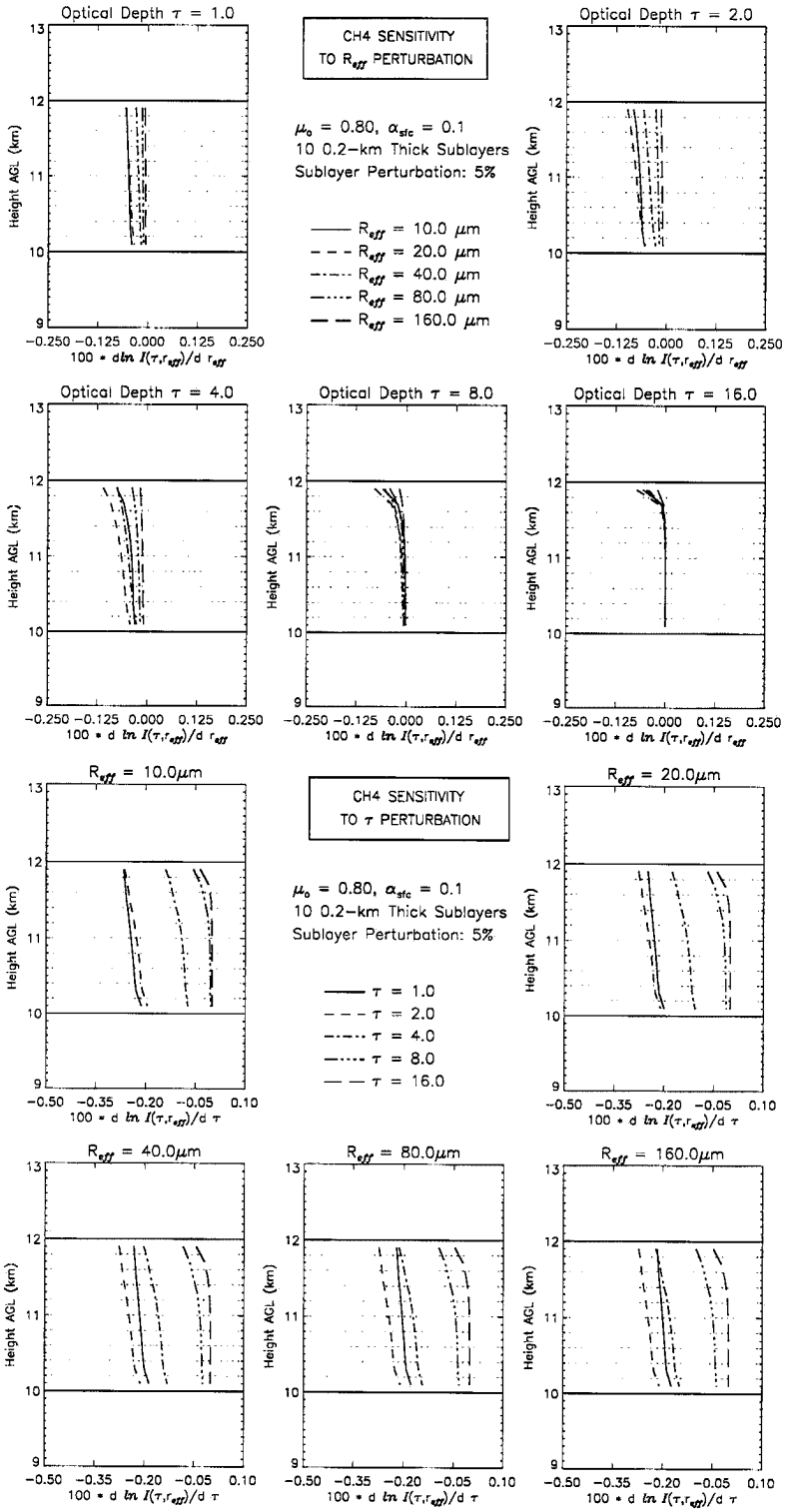

Figure 4.26: Sensitivity to cloud vertical inhomogeneity for a 2-km thick cirrus cloud: GOES Ch. 4

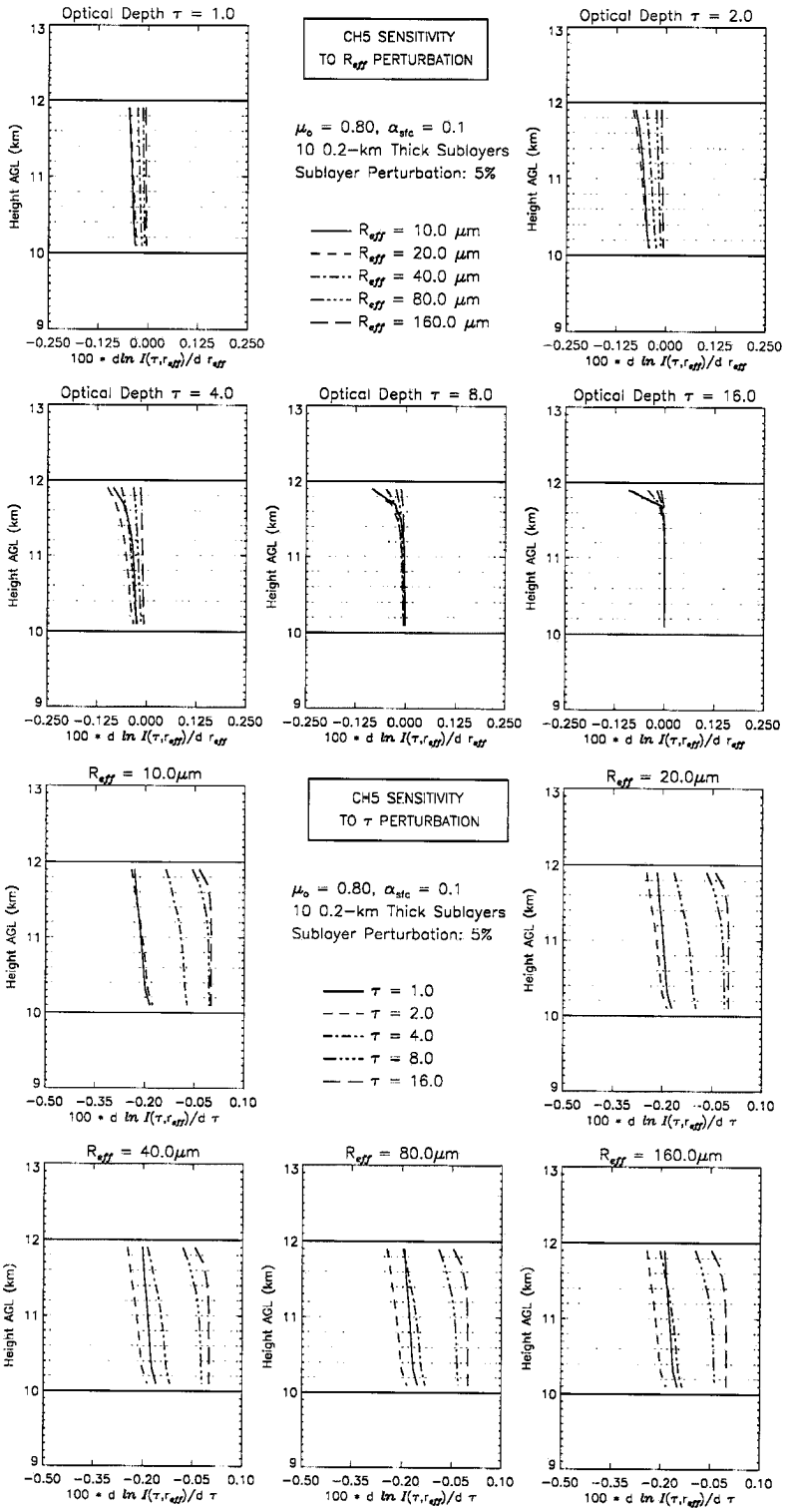

Figure 4.27: Sensitivity to cloud vertical inhomogeneity for a 2-km thick cirrus cloud: GOES Ch. 5

increases with increasing effective radii for clouds with optical depth less than $\tau = 2.0$ while higher optical depths eliminate sensitivity to changes in the scattering phase function.

2. Sensitivity to r_{eff} perturbances is larger for smaller r_{eff}. The asymmetry parameter increases rapidly in this regime and the single-scatter albedo decreases, translating to stronger forward-peaked scattering and enhanced absorption by larger particles, respectively. The result is lower cloud reflection of incident solar radiation, and a correspondingly lower perturbed measurement. For a satellite observing platform, the strongest differential effects are expected to occur for perturbances near cloud-top, as is observed in Figure 4.24.

- Channel 3:

1. Sensitivity to τ-perturbances begin to show vertical structure in the Ch. 3 plots. The downwelling solar radiation is all but negligible in this band, with only upwelling emissions from the warmer atmosphere below as a source. Again as a result of the satellite vantage point, sensitivities are strongest near cloud top and for the lower optical depths (where sensitivity to the scattering phase function remains appreciable).

2. Strongest sensitivities are again observed for smaller values of r_{eff} (see Ch. 2 r_{eff} discussion). The presence of strong water vapor absorption in Ch. 3 lowers the measured radiances in comparison to a window channel by obscuring the warmest surface emissions. This accounts for the small sensitivity magnitudes in these figures. For low τ and r_{eff} the perturbed measurements are slightly less than the base case (thus yielding a negative derivative) in the lower sublayers while the reverse is true for the uppermost sublayers. At larger optical depths, sensitivity within the lower sublayers weakens while rapidly increasing for the upper sublayers. The slight negative change to perturbed r_{eff} in lower sublayers is due to a decrease in the single-scatter albedo, ω_{o}. Lower values of ω_{o} imply stronger absorption and emission at the ambient cloud temperature (usually

lower than upwelling emissions from below the cloud), accounting for negative derivatives near cloud base. These effects vanish for increasing τ, as the upwelling emissions are obscured regardless of ω_o variations for this case. Upper sublayer sensitivities are associated with a "capping" of lower level emissions. Recalling that forward scattering increases with increasing asymmetry parameter, a cloud with a higher g will is optically thinner to upwelling emissions from below. This yields an enhanced perturbed radiance and a positive derivative. At lower optical depths, the competition between ω_o effects and capping effects neutralize each other at the zero-sensitivity cross-over point in these profiles.

- Channel 4:

  1. The structure of Ch. 4 sensitivity to τ perturbances is very similar to that of Ch. 3, with the main difference being that they are roughly an order of magnitude larger. The primary reason for this difference is the fact that Ch. 4 is situated in an atmospheric window, allowing for warmer surface emissions to reach cloud base than in the water-vapor-dominated Ch. 3 signal.

  2. The largest vertical sensitivities to perturbed r_{eff} are observed over the 0-40 μm range where the optical properties ω_o and g vary most rapidly. In Ch. 4, an increase in r_{eff} results in a corresponding increase in both of these optical properties, serving to enhance the transmission of warmer low-level emissions through the cloud to reach the satellite (thus resulting in the positive derivatives observed in Figure 4.26). The transmission effect weakens for larger optical depths and for larger r_{eff} (as ω_o and g reach asymptotic values which yield little change for a 5% perturbance of effective radius).

- Channel 5:

  1. Ch. 5 sensitivity to τ perturbances in the vertical is very similar to that of Ch. 4. The only subtle difference is a slightly lower magnitude associated with the Ch. 4 figures, owing to a less-transparent atmosphere in the 12.0 μm

split-window channel accompanied by slightly enhanced absorption by cloud water.

2. The sign and structural behavior of derivatives in Ch. 5 are again very similar to that of Ch. 4. Because absorption by water vapor is slightly stronger in Ch. 5, sensitivities are somewhat smaller in magnitude compared to those of Ch. 4, especially at the lower cloud sublayers (analogous to the Ch. 3 discussion pertaining to lower sublayers).

These results indicate that vertical variability of cloud optical properties do differ from the plane-parallel assumption and vary from channel to channel. The exercise was conducted to identify where the observing system was sensitive to these details. While the passive sensor retrievals conducted for this research employ strictly plane-parallel cloud approximations, active sensors may provide additional information on the vertical profile that can be included in the *a priori* information vector to further improve the retrievals beyond that afforded by correct cloud placement.

4.4.3 Forward model sensitivity to scattering phase function

An important consideration to assessing retrieval uncertainty is the assumption of phase function structure used in the forward model. A given effective radius for a cloud droplet distribution can be realized by an infinite array of possible size-distributions/particle-shapes and hence an infinite number of ways that the cloud interacts with radiation. While an *a priori* knowledge of the structure of typical phase functions found in real clouds (based on either Mie theory for water droplet clouds or Monte-Carlo raytracing simulations for complex ice crystal morphologies) enables us to discard a large subset of these structures in practice, disparities in simulated radiances among the remaining possibilities remain significant. This is especially true for ice clouds which often exhibit an extremely high (on the order of $10^5 - 10^6$) forward diffraction peak). The spherical approximations of Mie theory, much less the simple DHG parameterization so often used in retrieval work, do not hold for these cases.

To assign uncertainties to the simple DHG liquid/ice phase functions used in the retrievals, forward model simulations of a 1 km thick cloud with varying optical depth and DHG phase functions were compared to equivalent effective radii from tabulated phase function data of Deirmendjian (1969) (C1-cumulus parameterization) and Takano and Liou (1995) and Yang (1998) (raytracing results for ice crystals). To describe the method briefly, incident photons striking model ice crystal morphologies (e.g., hollow/solid/capped columns, bullet rosettes, dendrites, and aggregates) are traced using a hit-or-miss Monte Carlo model. When photons strike a boundary, they are reflected according to Fresnel reflection coefficients of or are otherwise transmitted. A stochastic process describes the absorption probability of a photon passing through the crystal interior.

Figures 4.28-4.39 depict absolute error surfaces for GOES Channels 1-5 plotted for all possible observation geometries. In the solar-component figures, an azimuth angle of $\phi - \phi_\circ = 0.0$ corresponds to the sun behind the satellite, and $\phi - \phi_\circ = 180.0$ corresponds to the sun in front of the satellite. The infrared channels are modeled as azimuthally symmetric ($m = 0$ only). These data, shown here only for $\mu_\circ = 0.8$ and $\tau = 1.0$, were computed for a range of $\mu_\circ$ from 0.0 to 1.0, and τ from 0.5 to 8.0. As diffuse radiation fields begin to dominate over single-scatter effects with increasing τ, the sensitivities decrease in turn. These data served as the basis for the estimation of phase function uncertainty for a given cloud phase and solar/viewer geometry. Plotted as insets on these figures are the DHG and tabulated scattering phase functions chosen in the comparisons for both water and ice clouds. The effective radius of water clouds (identified as having a mean cloud temperature greater than 273 Kelvin) was set to 10-microns, and a value of 32 microns was chosen to match to specifications for Yang *et al.* (1998) aggregate ice crystal data. χ-expansion of the forward-peak-truncated tabulated phase function data were performed as discussed in Chapter 2 to represent them in terms of Legendre polynomials in the forward model.

The comparisons indicate that differences between Ch. 1 cloud reflectances can be significant (in upwards of 90% at some angles), while errors for other channels are on the order of 10% (to negligible, in some IR channels) over the typical solar/observer

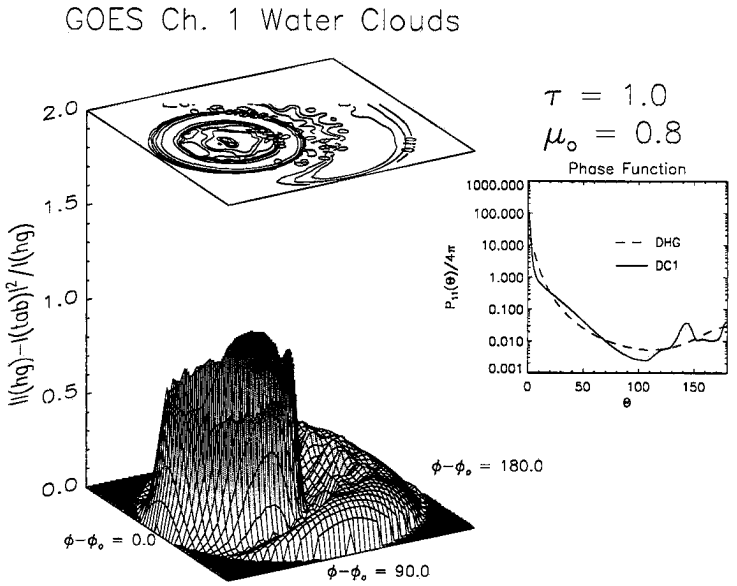

Figure 4.28: Absolute errors between DHG and tabulated water phase functions for GOES Ch. 1

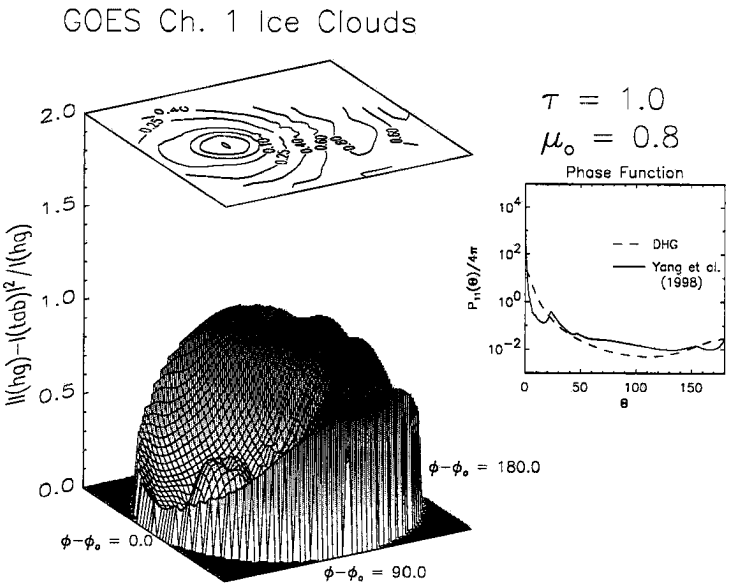

Figure 4.29: Absolute errors between DHG and tabulated ice phase functions for GOES Ch. 1

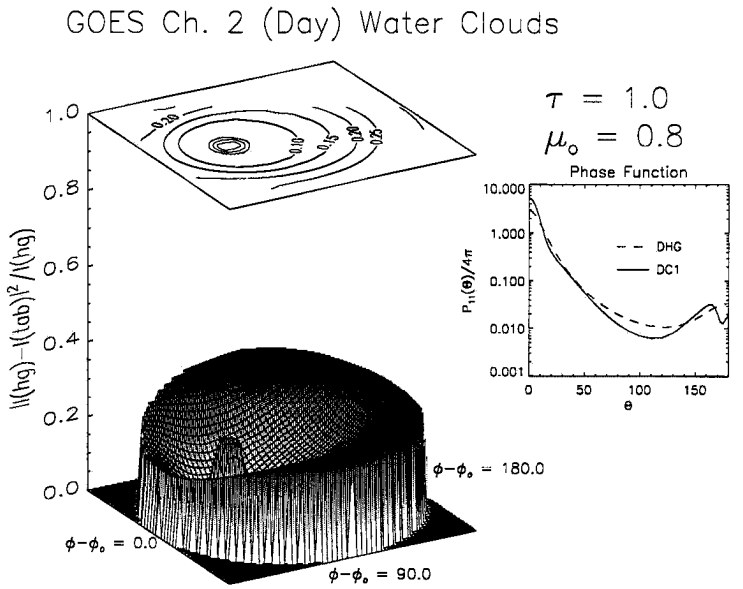

Figure 4.30: Absolute errors between DHG and tabulated water phase functions for GOES Ch. 2 (day-time case).

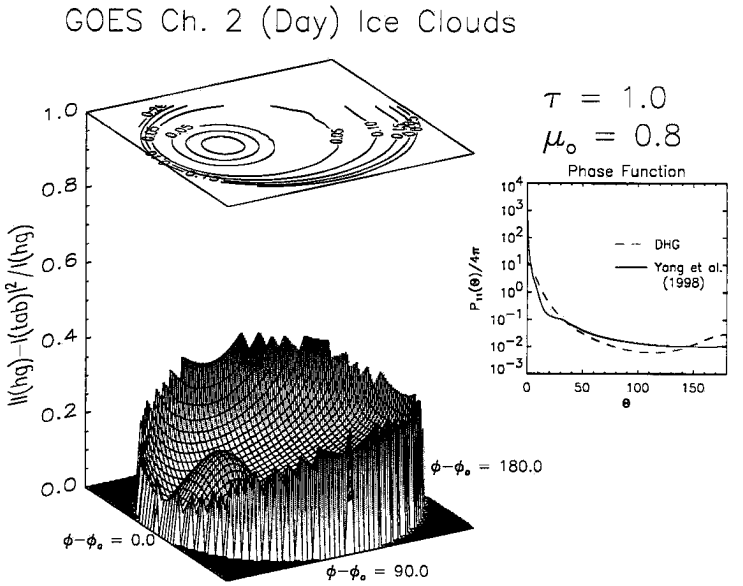

Figure 4.31: Absolute errors between DHG and tabulated ice phase functions for GOES Ch. 2 (day-time case).

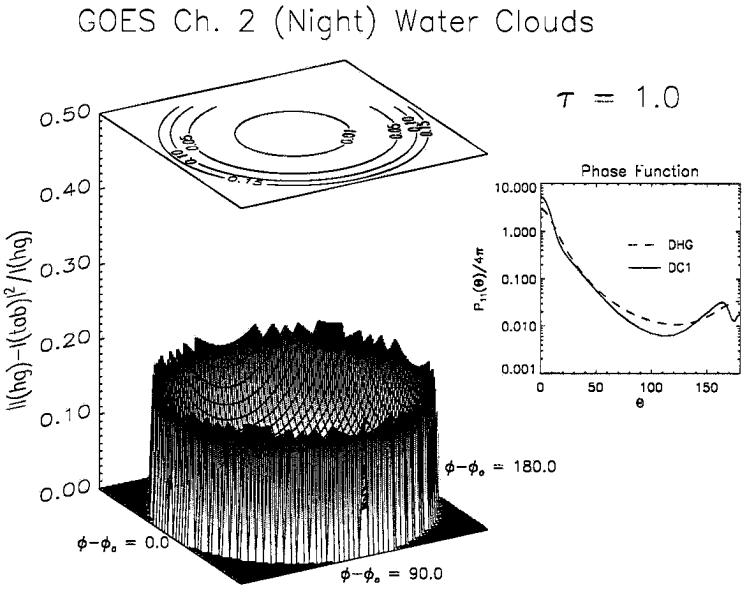

Figure 4.32: Absolute errors between DHG and tabulated water phase functions for GOES Ch. 2 (night-time case).

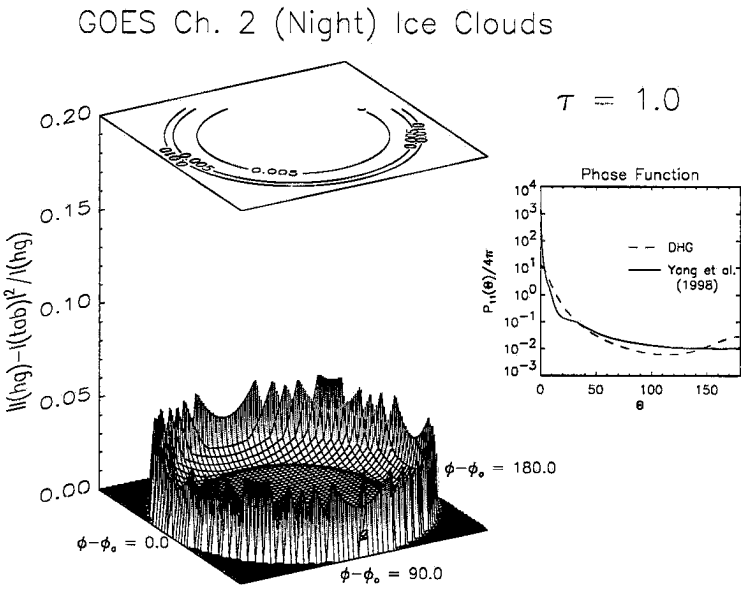

Figure 4.33: Absolute errors between DHG and tabulated ice phase functions for GOES Ch. 2 (night-time case).

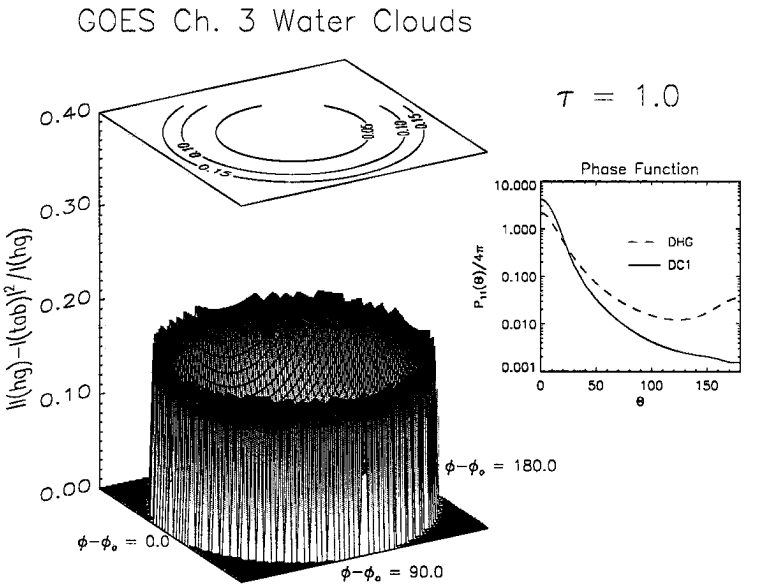

Figure 4.34: Absolute errors between DHG and tabulated water phase functions for GOES Ch. 3.

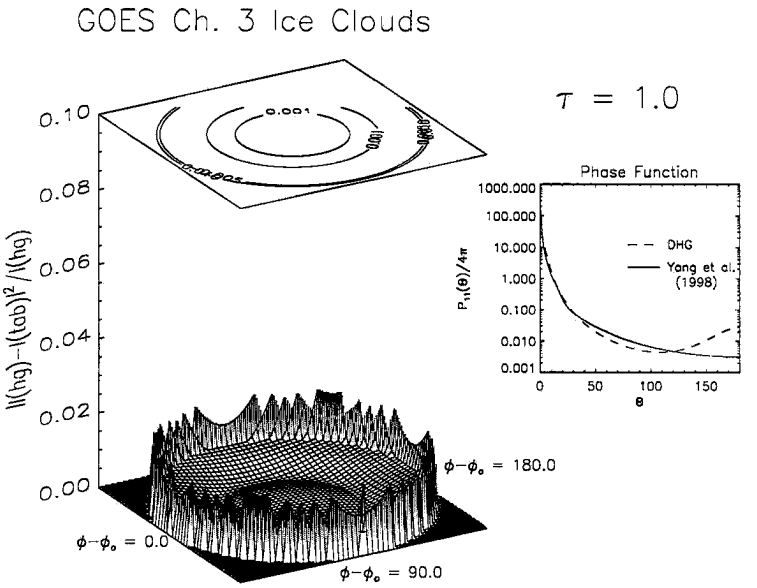

Figure 4.35: Absolute errors between DHG and tabulated ice phase functions for GOES Ch. 3.

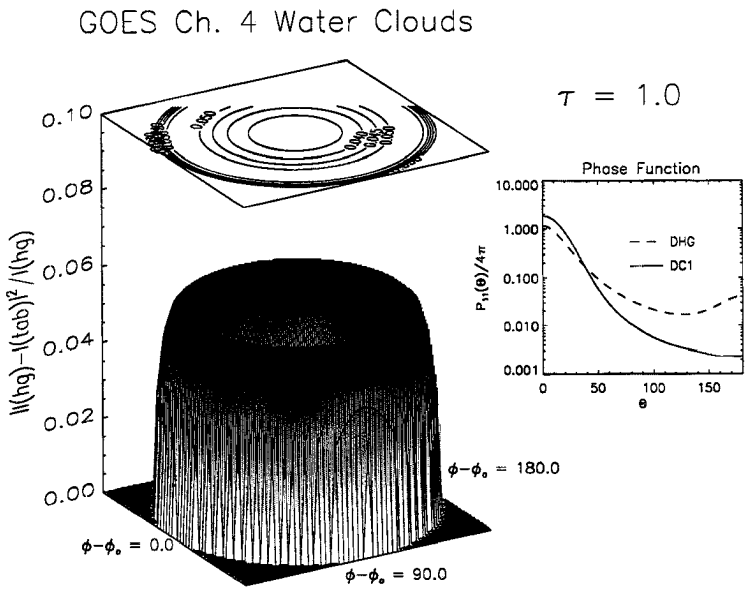

Figure 4.36: Absolute errors between DHG and tabulated water phase functions for GOES Ch. 4.

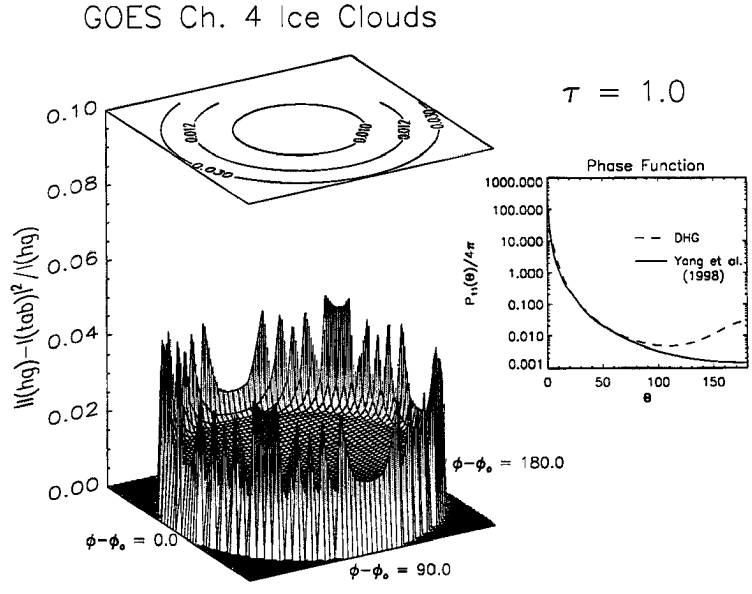

Figure 4.37: Absolute errors between DHG and tabulated ice phase functions for GOES Ch. 4.

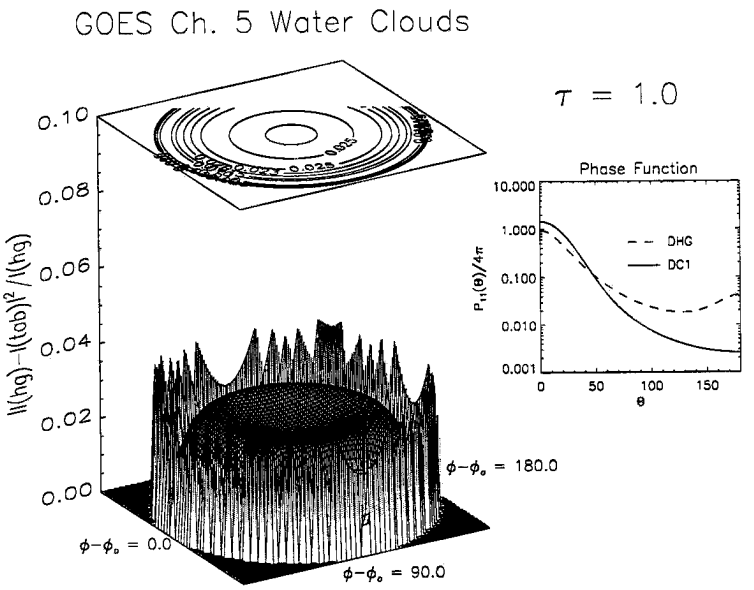

Figure 4.38: Absolute errors between DHG and tabulated water phase functions for GOES Ch. 5.

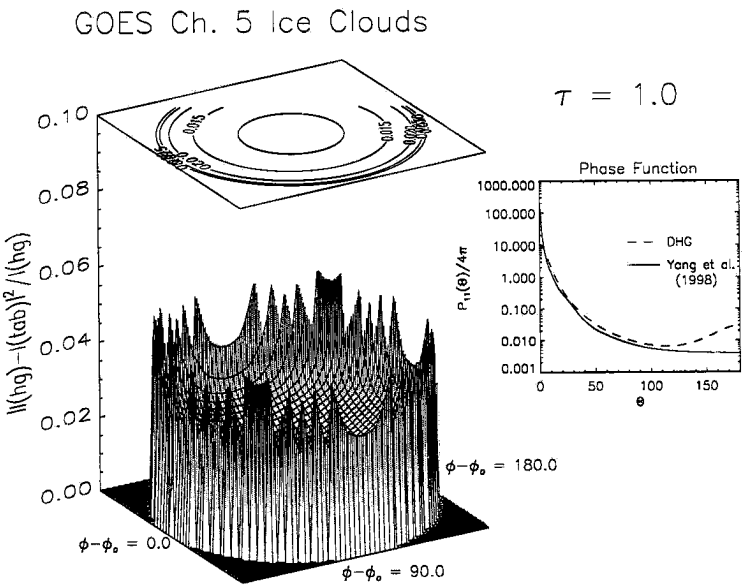

Figure 4.39: Absolute errors between DHG and tabulated ice phase functions for GOES Ch. 5.

geometries encountered in the retrievals of this research. It must be recognized that the tabulated phase function data, while more representative of true ice and water clouds, can not be regarded as absolute truth, as the spread among real-world clouds is significant. Consequently, there exists considerable uncertainty in the *assignment* of this uncertainty itself; a testament to the inadequacy inherent to most all contemporary cloud property retrievals.

4.4.4 Forward model sensitivity to *a priori* cloud height information

While methods to retrieving cloud top altitudes exist in the literature (see Minnis *et al.* (1992,1993) and Smith *et al.* (1996)), optical depths can only be estimated without introducing emittance parameterizations during the day-time (via Ch. 1 reflectance). Other methods, such as CO_2-slicing, provide approximate cloud top altitudes without any information on physical thickness. To examine the sensitivity of a single-layer satellite retrieval to uncertainty in cloud thickness, synthetic retrievals were performed using the forward model. Four cases of increasing optical profile complexity were created for an ice cloud between 8 and 10 km, comprised of four sub-layers of varying optical depth and effective radii. The forward model was then used to create an IR (night-time) measurement vector based on these "true" profiles. Retrievals based on these measurements were then computed under the assumption that the cloud top altitude was known *a priori* but cloud base was unknown (i.e., the currently capability of passive-sensors alone). The cloud base was decreased systematically from 9.9 to 6.0 km in increments of 0.1 km such that a $\pm 100\%$ range of cloud thickness uncertainty was spanned. The number of streams and profile resolution were simplified in the retrieval runs to represent forward model uncertainties. Solution disparities for the inhomogeneous profiles at the correctly-guessed 2-km cloud thickness are also affected by the assumption of a plane-parallel-cloud in the retrieval.

Results for these four cases are presented in Figure 4.40. Concentrating on the simple homogeneous layer case, retrieved optical depths are under-estimated for the cloud bases above the true level of 8-km and over-estimated for cloud bases lower than 8-km. Considering the decrease in temperature with height, a cloud with a colder average temperature

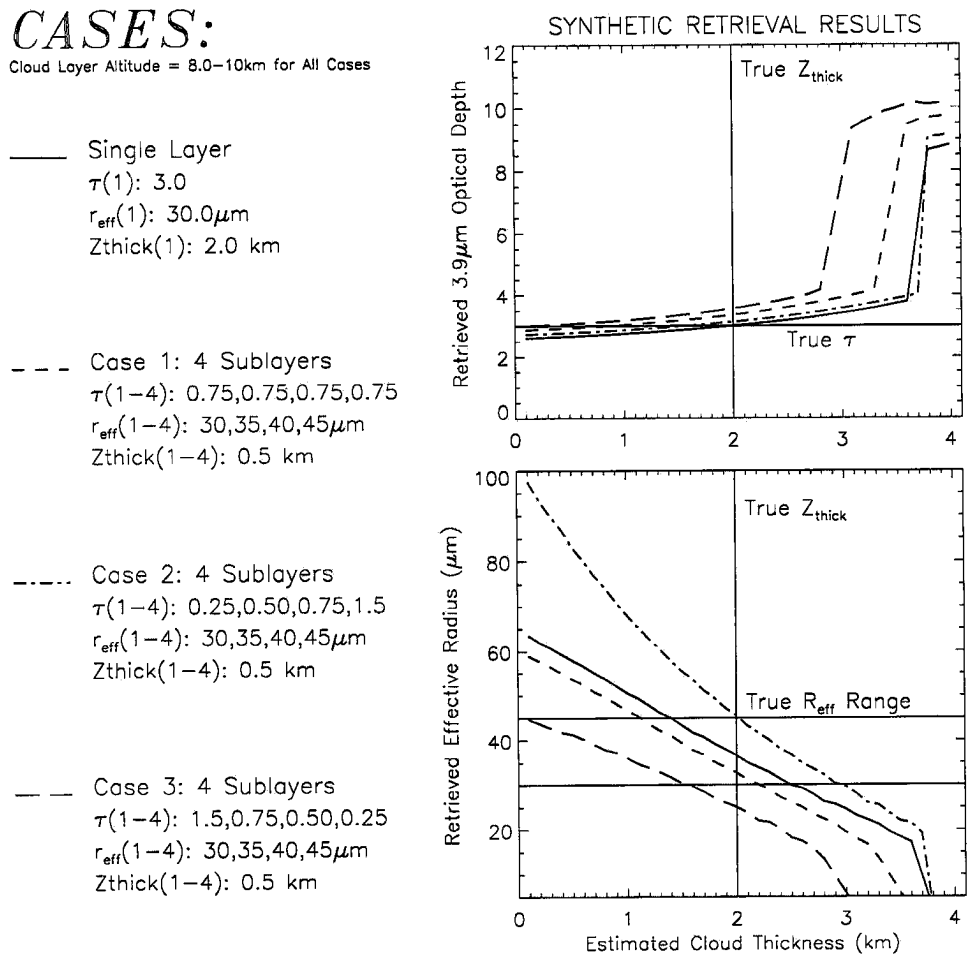

Figure 4.40: Analysis of IR-only retrieval uncertainty as a function of cloud physical thickness and vertical profile uncertainties. Sublayers are 0.5-km thick and listed from top down in the vertically inhomogeneous cases.

does not require as high of an optical depth to emit at a brightness temperature comparable to the base case, whereas the clouds with bases below 8-km require a higher optical depth such that the upper-portion of the cloud offsets the warmer emissions from the lower half of the cloud. The sharp increase in optical depth is due to a transition between atmospheric levels in the simplified retrieval profile. This emphasizes the uncertainty associated with the *a priori* temperature profile for night-time retrievals. Over-estimates of effective radii are retrieved for the higher-based clouds and under-estimates for the lower-based clouds. This reflects the estimation scheme's attempt to achieve a balance between the g, ω_o, and τ parameters in the forward model and measurements vector. Recalling the relationships illustrated in Figure 4.7, smaller r_{eff} translates to more isotropic-like scatter in all GOES Channels. Because warmer emissions from below need to be "blocked" in the over-estimated cloud base case (in order to match the cooler measurement vector) effective radii are lowered to prevent a strong upward transmission through the retrieved cloud. Conversely, larger effective radii are selected for the under-estimated cloud base in order to "warm the measurement up" by allowing additional emissions from the surface to transmit upward to the satellite. It is seen in these synthetic retrievals how the scheme uses the physics to tune toward an appropriate solution. There may exist parameter combinations that yield retrieval convergence but are not physically-realistic quantities. *A priori* constraints on the retrieval are imposed to filter-out these solutions.

To assign values of uncertainty due to cloud-misplacement/thickness errors from passive-only estimates, the forward model was used to construct a look-up table for each retrieval. The table was composed of discrete modeled radiances computed as a function of mean cloud height (for a 1 km thick cloud), optical thickness, effective radius, and solar/observer geometry for all channels. The selection of temperature/moisture profile, surface albedo, and solar/observer geometry were dependent upon the retrieval case considered. After first performing the retrieval with active cloud heights, the retrieval was re-run with passive cloud-height estimates. Given the τ and r_{eff} of the former retrieval, radiances for the equivalent cloud at the passively-estimated level was interpolated from

the look-up table and difference ratio taken, e.g.:

$$R = \frac{|I_{\text{act},\lambda}(\tau_\lambda, r_{\text{eff}}) - I_{\text{pass},\lambda}(\tau_\lambda, r_{\text{eff}})|}{I_{\text{act},\lambda}(\tau_\lambda, r_{\text{eff}})}, \tag{4.8}$$

where $I_{\text{act,pass}}$ are the cloud radiances at the active and passive cloud heights. It was anticipated from the height-dependent sensitivities to cloud optical properties that these uncertainties would be minimal for the visible channel, low-level clouds in the reflective and thermal IR, and middle-to-lower tropospheric clouds in the 6.7 μm channel. Contrastingly, the uncertainty would be maximized for the NIR and IR window channel observations of high-altitude, optically thin cirrus (in which case transmissivity is high). Because retrievals using active cloud heights did not always match perfectly the observation vector (owing to other uncertainties in the forward model) computations of uncertainty were based exclusively on the forward model. In this way, all other uncertainty conditions could be held fixed and a relative uncertainty calculated. Because the comparisons were made against the active *a priori* clouds, the uncertainty due to deviations from the passive-assumed cloud physical thickness of 1 km were embedded within these computations. The uncertainty fractions were included in the S_y model/measurement covariance matrix.

4.4.5 Forward model quadrature approximation uncertainties

Uncertainty associated with a limited polynomial expansion in the model was estimated by comparing the 64-stream retrieval resolution to a 256-stream high resolution run. As cloud optical depth and effective particle size are highly variant for cloud to cloud, appropriately high values of variance were assigned to the initial-guess values for these quantities (S_a) in the retrievals, such that they only constrained the solution to be within an acceptable, positive domain. All retrieval results presented herein were run under a minimum of 64 streams, where errors with respect to the benchmark 256 case fell below 0.5% in all channels (invoking the Delta-M scaling method).

4.4.6 Band sensitivity to surface/atmospheric emissions

Sensitivity to spectral variation of Planckian emissions for GOES-8 IR channels is shown in Figure 4.41. Contours of blackbody intensity ($\text{Wm}^{-2}\text{sr}^{-1}$ μm^{-1}) are plotted

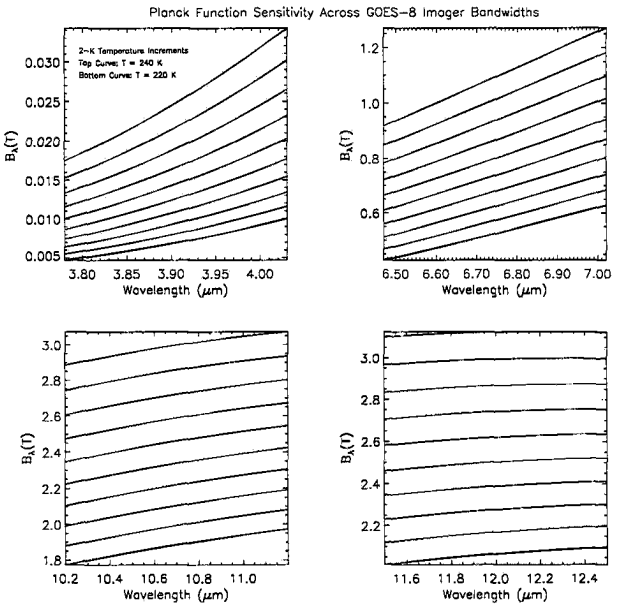

Figure 4.41: GOES-8 Channel 2-5 sensitivity to Planckian emission for typical upper-tropospheric cloud emitting temperatures.

over a typical range of ambient cirrus temperatures (values for water clouds show a similar structure with a slight shifting of the pattern to shorter wavelengths and higher values of intensity). The strongest relative changes are observed for Ch. 2 and 3, with the flatter response in Ch. 4 and 5 corresponding a region near the peak of emissions for these temperatures according to Wein's displacement law which states the wavelength $\lambda_{\max}$ (μm) of maximum emission for a blackbody is related to its temperature T by

$$\lambda_{\max} T = 2898^{\circ} K, \tag{4.9}$$

solved by determining $dB_{\lambda}(T)/dT = 0.0$ using Equation 2.13. These sensitivities aided in the choosing of appropriate band-intervals for these channels in the forward model.

4.4.7 Forward model sensitivity to surface albedo

For retrievals employing channels in the NIR and VIS, an important consideration is the dependency of the scene radiance on the surface albedo. Figure 4.42 indicates that sensitivity to surface albedo at all cloud optical depths in Ch. 1, while sensitivity falls to negligible values beyond $\tau \approx 7$ in the Ch. 2 case. Multiple scattering between cloud base and the surface (the propagator terms from Equation 2.44) leads to contributions in

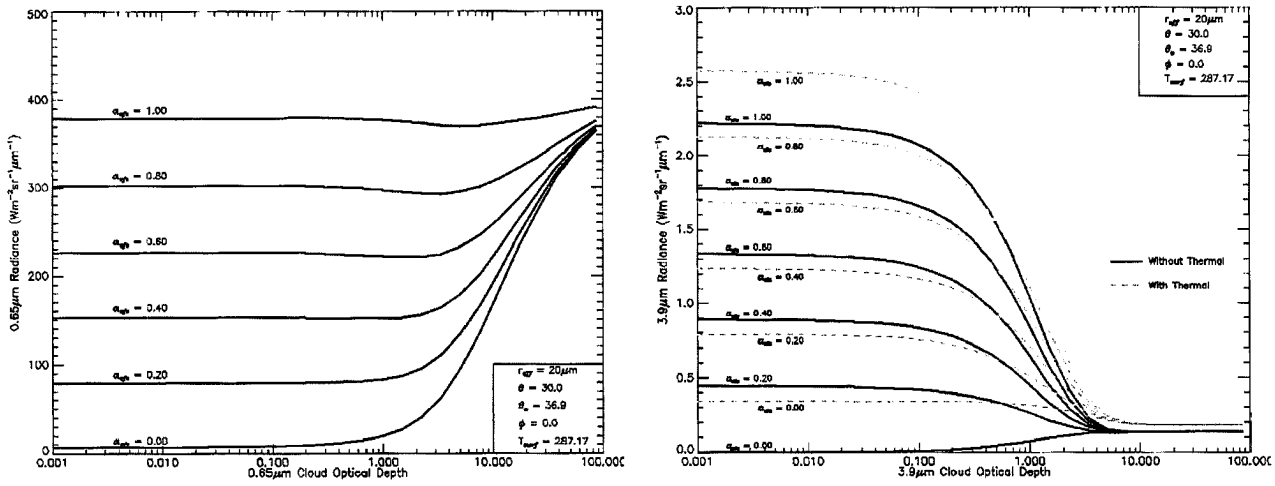

Figure 4.42: GOES Ch1 (0.65-μm, left panel) and Ch2 (3.9 μm, right panel) surface albedo sensitivities (Following Nakajima and Nakajima, 1995)for a 1km-thick water cloud with optical depth values as indicated. The 3.9 μm example shows full-scene (dashed) and solar-reflection only (solid) components for this case.

the former case, and a higher absorption at 3.9 μm removes the energy in the presence of multiple scattering in the latter. For thin clouds, it is clear that specification of the reflecting lower boundary can represent a critical source of *a priori* uncertainty. For satellite retrievals, nearby "clear-sky" pixels are often used as to estimate the surface albedo. Here, errors associated with surface heterogeneity (i.e., assuming the nearby pixel has the same surface properties as the pixel of interest) arise. For simplicity, most retrievals presented in this research were performed over uniform, dark ocean surfaces to minimize these uncertainties. Determination of surface albedo is discussed for each retrieval case individually.

4.5 Instrument Measurement Uncertainties

Measurement errors generally are comprised of a calibration coefficient error (ϵ_{calib}) and an absolute measurement error (shot noise, ϵ_{shot}). The reasonable assumption is made that errors are uncorrelated between different channel measurements, such that the off-diagonal elements of the S_y matrix are zero.

GOES 8 Noise Specifications				
Channel	*Bandwidth (μm)*	*IGFOV (km)*	*SSR (km)*	*Noise*
1	0.52-0.72	1.0 × 1.0	0.57 × 1.0	10-bit data ± 8 counts
2	3.78-4.03	4.0 × 4.0	2.3 × 4.0	0.15K @ 300K, 3.50K @ 230K
3	6.47-7.02	8.0 × 8.0	2.3 × 8.0	0.30K @ 230K
4	10.20-11.20	4.0 × 4.0	2.3 × 4.0	0.20K @ 300K, 0.40K @ 230K
5	11.50-12.50	4.0 × 4.0	2.3 × 4.0	0.20K @ 300K, 0.40K @ 230K

Table 4.2: GOES-8 imager channel bandwidth, instantaneous geometric field of view (IGFOV), sampled sub-point resolution (SSR), and noise specifications.

4.5.1 GOES Imager channel uncertainties

The main sources of uncertainty for GOES are the navigation of scene (determination of a pixel location), registration (the consistency of a given pixel's navigation from one image to the next) and the calibration of the imager channels. Sources of navigation/registration errors include i) Orbital Effects (the inclination, eccentricity and drift from the nominal equatorial sub-satellite point; parameters that are deterministic and therefore compensatable), ii) Structural/Thermal Distortion (resulting in shifting of the image–a pixel registration problem that is usually also compensatable), iii) Non-ideal Response (system noise), iv)Magnetic Storms, and v) Moving Components (structural vibrations of solar array, sail and boom, momentum wheel and imager optical axis due to scanner motions; an incompensatable uncertainty which must be minimized by design. Scan motions disturbing the spacecraft *attitude* are compensatable via image motion and mirror motion compensation.)

GOES instrument noise was computed according to NOAA protocols for signal-to-noise ratios (SNR) in channel 1 and noise-equivalent delta temperatures (NEΔT) for the IR channels (Weinreb *et al.*, 1997). Nominal values for noise in GOES-8 channels are listed in Table 4.2 If the Planck function is rewritten as

$$
\begin{aligned}
B(\nu,T) &= \frac{c_1\nu^3}{e^{c_2\nu/T}-1} \\
c1 &= 1.191062\times10^{-5}(\mathrm{mW/sr/m^2/cm^{-1}})/(\mathrm{cm^{-1}})^{-3} \\
c2 &= 1.4387863(\mathrm{K/cm^{-1}})
\end{aligned}
$$

Channel	GOES-8	GOES-9	GOES-10
2	0.1594	0.1065	0.0933
3	0.1394	0.1231	0.1324
4	0.1140	0.0710	0.0725
5	0.2032	0.1725	0.1516

Table 4.3: GOES imager IR channels on-orbit noise-equivalent delta-temperature (NEΔT) figures provided from NOAA/NESDIS

where ν is the central wavenumber (cm^{-1}) of the channel, then

$$\frac{dB}{dT} = \frac{c_1 c_2 \nu^4 e^{c_2\nu/T}}{T^2(e^{c_2\nu/T}-1)^2}. \tag{4.10}$$

NEΔT is the instrument noise in temperature units, and NEΔB is the instrument noise in units of radiance. These values are related to Equation 4.10 as follows

$$\frac{\frac{NE\Delta B}{NE\Delta T}|_{T_1}}{\frac{NE\Delta B}{NE\Delta T}|_{T_2}} \approx \frac{\frac{dB}{dT}|_{T_1}}{\frac{dB}{dT}|_{T_2}}, \tag{4.11}$$

where T_2 is the brightness temperature of the measurement, and T_1 is a reference temperature at which experimental values of NEΔT for the GOES Channels are provided in tables for all detectors. Table 4.3 provides figures of NEΔT for Ch. 2-5, detector A of GOES 8-10. Because NEΔB does not vary with temperature, Equation 4.11 reduces to

$$NE\Delta T|_{T_2} \approx NE\Delta T|_{T_1} \times \frac{\frac{dB}{dT}|_{T_1}}{\frac{dB}{dT}|_{T_2}}, \tag{4.12}$$

where the desired quantity $NE\Delta T|_{T_2}$ is the channel noise in the units of the measurement as required for the Rodgers error covariance (T. Baucom, personal communication).

For visible channel noise calibration, least-squares fits of pre-launch noise versus albedo were translated to fit the post-launch noise measured at 0% albedo (looking into deep space). The translated fit was used to compute the on-orbit noise at an albedo of 100%, and the on-orbit signal at this albedo was interpolated from pre-launch values (Baucom, 1998). The SNR was then defined as

$$SNR = \frac{Signal(\alpha = 100\%)}{Noise(\alpha = 100\%)}. \tag{4.13}$$

Detector	GOES-8	GOES-9	GOES-10
1	304.2	282.5	286.2
2	282.0	274.6	290.1
3	284.6	257.9	261.0
4	269.2	267.7	259.4
5	284.6	283.7	291.1
6	273.8	265.7	278.6
7	295.0	278.5	295.7
8	298.2	277.9	281.2

Table 4.4: GOES imager VIS channel on-orbit SNR (defined with respect to a scene albedo of $\alpha = 100\%$) figures for all detectors provided from NOAA/NESDIS

A relationship based on linear fits to pre-launch SNR versus target albedo

$$SNR = 279.3\alpha + 6.3, \tag{4.14}$$

(average fit to all detectors, which were very similar) was shifted to match the post-launch SNR at $\alpha = 100\%$ to obtain the in-orbit relationship. To compute the GOES Ch. 1 noise; 1) the radiance measurement was converted to albedo, 2) the correct version of Equation 4.14 was invoked to obtain the SNR, 3) the SNR was inverted to obtain the noise fraction, and finally 4) the noise fraction was multiplied by the measurement to obtain the uncertainty in units of the measurement as required by the Rodgers error covariance matrices.

GOES detector gain drift

An additional concern to the GOES measurements was the degradation of the visible channel sensitivity (defined in terms of amplifier gains) as first noted by Weinreb (1995). Causes for such degradation can range from the accretion of deposits on the reflecting mirrors within the optical assembly, electronic (amplifier) gain deterioration, or other hardware-related problems. Preliminary findings indicated that the GOES-8 visible detector, originally calibrated to 1.81 counts/[W m^{-2} sr^{-1} μm^{-1}] experienced a decrease to 1.65 over a period of 6 months in orbit. Follow-up tests revealed a continued degradation in upwards of 16% from pre-launch testing. Independent studies extrapolated from

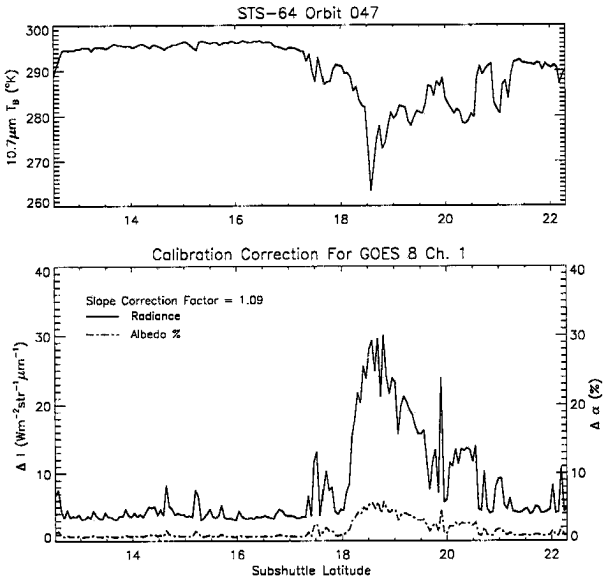

Figure 4.43: Example of GOES Ch. 1 calibration correction and its implications to the computed measured radiances and albedos. Top panel: Ch. 4 brightness temperature along a flight track as seen from GOES. Bottom Panel: Ch. 1 radiance and albedo differences (corrected minus degraded).

pre-launch values to present indicate a degradation rate of roughly 6.1%/yr (Ken Knapp, personal communication). GOES count-to-radiance calibration coefficients were corrected by the appropriate scaling factors (an example of this correction is shown in Figure 4.43.

4.5.2 SSP measurement uncertainty

A detailed error analysis for the SSP instrument calibration is given by Stephens *et al.* (1999). Based on extensive calibration both at the Sandia National Laboratory (SNL) and the Los Alamos National Laboratory (LANL) Optical and Infrared Laboratory using a 12 inch Labsphere integrating sphere, errors for the radiance channel was found to be no more than 2% and 4% for the visible and near-infrared portions of the spectrum, respectively. A nominal uncertainty figure of 3% was used for SSP calibration of radiances in the retrievals of this research (largely independent of temperature conditions). Three independent calibrations were performed on the instrument over a 2 year period, over which time the calibration was observed to remain stable.

4.6 Construction of the Error Covariance Matrices

Being a function of cloud height satellite/solar geometry, profile, and measurement magnitude, error estimation for a retrieval must be computed at run time (i.e., no ensemble error look-up tables are available). After all the components of forward model and measurement uncertainty for a retrieval point have been defined, they are combined to form the diagonal element of the S_y matrix as follows

$$\begin{aligned} S_y(i,i) &= \sum_{i=1}^{N} [\epsilon_i(P(\Theta)) + \epsilon_i(Quad) + \epsilon_i(PP) + \\ &\quad \epsilon_i(Profile) + \epsilon_i(Gas) + \epsilon_i(Meas)] \times y(i), \end{aligned} \tag{4.15}$$

where error terms on the right hand side of this equation are associated with uncertainty in phase function structure, number of streams, the plane-parallel approximation, temperature/surface-albedo/gaseous-absorber profile specification, the correlated-K gaseous absorption approach, and instrument calibration uncertainties. Cross covariances (off-diagonal components) between measurements are assumed to be zero (uncorrelated). These figures, specified in percentage, are converted to units of the measurements by multiplying by the appropriate element of the measurement vector, $y(i)$. The non-linearity of the Planck function requires that errors in the IR channels be computed first in terms of radiance and then converted to corresponding brightness temperature errors. The same care was taken for measurements of bi-directional reflection. For measurement elements formed by combinations of channels, errors were combined according to standard error analysis procedures for independent random errors. For addition/subtraction and quotients between two measurements I_a and I_b, for example, the associated errors (δ_a, δ_b) combine as

$$I_a \pm I_b \rightarrow \sqrt{\delta_a^2 + \delta_b^2} \tag{4.16}$$

and

$$\frac{I_a}{I_b} \rightarrow \sqrt{\left(\frac{\delta_a}{I_a}\right)^2 + \left(\frac{\delta_b}{I_b}\right)^2}. \tag{4.17}$$

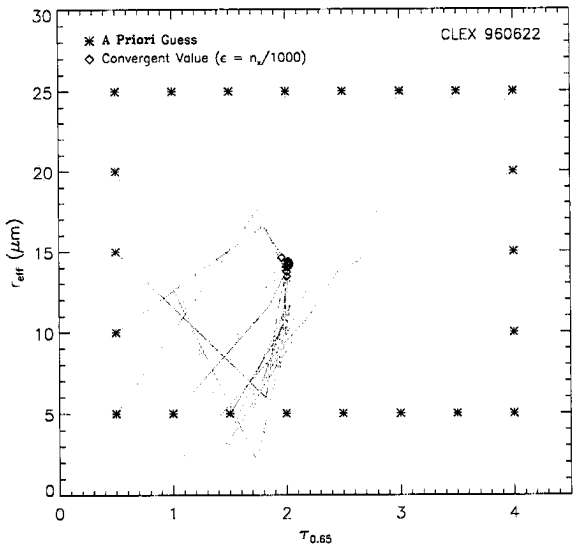

Figure 4.44: Example of the retrieval stepping toward convergence for a single retrieval point and multiple *a priori* parameter guesses.

Because the initial guess on the retrieved parameters (τ and r_{eff}) are based at best on only a very general climatology (for ice clouds an initial guess of $\tau = 1.0$ and $r_{\text{eff}} = 30\mu$m, and for water clouds $\tau = 5.0$ and $r_{\text{eff}} = 10\mu$m) with a large variance acknowledged, the diagonal elements of the S_a matrix are set to accordingly large variances such that the solution is not constrained to them from the onset of the retrieval. In cases where the retrieval has difficulty in finding a solution, however, these *a priori* guesses weigh in more heavily, with a corresponding decrease in the *a priori* matrix ($A(i,i)$ falling far below unity, and hence reflecting retrieval insensitivity to the i^{th} parameter).

4.7 Sensitivity to *A Priori* Parameter Estimates

As discussed in the previous chapter, a retrieval having sufficient sensitivity to the parameters it is attempting to retrieve ideally should display no significant biases to the *a priori* guesses (i.e., the *A Priori* Matrix elements should be close to unity). The iterative behavior of the retrieval as it steps towards convergence, however, can vary significantly as a function these guesses–owing to differences in model sensitivity which affect the elements of the Kernel functions and hence the stepping behavior of the retrieval vector itself (e.g., according to Equation 3.20). Figure 4.44 demonstrates this behavior for a single retrieval

point (based on a cloud with $\tau \approx 2.0$ and $r_{\text{eff}} \approx 15\mu$m and several different *a priori* starting points. The convergence criterion for this example was set at $\epsilon = n_x/1000$ (see Equation 3.30). While all the cases converge to the common solution within 4 iterations, the nature of the paths taken are clearly a function of the *a priori* guess. At larger effective radii, significant "overshoot" of the solution was observed. This is explained by the weaker model sensitivity (Kernel function) for larger r_{eff} owing to asymptoting of the cloud optical properties (g and ω_o) referring back to Figures 4.6-4.7. The weaker sensitivity encourages the model to increase the step size (by reducing the value of $\hat{S}_x^{-1}$ in the denominator of Equation 3.20). Similar overshooting behavior is observed for larger values of τ, where in this case the signal is becoming saturated (and thereby lowering the Kernel function components). In contrast, *a priori* values within regions of higher sensitivity exhibited a more direct step towards convergence. Based on these tests, the *a priori* vector for most retrievals of the work were set at $\tau = 1.0$ and $r_{\text{eff}} = 10\mu$m. For clouds having optical parameters in lower-sensitivity regimes of the forward model, the overshooting effect will still occur as the retrieval vector traverses towards the solution regardless of *a priori* guess. The choice of initialization in a region of higher model sensitivity, however, ensures that at least the retrieval begins the iterative process with its bearings straight.

4.8 Summary

This chapter introduced the passive instrumentation used in the retrievals of this work, developed a physical basis for what cloud properties are retrievable from these instruments (namely, cloud optical depth and effective particle radius. Nakajima and King (1990) emphasize that our interest in these parameters does not stem simply from the fact that they are readily retrievable quantities, but from the fact that cloud radiative properties (e.g., albedo, transmission, absorption) depend almost exclusively on these very parameters. This chapter also examined the sensitivities and uncertainties associated with the forward model and measurements. The components of the forward model and measurement uncertainty are combined to build the $S_{\tilde{y}}$ matrix of the Rodgers retrieval, and are essential to assessing the credibility of the retrieved parameters. The forthcoming

chapter presents examples of actual cloud r_{eff} and τ retrievals based on the observing systems and physical relationships outlined above. The degree to which accurate cloud height information (as provided by various active sensors) improves passive sensor retrievals may then be determined from the Rodgers diagnostic variables.

Chapter 5

CLOUD RETRIEVAL CASE STUDIES

5.1 Introduction

Having examined properties and sensitivities of the forward model, determined a suitable estimation approach, and outlined the physical basis for retrieval, the next step was to combine these tools to quantify how active sensors improve existing cloud property retrieval methods. This chapter summarizes the results of cloud optical property retrievals performed using several passive/active instrument observing systems from various experiments and IOPs conducted over the last several years. While the actual values of the properties retrieved are useful for comparison to independently-derived quantities (e.g., validation exercises), the *main* points of emphasis in these case studies are two-fold: i) illustrating the unique error-diagnostics available to the retrieval and, ii) quantifying the relative retrieval improvement afforded by *a priori* active sensor cloud height profiles. Numerous retrieval case studies drawing upon a multitude of observing platforms and cloud types have been assembled for this purpose. The reader is alerted to the fact that many of the cases presented here are redundant in terms of the message they convey, but all have been summarized here for the sake of reference (hence the girth of this chapter). Further, all cases contribute to a presentation of generalized results at the close of the chapter.

5.2 Cloud Ranging in Profile

Retrievals were performed for cases both with and without active sensor *a priori* cloud heights to assess the significance of this additional information on the cloud properties retrieved. The question is especially relevant to night-time (emission) retrievals, where an estimate of cloud location in the vertical (i.e., its emitting temperature) is needed. While

the assignment of cloud heights in the retrievals supplied with active sensor information were relatively straightforward, the same cannot be said for passive-only retrievals (especially at night, where not even cloud shadows are available). For simplicity in both retrieval and interpretation of results, case studies featuring primarily single-layer (water or ice) clouds were examined.

5.2.1 Active sensor cloud profiling

Ostensibly, the detection of cloud boundaries using active sensors is a straightforward matter of identifying large gradients in the backscatter profile and defining an appropriate threshold with respect to a defined background return strength. As with most measurements, however, there do exist caveats and "grey-areas" associated with this procedure. The active instruments used in the retrievals of this research were lidar (ground-, aircraft-, cloud detection lidar (CDL), space-based lidar (LITE)) and airborne cloud radar (ACR, developed and operated by the University of Massachusetts (UMass) and Jet Propulsion Laboratories (JPL)). Summarized briefly here are the procedures followed to obtain cloud boundary information from these data and their accompanying uncertainties.

Radar-derived cloud heights

Ignoring atmospheric attenuation, the general form of the radar equation is given as follows:

$$P(r) = \frac{C_{rad}}{r^2}\eta, \tag{5.1}$$

where $P(r)$ is the radar return power, C_{rad} is the radar system constant, and η is the radar reflectivity expressed in terms of the radar wavelength λ, particle dielectric constant magnitude $|K|^2$, and particle diameters D within the sample volume:

$$\eta = \frac{\pi^5}{\lambda^4}|K|^2 \sum_{vol} D^6. \tag{5.2}$$

The summation term is called the radar reflectivity factor, $Z(r)$. Solving for it using Equations 5.1-5.2 yields

$$Z(r) = \frac{P(r)r^2\lambda^4}{C_{rad}\pi^5|K|^2}. \tag{5.3}$$

Cloud edge information was computed from radar data using a detection algorithm which employed signal-to-noise ratio thresholding technique and hysteresis for stability. Each radar profile was comprised of 188 range bins. Within each profile, the gates are scanned from a point near (just above, to avoid ground clutter) the surface and compares the value of the SNR(dB) ($= 10log_{10}(SNR)$) to an effective SNR defined as

$$ESNR(dB) = SNR(dB) + 5log_{10}(\#Averages) + 3dB, \tag{5.4}$$

where $\#Averages$ is the number of radar pulses averaged together to compute the profile data. The 3 decibel offset is added to the threshold in an effort to filter-out spurious profile noise which might mistakingly be attributed to cloud. Without it, an 18% error in cloud detection is incurred, and its inclusion results in only minimal effects on cloud edge detection (G. Sadowy, personal communication). As defined, whenever the *ESNR* exceeds 0.0 decibels the bin is classified as cloudy. To further reduce the possibility of spurious noise contamination, a stability threshold of three continuous range gates inside (outside) of cloud is enforced in the assignment of in-cloud (out-cloud) status. The usage of SNR data is superior to reflectivity thresholding, since there exists a $(1/R^2)$ dependency in the latter such that a threshold at one range is not applicable to the entire profile (whereas SNR is a range-independent quantity). These data were combined with the GOES-8 measurements, instrument/solar angular geometry, and sounding data to retrieve single-layered cloud optical depths and effective cloud particle radii along the flight track. The uncertainty associated with cloud boundary placement for this instrument using this method generally is within $\pm$ 60 m.

Lidar-derived cloud heights

For a vertically-oriented lidar, the backscatter return as a function of height,$P_{lid}(z)$, can be expressed (entirely analogous to the radar equation) as:

$$P_{lid}(z) = \frac{C_{lid}\beta(z)}{z^2} exp\left[-2\int_0^z \eta(z)\sigma(z)dz\right], \tag{5.5}$$

where C_{lid} is the lidar system constant and $\beta(z), \sigma(z)$, and $\eta(z)$ are the range-dependent volume backscatter coefficient, volume extinction coefficient, and multiple-scattering correction factor, respectively. The latter three terms are unknown quantities which comprise

the attenuated backscatter coefficient

$$\beta'(z) = \beta(z) exp\left[-2\int_0^z \eta(z)\sigma(z)dz\right], \tag{5.6}$$

such that the lidar equation assumes the form

$$P_{lid}(z) = \frac{C_{lid}\beta'(z)}{z^2}. \tag{5.7}$$

The multiple-scattering correction factor, varying from 0 to 1, reduces the volume extinction term to account for enhanced cloud penetration of lidar photons by strongly forward-scattering particles.

Cloud profile data along LITE orbits were obtained from NASA Langley's Level II LITE database. Computed from the raw reflectivity returns, the CloudFinder algorithm (Winker and Vaughan, 1994) used to process the data invokes an altitude-dependent thresholding approach operating on attenuated scattering ratios:

$$R' = \frac{\beta'(z)}{c_{lid}\beta'_{mol}(z)}, \tag{5.8}$$

where $\beta'_{mol}(z)$ is the attenuated backscatter cross-section for the molecular atmosphere alone (a monotonically decreasing function of altitude). Clouds are classified whenever R' exceeds the threshold

$$T = 1 + \frac{T(z_o)}{\beta'_{mol}(z)}, \tag{5.9}$$

which increases monotonically with altitude to maintain a constant threshold with respect to increasing noise with altitude. Only night-time heights were available, as solar reflection adds very high noise to the day-time orbit profiles. An example of the cloud profiles retrieved from raw LITE imagery using the CloudFinder algorithm is given in Figure 5.1. Thin cirrus clouds are readily detected, as well as multiple layers of cloud. Important considerations for these data is the possibility of complete attenuation of the lidar beam in optically-thick clouds that results in a LITE-derived cloud base which is too high, and pulse stretching (Winker, 1997); an artifact of multiple scattering which leads to derived cloud bases which are too low. Figure 5.1 contains examples of both these effects. Complete attenuation of the lidar beam occurs within the deep convective cloud near 33

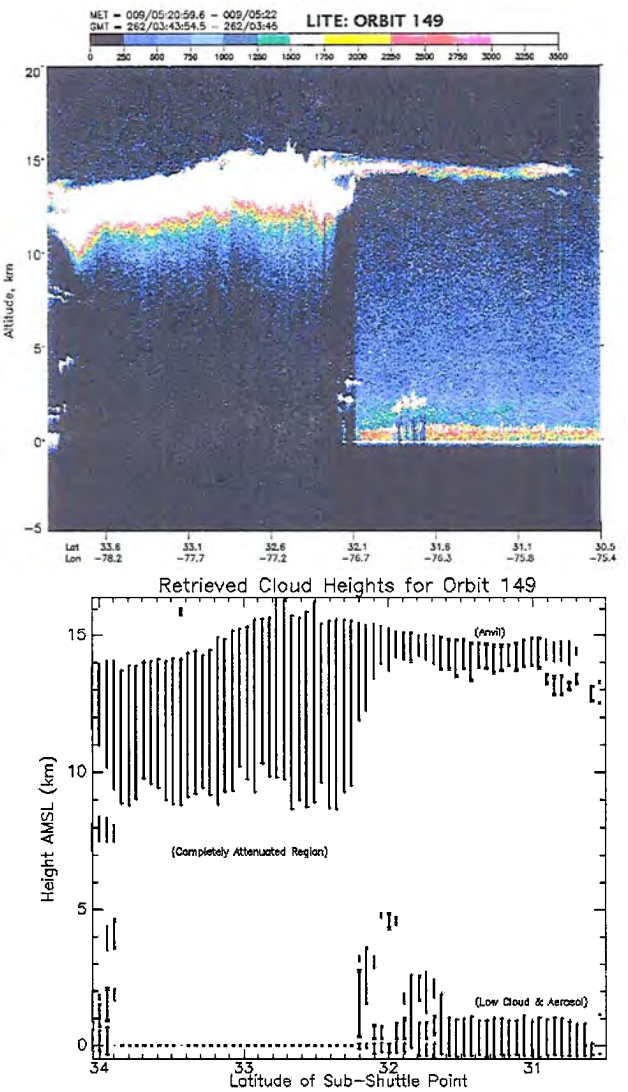

Figure 5.1: Example of cloud heights retrieved (lower) from a subsection of raw lite imagery (upper). Note complete attenuation of the lidar beam within the region of deep convection.

N and returns below the ocean surface are seen near 31-N. Cloud base is placed at the lowest observable base in the case of complete pulse attenuation, and at 0.3 km above the surface in cases of below-surface pulse stretching.

Studies (e.g., Winker and Poole, 1995; Miller and Stephens, 1999) have indicated that pulse stretching in cirrus is negligible while that of liquid water clouds can be significant (> 5 km below true cloud base in some occurrences). Miller and Stephens (1999) attempt to model these effects in terms of cloud optical properties (e.g., optical depth, structure of the scattering phase function, and physical cloud geometry). For night-time retrievals of optically-thick clouds, exact knowledge of cloud base may not effect adversely the retrieved results (satellite-measured emissions being characterized in this case by optical properties in the uppermost portions of the cloud).

The terrestrial/airborne cloud detection lidar (CDL), being considerably closer to cloud targets, does not experience pulse stretching effects as observed extensively in LITE data (this is fortunate, since for a ground-based instrument these would lead to an over-estimate of cloud top heights which could alter considerably the satellite-retrieved optical depth). Complete attenuation of the beam remains a problem, especially in cases where a radiatively significant cirrus layer may go undetected above an optically-thick lower-level water cloud. A thresholding method similar to the NASA Langley CloudFinder code was applied to define cloud boundaries in these CDL data.

5.2.2 Passive-only cloud height estimation

For retrievals based exclusively on solar reflection measured in window channels (notwithstanding the case of heavy aerosol loading) the accurate placement of clouds in the vertical is of secondary importance. Most retrievals require an absorbing/emitting channel to achieve sensitivity to particle size. In these cases, the location of the cloud in the vertical will determine its emitting temperature; information necessary for its accurate representation in the forward model. Some methods (e.g. Minnis, 1993) have invoked parameterizations of IR cloud emissivity as a function of visible reflectance to circumvent the need for this knowledge (in this case, the cloud height falls out as a by-product

of the retrieval). In other instances when available, cloud shadows may be used to approximate cloud top heights. Cloud top heights can also be estimated using the stereo parallax method (Bryson, 1978; Hasler, 1981) in cases when clouds are observed between two satellites without underlying cloud layers to an accuracy of roughly 1 km (Wylie, 1989). This research considers only the simple (and most common) case of single-satellite observations of a cloud scene. For the retrievals of this study, the best available passive method was applied for comparison against retrievals with active-derived *a priori* cloud profile information.

Ice clouds

For cirrus, the method of Szejwach (1982) was employed to approximate cloud heights from passive sensor measurements in the infrared. By showing that cloud emissivity is nearly the same for 6.5 μm (water vapor) and the 10.7 μm (infrared window) channels, it is argued that the brightness temperature difference observed between these two measurements (for a cloud residing above the majority of atmospheric water vapor) is due not to the cloud being more opaque in one channel but rather to the colder atmospheric upwelling eric emission measured at 6.5 μm. Following the notation of Szejwach (1982), the satellite-measured cloud reflectances in both channels are written as

$$\begin{aligned} R_{6.5}(T_{6.5}) &= \epsilon_{6.5} R_{6.5}(T_{cld}) + (1 - \epsilon_{6.5}) T_{atm,6.5} \\ R_{10.7}(T_{10.7}) &= \epsilon_{10.7} R_{10.7}(T_{cld}) + (1 - \epsilon_{10.7}) T_{atm,10.7} \end{aligned} \tag{5.10}$$

where T_{cld} is the ambient cloud temperature and T_{atm} are the effective emitting temperatures of the atmosphere below the cloud for the two channels. Equating the cloud emissivities allows Equations 5.10 to be combined as

$$R_{6.5}(T_{6.5}) = a R_{10.7}(T_{10.7}) + b, \tag{5.11}$$

where

$$a = \frac{R_{6.5}(T_{cld}) - R_{6.5}(T_{atm,6.5})}{R_{10.7}(T_{cld}) - R_{10.7}(T_{atm,10.7})} \tag{5.12}$$

$$b = \frac{R_{6.5}(T_{atm,6.5}) R_{10.7}(T_{cld}) - R_{6.5}(T_{cld}) R_{10.7}(T_{atm,10.7})}{R_{10.7}(T_{cld}) - R_{10.7}(T_{atm,10.7})} \tag{5.13}$$

In this way, a linear fit of simultaneous (6.5 and 10.7 μm) spectral radiance data from a semi-transparent cirrus may be extrapolated to the theoretical blackbody curve (corresponding to a completely opaque cloud at this level) to derive the ambient cloud temperature. A temperature sounding then allows for conversion of the derived mean cloud temperature to an equivalent altitude to be used in the retrievals of τ and r_{eff}. Examples of this procedure are included in the retrieval case studies. While the procedure cannot predict the cloud physical thickness or the presence of multiple cloud layers, and is applicable only for high clouds, it has been considered here as the "best guess" for night-time passive-only estimates of cirrus heights.

Water clouds

Because lower-tropospheric clouds are often embedded within the water-vapor, the GOES Ch. 3 Szejwach technique cannot be applied. Slicing techniques can be used here to retrieve single-layer cloud-top pressure in cases where there exists no overlying cirrus. Following Wylie *et al.* (1982), the all-sky (cloudy plus clear) satellite-observed radiance at wavelength λ from a single pixel is written as

$$\begin{aligned} I_{\lambda,\text{all}} &= (1 - N_{\text{cld}}\epsilon_{\lambda,\text{cld}}) \left(B(\lambda, \mathrm{T_{sfc}})\, Tr_\lambda(\mathrm{TOA}, \mathrm{P_{sfc}}) + \int_{\mathrm{P_{sfc}}}^{\mathrm{P_{cld}}} (\mathrm{B}(\lambda, \mathrm{T_p}) \frac{\mathrm{d}\, Tr_\lambda}{\mathrm{dp}}) \mathrm{dp} \right) \\ &+ N_{\text{cld}} B(\lambda, \mathrm{T_{cld}})\, Tr_\lambda(\mathrm{TOA}, \mathrm{P_{cld}}) + \int_{\mathrm{P_{cld}}}^{\mathrm{TOA}} (\mathrm{B}(\lambda, \mathrm{T_p}) \frac{\mathrm{d}\, Tr_\lambda}{\mathrm{dp}}) \mathrm{dp}, \end{aligned} \tag{5.14}$$

where Tr_λ is the atmospheric specular transmittance, $N_{mathrmcld}$ is the fraction of cloud in the satellite pixel, T_{cld} and P_{cld} are the temperature and pressure at cloud top, and $\epsilon_{\lambda,\text{cld}}$ is the specular cloud emissivity. This equation describes the contributions from surface emission, the atmosphere below the cloud, the cloud itself, and the atmosphere above the cloud (column-integrated weighted appropriately by atmospheric transmission). Quantities listed here as specular are in fact band-quantities corresponding to the instrument response function. For the case of a clear-sky measurement, Equation 5.14 reduces to

$$I_{\lambda,\text{clr}} = B(\lambda, \mathrm{T_{sfc}})\, Tr_\lambda(\mathrm{TOA}, \mathrm{P_{sfc}}) + \int_{\mathrm{P_{sfc}}}^{\mathrm{TOA}} (\mathrm{B}(\lambda, \mathrm{T_p}) \frac{\mathrm{d}\, Tr_\lambda}{\mathrm{dp}}) \mathrm{dp}. \tag{5.15}$$

Taking the difference between Equations 5.14 and 5.15 yields

$$\begin{aligned} I_{\lambda,\mathrm{all}} - I_{\lambda,\mathrm{clr}} &= -N_{\mathrm{cld}}\epsilon_{\lambda,\mathrm{cld}}(B(\lambda,\mathrm{T_{sfc}}) - \mathrm{N_{cld}}\epsilon_{\lambda,\mathrm{cld}}\int_{\mathrm{P_{sfc}}}^{\mathrm{P_{cld}}}(\mathrm{B}(\lambda,\mathrm{T_p})\frac{\mathrm{d}Tr_\lambda}{\mathrm{dp}})\mathrm{dp} \\ &+ N_{\mathrm{cld}}\epsilon_{\lambda,\mathrm{cld}}B(\lambda,\mathrm{T_{cld}})Tr_\lambda(\mathrm{TOA},\mathrm{P_{cld}}), \end{aligned} \tag{5.16}$$

which can be simplified via integration by parts to produce

$$I_{\lambda,\mathrm{all}} - I_{\lambda,\mathrm{clr}} = N_{\mathrm{cld}}\epsilon_{\lambda,\mathrm{cld}}\int_{P_{\mathrm{sfc}}}^{P_{\mathrm{cld}}}(Tr_\lambda(p)\frac{dB(\lambda,\mathrm{T_p})}{dp})dp. \tag{5.17}$$

This represents the "cloud signal" in the satellite measurement. The ratio of this difference quantity for two nearby spectral bands designated by λ_1 and λ_2 can be written as

$$\frac{I_{\lambda_1,\mathrm{all}} - I_{\lambda_1,\mathrm{clr}}}{I_{\lambda_2,\mathrm{all}} - I_{\lambda_2,\mathrm{clr}}} = \frac{N_{\mathrm{cld}}\epsilon_{\lambda_1,\mathrm{cld}}\int_{P_{\mathrm{sfc}}}^{P_{\mathrm{cld}}}(Tr_{\lambda_1}(p)\frac{dB(\lambda_1,\mathrm{T_p})}{dp})dp}{N_{\mathrm{cld}}\epsilon_{\lambda_2,\mathrm{cld}}\int_{P_{\mathrm{sfc}}}^{P_{\mathrm{cld}}}(Tr_{\lambda_2}(p)\frac{dB(\lambda_2,\mathrm{T_p})}{dp})dp}. \tag{5.18}$$

Provided that λ_1 and λ_2 are sufficiently close, the cloud emissivity terms cancel and the relationship provides a means to approximating cloud-top pressure. The left hand side is provided from satellite scene radiances (the cloudy pixel and a nearby clear-column pixel, with the underlying assumption that all atmospheric/surface parameters contributing to the measurement remain the same between the two), and the right hand side is computed from an *a priori* set composed of an appropriate temperature profile and profiles of atmospheric spectral transmittance as a function of cloud top pressure, P_{cld}. The best match between observations and calculated quantities yields the solution for cloud-top pressure. Because CO_2 is a well-mixed gas (minimizing uncertainty associated with computation of transmittance look-up tables), channels situated in the 15 μm band (dominated by CO_2 absorption) are most often used for this application. The resolution and accuracy of these data (along with measurement uncertainty and assumptions on the representativeness of the clear-sky pixel) determine the uncertainty associated with the slicing method.

As posed, no cloud thicknesses are available from this method. In the passive-only retrievals of water clouds without overlying cirrus it was assumed that the CO_2 slicing technique may be applied to retrieve the cloud top height to within an uncertainty of ± 1 km (following calculations of Wylie and Menzel, 1989). This is probably a reasonable approximation when considering that lower-tropospheric clouds tend to be more optically

thick than most cirrus, and for this reason even simple brighness-temperature/sounding height conversions will yield smaller uncertainties. For lack of a better alternative the geometric thickness of clouds in the passive-only retrievals of this work were set at fixed a value of 1 km (following ISCCP protocols). For the case of overlying cirrus, underlying water cloud layers were assumed to be missed entirely by the passive-sensor-only techniques.

5.3 LITE 940909-940920 Retrievals

This section summarizes retrieval case studies performed using GOES-8 imager data in conjunction with lidar cloud heights derived from Lidar In-space Technology Experiment (LITE) data. The retrievals in all cases to follow include a brief overview of the experiment, a presentation of the retrieved parameters and an error analysis as afforded by the Rodgers retrieval. Comparisons between active-plus-passive and passive-only retrievals were made to assess the benefit of the active data. When available, comparisons with independently-derived optical properties or related quantities (e.g., flux measurements) were computed as an independent test of the retrieval.

5.3.1 LITE Orbit 149 case

Overview

LITE was flown aboard the Space Shuttle Discovery during September of 1994. As the first civilian effort to operate an active instrument on the space platform for the purposes of environmental remote sensing, LITE sampled the atmosphere at near-nadir using a 532 nm Nd-YAG lidar instrument to provide detailed profiles of cloud and aerosol along the Discovery orbit track. Because of solar contamination of day-time lidar returns, only night orbits were considered for the LITE retrievals. Unfortunately, independent retrievals based on LITE data exclusively were unattainable from the data due to the instrument being operated in a high-gain mode which saturate the cloud backscatter returns. This did not preclude its applicability to detect cloud edges and hence provide high resolution cloud *boundary* information in a given profile. For the purposes of the passive retrievals which

assume a plane-parallel and vertically homogeneous distribution of cloud properties in the forward model, the boundary information without detailed internal structure sufficed. A full summary of the experiment, lidar hardware, and system overview are described in detail by Couch *et al.* (1991), McCormick *et al.* (1993), and Winker *et al.*, (1996).

Data from a portion of LITE orbit 149 within the GOES-8 field of regard constituted the *a priori* cloud height information (Fig. 5.2). Because no visible data were available for this night-time orbit, an observing system exploiting the spectral-differencing sensitivities observed by *Prabhakara et al.* [1988] and *Stone et al* (1990) using GOES-8 channels 2,4, and 5 was applied in an IR-only approach. Two-line-element (TLE) ephemeris data were used to compute 1-second resolution sub-shuttle positions which were used in turn to extract non-redundant GOES-8 pixel information from the imagery along the LITE flight track. The water vapor channel (Ch. 3) was used according to *Szejwach* [1981] in the passive-only estimation of cirrus heights as described earlier. For cases where no estimate of the cloud geometric thickness was available (i.e., the passive-only retrievals) a constant cloud thickness of 1 km was assumed. Along-track temperature and moisture profiles were extracted from ECMWF global initialization gridded analysis. Temperature, moisture, and ozone profiles were extrapolated "to space" (e.g., to an altitude of 100-km) using McClatchey profiles appropriate for the time of year and zone(s) traversed by the orbit.

To determine the presence of cirrus in the GOES-8 imagery (and thereby provide a quality-check for the correct co-location between the sub-sectored McIDAS GOES imagery and the LITE flight track), the Support of Environmental Requirements for Cloud Analysis and Archive (SERCAA) algorithm from the United States Airforce (CERES ATB Doc., 1995) was employed. This algorithm, performed on the pixel level and applicable to both day-time and night-time scenes, takes advantage of the spectrally variant emissivity of cirrus by uses the brightness temperature difference (BTD) between Ch. 4 and 5 to detect a cirrus "signature." Because in the absence of cirrus the BTD will be positive due to the enhanced absorption by water vapor in Ch. 5, the appropriate BTD threshold M is defined as a function of the Ch. 4 brightness temperature and observer viewing angle

$$T_{B4} - T_{B5} > M(T_{B4}, \Theta_{\text{obs}}). \tag{5.19}$$

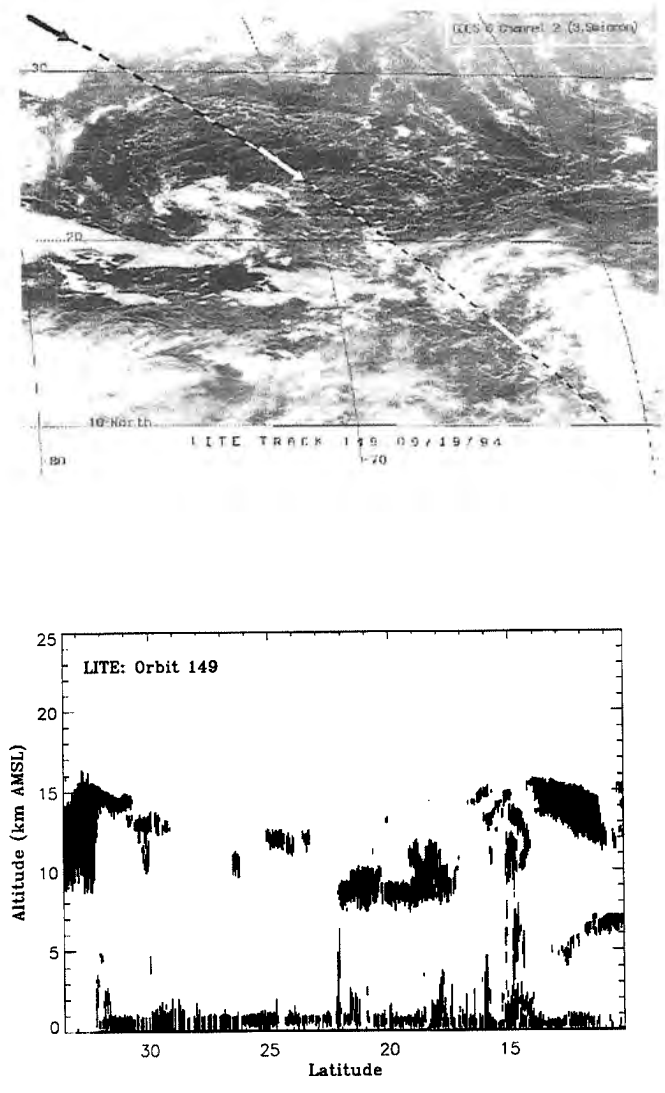

Figure 5.2: GOES-8 co-located LITE orbit 149 shown for the 3.9-μm imager channel (upper panel) and the corresponding LITE-derived cloud profile (lower panel).

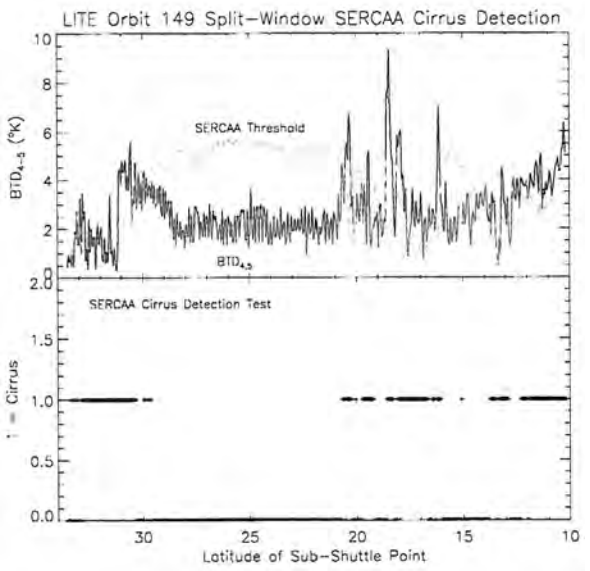

Figure 5.3: The SERCAA cirrus detection test applied to GOES-8 data for the LITE orbit 149 case.

The threshold values are provided for reference in Table 5.1. These thresholds increase for optically thinner cirrus (i.e., larger Ch. 4 brightness temperature) and higher observer zenith angles. In these cases the differential emission between Ch. 4 and Ch. 5 is maximized by water vapor absorption effects in the lower atmosphere. The most tangential observer angle ($\Theta = 60.0°$) views the most optically thick atmosphere (with respect to water vapor) and therefore exhibits the largest BTD thresholds. The results of the SERCAA cirrus detection test for GOES imagery co-located with LITE orbit 149 are shown in Figure 5.3. The upper panel illustrates the SERCAA threshold (dashed curve) plotted

$T_{B4}(K)$	$\Theta = 0.00°$	$\Theta = 36.87°$	$\Theta = 48.19°$	$\Theta = 55.15°$	$\Theta = 60.00°$
260	0.55	0.60	0.65	0.90	1.10
270	0.58	0.63	0.81	1.03	1.13
280	1.30	1.61	1.88	2.14	2.30
290	3.06	3.72	3.95	4.27	4.73
300	5.06	6.92	7.00	7.42	8.43
310	9.41	10.74	11.03	11.60	13.39

Table 5.1: Brightness temperature difference thresholds (M, in Equation 5.19) expressed as a function of the Ch. 4 brightness temperature (T_{B4}) and observer zenith angle (Θ) for the SERCAA cirrus detection test.

against the BTD, and detected cirrus is represented as points at 1.0 in the lower panel. When compared against the LITE-derived cloud heights of Figure 5.2), the coherence of cirrus detected by LITE and SERCAA indicates a successful co-location and extraction of GOES pixel data. A small amount of thin cirrus missed near 24 N, suggesting that the addition of active-sensor data will enable the detection and retrieval of high clouds that may otherwise be missed by passive-sensor techniques alone.

Retrieval results

The retrieval results, associated parameter uncertainty statistics, and *a priori* parameters for LITE Orbit 149 are shown in Fig. 5.4-5.5 for a ground track approximately 1400 km in length. Over this distance, a single layer of cirrus was encountered between 8 and 12 km accompanied by intermittent, boundary layer marine stratus clouds and aerosol. Single Henyey-Greenstein approximations to the scattering phase function were used for these IR-only retrievals as they better-matched the ice crystal data at these wavelengths (e.g., no strong backscattering lobe; referring back to the inset of Figure 4.37 in Chapter 4). Retrieved 3.9 μm cloud optical depths typically were less than 2.0, and effective particle radii ranged between 10 and 50 μm. The total uncertainty and contribution breakdown (obtained by switching on/off components of the S_y matrix and re-running the retrievals) based on the Rodgers-derived expressions of (3.26) are given in the central panels, and the associated *a priori* (3.21) elements are shown in the bottom panels.

In all τ retrievals, errors were of the order $\delta^2 = 0.2$, due largely to sensitivity of the Kernel function and phase function uncertainty. The values of the *a priori* parameter were near unity, indicating that the initial guesses for τ had little bearing on the retrieved values. Errors in the effective particle radius retrievals were much larger, and the error components reveal that the majority of this error was due to uncertainty in the scattering phase function–a figure seldom quantified in the literature. Regions of highest error were correlated strongly with lowest values of A. Thin cirrus were found in general to account for poorest retrieval performance (largest sensitivity to the phase function). The sensitivity of the forward model to changes in particle size decreased with increasing particle size. The retrieval therefore relied more heavily on *a priori* information for convergence in the cases

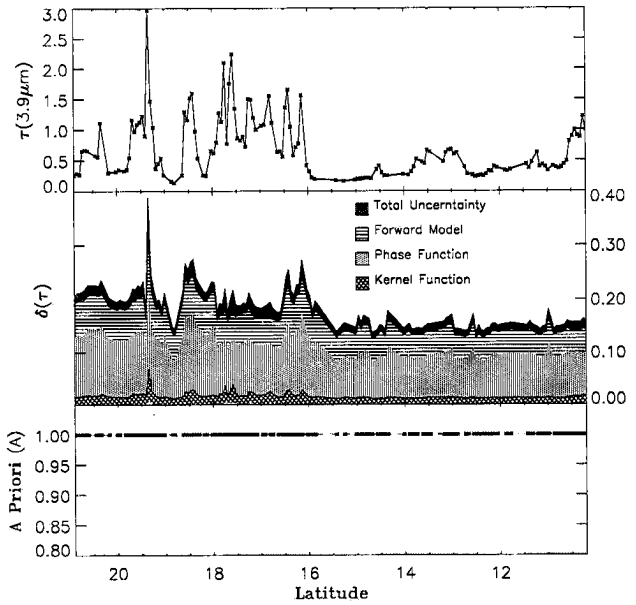

Figure 5.4: Optical Depth retrieval and uncertainty components for LITE Orbit 149.

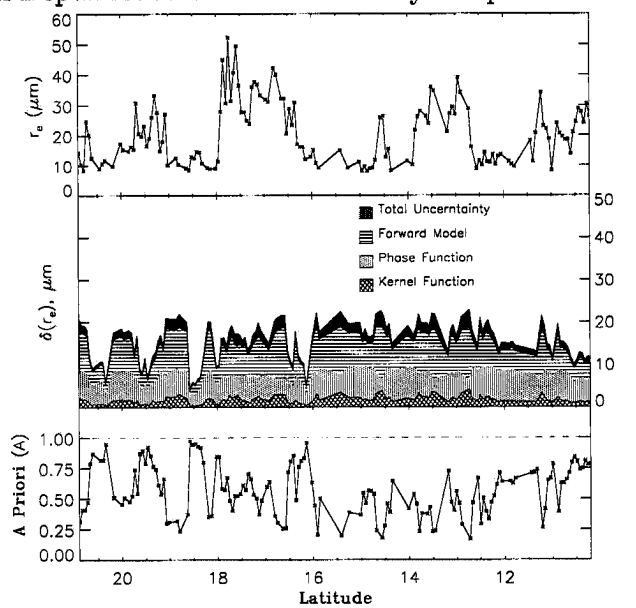

Figure 5.5: Effective radius retrieval and uncertainty components for LITE Orbit 149.

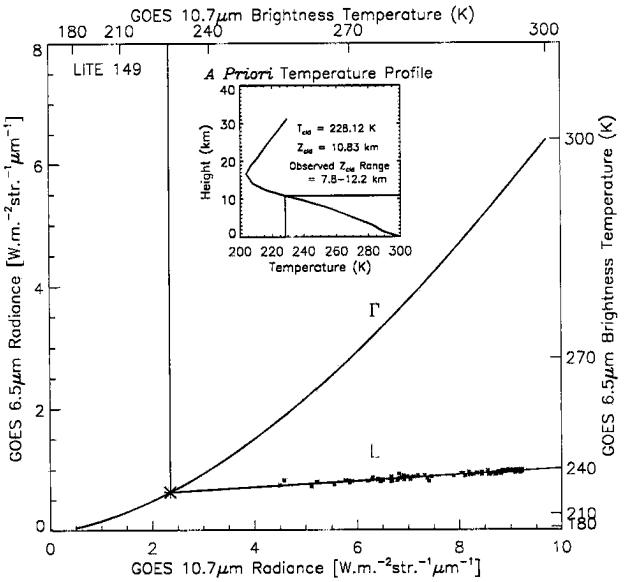

Figure 5.6: Passive sensor estimate of semi-transparent cirrus height for LITE Orbit 149 using GOES 6.5 μm water vapor and 10.7 μm IR window channels. Curve "Γ" is the theoretical blackbody relationship and line "L" is the linear fit to the observation set (following the method of Szejwach, 1982).

of thin, large-particle cirrus clouds. The Rodgers approach afforded this useful diagnostic information on where to place more/less confidence in the retrieval.

Passive-only retrieval uncertainty

An important point of emphasis to these case studies was the illustration of the benefits active-sensors provide to the retrieval of cloud properties. Because the active cloud profile information introduced constraints to the forward model with negligible error, differences between these retrievals and those employing passive-only cloud height estimates were regarded as a measure of retrieval improvement. The passive-only approximation to the cirrus cloud heights for the orbit section spanning $\approx$ 21 to 16 North Latitude for LITE orbit 149 is given in Figure 5.6. While the passive-only estimate of 10.83 km was well-within the observed range of 7.8- to 12.2 km, no information on cloud thickness was available.

Retrieved parameter differences were then computed for the two cases (with- versus without-*a priori* active cloud profile information) and expressed as a function of the differences between passive (e.g., Szejwach) and actively-derived cloud heights The results are

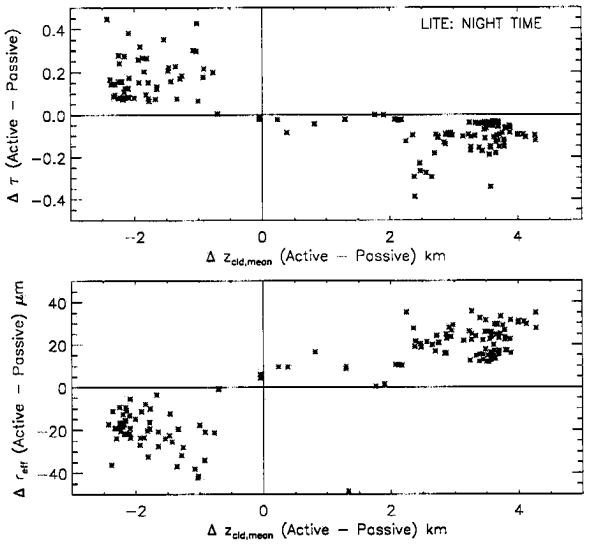

Figure 5.7: Comparison of retrieved parameter differences as a function of LITE-GOES estimated cloud heights.

shown in Figure 5.7. Discrepancies arising from a mis-representation of cloud location in the profile was evident in both parameters. In cases where the cloud was placed too high with respect to the true cloud height (a negative $\Delta Z_{\rm cld}$), the retrieved optical depths were smaller (positive $\Delta\tau$) and the effective particle radii were larger (negative $\Delta r_{\rm eff}$). The converse held when the cloud was placed too low in the profile, producing a distribution of points symmetric about the $\Delta Z_{\rm cld} = 0$ origin in Figure 5.7. In the former case of cloud height overestimation, the cloud was misplaced into a colder (higher) environment. In order for the forward model to reproduce the satellite brightness temperature measurements of this colder cloud, the cloud optical depth were made smaller. This enabled more upwelling radiation from the warmer surface and lower atmosphere to transmit through the cloud and reach the satellite. The larger particle sizes corresponded to larger values of asymmetry parameter (g) in the Mie look-up tables which in turn enhanced the forward scattering of the upwelling radiation (the single scatter albedo $\omega_{\rm o}$ varies in opposite directions as a function of effective radius at 3.9 μm and 10.7 μm). In the latter case where the cloud was misplaced into a relatively warmer (lower) environment, the parameters retrieved were again biased (now in the opposite sense) to match the observations. Higher optical depths were retrieved to absorb a greater portion of upwelling IR radiation, with

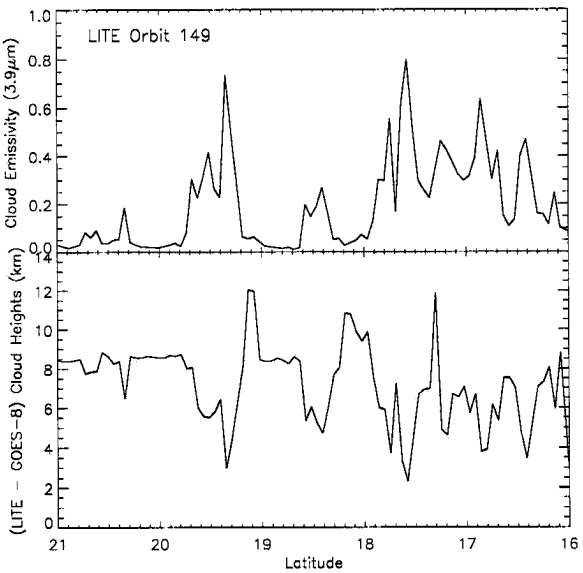

Figure 5.8: Comparison of retrieved cloud emissivities as a function of LITE-GOES estimated cloud heights.

lower effective particle radii to provide a lower value of asymmetry parameter and less forward scatter.

As expected, the retrieval biases described above diminished in the vicinity of $\Delta Z_{\text{cld}} = 0$ and were exacerbated as cloud misplacement was increased in either direction. Differences between active and passive-only retrievals at the $\Delta Z_{\text{cld}} = 0$ point were associated with differences between the true cloud thickness and that assumed (1 km) by the passive-only method. Because the lapse rate of temperature was slightly larger in magnitude (from soundings, ≈ -8.0 K/km) in the atmosphere below the true mean cloud height of 9.0 km than in regions immediately above (≈ -6.5 K/km), retrievals were more sensitive to the underestimations of cloud height for this particular case. This explains in part why the error distribution was larger in magnitude on the $\Delta Z_{\text{cld}} < 0$ side of Figure 5.7).

The problems associated with thin cirrus from a passive radiometer perspective are perhaps best illustrated in terms of cloud emissivity ϵ and its implications to satellite emission-based estimates of cloud height. The emissivity of a cloud having spectral absorption optical depth

$$\tau_{\text{abs}} = (1 - \omega_{\text{o}})\tau), \tag{5.20}$$

(λ subscripts omitted) and observer angle μ is defined as

$$\epsilon = 1 - e^{-\tau_{\text{abs}}/\mu}, \tag{5.21}$$

such that as the absorption optical depth increases ϵ approaches unity (i.e., behaving more as a blackbody emitter). Implicit to this discussion is the spectral dependence of ϵ (since τ_{abs} itself is a spectrally-dependent quantity). Conversely, the lower emissivity associated with optically thinner cirrus will produce a much warmer scene than the ambient environment of the cloud (owing to upwelling transmissions from below it) when viewed from above. Figure 5.8 demonstrates the relationship for the LITE Orbit 149 retrieval. Provided the retrieved effective particle radius, the corresponding $\omega_\circ$ from the Mie look-up table was obtained to compute τ_{abs} from the retrieved value of τ (integrating the extinction coefficient through the depth of the cloud). Emissivities were computed according to Equation 5.21 and are shown in the top panel of Figure 5.8. The cloud height differences shown in the lower panel were computed from mean LITE cloud heights and a those computed from GOES T_{B4}. The GOES brightness temperatures were mapped directly to a position in the vertical using a temperature sounding. The expected inverse relationship between ϵ and (LITE - GOES) cloud heights is evident, with the lowest emissivities corresponding to the largest height differentials. Because much of these data correspond to optically thin cirrus near 9 km, significant underestimates by GOES brightness temperatures of cloud altitude follow from the low emissivities. This is not as large of a concern for lower-level cloudiness, where ambient cloud temperatures are much closer to those of the underlying atmosphere and surface. Only in the rare cases when $\epsilon \rightarrow 0.8$ do the cloud height underestimates fall within 3 km of the LITE observations.

5.3.2 LITE Orbit 117 case

Overview

A portion of the descending orbit of LITE Orbit 117 (in view of GOES-8) crossed the North-Eastern United States and South-Eastward into the Atlantic and Caribbean (see Figure 5.9. While over land, the LITE cross section (region of interest shown in

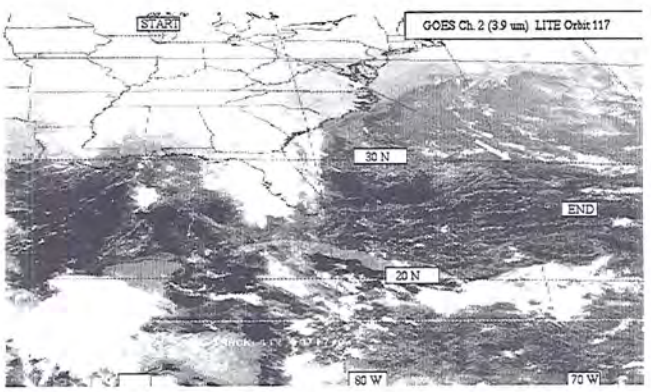

Figure 5.9: GOES-8 view of LITE Orbit 117 track. Trajectory of orbit is indicated by solid arrows along the ground-track.

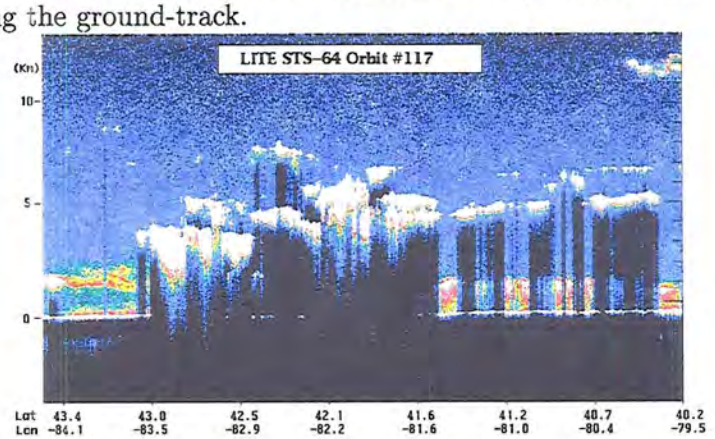

Figure 5.10: The raw LITE data corresponding to the North-West portion of the ground track shown in Figure 5.9.

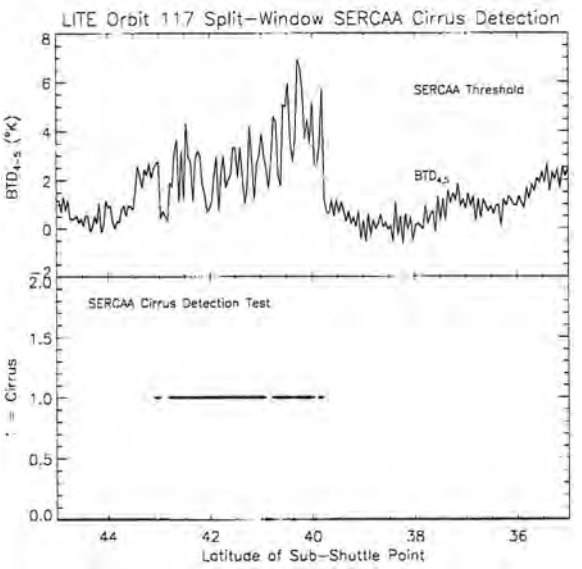

Figure 5.11: The SERCAA cirrus detection test applied to GOES-8 data for the LITE orbit 117 case.

Figure 5.10) bisected multi-level cloudiness associated with a mid-latitude cyclone. Based on established good agreement with soundings from numerous case studies, ECMWF profile analyses were considered as a viable alternative for areas where rawinsonde data were not available, and hence were extracted along this flight track for use as forward model input.

Similar to LITE Orbit 149, the SERCAA cirrus cloud detection algorithm was used to verify correct extraction of GOES-8 pixels along the LITE Orbit 117 flight track. The observed Ch. 4 - Ch. 5 BTD, SERCAA threshold, and detected cirrus pixels are shown together in Figure 5.11. The comparison indicated the presence of high cloud in the same location as the LITE cross section, verifying the correct co-location and extraction of GOES-8 data along the LITE track.

Retrieval results

The results for optical depth and effective radius retrievals are shown together with uncertainty and *A Priori* parameters in Figures 5.12 and 5.13, respectively. These optically-thick clouds tended to saturate the sensitivity of the IR-only retrieval method, and in many cases the uncertainty attributed to the Kernel function dominated the parameter

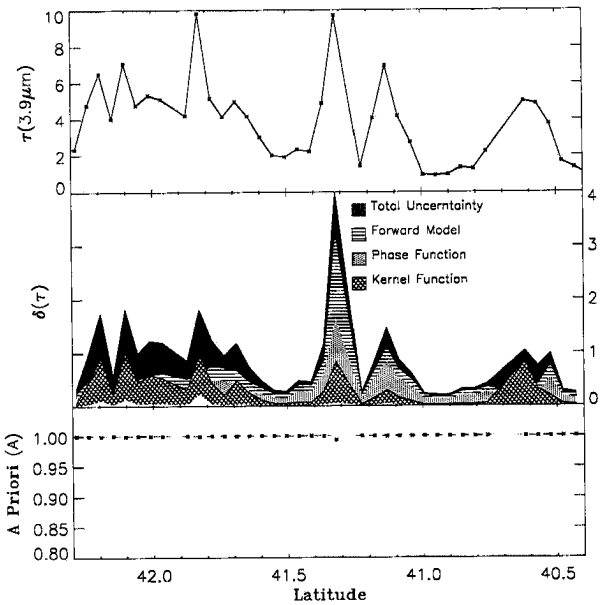

Figure 5.12: Retrieved cloud optical depth along the LITE Orbit 117 flight track.

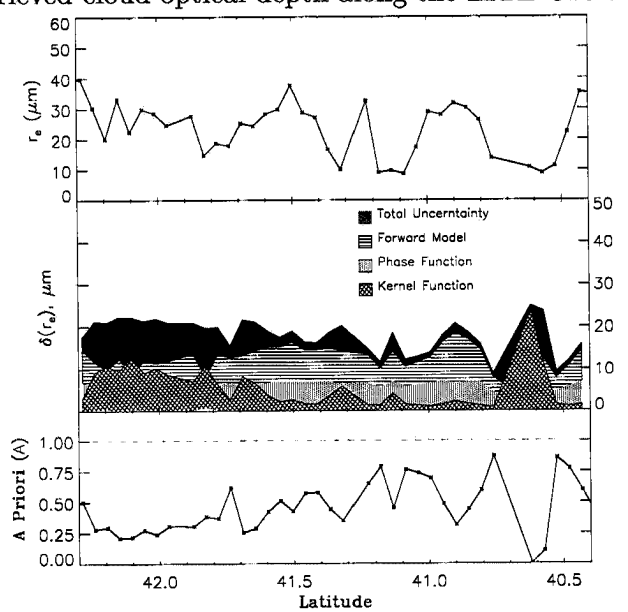

Figure 5.13: Retrieved effective radii along the LITE Orbit 117 flight track.

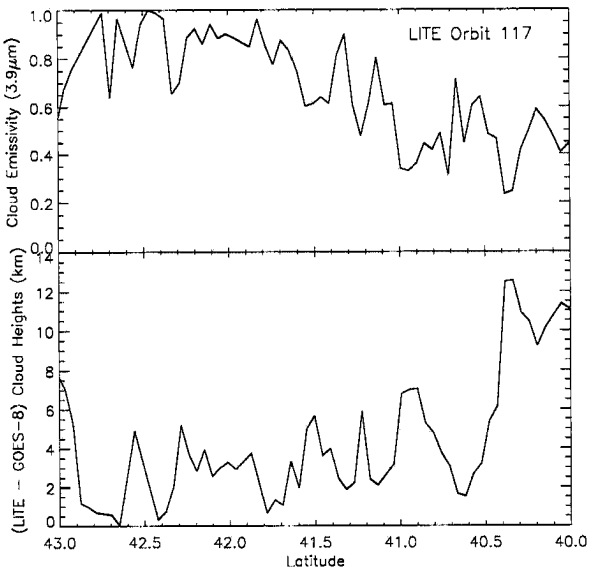

Figure 5.14: Retrieved cloud emissivity plotted against differences in cloud-height as estimated by active and passive-only techniques.

error. This point is evident particularly in the effective radius retrieval uncertainty near 42° N (a region of optically thick cloud), where the error is dominated almost entirely by model insensitivity. This illustrates some limitations of current IR-only retrievals for cases of optically thick clouds. The Rodgers retrieval raises the red-flags for these retrievals and identifies the dominant source of uncertainty.

Passive-only retrieval uncertainty

The 3.9 μm cloud emissivity derived from the retrieved optical properties and Mie theory was again plotted against differences in cloud height estimates between LITE and the GOES-8 Ch. 4 brightness-temperature-derived heights. The results of this exercise are plotted in Figure 5.14. High emissivity (i.e., close to unity) correspond with the large optical depths retrieved over the frontal cloudiness, and gradually fall-off as the orbit proceeds South-Eastward across the leading cirrus shield. The now familiar inverse relationship was observed to exist between the two curves. The presence of a 12 km cirrus cloud layer near the end of the retrieved track (see Figure 5.10) accounts for the correlation between relatively large emissivities and large ΔZ_{cld} cloud heights (for comparisons with

GOES-8 a single mean cloud height was defined for LITE, and this high cloud biases positively the estimate).

5.3.3 LITE case summary

The LITE case studies demonstrated the utility of active sensors on the space platform in improving the current cloud optical property retrieving capabilities of passive satellite radiometers. This is valid especially in the presence of thin cirrus, where very low cloud emissivities give rise to large uncertainty in the placement of clouds in the vertical by passive sensor methods alone. Plots of retrieval discrepancies as a function of cloud misplacement indicate that knowledge of the true cloud profile leads to significant changes (presumably toward improvement) in the retrieved parameters. The Rodgers approach allows for dissection of the total retrieval error into components due to quantified uncertainties in the forward model and measurements. In all, cloud profile data for 66 night-time LITE orbits were made available by NASA Langley Research Center. While this research focused on a few cases observed by GOES-8, additional cases observed by the wide array of GEO and LEO (e.g., AVHRR) environmental satellites have yet to be examined.

5.4 CLEX-1 Retrieval

In an effort to better understand the optical properties, distribution and structure of non-precipitating mid-level clouds, the Department of Defense (DoD) has sponsored a series of Complex Layered Cloud Experiments (CLEX). Those of interest to this work included funding for an airborne active sensor to supply cloud height profiles similar to those of LITE (for local areas as opposed to global data). This section summarizes a retrieval performed using data collected during June 1996 over the ARM Southern Great Plains (SGP) Cloud and Radiation Testbed (CART) site.

5.4.1 CLEX-1 Overview

CLEX-1 (the first of the CLEX series) was conducted during June of 1996 and included active sensor data from synthetic aperture radar (SAR). The case of interest considered June 22, 1996 flight leg, spanning from 12.7 to 14.4 UTC and centered around

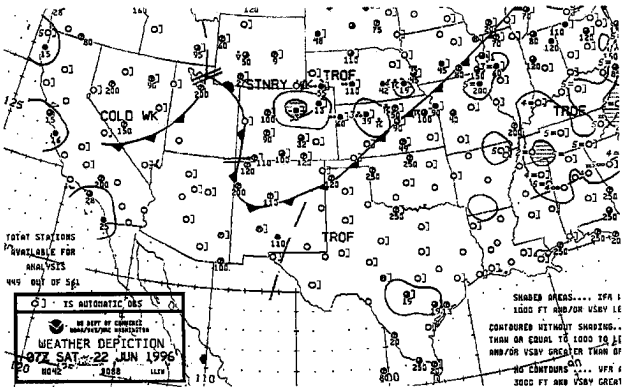

Figure 5.15: Surface analysis at 00-Z for 6/22/96 (CLEX).

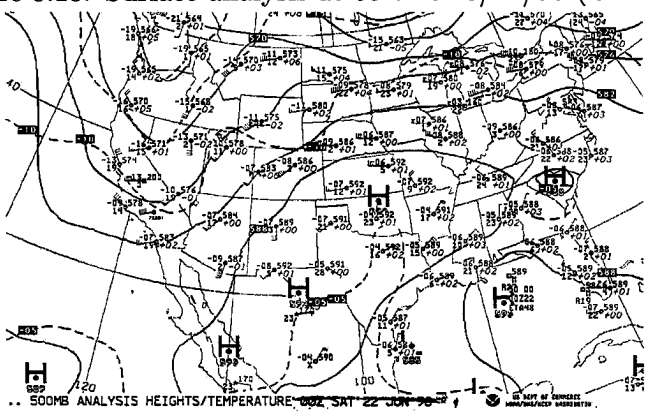

Figure 5.16: 500-mb analysis at 00-Z for 6/22/96 (CLEX).

the ARM SGP CART site (a 55,000 square mile area of remote sensing clusters in north-central Oklahoma and south-central Kansas with the central facility located in Lamont, OK).

Figures 5.15-5.16 depicts the synoptic-scale conditions responsible for generating the June 22^{nd} cloud field in terms of the surface and 500 mb pressure-surface analyses. On the previous day, a SW/NE-oriented surface cold front draping across central Kansas acted as a focus for late afternoon convection, with moisture-laden Gulf Coast air advected in from the S/SW. A nocturnal mesoscale convective complex (MCC) organized from this convection over SE Colorado and SW Kansas (tracking along the northern side of the long-wave ridge indicated in Figure 5.16) throughout the evening of June $21^{s}t$. The MCC advected slowly over Kansas and began to dissipate by late morning. Residual MCC anvil debris associated with the meso-vortex, and the focus of these retrievals, were dispersed in the system's wake.

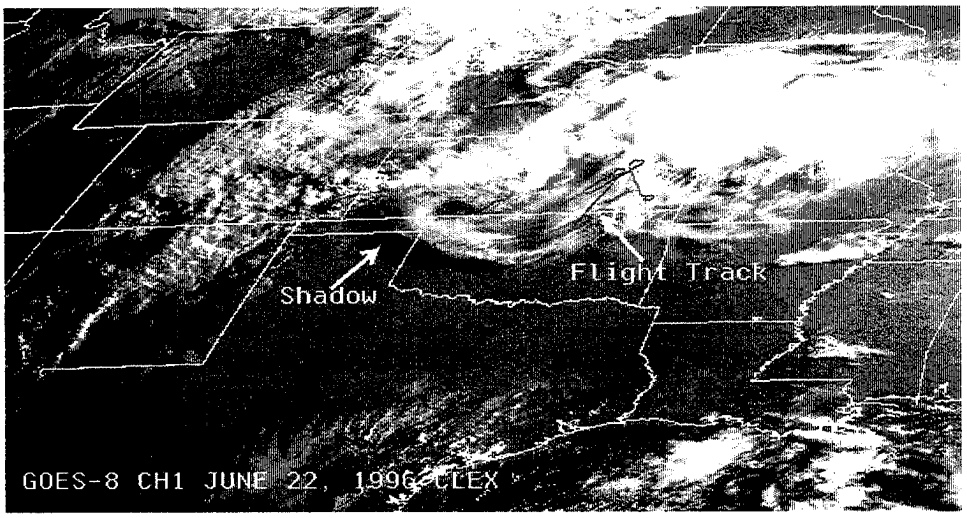

Figure 5.17: GOES-8 CH1 ($0.67\mu m$, Visible) image with DC-8 flight track superimposed for the 960622 CLEX-1 case.

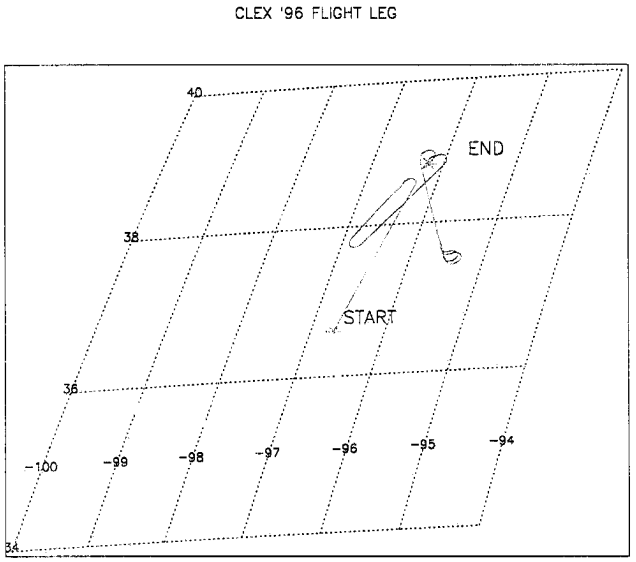

Figure 5.18: Map of DC-8 flight track for the 6/22/96 CLEX-1 case.

A DC-8 research aircraft, carrying the 94 GHz ACR flew over a substantial portion of NE Oklahoma and SE Kansas during the last phase of the MCC event. It encountered the dissipating anvil debris described above over a 3 hr period of the morning flight leg. Figures 5.17-5.18 show a GOES-8 visible image for this case with the DC-8 flight track superimposed upon it, and a closer view map of the flight track for clarity. Reports from the Wyoming King Air crew also flying in the same area describe complex layered clouds that were scattered in horizontal extent, with alto-cumulus and altostratus and cirrus above; many of the AC were precipitating ice crystals. Several changes in flight heading were made during the leg (this accounts for the "symmetry" of some sections of the RADAR return imagery as the DC-8 looped around and re-traversed the same cloud structures).

Because these observations were made during a morning flight, there was a low solar zenith angle. The cirrus layer in Figure 5.17 is visible in the GOES-8 Ch. 1 imagery, casting an extensive shadow to the West. Computing the cloud height based on shadow and cloud edge placed the cloud top at approximately 8 km, in agreement with the radar data (such estimation techniques are only applicable to day-time, single-layer cloud imagery). The residual MCC cirrus layer provided an ideal case study for this experiment and incidently one of the very few good data-takes accomplished during the span of the entire CLEX-1 IOP.

Measurements

The active instrument used in the CLEX-1 retrieval was the ACR. It was oriented nadir upon the DC-8 and provided high spatial resolution reflectivity profiles of the cloud top and base altitudes as described above. To place these retrievals within the broader scope of this research, we may consider the radar information as having been produced by an equivalent satellite-based instrument at a moderately coarser resolution. Plots of the radar reflectivity and derived cloud base/top heights are shown in Figures 5.19-5.20. The DC-8 flight track data were partitioned into 1 second resolution latitude/longitude points. The procedure followed for assembling the ACR retrieval data was as follows

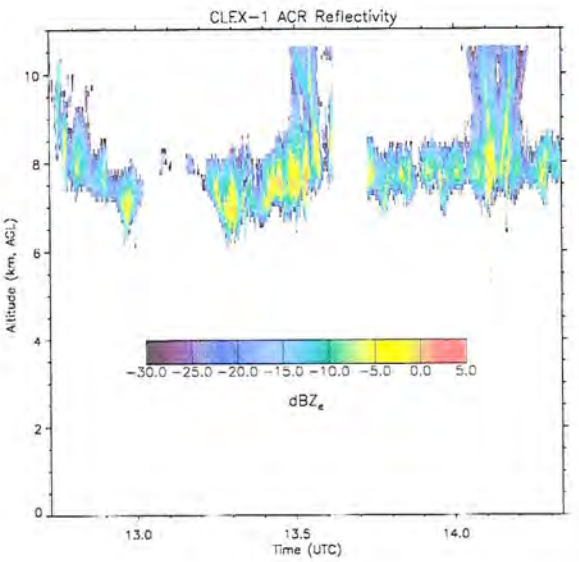

Figure 5.19: ACR cloud profile observations for the 6/22/96 CLEX-1 case.

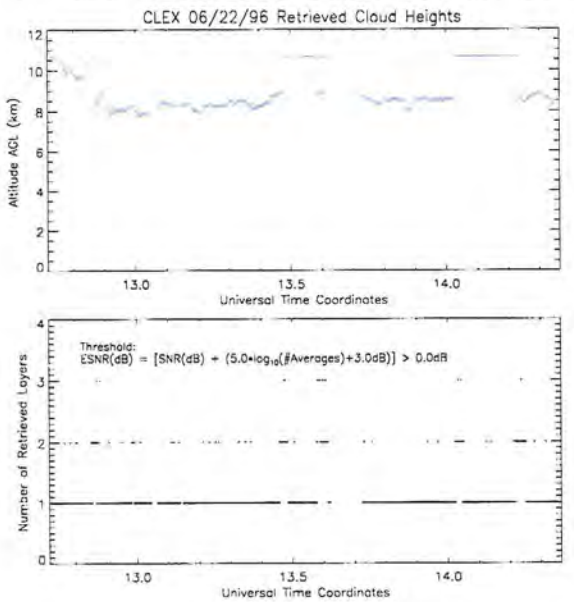

Figure 5.20: Retrieved cloud heights from ACR data using SNR thresholding. The lower panel denotes the number of "layers" detected in a given profile.

1. Identify candidate flight legs based on cloud field, data-availability, coverage, and construct flight-leg latitude/longitude/time files.

2. Use GVIEW package to extract GOES imager data along tracks defined in flight-leg files and consolidate into a single file of records.

3. Compute solar and satellite zenith and azimuth angles along the flight-leg.

4. Obtain either ECMWF gridded analysis data or rawinsonde data for profile temperature and moisture information.

The corresponding GOES-8 data (for this case, 4 sets of Ch. 1-5 imagery) were downloaded from the Cooperative Institute for Research of the Atmosphere (CIRA) archives at Colorado State University and processed with GVIEW software developed by Kelly Dean (of CIRA). The continental United States (CONUS) sector was obtained for the times spanning the flight leg and sub-sectored to the local region of the CLEX-1 IOP). Several sets of imagery spanning the duration of the flight were used in order to minimize flight-track/satellite cloud collocation errors due to cloud advection as well as retrieval errors owing to changes in the solar geometry.

Information from both ECMWF and CART-Site rawinsonde data were used for profiles of temperature moisture, wind speeds and directions, and absorber gas abundancy. The rawinsonde data were reported at 56 levels (dithered to 15 levels for input to the forward model). Figure 5.21 is a comparison between the ECMWF initialization field (used for retrievals where sounding data are not available) and a sounding within the model gridbox launched within one hour of initialization. The dewpoint temperature (T_d) was computed from the temperature (T) and relative humidity (H% / 100) using a Clausius-Clapeyron based empirical relationship

$$T_d = \frac{C_1 T}{B - TH}, \tag{5.22}$$

where C_1 = 5.42E+03. The water vapor mixing ratio (kg/kg) is computed according to

$$\begin{aligned} W &= \frac{R_{dry} C_2 H S}{R_{moist} P - S} \\ S &= H C_2 e^{\frac{-B}{T}}, \end{aligned} \tag{5.23}$$

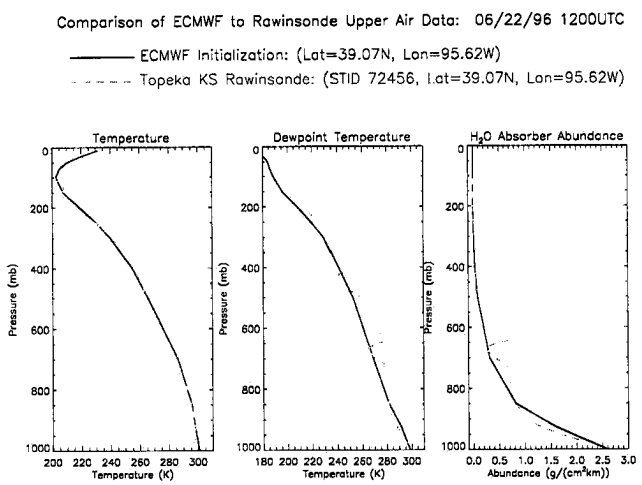

Figure 5.21: A comparison between the ECMWF model initialization field profile variables and those measured from a rawinsonde during CLEX-1.

where $C_2 = 2.53\text{E+}09$ and $R_{moist,dry}$ are the gas constants for moist and dry air (287 and 461.5 J K^{-1} Kg^{-1}, respectively). Water vapor abundance (A, in units of g cm^{-2} km^{-1}) is converted directly from the water vapor mixing ratio (R) according to

$$A = 100 \times R\rho_a, \tag{5.24}$$

with ρ_a being the density of air at a specific level in the atmosphere. Encouraging agreement was observed between the model and observed variables most relevant to GOES IR-channel-only retrievals.

Independent active sensor retrievals

Whenever available, it is desirable to obtain an independent (i.e., using different remote sensors) of the retrieved quantities as a check for consistency. Such estimates were available to the CLEX-1 study from parameterizations based on simple power-law relationships applied to the radar reflectivity. These empirical relationships are obtained in practice generally by assembling a large sample set of similar cases (e.g., cloud type, phase, particle habit, etc.), plotting the data, and performing a regression on the resultant distribution with radar reflectivity as the independent variable. The ice-cloud reflectivity parameterizations applied to the CLEX-1 ACR data were as follows:

- Ice Water Content:

  Source: Liao & Sassen (1994) for complex cirrus morphologies

  $IWC = 7.49 \times 10^{-2} Z_e^{0.78} \quad (gm^{-3})$

- Extinction Coefficient (W-band):

  Source: Sato et al (1981)

  $\sigma_{ext} = 3.51 \times 10^{-4} Z_e^{0.98} \quad (km^{-1})$

- Extinction Coefficient (At a visible wavelength):

  Source: Sassen and Liao (1996)

  $\sigma_{ext} = 0.965 Z_i^{0.81} \quad (km^{-1})$

- Effective Particle Radius:

  Source: Platt (1997)

  $R_{eff} = 1.73 \times 10^2 IWC^{0.39} \quad (\mu m)$

where Z_e in the first two expressions is the effective radar reflectivity factor (dBZ) for water. Because in practice it is usually not known *a priori* what the dominant phase of particles in the sample volume is, the standard value computed Equation 5.3 assumes the dielectric factor for water. This can be renormalized to ice values according to

$$Z_i = \frac{|K_w|^2}{|K_i|^2} \tag{5.25}$$

where $|K_{w,i}|^2 = (0.7175, 0.1772)$ are the dielectric factors for liquid water and ice at 95-GHz, respectively.

To compare optical depths derived between the active-only and passive retrievals, the extinction coefficient was integrated throughout the depth of the cloud (as defined by the active senor derived cloud boundaries) following Equation 2.2-2.3 and then converted from the radar wavelength (95 GHz $\approx$ 3 mm) to that of the satellite imager channel using Equation 3.28. To invoke Equation 3.28 the radar-retrieved effective radius was applied to Mie theory to obtain the requisite extinction efficiency (Q_{ext}). It is important to emphasize that the parameterizations listed above are climatological relationships (i.e,, best fits to a large sample) with a large variance associated with them. As there exists a great deal

of uncertainty with the empirical fits, they were intended to serve only as a first-order quality-check for comparison to the radiometer-retrieved quantities.

5.4.2 Retrieval results

Because this CLEX-1 case involved day-time observations, a bi-spectral retrieval approach based on the bi-directional reflectances in GOES Ch.1 and Ch.2 was chosen for the observation vector. The retrieved optical depth and effective radii for the CLEX-1 case are shown in Figures 5.22-5.23, respectively, along with a break-down of the uncertainty in terms of components. The retrieved 3.9 μm (corresponding to GOES-8 Ch. 2) cloud optical depths ranged over [0.1,10.0], and effective radii varied between 10 and 70 μm. The largest uncertainties in these retrievals again corresponded to the lower values of the *A Priori* parameter matrix. The strongest contribution to optical depth uncertainties were from the phase function. This is because the cloud optical depth is a stronger function of the visible channel reflection, and uncertainties computed for the ice crystal phase function assumptions were larger than most of the IR channels. The largest retrieved particles were observed in the cirrus turret features encountered along the flight track. Here, profile uncertainty and Kernel function insensitivities paid a greater contribution to the total retrieval uncertainty.

Independent radar-based retrieval validation

Examples of ACR retrievals of ice water content, extinction coefficient, and effective particle radius based on the reflectivity parameterizations listed above are shown in Figure 5.24. These empirical results are only as valid as the degree to which the training data from which the parameterizations were derived are representative of the observed cloud field. This caveat must be kept in mind whenever making comparisons between cloud properties derived from generalized reflectivity parameterizations and satellite retrievals. Nonetheless, they provide a useful first-order validation set for these retrievals when no other data is available.

One such application involves the use of the radar-derived extinction, cloud boundaries, and particle size to obtain a radar-estimate of the cloud optical depth. The ACR

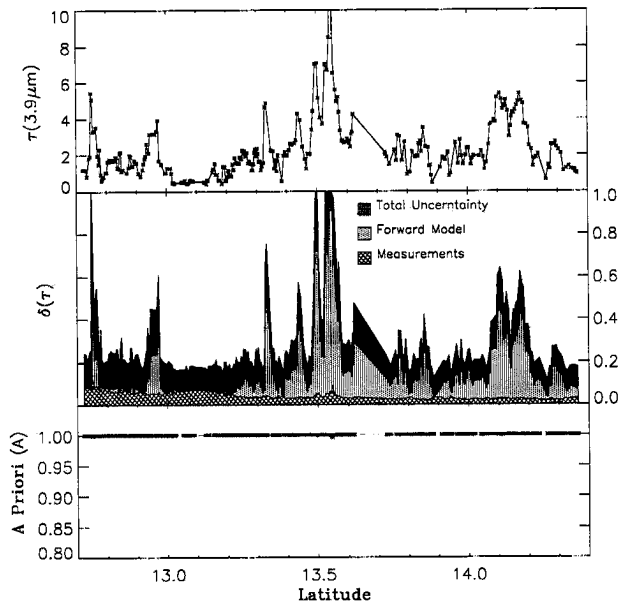

Figure 5.22: GOES-8 retrievals of cloud optical depth for CLEX 6/22/1996 (Top) and breakdown of uncertainty components (Bottom).

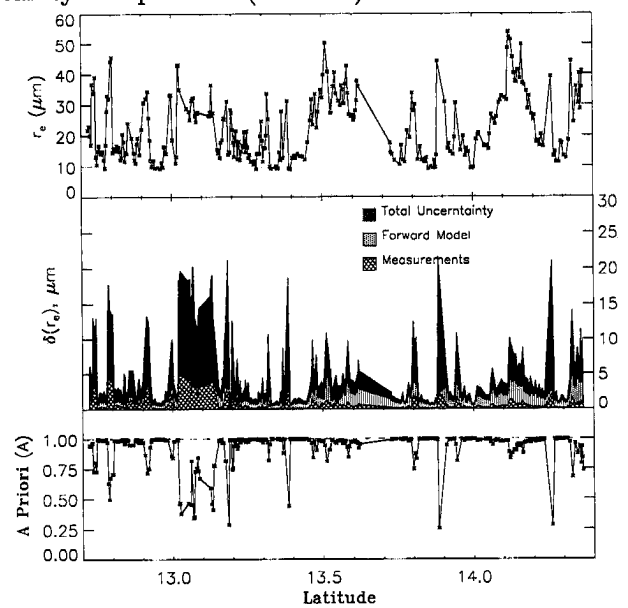

Figure 5.23: Corresponding GOES-8 retrievals of effective radii and uncertainties.

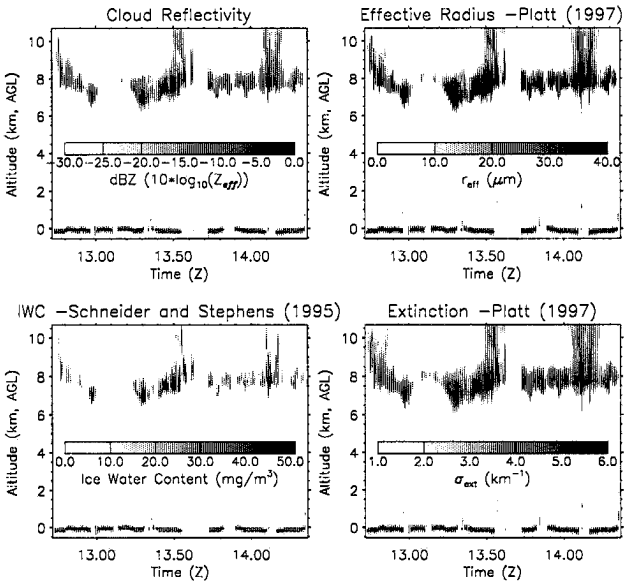

Figure 5.24: Empirical retrievals for CLEX 6/22/1996 from 95-GHz radar data.

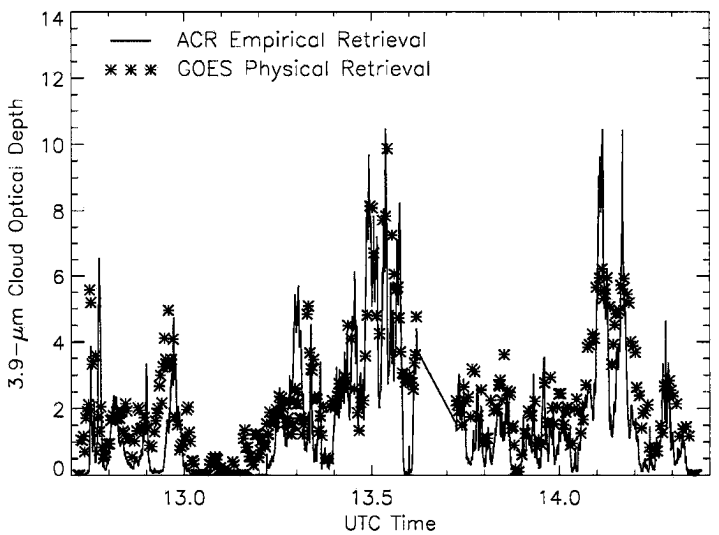

Figure 5.25: Radar/GOES-8 cloud optical depth retrieval comparison for CLEX-1 960622. 94 GHz radar-derived τ rescaled to GOES Ch. 2 using Mie Theory.

empirically-derived extinction coefficient was rescaled to 3.9 μm using Mie theory with a mean radar-estimate of the cloud droplet size and Equation 3.28. This rescaled extinction was then integrated over the entire depth of the cloud (as defined by the radar-retrieved cloud profile) to obtain an equivalent 3.9 μm optical depth comparable to the GOES-8 retrieved quantity. As shown in Figure 5.25, the comparison between the passive-only and active-only retrieved optical depths showed good general agreement. Fine-scale discrepancies were due to the GOES pixel resolution, cloud advection (i.e., a discrete versus nearly continuous temporal sample for GOES and ACR, respectively), errors associated with the assumptions involved with radar retrieval (empirical parameterization and rescaling to 3.9 μm using Mie theory and hence ice spheres), and *a priori* constraints imposed on the passive retrieval. These uncertainties are very difficult to quantify, and because this exercise was intended more as a validation of correct satellite co-location and first-order optical property retrieval, no attempt to resolve them further was made here. Even with all caveats considered, the comparison indicates still that a reasonable representation of the cloud optical properties has been retrieved from the satellite data.

Cloud-emissivity/cloud-height comparisons

An important consideration for cirrus is the implications their thin optical depths have on determining their correct altitudes. Figure 5.26 illustrates the inverse relationship that exists between retrieved cloud emissivity at 3.9 μm and the cloud height difference between the true cloud height (mean value) and that inferred from GOES-8 brightness temperatures alone for the cirrus shield observed in CLEX-1 on June 22, 1996. The latter assumes a cloud emissivity of unity for all clouds and places them in the vertical by matching to a temperature sounding. When a cloud has a high absorption optical thickness (i.e., a higher emissivity), it emits more as a blackbody at the temperature of its environment. Hence the GOES-8 brightness temperatures better represent the true cloud altitude. Conversely, optically thinner clouds (i.e., lower emissivity) allow emissions from the lower atmosphere and surface to transmit through the cloud and reach the satellite detectors. The satellite-inferred altitude for this case will be lower than that observed by

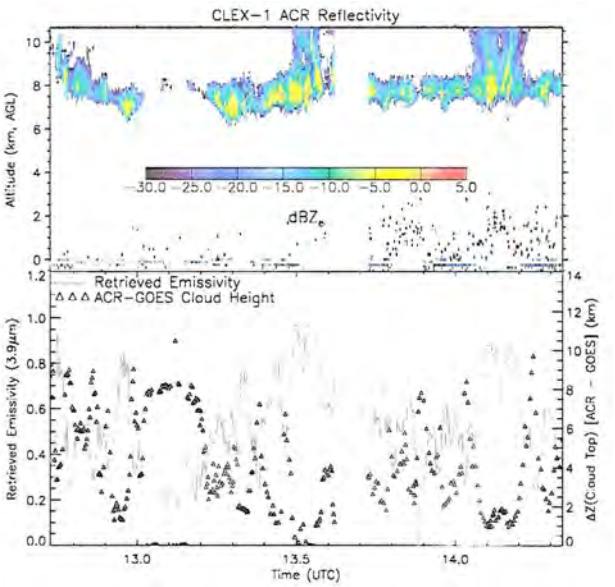

Figure 5.26: The inverse relationship between emissivity and ACR-GOES cloud heights for CLEX 6/22/96

active sensors, as the cloud appears warmer than its actual environment and is mapped by the soundings to lower (warmer) altitudes accordingly.

In the most optically thick regions of Figure 5.26 (corresponding to 3.9 μm emissivities on the order of 0.8) the ACR-GOES retrieved mean cloud height differences reduced to 1 to 2 km, while for the thinner cloud regions this difference extended to values in excess of 9 km. This illustrates the problems encountered by passive-only retrievals in placing thin clouds at their correct positions in the atmosphere. Optically thin cirrus, which plays an important role in trapping upwelling thermal radiation and thereby heating the atmospheric column below it, can be missed altogether by passive-only techniques. It might reasonably be expected that these uncertainties in cloud height location would manifest in large retrieval uncertainties for optically thin clouds, especially at night.

5.4.3 Passive-only retrieval uncertainty

For the passive-only estimate of cloud height, the approach of Szejwach (1982) was again employed (see Figure 5.27. A cluster of GOES pixels corresponding to the turrets observed in Figure 5.19 bias the fit toward colder cloud tops (the DC-8 aircraft did not fly above these clouds completely). When the Ch. 4 brightness temperatures used in

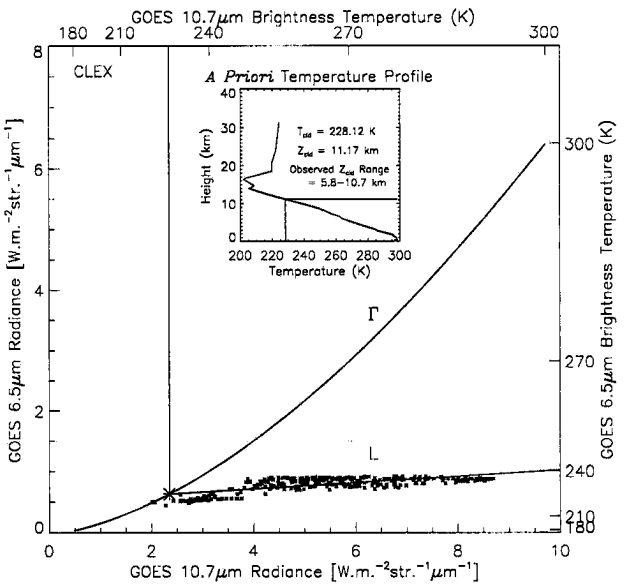

Figure 5.27: Passive sensor estimate of semi-transparent cirrus height for CLEX-1 using GOES 6.5 μm water vapor and 10.7 μm IR window channels. Curve "Γ" is the theoretical blackbody relationship and line "L" is the linear fit to the observation set (following the method of Szejwach, 1982).

the Szejwach height retrieval were truncated at 250 K (effectively removing the colder cluster), the fitted curve placed cloud tops at 10.5 km. The latter figure was used for the passive-only cloud retrievals in regions outside the cloud turrets, where the former figure was retained.

The top panel of Figure 5.28) shows the Szejwach-derived passive-estimate cloud plotted against ACR cloud top and base boundaries. The central panel shows cloud top and thickness differences, and the lower panel summarizes the percent differences in retrieved quantities. It was observed that the passive retrieval overestimated optical depth primarily in the few cases where the cloud physical thickness was underestimated (i.e., a positive cloud thickness difference in the center panel of Figure 5.28), while showing no apparent correlation to the cloud top height difference. In these cases, the passive-only retrieved effective radius (which generally was observed to be smaller in the passive-only retrievals) was significantly larger than the active retrievals. Because the passive cloud was geometrically thinner, a larger optical depth was required to produce the same cloud reflectance. This perturbance to τ resulted in a strong change to r_{eff} (according to the similarity condition) in order to match both channel observations.

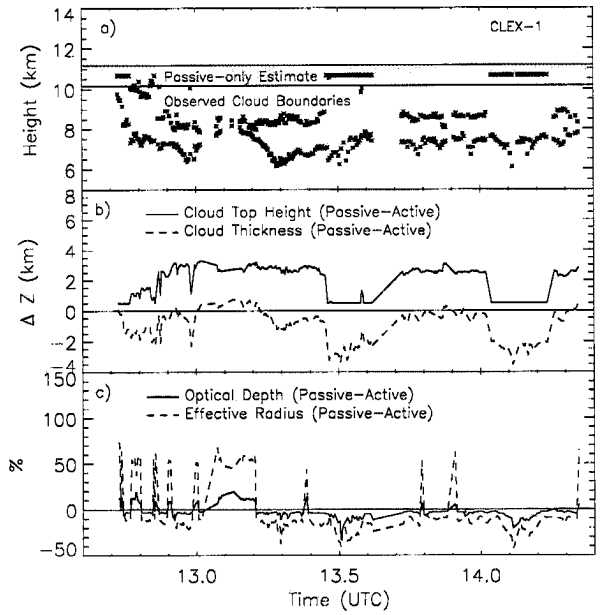

Figure 5.28: Comparison between cloud heights (top), thickness (center), and percent differences in retrieved parameters (bottom) between passive-only and active *a priori* cloud retrievals.

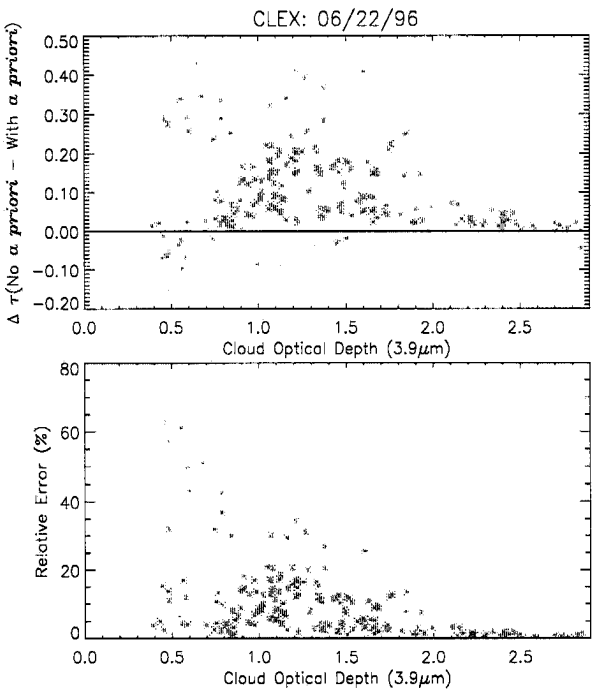

Figure 5.29: Analysis of retrieval results with and without *a priori* cloud height information.

A second method of approximating the cloud height from passive measurement was to use the Ch. 4 brightness temperatures and a sounding to place a 1 km thick cloud in the vertical. With the exception of strong inversion cases (none of which were encountered in these case studies), this approach will in general place a non-black ($\epsilon < 1.0$) cloud below its true level in the atmosphere. Retrievals based on this version of passive-only cloud height estimation were recomputed for the CLEX-1 case. Figure 5.29 is a scatter diagram of differences between passive-only (i.e., passive cloud heights estimated only from GOES-8 Ch. 4 brightness temperature and sounding) and ACR *a priori* optical depth retrievals plotted against the retrieval using active cloud profile information (considered here as "truth"). As anticipated from the emissivity vs. cloud-height-difference results, this effect was most dramatic for optically thin cirrus (where the ambiguity in true cloud height is highest). The retrieved values without true cloud height information are higher because the retrieval places them at lower (warmer) levels in the atmosphere. In order to produce the cooler brightness temperature observed by GOES, the cloud must be made optically thicker (such that the primary source of radiation is from the ambient temperature of the cloud itself and not from warmer regions below the cloud). These differences are significant and affect directly the modeled cloud radiative feedback processes associated with with cirrus clouds.

5.4.4 CLEX-1 case summary

The results of the June 22, 1996 CLEX-1 retrieval emphasize the need to know accurately the location of optically thin clouds in the vertical. The heights of these clouds are very often underestimated by passive sensing techniques, resulting in overestimation of true cloud optical depth. Thin cirrus cover a large fraction of the planet at any given time, and are associated with radiative heating of the atmosphere (by allowing transmission of down-welling solar radiation while absorbing thermal radiation from below). As such, the additional profile information provided by an active instrument aids in better representing the role of these radiatively important clouds in many climate modeling applications. The radar data were also shown to be useful in the independent validation of the satellite retrievals. Even though ACR profile data was used to compliment the forward model

information, these comparisons are not incestuous because the radar-only retrieval bases its estimates on 94 GHz *backscatter* properties whereas the GOES retrieval uses the radar height information only to constrain the cloud IR-*emissive* properties.

5.5 PACRIM 961101 Retrieval

5.5.1 Overview

The Pacific Rim Experiment (PACRIM) (also referred to as CLEX-2) flew NASA DC-8 aircraft across the Pacific ocean during late October and early November, 1996. The ACR used in the Summer synthetic aperture radar series (SAR, or CLEX-1) was oriented in the zenith. As a result, the profile of cloud below the level of aircraft flight altitude was not known. For these comparisons, retrievals were carried out assuming a common lower boundary condition (cloudy or clear) such that relative differences owing to uncertainties in cloud locations above the aircraft could still be examined. The flight track was observed by GOES-9 (the Western compliment to GOES-8 with a sub-satellite position of 135° W longitude and 0° Latitude). Although the imager channels nominally were the same as those of GOES-8, detector response functions vary from instrument to instrument. The appropriate response functions (pre-launch laboratory specifications) for GOES-9 were therefore used in the forward model for the PACRIM retrievals.

The PACRIM flights consisted of two main legs (one from San Francisco across the Eastern Pacific to Hawaii, and then from Hawaii across the South-Western Pacific to New Zealand) followed by several short-range closed-loop flights in the New Zealand/Eastern-Australia region. The retrieval examined for this case was at the beginning part of the second (Hawaii to New Zealand) leg. Figures 5.30-5.31 illustrate the portion of flight track retrieved as viewed from the GOES-9 vantage point. Virtual soundings over this open-ocean leg were estimated using ECMWF global reanalysis data.

The corresponding ACR observation data for this case are shown in Figure 5.32. Cold cloud tops in the satellite image appear as dark features while the warm ocean surface is relatively bright. This corresponds to the actual energy exposure of the detector, although most IR imagery is color-reversed by convention largely because we are accustomed to

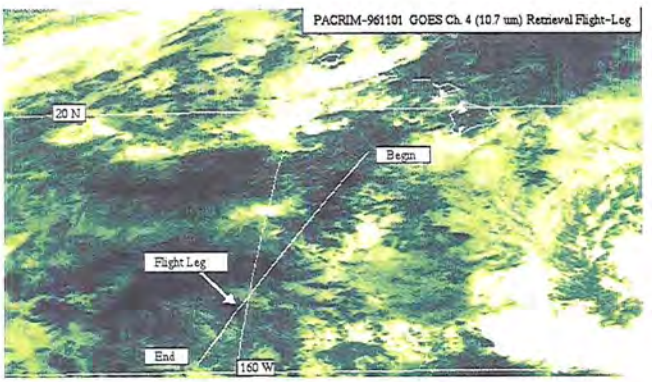

Figure 5.30: GOES-9 observations corresponding to the 11/01/96 PACRIM retrieval.

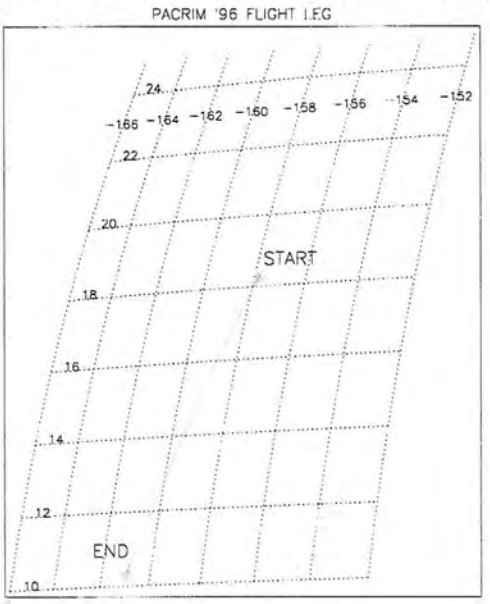

Figure 5.31: DC-8 flight track for the 11/01/96 PACRIM retrieval.

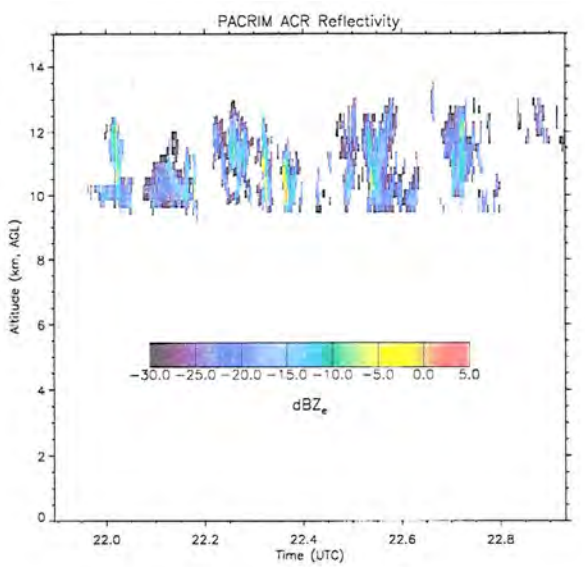

Figure 5.32: Along-track ACR cloud observations (oriented in the zenith) for the 961101 PACRIM retrieval.

viewing "white" clouds as they would appear in day-time visible imagery. The cirrus observed by the zenith-oriented ACR ranged in altitude from 9.5 to 13 km, with variable internal structure and geometric thickness along the flight track.

The retrieved cloud heights using a SNR-thresholding approach analogous to CLEX-1 are shown in Figure 5.33. Shown also on this figure is the varying altitude of the DC-8 aircraft (the radar data, which were given as a function of range from the instrument, were corrected for the aircraft altitude for all profiles as in CLEX-1). Although multiple layers were sometimes computed by the thresholding algorithm, these clouds were reduced to a single layer whenever the separation-distance between the layers was less than 0.5 km.

5.5.2 Retrieval results

The GOES-9/radar retrieval results for optical depth and effective radius are shown in Figures 5.34-5.35. Optical depth errors were found to be on the order of 15% and due largely to uncertainties associated with the scattering phase function. Effective radii were retrieved between 35 and 60 μm, with errors on the order of 15 μm. The larger particle sizes were associated with weaker forward model sensitivity (as the single scatter albedo

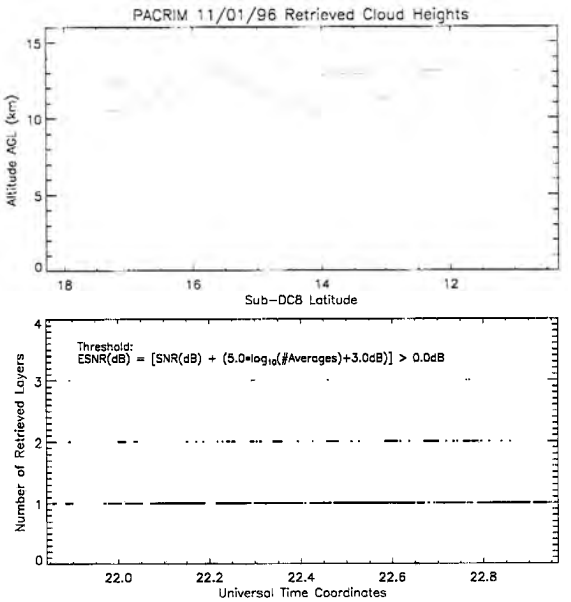

Figure 5.33: Retrieved cloud heights from ACR data using SNR thresholding. The dashed line in the upper panel denotes the DC-8 altitude. The lower panel denotes the number of "layers" detected in a given profile.

and asymmetry parameter approach their asymptotic limits according to Mie theory), leading to a strong contribution to the error by the Kernel function for these retrievals.

5.5.3 Passive-only retrieval uncertainty

The Szejwach method of defining cloud height from passive-only measurements is illustrated for the PACRIM case study in Figure 5.36. The well-behaved (linear) distribution of GOES-9 temperatures was indicative of a quasi-uniform layer of cirrus (with varying emissivity) over the region. The resultant cloud height estimate placed the cloud layer at roughly 12 km; squarely between the ACR-observed cloud range of 10 to 14 km. Due to the high variability of emissivity, cloud height estimation based on the GOES Ch. 4 brightness-temperature/sounding approach yielded cloud heights ranging from 2.25 to 10 km.

Similar to the CLEX-1 case study, retrieved cloud optical depths and single-scatter albedos were used to compute cloud emissivity at the GOES-9 zenith angle ($\mu \sim 33°$). Comparison of this retrieved quantity with cloud height differences between radar and GOES-9 Ch. 4 brightness temperature estimates along the DC-8 flight track is shown

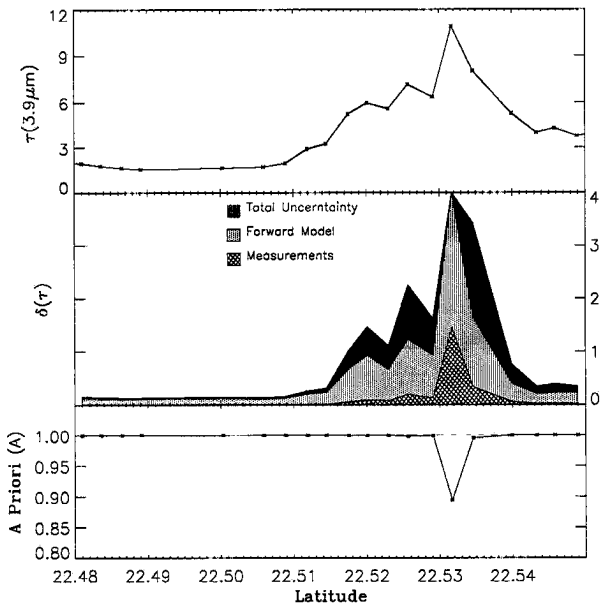

Figure 5.34: GOES-9 retrievals of cloud optical depth for PACRIM 11/01/1996 (Top) and breakdown of uncertainty components (Bottom).

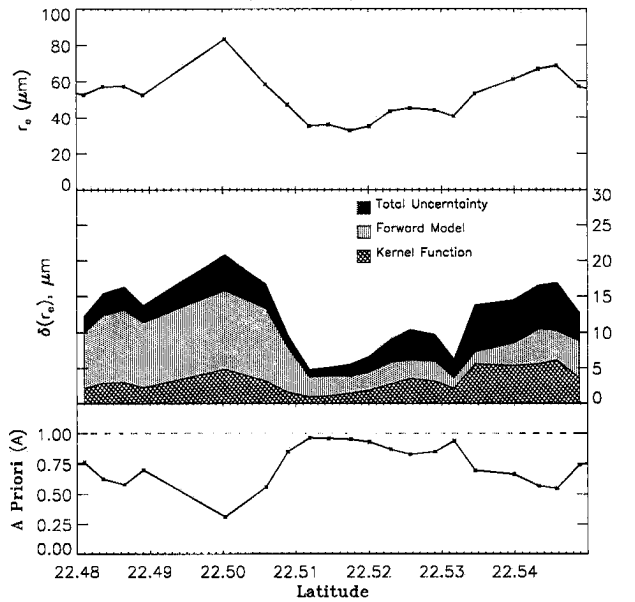

Figure 5.35: Corresponding GOES-9 retrievals of effective radii and uncertainties.

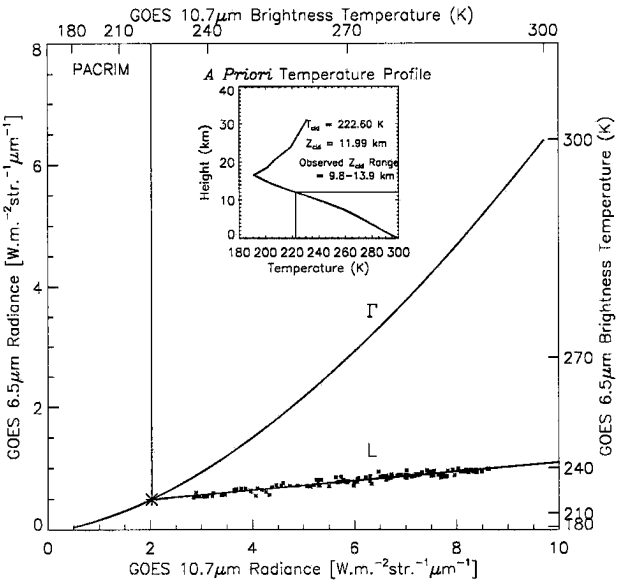

Figure 5.36: Passive sensor estimate of semi-transparent cirrus height for CLEX-1 using GOES 6.5 μm water vapor and 10.7 μm IR window channels. Curve "Γ" is the theoretical blackbody relationship and line "L" is the linear fit to the observation set (following the method of Szejwach, 1982).

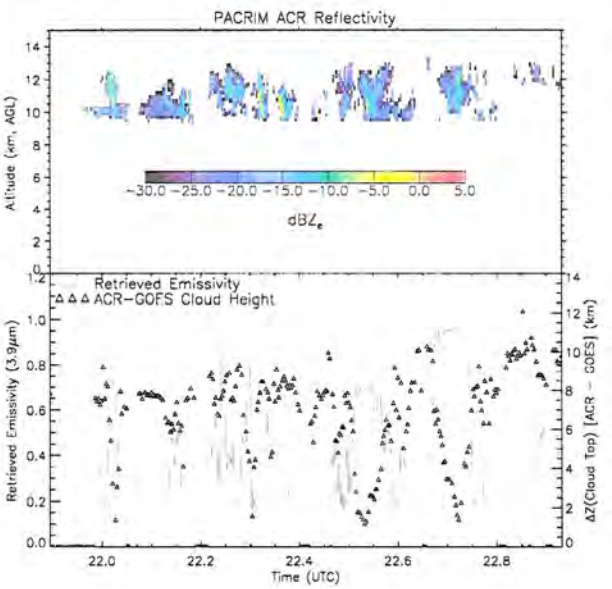

Figure 5.37: The inverse relationship between emissivity and ACR-GOES cloud heights for PACRIM 11/01/96

in Figure 5.37. Again, regions of high cloud emissivity correlate negatively with cloud height differences, and low emissivities correspond to the largest discrepancies between cloud height estimates. Slight shifts between retrieved maxima in τ and maxima in radar reflectivity in Figure 5.37 were due to cloud advection over the 1 hour, 20 minute segment of the flight leg (only one set of GOES-9 imagery was obtained for this particular case).

5.5.4 PACRIM case summary

Whereas the CLEX-1 case study examined cirrus comprised of debris from a continental mid-latitude MCC, the CLEX-2 (PACRIM) case dealt with cirrus of tropical origin. The differences in optical properties arising from differences in formation mechanisms and profile characteristics (e.g., depth and moisture content of troposphere) have yet to be quantified to the extent that this information could be applied, for example, to cloud parameterization in numerical weather prediction models. Active sensors on the satellite platform will enable retrievals of this kind to be performed on a great number of cirrus cases with minimal uncertainty owing to cloud placement in the vertical.

5.6 ARM-SWIOP 9/26/97-9/27/97 Retrieval

The complimentary role of surface-based active remote sensing systems in satellite cloud property retrievals was examined for observations from the ARM Short-Wave IOP (ARM-SWIOP) experiment conducted during September of 1997 at the ARM SGP CART site. The cloud profile information provided by the surface platform required a multi-time, single pixel satellite retrieval approach as opposed to extracting several pixels along flight tracks for a few times (aircraft experiments) or a great number of pixels for a single time (LITE). The primary benefit of surface observations is that they are by far the most convenient (in terms of cost and implementation) of the three platforms. Co-location of satellite data with a time series of surface observations requires ancillary data to determine cloud advection across the fixed site. Fortunately, this information usually can be obtained either from rawinsondes launched on-site or from satellite-derived cloud vector wind approximations (i.e., tracking cloud edges between temporally adjacent images, with some ambiguity arising from the assignment of altitude for the feature being tracked). The following discussion illustrates this approach.

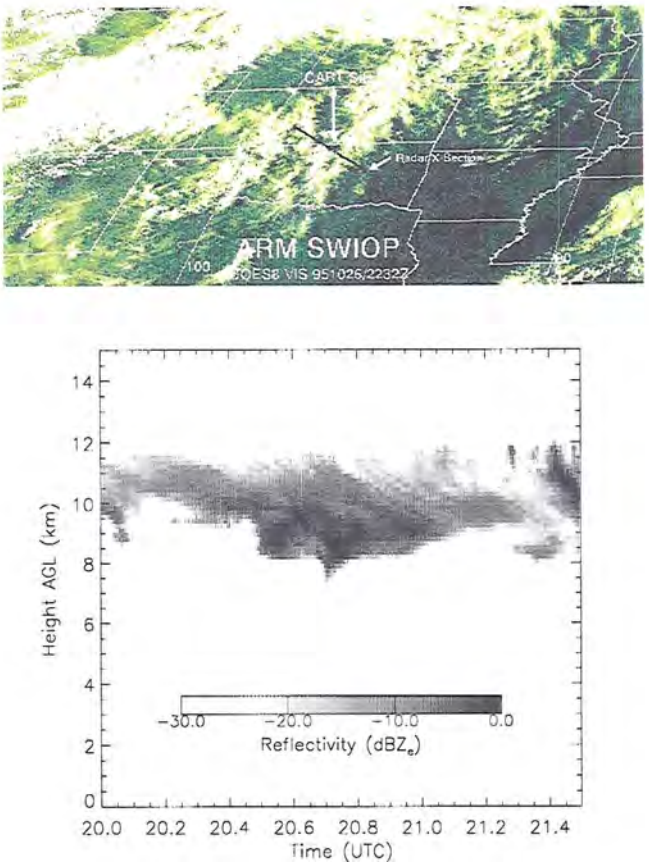

Figure 5.38: GOES-8 coverage of the ARM-SWIOP shown for the 3.9-μm imager channel (upper panel) and the surface-based cloud radar detected cirrus profile (lower panel).

5.6.1 Overview

Included in the instrument array of the ARM-SWIOP were the ACR (surface-based) and an Eppley Pyrgeometer. The former provided accurate profiles of cloud advecting over the SGP CART site facility near Lamont, OK, and the latter measured the downwelling broadband infrared flux. GOES-8 imager data for several image times (CONUS scans at 30 minute resolution) were obtained for the passive/passive+active retrieval computations. The pyrgeometer measurements provided the opportunity to validate independently, albeit indirectly, the satellite-retrieved cloud optical properties (applied as input to a 2-stream radiative transfer code to compute equivalent measurements of flux).

The data collected on 26-27 September, 1997 were obtained for conditions of a single-layer cirrus field. This cloud, at an altitude of approximately 10-km, advected South-Eastward over the ARM CART site during the late afternoon and early evening hours.

The day-time portion of the retrieval made use of solar reflectivity information in Ch. 1 and Ch. 2 while the night-time portion of the retrieval used an approach similar to the infrared-only techniques applied to the LITE retrieval. As mentioned above, rawinsonde data were enlisted to approximate the wind speed and direction at mid-cloud altitude (as inferred from the cloud radar). This information was used to advect the cloud field upstream and downstream of the CART site and, insodoing, create a virtual flight track traversed by the surface-based radar. Cloud height information was obtained from the cloud radar using a reflectivity-thresholding approach similar to the LITE CloudFinder technique. Fifteen GOES-8 image times (available at 30 minute intervals) spanned the 7.5-hour observation period.

5.6.2 Retrieval results

Figures 5.39-5.40 show retrieval results and uncertainty analysis for a portion of the ARM-SWIOP case. The cirrus clouds advecting over the CART site were characterized generally by optical depths on the order of $\tau_{0.65\mu m} = 2.5$, with occasional thicker regions exceeding $\tau_{0.65\mu m} = 5.0$. Retrieved effective particle radii ranged from 40 to 50 μm. *A priori* parameters again were very close to unity for the optical depth retrievals, while those for r_{eff} were on the order of 0.7 and correlated strongly with the phase function uncertainty. Uncertainty associated with the profile is lower than for the LITE retrievals because information was provided by rawinsonde rather than by ECMWF initializations. For the region of higher τ, r_{eff} uncertainty associated with Kernel function sensitivity increases (saturation of signal) and phase function contributions decrease (owing to increased multiple scattering). While such relationships are intuitive from elementary radiative transfer, the ability of the retrievals to quantify these components is an invaluable asset to analysis.

Independent pyrgeometer retrieval validation

The cloud properties derived from the satellite/radar retrieval were used as input to a simple 2-stream (flux) radiative transfer model [e.g., *Stackhouse and Stephens*, 1990] to simulate the downwelling broadband infrared (3.8 μm to 500 μm) flux at the surface. The 2-stream model includes a correlated-K handling of gaseous absorption. To better match

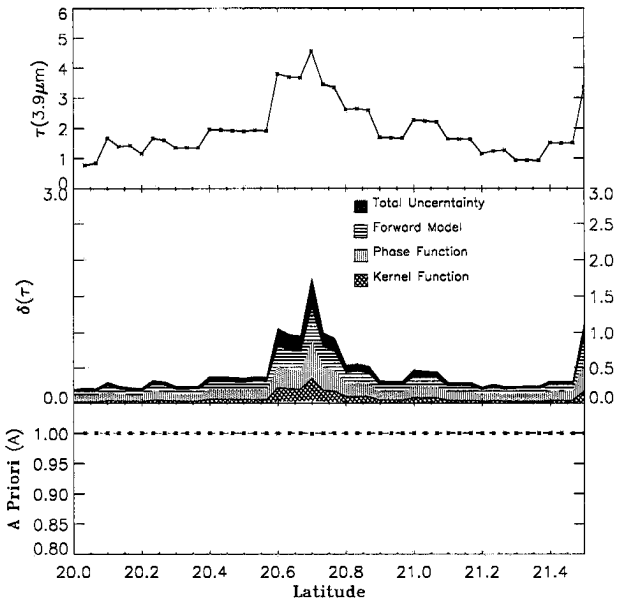

Figure 5.39: Optical depth retrieval and uncertainty for ARM-SWIOP.

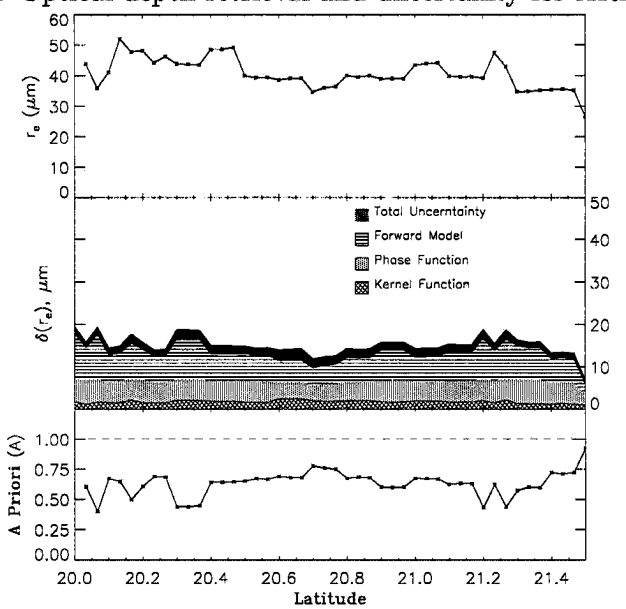

Figure 5.40: Effective radius retrieval and uncertainty for ARM-SWIOP.

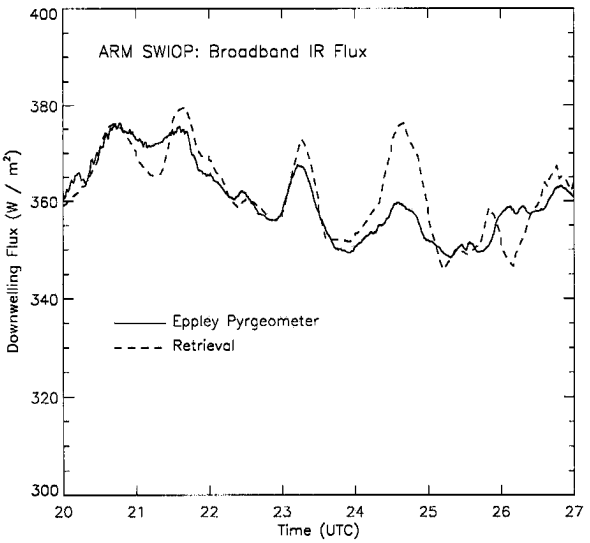

Figure 5.41: Comparison of retrieved broadband IR (3.8 μm to 500 μm) flux compared with a ground based Eppley pyrgeometer located at the ARM CART site. 10 km cirrus were advecting over the site during the 7.5 hour observation period.

the single-pixel values provided by the retrieval to the pyrgeometer integrated field of view, a boxcar average smoothing technique was applied to the retrieved fluxes. The width of the smoothing, determined from the cloud advection speed, cloud height, and the cosine response of the pyrgeometer, was equivalent to a 23 minute time window in the retrieval data. These smoothed fluxes were then compared to the pyrgeometer measurements as an independent validation of the satellite retrieval. It should be recognized that even though a model-based retrieval has been fed into another model to compute broadband fluxes, this validation is non-incestuous because the pyranometer observations remain completely independent of these retrieval/modeled fluxes. In other words, if the cloud properties retrieved were in error, then there is no reason that the 2-stream fluxes should match the observations.

The results of this exercise are shown in Figure 5.41. Captured in this figure are the broad-scale features of the cloud layer. Regions of higher downwelling flux correspond to optically thicker cirrus (which emit more radiation downward to the surface). While overall agreement is good, some areas show significant disagreements. These may be attributed to the non-plane-parallel quality of the actual cloud field. For example, a optically thick

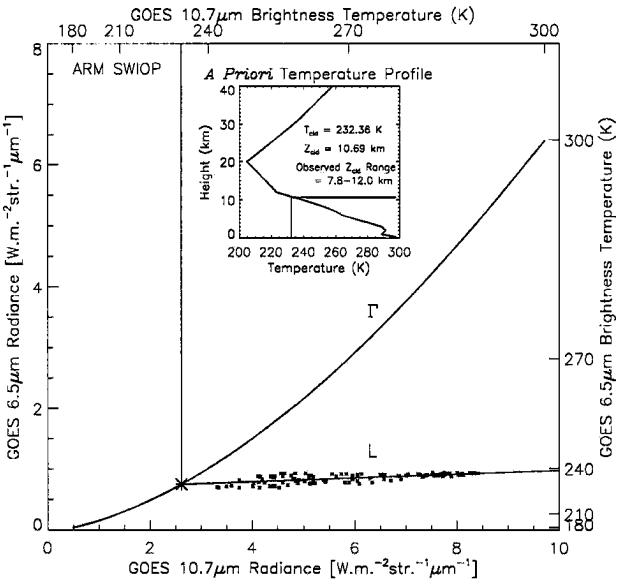

Figure 5.42: Passive sensor estimate of semi-transparent cirrus height for the ARM-SWIOP using GOES 6.5 μm water vapor and 10.7 μm IR window channels. Curve "Γ" is the theoretical blackbody relationship and line "L" is the linear fit to the observation set (following the method of Szejwach, 1982).

cloud pixel retrieved locally would then be attributed to the entire scene in the 2-stream flux computation, resulting in a much larger downwelling flux value than that of the heterogeneous scene observed by the pyrgeometer. Conversely, retrieval on an optically thin cloud in the midst of thicker surrounding field will result in an underestimate of the downwelling flux compared to observations. Incorporation of three-dimensional active sensor information and flux averaging of adjacent satellite-pixel retrievals would further mitigate the observed differences beyond boxcar averages. Overall, extrema straddle the observations as the advecting cloud field varies about the plane-parallel assumption. That this was observed in the absence of a positive or negative bias is an indication that the retrieved parameters of the cloud field were representative of the areal-averaged flux measurements.

5.6.3 Passive-only retrieval uncertainty

The Szejwach (1982) cloud height estimates for the ARM-SWIOP case are presented in Figure 5.42. The single-layer cirrus case provided a low-variance linear fit with a reasonable cloud top altitude of 10.7 km (actual observed range was 7.8 to 12 km). The differences between retrievals using active sensor cloud heights and passive-only techniques

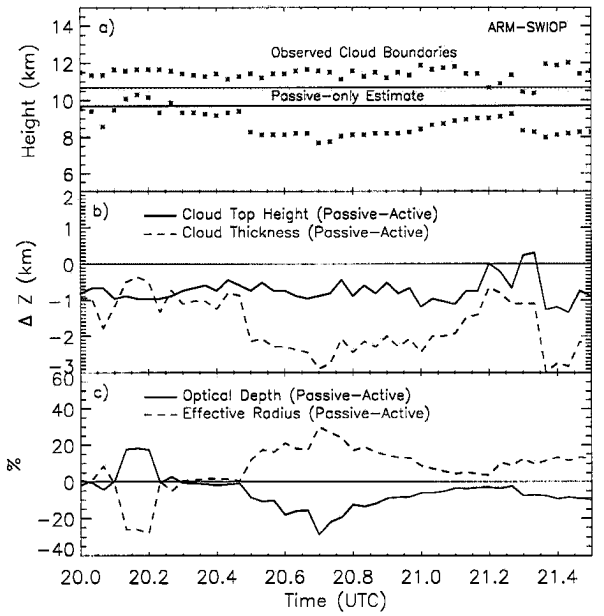

Figure 5.43: Differences in retrieved parameters between active-*a priori* and passive-only approaches: a) The active (points) and passive (following Szejwach (1982), shaded) cloud height estimates, b) Differences between passively- and actively-retrieved cloud heights (solid) and thickness (dashed), and c) Percent-difference between retrieved optical depths (soli) and effective radii (dashed) for the two retrievals.

are illustrated in Figure 5.43. Differences in cloud top and physical thickness are shown in the top panel and corresponding percent-differences in the lower panels. The assumed physical thickness of 1 km for the passive-only retrievals resulted in an underestimate error (solid, in panel (a) of Figure 5.43) of roughly 1 km. The thickness (dashed) underestimation ranges from 1 to 3 km. It is noted that near the time 20.7 (UTC) a maximum in retrieved parameter differences between the two retrievals corresponds with a maximum in passive-only underestimation of the physical cloud thickness. Here, the passive-only retrieval slightly underestimated τ while grossly overestimating r_{eff}. The passive cloud profile estimate being physically thinner and at a higher mean altitude than the true cloud layer, requires an entirely different combination of τ and r_{eff} for the forward model to reproduce the same observed radiation field.

5.6.4 ARM-SWIOP case summary

The ARM-SWIOP case demonstrated the application of ground-based active data in improving satellite cloud retrievals. In order to extract the appropriate satellite pixels cor-

responding to the surface observations, winds at mean cloud altitude were used to advect up- and down-stream of the central facility in the GOES imagery. After box-car averaging to approximate the field-of-view of the surface pyrgeometer, IR downwelling fluxes derived from the retrieved cloud optical properties were compared against the observations. Such comparisons are useful in ascertaining to what degree the retrieved optical properties along a profile can be used to represent the important radiative forcing effects of horizontally heterogeneous.

5.7 ARESE 10/26/95 and 10/30/95 Retrievals

The retrieval technique presented in this research was intended to be versatile in the ability of the forward model to accommodate observations from a wide array of remote sensing systems. Whereas the cases presented above all dealt with GOES satellite imagery as the passive-component, these retrievals could conceivably have been reproduced from (for example) observations made by the Advanced Very High Resolution Radiometer (AVHRR), the Defense Meteorological Satellite Program (DMSP) satellites, or the Moderate Resolution Imaging Spectroradiometer (MODIS) Airborne Simulator (MAS) instrument. This section presents retrievals based on active sensors working in conjunction with the CSU SSP operating from the manned/unmanned aircraft platform. The appeal of these instruments operating on the latter (unmanned aircraft) platform lies in the relative cost-effective deployment of these aircraft for extended, high-altitude global observations in remote parts of the Earth. Further, these solar-powered vehicles conceivably could be coordinated with satellite active/passive observations to enable IOP-quality observations at most any poorly accessible area of the world.

5.7.1 Overview

The ARM Enhanced Shortwave Experiment (ARESE) took place during October, 1995. Among the instruments flown aboard the DoE Egrett aircraft during this IOP was the SSP and the CDL. The former provided spectral radiance and flux measurements (40 channels) spanning the range of 0.4 to 1.1 μm (for use in forward model observation vector), and the latter provided a two-dimensional slice of the cloud profile along the

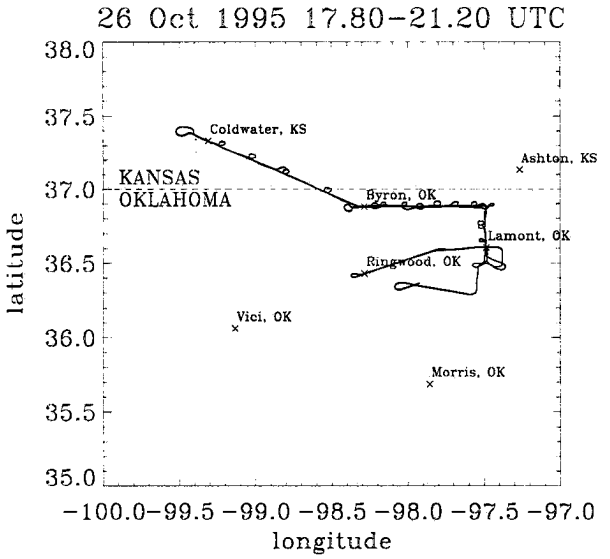

Figure 5.44: Flight tracks for ARESE October 26, 1995 cirrus case.

Egrett flight track similar to that provided by LITE (for use in the *a priori* constraint on cloud profile). Both instruments were mounted on the belly of the aircraft and recorded nadir observations of cloud and surface reflective properties. As this version of the SSP did not extend far enough into the middle IR to achieve sensitivity to particle size from solar reflection, these retrievals were forced to constrain (based on cloud climatology) the effective particle size and retrieve only cloud optical depth. For these retrievals, effective particle radii for cirrus were constrained to 30 μm as a typical value (C.M.R. Platt, personal communication) and water clouds in the October 30th case were set to 10 μm. Because reflection at visible wavelengths is not a strong function of particle size, errors associated with an incorrect assumption of this quantity were assumed to be small.

October 26th ARESE case

On October 26, 1995, the Egrett took off at 1748 UTC and flew a 2.5 hour leg between the ARM central facility at Lamont, OK and Coldwater, KS (the flight track is shown in Figure 5.44. The SSP and CDL observed a single-layer of cirrus over this duration. The spectral surface albedos for this case were derived from clear-sky SSP radiance observations (Partain *et al.*, 1999) and a forward model. The derived albedo accounted also for aerosol scattering effects below the altitude of the aircraft.

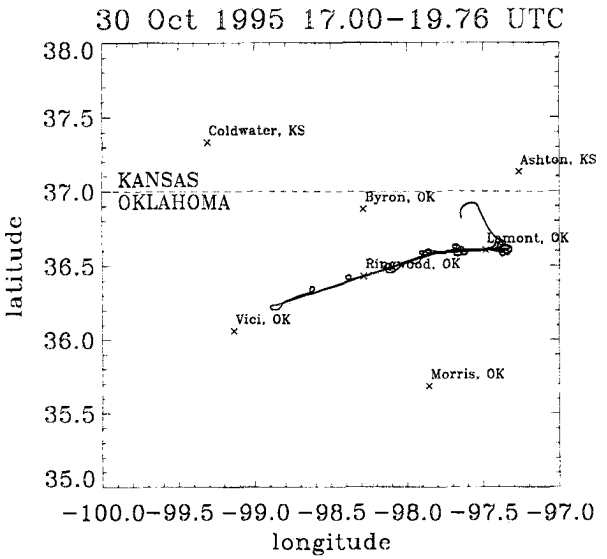

Figure 5.45: Flight tracks for ARESE October 30, 1995 cirrus+low-cloud case.

Also on-board the Egrett was the Total-Direct-Diffuse Radiometer (TDDR) instrument (Valero *et al.*, 1989), designed to measure solar radiation in several narrow (10-nm) spectral band-passes and also the broadband (0.25 to 3.0 μm) solar flux. The instrument achieves decoupling of the direct and diffuse components of downwelling solar flux by including an oscillating shadow ring. In this way the TDDR is superior to sun-tracking photometers which are both complex and difficult to maintain tracking accuracy. The TDDR was mounted next to the SSP recording nadir observations of solar reflection at cloud top. Several results presented for these retrievals were converted to equivalent fluxes for comparison against the TDDR measurements.

October 30th ARESE case

On October 30, 1995, the Egrett flew above a two-layer cloud field composed of thin cirrus at 10 km and a thick lower-level stratus cloud between 1 and 2.5 km. Figure 5.45 shows the flight path spanning the period 1700-1945 UTC between Lamont and Vici, OK. The high optical depth of the lower layer attenuated completely the CDL signal before reaching the surface. As a result, rawinsonde data launched from the CART site were used to define an approximate cloud base for the lower cloud using the cloud condensation level (at roughly 1-km). Surface albedos for this case were derived in a similar fashion to those

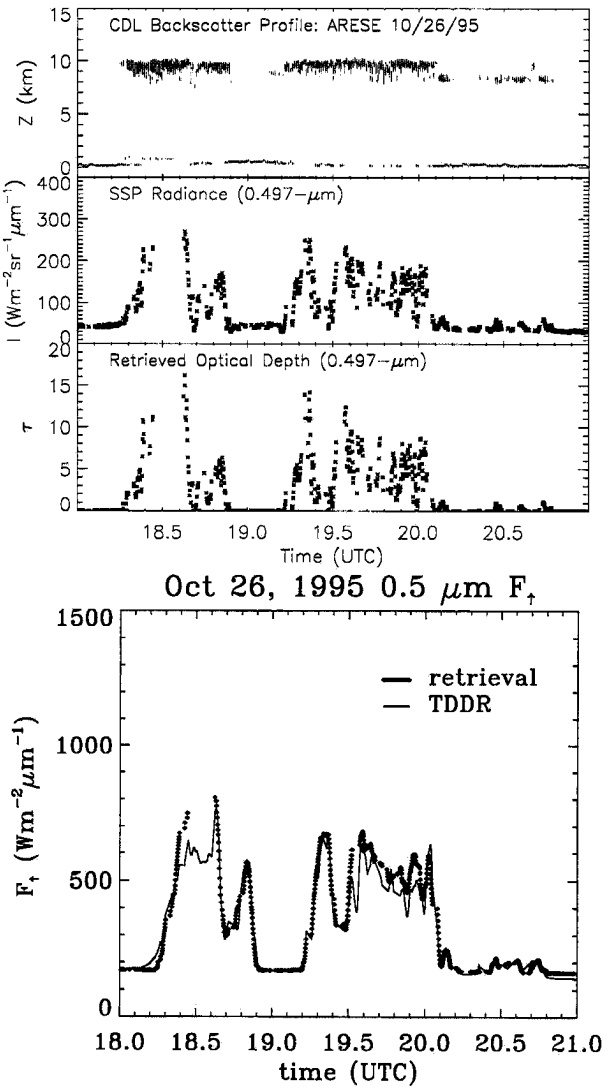

Figure 5.46: Optical depth retrievals and derived spectral flux comparisons with TDDR measurements for the ARESE October 26, 1995 cirrus case.

of the October 26 case. The TDDR instrument was again flown in a nadir orientation along side the SSP.

5.7.2 Retrieval results

Figures 5.46-5.47 summarize the retrieval results for the two ARESE flight legs considered. The top three-panel plot depicts the CDL-observed cloud profile, the corresponding spectral radiance (shown here at $\lambda = 0.497$-μm), and the retrieved values of cloud optical depth at this wavelength. Gaps in the SSP/retrieval data corresponded to portions of the flight leg where SSP data was unavailable. It was noted that in regions of higher optical

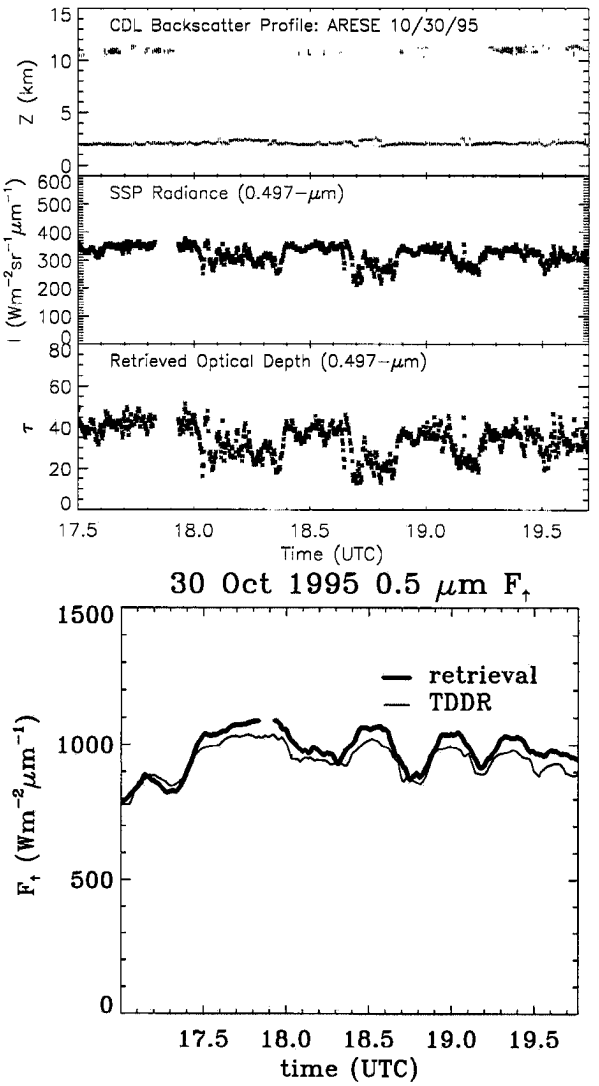

Figure 5.47: Optical depth retrievals and derived spectral flux comparisons with TDDR measurements for the ARESE October 30, 1995 cirrus case.

depth (e.g., $\tau > 5.0$), the CDL did not penetrate the clouds completely (as indicated by the absence of a surface return). Because the CDL was designed for cloud altimetry (as opposed to cloud profiling) a more suitable choice of active sensor for use in this retrieval would have been the millimetric radar. Knowledge of correct cloud top altitude, however, remains superior to having no *a priori* information whatsoever. The high measured reflectances during the 30^{th} case were dominated by the optically thick lower cloud. At these large optical depths, sensitivity to changes in the optical properties is very weak. Shown in the lower, single-panel plots on each figure are two curves–one corresponding to a two-stream flux model (which accepted as input the retrieved cloud optical properties), and the second corresponding to actual measurements of the spectral flux as observed by the Total-Direct-Diffuse Radiometer (TDDR) instrument. This exercise may be regarded as an independent validation of the SSP-measurements and retrieval. While good agreement was observed for these visible-wavelength spectral flux comparisons with the TDDR owing to the similarity condition, uncertainty in the assumption on particle size would manifest in the near- and thermal-IR (where cloud absorption becomes a strong function of the particle size distribution).

5.7.3 ARESE case summary

The ARESE case studies illustrate the versatility of the retrieval developed for this research by applying it to an observing system other than GOES-8/9 satellites. The optical depth retrievals on cirrus and cirrus with low-level cloud were converted to hemispheric upwelling flux and validated against independent TDDR measurements. The agreement between retrieved and observed fluxes indicates that either the assumption on particle size was not a strong factor in the retrieval, or that the forward model tuned the optical depth accordingly to accommodate for the fixed effective radius. Based on simulations conducted with a variety of effective radii, the latter mechanism also appeared to play a non-negligible factor in these retrievals. Despite the generally small magnitude of visible reflection variation with particle size, these differences are not negligible. As a result, a slightly different optical depth will be retrieved for a given effective radius constraint.

The retrieval itself is not to blame for these differences, for it is only being "told" that the true effective radius was a specific value with no uncertainty (in order to constrain the forward model at this value) attached. As a result, all variability in reflectivity observations must be accounted for by variance in the cloud optical depth. The model has no way of knowing the origin of that *a priori* data and must therefore take the information at face value. When these parameters are in turn used as input to a 2-stream model, the resultant fluxes are identical for all the τ, r_{eff} pairs arising from different constraining values of r_{eff}. This is illustrates the similarity condition for cloud reflection, which describes the infinite possibilities of optical properties which yield the same measured cloud reflection. This is why we seek to constrain our solution with measurements at water-absorbing window bandwidths situated at near- and thermal-IR wavelengths whenever possible.

5.8 SUCCESS 4/20/96 and 4/27/96 Retrievals

Retrieval case studies presented in this section were conducted for two flights conducted during the Sub-sonic Aircraft and Cloud Effects Special Study (SUCCESS). The data were collected during April and May of 1996 near the ARM CART site. As a piggyback mission in connection with SUCCESS, ARM funded the deployment of the SSP, TDDR and CDL instruments. Several cases of cirrus and low-level cloud layers were encountered over the course of the flights. Retrievals from two of the cirrus days are shown here.

5.8.1 Overview

SUCCESS flight tracks are shown for two legs on April 20^{th} and 27^{th} in Figure 5.49. Both flight patterns were highly irregular with multiple overflights of the CART site facility. Co-location with satellite pixels for such cases is difficult due to the highly variable position of the aircraft, the advection of cloud, and the temporal resolution of the satellite imagery. Whenever possible, it is desirable to have all instruments operating upon the same platform to eliminate the uncertainty of co-location. As in the ARESE cases, the SSP, TDDR, and CDL were mounted together on the base of the aircraft to record simultaneous

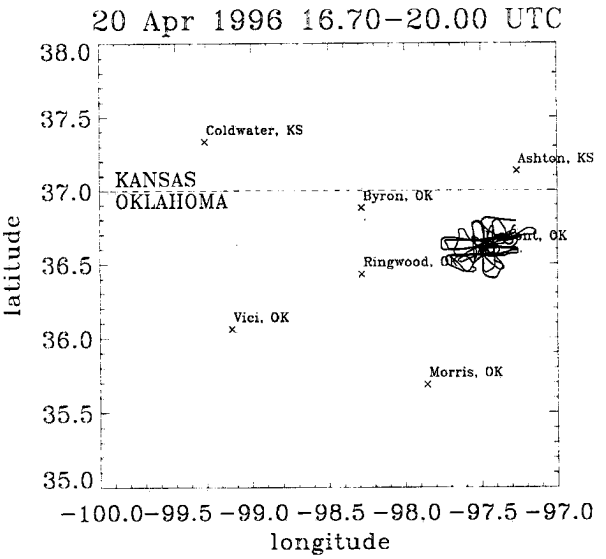

Figure 5.48: Flight track for SUCCESS April 20, 1996 cirrus case.

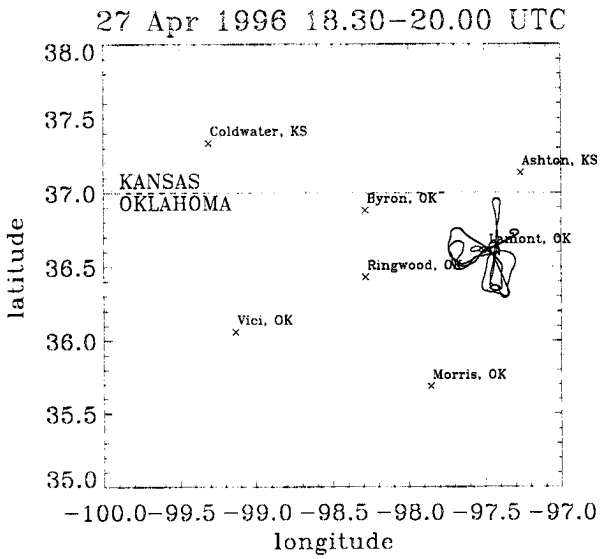

Figure 5.49: Flight track for SUCCESS April 27, 1996 cirrus case.

observations of the same cloud fields. The same problem with SSP insensitivity to the near-IR precluded the retrieval of particle size and necessitated again the *a priori* constraint on effective radius at 30 μm. To account for the high forward and backscatter peaked scattering phase functions associated with most cirrus (especially at visible wavelengths), a tabulated ice-crystal phase function from Takano and Liao (1995) was employed with δ-M scaling to expand it as a Legendre polynomial series with a reasonable number (here, 65) of χ-expansion terms.

5.8.2 Retrieval results

Figures 5.50-5.51 summarize the observations and optical depth retrievals performed for the SUCCESS flight legs described above in similar fashion to those presented for the ARESE case. Again, the optically thinner clouds ($\tau < 5$) were penetrated entirely by the CDL on the 20$^{\text{th}}$ case, while optically thicker clouds were devoid of CDL surface returns on the 27$^{\text{th}}$. Using these retrieved optical depths along with the assumed particle size, 0.5 μm spectral fluxes computations were compared to TDDR measurements for both cases. The results are shown in the lower single-panels of Figures 5.50-5.51. A slight underestimate of the reflected spectral flux may be related to an underestimate of the surface reflectance spectrum or lower-atmosphere aerosol content for these cases as simulated in the 2-stream model. Surface albedos for the SUCCESS cirrus retrievals were computed from a different day (over the same area) when clear skies prevailed. The bias was observed predominantly in the lower-reflectance portions of cloud. An important point to also keep in mind when considering comparisons with the TDDR is that the retrieval-fluxes are based on a plane-parallel cloud whose properties everywhere are described by those retrieved at nadir. The TDDR, on the other hand, observes the true cloud field which includes horizontal heterogeneity. It might be expected that for a heterogeneous field, then, the distribution of over- and under-estimates between the model and TDDR observations would be nearly equal. This suggests that a possible forward model bias (introduced in the vector of unretrieved parameters) existed in these SUCCESS cases. This emphasizes the importance of correct surface albedo specification in the forward model, especially

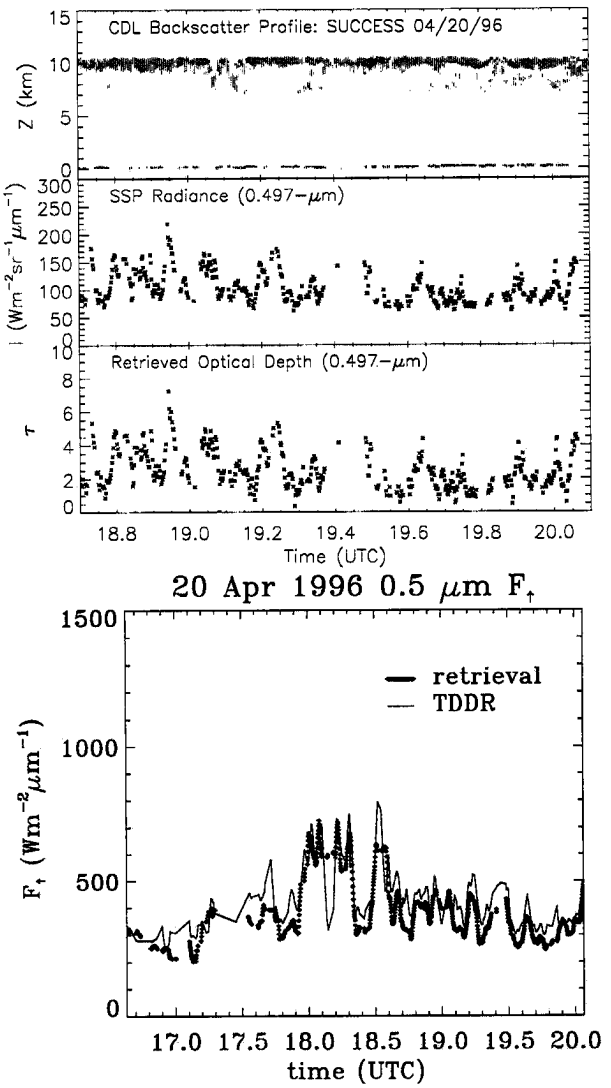

Figure 5.50: Optical depth retrievals and derived spectral flux comparisons with TDDR measurements for the SUCCESS April 20, 1996 cirrus case.

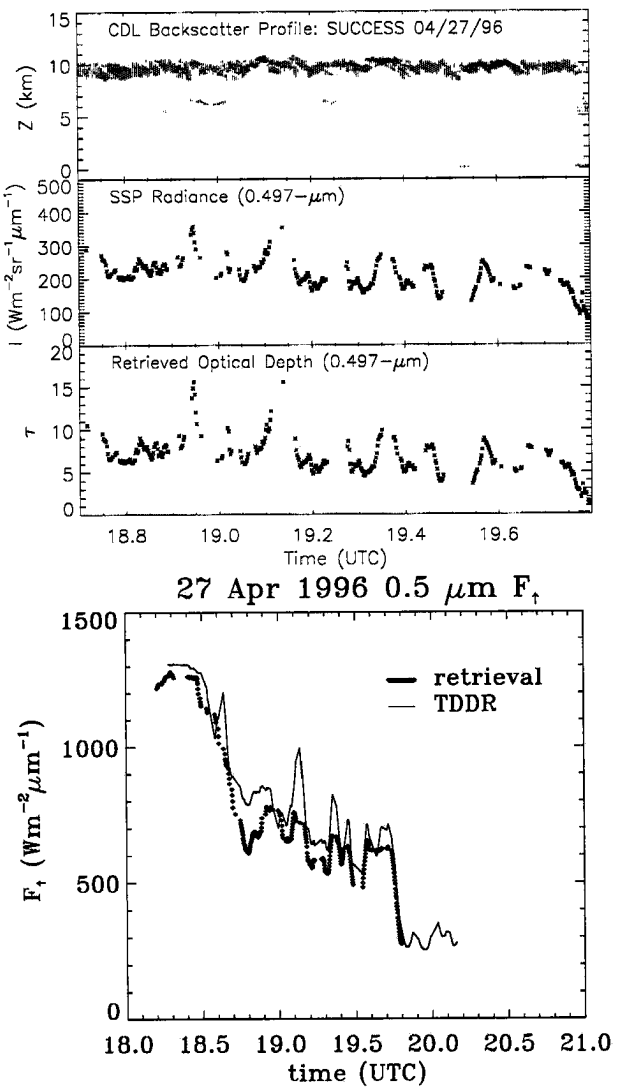

Figure 5.51: Optical depth retrievals and derived spectral flux comparisons with TDDR measurements for the SUCCESS April 27, 1996 cirrus case.

when dealing with day-time retrievals over land surfaces (where vegetation in particular displays high spectral variability across visible and near-infrared wavelengths).

5.8.3 SUCCESS case summary

The SUCCESS cirrus cases, while presenting results very similar to those of ARESE, provided additional cirrus retrieval data to be included in an ensemble-case assessment of results derived from the new retrieval method. The optical properties were used as input to a 2-stream model and fluxes compared against those observed by the TDDR. An underestimate error observed in these flux comparisons was due most likely to the error associated with the assignment of surface albedo. This speaks to why retrieval-oriented experiments gravitate toward cases over the ocean where the background surface albedo is more uniform, small in magnitude, and relatively spectrally flat compared to heterogeneous land surfaces.

5.9 ARM-UAV 4/30/99 Kauai Retrieval

The ARM-UAV flight series, conducted during April-May, 1999, consisted of two aircraft and a large array of instruments. On April 30, the UAV (Altus II) flew the SSP (oriented nadir) at high altitude (near 16 km) above tropical cirrus while the Twin Otter flew the ACR (oriented in the zenith) at lower altitudes (near 3 km). The Otter's altitude and heading was selected to match as closely as possible the track of the UAV (formation flying) such that the same clouds were sampled simultaneously by all instruments. Included on the Altus-II payload were the CDL and TDDR instruments, and a second TDDR flew aboard the Otter. A second SSP was added to the Otter during these experiments, but was not installed in time for the preferred cirrus studies examined here.

5.9.1 Overview

The primary objective of the April 30 (S99-4) flight was to collect cirrus data. The cirrus at the onset of the experiment occurred between 11.0 and 13.5 km and were optically thin. Over the course of the afternoon, the layer thickened both geometrically to a range between 7.0 and 14.0 km. The Altus took off at 1915 Z and landed at 0236 Z. This

retrieval used observations made between 2030 and 0030 (May 1) (or 1030-0230 local military time). Although a Lagrangian (i.e., following the same air parcel in time) sample was not made, it could be inferred from multiple track legs that the large-scale cloud structure was evolving from a single layer near 12.5 to 14 km toward a two-layer structure (with a lower cloud forming near 7 to 9 km) and finally to a thick, single layered cloud spanning the full range from 7 to 14 km. GOES-10 imagery loops revealed the cirrus layer, which was tied synoptically to an approaching baroclinic wave, advected into the IOP region from the W/SW and deepened (as inferred by colder cloud tops) over time. Identified from rawinsonde observations was a very deep, dry layer below 7 km, defining clearly the ACR-observed base of the cirrus layer.

The varying altitude of the Twin Otter aircraft necessitated sample-by-sample range-correction of the cloud radar returns. This was done by shifting upward the data by an integral number of range gates corresponding to the aircraft altitude. The empirical relationships from Sassen & Liao (1996) and Platt (1997) were used for radar-reflectivity-based estimates of water content, extinction (from which optical depth was derived), and particle size. Cloud heights were determined from reflectivity thresholding/stability techniques (no SNR data were available) as described earlier. Also available were ECMWF reanalysis shortrange forecasts to support the forward model profile requirements. The UAV departed from the airfield on the Western coast of Kauai and headed West to a position near (22.1° N,160.8° W). From this point, multiple legs of the same North-East/South-East (up to roughly 22.8° N,159.9° W) line were flown with the Twin Otter, which flew in co-location at an altitude of 3 km. For comparisons with the ACR, only points within ±1-minute and ±4 km (with respect to the ground track) were considered as being "co-located" observations (i.e., all realignment maneuvers and *en route* portions of the flight legs were discarded in Otter/Altus comparisons).

As an additional source of independent retrieval information, imager data from GOES-10 were obtained from CIRA for this case and pixel information extracted along the Altus flight track. Three-way intercomparison between SSP, ACR, and GOES-10 required co-location of the two aircraft and satellite imagery in both space and time. A temporal/spatial requirement of ±2 minutes, 4 km was enforced between the Altus and Twin

Otter (using aircraft navigation files). Although chosen somewhat arbitrarily, the thresholds decided upon were considered as sufficient for advection speeds and horizontal scales typical of cirrus. GOES-10 imagery (Ch. 1-5) was collected at 15 to 30 minute intervals throughout the duration of the Altus/Twin-Otter formation flights. Similar to the ARM-SWIOP case, the retrieval compared at run-time the time-stamped aircraft observations to the GOES image scan times in order to utilize observations from the closest temporal match in the imagery (minimizing errors due to between-scan cloud advection). Clearsky scenes were used to adjust the forward model ocean surface albedo to match the observations.

5.9.2 Retrieval results

An example of ACR-derived retrieval products from a NE/SW leg of the Kauai 04/30/99 cirrus flights is shown in Figure 5.52. The upper-left panel depicts the flight tracks for both the Twin Otter and Altus-II, with the light-shaded portion of the track corresponding to temporal and spatial aircraft co-location as described above. The inscribed dashed-line boxes define areas analyzed by ECMWF specifically for this case to provide profile information for the forward model (the examination of model cloud products included as part of these data is a subject of the ensuing chapters). The upper-right plot shows ACR profiles of reflectivity and ice water content and effective particle radii computed as a function of the reflectivity according to the empirical parameterizations of Sassen and Liao (1996) and Platt (1997). In the lower-left plot, extinction coefficients at a visible wavelength (again using Sassen and Liao, 1996, not shown) were integrated through the depth of the cloud profiles as defined by the cloud-edge detection algorithm to obtain cloud optical depths. The lower-right panel is an example of a cumulative frequency in altitude diagram (CFAD) based on the entire leg of radar data shown. CFADs contain a great wealth of information about cloud microphysics and bulk properties of the internal structure that are often less obvious when observing the cloud in time series. For example, the increase of reflectivity toward cloud base suggests particle growth is followed by a sharp decrease owing to evaporation in a dry layer below the level indicated. In mixed-phase clouds, the melting level is often clearly evident in CFADs as marked spike

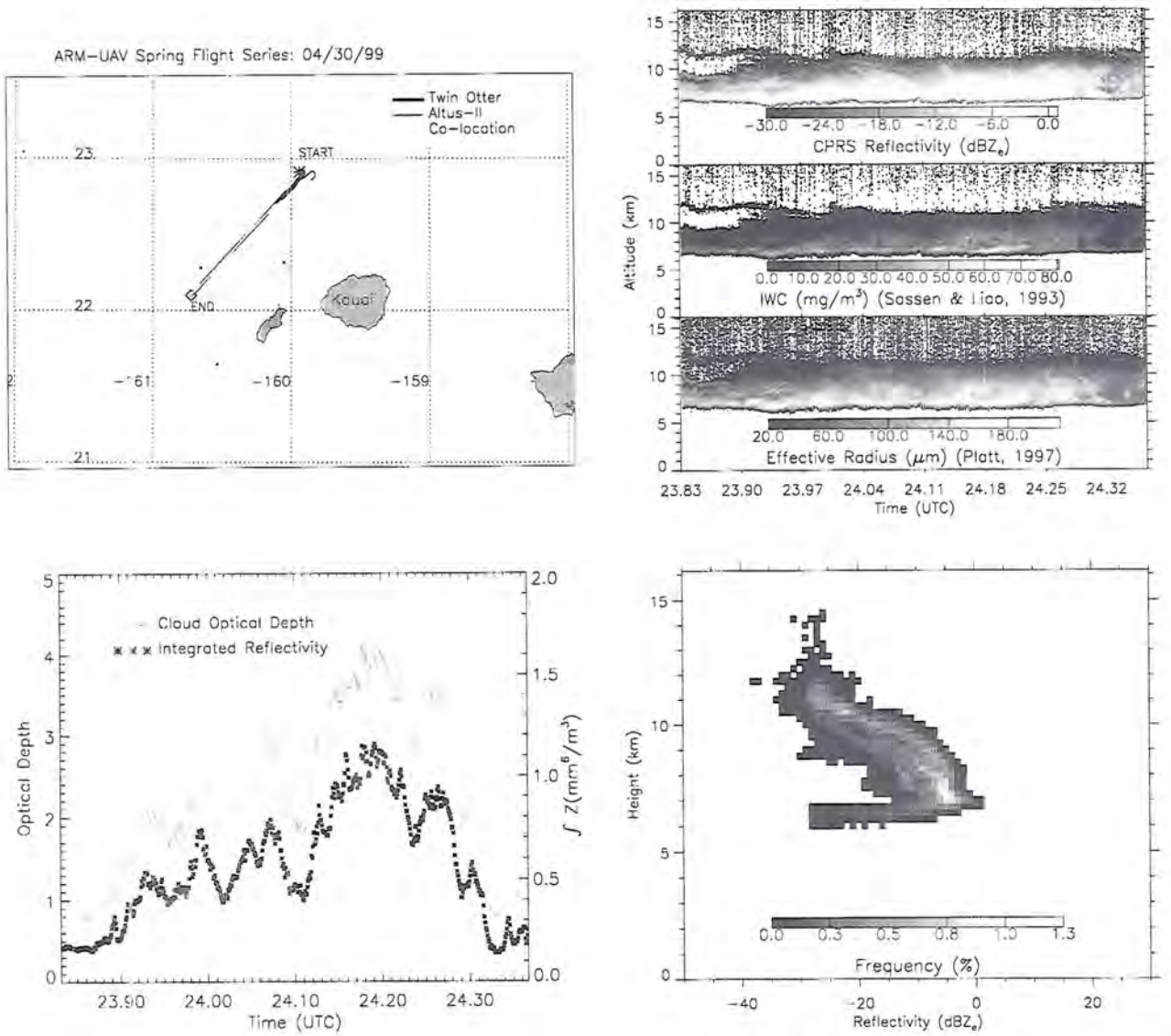

Figure 5.52: ACR results for 04/30/99 ARM-UAV flight track showing flight line (upper left), reflectivity derived products (upper right), column-integrated reflectivity and optical depth (lower left), and frequency distribution of reflectivity in space (lower right). See text for details.

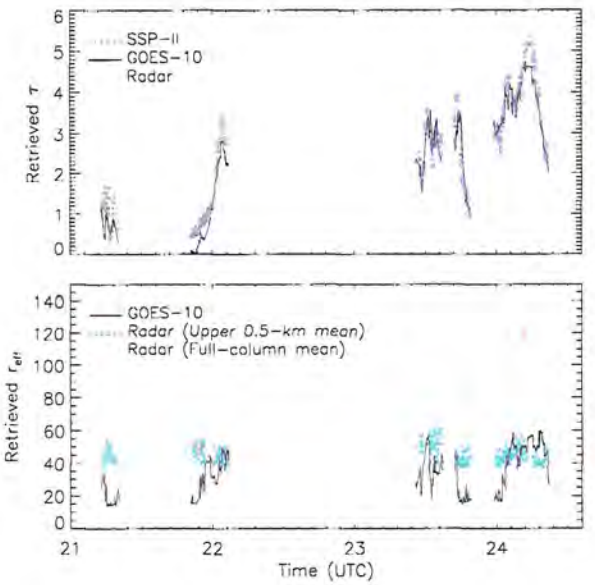

Figure 5.53: ARM-UAV Kauai cirrus optical depths as retrieved independently by GOES-10, the SSP, and from empirical radar relationships applied to the ACR (τ: Sassen and Liao, 1996; r_{eff}: Platt, 1997). Retrievals correspond to the periods where the Altus and Twin Otter were co-located.

in the maximum reflectivity. Such ensemble cloud statistics also are useful in comparing to model-fields of water and ice content (after converting empirically from model parameters to equivalent radar reflectivities or vice-versa). The data are also useful, for example, in Department of Defense (DoD) applications where target detectability through cloudy slant-paths as probed with laser optics must considered.

The retrievals of optical depth and effective radii for the co-located Kauai data are shown in Figure 5.53 for all three observing systems. Uncertainties associated with these parameters (not shown) are of the same order as cirrus case study retrievals presented earlier. For the GOES and SSP physical retrievals, a hollow-column ice crystal morphology phase function (with associated asymmetry parameter and single-scatter albedos as a function of wavelength and effective size) from the tabulated data of Yang *et al.* (1998) was employed as a χ-expansion in the forward model. This lowers the uncertainty associated with the phase function (compared to a double Henyey-Greenstein approximation), however uncertainty still exists among the variants of crystal shapes possible in cirrus. Retrieved optical depths using these ice phase functions tend generally to be

smaller than their best-fit double Henyey-Greenstein counterparts, owing to their relatively strong backscatter peaks at visible wavelengths (allowing for a smaller estimate of τ to produce the same observed solar backscatter). The optical depths for the physical retrievals were found to be similar, with some underestimation by GOES owing to subpixel variability (e.g., a partially-filled pixel yielding a lower value of average reflectivity compared to the more localized footprint by the SSP). The radar-only empirical (Sassen and Liao, 1996) retrieval of τ was consistently lower than those of the solar reflection based methods. Comments regarding this under-bias are reserved for the discussion of the CloudSat/PICASSO observing system to follow. Effective radii between the physical and empirical method (Platt, 1997) differed significantly when comparing against the column-mean radar-derived effective radii.

Shown in the lower panel of Figure 5.53 are effective radii retrieved by the the GOES-10 and empirical radar methods. Because the upper limit on the spectral range of the SSP was 1.1 μm, no cloud particle information was available. The radar relationship calculates an effective radius for each gate based on the reflectivity, and so a column mean effective radius was computed for comparison against the single GOES-10 values. These comprise the points that extend well above 100 μm, in considerable disagreement with the GOES results with maximum r_{eff} near 60 μm. The large differences were due to contributions to the mean radar-derived reflectivity near cloud base. The point to remember with retrievals based on solar reflection is that the reflection measured generally is not a function of a cloud-averaged mean r_{eff}, but rather of some value closer to the cloud top. The degree to which solar radiation will penetrate the cloud top is a function of the water/ice absorption at the wavelength in question. The 1.65 μm water vapor window channel, while offering sensitivity to particle size, has weaker absorption than at 3.9 μm. As a result, reflection measured at the former wavelength is representative of a deeper level (i.e., more penetration) within the cloud, whereas the measurement at 3.9 μm is more representative of particles closer to the cloud top. A study by

Nakajima and King (1990) investigate this property for the case of marine stratocumulus observed during the First ISCCP Regional Experiment (FIRE) conducted off the

San Diego coast in July 1987. They show that for marine stratocumulus (where particle size increases with height in the cloud) the effective radius retrieved from solar reflection at 3.9 μm is roughly 90% of the cloud top r_{eff} when $\tau \geq 5.0$. To compensate for this effect, a new radar-derived effective radius comprising a mean of the uppermost 0.5 km of cloud was computed. These data fell much closer to the GOES-10 retrievals. Discrepancies that persisted for the optically thinnest clouds were be explained in part by the lack of radar sensitivity to a majority of the profile (thereby computing a mean based on the larger particles that were detected while missing the smaller component). The subject of detectability is therefore key when assessing the utility of active sensors. As will be shown for this case, the same cloud may appear very different when observed by different instruments.

5.9.3 Application to CloudSat Algorithm Development

While the retrievals presented in this chapter place a strong emphasis on the how active sensors complement existing passive sensor techniques, the use of active sensor data to progress other active sensor applications should not go unconsidered. With the pending launch of the first civilian millimetric radar (CloudSat) in 2003, there is much to learned in terms of what clouds/cloud-properties it will be able to detect. More importantly from the perspective of the science goals to be drafted in the ATBD, questions regarding what level of information will be *missed* and the associated radiative implications must be addressed. A means to addressing some of these questions involves the use of airborne/surface cloud radar observations as an antecedent data source (i.e., an observation-based model of CloudSat).

Figure 5.54 illustrates this thought process as applied to data available from various DoE/ARM IOPs conducted over the last several years which include active sensor observations. In the diagram, the closed loop depicts the current, pre-launch period during which time algorithm development may be achieved by recasting antecedent data into a "virtual CloudSat platform" by averaging and thresholding techniques. Results from these exercises will help ascertain where clouds are missed, for what reasons, and the implications of these shortcomings to applications such as model assimilation. Once the satellite becomes

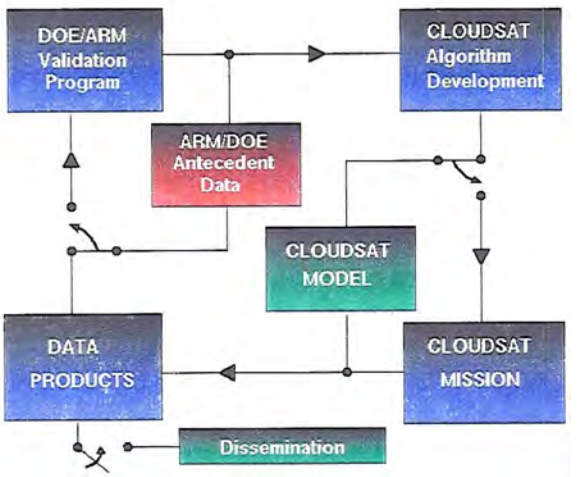

Figure 5.54: Conceptual cartoon illustrating the developmental stage of CloudSat algorithms using active-sensor antecedent data collected from existing IOPs.

operational in 2003, all nodes shown in Figure 5.54 switch to the outer loop as indicated by transition arrows, where the developed algorithms are applied to actual CloudSat data to produce end-products (i.e., level 1 and higher data products). In the operational phase, the role of surface IOPs change from developmental to validation oriented.

While discussed here in terms of DoE/ARM, in principle the source of these antecedent data is entirely arbitrary. Smoothed and degraded to an equivalent orbit-altitude footprint (e.g., 3 km after shot-averaging for CloudSat) and vertical resolution (e.g., 0.5 km for CloudSat), optical properties derived from the simulated CloudSat data can be compared against results from the original full-resolution data. Further, passive satellite retrievals employing *a priori* active cloud heights (as outlined in many of the case studies covered in this chapter) can be used to validate and improve upon existing radar retrieval parameterizations. In this way, multiple components of existing active sensor data are applied non-incestuously to the development of future active remote sensor platforms.

The ACR reflectivity for an earlier leg of the 04/30/99 Kauai flight were rebinned to CloudSat resolution (shown in the left panel of Figure 5.55. The result was a smoothed field of area-averaged reflectivity. As expected, the largest departures with respect to the full resolution ACR profile occurred in regions of high spatial heterogeneity (e.g., multi-level cloud and near cloud edges), leading to an underestimate of radar-derived cloud optical depth (right panel of Figure 5.55) in those regions. The most notable effects for

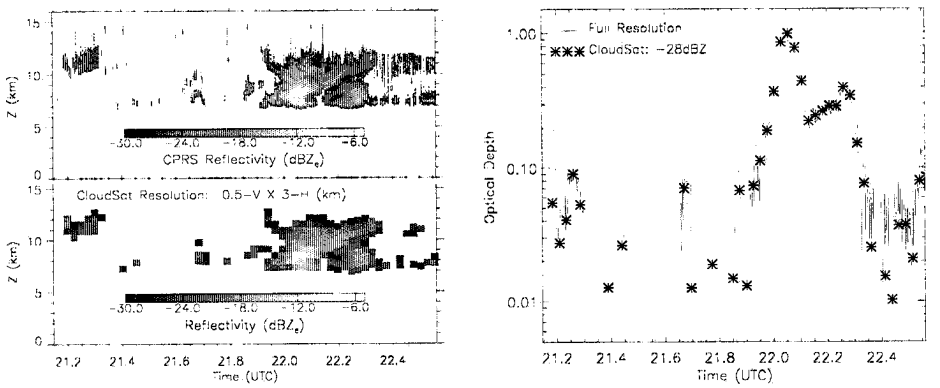

Figure 5.55: Rebinning/reflectivity-averaging of Kauai ACR data to CloudSat resolution (0.5-km vertical and 3.0-km horizontal, left panel), equivalent CloudSat-derived visible optical depths (right panel).

this particular flight leg were observed for the portion of the leg between 22.3 and 22.5 UTC, where two layers of intermittent optically-thin cirrus often fell below the -28 dBZ threshold after smoothing to CloudSat spatial resolution.

Three flight legs of cirrus data were analyzed for this portion of the ARM-UAV Kauai IOP. For each leg, radar reflectivity (dBZ) and optical depth were tallied at both full (ACR) and at CloudSat spatial resolution. These data were assembled to compute ensemble PDFs of these quantities. The results for both ACR (thresholded at a nominal sensitivity of -28 dBZ_e) and CloudSat (computed from spatial averaging of the thresholded ACR data) resolutions are shown in Figure 5.56. The negative shift in the CloudSat reflectivity distribution was attributed to loss of information near cloud edges sharp inner-cloud gradients of reflectivity (i.e., smoothed ACR reflectivities falling below the -28 dBZ_e minimum sensitivity threshold. How this loss translated to differences in the distribution of CloudSat-derived cloud optical depth is shown in the lower panel PDF in Figure 5.56. The inset figure provides a zoom-in of the PDF curves evaluated at the lowest optical depths and shows an enhanced distribution for the CloudSat resolution curve (owing to the degrading of cloud reflectivity in the averaging process). Because the reflectivities corresponding to these very low τ occurred below the -28 dBZ_e threshold, most of these clouds will be missed altogether on the actual CloudSat platform. Repeating the exercise for a range of minimum detectable signals (MDS) enables the determination of baseline

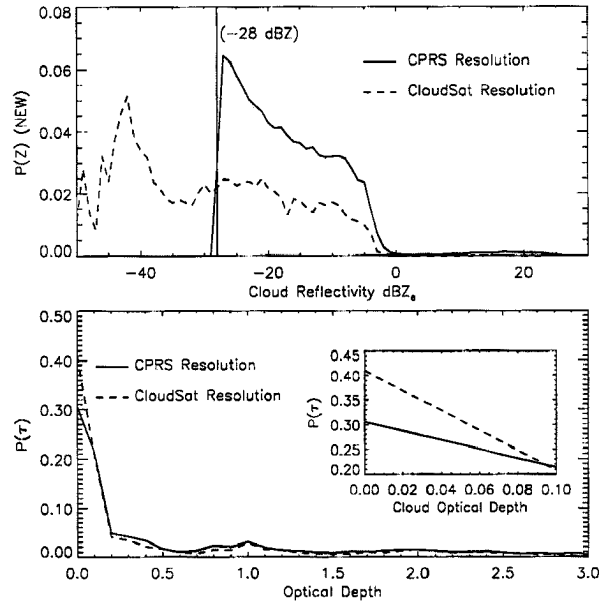

Figure 5.56: PDF comparisons of reflectivity and optical depth between ACR- and CloudSat-resolution. See text for details.

MDS corresponding to a specific retrievability goal (e.g., at what MDS are cirrus with $\tau < 0.1$ lost?) as what might be quoted within the algorithm theoretical basis document (ATBD).

The original CloudSat proposal included as part of its observing system a cloud lidar similar to that used in LITE. Due to budget constraints, this component was omitted from the final draft of the accepted proposal, but was mitigated in part by the decision for CloudSat to formation fly with PICASSO-CENA. The two active instruments (cloud radar and lidar) are by no means redundant. While the radar has the capability to penetrate and provide detailed cross-sections through optically thick clouds, it suffers from insensitivity to optically thin clouds and aerosol. Because the lidar utilizes a visible-wavelength active signal, the size parameters associated with smaller particles are again large, yielding an appreciable backscatter return from these constituents. The drawback to the lidar is that the signal is quickly attenuated in optically thick media. Fortunately, nature has conspired to form its most optically thin clouds in the upper troposphere, such that a spaceborne lidar can measure them above the problematic heavy-attenuators residing below. The dual cloud radar/lidar system captures information at both optical limits, thereby providing an ideal system for observing the cloud profile.

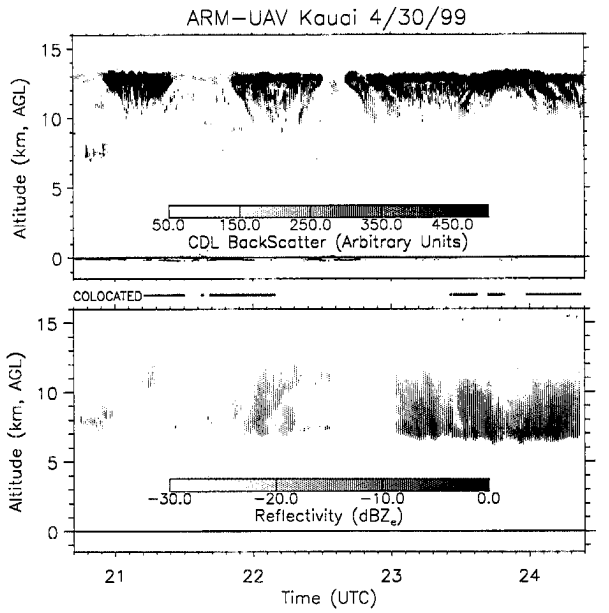

Figure 5.57: ARM-UAV Kauai observations of cirrus clouds by the CDL and the ACR. Note differences in sensitivity between the two instruments. Co-location times are indicated between the two panels.

Figure 5.57 exemplifies this concept for the Kauai cirrus case study presented above. The cloud lidar data is shown in the upper panel, and the corresponding cloud radar data is provided in the lower panel (co-location between the two aircraft as defined by the space/time criteria outlined above is shown in-between these panels as a segmented line). At first glance, the two images appear almost as entirely different cloud structures. In the CDL data, a sharp upper boundary near 13 km is observed, and fades to a variable and at times indistinguishable base. We recall from previous retrieval case studies (e.g., ARESE, SUCCESS) that the lidar beam often suffers complete attenuation in optically thicker regions of cloud; a property that correlates with the occasional disappearance of the strong surface return. The cloud radar, on the other hand, portrays this same series of cirrus as having an equally sharp base near 7 km with a tapering-off of the signal toward an ill-defined cloud top altitude varying between 10 and 12 km. Cirrus climatology provides us with a clue as to why such marked differences exist between the two observing systems. At the level of formation (cloud top) cirrus particles generally are small, growing larger and larger as they sediment toward the base. The sharp cut-off corresponds to a very dry layer (observed from sounding) below this level. In the framework of the radar/lidar

system, the radar will more readily see the larger (lower) particles and the lidar will see the smaller (upper) particles. The lidar signal is completely attenuated by the larger particles near cloud base, while the radar completely transmits through the very small upper-cirrus particle (yielding zero backscatter at the respective detectors for entirely contrasting reasons).

5.9.4 Kauai case summary

Tropical cirrus were examined with aircraft/spaceborne radiometers in conjunction with airborne active instruments. Important considerations for interpreting cloud effective radii as retrieved by passive instruments in the presence of a vertically varying profile (as most often is the case for clouds in our atmosphere) was illustrated. The ARM-UAV program presents the intriguing capability of extensive spatial and temporal observations with a multi-sensor payload. These Kauai retrievals showcased the utility of multi-platform active sensors in both the improvement/enhancement of existing retrieval methods and development of future remote sensing applications.

5.10 CAVEX 6/30/99 Monterey Retrieval

The Monterey Coastal Stratus Experiment (MCSE), funded by the Office of Naval research, involved a month-long survey of marine stratus off the California coastline during June, 1999. The experiments flew the MAS instrument aboard the high-altitude NASA ER-2 aircraft, recording multispectral radiance imagery of the cloud decks below. A piggy-back to this experiment supported by the DoE ARM/UAV program was the CloudSat Antecedent Validation Experiment (CAVEX). It included a second aircraft (the DoE Twin Otter) equipped with the UMass/JPL ACR oriented in the nadir. As most retrieval case studies examined in this research focused on cirrus (active sensor cloud height information is more crucial for cirrus, while marine stratus cloud temperatures are very close to the underlying ocean surface temperature), the stratus experiment provided an important opportunity to assess the retrieval's performance on liquid water clouds.

On June 30, 1999, a widespread 300 m thick layer of quasi-uniform low-level marine stratus (advection fog) was present along the Northern California coastline. This layer was

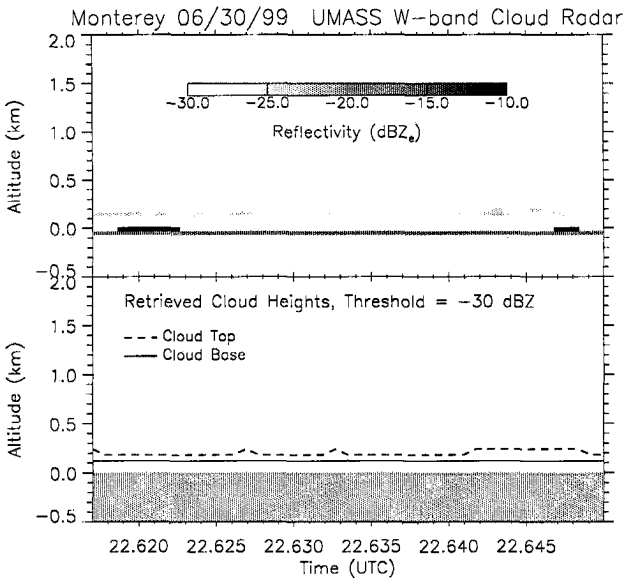

Figure 5.58: Radar estimation of marine stratocumulus cloud heights for the June 30, 1999 Monterey Coastal Stratus Experiment.

overflown by both MAS and the cloud radar. The observed radar reflectivity and derived cloud boundaries for this case are shown in Figure 5.58. Also flown aboard the ER-2 was the Solar Spectral Flux Radiometer (SSFR; Pilewskie *et al.*, 1998) instrument measuring downwelling spectral flux. This data was used to make minor corrections to the forward model's upper-atmospheric aerosol profile. The model atmosphere essentially was "tuned" to match the SSFR spectral measurements. MAS channels centered at wavelengths of 0.56, 1.61, 2.13, and 3.91 μm were used in the observation vector, and a bi-spectral grid approach was applied to obtain sensitivity to both optical depth and effective radius.

5.10.1 Retrieval results

Retrieved optical depth and effective radii for the CAVEX case study are presented in Figure 5.59. Visible (0.556 μm) optical depths (upper panel) for these clouds typically were on the order of 4.0, with effective radii (lower panel) between 10 and 13 μm. The effective radii were consistent with *in situ* samples taken on on similar clouds from previous days (due to an on-board computer failure on June 30, the aircraft carrying the *in situ* instruments unfortunately did not fly). Depicted on the same figure are the retrievals conducted without the SSFR downwelling solar flux corrections. The main effect

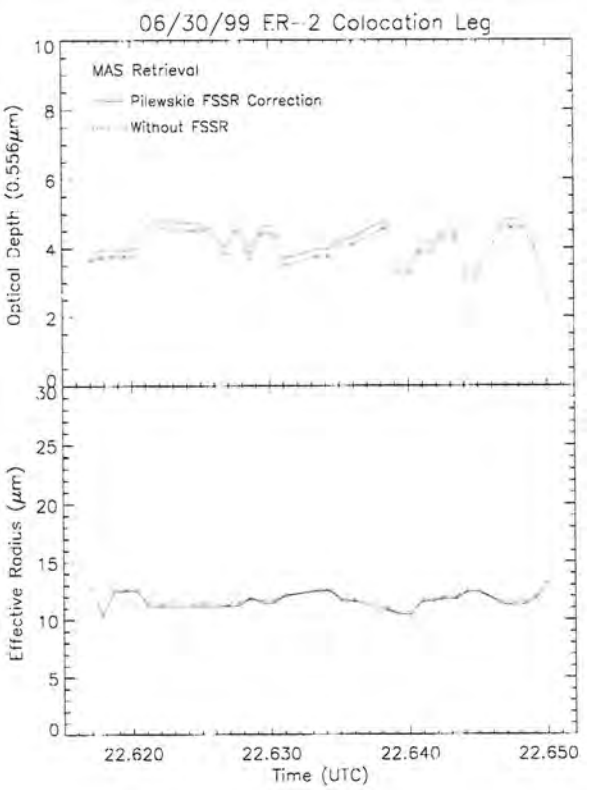

Figure 5.59: MAS retrievals of cloud optical depth and effective radius for marine stratocumulus off the coast of Monterey, CA on June 30, 1999 (including SSFR downwelling flux corrections).

of the corrections was a slight lowering in the retrieved optical depths. This is explained physically by noting that without account for the additional attenuation by the upper atmosphere in the model, a larger downwelling solar flux will be incident upon the cloud top. In this way, a lower cloud optical depth is required in the forward model to produce the same reflection measured by MAS. The very slight increase in retrieved effective radius follows this same argument, as smaller r_{eff} are associated with smaller g according to Mie theory. This translates to a stronger component of scatter in the back-hemisphere which produces a correspondingly higher cloud reflectivity. With a stronger downwelling solar flux (without the SSFR correction), the forward model does not need to make the cloud as reflective in order to match the observations, and the retrieved particle sizes are slightly (at most, 0.5 μm) larger as a result. This exercise reinforces the tenet that every additional piece of *a priori* information that can serve as an additional constrain the retrieval should be included in the forward model whenever available.

5.10.2 CAVEX case summary

This MCSE/CAVEX case study examined marine stratocumulus deck observed by MAS. SSFR data were introduced to constrain the model aerosol/rayleigh scatter contributions. The versatility of this retrieval in terms of its ability to handle measurements from these different remote sensing observing systems has again been demonstrated. Retrieved particle size were consistent with size distributions observed often in pristine maritime stratocumulus. While for the case of solar-reflection channel retrievals of shallow boundary layer clouds the active sensor cloud profiles do not play an important role in constraining the forward model, they can continue to serve as a useful validation tool in independent estimation of radiometer-retrieved properties.

5.11 Ensemble retrieval statistics

Gathering the results from all single-layer cirrus retrievals afforded the opportunity for a quantitative, generalized uncertainty comparison between active+passive and passive-only retrieval approaches. Shown in Figures 5.60-5.61 are frequency distributions (probability density functions, or PDFs) of retrieved parameter percentage error for all clouds

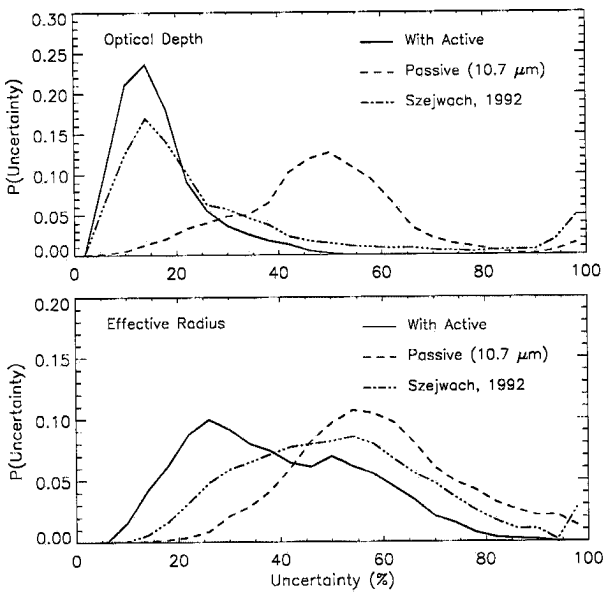

Figure 5.60: Frequency distribution of error comparison between active+passive and passive-only retrievals for optical depth (top) and effective radius (bottom). Case 1: IR-only retrievals, all clouds.

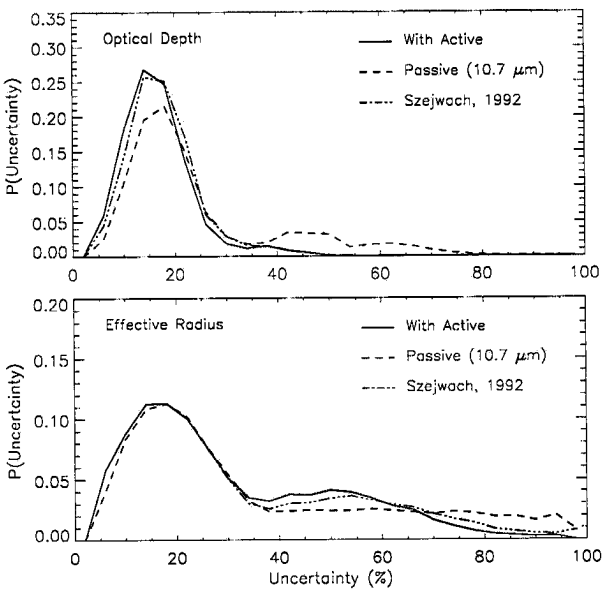

Figure 5.61: Case 2: Solar-reflection retrievals, all clouds.

using IR-only (e.g., Prabhakara *et al.*, 1988) and solar-reflection retrieval methods (e.g., King *et al.*, 1992). In all plots to follow in this discussion, the "active only" (solid) curve corresponds to retrievals using *a priori* cloud height constraints from active sensors. The "10.7 μm" (dashed) curve summarizes uncertainties arising from the placement of clouds in the atmosphere based on a temperature sounding and the brightness temperature as measured by GOES Ch. 4. Finally, the "Szejwach" curve (dashed-dot) provides a best-attempt by passive-only techniques comparable in accuracy to what can be provided from CO_2-slicing. Together, the passive only curves define the range of accuracy available to retrievals without active sensor contributions. While these distributions were very similar for the reflection-based retrievals (see Figure 5.61), significant departures were observed in the emission-based (night-time) method (Figure 5.60. In the case of solar reflection, the main penalty for cloud misplacement arose from the relatively minor effects of the aerosol loading and the Rayleigh scattering profile. On the other hand, emission-based retrievals were especially susceptible to errors associated with optically thin clouds (whose low emissivities translate to significant underestimates of cloud height).

To examine the details of the ensemble frequency distributions, the PDFs were re-computed for the categories of "optically thin" ($\tau \leq 1.0$) and "optically thick" ($\tau > 1.0$) clouds. The selection of these thresholds, while arbitrary, corresponded roughly to the transition between single and multiple-scattering regimes (with errors associated with the scattering phase function and cloud height placement are strongest in the former). The results for emissive and reflective retrievals of optically thin clouds are shown in Figures 5.62 and 5.63, respectively.

In Figure 5.62, distributions of optical depth uncertainty narrow in variance about roughly the same mean values, while the effective radii distributions shift toward higher error. This shift is most dramatic in the *a priori* cloud height retrieval, indicating that even with correct placement of these optically thin clouds, considerable uncertainty remains due to the high uncertainty associated with the scattering of the ice poly-dispersions (the effects of this uncertainty is strongest for low scattering orders, or small optical depths).

In Figure 5.63, significant differences with respect to the ensemble cloud distributions are apparent due to the placement of cloud using the passive-only method. Here, the

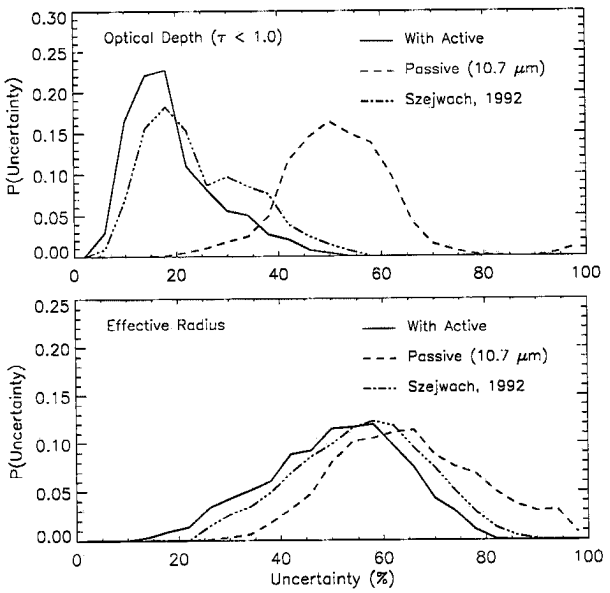

Figure 5.62: Frequency distribution of error comparison between active+passive and passive-only retrievals for optical depth (top) and effective radius (bottom). Case 1: IR-only retrievals, only clouds with $\tau \leq 1.0$.

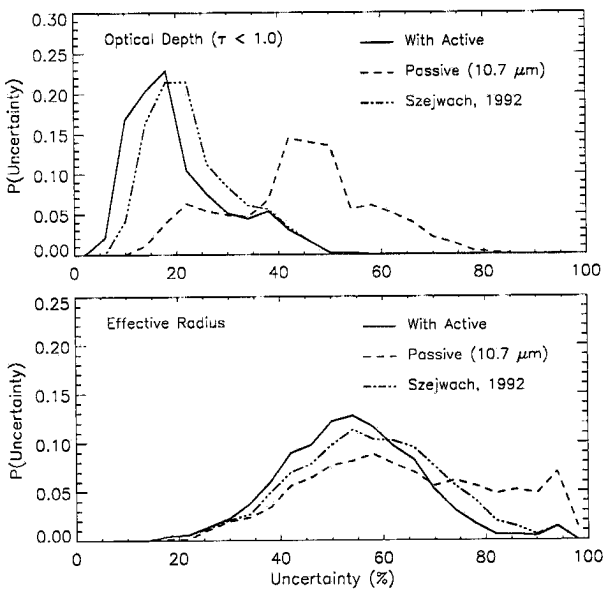

Figure 5.63: Case 2: Solar-reflection retrievals, only clouds with $\tau \leq 1.0$.

small scattering effects of the aerosol/rayleigh profile become significant with respect to the magnitude of cloud optical depth. As in the thermal retrievals, the distributions of effective radii are observed also to shift significantly toward higher error due to single-scatter phase function uncertainty. Contributions by the thin clouds explains the weak bi-modal appearance of the effective radii uncertainty PDFs for both the thermal and reflective retrieval cases.

Error PDFs for emissive and reflective retrievals of optically thick clouds are shown in Figures 5.64 and 5.65, respectively. These distributions resemble closely the ensemble distributions with the bimodal component (introduced by the optically thin clouds) removed. It is clear from Figure 5.65 confirms that for single-layer cirrus little is gained from adding *a priori* cloud height information. This will not be true for the more general case of multi-layered cloud profiles (in which case the active sensor will again provide a superior day-time retrieval by detecting the cloud layers missed by passive-only techniques). Quantification of the multi-layer problem is a strong function of the cloud profile and the subject of ongoing research.

Finally, the relative improvement to the retrieved parameter uncertainties are shown in Figures 5.66-5.67 as a function of the difference between active and passive-only estimates of mean cloud height. Relative differences in uncertainties were small, as would be expected, in all cases where ΔZ_{cld} is small. In the IR-only retrievals, these uncertainties grew rapidly with increasing ΔZ_{cld}. While these difference appeared to grow monotonically for optical depth, a rapid increase (corresponding to a low sensitivity to particle size for optically thick clouds as $\Delta Z_{\text{cld}} \rightarrow 0.0$) followed by gradual decrease with increasing ΔZ_{cld} was observed for effective radii in Figure 5.66. Because of weaker sensitivity of cloud optical properties at larger particle sizes, the relative error differences computed for many of the thin cirrus retrievals (large ΔZ_{cld}) did not grow (and in some cases, decrease) with increasing ΔZ_{cld}. The reflection-based retrievals exhibited lower relative uncertainties that grew with increasing ΔZ_{cld} at a rate following the increase of Rayleigh scatter toward the surface. Similar to the emissive retrievals was a slight trend toward lower r_{eff} relative uncertainty with increasing ΔZ_{cld}.

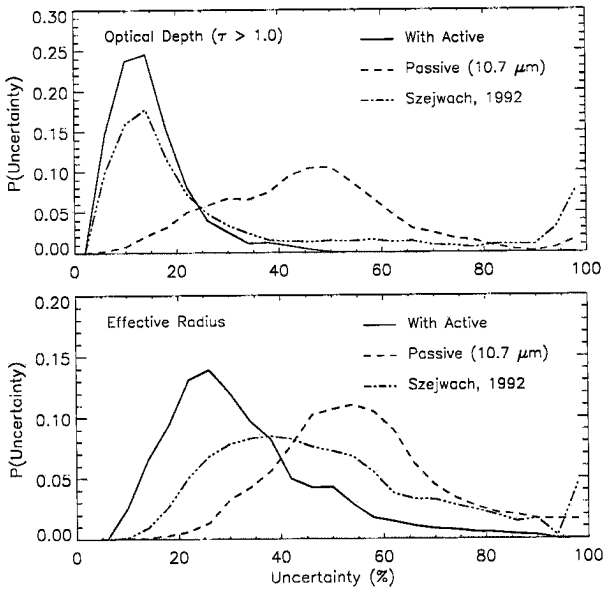

Figure 5.64: Frequency distribution of error comparison between active+passive and passive-only retrievals for optical depth (top) and effective radius (bottom). Case 1: IR-only retrievals, only clouds with $\tau > 1.0$.

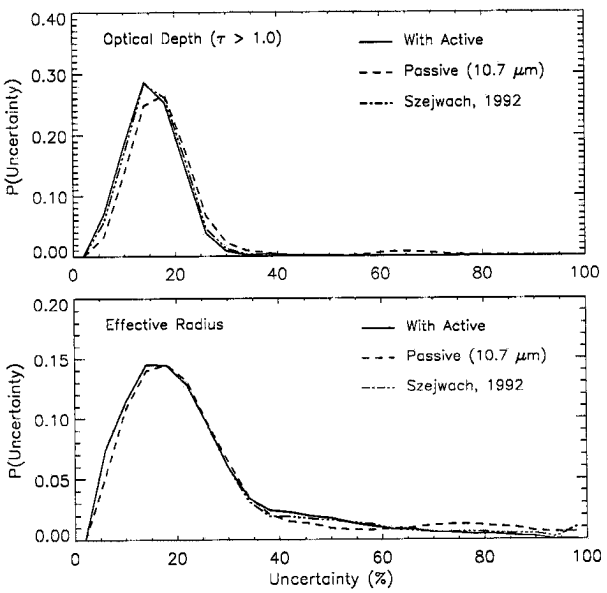

Figure 5.65: Case 2: Solar-reflection retrievals, only clouds with $\tau > 1.0$.

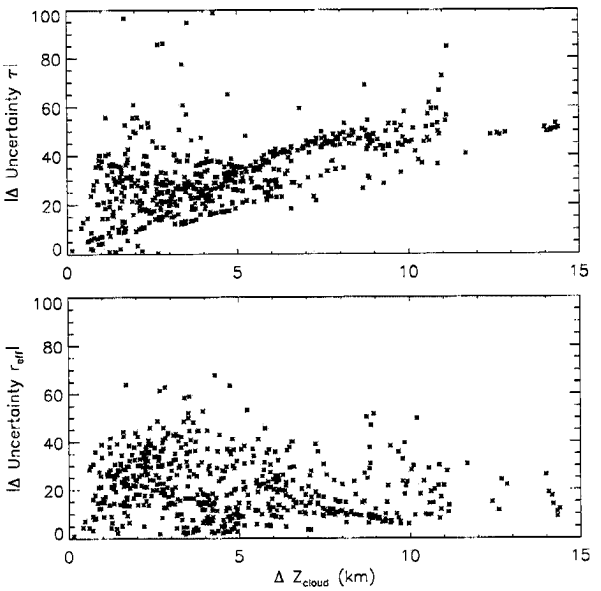

Figure 5.66: Differential percent-error between active+passive and passive-only retrievals plotted as a function of the difference between active and passive-only estimates of cloud height. Case 1: IR-only retrievals

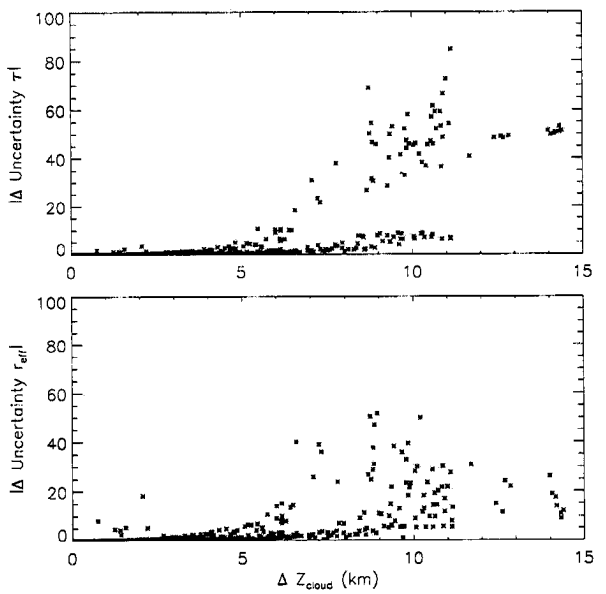

Figure 5.67: Case 2: Solar-reflection retrievals

5.12 Summary

Presented in this chapter were several retrieval case studies employing active sensor information (from both surface/airborne cloud radar and surface/airborne/spaceborne lidar) as an *a priori* constraint to passive instrument measurements (e.g.,cloud reflection and emission by GOES, SSP, and MAS). The main emphasis of these cases were night-time retrievals of cirrus using the forward model and inversion theory described in Chapter 4. Cirrus play a very important greenhouse role in the climate-feedback system. Being optically thin, these clouds often are difficult to detect and range in the vertical by passive instruments. As a result, improved retrievals of their optical properties are desired throughout the modeling and measurement communities alike. Not surprisingly, the most significant improvements to retrieval uncertainties by this new method were shown to occur for cirrus in night-time retrieval situations. Perhaps more surprisingly was the magnitude of this improvement with respect to CO_2 slicing-equivalent methods as illustrated in the ensemble results (e.g., greater than 20% for r_{eff} and 10-20% for optically thin cirrus at night). Extrapolating to global scale observations (e.g., as will be provided by the CloudSat/PICASSO-CENA tandem) we stand poised to learn a great deal more about cirrus in terms of both their distribution and radiative impact in our atmosphere.

The Rodgers (1976) inversion approach provided a decomposition of the uncertainty and diagnostics for retrieval performance. Retrievals were performed both with and without cloud profile information to examine the changes in retrieved optical depth and effective particle radius uncertainties. The constraints were shown to yield marked improvements in these quantities, particularly for the night-time (or IR-only) cases. The component of uncertainty owing to the scattering phase function dominated, as the structure of this parameter is highly variable and difficult to ascertain from measurement at a single viewing angle. It should be noted here that while the retrievals presented here were based on GOES imagery, alternative instrumentation which enables the phase function uncertainty to be further constrained exists. The Polarization and Directionality of the Earth's Reflectances (POLDER) is capable of observing pixels from 14 different viewing directions (each corresponding to a different scattering angle typically over the range from

60° to 180°. This enables a sampling of the phase function sufficient to rule-out particular habits (e.g., hexagonal plates and columns) as being dominant. *Doutriaux-Boucher et al.* [2000] use these data to assess the sensitivity of retrieved cirrus optical thicknesses to *a priori* phase function assumption. The Along Track Scanning Radiometer (ATSR-2) (e.g., *Baran et al.* [1999a]) instrument provides dual-viewing which *Baran et al.* [1999b] apply in a similar way to POLDER in constraining the phase function of cirrus (in terms of identifying a "dominant crystal habit"). Such multi-directional imagery is not available to the GOES platform, necessitating an *a priori* assumption on the crystal habit.

Retrieval products derived from this new method provide a confident assessment of cloud radiative forcing than what could be provided by a passive-only retrieval with inherently larger uncertainties attached. Wherever possible, independent estimates of the cloud optical properties were computed and compared to those retrieved for validation. Discrepancies that existed between the two sets of results, however, were often difficult to interpret due to differences in sample size between the two observing systems and/or the empirical foundation of the latter method. This appeals to the desirable situation of a multi-sensor observing system where co-location and sampling issues are deterministic.

Chapter 6

NWP CLOUD COVER VALIDATIONS

6.1 Introduction

Historically, numerical weather prediction (NWP) and climate modeling have evolved as two separate and distinct disciplines in atmospheric science. The recognition of the latter as being a logical extension of the former has been stymied in practice by an inadequate representation of cloud, and hence cloud radiative feedbacks, in GCMs (see Cess *et al.*, 1990). Clouds play an integral dual role in the dynamic climate system; acting not only in passive response (e.g., growth and dissipation in response to the atmospheric circulation) but also as physical drivers (in the context of radiative diabatic heating responsible for these circulations). Representing closure of the hydrological cycle, the formation and dissipation of cloud may be regarded as the most readily-observable signature of the underlying moisture and circulation fields. The level of approximation to which a NWP model can reproduce the observed cloudy/clear field, then, is a very important indirect indicator of its ability to characterize atmospheric circulation on time and spatial scales appropriate to discussions of climate and climate variability. Proper treatment of clouds in both capacities requires incorporating them into the model at the most fundamental level. This has stood as a formidable challenge to the improvement of forecasting skill, and by extension, the validity of climatology studies that consider model data. To date, the cloud modeling and cloud measurement communities have stood as largely disjoint entities, and it is likely that the focus and development of both disciplines have suffered for it.

Understanding the complex, non-linear way in which clouds affect the Earth's climate system hinges upon a better understanding of cloud spatial, temporal, and microphysical

properties/distributions on the global scale. Discussion to this point has centered primarily on how passive-sensor cloud property retrievals benefit from the inclusion of active senor cloud profile data. This chapter considers spaceborne, airborne, and surface-based active sensors in the validation and development of global NWP models. Advances in the parameterization of clouds in global circulation models (GCMs) are contingent upon our ability to validate them on a global level. The relevant goals sought by this research are outlined as follows: 1) to assess the current level of cloud-*fraction* forecasting skill in the state-of-the-art among contemporary NWP models, and 2) to employ the retrieval scheme outlined in previous chapters to extend this assessment to model cloud-*radiative properties* in the context of liquid/ice water contents. The realistic treatment of clouds in terms of their non-linear radiative feedback processes requires that the model represent correctly both the spatial and bulk-microphysical properties. In this research, ECMWF prognostic cloud forecasts were matched against active sensor observations on both global (LITE) and local (e.g., ARM IOPs) scales. Results from the former represent a first-look at NWP global forecast performance using active data from the space platform; an exercise which one day might lead to the assimilation of such data into model initialization fields at the operational level.

6.2 Background

The intent of this study was to examine differences between cloud distributions as observed from an active remote sensor and those predicted in short-range (e.g., 24 to 30 hour) ECMWF forecasts matched to the observations. The choice to use ECMWF was based largely upon the sophisticated nature of their cloud scheme and encouraging results of comparisons with surface radar observations (Mace *et al.*, 1998). Lau and Crane (1995) use ISCCP cloud data and ECMWF analyses to examine the spatial and temporal variability of cloud, and Klein and Jakob (1998) extend the study to include a direct comparison between ECMWF composite simulations of frontal clouds with the ISCCP data. While ISCCP data are based on operational weather satellites and therefore provide global coverage, little information about the distribution of cloud in the vertical.

The material presented in this dissertation differs significantly from previous studies in the spatial scale at which high resolution cloud profile information were available for validating the cloud forecasts.

6.3 Model and Observational Data

6.3.1 ECMWF model data

The ECMWF global spectral model provided global data at triangular truncation of wavenumber 319, with 31 vertical model levels defined by hybrid coordinates (T319L31). The data were output on a reduced Gaussian grid (i.e., a variable number of longitudinal points as a function of latitude, with the maximum number at the equator decreasing toward either pole). This grid was then interpolated to a regular 1 degree (equal angle, corresponding roughly to 110 × 110 km grid boxes) resolution for co-location with LITE orbits. Higher resolution was available at 0.5 degrees (60 km) but was not warranted, as the model fields were relatively smooth (A. C. M. Beljaars, personal communication). Flux levels, which straddle the model levels, defined the interfaces between adjacent profile bins. Profile heights for a given gridbox were calculated by adding the model surface elevation as an offset to these flux levels (converted from pressure to height via the hypsometric equation).

An important step toward the physical treatment of cloudiness in GCMs was made by ECMWF when it adopted a prognostic cloud scheme into its integrated forecasting system (IFS). In contrast to diagnostic approaches, where clouds are considered essentially as by-products of instantaneous environmental vectors of state, prognostic schemes represent clouds as evolving variables within the Earth-atmosphere system. The considerable increase to model complexity is offset by the newfound physical representativeness of model clouds and their impact on traceability in the model hydrological cycle. Introduced by Tiedke (1993) with revisions by Jakob (1994), the prognostic cloud parameterization is based on gridbox budget equations for cloud fraction a and cloud condensate (water + ice) l. Following the notation of Jakob and Klein (1998),

$$\frac{\partial a}{\partial t} = A_a + S_a - D_a \tag{6.1}$$

$$\frac{\partial l}{\partial t} = A_l + S_l - D_l, \tag{6.2}$$

where A, S, and D are advection, source, and dissipation terms, respectively. Cloud formation is connected to processes of synoptic ascent, horizontal transport of cloud water by convective systems, diabatic cooling (e.g., stratiform clouds), and turbulence in the boundary-layer. The sink term is comprised of turbulent mixing of cloud air with subsaturated environmental air, adiabatic/diabatic heating, and loss by precipitation. As complex parameterizations for precipitation based on evolution of droplet spectra remain too computationally expensive for contemporary resources, a simple parameterization based on Sundqvist (1988) was first adopted; applied to both water and ice.

The revisions by Jakob (1994) include an extension of the scheme to handle mixed-phase thermodynamics by introducing a temperature-dependent liquid water condensate fraction. The precipitation process for ice, which when compared with observations suggested an over-efficient release of precipitation, was recast as a function of the mean fall speed of ice crystals according to Heymsfield and Donner (1990). As observations also indicated that the original scheme failed to dissipate low level clouds fast enough and produced spurious rain from maritime low level clouds, a modification to the cloud top entrainment that included the mixing invoked by cloud top radiative cooling was also introduced. The benefits of these revisions led to their implementation in the new ECMWF reanalysis system.

Cloud generated in a model grid box is assumed to extend vertically (and uniformly) over the entire model layer depth and similarly over the horizontal extent of the grid box. Jakob and Klein (1994) conduct an exploratory study on the effects that vertical variation in cloud fraction on the sub-grid scale have on the parameterization of microphysical processes. Their technique involves partitioning horizontally each model grid box into an array of smaller boxes each assigned a cloud fraction of either zero or unity according to the total grid box cloud fraction and the maximum-random overlap (see Morcrette and Fouquart, 1986) assumption for cloud fraction used in the radiation parameterization. Each sub-grid box is solved individually using the original, unaltered microphysical parameterization, and the averaged products are compared to the original full-box runs. The

results point to an overestimation of evaporation (precipitation spread out over the entire grid box). Jakob and Klein (1994) note that a balance between the sophistication of cloud microphysical parameterizations with cloud microphysics (e.g., cloud/precipitation fractions and overlap) should be sought in GCMs. Toward development of an understanding of this balance, they state further that a necessary step is the validation of the vertical cloud variation produced by the parameterization. The work of Mace *et al.* (1998) is mentioned in this context, but adding that

> The study is however limited to cloud occurrence statistics at one location and therefore does not cover the variety of cloud situations encountered globally.

It is here where the LITE data employed in this research, and active sensors on the space platform in general, can serve to bridge the gap that exists currently between what the modeling community requires and the the measurement community can provide. A specific goal of this research was to exemplify the utility of near-instantaneous synoptic-scale active sensor data in the arena of numerical weather prediction.

6.3.2 Observation data: LITE cloud profiles

A total of 66 orbits comprising the night-time-only subset of the LITE database were used in these comparisons. The data and derived cloud heights were processed at the NASA Langley Research Center (LaRC) and obtained from the Distributed Active Archive Center (DAAC). Again, because of solar contamination effects, day-time orbits were discarded (with a millimetric radar as is proposed for CloudSat, similar profile data will be available for both day-time and night-time orbits). Even so, the active-sensor night-time sampling was exotic compared to contemporary active datasets, and afforded the first opportunity for global validation of the 3-D cloud field produced by a single NWP forecast.

Associated with the LITE data are caveats that warrant further consideration here. Some lidar observations may miss the lower portions of optically-thick ($\tau > 10.0$) clouds (including cloud base) due to complete attenuation of the beam. In these circumstances, all

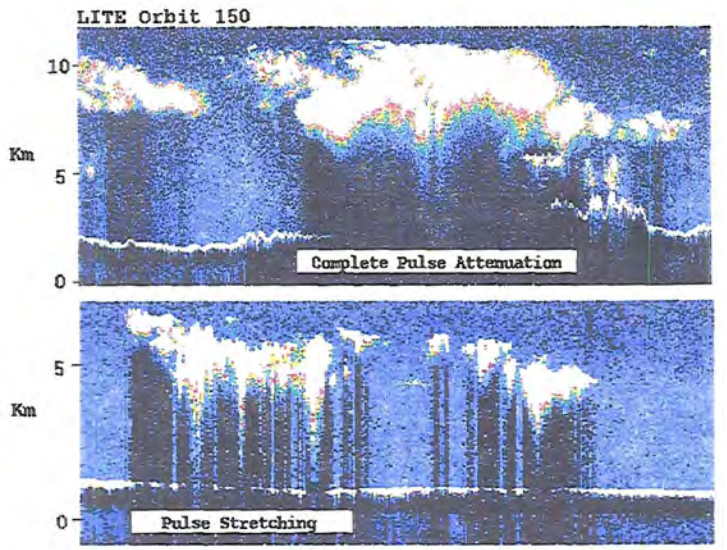

Figure 6.1: Examples of lidar pulse attenuation (Top) and pulse stretching (Bottom) caveats associated with some LITE cloud profiles.

clouds that occur at or below the level of complete attenuation are unreported (Figure 6.1, top panel). This effect is observed most often in liquid-phase clouds (and optically-thick marine stratus and deep convection, in particular). Because of high forward-scattering characteristic of most ice crystal dispersions, the LITE beam penetrates all but the most optically-thick cirrus. This point is illustrated graphically in the work of Platt and Winker (1996) in their analysis of changes in the LITE multiple scattering return using a real-time variable detector field of view annulus.

Another lidar phenomenon which leads to reports of false cloud base altitude is termed "pulse stretching" (Winker and Poole, 1995; Figure 6.1, bottom panel). This is an lidar data acquisition artifact that results in backscatter that is not representative of true return at the level in question. The misranged information results from in-cloud multiple scattering (MS) of the lidar photons. The time required for multiply-scattered photons to scatter within the cloud before returning to the detector manifests in a temporal delay of the energy return. Because a single-scatter assumption is imposed necessarily (i.e., all returns are assumed to have interacted with only one pulse volume within the cloud), the temporal delay associated with MS photons is processed as a cloud return that is often ranged to greater distances away (on the order of kilometers in some instances) from the

instrument. This results in an ambiguous far-boundary to the cloud profile which fades with range. These stretched returns occur predominantly in water clouds while markedly less so in cirrus, owing again to differences in cloud optical properties between the two cloud types. Miller and Stephens (1998) investigate the relationships between these optical properties and the magnitude of pulse stretching as modeled for marine stratocumulus and cirrus in the context of LITE. Their findings indicate that pulse stretching becomes significant in the former beyond $\tau \geq 5.0$, while making a minimal contribution to returns in the latter cloud class. Both pulse stretching and loss due to pulse attenuation are functions of the instrument power, sensitivity, and field-of-view. Until further hardware advances are made, limitations on all these factors will require the consideration of both pulse stretching and attenuation effects for all applications of spaceborne lidar.

Due to these lidar caveats, erroneous "false alarms" (pulse attenuation resulting in a clearsky observations in the presence of correctly-forecasted model cloudiness) and "misses" (pulse stretching adding false cloud observations below the true cloud base and penalizing the model for its potentially correct clearsky forecast) in these comparisons are possible in lower-level clouds and areas of deep convection. These classifications are discussed in more detail below. Presently there exists no remedy to these problems other than to include them in the discussion of the intercomparison uncertainties and filter them from the statistics calculations (discussed below) wherever possible. Even with these deficiencies, however, these LITE data far exceed the capabilities of current satellite observing systems for detecting the fine-scale structure of cloud profiles.

6.3.3 Observation data: ACR and CDL cloud profiles

While the global-scale validation of forecast cloud distribution afforded by LITE was very useful in assessing the spatial forecasting of meso- and synoptic-scale cloud structures, the high gain setting of LITE data meant that no independent retrievals of cloud optical properties could be performed (cloud signals were saturated). To answer the question of forecasted cloud content, additional cases offering active data over the range of tens of kilometers (e.g., ARM IOPs) were also examined. Unlike LITE, many of these cases also provided independent radiance, flux, and radar/lidar reflectivity data useful in

Model Param #	Symbol	Description	Units
129	Z	Geopotential (Surface)	m^2/s^2
130	levT	Level Temperatures	K
131	U	Zonal Wind Velocity	m/s
132	V	Meridional Wind Velocity	m/s
133	Q	Specific Humidity	kg/kg
135	W	Vertical Wind Velocity	Pa/s
152	LNSP	Log Surface Pressure	ln(hPa)
235	SKT	Skin (surface) Temperature	K
246	CLWC	Cloud Liquid Water Content	kg/kg
247	CIWC	Cloud Liquid Water Content	kg/kg
248	CF	Cloud Fraction	[0-1]

Table 6.1: Model fields available to the LITE/ECMWF correlative study

determining the cloud content and optical properties. In most of these cases, either the ACR or CDL was used as the active sensor for cloud heights and reflectivity-derived cloud properties. Together with passive observations from satellites and/or the SSP, these active data were employed in the same fashion as LITE to provided retrievals of optical depth from measurements of spectral cloud reflectance.

6.4 Forecasted Cloud Cover Validation

Short-range (24 to 30 hours) model forecasts were provided by ECMWF to validate within 30 minutes of specified LITE night-time orbit overpasses. The argument for using this forecast range is as follows: to test the prognostic cloud generation, short range forecasts were desired in order to have the synoptics reasonably accurate, while also avoiding the spin-up period of the model fields from initialization. Normally, a forecast forecast range on the order of 12-hrs would be selected, but for these LITE cases no initial cloud fields were available. As such a minimum of 24 hours (from experimentation, ECMWF clouds do not take longer than 24 hours to spin-up) was chosen for the LITE forecasts. In the IFS, the cloud field from the previous first-guess forecast is separated from the other model variables (which undergo changes by analysis and initialization) and is passed as initial conditions to the next forecast where it adjusts rapidly to the new synoptic conditions (Jakob, 1999).

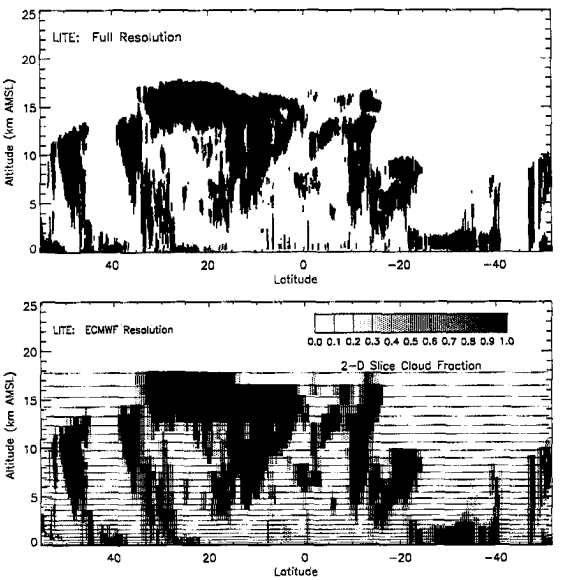

Figure 6.2: Recasting of high-resolution LITE (Orbit 123) data to coarser ECMWF resolution. Averaged hybrid ECMWF vertical levels are indicated as horizontal lines in the lower panel.

ECMWF grid boxes coinciding with the flight track were identified and the model parameters and surface elevation extracted. The resultant profiles to be compared with the LITE observations were thereby composed of adjacent model grid boxes, with a variable amount of lidar shots contained in each. The fields contained in these "model flight tracks" and their associated units are listed in Table 6.1. The field of interest to this particular exercise was the prognostic cloud fraction (CF) parameter which varies from 0 to 1 (completely clear to completely overcast, respectively) at a given level within a model gridbox.

In order to compare model CF to observations, the high-resolution LITE data first was recast to the coarser vertical and horizontal resolution of the model grid. Model hybrid flux levels, specified in pressure coordinates, were converted to equivalent altitudes by computing the layer geometric thickness (in km) between η-levels i and $i+1$ via the hypsometric equation:

$$\Delta Z = \frac{H_s ln(P_i)/ln(P_{i+1})}{1000}, \tag{6.3}$$

where P_i is the pressure (mb) at level i ($P_i > P_{i+1}$), and H_s is a scale height given by

$$H_s = R\overline{T}/g \tag{6.4}$$

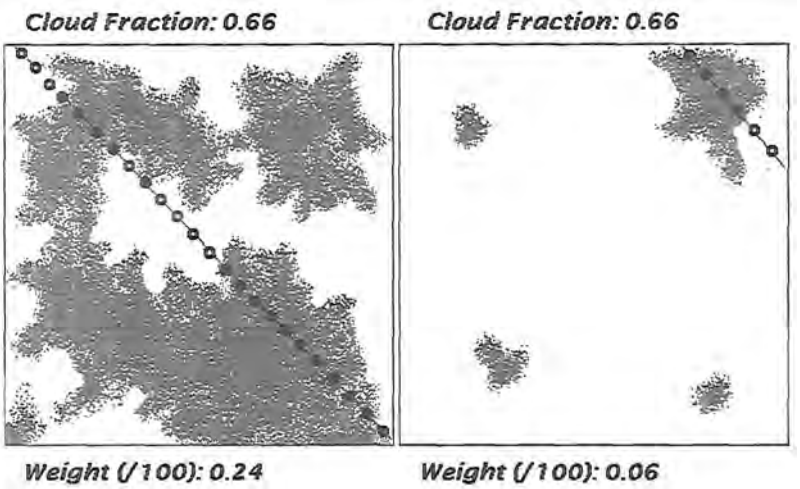

Figure 6.3: Sampling accommodations 1: The weighting of LITE-derived cloud fraction according to profile density.

where R is the gas constant for dry air (287.04 J K^{-1} kg^{-1}), g is the global average of gravity at mean sea level (9.80655 m s^{-2}), and $\overline{T}$ is the model mean temperature of the layer. The surface geopotential height (another model field) provides the lower boundary condition.

In an attempt to reconcile the differences between LITE's 2-dimensional slice and the 3-dimensional model grid-box profile, a pseudo-cloud-fraction parameter for the LITE data (CF_{LITE}) was computed at each level by normalizing the number of cloud hits found at that level by the total number of profiles in the grid box:

$$\mathrm{CF_{LITE}(g,z)} = \left[\sum_{\mathrm{i=1}}^{\#_{\mathrm{prof}}(\mathrm{g})} \mathrm{L_i(g,z)} \right] / \#_{\mathrm{prof}}(\mathrm{g}), \tag{6.5}$$

where $\#_{\mathrm{prof}}$ is the number of LITE profiles contained in the current ECMWF horizontal gridbox g at model level z, and L is a binary flag designating cloud detection by the lidar (equal to 1 if a cloud was detected) at level z. In this way, an active sensor slice cloud fraction parameter between 0 and 1 was computed for each grid box at the model grid resolution.

To further account for the sampling differences between LITE and ECMWF, a weighting scheme which considered both the density of LITE profile information (Eq. 6.8) *and*

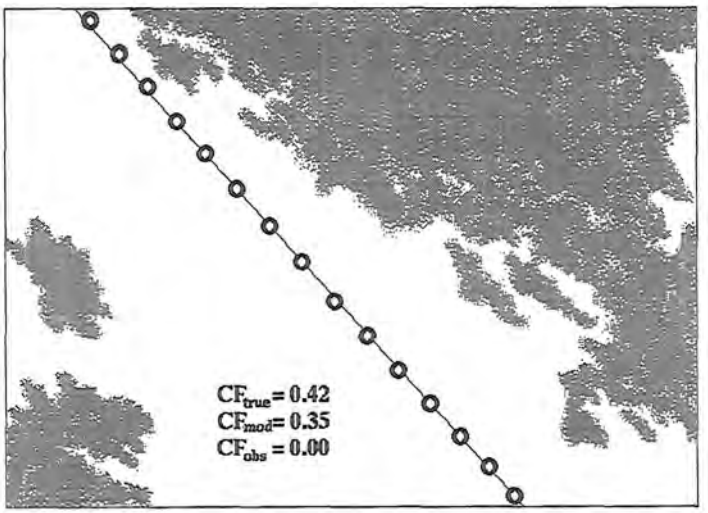

Figure 6.4: Sampling accommodations 2: Motivation for the weighting of false alarm statistics.

the likelihood of sampling uncertainty was introduced. To motivate the usage of such a weighting scheme, a hypothetical example of two LITE tracks through the same ECMWF pixel (at an arbitrary level) is shown in Figure 6.3. While it is clear that the case in the left panel cannot represent the full cloud fraction of the box, it is argued statistically to be more representative than cases such as the example in the right panel. The statistics were weighted by the density of observation data within each grid and at all levels considered.

False alarm contributions were weighted (W) by cloud fraction in the following way. A model $CF_{ECMWF} = 1.0$ and observed $0.0 < CF_{LITE} < 1.0$ produces a false alarm penalty of magnitude B = 1.0 - CF_{LITE}. In this way, a full false alarm penalty was incurred whenever $CF_{LITE} = 0.0$. Similarly, a $CF_{ECMWF} > 0.0$ coinciding with $CF_{LITE} = 0.0$ was assigned a false alarm value equivalent to CF_{ECMWF}. The motivation for the latter weighting is presented in Figure 6.4, which shows an example of a "false negative" in the LITE observations. In this way, a small CF which may have existed within the grid box but outside the LITE orbit cross section does not incur the full false alarm penalty. No weighting actions were taken for cloudy/clear hits or for misses.

For a quantitative assessment of model performance from LITE observations, a statistical analysis similar to that of Mace *et al.* (1998) was performed. The analysis involved

Cloud Cover		*Action*	
Model	Observed	Unweighted	Weighted
> 0	> 0	A = A + 1	A = A + 1, B = B + (1 - CF_{LITE})
> 0	$= 0$	B = B + 1	B = B + CF_{ECMWF}
$= 0$	> 0	C = C + 1	C = C + 1
$= 0$	$= 0$	D = D + 1	D = D + 1

Table 6.2: ECMWF/LITE Cloud Cover statistics rules for weighted and unweighted schemes. The "+ 1" indicates an increment in the hits/misses/false-alarms fields as outlined in Equation 6.7.

looping over all the gridboxes and levels for a single orbit and tallying the agreements and disagreements between the model forecast and rebinned LITE observations. These statistics were then combined to yield ensemble-orbit diagnostic information for important aspects of the cloud forecast. The following parameters characterize the statistical analysis:

$$A = \text{cloud hit}, \tag{6.6}$$

$$B = \text{false alarm},$$

$$C = \text{cloud miss},$$

$$D = \text{clearsky hit}, \tag{6.7}$$

where (A, C, D) define agreements/disagreements between the model and rebinned observations and B classifies forecasts of cloud when the observations reported clear sky. As discussed above, because the amount of LITE cloud profile information in a model grid box varied according to the orbit path of intersection, the parameters were computed as

$$[A, B, C, D]^T = \sum_{i=0}^{N} P_i \cdot [A_i, B_i, C_i, D_i] \cdot [1., W_i, 1., 1.]^T, \tag{6.8}$$

where N is the number of ECMWF grid boxes spanned by the LITE orbit and P_i is the fraction of LITE profiles in the i^{th} grid box.

For every model grid box and level, elements of Equation 6.7 were tallied according to the presence/lack of clouds in the model and observed data. A summary of the rules and

component assignments are given in Table 6.2 for both the unweighted and false-alarm-weighted versions of the statistics. It is noted that while the false alarm score benefits (i.e., is reduced) in the $CF_{\mathrm{ECMWF}} > 0, CF_{\mathrm{LITE}} = 0$ case, this is compensated for in part by the introduction of additional false alarm contributions to the $CF_{\mathrm{ECMWF}} > 0, CF_{\mathrm{LITE}} > 0$ case. The weighting scheme, though inexact, provided perhaps a more fair comparison between the model and observations than the hard-line unweighted method. Both versions of the computed statistics are included in Appendix B.

Using the ensemble-track hit/miss/false-alarm data, the statistical definitions for hit rate (HR), threat score (TS), probability of detection (POD), and false alarm rate (FAR) follow from Wilks (1995) as

$$\begin{aligned} HR &= \frac{A+D}{A+B+C+D}, & TS &= \frac{A}{A+B+C}, \\ POD &= \frac{A}{A+C}, & FAR &= \frac{B}{A+B} \ . \end{aligned} \tag{6.9}$$

HR is the fraction of correctly-forecasted (cloudy *or* clearsky) grid boxes, while TS excludes the clear sky component and concentrates only on the cloud component. The ratio of cloud hits to the total number of *observed* clouds is given by the POD, and the FAR offers a metric for cloud over-forecasting in the model. A perfect forecast would therefore entail HR = TS = POD = 1.0 and FAR = 0.0 (i.e., no misses or false alarms). A diagnostic flag in the Level II LITE data denoted whether or not a surface return was detected in the LITE profile. If the flag indicated no surface return (i.e., complete attenuation of the lidar pulse) then statistics were not computed for levels below the lowest cloud level detected in the LITE profile. Otherwise, CF statistics were computed at all levels except those where LITE detected cloud below the surface (e.g., pulse stretching in marine stratocumulus).

6.4.1 Spatial distribution results

An example of the ECMWF/LITE comparisons is shown for LITE orbit 124 in Figure 6.5. These comparisons were the very first of their kind, afforded by spaceborne active sensor data which someday will become commonplace on the space platform. The ground

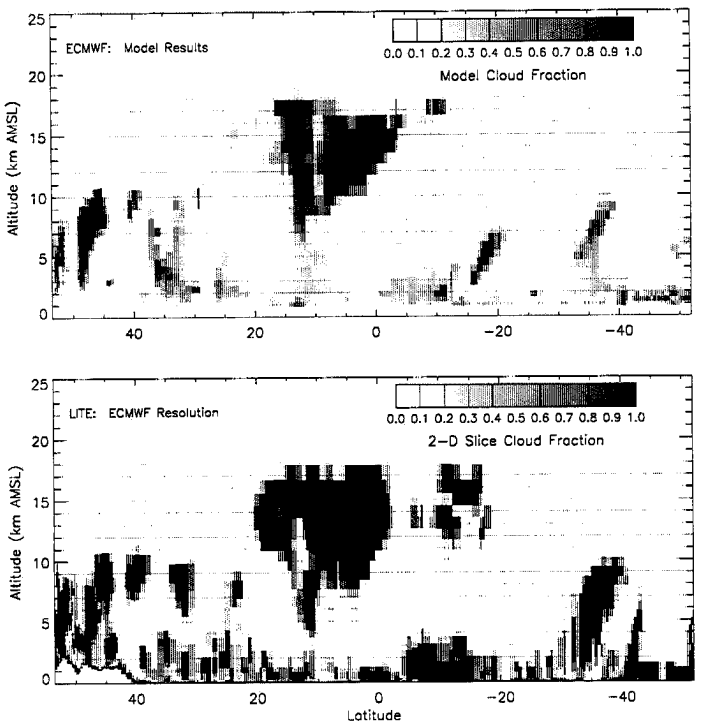

Figure 6.5: Cloud fraction comparison for LITE orbit 124 (September 16, 1994, 14:25-15:00 UTC, spanning the tropical western Pacific warm pool).

track of the orbit shown begins in central Russia and traverses North-Eastern China, South Korea, the tropical western Pacific (TWP) Warm Pool, and South-Eastward across New Zealand. The coarse appearance of the LITE data is due to the rebinning procedure followed to match the horizontal and vertical resolution of the model. The remarkable agreement between the observed and forecast cloud fields on the synoptic scale gave cause for considerable excitement (and disbelief) when they were first produced. Qualitatively, the vertical extent and placement of deep convection in the Inter-Tropical Convergence Zone (ITCZ), migratory mid-latitude disturbances, and subsidence zones appear to be in good agreement with the observations for this case. The other 65 orbit comparisons included in Appendix B indicate that this level of agreement indeed was not an event of chance. That these 24-hour forecasts included no cloud assimilation data whatsoever is a testament to the level of accuracy that exists in the temperature, pressure, moisture, and vertical motion fields in the ECMWF forecasting product.

Orbit	$\%_{MOD}$	$\%_{OBS}$	HR	TS	POD	FAR
079	0.224	0.264	0.858 (0.891) [0.923]	0.496 (0.660) [0.784]	0.549 (0.730) [0.875]	0.161 (0.127) [0.117]
083	0.302	0.314	0.880 (0.940) [0.946]	0.649 (0.854) [0.884]	0.690 (0.908) [0.948]	0.083 (0.065) [0.071]
085	0.233	0.287	0.794 (0.822) [0.836]	0.364 (0.558) [0.650]	0.425 (0.649) [0.760]	0.283 (0.201) [0.182]
115	0.274	0.278	0.854 (0.897) [0.912]	0.546 (0.713) [0.775]	0.612 (0.799) [0.876]	0.165 (0.130) [0.119]
116	0.296	0.358	0.851 (0.891) [0.923]	0.607 (0.753) [0.844]	0.643 (0.800) [0.902]	0.084 (0.072) [0.065]
123	0.423	0.371	0.838 (0.879) [0.903]	0.646 (0.779) [0.845]	0.726 (0.877) [0.958]	0.146 (0.125) [0.122]
124	0.376	0.315	0.867 (0.902) [0.921]	0.648 (0.785) [0.850]	0.726 (0.880) [0.960]	0.142 (0.120) [0.119]
128	0.114	0.222	0.877 (0.915) [0.935]	0.408 (0.624) [0.728]	0.418 (0.642) [0.755]	0.057 (0.044) [0.046]
129	0.191	0.191	0.888 (0.911) [0.925]	0.475 (0.642) [0.730]	0.562 (0.760) [0.866]	0.247 (0.194) [0.178]
131	0.258	0.269	0.873 (0.915) [0.940]	0.578 (0.765) [0.837]	0.635 (0.847) [0.952]	0.166 (0.112) [0.126]
134	0.314	0.286	0.846 (0.881) [0.893]	0.549 (0.707) [0.769]	0.627 (0.807) [0.884]	0.185 (0.149) [0.145]
145	0.216	0.274	0.864 (0.911) [0.928]	0.526 (0.729) [0.800]	0.569 (0.790) [0.869]	0.127 (0.095) [0.090]
148	0.224	0.188	0.887 (0.920) [0.944]	0.475 (0.680) [0.800]	0.547 (0.782) [0.929]	0.218 (0.161) [0.148]
149	0.369	0.241	0.862 (0.884) [0.907]	0.573 (0.701) [0.794]	0.663 (0.811) [0.927]	0.191 (0.163) [0.153]
150	0.392	0.325	0.840 (0.885) [0.899]	0.606 (0.759) [0.814]	0.682 (0.855) [0.925]	0.156 (0.129) [0.129]
TOT	0.289	0.284	0.859 (0.897) [0.916]	0.555 (0.721) [0.798]	0.621 (0.808) [0.900]	0.161 (0.129) [0.124]

Table 6.3: Performance statistics computed for a subset of the LITE orbit cases. Parenthetical figures are allowances for ( ): ± 1 bin in the horizontal and vertical, and [ ]: ± 1 bin in the horizontal and ± 2 bins in the vertical. See text for explanation of statistical fields. (From Miller *et al.*, 1999)

Table 6.3 presents tabulated statistical results for a subset (15) of the LITE orbits considered in this study (taken from Miller *et al.*, 1999). The "%" columns indicate the ensemble fraction of the data occupied by *any* amount of cloud, and the remaining columns contain the statistical figures outlined above. To address the possibility of a false alarm being in fact a "near-hit" (i.e., either the LITE flight track missed cloud that was within the model box according to Figure 6.4, or the model shifted slightly the cloud structure in either the horizontal or vertical), a window of acceptance (in the form of $\pm$ grid boxes) was applied to the intercomparisons and the statistics were re-computed. The results are included in Table 6.3 as parenthetical figures. The improvement in statistical performance reflects the strong correlation observed by the naked eye in Figure 6.5 and indicates that, to within the specified margins of error (e.g., ± 1 model bins in the vertical as indicated in Figure 6.2), the model forecasts the spatial distribution of observed cloud fields reasonably.

6.4.2 Ensemble statistics from LITE

The ensemble of LITE orbits amounts to only ten days of tenuous (with respect to the surface area of the globe) sampling, and therefore cannot be applied to cloud climatology studies. However, the composite data may still prove useful in identifying areas of potential model bias (e.g., underestimation of cloud at a given height range, overestimation of a certain class of cloud, regional affects). In the case of a prognostic cloud scheme, these

statistics are especially helpful, as biases speak directly to the mishandling of specific and identifiable physical processes/forcing tied to cloud water budget equations at both small and large spatial scales.

Combining the cloud information for all 66 LITE orbits processed provided a quasi-global validation database. Statistics computed from the ensemble-orbit data allowed for identification of possible model biases. Before comparing to LITE observations, model cloud fraction along the LITE flight tracks were gathered in 4 km height bins and probability density functions (PDFs) were computed for low (0-4 km), middle (4-8 km), high (8-12 km), and clouds above 12 km. These PDFs are shown in Figure 6.6. From the structure of the curves, several general statements about the model cloudiness can be made. First, the tendancy in cloud fraction is toward either mostly clear or mostly cloudy, with a relative minimum of "partial cloudiness" near CF = 0.5. This tendancy is consistant with the observation that the presence/absence of cloud is most often associated with the atmospheric circulations responsible for encouraging/inhibiting cloud development (such that statistically-speaking clouds occur in quantity or not at all). The structure of the PDF holds for all levels of cloud, but is most prevalent for the high clouds. Because cirrus clouds often are associated with organized synoptic-scale circulations (e.g., the ITCZ, mid-latitude cyclones and jet streams) and their coverage when present tends to be large with respect to the model grid resolution. With the exception of widespread decks of marine stratocumulus, clouds inhabiting the lower troposphere are more variable in shape, size and distribution. This is observed in the PDFs by relatively greater values at lower cloud fraction at the expense of lower values at greater cloud fraction.

Figure 6.7 shows model and LITE-derived mean and variance of cloud fraction along the LITE orbits. For the computation of LITE pseudo-cloud-fraction, the parameters computed by Equation 6.5 were used. Because of sampling coarseness, cloud fraction reported by LITE was heavy-side biased (i.e., toward 1.0 when clouds were encountered in a model gridbox). Because of the tendancy of clouds to cluster, when LITE encounters a cloud there is a better chance that adjacent lidar shots in the gridbox slice will also be cloudy. These results were composed only of profiles where non-zero cloud fraction was encountered. Given the small (typically ≈ 10, ranging from 1-20) number of lidar shots that

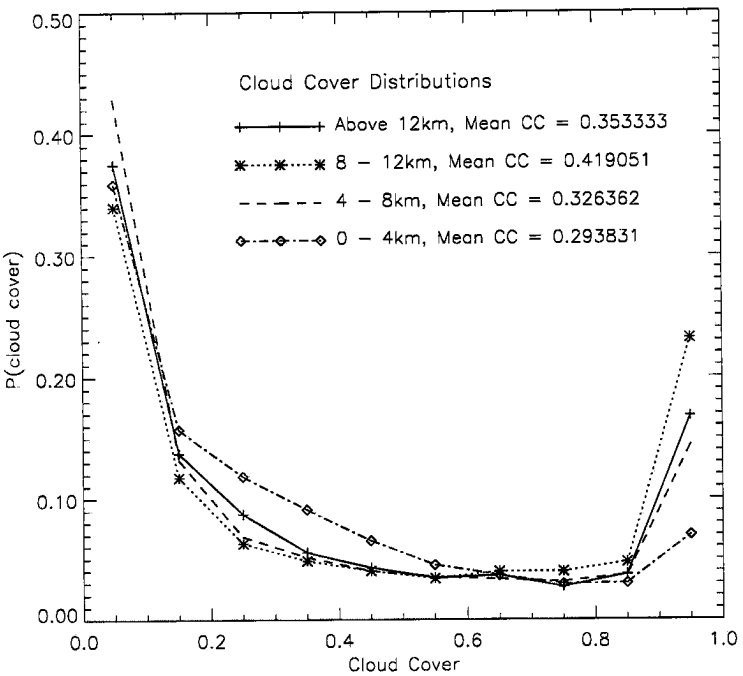

Figure 6.6: Probability density functions of model cloud fraction along LITE orbits as a function of grouped cloud heights.

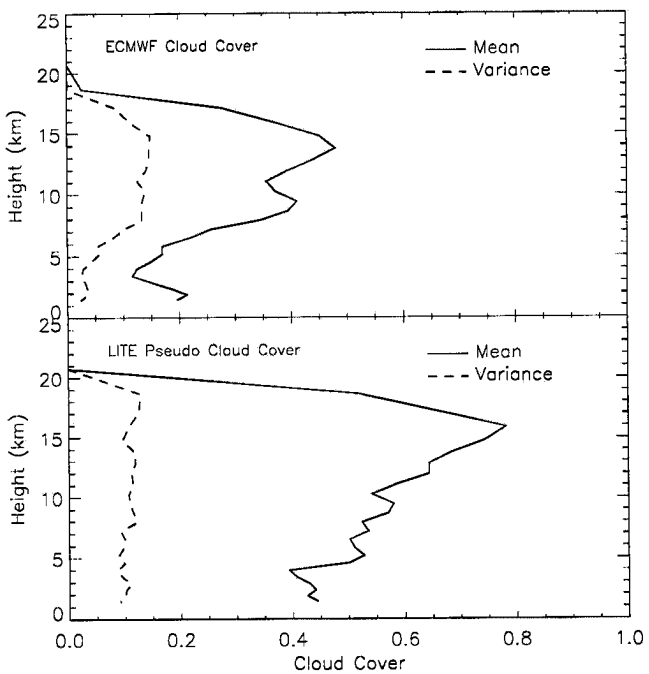

Figure 6.7: ECMWF ensemble mean and variance of cloud fraction along LITE orbits.

occur within a single gridbox, the clumping-nature of clouds explains the heavy-side bias. The approximation, albeit inexact, was nonetheless a step above assuming a persistant CF of unity. Further, the *shape* of the LITE-derived CF is argued to be representative of the true CF in a statistical sense. The variance of cloud fraction parameters was computed as a function of height according to

$$\delta^2_{\mathrm{CF}}(z) = \frac{1}{N-1}\sum_{i=1}^{N}(\mathrm{CF_i}(z) - \overline{\mathrm{CF}}(z))^2, \tag{6.10}$$

where N is the total number of profiles (all orbits) at model level z and $\overline{\mathrm{CF}}$ is the mean cloud fraction at that level. Corroborating Figure 6.6, the maximum mean cloud fraction was observed to peak near 0.5 for 10 km cirrus, a local minimum of 0.2 existed at mid-levels (near 5 km), and cloud fraction again increased for the lowest clouds (capturing marine stratus segments of the orbits). The LITE pseudo-CF, while biased toward unity as discussed above, revealed a structure very similar to that of the model results. It was concluded from this exercise that the NWP model generated, at least to first order, realistic cloud distribution characteristics (to the extent that the LITE pseudo cloud fractions were representative of the grid-averaged cloud fraction statistics).

An idea of where the model tends to generate clouds in the profile compared to observations is given in the probability density functions of Figure 6.8. It is important to recognize that the curves do not contain information on how *much* cloud occurred at a given level, they do indicate where in the profile clouds were found most frequently. The "kink" feature in the LITE data near 4-km is likely due to the aggregate effects of pulse attenuation (below which level cloud returns are lost). This skews the observation data and results in stronger values of PDF for the high clouds. Repeating the exercise using a cloud radar (e.g., CloudSat) would not encounter the significant losses owing to pulse extension, but may not detect a portion of the upper-level cirrus below the sensitivity of the instrument (e.g., -28 dBZ). Combining data from the formation-flying CloudSat and PICASSO/CENA (the latter carrying a 532 nm lidar) satellites would mitigate both loss-related issues.

Statistics that offer a comparison of the frequency of cloud generated by the model verses that observed is given in Figure 6.9. In the top panel, ECMWF (dashed) and

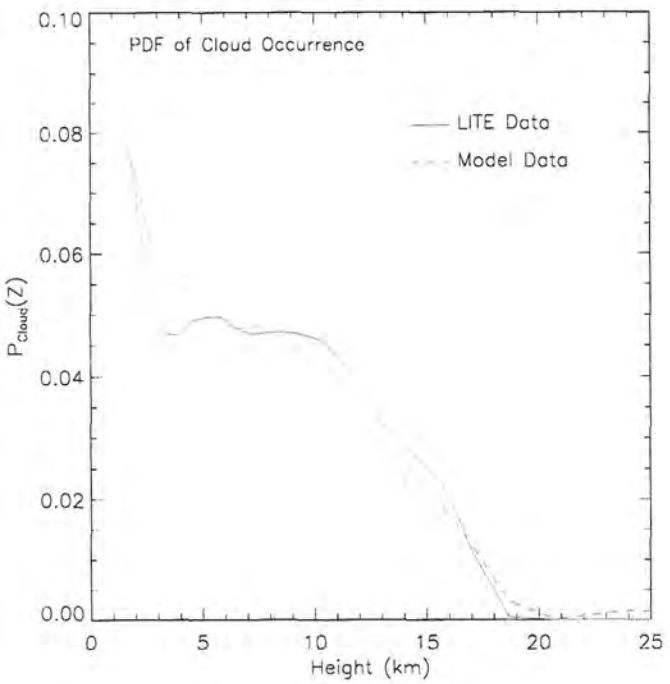

Figure 6.8: Probability density function of model vs. observed cloud height along LITE orbits.

LITE (solid) cloud occurrence frequencies are plotted against height. For these curves, the magnitudes of cloud fraction (model or pseudo-estimate) were not considered. If any cloud was detected at that level the count tally of clouds detected was incremented by one. The final count at each level was then normalized by the total number of model columns for all orbits considered (cloudy+clear), resulting in a percent cloud occurrence at each level in the atmosphere. Differences between the observed and model curves are shown in the lower panel of Figure 6.9.

Three regimes of interest in this figure are the strong negative difference for clouds layers less than 9-10 km in altitude, a region between 10 and 16 km where differences are small (or even slightly positive), and a region above 16 km where again the differences become negative. Although at first perhaps counterintuitive, the area of greatest concern to the ECMWF model may in fact be the regime between 10 and 16 km where "agreement" between the model and observations is nominally the best. To make sense of this statement, recall that for these curves, *any* amount of cloud contributes a full count to

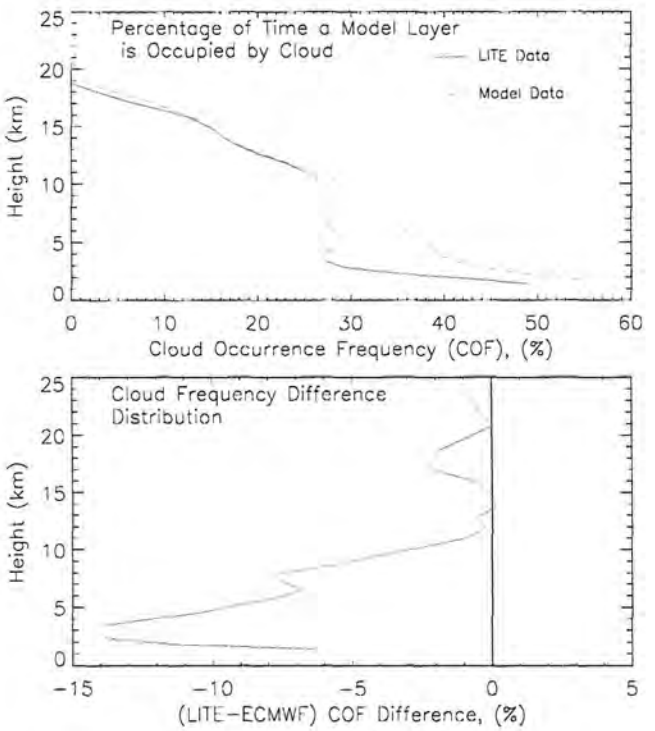

Figure 6.9: Top panel: percentage of time a model layer is occupied by cloud. Bottom panel: corresponding difference between observations and model

the tally at a given level. Because the ECMWF gridbox spans a massive area with respect to the small cross section of the LITE observations, the chances of the model reporting a finite cloud fraction are inherently much greater than for LITE (not to be confused with the discussion above regarding heavy-side biases in LITE-derived pseudo cloud fraction). The expected result is for the model frequency curve to exceed LITE at all levels. A red-flag is thus raised whenever the statistics indicate LITE observations very close to the model and certainly when exceeding it. If this bias is valid, it suggests that either the model does not generate enough cirrus by way of deep convection or synoptic-scale forcing (e.g., jet streaks), or these cirrus are dissipated too quickly by model sink terms in the prognostic equations.

A counter-argument to the interpretation of low LITE-ECMWF frequency differences being indicative of a biasing problem can be made by considering the climatology of upper-level cloud distributions. Either generated widely by synoptic-scale forcing or spread-out from local sources of convection by strong upper-level winds, cirrus tend to span greater

horizontal distances compared to lower tropospheric/boundary-layer clouds. These more uniform cloud fields offer a greater probability of detection by the LITE cross section and hence a better agreement between observations and a correct model forecast. The trend toward ECMWF > LITE (the negative regime below 10-km in the lower panel of Figure 6.9 with decreasing altitude corroborates this hypothesis, as lower-level cloudiness is tends to be more sporadic (e.g., fair weather cumulus)–decreasing the probability of LITE detection (again, exceptions to this low-cloud generalization being stratus and organized storm systems) of a representative fraction in a given model gridbox. The largest negative differences in this regime were also contributed to by the lidar pulse attenuation problem (this is not an issue for the upper-level cirrus). Curiously, the differences are again considerably negative at levels near 17 km. If the argument for agreement between 10 and 16 km is valid, then the bias would indicate either an overproduction or over-residency time for very high model cloudiness. Considering the increase of tropopause height toward the Equator, it may be concluded that the majority of these statistical $\sim$ 17 km cloud fraction disagreements occurred for tropical cirrus lofted high into the atmosphere by deep ITCZ convection.

Cloud fraction statistics for the ensemble of LITE orbits were computed as a weighted (by number of LITE profiles contained in each orbit segment) average of the individual orbit statistics. To provide a more detailed analysis in terms of cloud distributions in the vertical and in zones of different synoptic-scale forcing, the statistics were recomputed as a function of cloud heights and latitudinal zones. Specifically, low (0-4 km), middle (4-8 km) and high (above 8 km) cloud comparison statistics were computed using the rebinned LITE and model height field. Zonal statistics were computed for the Tropics (defined for orbit between the tropics of Cancer (23.5 N) and Capricorn (23.5 S)) and Extra-Tropics (all orbits outside of the Tropics). As synoptic-scale forcing generally is much weaker in the Tropics than in the Extra-Tropics (the extent of most baroclinic waves), this demarcation was of particular interest to ECMWF for assessment of the prognostic scheme (the older diagnostic scheme was reputed to perform worse in regions of weak forcing).

Results for the ensemble LITE statistics are shown in Figure 6.10. As expected from visual inspection of the case-by-case model and observed cloud fields (see Appendix B),

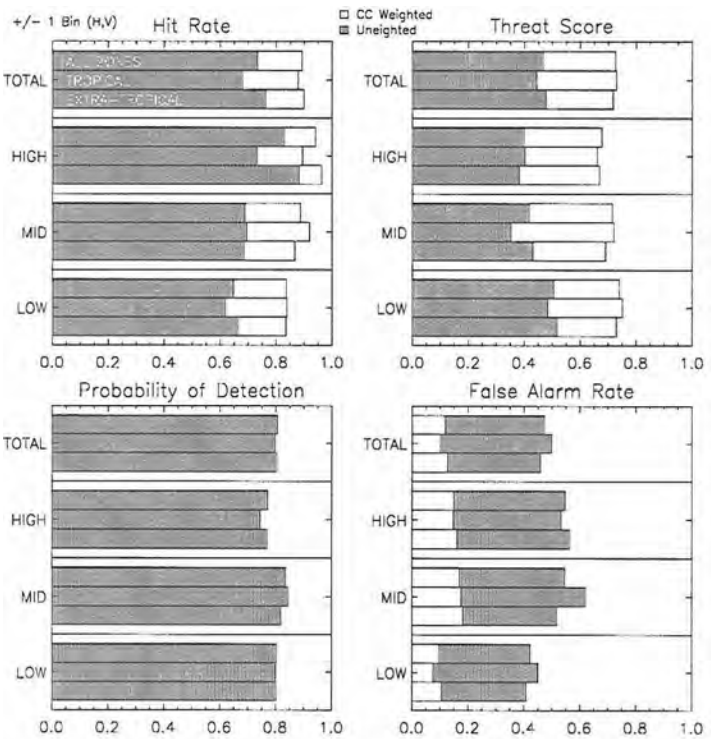

Figure 6.10: Ensemble-orbit statistics as defined in 6.9 for the ECMWF/LITE comparisons (Shown: $\pm$ 1 bin H/V). Statistics are decomposed into Total-column, Low (0-4 km), Middle (4-8 km), and High (¿ 8 km) cloudiness for Tropics and Extra-Tropics.

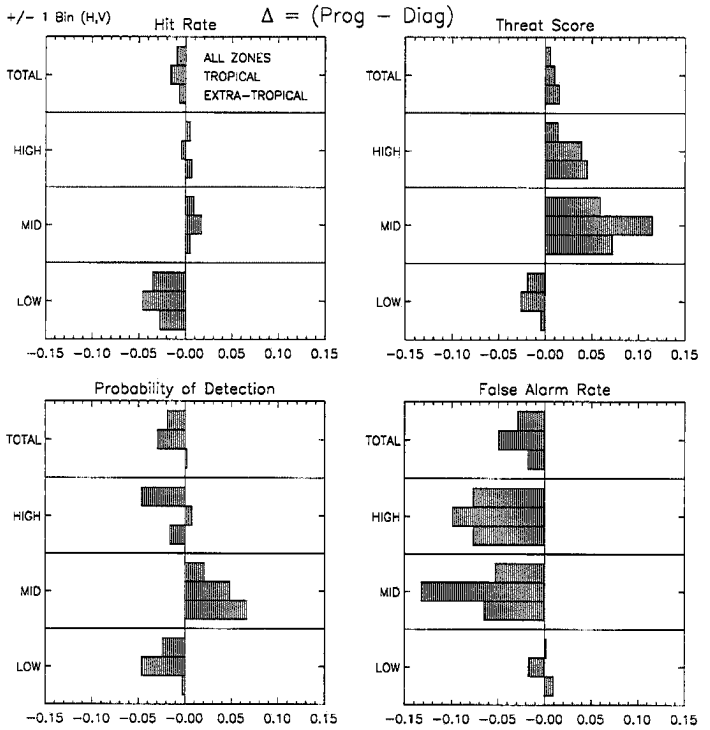

Figure 6.11: Differential statistics computed for comparison of the ECMWF prognostic (now implemented) and older diagnostic cloud parameterization schemes.

the statistics indicated that the model forecasts in general produce reasonable results with respect to the observations. For the ensemble cloud-fraction-weighted figures (white bars), hit rates were near 90%, threat scores exceeded 70%, probabilities of detection approached 80%, and false alarm rates were below 15% for all zones. Statistics as a function of cloud height show slightly better performance for lower-level clouds in all zones. Having never before been validated at these spatial scales and vertical resolution, these results have been regarded by ECMWF as very encouraging, and this research has helped to spawn new interest in the assimilation of global active sensor data in NWP models.

A comparison between the prognostic and older diagnostic scheme was carried out for a 15 orbit subset of the LITE database. The differences between prognostic and diagnostic computed statistics are shown in Figure 6.11. The statistics were computed with cloud fraction weighting and a $\pm$-1 bin window of acceptance in the horizontal and vertical dimensions. A general improvement in threat score was observed for the prognostic scheme, with the exception of low (0-4 km) cloudiness. The most significant improvement afforded

by the prognostic scheme (at least for the orbits considered) was for mid-level cloudiness. As expected, Tropical cloud forecasts (weak synoptic-scale forcing) improved significantly over the diagnostic scheme. Interestingly, the diagnostic scheme out-performed the prognostic scheme in the forecasting of low-level cloudiness for all zones. Because the higher threat scores and probabilities of detection are not offset by correspondingly higher false alarm rates, this was not simply a matter of the diagnostic scheme generating a greater amount of low-level cloud. One possible explanation is that the prognostic scheme is not being constrained sufficiently with relative humidity and strength of inversion in the surface layers. An increase in model vertical resolution in the region of the planetary boundary layer (PBL) may also serve to remedy any numerical components to this problem.

6.5 A Collection of Local Case Studies

In addition to the validation of multiple grid boxes for a single forecast (the LITE study), multiple forecasts time steps for a single grid location were performed for numerous airborne/surface campaigns (the non-LITE retrieval cases presented in Chapter 5) that were associated with limited spatial extent. The main advantage of the local platform was the presence of a larger array of remote sensing devices equipped to complement the active sensor data. Also, these cases allowed for a *temporal* analysis of the model forecasts (e.g., the advection of a cloud field into the region of observation). These local cases enlisted the Diagnostiques des Domaines Horizontaux (diagnostics for horizontal domains, or "DDH") ECMWF model architecture to provide forecasts over specified points/areas matched to the flight tracks or ground station. For convenience, the DDH case studies chosen corresponded to several of the retrieval cases presented in Chapter 5. A collection of results for these studies is included here.

Similar to the problems encountered with LITE, an unavoidable source of uncertainty existed in the assessment of cloud-fraction forecast performance due to sampling differences between the model fields and active-sensor observations. While the model cloud data are volumetric (spanning an entire grid box) quantities, the active data comprise a two-dimensional cross section (along the aircraft flight track) within this volume. A direct

comparison between model/observation cloud fraction is thus ill-posed, as the distribution of actual cloud within the volume encompassed by the model grid box is unknown (in some cases, the flight tracks loop back on themselves and thus sample a greater horizontal extent of the ECMWF volume, but even in this case additional uncertainties arise owing to cloud advection over the duration of the flight). As such, the same caveats associated with ECMWF/LITE false alarms, etc., applied also to the local DDH case studies. In the LITE study, one could make the argument that the large quantity of samples in the ensemble of orbits approached a reasonable sample set for statistical analysis. The same cannot be said of the DDH cases, where at most only a few gridboxes were applicable for any given case (with several time steps spanning the duration of the experiments). The poor sampling issues would thereby be amplified by the sparse number of points considered, leading to a possible misrepresentation of model performance. Considering these problems, no observation-based "pseudo cloud fractions" were computed for these local case studies. The emphasis instead was placed on evaluating the *temporal evolution* of cloud distribution (e.g., multi-layer cloud evolution/dissipation) at a fixed location (within the confines a single model grid-box volume).

6.5.1 ARESE 10/26/95 and 10/30/95

Single-box DDH forecasts (encompassing the Egrett flight track) centered near the SGP CART site (36.5-N,97.5-W) were produced by ECMWF for the local ARESE cases. Initialized at 00-UTC, forecast time steps between 17 and 20 hours at 20 minute temporal resolution were extracted for the comparisons. Generated were model fields of cloud fraction (0-1 fraction), specific liquid water content (kg/kg) and specific ice water content (kg/kg), along with profiles of temperature, pressure, and humidity at 31 hybrid flux levels. In order to obtain a one-to-one comparison between model and observations, the CDL data were binned to the temporal resolution of the model (spatial resolution is embedded in the specification of the DDH field; chosen either for a single-grid point or fields averaged over a specified area). Figure 6.12 illustrates the procedure of rebinning airborne CDL data to DDH resolution for this case study (cases to follow omit this example, and readers are referred to Chapter 5 for the depiction of the cloud fields at active-sensor resolution).

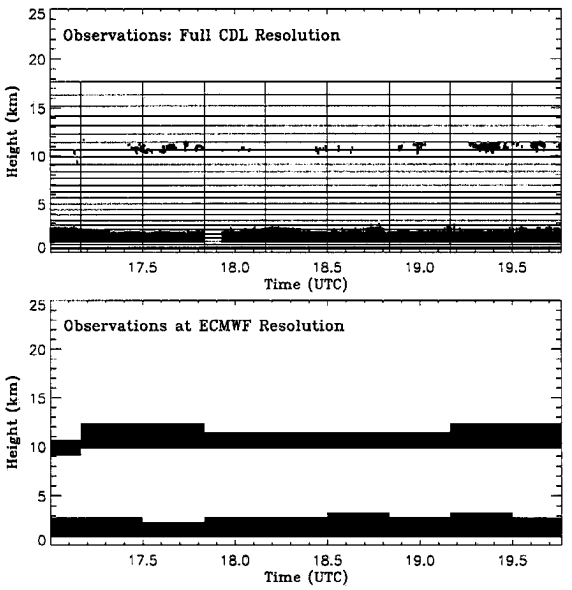

Figure 6.12: CDL observations rebinned to ECMWF vertical resolution.

Comparisons between model and observed cloudiness for both ARESE cases are shown in Figures 6.13-6.14. The onset of cloudiness near 8 km in the 26th case was captured at the 20 minute DDH resolution, along with a sparse distribution of lower-level cloud that was not observed at the CART site location (but may have existed somewhere within the surrounding domain). The 30th demonstrated accurate forecasting in both height and thickness for a two-layer cloud system during the 3 hour observation period. Because the lower cloud layer was optically thick, the CDL could not penetrate it fully. The base altitude was therefore approximated from rawinsonde observations (Figure 6.15, with observed cloud shaded).

6.5.2 SUCCESS 4/20/96 and 4/27/96

The SUCCESS flights conducted during April, 1996 (retrievals discussed in the preceding chapter) provided excellent case studies of continental cirrus near the ARM SGP CART site. Airborne CDL data were binned to the DDH resolution and cloud fraction comparisons are shown in Figure 6.16. On the 20th case, the forecasts predicted accurately the presence and longevity of the observed 7 to 11 km cirrus. Model cloud thickening (or higher occurrence of cloud) toward 1900 Z was also in agreement with the suggested trend in the observations (toward a persistent presence of cloud between 7 and 11 km), although

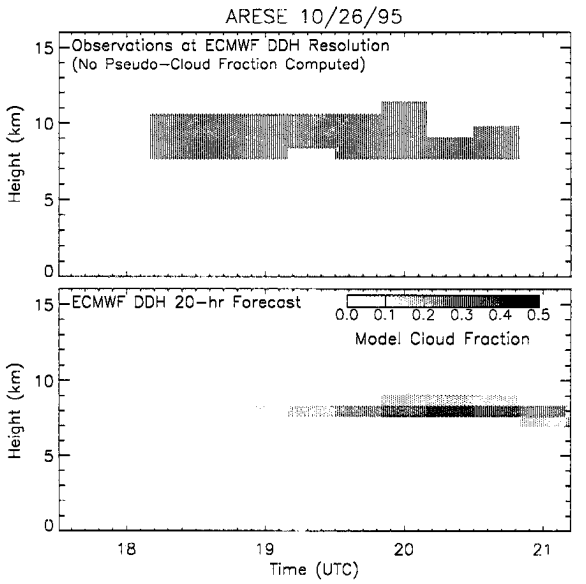

Figure 6.13: Comparison between CDL (rebinned to model resolution) and ECMWF cloud fraction forecast for ARF

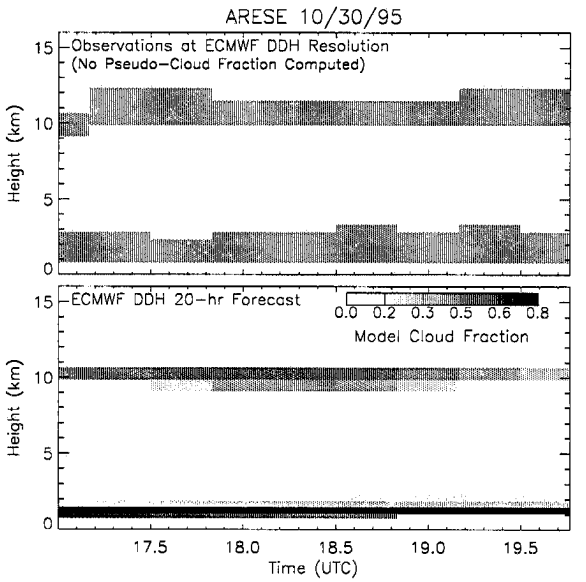

Figure 6.14: Comparison between CDL (rebinned to model resolution) and ECMWF cloud fraction forecast for ARESE 10/30/95.

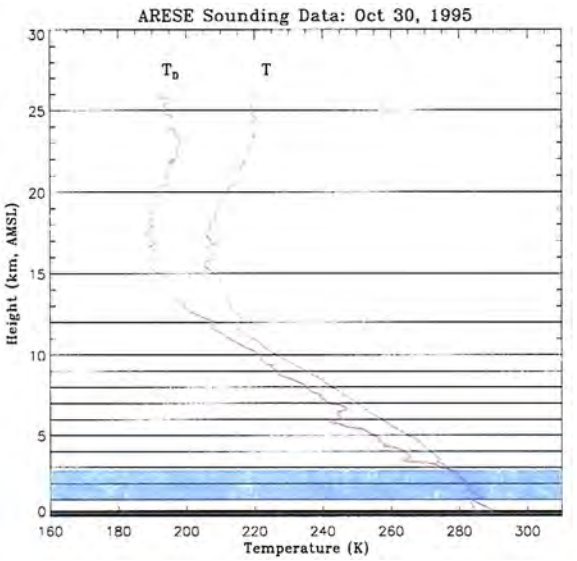

Figure 6.15: Rawinsonde data used to approximate lower cloud layer base for ARESE 10/30/95. Shaded is the observed location of the lower cloud layer.

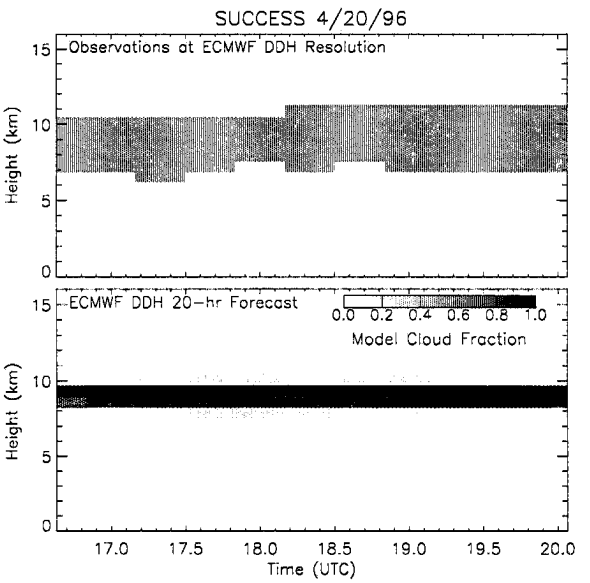

Figure 6.16: Comparison between CDL (rebinned to model resolution) and ECMWF cloud fraction forecast for SUCCESS 4/20/96.

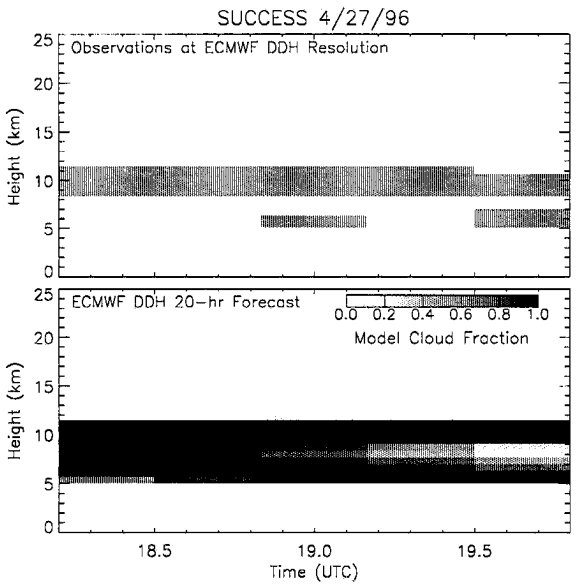

Figure 6.17: Comparison between CDL (rebinned to model resolution) and ECMWF cloud fraction forecast for SUCCESS 4/27/96.

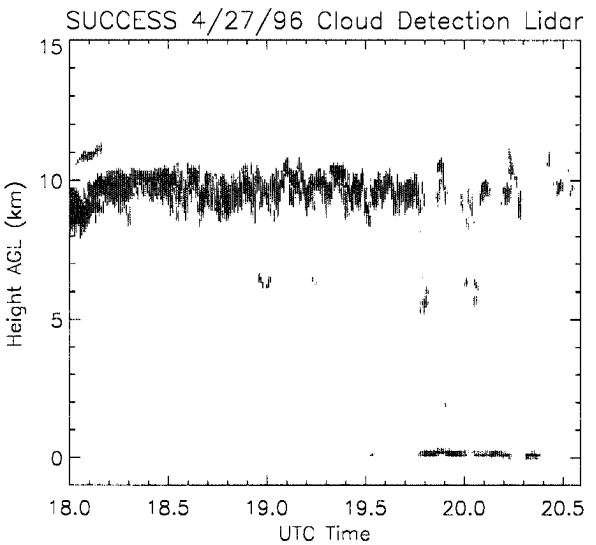

Figure 6.18: Full-resolution CDL data for comparison to Figure 6.17.

sampling uncertainty again rendered difficult this interpretation. The comparisons for 4/27/96 (Figure 6.17) indicate a correct forecast of cirrus, but the model cloud was several kilometers thicker than that indicated by the CDL. It should be noted, however, that the CDL return was completely attenuated for observations between 1800 and 2000 Z, such that the true cloud base was unretrievable. If the cirrus morphology was consistent with that of the Kauai ARM-UAV 4/30/99 case the true cloud base likely extended several kilometers below the CDL-indicated base, thereby achieving better agreement with the forecasted boundaries. Toward the end of the period (e.g., near 1900 Z) the forecast began to dissipate and split the cloud into two distinct layers with broken cloud in between. Observations at full resolution (shown in Figure 6.18 corroborate this trend. The change toward optically thinner model clouds (e.g., near 1900 Z in Figure 6.17) corresponds closely with the first appearance of a lower cloud layer near 6 km and the first indications of a surface return in the lidar data.

6.5.3 CLEX-1 and PACRIM

The CLEX-1 and PACRIM (CLEX-2) experiments, flying the ACR on the DC-8 aircraft, were considered as part of the same Summer Synthetic Aperture Radar (SAR) flight series. The cloud reflectivity data were binned to model resolution and the comparisons with ECMWF 24 hour forecasts are shown in Figures 6.19-6.20. In CLEX-1 the model failed to forecast any of the observed cirrus over the entire duration of observations. That these cirrus were associated with an MCS may explain in part the poor forecast performance, as the complex mesoscale circulations set up by buoyancy and pressure perturbations associated with MCSs are not accounted for in the model. Because the ACR was oriented in the zenith for the PACRIM case, no active data were available for the atmosphere below aircraft altitude (below 9 km). The forecast of the tropical cirrus layer lagged the observations by roughly one-half hour and overestimated height by several kilometers. These cases represent a small subset of the many areas of existing model deficiency that can be identified and explored through the use of active sensor cloud data on both the synoptic- and mesoscales.

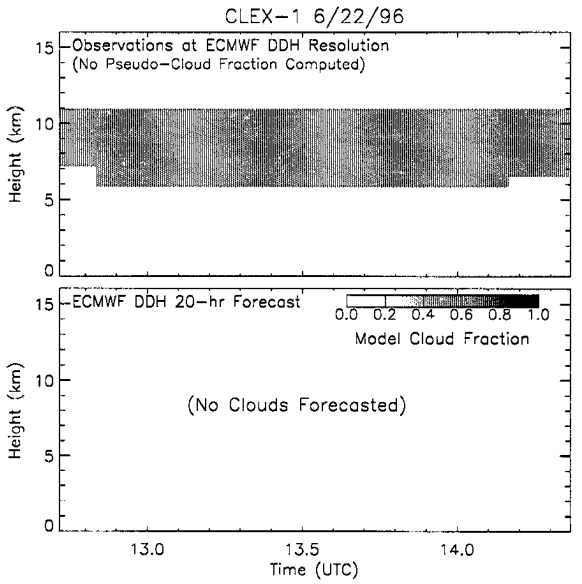

Figure 6.19: Comparison between CDL (rebinned to model resolution) and ECMWF cloud fraction forecast for CLEX 6/22/96.

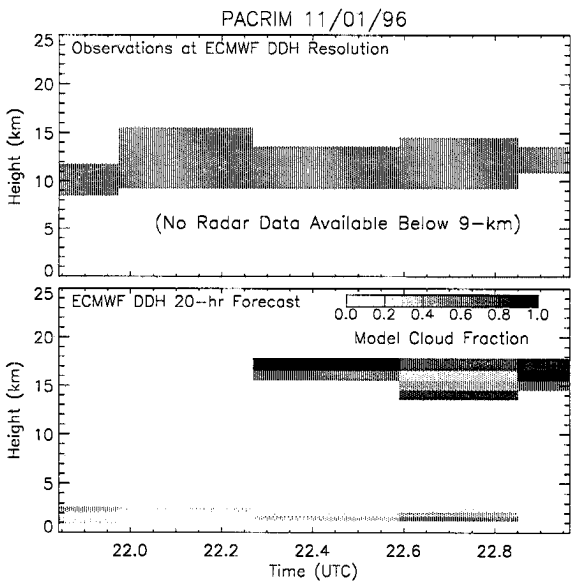

Figure 6.20: Comparison between CDL (rebinned to model resolution) and ECMWF cloud fraction forecast for PACRIM 11/01/96.

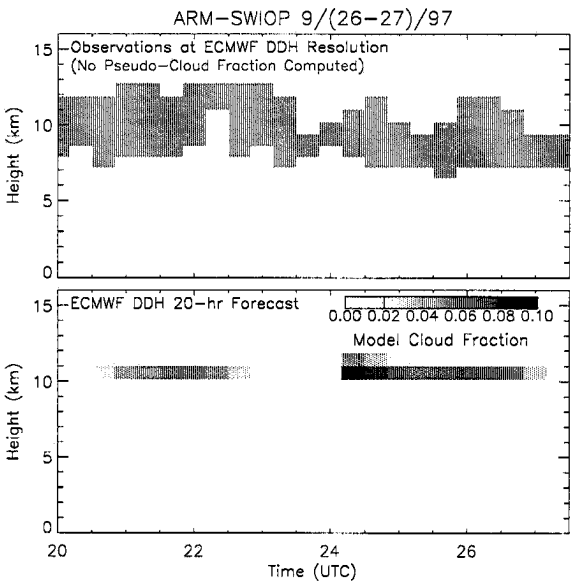

Figure 6.21: Comparison between CDL (rebinned to model resolution) and ECMWF cloud fraction forecast for ARM-SWIOP 9/(26-27)/97.

6.5.4 ARMSWIOP

DDH forecasts compared against CDL ground-based observations from the ARM-SWIOP are shown in Figure 6.21. While the level of cloud was found to be in agreement with the lidar observations, the more interesting feature of this comparison is the forecasted gap between 2200 and 2400 Z. Examination of the satellite and radar imagery (see Figure 5.38 from Chapter 5) revealed that this gap did in fact exist in the observations (in the satellite image of Figure 5.38, the region just to the North-West of the CART site as the flow advected South-Eastward along the direction designated by the virtual flight track line). The rebinning of observations to DDH resolution effectively fills-in the gap due to the presence of an intermittent cloud. The timing between the forecast and observed gap was remarkably close, indicating that the forecasted synoptic-scale flow was correct in the 24 hour forecast. The ability to validate model flow fields as illustrated here is one obvious advantage of these field observations.

6.5.5 ARM-UAV Kauai 4/30/99

The ARM-UAV Kauai 4/30/99 flight provided an opportunity to examine not only cloud location (as observed by both CDL and ACR) and microphysics (as retrieved from

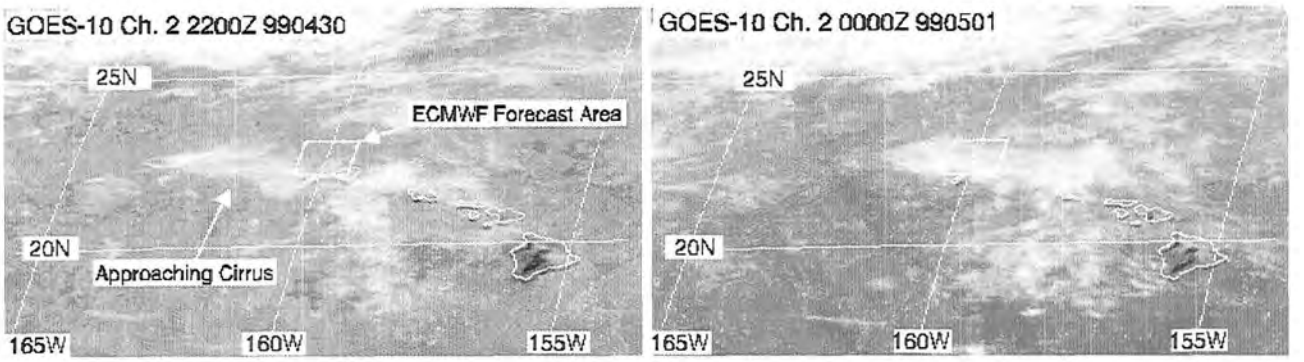

Figure 6.22: GOES-10 Ch. 2 (3.9-μm imagery of the Hawaiian archipelago during the ARM-UAV spring flight series 4/30/99 experiment. Two-hour interval imagery reveals an deck of cirrus that advected into the region over 2200-0000Z.

radar, SSP, and GOES-10) but also the model's temporal coherence with the observed cloud advection. Because the flight tracks looped back and forth across a single South-West/North-East segment confined within the ECMWF analysis area, the observations could be considered to first order as a stationary measurement of cloud evolution within the model grid-box (and a better sample than the single-point measurement as in the ARM-SWIOP). Figure 6.22 shows GOES-10 imagery at a two-hour interval collected during the 4/30/99 UAV experimental flights. Indicated in the 2200 Z image is the Hawaiian archipelago, the ECMWF forecasted area, and the cirrus deck that advected into the area from the West/SouthWest. At 2200 Z the Twin-Otter, heading South-West along the prescribed formation flight track with the Altus-II, returned to base for refueling. Prior to this time, few cirrus were observed (top panel of Figure 6.22), and while heading back to the Kauai airfield first encountered the leading edge of the cirrus shield. By 2400 Z, the Twin-Otter (having again taken to the air) observed a thick well-established cirrus layer (bottom panel of Figure 6.22).

The model/observation comparisons over the full span of Twin-Otter flight data are shown in Figure 6.23. The ACR observations were left at full resolution in the figure to capture the evolution of the cloud field. The model forecasts a cloud layer at roughly the correct altitude, but over-forecasts the amount of cloud at the onset and then begins to produce a cloud between 13 and 14 km that was not observed by either the ACR or CDL. It should be noted in referring to the earlier image (2200 Z) in Figure 6.22 that

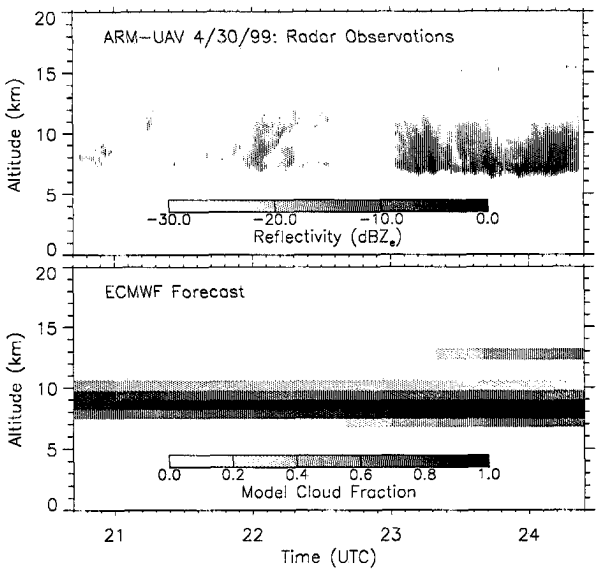

Figure 6.23: Comparison between ACR (given at full resolution to show changes in cloud field over time) and ECMWF prognostic cloud fraction forecast for ARM-UAV 4/30/99.

a finite amount of cloud did exist in the model area at this time (the flight track was on the Northern edge of the box and hence observed only intermittent cirrus). Although more difficult to discern in the grey-tone version of Figure 6.23, a notable increase in the forecasted cloud fraction was observed in the model layers between 7 and 8 km (CF: $0.05 \rightarrow 0.20$ and $0.66 \rightarrow 0.82$), possibly representing the advection of the observed thicker cloud deck into the region. By 2400 Z the model cloud fraction had increased to unity in two adjacent layers corresponding to the observed cloud level, and values of specific ice water content (not shown) increased by 25% from 0.08 to 0.1 kg/kg throughout the depth of the cloud.

6.5.6 CAVEX Monterey 6/30/99

In a recent assessment of global cloud cover in the ECMWF reanalysis product using ISCCP data, Jakob (1999) notes several areas of model cloud bias tied cloud class and geographic region. Among the findings is an underestimation of stratocumulus cloud off the western coasts of the subtropical continents by 15%. The CAVEX retrieval outlined in Chapter 5 was included in this research specifically to address this aspect of the prognostic cloud scheme. Shown in Figure 6.24 are comparisons of model and radar derived cloud

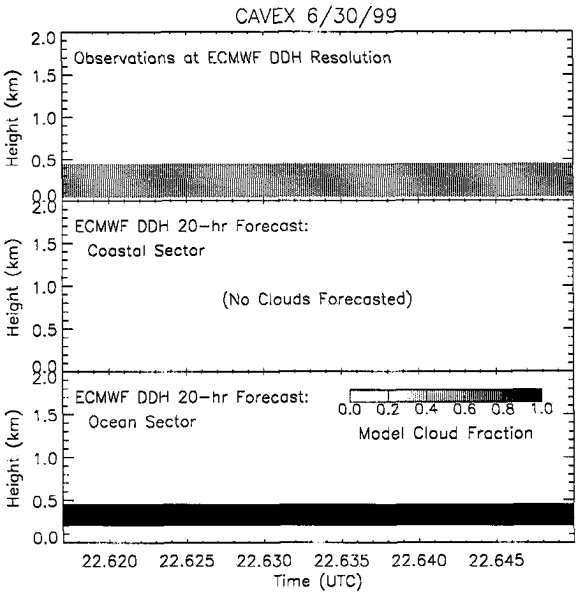

Figure 6.24: Comparison between radar (rebinned to model resolution) and ECMWF cloud fraction forecast for CAVEX 6/30/99. See text for details of coastal and ocean sectors.

fraction for a short segment of the 6/30/99 CAVEX flight. The observations were made at (38.75 N, 124.5 W). The center panel of Figure 6.24 shows the model forecast for this location (labeled "coastal sector"), and the lower panel corresponds to a sector further to the West (38.75 N, 129.5 W) (labeled "ocean sector"). While the coastal sector failed to forecast the observed marine stratus, the presence of this synoptic-scale feature in the model was verified by the off-shore sector. These findings were consistent with Jakob (1999) and point to possible deficiencies in the prognostic scheme in situations of weak synoptic-scale forcing (in the case of Monterey marine stratocumulus, weak subsidence associated with the stationary high pressure system over the Pacific Ocean). Increases in model vertical resolution have yielded some improvements, indicating that numerical problems are also at play (C. Jakob, personal communication).

6.6 Summary

This chapter explored the application of active sensors to the validation and assessment of forecasts employing the ECMWF prognostic cloud scheme. The opportunity for global active sensor validations of a NWP model was demonstrated using LITE data.

The sixty-six night-time orbits provided a wealth of data from which various forecast performance statistics were computed. A great deal of information is present in any given LITE orbit, and a more detailed statistical analysis of cloud structure in connection to the synoptic and/or mesoscale forcing remains to be addressed. Short-range cloud fraction forecast performance of ECMWF (with focus on both spatial and temporal coherence) has also been investigated using a collection of field case studies and the DDH model format. Because only a few cases were considered here, no general statements regarding forecasting tendencies were warranted. Emphasized instead is that opportunities for this nature of comparison do exist and should be explored further in the context of the TRMM, CloudSat, and PICASSO-CENA missions among others to transpire within the next decade.

While by no means suggesting that the problem of parameterized cloud treatment in NWP models has been resolved by virtue of the findings presented in this research, the model/observation results were considered nonetheless as an encouraging commentary on our current ability to represent the three-dimensional distribution of cloud in GCMs. This raises important questions regarding to what extent certain aspects of the ECMWF reanalysis may provide useful information to current research activities–either in the context of an ancillary data source or as a plenary tool. As an example of the latter, the mission coordinators for CLEX-5 have considered employing ECMWF short-range forecasts of cloud fraction as guidance for when to mobilize and where to deploy research aircraft dedicated to their field observation campaigns. By the same token, plans for future CLEX IOPs include observational sampling geared toward minimizing sampling ambiguities in comparisons against forecasted fields at available model resolution. As a better awareness between the two communities evolves, so also will the quality and utility of results stemming from future IOPs.

Chapter 7

NWP CLOUD MICROPHYSICS VALIDATIONS

7.1 Introduction

While the results of Chapter 6 embodied a necessary condition, the correct placement of cloud in the atmosphere is not a sufficient criterion for the correct modeling of cloud radiative and hydrological feedback processes. How a cloud interacts with radiation is also determined by its optical properties, which in turn are related directly to its physical makeup (e.g., cloud phase, the size distribution of droplets/crystals, the water/ice mass of cloud material, etc.), geometry, distribution, and position in the vertical. Therefore, a thorough model validation requires the examination of both cloud spatial distribution and properties of the clouds themselves. In addressing this latter condition of "cloud content," this chapter attempted to tie together the two main concepts of the dissertation; the multi-sensor approach to cloud property retrievals and NWP cloud parameterization validation, by appealing to results derived from the the former in addressing the latter. By doing so, the framework is established for better understanding the relationships between detailed (e.g., multi-layered) cloud structure and the atmospheric circulation; this, in the context of models empowered with the additional information provided by space-borne active sensor data.

One method of addressing the cloud content requirement involves the matching of forecasted fields to equivalent parameters derived from physical cloud property retrievals. The apparent skill displayed by ECMWF forecasts of cloud distribution (e.g., the LITE comparisons) begs the question "To what extent are model cloud *microphysical* properties representative of real clouds?" With global active sensor data, we can begin to address this question in a non-statistical manner. That is, because the model clouds correspond

to specific active sensor observations, the optical properties of the clouds may be examined on a case-by-case basis as opposed to the more traditional ensemble comparison delineated by cloud class (e.g., cirrus, cumulus, stratus, etc.). While questions regarding model climatology are deferred more appropriately to the latter genre of analysis, the non-statistical method provides detailed insight (e.g., biases tied to specific geographic locations or synoptic conditions that go on to affect the global model cloud climatology) that may otherwise be lost amidst the ensemble data.

To compile a database from single-point forecasts sufficient for use in statistical analysis (comparable to what was done with the LITE data), an extended (e.g., months of data) observation period is required. Rather than examining further the cloud spatial distribution forecasting performance (while being cautious to clarify that the LITE study is not considered here as exhaustive in this capacity), the emphasis of these cases was placed instead on cloud optical properties as defined by water/ice content, optical depth and effective particle radius. There exist several possible metrics from which to chose, some of which will be more definitive for model validation than others. For this research, cloud optical depth (which is a proxy for cloud water content and hence related to model prognostic parameters) was emphasized as much for convenience as for its impact on the distribution of radiation.

7.2 Recasting of Observational/Model Parameters to Comparable Fields

Comparison between model fields and retrieved optical properties required conversion to equivalent parameters (e.g., retrieved optical depth and particle size converted to model fields of liquid/ice water content, model cloud parameters converted to equivalent cloud radar reflectivity, etc.). Generally, these conversions are based upon either physical relationships derived from theory and modeling or empirical relationships using a statistical database (e.g., a best-fit to a dispersion of observational data). Both methods may be used to obtain useful information so long as the approximations, uncertainties, and limitations implicit to each method are understood. Summarized in this section are the approaches taken in this analysis toward the comparison of model and retrieved cloud property fields.

7.2.1 Physically-based conversions

Whenever possible, it is best to avoid empirical relationships in favor of physically traceable relationships (since the former seldom are universally applicable, and uncertainties are poorly quantifiable). Following Stephens (1978), we derive here from first principles a relationship between optical depth, effective particle radius, and liquid water path. Beginning with the explicit definition for optical depth:

$$\tau = \int_{\Delta z} \int_0^\infty n(r) \pi r^2 Q_{\text{ext}} dr dz,$$

we consider the case where the size parameter $x = 2\pi r/\lambda$ is large (i.e., particles that are large with respect to the wavelength of incident radiation). This assumption holds in general for most cloud particles within the optical (0.3 to 14 μm) portion of the spectrum. In this "extinction paradox" regime (so-called because the extinction efficiency Q_{ext} approaches a constant value of 2.0 as opposed to the more intuitive value of unity) the extinction efficiency falls out of the integral as a constant, and applying the definition for effective radius

$$r_{eff} = \frac{\int_0^\infty n(r) \pi r^3 dr}{\int_0^\infty n(r) \pi r^2 dr},$$

the expression for optical depth may then be rewritten as

$$\tau = 2 \int_{\Delta z} \int_0^\infty \frac{n(r) \pi r^3 dr}{r_{eff}} dz. \tag{7.1}$$

Introducing reciprocal constants (i.e., multiplying by a selected form of unity)

$$\tau = 2 \frac{3}{4\rho} \int_{\Delta z} \int_0^\infty \frac{n(r)(4\pi r^3 \rho/3) dr}{r_{eff}} dz,$$

enables the integral over particle size to be expressed as a function of the height-dependent liquid (ice) water content $w(z)$

$$\tau = \frac{2}{3\rho} \int_{\Delta z} \frac{w(z)}{r_{eff}} dz. \tag{7.2}$$

Integration over the entire depth of the cloud (Δz) yields the liquid (ice) water path W, and invoking the assumption that r_{eff} is constant with height results in a final simplified expression for the cloud optical depth:

$$\tau = \frac{3W}{2\rho r_{eff}}. \tag{7.3}$$

This relationship may be used to convert model fields of cloud water and parameterized particle sizes to equivalent optical depths. Conversely, the retrieved values of τ and r_{eff} may be converted to a model-equivalent liquid water path by solving Equation 7.3 for W

$$W = \frac{2\tau\rho r_{eff}}{3}.$$

Model liquid/ice water contents were computed from the specific (kg/kg) fields. In-cloud LWC/IWC can be obtained by normalizing by model cloud fraction. Doing so, however, may lead to an over-bias of the model results for the case of a partly cloudy scene. In rebinning the observations to model resolution, both cloudy and clear regions of the flight track (for example) are averaged, thereby embedding the "pseudo cloud fraction" within the observed fields. In the ideal case where the pseudo and true cloud fractions coincide, the smoothed fields would in principle be equivalent to the smoothed model fields. As such, no cloud fraction normalizations were performed and the model fields were thereby considered statistically as representative of an arbitrary flight track within the gridbox. An alternative approach would be to consider only the cloudy portion of the observations in the rebinning to model resolution and then to compare against model fields normalized by the model cloud-fraction. While ostensibly this may provide a more straightforward cloud intercomparison by removing ambiguities arising from the cloud fraction, this filtering would render less meaningful the discussion of energetics in terms of model vs. observed fluxes. How best to apply non-traditional (e.g., active sensor) data to model validation/assimilation is one of the many difficult questions posed to this area of research that remains unresolved.

A fixed effective radius of 10.0 μm for model water clouds over land, 13 μm over the oceans, and a temperature-dependent relationship for ice clouds were assumed by the ECMWF cloud parameterizations. The ice relationship is taken directly from Ou and Liou (1995), with imposed minimum and maximimum values of 40 and 130 μm, respectively. A temperature-dependent parameterization for the water phase (Jakob, 1994) assumes that all condensate below -23° C is ice and everything above 0^{circ} C is liquid. Between these temperatures the water fraction reflects a compromise between the minimum observed

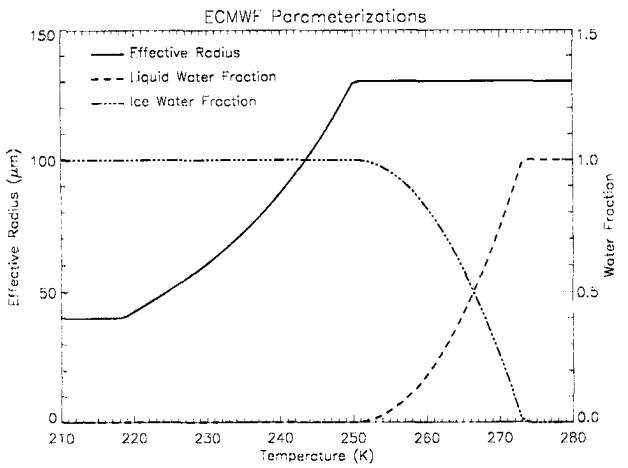

Figure 7.1: ECMWF parameterizations for ice effective radii (μm) and ice/liquid water fraction as a function of temperature.

temperature of super-cooled water prior to homogeneous freezing and newer observations which indicate that liquid water is seldom present below -10° C. These parameterizations, which were employed to compute model equivalent optical depths, are shown together in Figure 7.1.

The physical relationship developed above is only as valid as the assumptions that $Q_{\text{ext}} = 2$ (the extinction paradox condition) is satisfied and the effective radius is *constant* throughout the cloud profile. The former (large particle) condition generally is satisfied for sub-micron wavelength solar radiation where scattering by cloud particles on the order of several microns in size (e.g., $2\pi r \gg \lambda$). The latter condition is less often observed in nature (e.g., profiles of effective radii in stratus grow with height under weak lifting conditions, while those in many cirrus are largest at cloud base due to sedimentation as was illustrated in the ARM-UAV Kauai 4/30/99 retrievals). The uncertainty is then proportional to the cloud profile variability. A cloud profiling radar may prove useful in obtaining a quantitative assessment of this uncertainty, but this topic has been left unexplored by this research.

7.2.2 Empirically-base conversions

The alternative method of comparison involves the conversion of radar reflectivity to physical/optical cloud properties through an empirical relationship (e.g., those listed

and described in Chapter 6). Similarly, inversions of the radar-reflectivity/water-content relationships can be applied to model water-content fields to compute model-equivalent reflectivities for direct comparison against radar observations (a topic that is explored in more detail further along). The conversion from profiles of model cloud liquid/ice water content to those of equivalent radar reflectivity may also prove useful in the simulation of a "virtual CloudSat" (to the extent that these model fields can be shown as representative of Nature–the question addressed in this chapter). Uncertainties associated with these empirically-based approaches are tied directly to the representativeness of the cloud data used to compute the fit. As these uncertainties are often large and highly variable from cloud to cloud, the physically based method is the desirable alternative whenever available, with the empirical products serving as a low-weighted source of independent validation data.

7.2.3 Optical property comparison protocols

The same sampling problems encountered in the model/observation comparisons of cloud fraction were present also in those for cloud optical properties. The model reports cloud liquid/ice water content at a given level as a single value spread out (diluted) over the entire model layer. To convert this quantity to the "in-cloud" equivalent value, the water content was normalized by the cloud fraction at that level (such that a cloud fraction of unity will result in no change while a smaller cloud fraction will increase the water content within now-undiluted cloud). The conversion to optical depth following Equation 7.3 is then performed. The physical retrievals must also be converted to model resolution. Each retrieval point corresponds to a single column along the flight track (or in the case of DDH, time), and it is usually the case that clouds with variable heights and optical depths exist within the same model gridbox or DDH time slot.

There are two smoothing issues at hand: first, the optical depth within a single column must be smoothed to model vertical resolution, and second, these partitioned columns must be combined to form a horizontally-averaged column. The resultant data are of the same resolution as the model in both the vertical and horizontal (or time, in the case of DDH) dimensions. The first step was accomplished by normalizing the retrieved

optical depth by the true cloud thickness (as determined by active sensor measurements) to obtain the corresponding extinction coefficient. A loop over the model levels determined in which layers the full-resolution cloud fell. For these layers, the optical depth was computed by multiplying the extinction coefficient by the fractional occupation of the cloud within the layer. For example, if a model layer resided between 4 and 5 km and the true cloud spanned 3 to 4.7 km with an extinction coefficient of 1.0/km, then the optical depth assigned to that model layer would be (4.7-4.0 km)$\times$1.0/km = 0.7. If the cloud spanned the model layer completely, the full layer thickness was used in computing τ. The retrieval was thereby smoothed to model vertical resolution with no information lost in the process. To complete the rebinning, all retrieval columns within a the model horizontal grid (time) span were assembled and the optical properties at each level averaged together to yield a final retrieved quantity. It is noted that by this smoothing method the "pseudo cloud fraction" used in the cloud fraction comparisons of Chapter 6 is implicit to these optical property comparisons.

By the method described above, liquid/ice water contents may be compared one-to-one at the model resolution. In principle, comparisons of column-integrated optical depth do not require the first rebinning (i.e., to model vertical resolution step), but carrying out the full procedure will reduce to an equivalent average τ if done correctly. The vertical resolution rebinning allows for discrimination of cloud layers in a multi-layer case. The main assumption implicit to the procedure is that extinction is constant with profile. As discussed earlier, this generally is not the case. As presented and applied to the case studies of Chapter 5, the passive/active retrievals provide a single value representative of the column-integrated cloud optical depth. For this reason, comparisons of column-integrated optical depth (which by its very definition circumvents the caveat of vertical inhomogeneity) were emphasized for these assessments of forecasted cloud properties.

7.2.4 Sampling considerations

As with the cloud fraction comparisons, the problem of point (or flight track) observations versus three-dimensional area model fields existed in the cloud property comparisons as well. In the case of a broken cloud field in which a distribution of cloud optical depths

(for example) exist, there is no reason to expect that the point/track observation will correspond to the areal mean value of the gridbox. It is, however, expected to fall somewhere within the distribution of optical depths characterizing all clouds within the gridbox. To compare the data in a statistical sense, then, it is perhaps more useful to discuss the agreement/disagreement in terms of parameter distributions. This requires a synthetic increase of the model resolution while adhering to physics and maintaining conservation of the coarse field parameters.

To compute a distribution of model cloud optical depths from a single, 31 level model gridbox (each level characterized by prognostic cloud fraction and ice/liquid water content parameters), a technique following Jakob and Klein (1999) was applied to the ECMWF forecast grid. In this method, each gridbox was assumed to be composed of 100 "pixels". Maximum/random overlap of cloud in adjacent layers was considered, and each pixel was assigned an integer value of either completely clear or completely cloudy (the total number of cloudy pixels divided by 100 yields the original cloud fraction for the gridbox/level in question). The optical depth at a given pixel was then computed by summing over the total column, with contributions dependent on whether the pixels were 0 or 1 in that sub-column. The result was a distribution (between 1 and 100 elements) of optical depths whose mean value was the same as that computed in the original, un-pixelized column.

Because maximum-random overlap was enforced, the pixel optical depths are more realistic than a purely random distribution of cloudy/clear pixels. The pixel field of optical depths should not, however, be interpreted as applicable to a one-to-one comparison along a flight track, since no information is available on *where* in the horizontal domain these overlapped clouds occur. The result is used instead for statistical validation–the observations should fall somewhere within the model spread. Further, compiling these distributions over a time series or extended flight track allows for a statistical distribution of observations to be assembled for comparison against the model. It is this latter mode (with a large database classified by cloud type, synoptic situation, geographic location, etc.) that holds perhaps the greatest promise for unambiguous identification of model biases by active observing systems.

7.2.5 Flux comparisons

A 2-stream radiative transfer model based on the method described by Stephens *et al.* (2000) was employed to calculate the broadband shortwave (0.2- to 4.0-μm) and longwave ($4.5 \rightarrow \infty$ μm) fluxes at the surface and top-of-atmosphere. Required as input were profiles of temperature, pressure, relative humidity, cloud specific liquid/ice water content, cloud fraction, and the solar zenith angle. The model-resolution averaged values of the retrieved cloud liquid/ice water contents (as converted from τ and r_{eff} according to Equation 7.3) were used for these flux calculations. Boundary (surface and TOA) fluxes were computed for model and observation fields to provide a quantitative measure of the differences in bulk energetics arising from errors in the model cloud optical properties. Because many of the profile data (especially in the case of LITE) were not available as independent measurements, ECMWF data were used. As a result, only the relative differences between model and observed fluxes (arising from differences in cloud water contents) were emphasized, as opposed to direct validations against flux observations.

7.3 Selected Case Studies

Presented in this section are model/retrieval cloud property comparisons selected from the retrieval case study results of Chapter 5. While all cases were processed and are included in the ensemble results, only three representative examples were included here in the interest of space. Also examined was the impact of cloud optical property model discrepancies on the transfer of atmospheric radiation (i.e., in terms of boundary fluxes and cloud radiative forcing). While clearly insufficient in quantity to identify decisively areas of model biases in the parameterization of global cloudiness, these data may contribute toward addressing these questions in connection with data resources from ARM, CloudSat, and antecedent CloudSat algorithm-development programs. These efforts are geared toward providing a better handle on model energetics and possible areas of deficiency in the currently implemented cloud scheme.

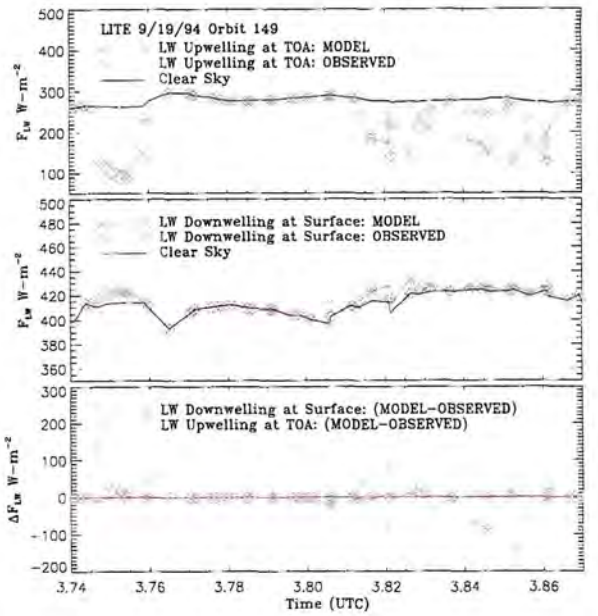

Figure 7.4: Corresponding two-stream boundary fluxes derived from forecasted and observed profiles of LITE Orbit 149 cloud liquid/ice water contents, along with modeled clearsky values for reference.

7.3.1 LITE Orbit 149 (Atlantic) 9/19/94

After rebinning observations to model resolution and implementing the requisite field-conversions as outlined above, retrieved cloud optical depths were compared against co-incident model forecasted clouds. The comparison for LITE Orbit 149 is shown in Figure 7.2, and the corresponding PDF is given in Figure 7.3. By omitting any additional model clouds that were not observed as well as those observed but not forecasted, the comparison effectively filters out the false alarm and miss contributions to the ensuing flux analysis. This was argued to yield a better direct comparison of the cloud and cloud optical properties of interest here (whereas issues of cloud distribution discrepancies were the subject of the previous chapter). The trends captured in Figure 7.2 are truly striking when considering that the spatial, temporal, and optical coherence were all constraining simultaneously this forecast comparison. The model cirrus encountered between 3.81 and 3.86 Z exhibited a slight over-bias with respect to the retrievals (this can also be inferred in a general sense when exmaining Figure 7.3. The region of large τ near 3.75 Z corresponded to a deep convective system (refer back to Figure 5.1 in Chapter 5). LITE experienced full attenuation in this cloud, and the night-time retrievals, as discussed in Chapter 4,

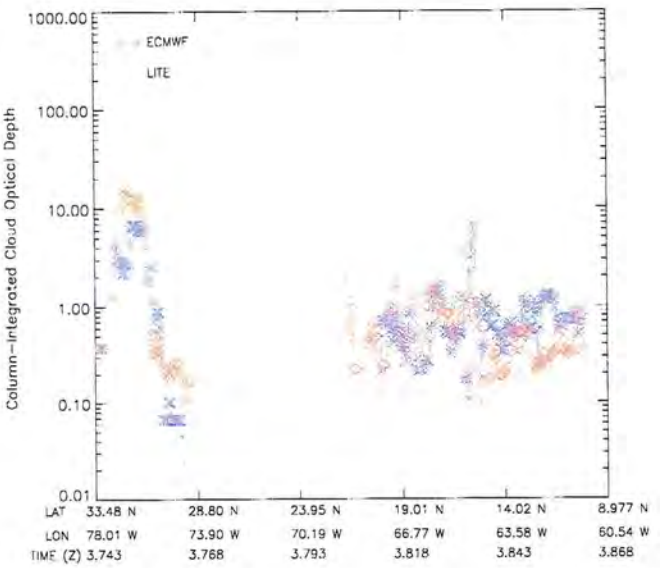

Figure 7.2: Comparison between optical depths derived from GOES measurements and those converted from model cloud water forecasts for LITE Orbit 149.

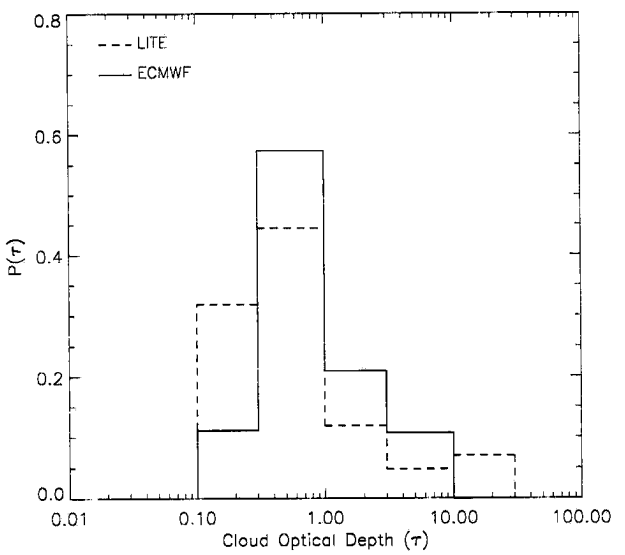

Figure 7.3: Corresponding PDF of retrieved and modeled cloud optical depths.

saturate near $\tau = 10.0$ (i.e., the cloud brightness temperature approaches that of its ambient environmental temperature and no further sensitivity to increases in τ is available). The true optical depth for this cloud system was likely much higher than indicated, and the close correspondence between model and observations for this cloud is probably more coincidental than meaningful (although constraining the ECMWF cloud to the apparent depth observed by LITE will yield a better approximation to the GOES retrieval, which effectively was retrieving properties near the cloud-top).

The corresponding TOA upwelling and surface downwelling fluxes (longwave only for this night-time case) as modeled from the profiles of cloud mean liquid/ice water content are shown in Figure 7.4. Shown for reference is the clearsky flux (computed from the same two-stream model, temperature/humidity profiles, and solar zenith angles but with cloud liquid/ice water contents set to zero), with variability owing to the changing along-track surface/atmospheric temperature data. Clouds with higher optical depths correspond to decreases in the TOA upwelling longwave and increases in downwelling surface fluxes with respect to clearsky values. In the lowest panel are along-track difference curves. The most notable differences were observed for TOA outgoing radiation, where the presence of cloud was often observed to prevent over 50% of the upwelling emissions from escaping to space. The effect on the downwelling surface flux was not as great for these upper-tropospheric clouds (since the broadband quantity is dominated by water vapor in the lower troposphere). The largest differences were observed in the vicinity of the deep convective cloud and arose due to a slight mislocation of the forecasted cloud field

7.3.2 ARESE (SGP) 10/30/95

The model and rebinned retrieved cloud optical depths for the ARESE 10/30/95 case are shown together in Figure 7.5. The column optical depth was dominated by the lower-level stratus cloud. Error bars on the retrieval curves are on the order of 10%, while the bars on the model curve represent the 1-σ of the subgrid distribution of model optical depths described above. The corresponding comparison of cloud water content (in the form of a column-integrated water path) is given in Figure 7.6. It was observed that the water path curves were in closer agreement than the optical depths. This was

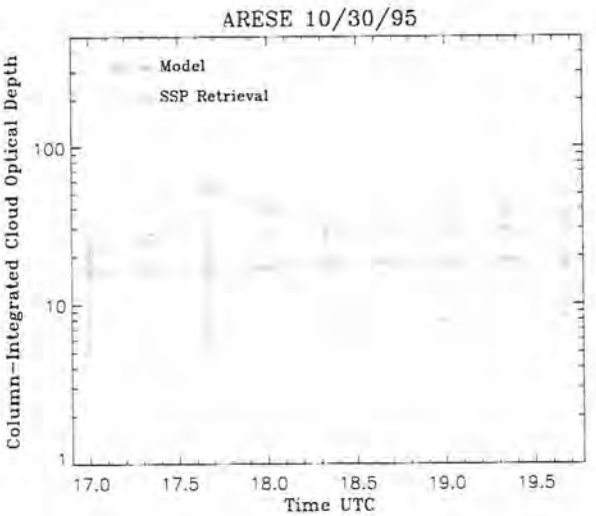

Figure 7.5: Comparison between optical depths derived from SSP measurements and those converted from model cloud water forecasts for ARESE 10/30/95.

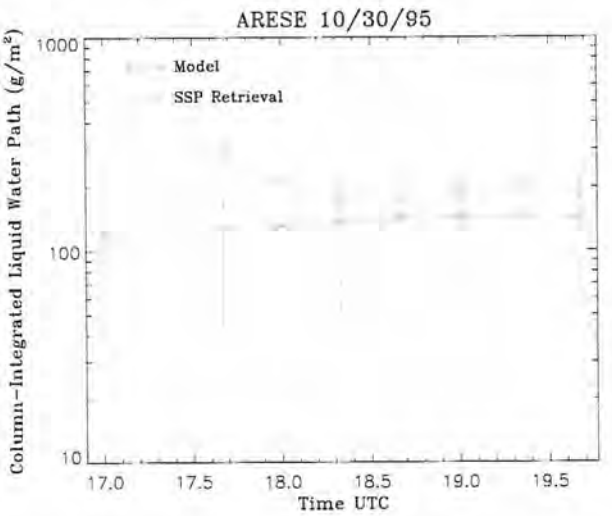

Figure 7.6: Comparison between water paths derived from SSP measurements and model forecasts for ARESE 10/30/95.

due to differences in the retrieved and model-assumed effective particle radii, which relate optical depth and water path according to Equation 7.3. While the model and observed τ remained within an order of magnitude, the discrepancies could by no means be considered as negligible. The radiative implications of these differences on the boundary fluxes of the atmospheric column (as measurable from surface and satellite-based instruments) must also be considered.

Figure 7.7 summarizes the shortwave and longwave flux comparisons for ARESE 10/30/95. The discrepancies in model-observed longwave were small, since both lower-layer clouds were optically thick. Nearly 80% of the downwelling solar flux was blocked, and an estimated three-fold enhancement in shortwave albedo was computed for both model and retrieved clouds. The maximum shortwave transmission and reflection disagreement between 30 and 60 W m^{-2} in the region of greatest τ differences near 17.5 Z. Shown in Figure 7.8 are differences in cloud radiative forcing:

$$\mathrm{CRF_{SW/LW}} = \mathrm{F^{\uparrow}_{TOA,SW/LW}(clear)} - \mathrm{F^{\uparrow}_{TOA,SW/LW}(cloud + clear)} \tag{7.4}$$

(defined as the difference The net cloud forcing is the sum of the longwave and shortwave components. This is a direct measure of the effect of the presence of cloud on the surface/atmosphere energy budget. As defined, longwave cloud forcing is a positive quantity (i.e., emission from clouds generally is lower than that of the underlying surface owing to colder cloud temperatures, making the clear-allsky flux difference positive) and the shortwave forcing is a negative quantity (i.e., clouds generally reflect a greater amount of solar radiation than the underlying surface, rendering this same difference negative). For the ARESE case, the net cloud forcing was dominated by the shortwave component, and the calculated differences (here, on the order of 20 W m^{-2}) provide a metric for how cloud optical property differences translate to atmospheric energetics. These errors will propagate throughout the model as discrepancies in surface/atmospheric heating and lead ultimately to different circulation patterns and a divergence from Nature with time.

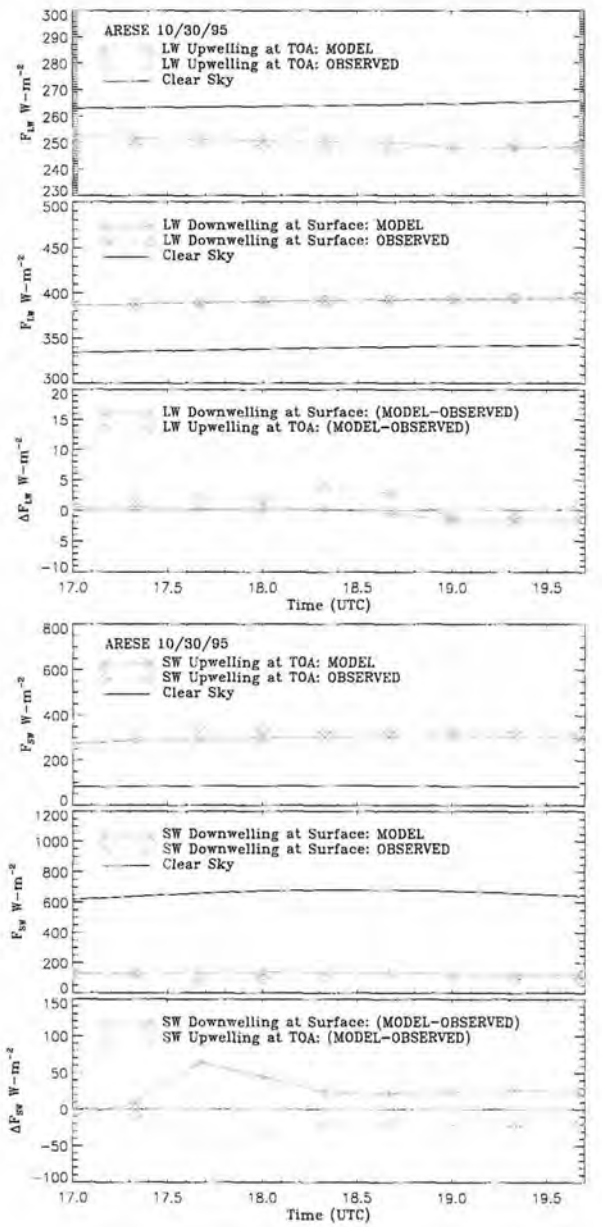

Figure 7.7: Corresponding two-stream boundary fluxes derived from forecasted and observed profiles of ARESE 10/30/95 cloud liquid/ice water contents, along with modeled clearsky values for reference.

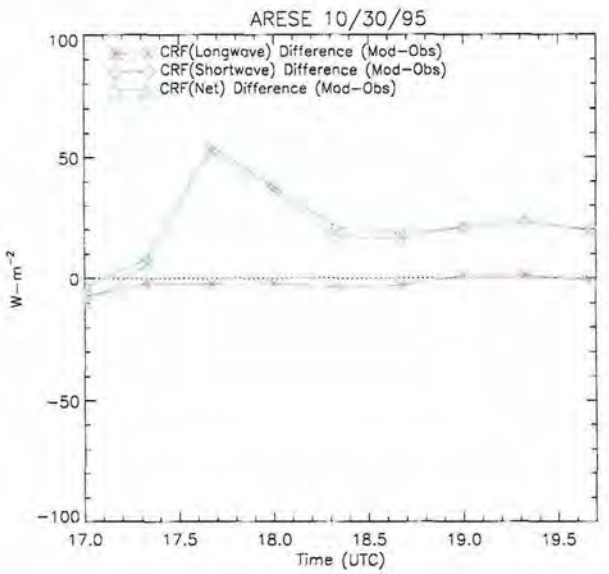

Figure 7.8: Differences between model and observed cloud radiative forcing derived from 2-stream TOA cloudy and clearsky flux results.

7.3.3 ARM-UAV (Kauai) 4/30/99

As a final example of model/observed cloud property comparisons, the data from the ARM-UAV Kauai 4/30/99 experiment was examined (recalling from Chapter 6 that the model forecast of cloud performed quite well in a spatial sense). The optical depth comparisons presented in Figure 7.9 indicated that while the trend toward increasing cloud ice content with time was captured, the forecast underestimated persistently the amount of cloud ice. Because the retrieval data were patchy up until 2300 Z (the cirrus layer had not yet advected completely into the area and the Twin Otter made a refueling stop), the focus of discussion is on the period between 2300 and 2430. Over this period, the observed cloud optical depth was nearly an order of magnitude greater than the forecast. The model verses observed water path comparison is shown in Figure 7.10, and shows better agreement than optical depth. This was again explained by the values of model effective radii, which were twice as large on average (74 μm, verses 32 μm) than the retrieved quantities. Even with this improvement, however, the mean ice water paths over the focus period were much lower (a factor of 2) than observations.

The corresponding longwave and shortwave boundary fluxes are shown in Figure 7.11, and the cloud radiative forcing computed from these fluxes is given in Figure 7.12. Over

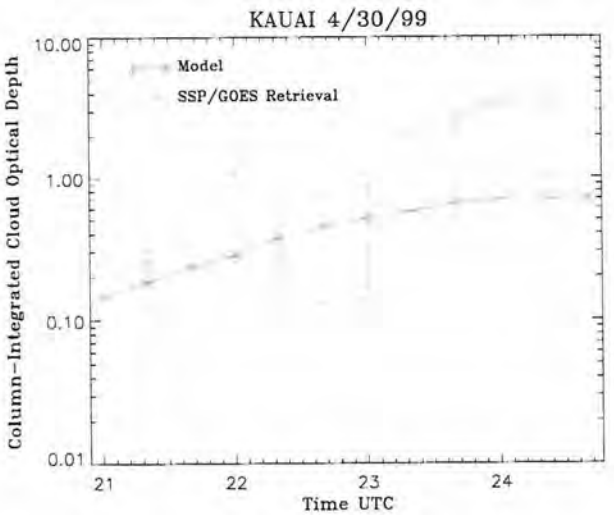

Figure 7.9: Comparison between optical depths derived from GOES/SSP measurements and those converted from model cloud water forecasts for ARM-UAV Kauai 4/30/99.

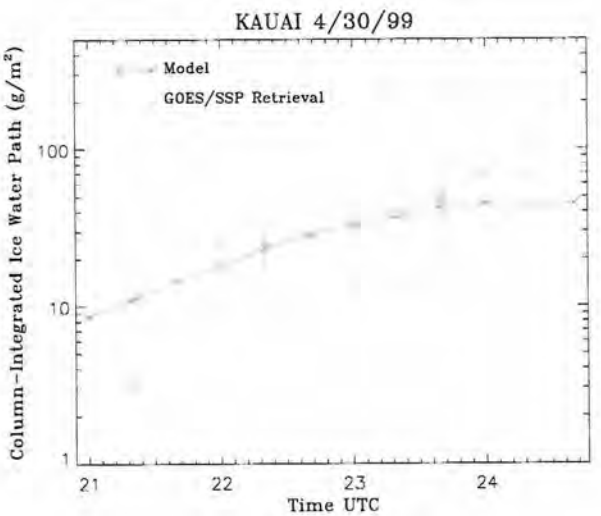

Figure 7.10: Comparison between water paths derived from GOES/SSP measurements and model forecasts for ARM-UAV 4/30/99.

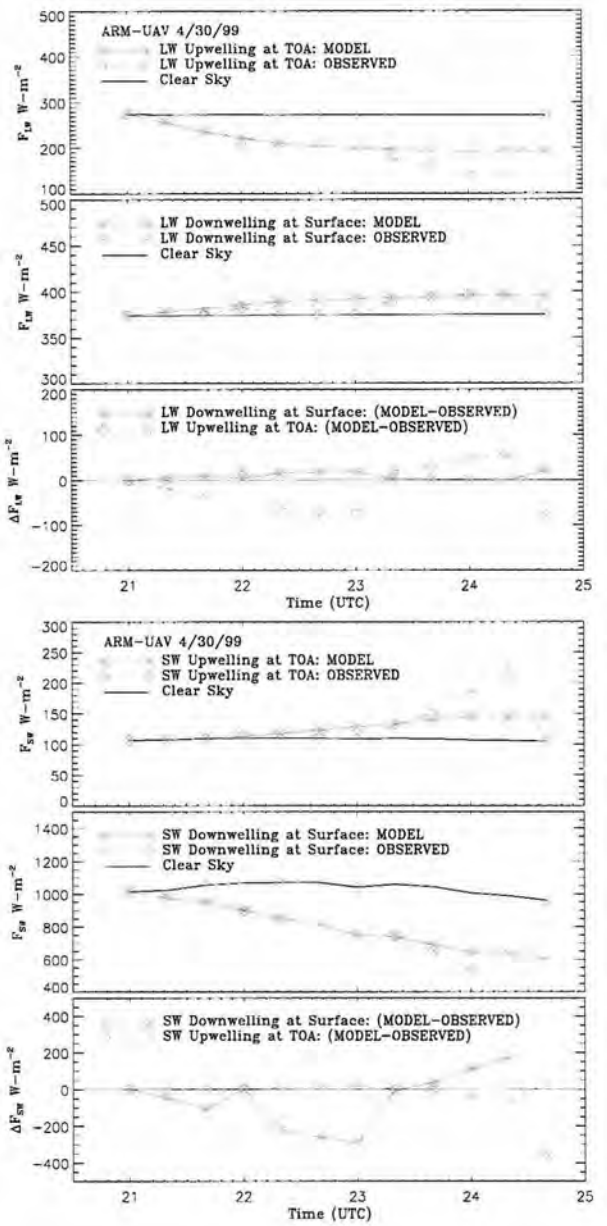

Figure 7.11: Corresponding two-stream boundary fluxes derived from forecasted and observed profiles of ARM-UAV Kauai 4/30/99 cloud liquid/ice water contents, along with modeled clearsky values for reference.

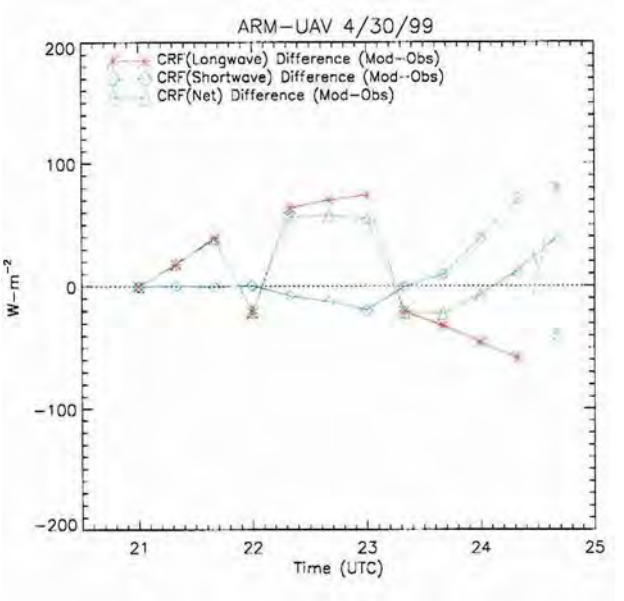

Figure 7.12: Differences between model and observed cloud radiative forcing derived from 2-stream TOA cloudy and clearsky flux results.

the focus period of these comparisons, the model was observed to underestimate the TOA outgoing longwave between 20 and 60 W m^{-2} (or roughly 11% of the clearsky value) while differences in downwelling longwave flux at the surface were minimal (similar to the cirrus of the LITE case). The strongest differences in the shortwave were found in the downwelling fluxes at the surface, where the averaged model underestimate was $\approx$10%. The CRF differences, shown in Figure 7.12, indicated model underestimates of forcing that increased with time. The divergence of agreement may have be due to an error in the available moisture, the strength of the synoptic-scale forcing, or the cloud scheme. Tying active sensor data together with other measurements capable of fully characterizing the system is therefore essential to isolating problems tied to the model cloud parameterization.

7.3.4 Ensemble results

Optical depth data from all retrieval case studies outlined in Chapters 5 and 6 were pooled together for a bulk comparison against the model forecasts. The top panel of Figure 7.13 is a scatter diagram of τ with the 1:1 correspondence line indicated. Most of these case studies involved observations of cirrus with relatively low optical depths (e.g.,

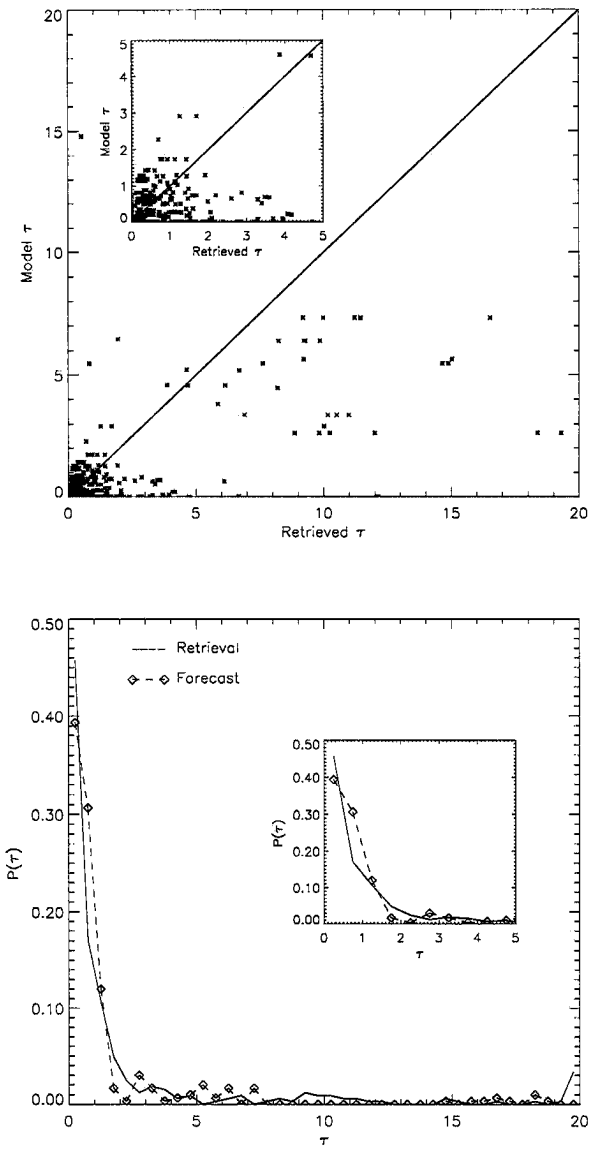

Figure 7.13: Ensemble observed vs. model optical depth scatter plot (Top) and corresponding PDF comparison for all case studies presented.

$\tau < 5.0$), and so and inset figure was included over this range. Probability density functions of optical depth for these same data are shown in the lower panel of Figure 7.13. The level of agreement, while showing significant room for improvement, does suggest that in a bulk sense the cloud optical properties produced in these shortrange forecasts fall within an order of magnitude with observed data. Considering the highly constrained nature of these comparisons, these results should not be interpreted as discouraging. Clearly, the problem at hand requires a great deal more data of this kind. Mace *et al.* (1999) begin to compile this scale of data in their characterization of cirrus from an entire year of continuous cloud radar data at the ARM-SGP site.

7.4 Relevant Applications

If model cloud water contents may be considered as representative of true cloud fields to first-order (and spatial distributions have already been demonstrated to satisfy this minimal criterion), the doors are opened to a large number of applications involving model reanalysis data. Treating the model forecast fields as virtual observations, for example, would allow for active sensor algorithm development activities (e.g., addressing cloud detectability issues in the context of the CloudSat/PICASSO ensemble system). Discussed briefly here are examples of studies that turn the problem around by generating from model forecasts of cloud distribution and content a global source of virtual active sensor data.

7.4.1 Model-derived active profiles: toward assessing the CloudSat observing system.

To date, the LITE database is our only source of global cloud profile information. The comparisons against shortrange forecasts in Chapter 5 indicated that global cloudiness tied to the atmospheric global circulation was being handled considerably well by the ECMWF cloud scheme. If the water content information contained in these realistically distributed clouds is also representative of true clouds to first order (the case studies shown in this chapter, while not demonstrating perfect agreement, would at least appear to support this criterion) then model-equivalent "LITE" profiles could be used as a head-start toward

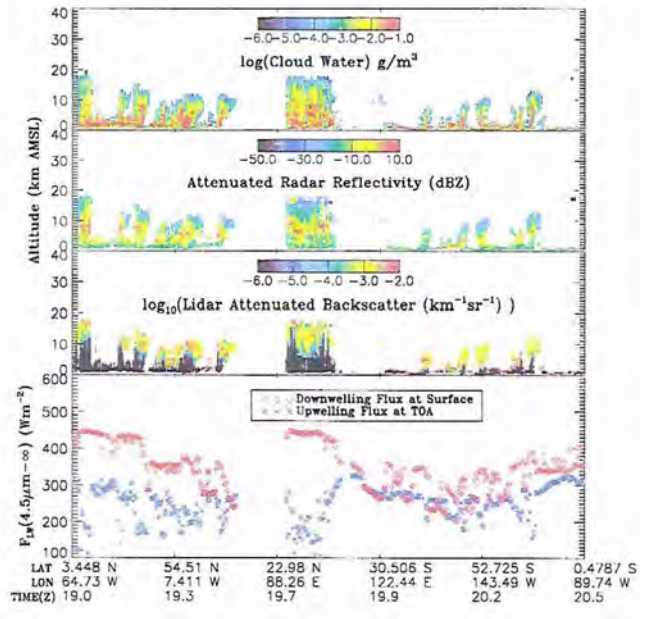

Figure 7.14: W-band radar reflectivity and 532 nm lidar backscatter simulated from a track of forecasted ECMWF cloud data (corresponding to LITE Orbit 047). The instruments are oriented in nadir mode.

understanding the utility and limitations of active data from space that has yet to become available.

As one example, model cloud water contents can be used to attenuate a radar or lidar pulse, thereby simulating the observable profile. This is demonstrated for a portion of LITE orbit 047 in Figure 7.14. The top panel shows liquid and ice water contents as provided by the model, the two center panels show the simulated radar reflectivity and lidar backscatter return (including in-cloud attenuation), and the lowest panel shows boundary fluxes computed from the same 2-stream model described above. Parameterizations for radar reflectivity and extinction for ice clouds were taken from Sassen and Liao (1996). For liquid-phase clouds, a log-normal size distribution was assumed of the form:

$$N(r) = \frac{N_T}{\sqrt{2\pi}\ln\sigma r} e^{\frac{-\ln^2(r/r_g)}{2\ln^2\sigma}}, \tag{7.5}$$

where N_T is the droplet concentration (mm^{-3}), σ is the distribution width parameter, r is the droplet radius and r_g is the geometric mean radius of the distribution. From this relationship, the liquid water content, equivalent radar reflectivity, effective radius, and

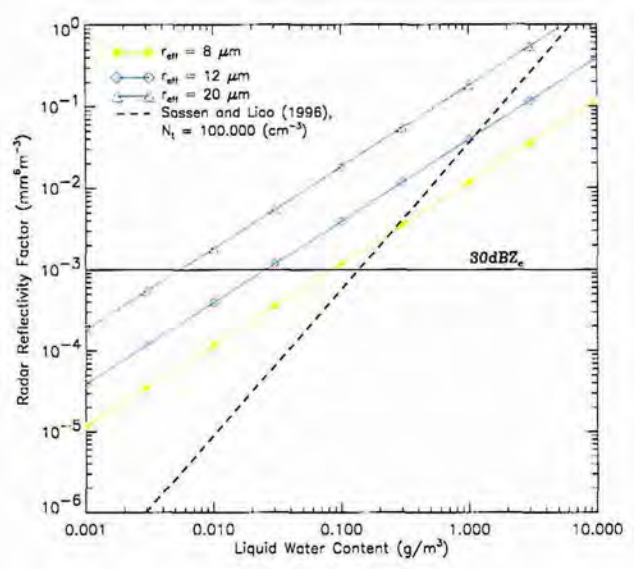

Figure 7.15: Z-LWC relationship corresponding to Equation 7.8 for varying effective radii. Shown for reference is the CloudSat -30 dBZ$_e$ sensitivity threshold. (Developed with the assistance of R. Austin)

extinction coefficient are given by

$$\text{LWC} = \frac{4}{3}\pi\rho N_T r_g^3 e^{(9/2)\ln^2\sigma} \tag{7.6}$$

$$Z_e = 64 N_T r_g^6 e^{18\ln^2\sigma} \tag{7.7}$$

$$r_{\text{eff}} = r_g e^{(5/2)\ln^2\sigma} \tag{7.8}$$

$$\sigma_{\text{ext}} = 2\pi N_T r_g^2 e^{2\ln^2\sigma}, \tag{7.9}$$

respectively, with $\sigma \approx 1.3$ approximated from several cloud distributions presented in Nicholls (1987). Solving Equation 7.7 for r_g^3 and substituting into Equation 7.8 yields a relationship between the radar reflectivity and the liquid water content in terms of the cloud effective radius. This relationship is shown for various values of r_{eff} in Figure 7.15. As physically expected, the reflectivity parameterized at a fixed value of liquid water content is higher for larger-sized particles.

Lidar backscatter (in (km-sr)$^{-1}$) was computed according to

$$\beta(z) = \frac{\sigma_{\text{ext}} k}{4\pi}, \tag{7.10}$$

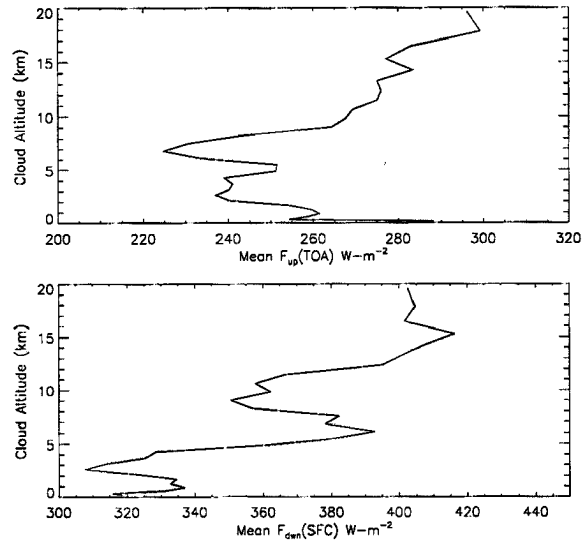

Figure 7.16: Mean boundary fluxes shown as a function of mean cloud height for all LITE orbits using ECMWF prognostic fields.

where k is the water/ice fraction-weighted backscatter to extinction ratio and z is the range in the cloud. Attenuation of the signal involved the integration of the extinction to the depth of interest (τ') and the subsequent calculation of the two-way transmission

$$\mathrm{T} = \mathrm{e}^{-2\tau'}. \tag{7.11}$$

Extinction coefficients for ice and water clouds were weighted by the representative fractions of each phase in the mixed-phase portions of the clouds:

$$\sigma_{\mathrm{ext}} = f_{\mathrm{liq}}\sigma_{\mathrm{ext}}(\mathrm{wat}) + (1 - \mathrm{f_{liq}})\sigma_{\mathrm{ext}}(\mathrm{ice}) \tag{7.12}$$

No accommodations were made for attenuation due to water vapor and oxygen in this exercise. Li *et al.* (1999) demonstrate with colocated radar observations from aircraft and surface that the attenuation suffered by nadir-mode airborne (space-borne) cloud radars is significantly less than the surface-based counterparts.

Provided a realistic profile of clouds, such model-derived quantities can prove very useful in assessing which clouds are the most radiatively important and in estimating the potential improvement to model fluxes provided by instruments of varying sensitivity. This point is illustrated further by Figure 7.16, where the mean values of upwelling TOA and

downwelling surface longwave fluxes for all 66 night-time LITE orbits listed in Appendix B are shown as a function of the mean cloud height. These heights were computed by normalizing the profile of liquid/ice water contents by the integrated water path and assigning the cloud height according to the center of mass. This simple procedure was performed for all cloud profiles, including multi-layered clouds (where the center of mass could fall in a clearsky portion of the profile). Because of the crude nature of this exercise, only the general structure of Figure 7.16 should be considered. For upwelling TOA fluxes (top panel), the highest clouds tend to be optically thin, and therefore correspond to upwelling fluxes comparable to clearsky surface or low-cloud emissions. The strongest effect was found for mid-level clouds (which included deep convection with calculated centers of mass at mid-levels). This was intuitive, as clouds with a mid-troposphere center of mass are generally of the convective (optically thick) variety. A corresponding spike at mid-levels for the downwelling surface fluxes (lower panel of Figure 7.16) was also noted, with an additional peak associated with the insulator properties of upper-tropospheric cirrus. Low clouds, having temperatures close to those of the surface, were seen to influence minimally the surface downwelling longwave flux (with values comparable to the TOA longwave flux for the low and optically-thin high clouds in the upper panel of Figure 7.16). The local minima near 10-km may be attributable to cases where multiple cloud layers (e.g., cirrus overlying a lower tropospheric cloud), where a compromise between the small effects of lower clouds and larger effects of upper cloud is realized.

7.4.2 Model-based cloud detectability applications

An active area of research relevant to space-borne active remote sensing is determining at what level of precision clouds must be detected to ensure a desired level of accuracy in model atmospheric fluxes. Here, the model clouds can serve as a realistic test-bed for this assessment, provided again that the model cloud distribution and water content are realistic at least to first order. Figure 7.17 depicts a portion of the forecasted LITE profile along Orbit 073 as detected by various thresholding levels of a W-band radar and a 532 nm lidar. Attenuation of the active signals were considered as described above, and accounted for for an under-detection bias in the lowest cloud layers (corresponding to

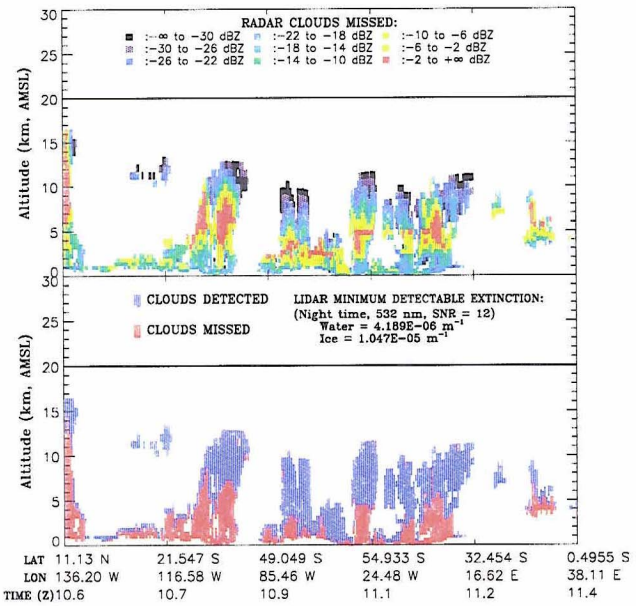

Figure 7.17:

deep convection) to varying degrees in both instruments. Thresholds for the radar were defined by reflectivity (in dBZ_e, and thresholds for the lidar instrument were taken from specifications for PICASSO. The radar detection (upper panel) indicated that optically thin, small-particle cirrus near the cloud tops were often missed (e.g., the 11 to 13 km cirrus near 10.65 Z, whereas these clouds were readily detected by the lidar. Conversely, the higher extinction associated with the lidar translated to a considerable under-detection of cloud that was captured by the radar.

The detection problem can be looked at in a statistical sense by computing the height-dependent frequency of cloud occurrence as detected by the instruments verses the that of true cloud field. This is illustrated in Figure 7.18, using an MDS of -26 dBZ_e for the radar and the PICASSO threshold for the lidar. In these simulations, the overall distribution of cloud heights estimated by the radar was superior to the lidar, owing to its ability to penetrate and hence detect more frequently the optically thick clouds residing at middle and lower levels. Figure 7.19 shows the fraction of cloud detected by each instrument with respect to the true (model field) distribution. An improvement in detection of the high-altitude cirrus was achieved by the lidar at the expense of underestimating severely the number of middle and lower-level clouds present. It would, however, be erroneous

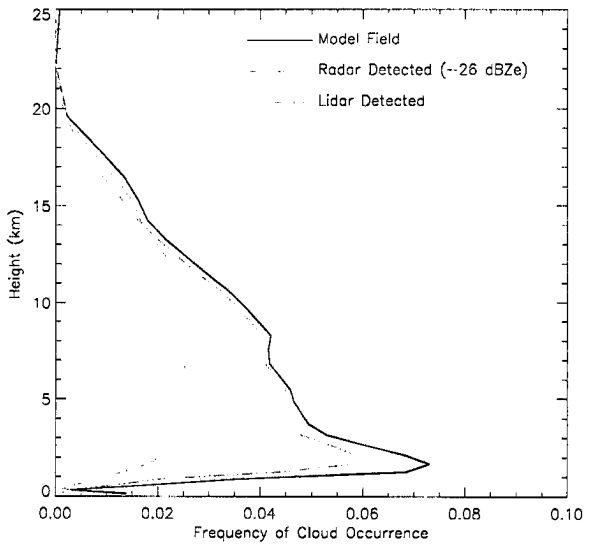

Figure 7.18: Frequency of lidar/radar cloud detection as a function of height for all 66 LITE night-time orbits using along-track ECMWF forecasts of cloud water and distribution fields.

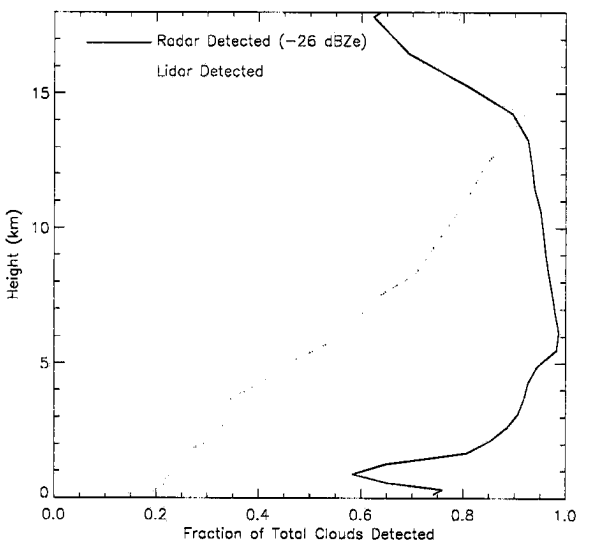

Figure 7.19: Fraction of total cloud detected as a function of height corresponding to Figure 7.18.

to conclude that the lidar is therefore an inferior instrument, especially when considering the global pervasiveness and radiative importance of optically thin (to sub-visual, e.g. $\tau \approx 0.02$) cirrus clouds that often go undetected by the W-band radar. A balance between sensitivity and attenuation must always be considered in the context of the problem at hand.

7.5 Summary

This chapter called upon the retrieval materials presented earlier for the purpose of validating ECMWF cloud microphysics. While the composite cloud-cover/microphysics study presented over the last two chapters indeed scratches only the surface of the work that needs to be done in the area of model cloud validation (and ultimately, assimilation of these data into the model initialization fields), it offers an outline for proceeding toward a more extensive undertaking. Further, it sought to provide a flavor for the great wealth of potential validation data that exists already (e.g., within the ARM archives)–waiting to be exploited for these very purposes.

To compare between model and observed cloud properties, conversions between liquid/ice water content, cloud optical depth, and radar reflectivity were performed after averaging appropriately the observations to model spatial/temporal resolution. To account in part for sampling inconsistencies between the point/track and areal data, a technique following Jakob and Klein (1999) that enables distributions of prognostic cloud parameters to be computed from a single gridbox and cloud fraction was used. To gain insight on differences between model and observed cloud radiative forcing, shortwave and longwave boundary fluxes were computed from profiles of model and retrieved cloud liquid/ice water contents input to a 2-stream radiative transfer code. The ensemble results were too sparse and variable to provide a meaningful assessment of biases. However, they demonstrated that the forecasted model fields of cloud liquid and ice water contents were, to first order, representative of retrieval-derived quantities.

Combining this result with the spatial results from Chapter 5 suggested that NWP reanalysis data may in fact provide more than simply diagnostic utility. Examples were

presented where the model clouds was considered as virtual measurements for the purpose of studying detectability by hypothetical space-borne active sensors, thereby serving as an antecedent source of detailed global cloud water content profile data to CloudSat and Picasso algorithm development where none had existed. In turn, observations and products derived from these future platforms will serve to improve upon the existing NWP cloud schemes. In this way, a symbiotic relationship is seen to emerge between model development and remote-sensing. This is argued to be the key relationship which must be cultivated now and reinforced into the future; serving to focus the best and brightest ideas of remote sensing and modeling upon a common interest.

Chapter 8

SUMMARY AND CONCLUSIONS

This dissertation, while ostensibly broad in scope, sought to address specific issues concerning the use of active remote sensors in the the atmospheric sciences. Namely, active sensor data were enlisted to improve our understanding of clouds in terms of their spatial and temporal distributions, their optical properties, and our ability to capture cloud and cloud processes in GCMs. The instruments themselves are not new, but then neither was the wheel when Henry Ford designed the first Model-T automobile. That is to say, it is *how* the technology is applied that matters most. This dissertation attempted in its own right to apply active sensors in a novel way: first, within a retrieval method tailored to reveal their quantitative benefits to passive retrievals, and then for a global validation of NWP cloud cover.

Only now are we beginning to realize the ways our own actions (with the progeny of Henry Ford's creation paying no small contribution here) can influence our environment in adverse and potentially harmful ways. The improvement of our grasp of the cloud link to the hydrological cycle and planetary energy balance is a significant step toward understanding how tomorrow's climate will behave in response to the external forcing we impose upon it today. A popular contemporary view on the subject of global warming is that the restoring (negative) feedback of clouds in response to greenhouse warming renders mute the entire topic. What has been overlooked altogether by this reasoning is the inherent link between changes in cloud cover changes and the atmospheric circulation. An infinite number of climate states may conspire to produce the same "globally-averaged temperature" coronated as the *de facto* metric of the greenhouse effect. Consequently, a constant globally-averaged temperature arising from cloud radiative responses may yet

spell agricultural catastrophe in the wake of even minor shifts in climate circulations. That this hypothesis has been formulated during a time when no definitive understanding of even the most fundamental cloud distribution and optical responses to external forcing exists renders it remarkably short-sighted. Clearly, it has become our charge to act as responsible stewards to this planet, the place that our own descendents will call "home" for millennia to come. A more detailed depiction of the climate signal flow diagram, including those feedbacks attributed to cloud processes, is a necessary step toward assuring educated policy decisions in the future.

8.1 Summary and Results

A major component of this dissertation was the development of a technique for retrieval of cloud optical properties using actively-sensed cloud height estimates to complement traditional passive radiometer (e.g., radiance, brightness temperature) measurements. The forward model component of the retrieval, presented in Chapter 2, was founded on the interaction principle and doubling/adding theory for plane-parallel media, and was verified against independent Van de Hulst, DISORT and Monte Carlo benchmarks. It attempted to capture an extensive component of the physical atmosphere by including atmospheric gaseous absorption, aerosol, detector response functions, and a computationally efficient accommodation for highly-asymmetric scattering phase functions. This forward model was designed to be versatile, such that a wide array of instruments could be accommodated in a single retrieval.

The basic philosophy of retrieval theory (the combination of the forward model and the estimation problem) and application of these principles to the problem at hand was considered in Chapter 3. The estimation component of this problem, the rationale for using the optimal estimation theory of Rodgers (1976), and its advantages from the standpoint of providing important error-diagnostic parameters were also presented in detail. A strong point of this estimation approach is its explicit assignment of error for each measurement and component of the model uncertainty, thereby providing a valuable quantitative assessment of the total retrieval uncertainty with all contributions accounted for. By virtue

of the forward model, the general retrieval is adaptive; with the ability to assimilate a potentially large number of instruments including active, passive, and model data. Having outlined the two main components of the retrieval, a description of their implementation from an operational perspective was provided as a guideline for reproduction of these retrievals.

A series of sensitivity studies were performed using the forward model described above. This discussion was intended to familiarize the reader with the basic tenets and considerations for cloud remote sensing in the scattering, absorbing, and emitting atmosphere, provide a short literature background on what has already been done in the area of cloud retrievals, and specifically to illustrate which (and over what ranges) optical properties were retrievable using the forward model developed in the previous chapter. The passive instruments (e.g., GOES Imager, SSP) used in the retrievals were introduced and cloud radiative properties specific to the spectral bandwidths of their detectors (channels) were discussed. Techniques for both day-time and night-time retrievals and the advantages and limitations inherent to both were presented as a launching point into the discussion of how accurate cloud boundary information from active sensors could lead to a significant improvement in retrieval accuracy. The uncertainties tied to the forward model and the measurements were examined, and techniques for combining them into the Rodgers model/measurement error covariance matrix was outlined.

Eleven retrieval case studies using the retrieval method developed in Chapters 2-4 were examined to demonstrate quantitatively the advantages of using active sensor cloud profile information in the retrieval of τ and r_{eff}. A supplemental discussion of cloud height estimation using passive-only (and active) techniques was provided as background for the comparisons between retrievals with and without active cloud heights. The diversity of active sensor platforms employed, ranging from surface to satellite, illustrated the versatility of the retrieval. A wide array of cases were processed in anticipation of applying their results to NWP model validations. In each case study, the retrieved values of τ and r_{eff} were presented along with a breakdown of the errors incurred from the forward model, measurements and Kernel function sensitivity according the Rodgers parameters,

and comparisons against the passive-only retrievals were also made. Whenever available, retrievals based on independent measurements and/or techniques were used as checks against the current method. In a brief excursus, active sensors deployed in field programs were shown to be of value as an antecedent source of information for space-borne cloud radar algorithm development.

Chapter 6 shifted gears to a discussion of active sensors applied to the validation of numerical weather prediction models. For this study, a collaborative effort with ECMWF was organized with the principle goal being comparisons of short-range forecasts against observations from the extensive LITE database. This represented a first opportunity to perform a validation of a single global forecast of cloud cover in the vertical using active remote sensor data. A statistical analysis similar to an analogous surface-based study done by Mace *et al.* (1998) was adopted for assessment of the along-track cloud cover forecasting performance. In addition to the full-track analysis, these statistics were subdivided into contributions from the Tropics, extra-Tropics, and low-, middle-, and high-cloud regimes. Care was taken when assembling these statistics to account for the limitations of the LITE data in terms of pulse stretching and particularly pulse attenuation. Owing to the ill-posed sampling problem arising from 2-D active sensor cross sections and 3-D model gridbox data, an attempt to mitigate in part these uncertainties was proposed. This involved computing a pseudo-cloud fraction for the LITE observations, weighting all statistics according to the density of LITE shots in the model gridboxes, and weighting of false alarm penalties by the model and pseudo- cloud fractions. The statistical results from both methods were presented to form a lower and upper bound on the overall model performance. In addition to "snap-shot" comparisons using LITE data, more traditional comparisons of multi-time ECMWF forecasts at a single model gridbox (DDH) were done for the field program case studies of Chapter 5. This rounded off the cloud cover study by providing an opportunity to asses the model's ability to represent the evolution of cloud systems in both space and time over an extended period.

In an attempt to bring together the observational and modeling components of this research under the common theme of active sensor applications, Chapter 7 called upon

the retrieval results of Chapter 5 and the cloud cover validations of Chapter 6 to complete the assessment of model cloud forecasts from the cloud-content perspective. As few GOES τ, r_{eff} retrieval opportunities were available during 1994 (GOES-8 was not yet in operational mode and GOES-7 lacked the useful 3.9 μm window channel) the study enlisted also results from the field program case studies presented in Chapter 5. The protocols for converting model and measurements to comparable fields was treated in terms of both physical and empirical approaches. The method of rebinning retrieved optical properties to model resolution was outlined, and the 2-D/3-D sampling problem was accounted for by computing sub-gridscale distributions of model cloud properties based on the grid-mean value and the model cloud fraction. Selected case studies were presented for comparisons of cloud optical depth, boundary fluxes (using a broadband shortwave/longwave 2-stream radiaitve transfer code), and cloud radiative forcing. These represented highly-constrained comparisons which tested the spatial, temporal, and microphysical components of the model forecast. Ensemble statistics for these comparisons were also presented. The findings of the composite validation raised immediately the possibility of using these NWP globally-forecasted cloud products as a source of virtual observations to various research activities. This concept was exemplified by converting the model cloud fields matched to LITE orbits into equivalent fields of radar reflectivity and lidar backscatter. These in turn, under the assumption of realistic model cloud water contents, were used to address cloud detectability concerns in the context of the CloudSat mission. In this way, a clear link was formed between the interests of the modeling and measurement communities; an ideal which embodies the heart of this research.

The main results compiled over the course of this research are summarized as follows:

- An important product of this research (and presented in Miller *et al.*, 1999) was the development of a new cloud property retrieval method that applies active sensor cloud height data to a sophisticated and versatile forward model and an optimal estimation approach following Rodgers (1976). The latter provides retrieval performance diagnostics which take account for the uncertainties tied to measurements,

components of the forward model, and *a priori* information, providing a convenient assessment of both the accuracy and quality of the information retrieved. The forward model was designed to be adaptive (with respect to observing system components), with the ability to model a wide array of passive remote sensors operating throughout the optical spectrum. Specific examples applied to GOES, SSP, and MAS multi-spectral measurements were shown.

- By adding an additional constraint to the retrieval, the inclusion of active sensor information was shown to reduce considerably the uncertainties of cloud optical depth and effective radius. The most significant ($> 20\%$) improvements were achieved for retrievals of thin cirrus at night, where IR-only methods often encounter the most difficulty in cloud height estimation. Daytime retrievals, which involve solar reflection measurements and rely less on the thermal properties of the cloud, were improved only minimally (correct placement in the Rayleigh and aerosol profile) by the active constraints. There remained considerable (25-50%) uncertainty in the effective radius retrievals, owing to corresponding uncertainties in the scattering phase function. This was especially true of optically thin ($\tau < 1.0$) clouds, where single-scattering contributions are significant. Results were shown to be consistent with independent measurements and the general findings of previous investigators.

- The utility of active sensors operating on the space platform has been illustrated by the ECMWF/LITE cloud validation study (see also, Miller *et al.*, 1999). Strong positive correlations between short-range forecasts of cloud cover using the Tiedke (1993) prognostic scheme and observations were demonstrated in 66 night-time orbits of LITE. Ensemble-orbit statistics place hit rates between 75 and 90%, threat scores between 45 and 75%, probabilities of detection at near 80%, and false alarm rates between 10 and 45%, with the best-case and worst-case bounds of these ranges determined by the weighted and non-weighted comparison approaches, respectively.

- Comparisons of model vs. retrieved cloud content (limited in scope by the case studies examined to primarily cirrus clouds), although agreeing typically within first

order, suggested room for considerable improvement. These discrepancies imply that NWP models cannot yet capture the realistic radiative feedback roles of cloud in the atmosphere in a general sense. The level of agreement currently exhibited should nonetheless be regarded as encouraging, with strong prospects for improvement through continued and more extensive active-sensor/model validation activities. In particular, the research highlighted the immediate windfall of a space-borne active-instrument observing system to the validation and further development of cloud parameterizations in GCMs.

- The results indicated that ECMWF global forecasts of cloud have already achieved a level of realism which may allow for their limited application as a source of virtual observations to research.

No significant improvements to predictions of climate change can be realized without first closing the feedbacks which tie clouds to radiation, humidity, and the atmospheric circulation. The modeling community cannot approach this problem without the support of detailed observational cloud database. The needs of the modelers should thus serve as a guideline to remote sensing orchestrations, and the modeling community must in turn make a concerted effort to make optimal use of these data and communicate effectively the nature of additional observations needed--thereby driving the technological evolution of the remote sensing community. This is the symbiotic relationship that this research has sought to highlight, here in the context of the active sensor. As we enter the 21st century, a new observing platform suite that includes active sensors similar to those presented in this research will provide detailed information essential to meeting this objective. To gain an historical perspective on observations directed toward developing an understanding for the global cloud climatology, we recognize CloudSat as representing the leap from ISCCP (i.e., multi-spectral passive) based methods to a nadir active+passive system which contains information on vertical structure. At this stage, some assumption on the horizontal extent of cloud outside the cross section must be made for application of these data in model assimilation or cloud climatology studies. The next step in this transition is the

active/passive *scanning* system which will provide a true three-dimensional observation of clouds (and thereby resolving the sampling problems encountered in this research) as opposed to the CloudSat "cat-scan." The enormous stream of observational data available for ingestion by global NWP models at this point will almost certainly shift the onus of progress back to the models and their ability to identify and assimilate the most important information in a time-efficient way. There is little doubt that Lewis Fry Richardson (regarded as the father of modern-day numerical weather prediction) would have found this an enviable dilemma.

8.2 Future Work

In addressing points relevant to the fate of this particular research, it is first noted that despite efforts to include several important aspects of the observing system the handling of cloud in the forward model remains crude with respect to the real world. Here, work in progress includes the development of water/ice crystal phase function parameterizations to better represent the complex behaviors of cloud scattering above and beyond that approximated by the double Henyey-Greenstein parameterization. With the availability of 3-dimensional active instrument profiles, areal (as opposed to flight track) retrievals will require the inclusion of horizontal transport either to capture cloud horizontal inhomogeneity or quantify the errors attributed to the higher dimensional nature of the transport. With the the increasing number of proposed environmental satellites which include active sensors (both radar and lidar) as an integral component to their observing system payloads, consideration for improvements to cloud property retrievals is timely.

In connection to the active-sensor model validation materials, work in progress includes a collaborative agreement between CSU and the DAO at NASA/GSFC to conduct an exploratory assessment of the Goddard Earth Observing System v. 3 (GEOS-3) global model similar in scope to the ECMWF/LITE study, with an additional emphasis placed on ARM observations in the TWP and an eye toward developing techniques for future assimilation of these active sensor data at the operational level. To better understand what other information (besides cloud profiles) exists in space-borne lidar, an unsolicited NASA proposal (C.M.R. Platt, principle investigator) to develop/refine the retrieval of high cloud

properties from LITE data is also currently underway. Finally, numerous experiments tied to the antecedent validation of algorithms to be implemented in the post-processing of CloudSat data have been proposed, and will offer additional opportunities to build upon the model/retrieval validation database presented in this dissertation.

In 1861, Admiral Robert FitzRoy (British naval officer and meteorologist) provided in his "storm warning service" the first synoptic forecasting tool for the maritime industry. Because of its limited coverage and sparse observational network, it suffered many failures and FitzRoy soon came under the public fire as a charlatan to his field. Overcome with grief by these brazen and increasingly personal beratements, a beleaguered FitzRoy chose to end his own life and all the misery that science had brought to it. The general public, of course, did not understand the revolutionary significance of that first step and where it might one day lead. Today, we all benefit from the initiative shown by FitzRoy and others who have assumed pro-active roles in our field. By virtue of increased observational technology and a growing bed of knowledge, we are now equipped to undertake yet another daunting challenge; one which will lead ultimately to an understanding of cloud processes sufficient to capture and model their dynamic influences on the climate system. The space-borne active sensor will play no small part in affording us this opportunity.

REFERENCES

Arakawa, A., and W. H. Schubert, 1974: The interactions of a cumulus cloud ensemble with the large-scale environment. Part I. *J. Atmos. Sci.*, **31**, 674-701.

Arking, A., and J. D. Childs, 1985: Retrieval of cloud cover parameters from multispectral satellite images. *J. Climate Appl. Meteor.*, **24**, 322-333.

Baran, A. J., S. J. Brown, J. S. Foot, and D. L Mitchell, 1999a: Retrieval of tropical cirrus thermal optical depth, crystal size and shape using a dual view instrument: A tropical cirrus anvil case. *J. Atmos. Sci.*, **56**, 92-110.

—, P. D. Watts, and P. N. Francis, 1999b: Testing the coherence of cirrus microphysical and bulk properties retrieved from dual-viewing multispectral satellite radiance measurements. *J. Geophys. Res.*, **104**, No. D24, 31673-31683.

Baucom, J., 1998: Imager visible channel noise calibration. NOAA/NESDIS Report # IS2001, Phase ACT, 4pp.

Bohren, C. F., and D. R. Huffman, 1983: *Absorption and scattering of light by small particles.* (John Wiley & Sons), p. 309.

Bryson, W. R., 1978: Cloud height determinations from geosynchronous satellite images. Ph.D. Dissertation, Univ. of Wisc.-Madison. Microfilms Inter. 7817097, 91 pp.

CERES Science Team, 1995: Clouds and the Earth's radiant energy system (CERES) algorithm theoretical basis document. *NASA Ref. Publication 1376*, Vol. 3, 242pp.

Cess, R. D., G. L. Potter, J. P. Blanchet, G. J. Boer, M. Déqué, V. Dymnikov, V. Galin, W. L. Gates, S. J. Ghan, J. T. Kiehl, A. A. Lacis, H. Le Treut, Z. -X. Li, X. -Z Liang, B. J. McAvaney, V. P. Meleshko, J. F. B. Mitchell, J. -J. Morcrette, D. A. Randall, L. Rikus, E. Roeckner, J. F. Royer, U. Schlese, D. A. Sheinin, A. Slingo, A. P. Sokolov, K. E. Taylor, W. M. Washington, R. T. Wetherald, I. Yagai, and M. -H. Zhang, 1990: Intercomparison and interpretation of climate feedback processes in 19 atmospheric general circulation models. *J. Geophys. Res.*, **95**, 16601-16615.

Chandrasekhar, S., 1960: *Radiative Transfer*, (Dover, New York).

Coakley, J. A., Jr. and Davies, R., 1986: The effect of cloud sides on reflected solar radiation as deduced from satellite observations. *J. Atmos. Sci.*, **43**, No. 10, 1025-1035.

Couch, R. H., and Coauthors, 1991: Lidar In-space Technology Experiment (LITE): NASA's first In-Space lidar system for atmospheric research. *Opt. Eng.*, **30**, 88-95.

Curran, R. J., and M. -L. C. Wu, 1982: Skylab near-infrared observations of clouds indicating supercooled liquid water droplets. *J. Atmos. Sci.*, **39**, 635-647.

Dave, J. V., and B. H. Armstrong, 1970: Computations of high-order associated Legendre polynomials. *J. Quant. Spect. Rad. Trans.*, **10**, 557-562.

Deirmendjian, D., 1969: *Electromagnetic scattering on spherical polydispersions* (Elsevier, New York).

Doutriaux-Boucher, M., J. -C. Buriez, G. Brogniez, L. Labonnote, and A. J. Baran, 2000: Sensitivity of retrieved POLDER directional cloud optical thickness to various ice particle models. *Geophys. Res. Lett.*, **27**, No. 1, 109-112.

Dowling, D. R., and L. F. Radke, 1990: A summary of the physical properties of cirrus clouds. *J. Appl. Meteor.*, **29**, 970-978.

Duda, D. P., 1994: *Macrophysical and microphysical influences on radiative transfer in two dimensional marine stratus.* Ph.D. Dissertation, Colo. State Univ., Dept. of Atmos. Sci., Fort Collins, 202pp.

Drummond, C. K., *A novel k-distribution parameters development system and its application to MAS/SUCCESS channels* M.Sc. Thesis, Colo. State. Univ., Dept. of Atmos. Sci., Fort Collins, 84pp.

Engelen, R. J., and G. L. Stephens, 1997: Infrared radiative transfer in the 9.6μm band: application to TOVS ozone retrieval. *J. Geophys. Res.*, 6929-6940.

—, and —, 1998: Characterization of water vapour retrievals from TOVS/HIRS and SSM/T-2 measurements. *Quart. J. Roy. Meteor. Soc.*, (In Press).

Greenwald, T. J., and G. L. Stephens, 1988: Application of doubling-adding radiation model to visibility problems. *CIRA Report*, 89pp.

Hammersley, J. M., and D. C. Handscomb, 1964: *Monte Carlo Methods.* (Wiley, New York), 178pp.

Hansen, J. E., and J. B. Pollack, 1970: Near-infrared light scattering by terrestrial clouds. *J. Atmos. Sci.*, **27**, 265-281.

—, and L. D. Travis, 1974: Light scattering in planetary atmospheres. *Space Sci. Rev.*, **16**, 527-610.

Hasler, A. F., 1981: Stereographic observations from geosynchronous satellites: an important new tool for the atmospheric sciences. *Bull. Amer. Meteor. Soc.*, **62**, 194-212.

Harrison, E. F., P. Minnis, B. R. Barkstrom, V. Ramanathan, R. D. Cess, and G. G. Gibson, 1990: Seasonal variation of cloud radiative forcing derived from the Earth Radiation Budget Experiment. *J. Geophys. Res.*, **95**, No. D11, 18687-18703.

Heidinger, A. K., and G. L. Stephens, 1998: *Nadir sounding of clouds and aerosols in the O_2 A-band.* Ph.D. Dissertation, Colo. State Univ., Dept. of Atmos. Sci., Fort Collins, 225pp.

Heymsfield, A. J., and L. J. Donner, 1990: A scheme for parameterizing ice-cloud water content in general circulation models. *J. Atmos. Sci.*,, **47**, 1865-1877.

Inoue, T., 1985: On the temperature and effective emissivity determination of semi-transparant cirrus clouds by bi-spectral measurements in the 10μm window region. J. Met. Soc. Japan, **63**, 88-89.

Jakob, C., 1994: The impact of the new cloud scheme on ECMWF's integrated forecasting system (IFS), *Proc. of ECMWF/GEWEX Workshop on Modelling, Validation and Assimilation of Clouds,* 277-294.

—, and S. A. Klein, 1999: The role of vertically varying cloud fraction for the parameterization of microphysical processes in the ECMWF model. *In Preparation.*

—, 1999: Ice clouds in numerical weather prediction models- progress, problems and prospects. Book submission pending, 16pp.

—, 1999: Cloud cover in the ECMWF reanalysis. *J. Climate,*, **12**, 947-959.

Johnson, L. W., and R. D. Riess, 1982: *Numerical Analysis*, Addison-Wesley, 448pp.

Joseph, J., W. J. Wiscombe, and J. A. Weinman, 1976: The delta-Eddington approximation for radiative flux transfer. *J. Atmos. Sci.*, **33**, 2452-2459.

King, M. D., Y. J. Kaufman, W. P. Menzel, and D. Tanré, 1992: Remote sensing of cloud, aerosol and water vapor properties from the moderate resolution imaging spectrometer (MODIS). *IEEE Trans. Geoscience and Remote Sensing*, **30**, 2-26.

Kleepsies, T. J., 1995: The retrieval of marine stratiform cloud properties from multiple observations in the 3.9-μm window under conditions of varying solar illumination. *J. Appl. Meteor.*, **34**, 1512-1524.

Klein, S. A., and C. Jakob, 1998: Validation and sensitivities of frontal clouds simulated by the ECMWF model. *Mon. Weather Rev.*, In press.

Kosarev, A. L., and I. P. Mazin, 1989: Empirical model of physcial structure of the upper level clouds of the middle latitudes. *Radiation Properties of Cirrus Clouds*, Nauka, 29-52.

Kratz, D. P., 1995: The correlated k-distribution technique as applied to the AVHRR channels. *J. Quant Spectrosc. Radiat. Transfer*, **53**, 501-517.

Lau, N. -C., and M. W. Crane, 1995: A satellite view of the synoptic-scale organization of cloud properties in midlatitude and tropical circulation systems. *Mon. Weather Rev.*, 1984-2006.

Liao, L., and K. Sassen, 1994: Investigation of relationships between Ka-band radar reflectivity and ice and water contents. *Atmos. Res.*, **34**, 231-238.

Liou, K. -N., 1992: *Radiation and cloud processes in the atmosphere* (Oxford University Press, New York) 487pp.

—, and T. Sasamori, 1975: On the tranfer of solar radiation in aerosol atmospheres. *J. Atmos. Sci.*, **32**, 2166-2177.

–, S. C. Ou, Y. Takano, F. P. J. Valero, and T. P. Ackerman, 1990: Remote sounding of the tropical cirrus cloud temperatures and optical depth using 6.5 and 10.5 μm radiometers during STEP. *J. Appl. Meteor.*, **29**, 716-726.

Mace, G. G., C. Jakob, and K. P. Moran, 1998: Validation of hydrometeor prediction from the ECMWF model during winter season 1997 using millimeter wave radar data. *Geophys. Res. Lett.*, **25**, 1645-1648.

Mace, G. G., E. E. Clothiaux, and T. P. Ackerman, 1999: The composite characteristics of cirrus clouds; bulk properties revealed by one year of continuous cloud radar data. *J. Climate*, (In Press).

Marchuk, G. I., G. A. Mikhailov, M. A. Nazaraliev, R. A. Darbinjan, B. A. Kargin, and B. S. Elepov, 1980: *The Monte Carlo methods in atmospheric optics.* (Springer-Verlag, New York), 208pp.

Marks, C. J., and C. D. Rodgers, 1993: A retrieval method for atmospheric composition from limb emission measurements. *J. Geophys. Res.*, **98**, No. D8, 14939-14953.

McClatchey, F. A., *et al.*, 1972: *Optical Properties of the Atmosphere* Air Force Cambridge Research Laboratories,AD-753 075, 24pp.

McCormick, M. P., D. M. Winker, E. V. Browell, J. A. Coakley, C. S. Gardner, R. M. Hoff, G. S. Kent, S. H. Melfi, R. T. Menzies, C. M. R. Platt, D. A. Randall, and J. A. Reagan, 1993: Scientific investigations planned for the Lidar In-Space Technology Experiment (LITE). *Bull. Amer. Meteor. Soc.*, **74**, No. 2, 205-214.

McKee, T. B., and S. K. Cox, 1974: Scattering of visible radiation by finite clouds. *J. Atmos. Sci.*, **31**, 1885-1892.

Menzel, W. P., W. L. Smith, and T. R. Stewart, 1983: Improved cloud motion wind vector and altitude assignment using VAS. *J. Climate Appl. Meteor.*, **22**, 377-38.

Menzel, W. P., and J. F. W. Purdom, 1994: Introducing GOES-I: the first of a new generation of geostationary operational environmental satellites. *Bull. Amer. Meteor. Soc.*, **75**, No. 5, 757-781.

Miller, S. D., G. L. Stephens, and A. C. M. Beljaars, 1999: A validation survey of the ECMWF prognostic cloud scheme using LITE. *Geophys. Res. Lett.*, **26**, No. 10, 1417-1420.

—, and G. L. Stephens, 1999: Multiple scattering effects in the lidar pulse stretching problem. *J. Geophys. Res.*, **104**, No. D18, 22205-22219.

—, C. K. Drummond, G. L. Stephens, A. K. Heidinger, and P. T. Partain, 1999: A multi-sensor satellite cloud property retrieval scheme. *J. Geophys. Res.*, In press, 30pp.

—, 1999: Physical decoupling of the GOES daytime 3.9-μm channel thermal emission and solar reflection components using total solar eclipse data. *Int. J. Remote Sens.*, In press, 27pp.

Minnis, P., P. W. Heck, D. F. Young, 1993: Inference of cirrus cloud properties using satellite-observed visible and infrared radiances. II–Verification of theoretical cirrus radiative properties. *J. Atmos. Sci.*, **50**, No. 9, 1305-1322.

Minnis, P., D. F. Young, K. Sassen, J. M. Alvarez, and C. J. Grund, 1990: The 27-28 October 1986 FIRE IFO cirrus case study: cirrus parameter relationships derived from satellite and lidar data. *Mon. Wea. Rev.*, **118**, 2402-2425.

—, K. -N. Liou, and Y. Takano, 1993: Inference of cirrus cloud properties using satellite-observed visible and infrared radiances. Part I: parameterization of radiance fields. *J. Atmos. Sci.*, **50**, No. 9, 1279-1304.

—, P. W. Heck, and D. F. Young, 1992: Inference of cirrus cloud properties using satellite-observed visible and infrared radiances. Part II: verification of theoretical cirrus radiative properties. *J. Atmos. Sci.*, **50**, No. 9, 1305-1322.

Morcrette, J. -J., 1990: Evaluation of model-generated cloudiness: Satellite-observed and model-generated diurnal variability of brightness temperature. *Mon. Weather Rev.*, **119**, 1205-1224.

—, and Y. Fouquart, 1986: The overlapping of cloud layers in shortwave radiation parameterizations. *J. Atmos. Sci.*, **43**, 321-328.

Nakajima, T. Y., and M. D. King, 1990: Determination of the optical thickness and effective particle radius of clouds from reflected solar radiation measurements: Part I: theory. *J. Atmos. Sci.*, **47**, No. 15, 1878-1893.

—, —, and J. D. Spinhirne, 1991: Determination of the optical thickness and effective particle radius of clouds from reflected solar radiation measurements: Part II: marine stratocumulus observations. *J. Atmos. Sci.*, **48**, No. 5, 728-750.

—, and T. Nakajima, 1995: Wide-area determination of cloud microphysical properties from NOAA AVHRR measurements for FIRE and ASTEX regions. *J. Atmos. Sci.*, **52**, No. 23, 4043-4059.

Nicholls, S., 1987: A model of drizzle growth in warm, turbulent, stratiform clouds. *Quart. J. Roy. Meteor. Soc.*, **113**, 1141-1170.

Ockert-Bell and D. L. Hartmann, 1992: The effect of cloud type on the Earth's energy balance: Results for selected regions. *J. Climate*, **5**, 1157-1171.

Ou, S. C., K. -N. Liou, W. M. Gooch, and Y. Takano, 1993: Remote sensing of cirrus cloud parameters using advanced very-high-resolution radiometer 3.7- and 10.9μm channels. *Appl. Opt.*, **32**, No. 12, 2171-2180.

—, K. -N. Liou, Y. Takano, N. X. Rao, Q. Fu, A. J. Heymsfield, L. M. Miloshevich, B. Baum, and S. A. Kinne, 1995: Remote sounding of cirrus cloud optical depths and ice crystal sizes from AVHRR data: verification using FIRE II IFO Measurements. *J. Atmos. Sci.*, **52**, No. 23, 4143-4158.

—, and K. -N. Liou, 1995: Ice microphysics and climatic temperature feedback. *Atm. Res.*, **35**, 127-138.

Phalippou, L., 1996: Variational retrieval of humidity profile, wind speed and cloud liquid-water path wit the SSM/I: potential for numerical weather prediction. *Q. J. R. Meteor. Soc.*, **122**, No. 530, 327-354.

Pilewskie, P., A. F. H. Goetz, D. A. Beal, R. W. Bergstrom, and P. Mariani, 1998: Observations of the spectral distribution of solar irradiance at the ground during SUCCESS, *Geophys. Res. Lett.*, **25**, 1141-1143.

Platnick, S., and F. P. J. Valero, 1995: A validation of a satellite cloud retrieval during ASTEX. *J. Atmos. Sci.*, **52**, No. 16, 2985-3001.

Platt, C. M. R., and G. W. Paltridge, 1976: *Radiative processes in meteorology and climatology.* (Elsevier Scientific Publishing Company, New York), 318pp.

—, D. W. Reynolds, and N. L. Abshire, 1980: Satellite and lidar observations of the albedo, emittance and optical depth of cirrus compared to model calculations. *Mon. Wea. Rev.*, **108**, 195-204.

—, and D. M. Winker, 1996: Multiple scattering effects in clouds observed from LITE. *SPIE, Opt. in Atmos. Prop and Adapt. Sys.*, **2580**, 60-71.

—, 1997: Size spectra, extinction and ice/water content of frontal and capping cirrus clouds. *J. Atmos. Sci.*, **54**, 2083-2098.

Prabhakara, C., R. S. Fraser, G. Dalu, M. -L. C. Wu, and R. J. Curran, 1988: Thin cirrus clouds: seasonal distribution over oceans deduced from Nimbus-4 IRIS. *J. Appl. Meteor.*, **27**, 379-399.

Rao, N. X., Ou, S. C., and Liou, K. N., 1995: Removal of the solar component in AVHRR 3.7-μm radiances for the retrieval of cirrus cloud parameters. *J. Appl. Meteor.*, **34**, 482-499.

Rawlins, F., and J. S. Foot, 1990: Remotely sensed measurements of stratocumulus properties during FIRE using the C130 aircraft multi-channel radiometer. *J. Atmos. Sci.*, **47**, No. 21, 2488-2503.

Ries, V. T., 1995: *Calibration of the scanning spectral polarimeter and measurement of the sky light polarization.* M.Sc. Thesis, Colo. State Univ., Dept. of Atmos. Sci., Fort Collins, 104pp.

Rodgers, C. D., 1976: Retrieval of atmospheric temperature and composition from remote measurements of thermal radiation. *Rev. of Geophys. and Space Phys.*, **14**, No. 4, 609-624.

—, 1990: Characterization and error analysis of profiles retrieved from remote sounding measurements. *J. Geophys. Res.*, **95**, No. D5, 5587-5595.

Rossow, W. B., and L. C. Gardner, 1993: Cloud detection using satellite measurements of infrared and visible radiances for ISCCP. *J. Climate.*, **6**, No. 12, 2341-2369.

Sagan, C., and J. B. Pollack, 1967: Anisotropic nonconservative scattering and the clouds of Venus. *J. Geophys. Res.*, **72**, 469-477.

Sassen, K. and L. Liao, 1996: Estimation of cloud content by W-band radar. *J. Appl. Meteor.*, **35**, 932-938.

Sato, N., K. Kikuchi, S.C. Barnard, and A.W. Hogan, 1981: Some characteristic properties of ice crystal precipitation in summer season at South Pole Station, Antarctica. *J. Meteor. Soc. Japan*, **59**, 772-780.

Shettle, E. P., and R. W. Fenn, 1979: Models for the aerosols of the lower atmosphere and the effects of humidity variation on their optical properties. *Env. Res. Papers*, USAF Geophys. Lab. No. 676, 94pp.

Simpson, J., R. F. Adler and G. R. North, 1988: A Proposed Tropical Rainfall Measuring Mission (TRMM) satellite. *Bull. Amer. Met. Soc.*, **69**, No. 3, 278-294.

Slingo, J. M., 1987: The development and verification of a cloud prediction scheme for the ECMWF model. *Quart. J. Roy. Meteor. Soc.*, **113**, 899-927.

Smith, W. L., Jr., L. Nguyen, D. P. Garber, P. Minnis, D. F. Young, D. M. Winker, M. P. McCormick, W. L. Smith, and H. L. Huang, 1996: Comparisons of cloud heights derived from satellite, aircraft, surface lidar and LITE data. *IRS '96: Proc. of the Int. Rad. Symp.*, 603-606.

Stackhouse, P. W., Jr., 1995: *The effects of two dimensional inhomogeneity on ice cloud radiative properties.* Ph.d. dissertation, Colo. State Univ., Dept. of Atmos. Sci., Fort Collins, 250pp.

Stamnes, K., S. -C. Tsay, W. Wiscombe, and K. Jayaweera, 1988: Numerically stable algorithm for discrete-ordinate-method radiative transfer in multiple scattering and emmitting layered media. *Appl. Opt.*, **27**, 2502-2509.

Stephens, G. L., 1978: Radiation profiles in extended water clouds. Part I: Theory - Part II: Parameterization schemes. *J. Atmos. Sci.*, **35**, 2111-2132.

— and C. M. R. Platt, 1987: Aircraft observations of the radiative and microphysical properties of stratocumulus and cumulus cloud fields. *J. Climate Appl. Meteor.*, **26**, 1243-1269.

—, S. -C. Tsay, P. W. Stackhouse, Jr., and P. J. Flatau, 1990: The relevance of the microphysical and radiative properties of cirrus clouds to climate and climatic feedback. *J. Atmos. Sci.*, **47**, No. 14, 1742-1753.

—, R. F. McCoy, Jr., R. B. McCoy, P. Gabriel, P. T. Partain, S. D. Miller, and S. Love, 1999: A multipurpose scanning spectral polarimeter (SSP): Instrument description and sample results. *J. Atmos. Ocean. Tech.*, In press, 28pp.

[Stephens *et al.* (1998)] —, D. G. Vane, and S. J. Walter, 1998: The CloudSat mission: a new dimension to space-based observations of cloud in the coming millenium. *Submitted to Bull. Amer. Met. Soc.*, 20p.

[Stephens *et al.* (2000)] —, P. Gabriel, and P. T. Partain, 2000: Parameterization of atmospheric radiative transfer 1: Validity of simple models. *Submitted to J. Atmos. Sci.*, 12p.

Stone, R. S., G. L. Stephens, C. M. R. Platt, and S. Banks, 1990: The remote sensing of thin cirrus cloud using satellites, lidar and radiative transfer theory. *J. Appl. Meteor.*, **29**, No. 5, 353-366.

Sundqvist, H. 1988: Parameterization of condensation and associated clouds in models for weather prediction and general circulation simulation. *Physically-Based Modelling and Simulation of Climate and Climate Change,* M. W. Schlesinger, Ed., Kluwer, 433-461.

Szejwach, G., 1982: Determination of semi-transparent cirrus cloud temperature from infrared radiance. Application to METEOSAT. *J. Appl. Meteor.*, **21**, 384-393.

Takano, Y., and K. -N. Liou, 1995: Radiative transfer in cirrus clouds. Part III: Light scattering by irregular ice crystals. *J. Atmos. Sci.*, **52**, 818-837.

Tiedtke, M., 1993: Representation of clouds in large-scale models. *Mon. Weather Rev.*, **121**, 3040-3061.

Toon, O. B., and J. B. Pollack, 1976: A global average model of atmospheric aerosols for radiative transfer calculations. *J. Appl. Meteor.*, **15**, 225-246.

Twomey, S., H. Jacobowitz, and H. B. Howell, 1966: Matrix methods for multiple-scattering problems. *J. Atmos. Sci.*, **23**, 289-296.

—, 1977: *Introduction to the Mathematics of Inversion in Remote Sensing and Indirect Measurements.* (Dover Publications, Inc., New York), 243 pp.

—, and T. Cocks, 1989: Remote sensing of cloud parameters from spectral reflectance in the near-infrared. *Beitr. Phys. Atmosph.*, **62**, No. 3, 172-179.

U.S. Department of Energy, 1990: ARM program plan. *DoE/ER-0441*, Washington, D.C., 74pp.

Valero, F. P. J., T. P. Ackerman, and W. J. Y. Gore, 1989: The effects of the arctic haze as determined from airborne radiometric measurements during AGASP II. *J. Atmos. Chem.*, **9**, 225-244.

van de Hulst, H. C., 1980: *Multiple light scattering tables, formulas, and applications* , Vol. 2, (Academic Press, New York), 739pp.

Wielicki, B. A., J. T. Suttles, A. J. Heymsfield, R. M. Welch, J. D. Spinhirne, M. -L. C. Wu, D. O'C. Starr, L. Parker and R. F. Arduini, 1990: The 27-28 October 1986 FIRE IFO cirrus case study: comparison of radiative transfer theory with observations by satellite and aircraft. *Mon. Wea. Rev.*, **118**, 2356-2376.

—, B. A. Baum, J. A. Coakley, Jr., R. N. Green, Y. Hu, M. D. King, B. Lin, D. P. Kratz, P. Minnis, and L. L. Stowe, 1997: Clouds and the earth's radiant energy system (CERES) algorithm theoretical basis document. *CERES ATBD Subsystem 4.0 Overview*, Release 2.2.

Weinreb, M., B. Goddard, and P. Celone, 1995: Relative gain of visible channels of GOES-8 and -9 imagers. NOAA/NESDIS Memorandum, 13pp.

—, Jamieson, M., Fulton, N., Chen, Y., Johnson, J. X., Bremer, J., Smith, C., and Baucom, J., 1997: Operational calibration of the imagers and sounders on the GOES-8 and -9 satellites. NOAA Technical Report NESDIS 44, U. S. Dept. Commerce, National Oceanic and Atmospheric Administration, Washington, D. C.

Wilks, D. S., 1995: *Statistical methods in the Atmospheric Sciences: An Introduction*, Academic Press, San Diego, Calif., 427pp.

Winker, D. M., and M. A. Vaughan, 1994: Vertical distribution of clouds over Hampton, Virginia observed by lidar under the ECLIPS and FIRE ETO programs. *Atmos. Res.*, **34**, 117-133.

—, and L. R. Poole, 1995: Monte-Carlo calculations of cloud returns for ground-based and space-based lidars. *Appl. Phys. B*, **60**, 341–344, 1995.

—, R. H. Couch, and M. P. McCormick, 1996: An overview of LITE: NASA's lidar in-space technology experiment. *Proc. IEEE*, **84**, No. 2, 164-180.

—, 1997: Simulation and modelling of multiple scattering effects observed in LITE data. *Advances in Atmospheric Remote Sensing with Lidar.* (Springer Verlag, New York 1997), 185-188.

Wiscombe, W. J., 1976: Extension of the doubling method to inhomogeneous sources. *J. Quant Spectrosc. Radiat. Transfer*, **16**, 477-489.

—, 1976: On initialization, error and flux conservation in the doubling method. *J. Quant Spectrosc. Radiat. Transfer*, **16**, 637-658.

—, 1977: The delta-M method: rapid yet accurate radiative flux calculations for strongly asymmetric phase functions. *J. Atmos. Sci.*, **34**, 1408-1422.

Wylie, D. P., and W. P. Menzel, 1989: Two years of cloud cover statistics using VAS. *J. Climate*, **2**, 380-392.

—, and W. P. Menzel, W. P. Menzel, H. M. Woolf, and K. I. Strabala, 1994: Four years of global cirrus cloud statistics using HIRS. *J. Climate*, **7**, 1972-1986.

Yang, P. and K. -N. Liou, 1998: Single-scattering properties of complex ice crystals in terrestrial atmosphere. *Contr. Atmos. Phys.*, **71**, No. 2, 223-248.

Appendix A

SLADRT MODEL INPUT STRUCTURE

A.1 Contents

Provided in this appendix is a brief documentation of the shortwave/longwave adding/doubling radiative transfer (SLADRT) model developed and applied as the forward model in the retrieval work of this research. The intention is to provide the reader with the fundamental information needed to understand the basic architecture and run the model under minimal duress. An overview of input formats and general instructions for running the executable are provided.

A.2 Sample Input Card

The foundation of SLADRT is a simple doubling/adding code which may be regarded for this discussion as a black box (refer to main text for details of theory). The complexity of SLADRT arises from the peripheral routines which set up the profile and provide the user with the freedom to run the code at various levels of complexity. Provided in Table A.1 is a sample input card used by the SLADRT driver routine. The data provided are read sequentially and characterize completely (to varying levels of approximation) the surface and atmospheric constituents as well as the observing system. Because the model handles varying levels of profile complexity, several input formats are included with each designated by an index dictating the architecture of subsequent formatted reads. The following is a line-by-line description of the input fields and format options handled by SLADRT for this particular example (with references to other formats included).

- Line 0: Run descriptor comment

Parameters	*Field Descriptor*
Text String	Run Descriptor Comments
4 8 6 4 gauss	# Upwellng Strms, # Leg Coeffs, # Azms, Numorder, Quad
1	Surface Reflection Index
N Y	Gas Flag, Rayleigh Atmos Flag
0 0 1	Mono/Band Flag, TOA Flag; Normalized Flux Flag
1.375	Wavelength (um) -or- (Instrument#; Channel#)
0 0	Subtract-Solar Flag, Subtract-Thermal Flag
0 0 2	Profile Flag, Extension Flag, Profile #
0 1 1 1.0	Aerosol Flag, Model#, Vis Prof#, Total τ
Y 0	Output Flag, Outfile Format Index
rtcode.out	Output name
N	Bandweight Flag
bandfile.dat	Bandweight File Name
1 0	# Layers, Layer Format Index
1.0 1.0 0.0 0.0 0.0 279.	Format-Dependent Layer Information
285 1.0 0.10 1013.25	SURFACE: T, Emissivity, Albedo, Pressure
0	# Cloud Layers
1.0	μ_o
2	Number of User-Specified Points
0 89.427 0.0	Pt1: Level, Zenith, Azimuth
0 87.134 0.0	Pt2: (etc.)

Table A.1: Sample input card for SLADRT. See text for detail description of fields and options.

- Line 1: Specifying the number of streams in a single hemisphere (e.g., an entry of 4 implies an 8-stream run); The number of Legendre expansion coefficients used for the integration; The number of azimuthal angles at which to compute the radiance field; The number of Fourier expansion coefficients ($m \geq 0$) to use in the azimuthal expansion (not applicable for longwave calculations).

- Line 2: Surface reflection option: 0=No surface reflection, 1=Lambertian reflector, 2=Specular reflector

- Line 3: Flag (Y/N) for inclusion of correlated-K gaseous absorption (currently CK files are available only for specific GOES instrument and channel combinations); Flag (Y/N) for inclusion of a molecular (Rayleigh) scattering atmosphere (height and wavelength dependent)

Index	*Description*
1	Tropospheric
2	Mid-Latitude Summer
3	Mid-Latitude Winter
4	Sub-Arctic Summer
5	Sub-Arctic Winter
6	Arctic Summer
7	Arctic Winter

Table A.2: McClatchey atmospheric profile options.

Index	*Description*
1	Tropospheric
2	Rural
3	Urban
4	Maritime

Table A.3: Aerosol model options.

- Line 4: Index 0 for monochromatic calculations or 1 for band calculations; Index 0 for computation of radiances at all intermediate atmospheric levels specified or 1 for only TOA and surface boundary fields; Index 0 for un-normalized solar spectral flux or 1 for normalized to unity

- Line 5: If monochromatic calculations, then wavelength in microns; If band calculations, then Instrument index (e.g., GOES = 0) and Channel index

- Line 6: Index 0 to neglect the solar component from calculations or 1 to include it; Index 0 to neglect the thermal component from calculations or 1 to include it

- Line 7: Index 0 to not use a standard McClatchey profile or 1 to include (if 1, then the input lines containing the layer profile information are excluded from the input card); Index 0 to not extend the profile to 100-km (using McClatchey soundings) or 1 to extend it; Index of McClatchey atmosphere to use (specified even if not actually using) according to Table A.2. NOTE: The extension to space option is currently only compatible with layer input format = 2

Index	*BL*	*TABL*	*STR*
1	50	50	None
2	5	23	Background
3	50	50	High Volcanic
4	5	23	High Volcanic

Table A.4: Aerosol horizontal visibility (in km) options. BL=boundary layer (0- to 2-km), TABL=troposphere above BL (2- to 10-km), STR=stratosphere.

Index	*Parameters*
0	τ(aer+gas+cld), ω_o, g_1, g_2, g_{eff}, T(K)
1	τ(aer), τ(gas), ω_o(aer), g(aer), Z(top, km), Z(thickness, km), T(K)
2 (format line)	# absorbers, ident_1, unit_1, $(\cdots)$, ident_i, unit_i, $\text{unit}_{\text{pres}}$, unit_T, unit_Z
3	absorber_1, $\cdots$, absorber_i, P, T, Z

Table A.5: SLADRT layer input formats.

- Line 8: Flag 0 for inclusion of aerosol information, 1 to omit; Index for aerosol model as listed in Table A.3; Index for visibility profile as listed in Table A.4; Total aerosol optical depth (default is 1.0). NOTE: The inclusion of aerosol requires water vapor profile information (which determines the size and hence optical properties of the aerosol). Therefore, the inclusion of aerosol is only valid for layer input format = 2

- Line 9: Flag (Y/N) for output of results to a dedicated file; Index 1 for abbreviated output format, 0 for full radiance field

- Line 10: Output file name (string)

- Line 11: Flag (Y/N) for instrument response function (applicable only for band calculations)

- Line 12: Instrument/channel-specific bandweights file (includes discretized solar spectral flux where applicable)

- Line 13: Index for number of layers (¿ 0 and unlimited); Index for layer input format as outlined in Table A.5. For Layer input format = 2, a second line of input

Index	*Absorber*
1	H_2O
2	O_3
3	CO_2
4	CH_4
5	N_2O

Table A.6: Gaseous absorber identification for layer input format 2.

Index	*Unit*
1	Abundance (g/cm^2-km)
2	Density (g/m^3)
3	Dew point T (K)
4	Relative Humidity (%)
5	Mixing Ratio (g/kg)
6	Pressure (Atm-cm/km)
7	Number Density (per/cm^3)

Table A.7: Gaseous absorber units for layer input format 2.

is required which describes the number of gaseous absorbers present, their units, and the units of pressure, temperature, and level heights for the ensuing layer records according to Tables A.6-A.8.

- Line 14: Formatted layer information (in the sample card case, a single layer of input format = 0 from line 12)
- Line 15: Surface parameters: temperature (K), emissivity (0.0-1.0), albedo (0.0-1.0), pressure (mb)
- Line 16: Number of cloud layers to insert in profile ($\geq$ 0 and unlimited)
- Line 17: Formatted cloud information as specified in Table A.9. NOTE: the first value on each cloud record is that cloud's format (such that multiple cloud formats may coexist if desired)
- Line 18: Number of user-specified points (unlimited) at which to output radiance field.

Index	*Pressure Unit*	*Temperature Unit*
1	mb	K
2	Atm	C
3	N/A	F

Table A.8: Pressure and Temperature units for layer input format 2.

Index	*Format*
1	Z_{top}(km), Z_{bot}(km), τ, ω_o, g_1, g_2, g_{eff}
2	Z_{top}(km), Z_{bot}(km), τ, r_{eff}, Mie file
3	Z_{top}(km), Z_{bot}(km), τ, ω_o, χ-expansion File

Table A.9: Cloud layer input formats. Further description of the Mie and χ-expansion supplementary files are provided in the text.

- Line 19: Level number (TOA=0) observer zenith (degrees), and observer azimuth (degrees) for user-specified point #-1
- Line 20: Level number (TOA=0) observer zenith (degrees), and observer azimuth (degrees) for user-specified point #-2 (etc.)

The quadrature abscissas available to the forward model are Lobatto and Gaussian. For many retrievals (e.g., SSP) where the instrument is oriented in the nadir, the Lobatto quadrature (which includes a point at 0-degrees) is a convenient choice. Cubic splining of the calculated intensity field is used to obtain intensity values at points in between the discrete ordinates. To minimize errors associated with interpolation of the radiance field, the user angles should be as close as possible to an existing quadrature node. It is a simple modification to the code to include an additional quadrature point pair (i.e., one in each hemisphere) corresponding to the desired viewer zenith. The weights assigned to these added nodes are set to zero.

A.2.1 Comments on layer input formats

The layer input format selected reflects the level of complexity (or available information) of a given run. Format "0" specifies ω_o, g and τ as consolidated terms (i.e.,

gas, cloud, and aerosol together). This format was used for the most general and basic applications such as model validation against DISORT and Van de Hulst benchmarks. Format "1" allows for assignment of ω_o, g and τ in terms of its cloud, aerosol, gas, and Rayleigh components, thereby giving the user more control over the atmospheric profile. Format "2" changes the architecture from layers to levels (i.e., information at a discrete height/pressure-level in the atmosphere). Gaseous absorbers are specified individually. Detailed cloud information may be specified with the cloud layer format section of the input block (discussed in more detail below).

A.3 Computing Layer Optical Properties

The total optical depth of an atmospheric layer is obtained by adding the individual contributions from cloud, gas, aerosol and Rayleigh

$$\tau = \tau_c + \tau_g + \tau_a + \tau_r, \tag{A.1}$$

where an empirical relationship from *Paltridge and Platt* [1976] describes the molecular (Rayleigh) optical depth as a function of altitude

$$\tau_r = 0.0088\lambda^{-4.15+0.2\lambda}e^{-0.1188z-0.00116z^2}. \tag{A.2}$$

Here, z represents a level-height in the atmosphere and λ denotes the spectral dependence of molecular scatter. Figure A.1 illustrates the λ^{-4} dependence of the Rayleigh optical depth over the portion of the electromagnetic spectrum where its contributions are significant.

Combined layer single-scatter albedos are obtained by an extinction-weighted scaling according to

$$\omega_o = \frac{\omega_{o,c}\tau_c + \omega_{o,a}\tau_a + \omega_{o,r}\tau_r}{\tau_c + \tau_g + \tau_a + \tau_r}, \tag{A.3}$$

where generally $(\omega_{o,g}, \omega_{o,r})$ are taken to be (0,1). The combined phase function is also scaled according to

$$P(\Theta) = \frac{\omega_{o,c}\tau_c P_c(\Theta) + \omega_{o,a}\tau_a P_a(\Theta) + \omega_{o,r}\tau_r P_r\Theta}{\omega_{o,c}\tau_c + \omega_{o,a}\tau_a + \omega_{o,r}\tau_r} \tag{A.4}$$

The "gas terms" are omitted from (A.3) and (A.4) because $\omega_{o,gas} = 0$, with its bulk scattering properties accounted for in the Rayleigh extinction term.

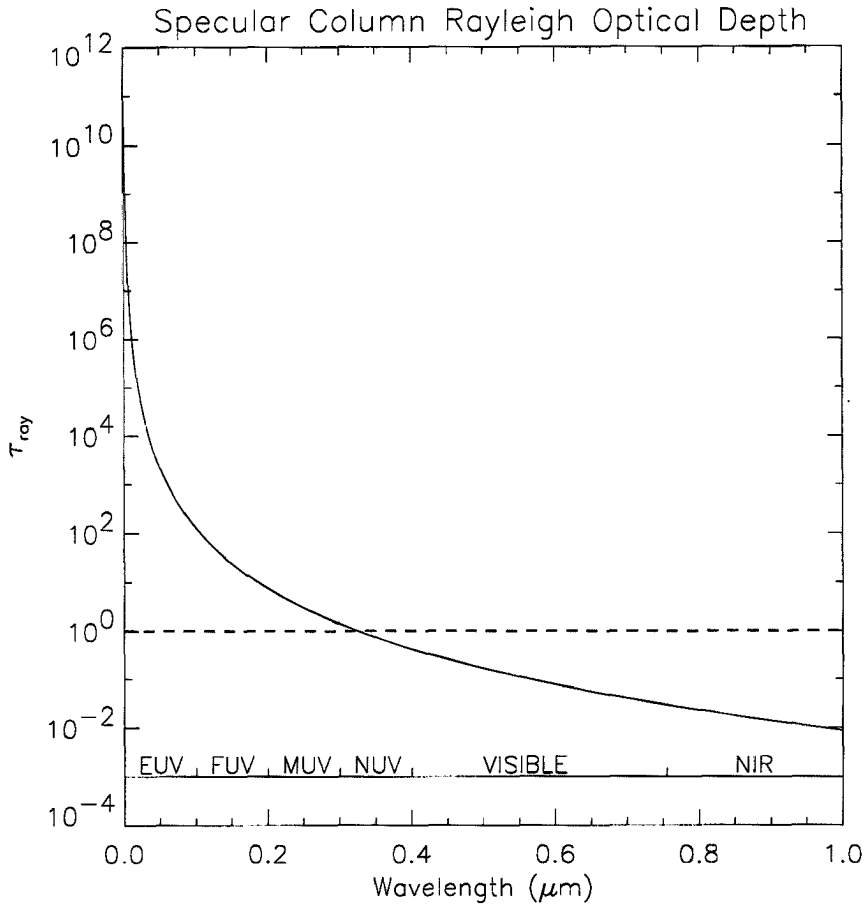

Figure A.1: Spectral Rayleigh column optical depth. Indicated are Extreme-, Far-, Middle-, and Near- Ultra Violet, Visible, and Near-Infrared

A.4 Cloud Layer Formats

The cloud module SLADRT inserts cloud layers into an existing profile, combines the specified cloud properties with the existing optical properties and interpolates atmospheric profile parameters for the new profile levels accordingly. The three levels of complexity for cloud insertion, specified in the input as cloud input formats listed in table A.9, are as follows:

- 0: Cloud top/base heights, optical depth, single scatter albedo and double Henyey-Greenstein phase function parameters specified at input. Pro: A simple format for diagnostic runs. Con: Enables a wide variety of potentially unrealistic clouds to be simulated.

- 1: Cloud top/base heights, optical depth, effective particle radius, and Mie look-up table name. Pro: Can create diverse database of spectrally dependent cloud optical properties with varying size distributions, useful for retrieval applications. Con: Based on spherical particles (which compromises applicability to ice clouds), still uses a double Henyey-Greenstein approximation to the phase function with an effective asymmetry parameter taken from the look-up tables.

- 2: Cloud top/base heights, optical depth, single-scatter albedo, and Legendre expansion coefficients (χ) file name. Pro: Combined with the δ-M scaling method, enables realistic, highly asymmetric scattering phase functions (e.g., cirrus) to be modeled in a numerically efficient way. Con: Still requires more expansion terms than simple phase function geometries, limited to availability of phase function data.

For the retrievals of this research, cloud formats 1 and 2 were used, with an emphasis on format 2 for cirrus clouds. A large database of ray-tracing phase function data for rough/smooth aggregates, bullets, solid/hollow columns, dendrites, and plates has been compiled by Yang *et al.* (1998). These data include the phase function structure, single-scatter albedo, asymmetry parameter and extinction at discrete wavelengths and 24 size distributions (each characterized by an effective radius). This offers a systematic way of varying the optical properties needed for iterative retrieval algorithms. A vertically inhomogeneous cloud can be approximated by stacking an arbitrary number of plane-parallel cloud layers together, each with its own optical makeup.

The Mie lookup tables were computed from a standard Mie-scattering code using a modified-gamma size distribution. The tables were computed for wavelengths spanning 0.3- to 20.0-μm at a resolution of 0.05-μm. Effective radii at each wavelength spanned 2- to 302-μm at 4-μm intervals (75 records). Dispersion factors (characterizing the width of the size distributions) of 1, 2, and 4 were computed for both water and ice spheres. Computed at each wavelength and effective radii were the single-scatter albedo, asymmetry parameter, and extinction normalized to a water content of 1.0 g/m^3. The asymmetry parameter was used to compute the Henyey-Greenstein phase function, and was used as

the effective asymmetry parameter in the double Henyey-Greenstein parameterization as described in Chapter 2.

The χ Legendre expansion coefficients were computed from tabulated phase function data according to

$$\chi_l = \frac{2l+1}{2} \int_{-1}^{1} \mu P(\mu) P_{\mathrm{LEG}}(l,\mu) d\mu, \tag{A.5}$$

where $P(\mu)$ is the tabulated, azimuthally symmetric phase function normalized by 4π (such that the integration over μ yields 2.0) and $P_{\mathrm{LEG}}(l,\mu)$ are the Legendre polynomials for the l^{th} expansion coefficient. To achieve the fit in a reasonable number of terms, the forward peak of the scattering phase function was truncated and the residual accounted for by the δ-M weight.

A.5 Running SLADRT

All source, object, and data files for SLADRT exist in separate directories. A makefile performs the compiling and linking of the source files. Diagnostic flags (which turn on/off various verbose statements in the subroutines) are also controlled by the makefile. The executable produced by a successful make is named "sladrt", and the code is run at the command prompt by feeding to it an input file (here, "input") according to

```
prompt>> sladrt input
```

In its current form, SLADRT outputs to screen several intermediate computational results. These may be commented out in the source code or simply directed to a diagnostics text file by appending the above command as follows

```
prompt>> sladrt input > diagnostics
```

For the retrieval work of this research (where SLADRT is called repetitively) an IDL interface was used to write the input files, spawn a call to SLADRT, and subsequently read the output file as described in the implementation architecture sub-section of Chapter 3.

A.6 Pitfalls

While much time, effort, and heartache has been dedicated to making SLADRT a robust and useful utility, the user inevitably will encounter previously unidentified problems with various input formats. Because the SLADRT interface allows for so many levels of input complexity, many potential areas of data incompatibility exist. Most of these problems center around the layer vs. level input architecture, and have been identified and treated whenever encountered. In the current version of SLADRT, gaseous absorption is handled only by the instrument/channel option (i.e., single wavelength computations, which would require the inclusion of a line-by-line gaseous absorber database, is not handled), and operates exclusively in layer input format "2" mode (level absorber data). At its current status of robustness, SLADRT should be able to handle the needs of most radiative transfer calculations. Due to the convoluted nature of SLADRT input interface to its radiative transfer black box, any modifications to this code may result in unpredictable results. It is strongly advised to maintain a back-up file directory and to check against benchmark runs throughout the revision process.

Appendix B

ECMWF/LITE DATABASE

B.1 Contents

This appendix contains a complete summary of ECMWF/LITE cloud profile comparisons for all 66 night-time LITE orbits. These data reveal details of model performance that are lost to the ensemble statistics plots. They also comprise a useful reference for future research which may seek to isolate a particular aspect of the model not addressed by the statistical analysis conducted in this research (e.g., forecast performance for clouds associated with a specific synoptic-scale situation or in the vicinity of a certain geography/orography). When considering the many different cloud structures encountered in just a single LITE orbit, a case-by-case presentation of the fine-scale model forecast performance at length was deemed both relevant to the scope of this research and worthwhile to interests beyond it.

B.2 Format

The data are shown both as qualitative comparisons plots of LITE observations against model forecasted cloud cover and statistical performance summaries for each orbit. Chapter 6 of this dissertation outlines the statistical approach adopted for the quantitative comparisons. Presented there are the ensemble-orbit results based on these individual case data. The following is a brief review of the plotting format (applicable to all 66 LITE orbits).

B.2.1 Orbit and cloud cover qualitative comparisons

The first plot is composed of three panels. The upper left panel provides information about the STS-64 (LITE) orbit number, the date and time (universal), and the time-step

(i.e., forecast length) of the model. Most forecasts for these comparisons were on the order of 24-hours (sufficient time for model spin-up and cloud development). The upper-right panel provides a graphical depiction of the orbit coverage with "Start" and "End" positions annotated. This is useful to quick-look browsing for cases that include ITCZ convection, for example. The lower plot presents the model cloud cover (top) corresponding (values between 0 for clear and unity for overcast) to the LITE observations (bottom). Here, the LITE data has been rebinned to the model resolution in both the horizontal and vertical, and a pseudo-cloud-fraction has been computed (see Chapter 6) which results in observed cloud fractions also ranging over (0,1). Statistics computed both with and without consideration of these pseudo-cloud-fractions are presented in this appendix. All surface returns have been filtered out from the LITE data (i.e., any colored pixel displayed corresponds to an observed cloud). Caveats associated with the LITE observations (e.g., pulse attenuation and pulse stretching) have *not* been removed from these plots, but have been filtered prior to computation of statistics.

B.2.2 Ensemble and spatially-partitioned statistics

The two bar-plots following the qualitative cloud cover comparisons present the statistics computed according to Chapter 6 for the Hit Rate, Threat Score, Probability of Detection, and False Alarm Rate (each as an individual panel in these four-panel plots). As defined, all of these statistics vary between zero and one (as indicated on the abscissa. Each of the four panels is delineated into four horizontal sections to provide statistics for low (defined as 0-4 km), middle (4-8 km), high (above 8-km), and total column cloudiness. For each of these categories there are three horizontal bars demarcating the zonal-breakdown of statistics into categories of 1) total, 2) tropical (23.5S-23.5N Latitude), and 3) extra-tropical (the difference between 1 and 2) coverage. Finally, for each bar there are light and shaded components corresponding to the statistics computed with and without consideration of cloud fraction weighting, respectively For a given statistic, the smaller of the two values is over-plotted upon the larger such that it can be viewed. The weighting protocol does not alter the Probability of Detection statistics.

The entire plot is produced twice to examine the statistical differences arising from allowing a "window of acceptance" in the horizontal and vertical dimensions. The "±0 Bin (H,V)" indicates that a one-to-one comparison at the resolution of the model was performed, while a "±1 Bin (H,V)" displays smoothed statistics computed by a window of acceptance in both the vertical and horizontal of one bin/grid-box. The latter statistics were considered after noting visually that some comparisons possessed forecasted cloud structures very similar to observations but offset slightly in space (such that the one-to-one statistical analysis produced very poor scores belying the apparently strong spatial coherence of the fields). For a fair comparison, both sets of statistics are shown for each case. The unweighted, no-window results may be regarded as a "glass is half-empty" presentation, while the weighted, ±1 Bin (H,V) assumes the "half-full" counterpart. The true model performance resides somewhere between these extremes.

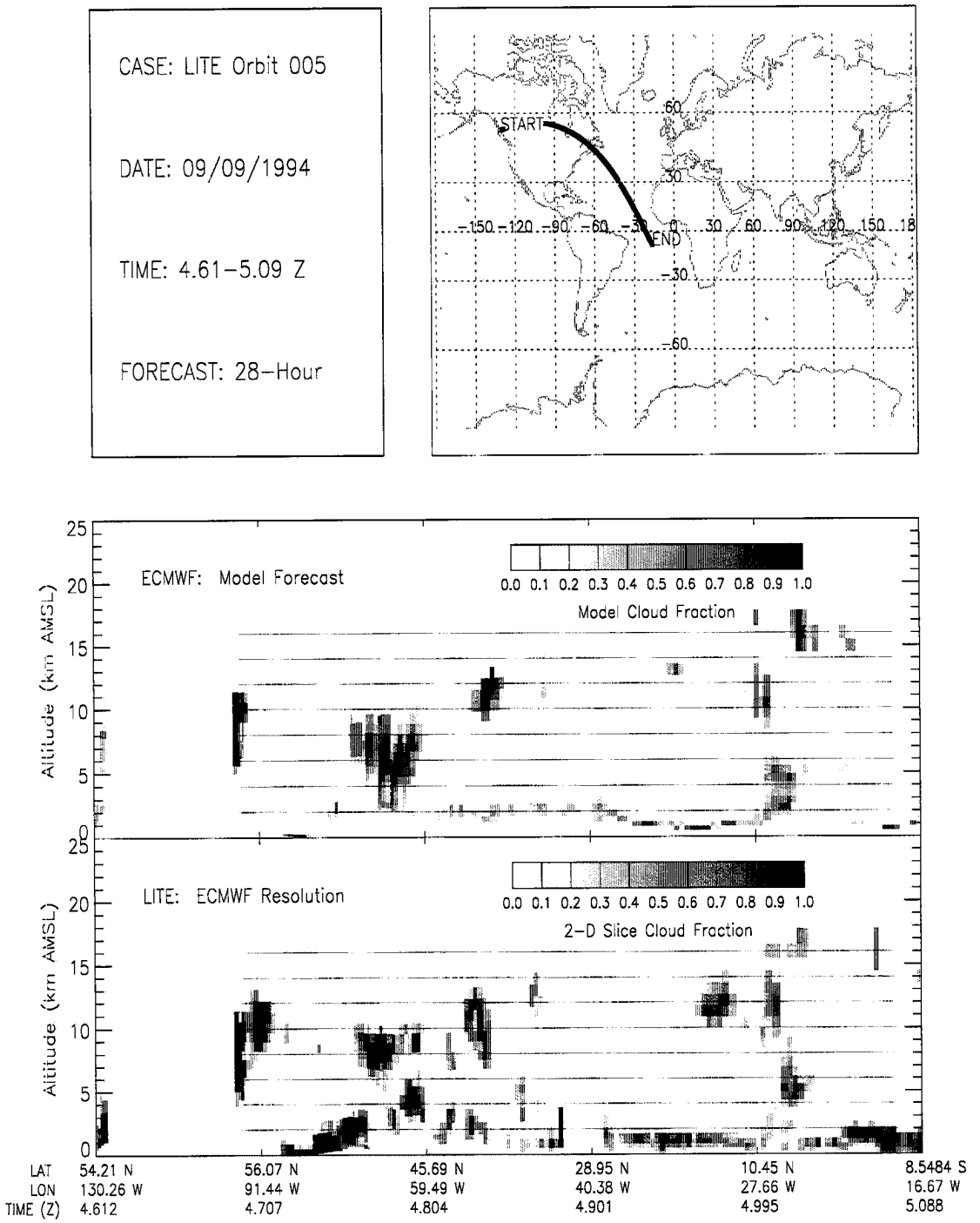

Figure B.1: LITE Orbit 005 Cloud Cover Comparison.

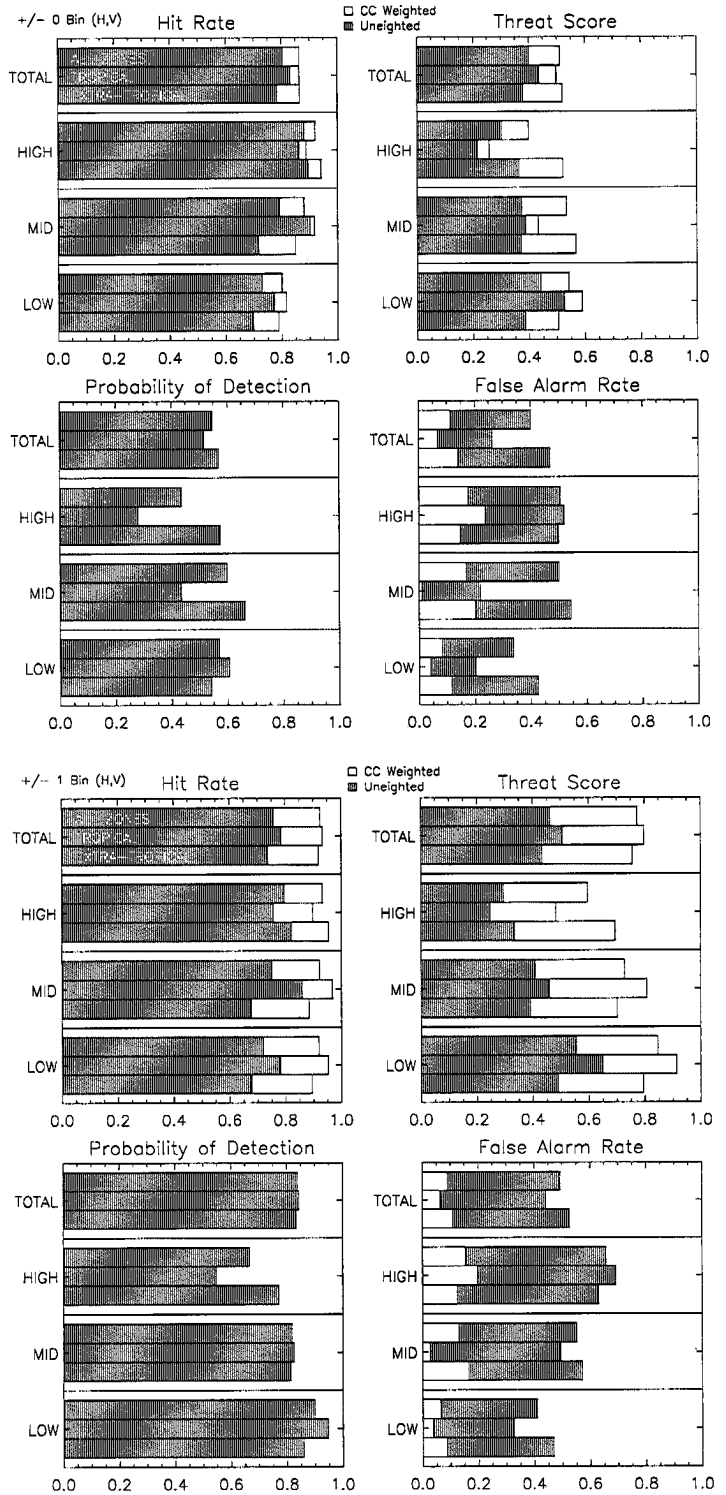

Figure B.2: LITE Orbit 005 Cloud Cover Statistics.

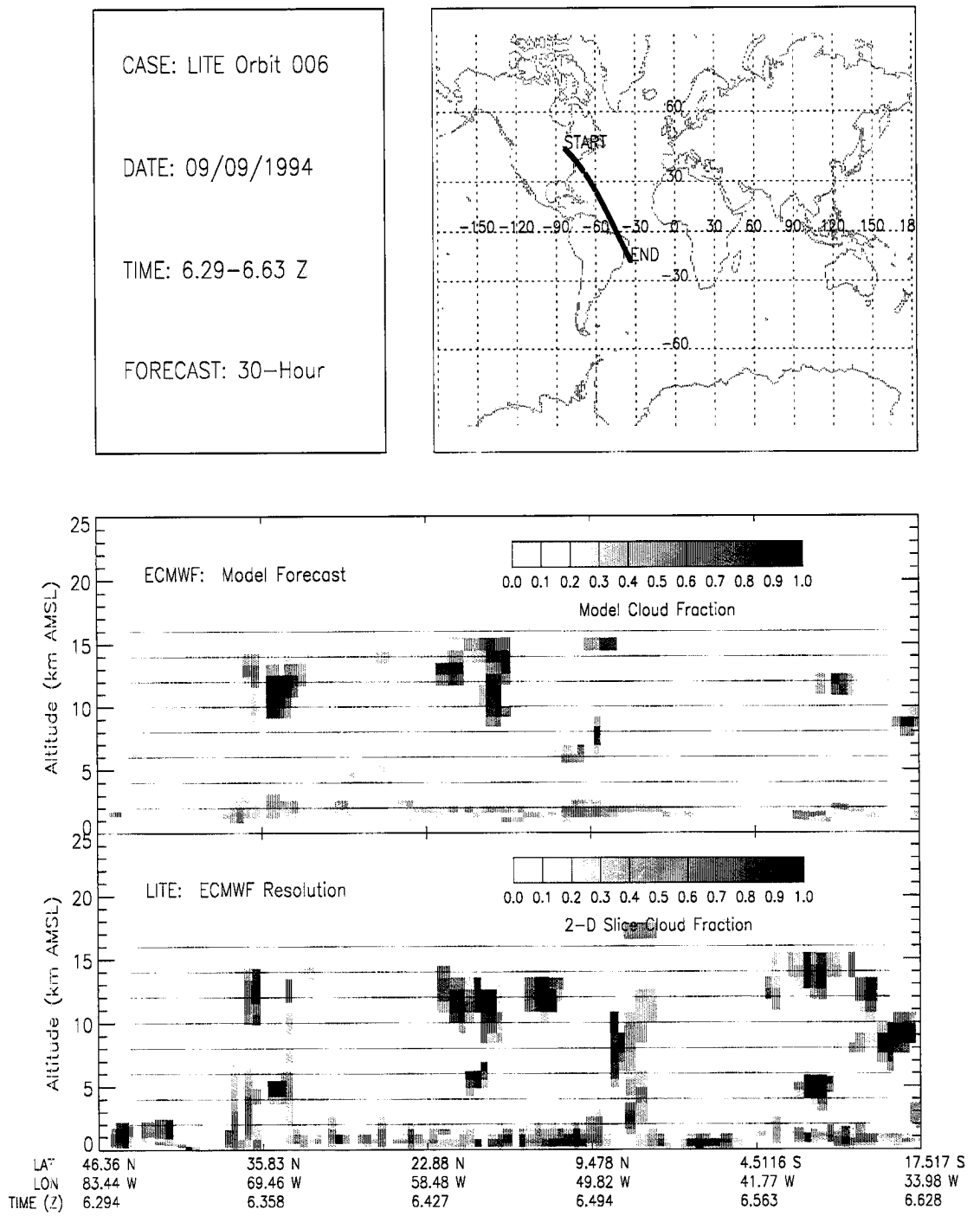

Figure B.3: LITE Orbit 006 Cloud Cover Comparison.

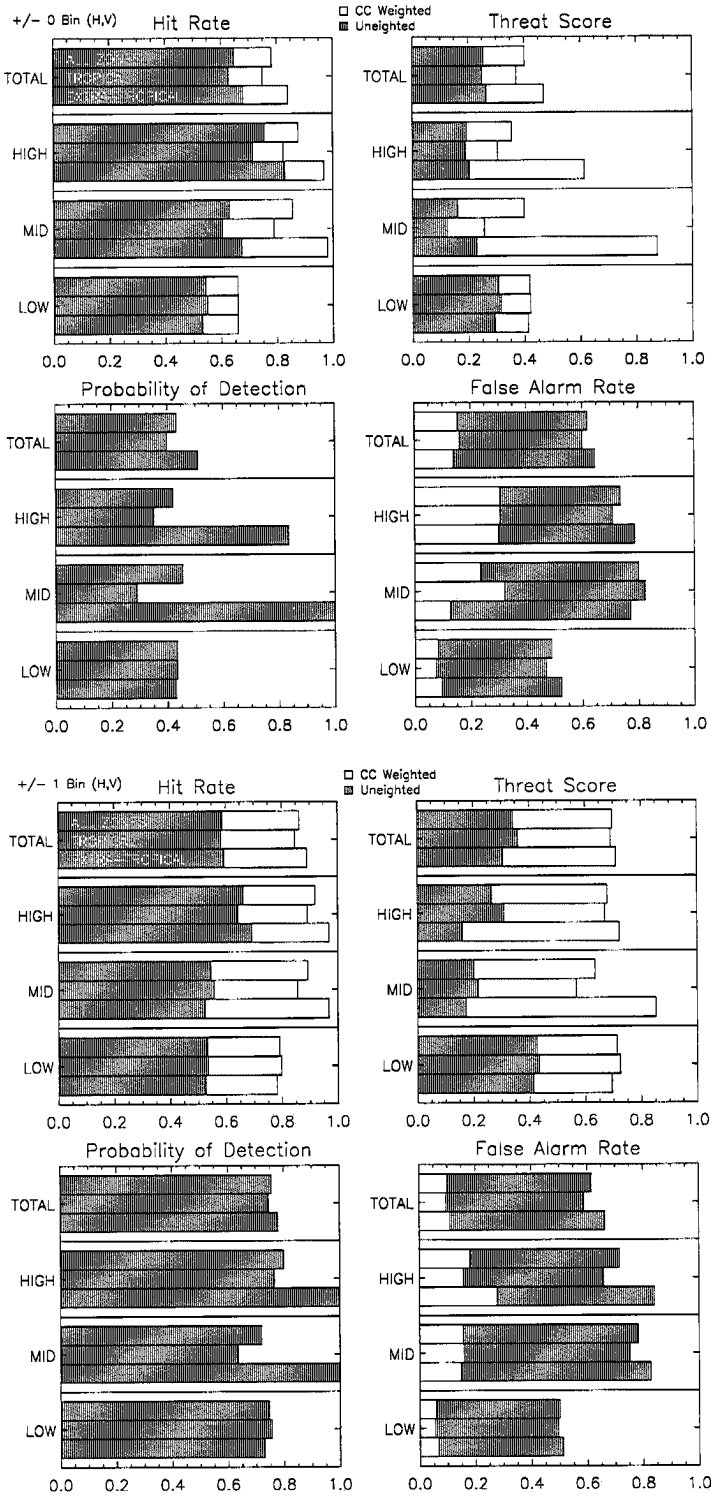

Figure B.4: LITE Orbit 006 Cloud Cover Statistics.

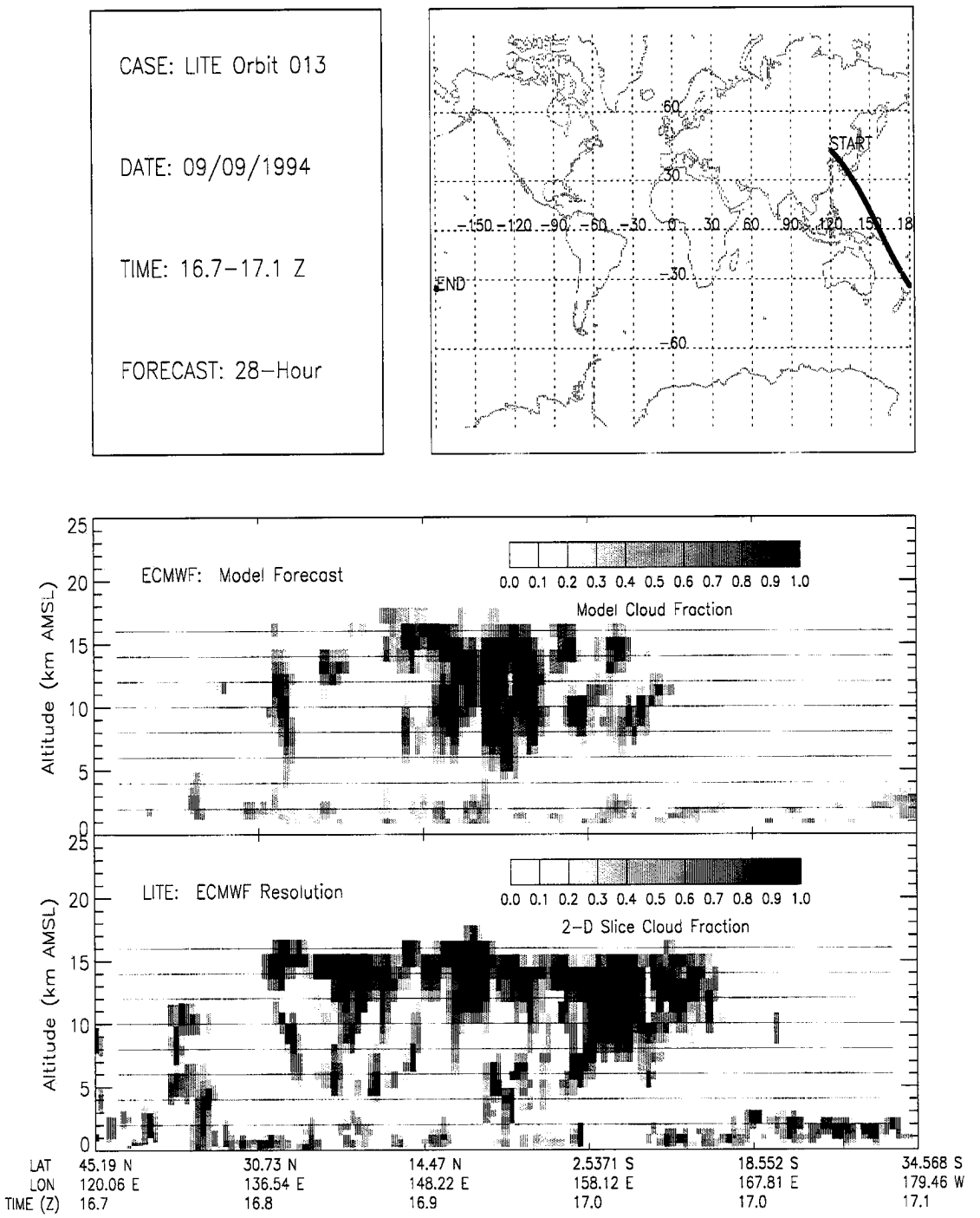

Figure B.5: LITE Orbit 013 Cloud Cover Comparison.

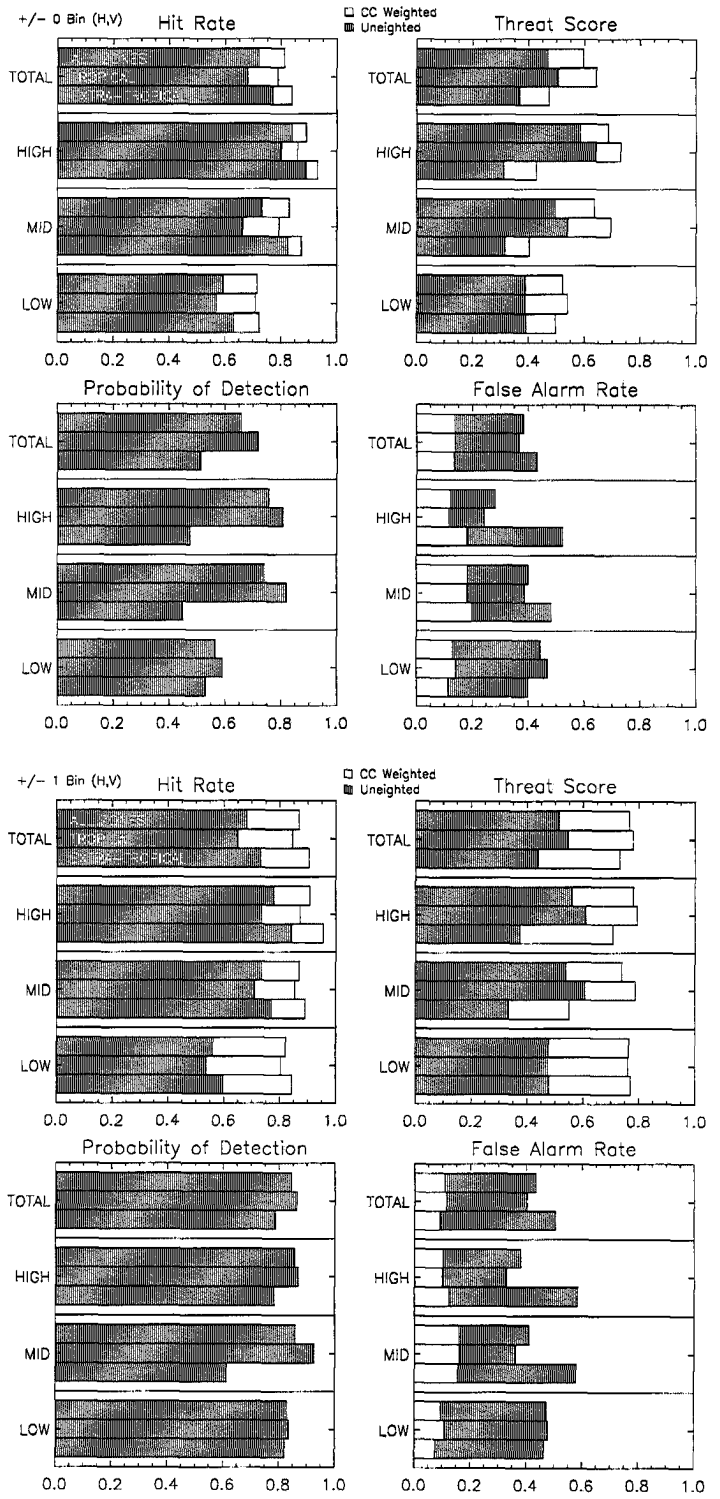

Figure B.6: LITE Orbit 013 Cloud Cover Statistics.

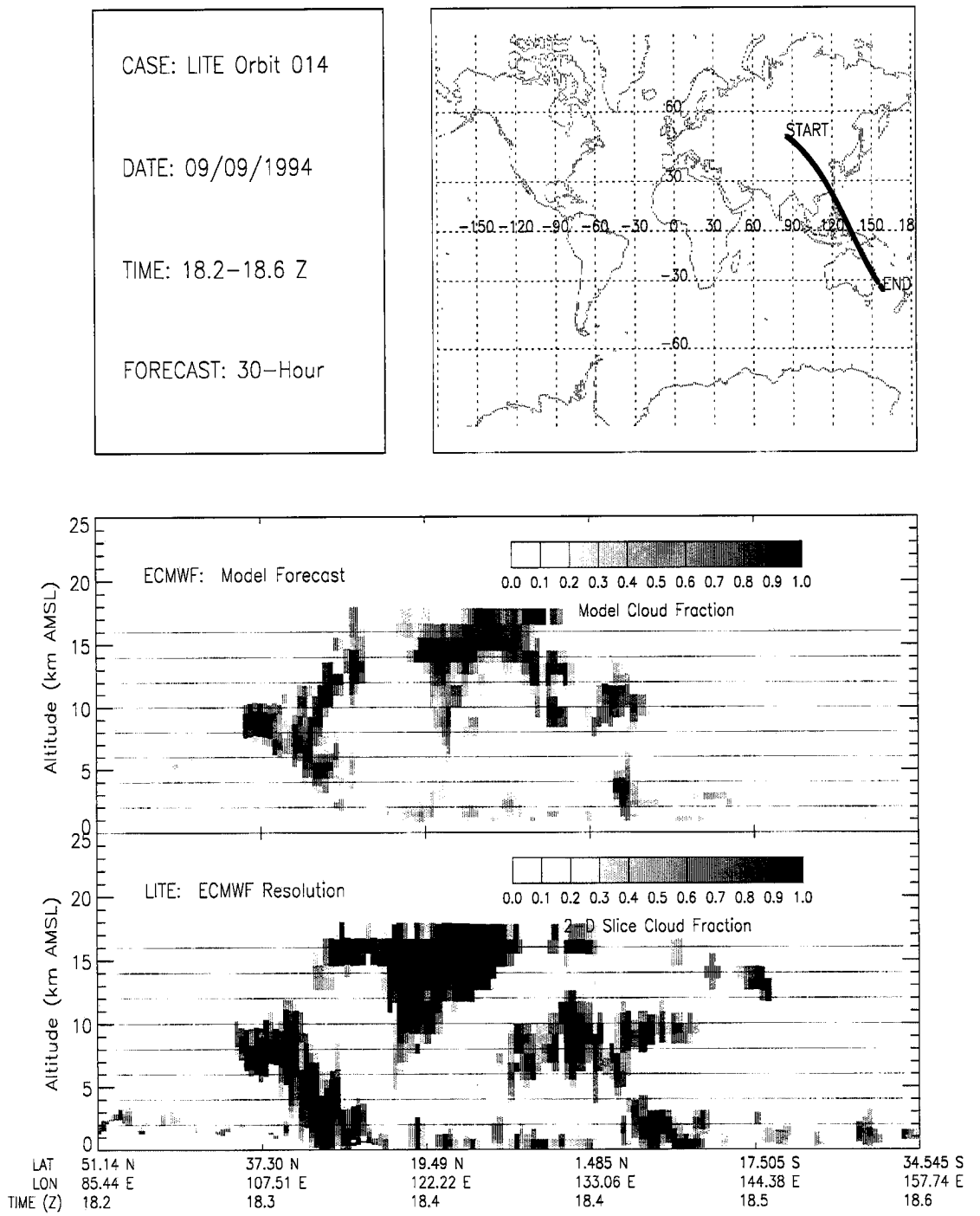

Figure B.7: LITE Orbit 014 Cloud Cover Comparison.

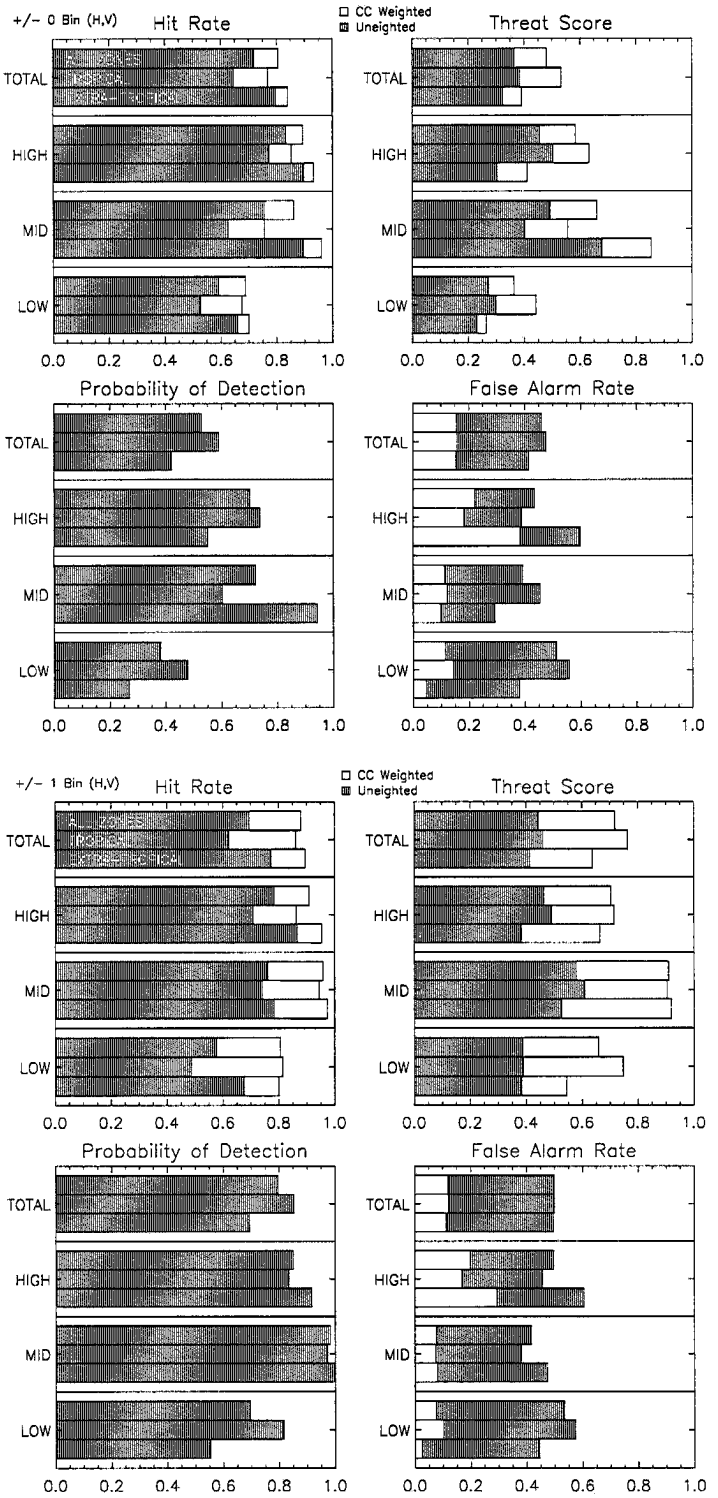

Figure B.8: LITE Orbit 014 Cloud Cover Statistics.

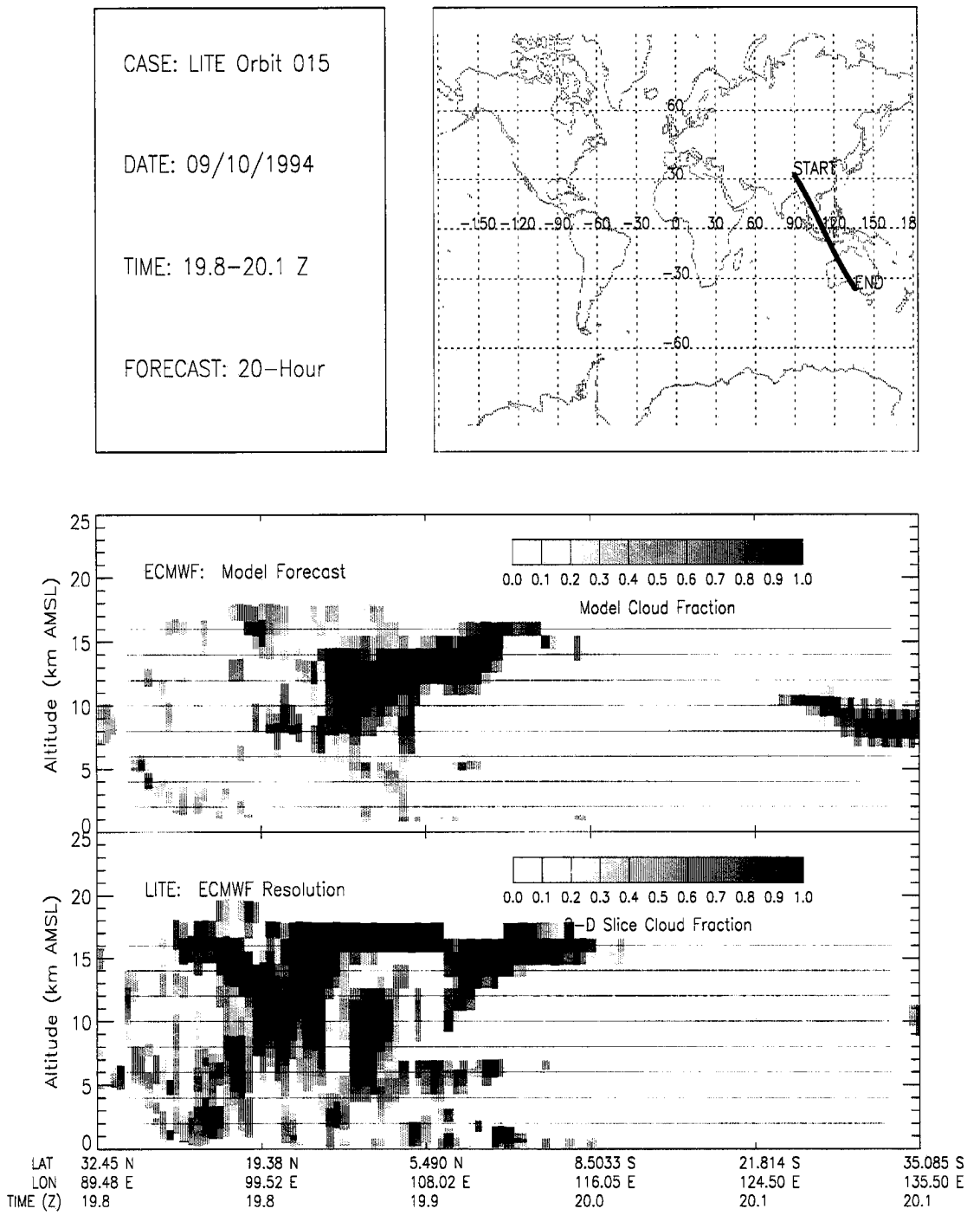

Figure B.9: LITE Orbit 015 Cloud Cover Comparison.

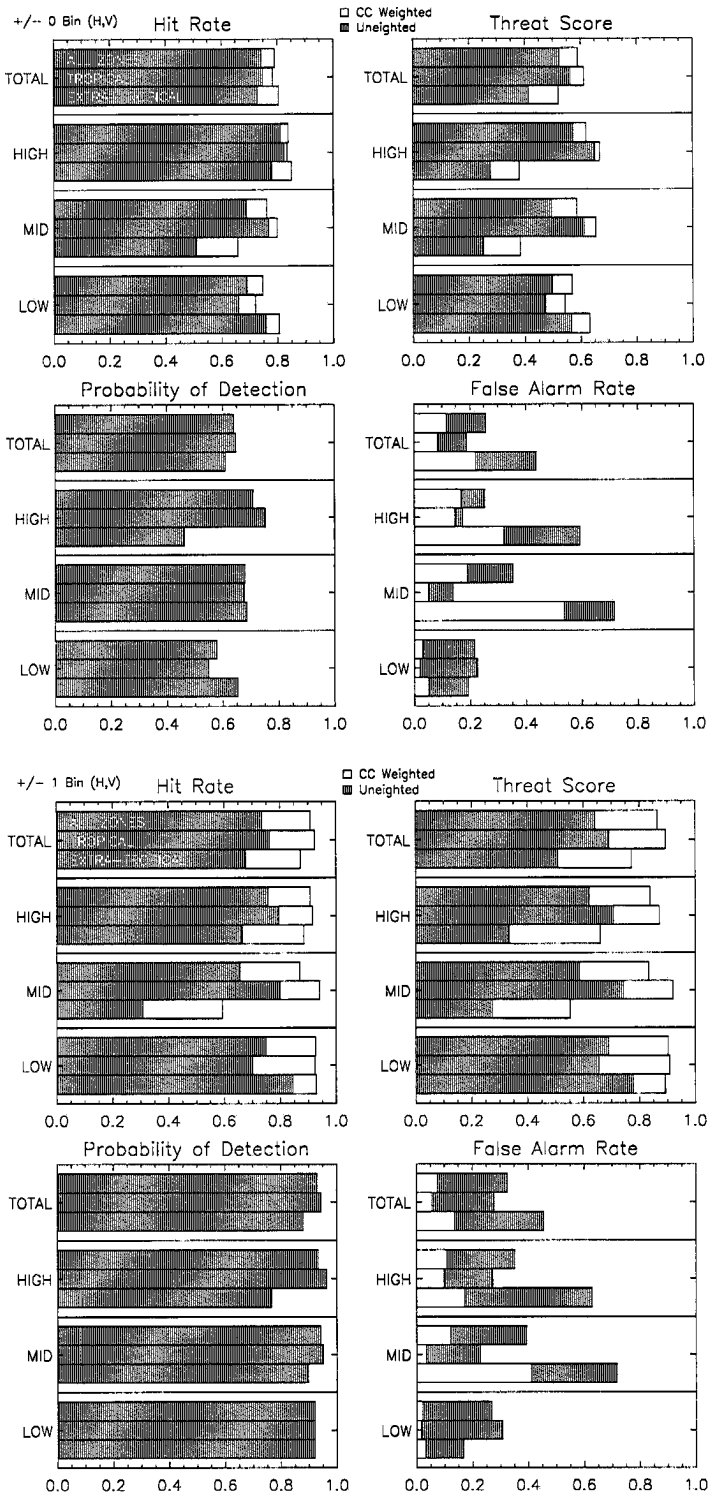

Figure B.10: LITE Orbit 015 Cloud Cover Statistics.

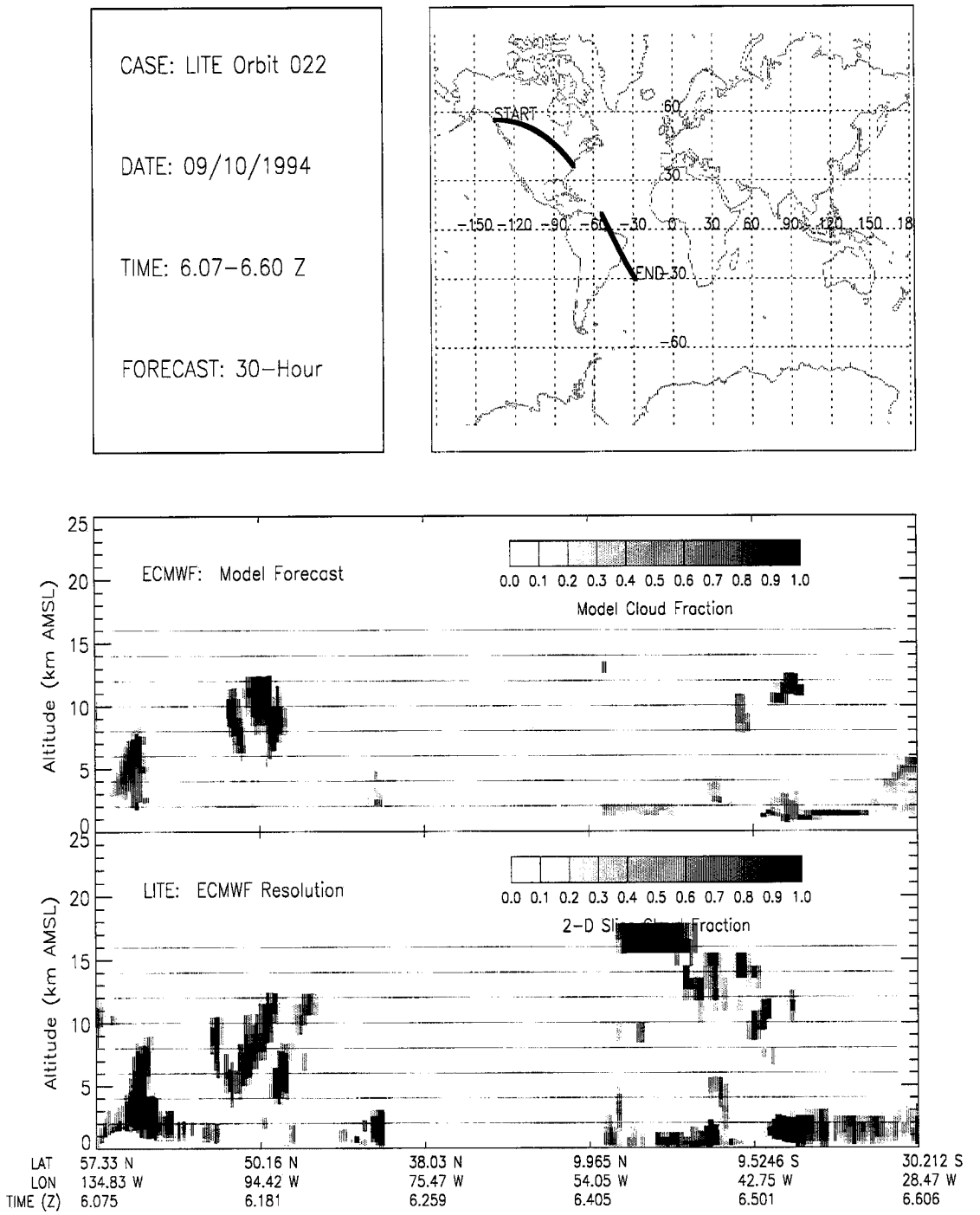

Figure B.11: LITE Orbit 022 Cloud Cover Comparison.

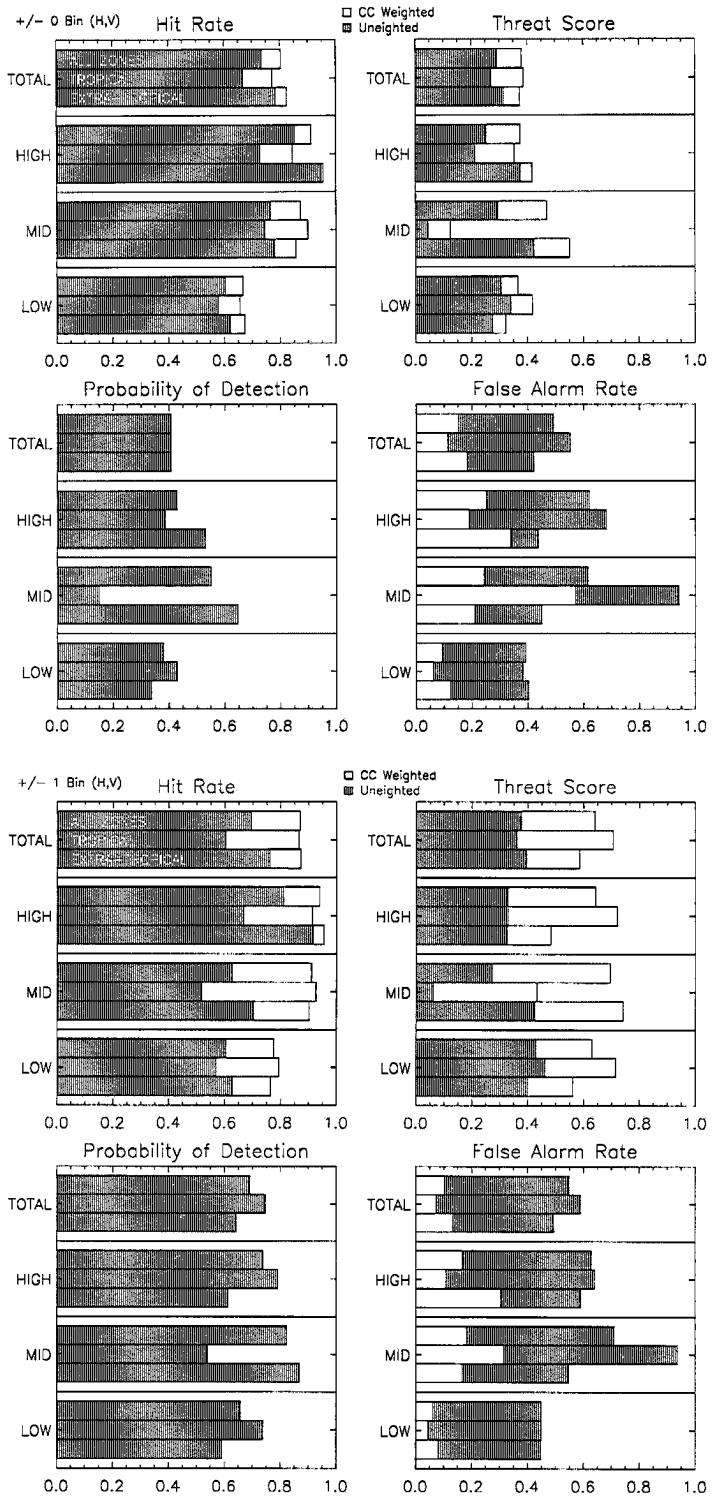

Figure B.12: LITE Orbit 022 Cloud Cover Statistics.

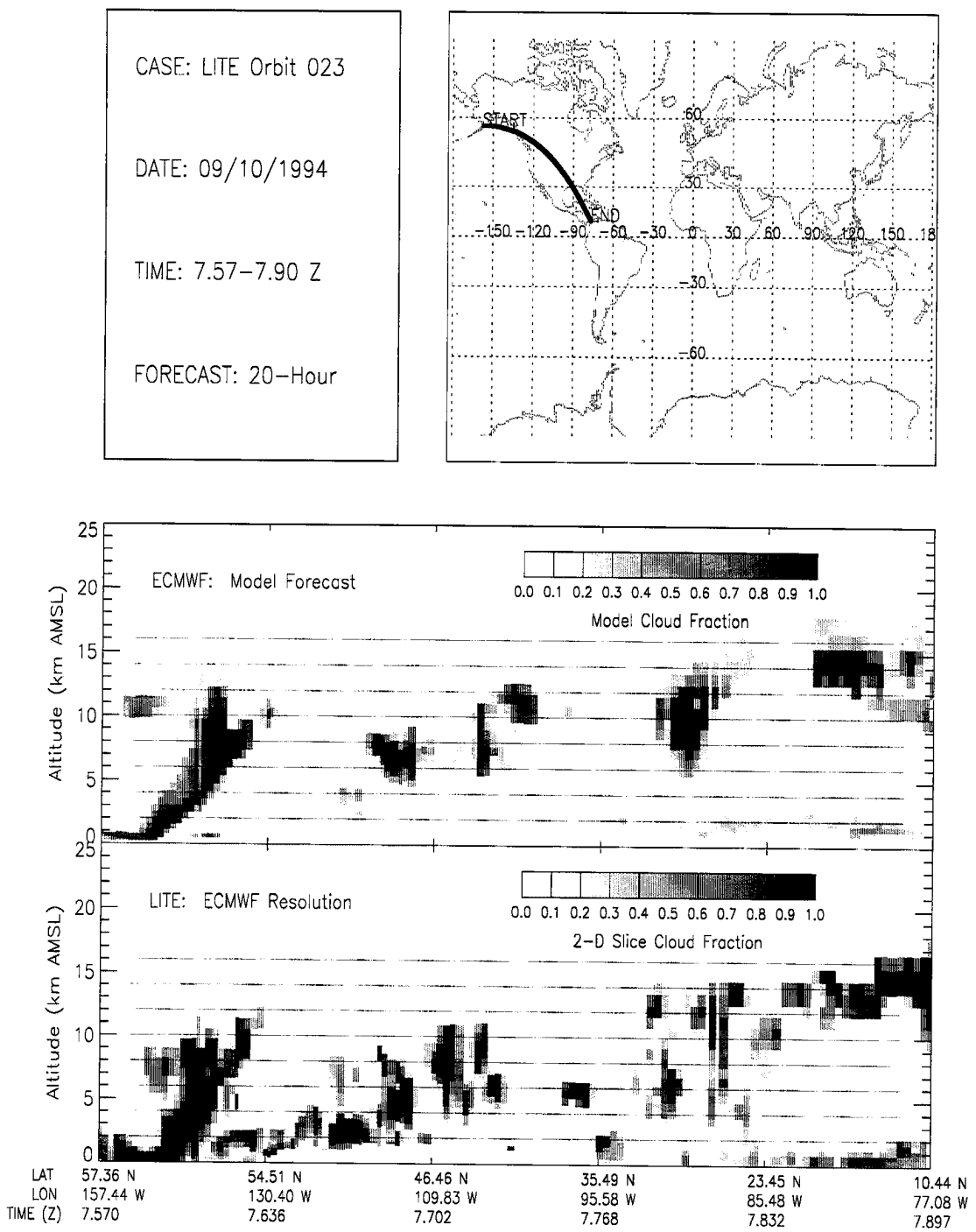

Figure B.13: LITE Orbit 023 Cloud Cover Comparison.

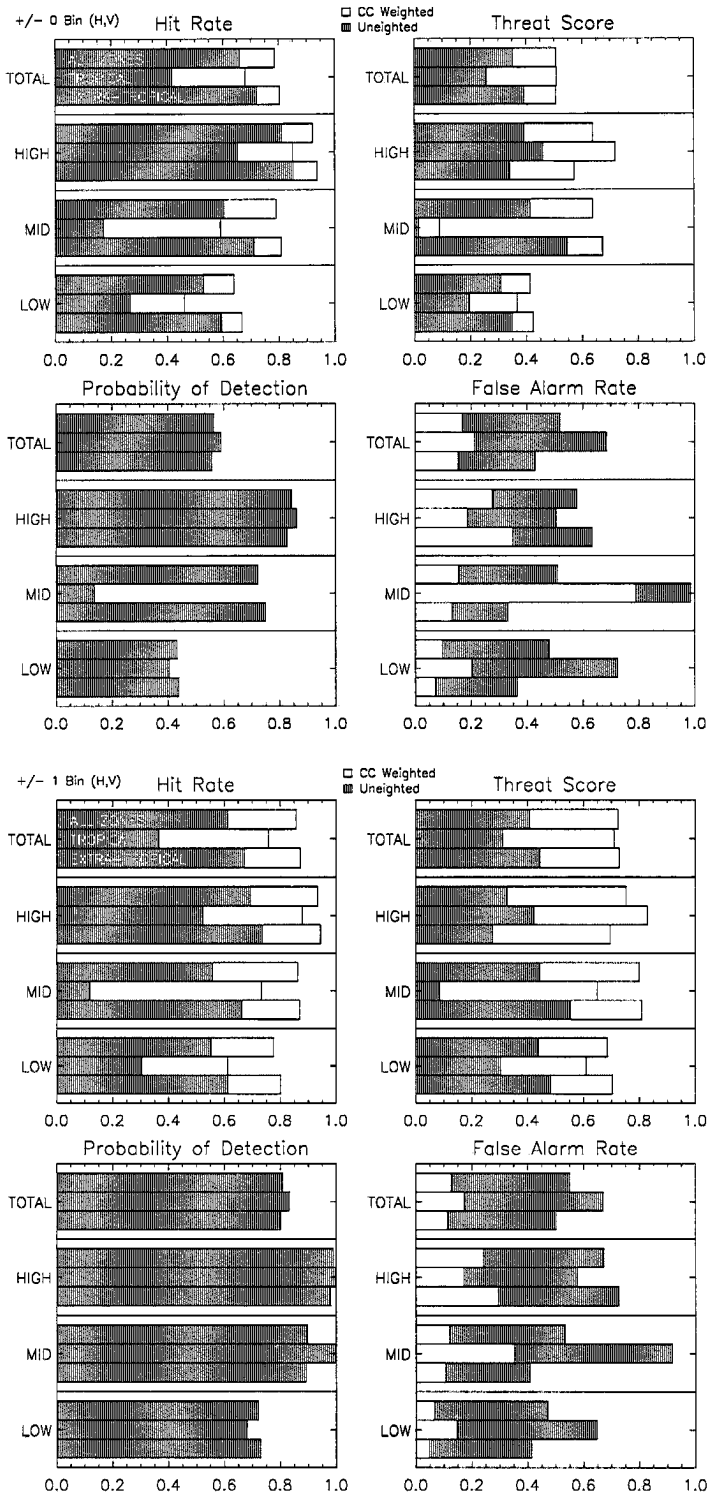

Figure B.14: LITE Orbit 023 Cloud Cover Statistics.

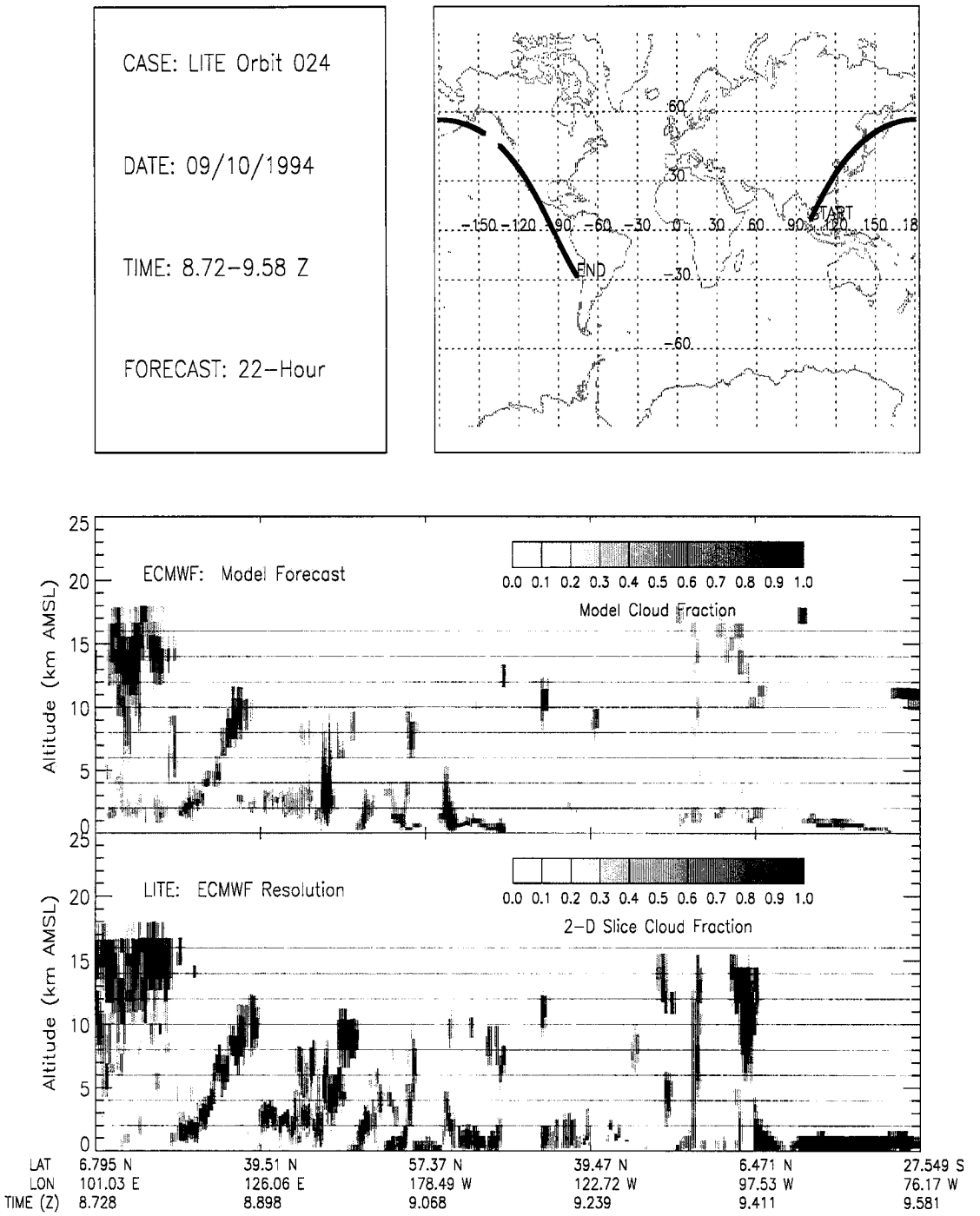

Figure B.15: LITE Orbit 024 Cloud Cover Comparison.

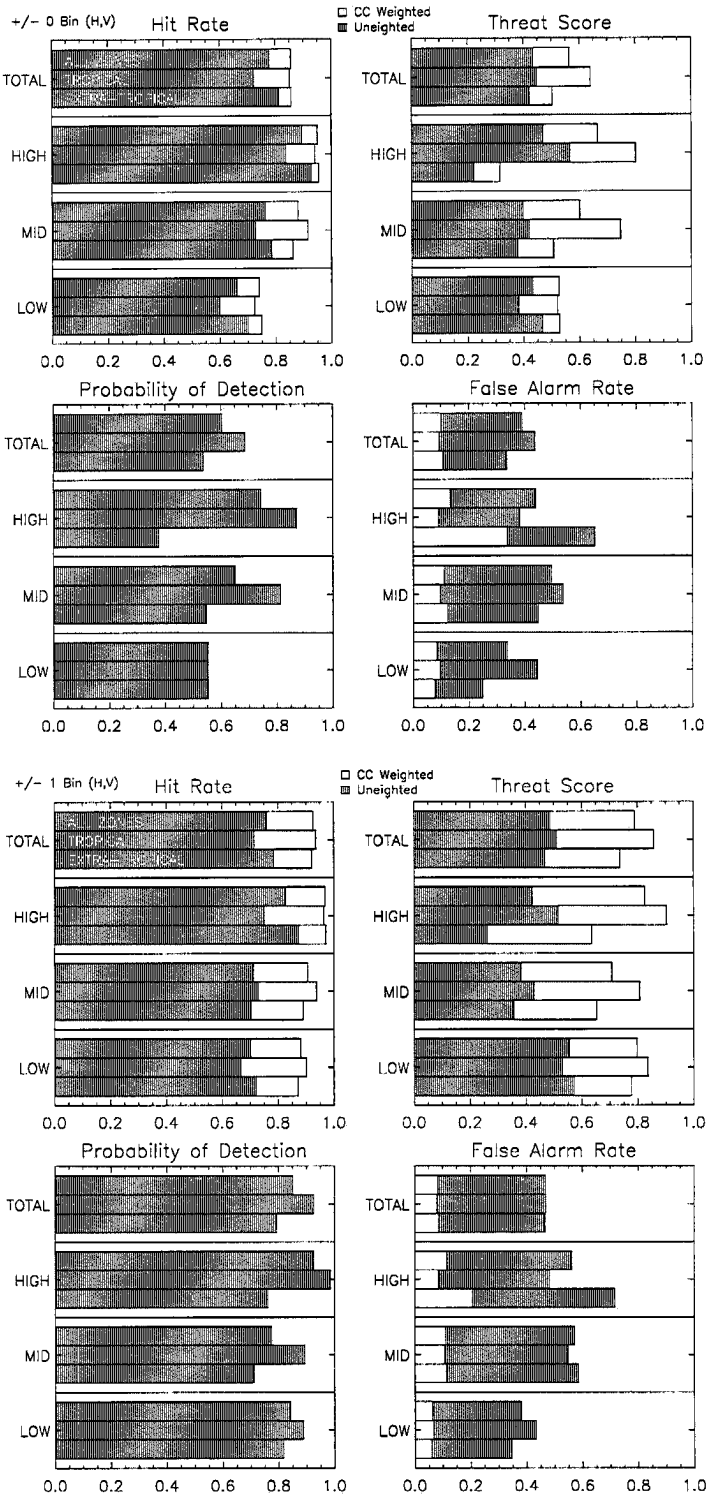

Figure B.16: LITE Orbit 024 Cloud Cover Statistics.

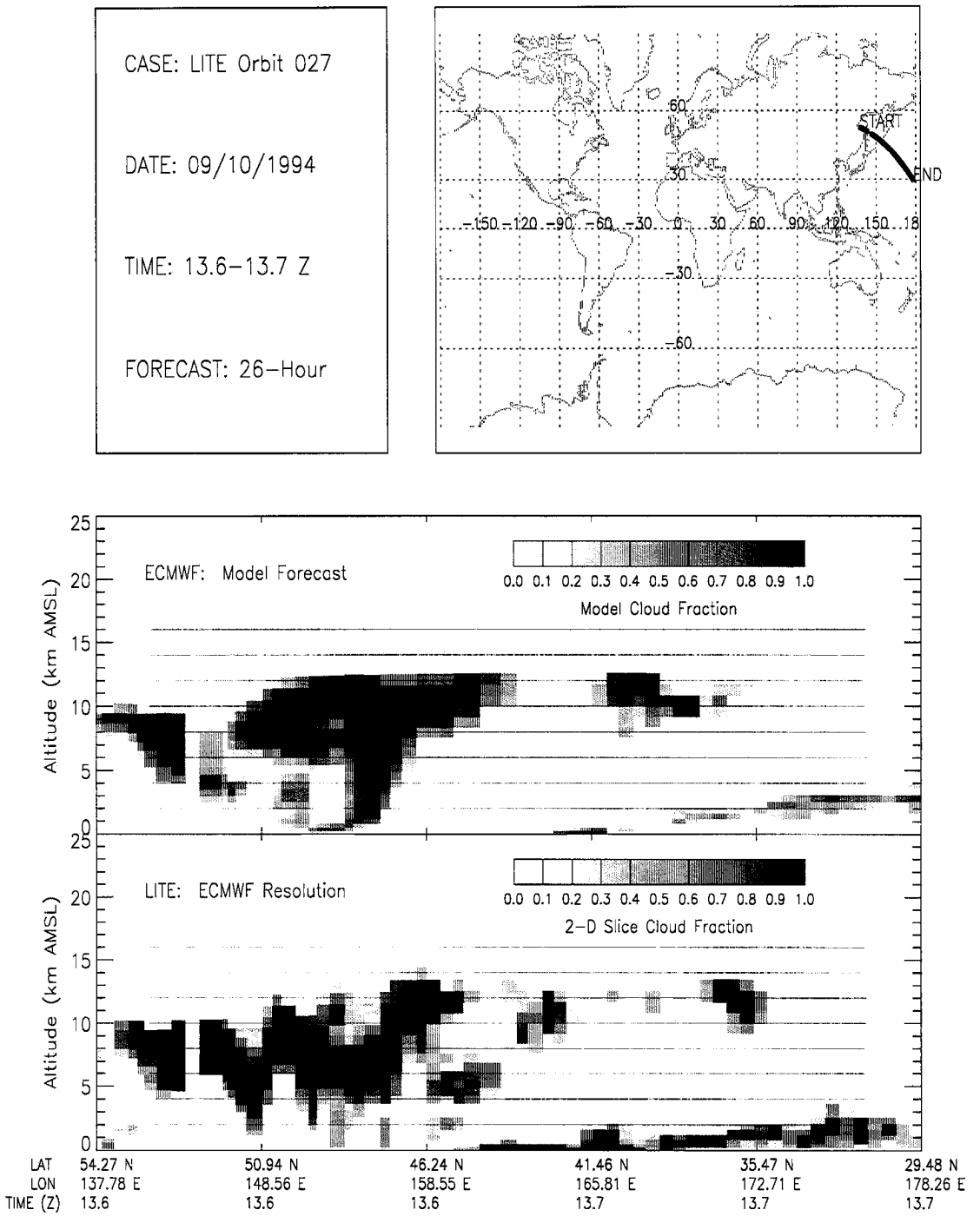

Figure B.17: LITE Orbit 027 Cloud Cover Comparison.

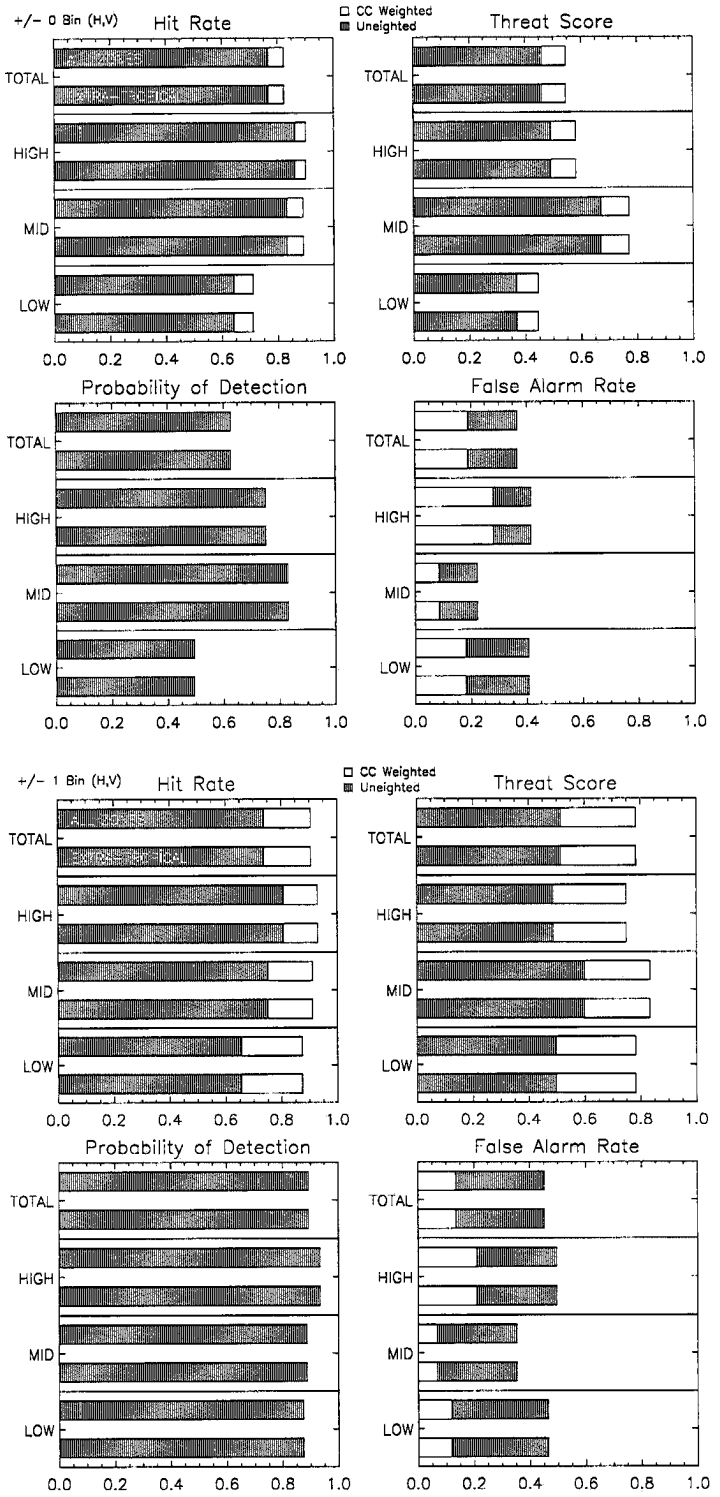

Figure B.18: LITE Orbit 027 Cloud Cover Statistics.

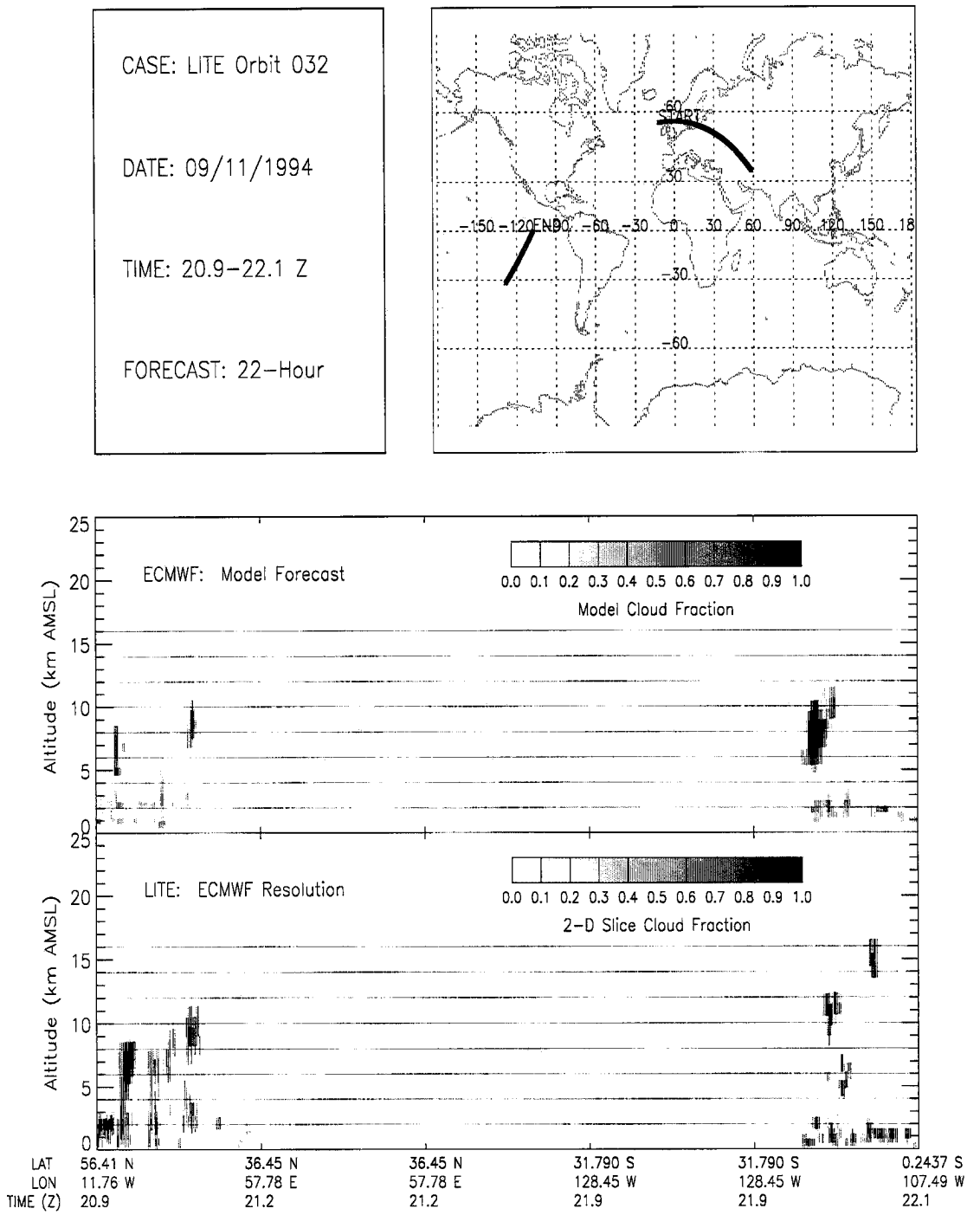

Figure B.19: LITE Orbit 032 Cloud Cover Comparison.

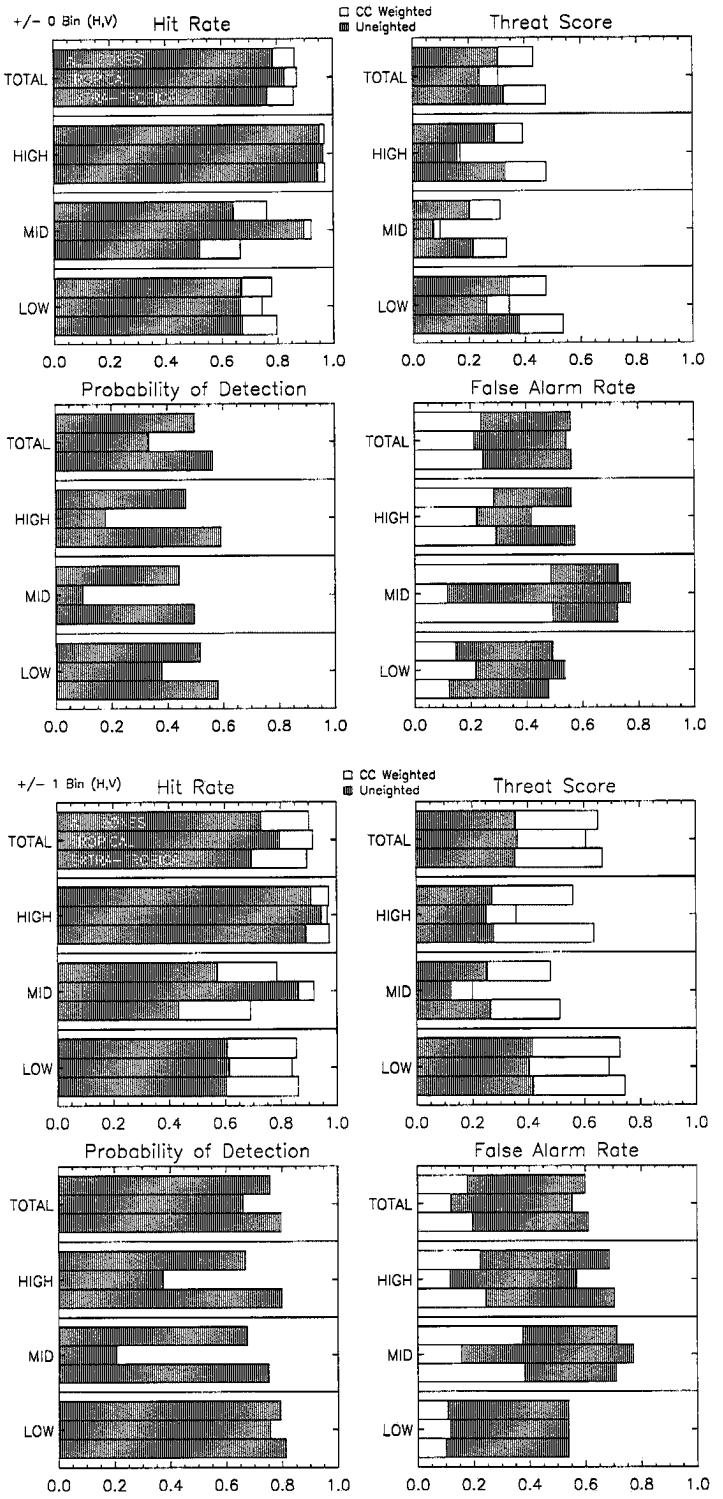

Figure B.20: LITE Orbit 032 Cloud Cover Statistics.

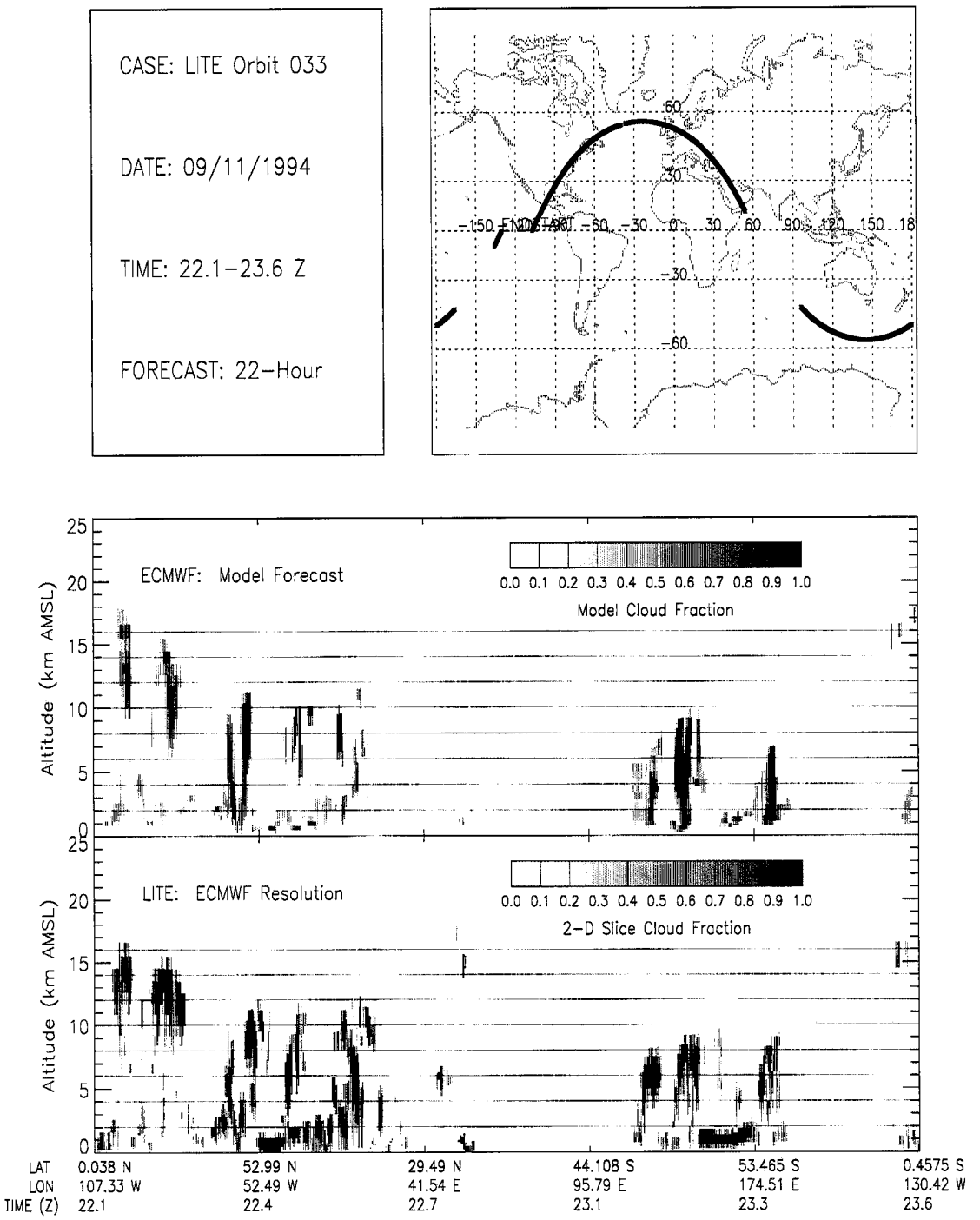

Figure B.21: LITE Orbit 033 Cloud Cover Comparison.

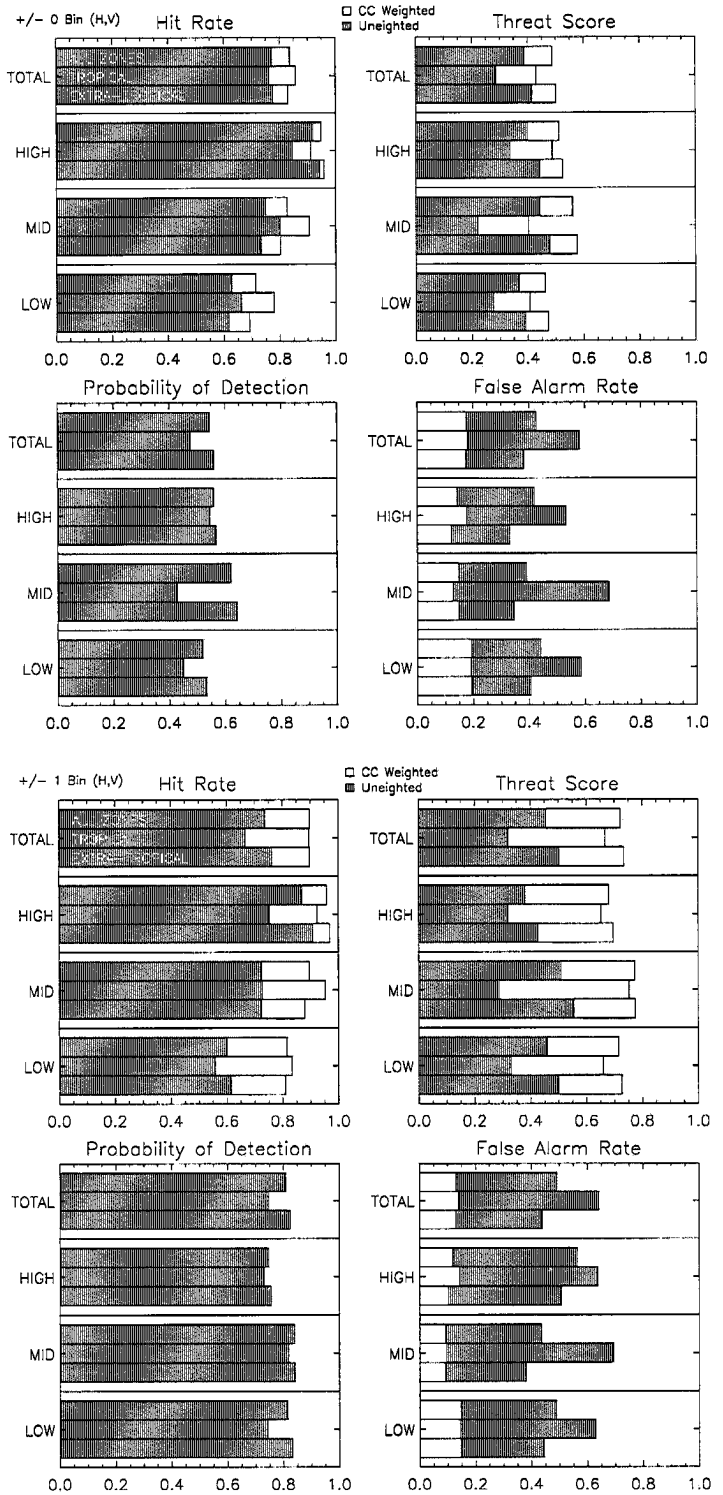

Figure B.22: LITE Orbit 033 Cloud Cover Statistics.

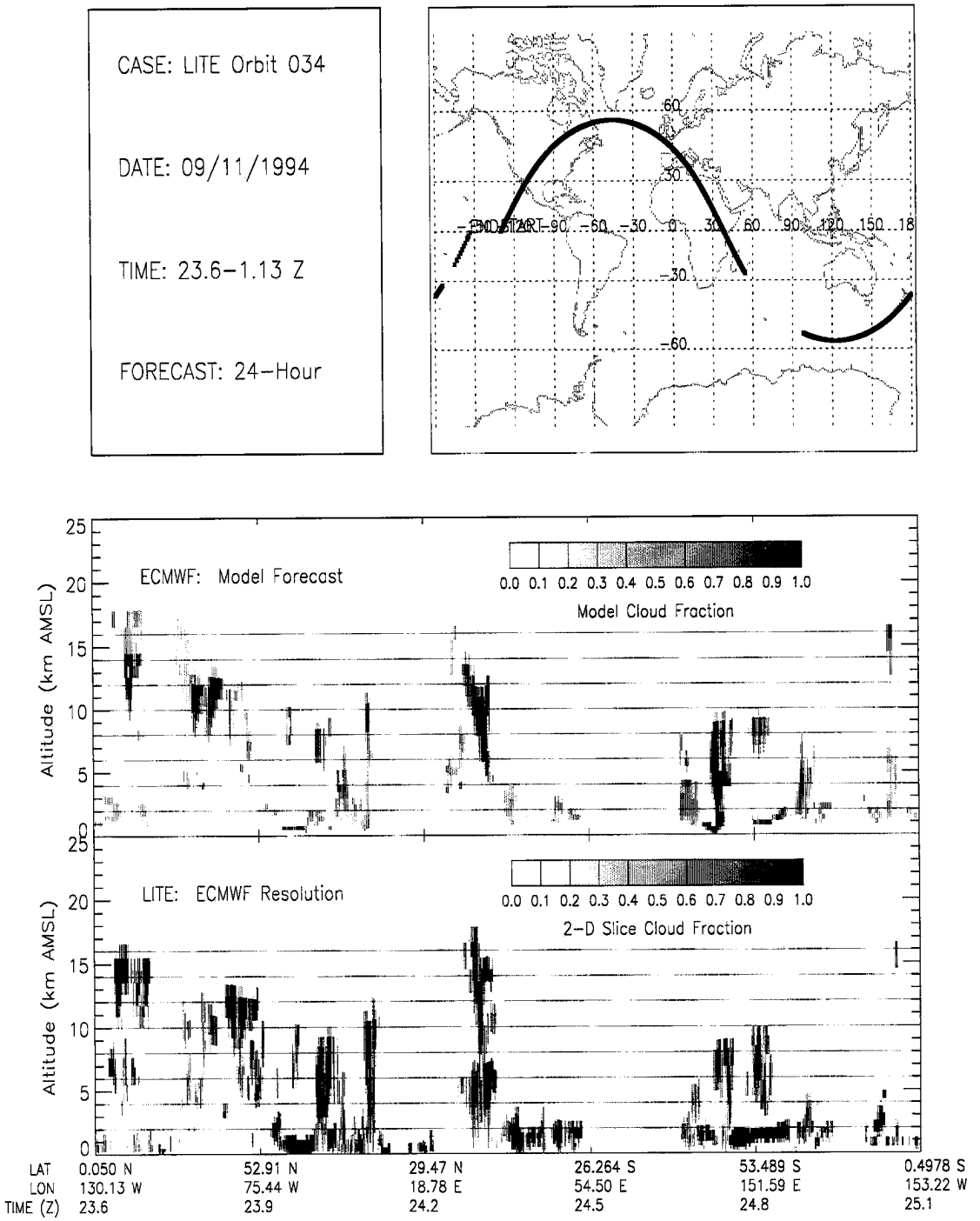

Figure B.23: LITE Orbit 034 Cloud Cover Comparison.

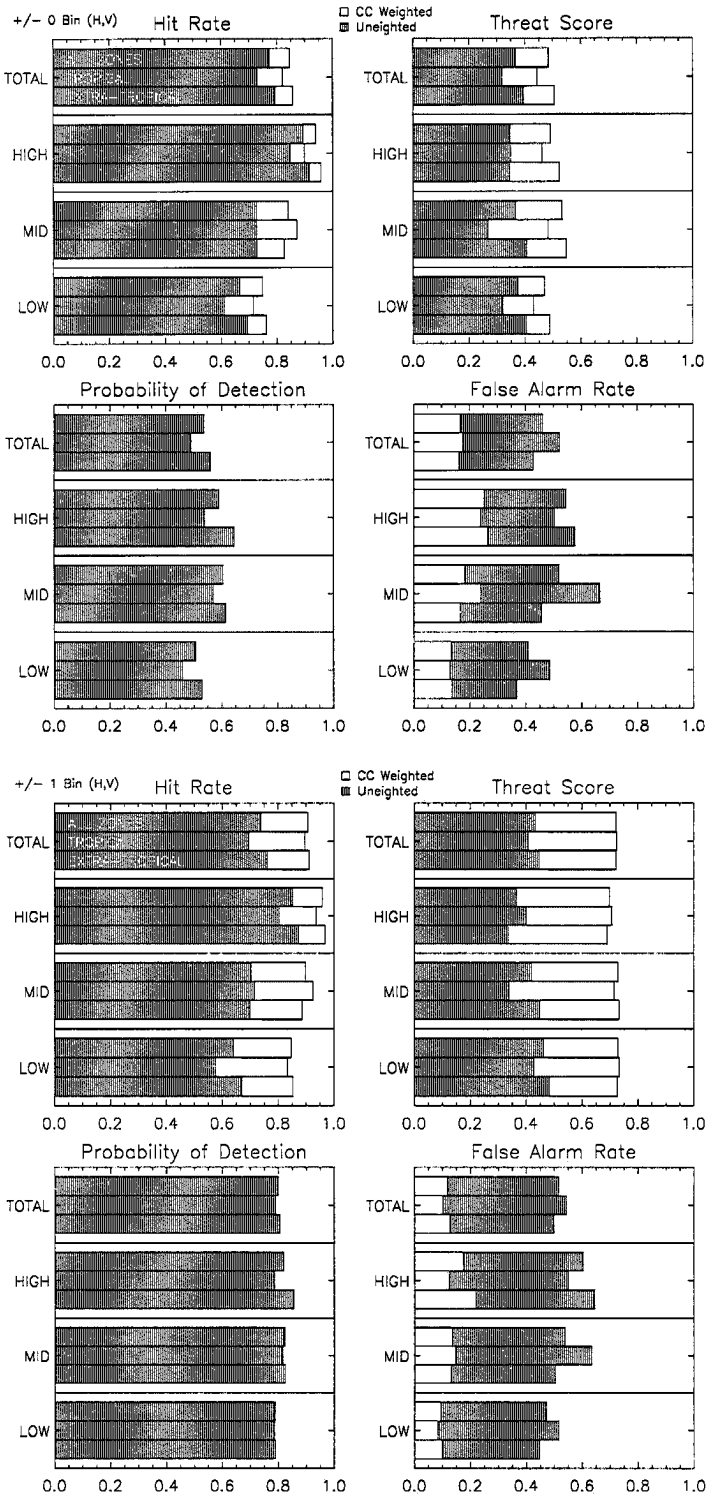

Figure B.24: LITE Orbit 034 Cloud Cover Statistics.

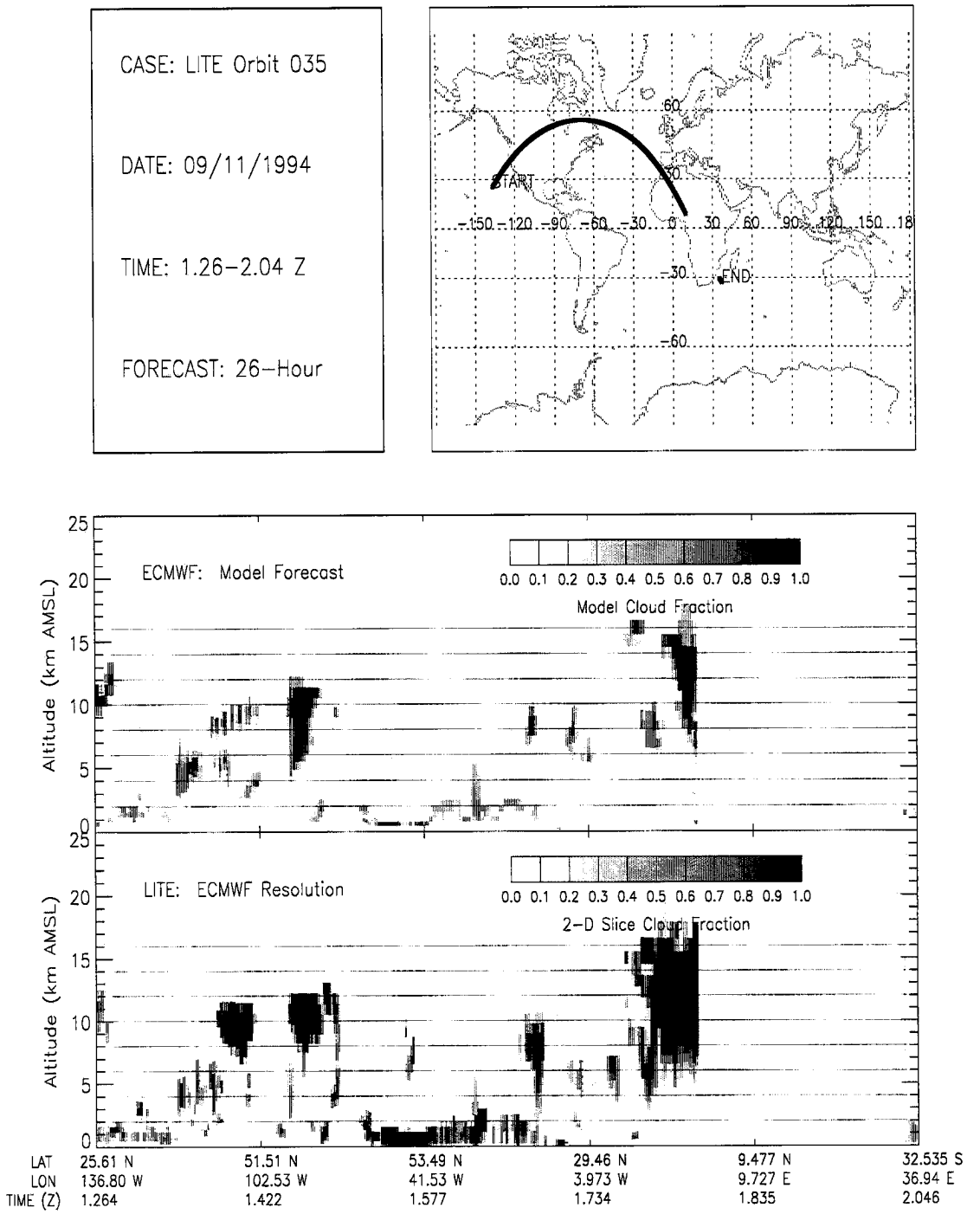

Figure B.25: LITE Orbit 035 Cloud Cover Comparison.

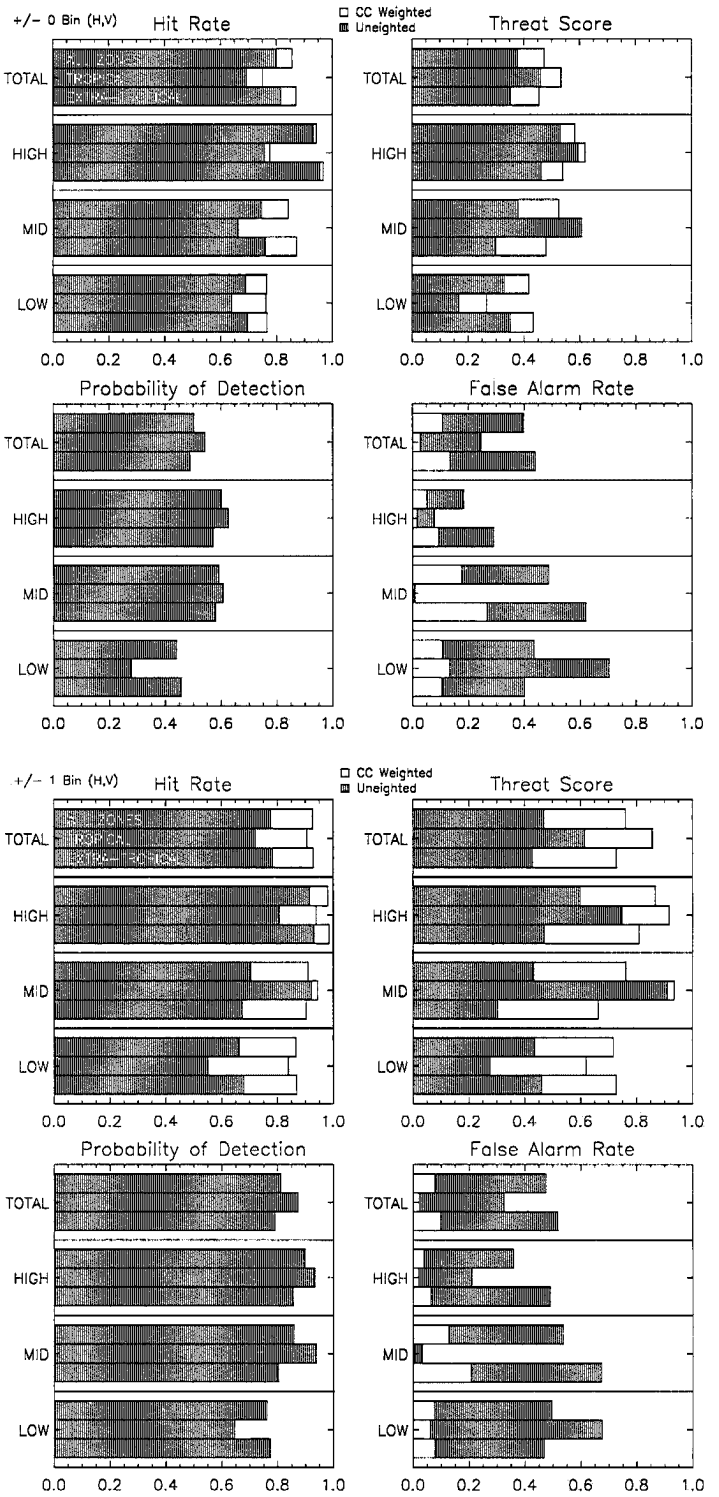

Figure B.26: LITE Orbit 035 Cloud Cover Statistics.

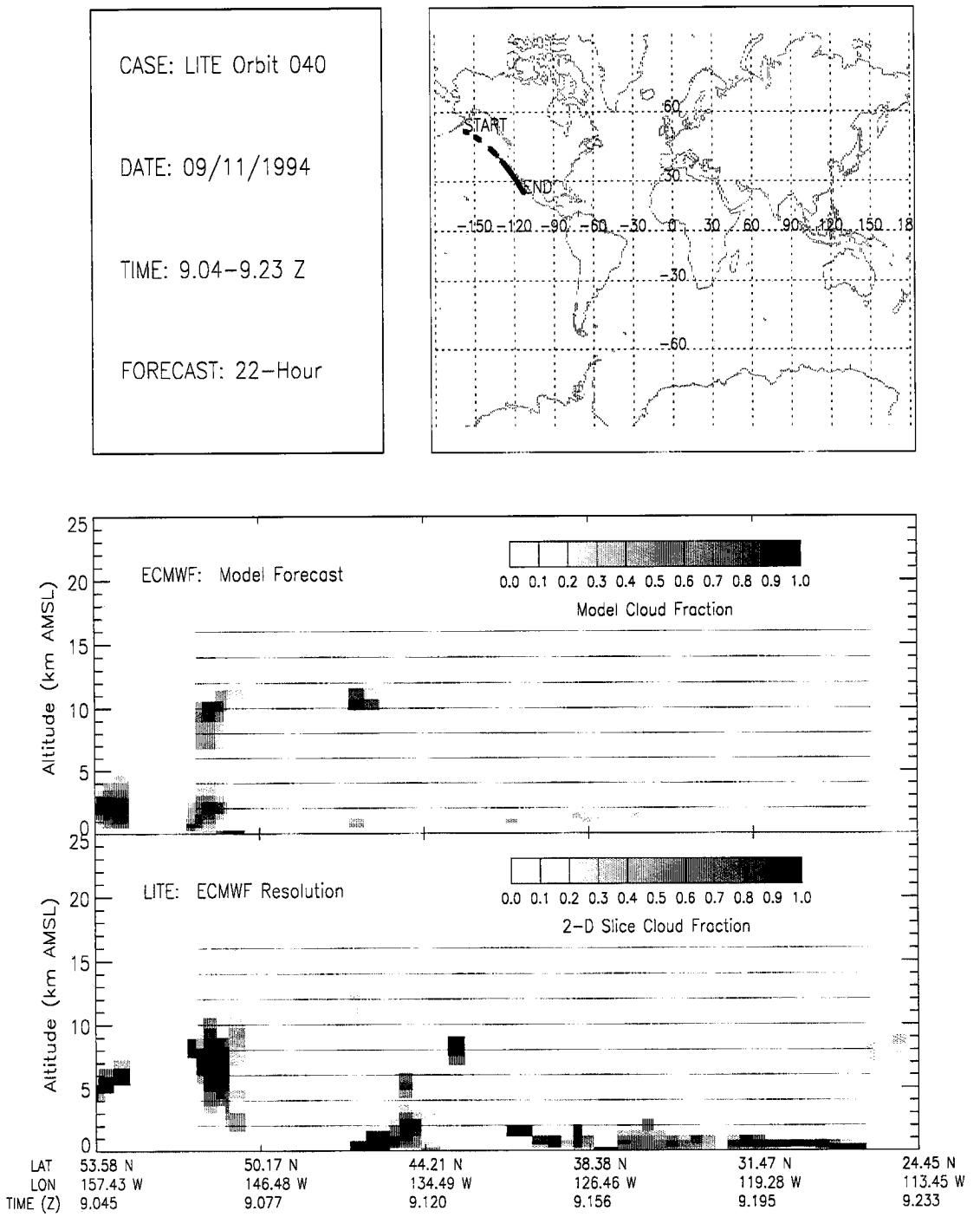

Figure B.27: LITE Orbit 040 Cloud Cover Comparison.

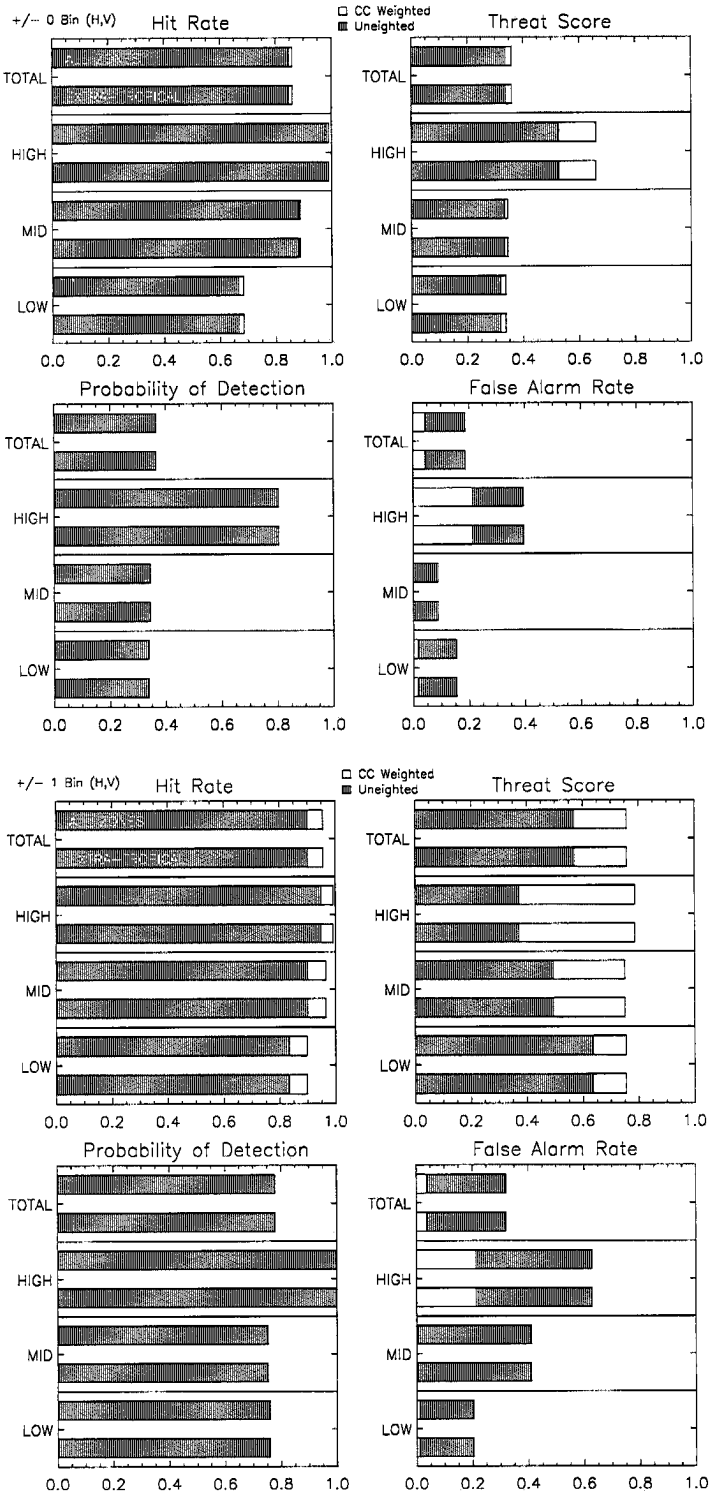

Figure B.28: LITE Orbit 040 Cloud Cover Statistics.

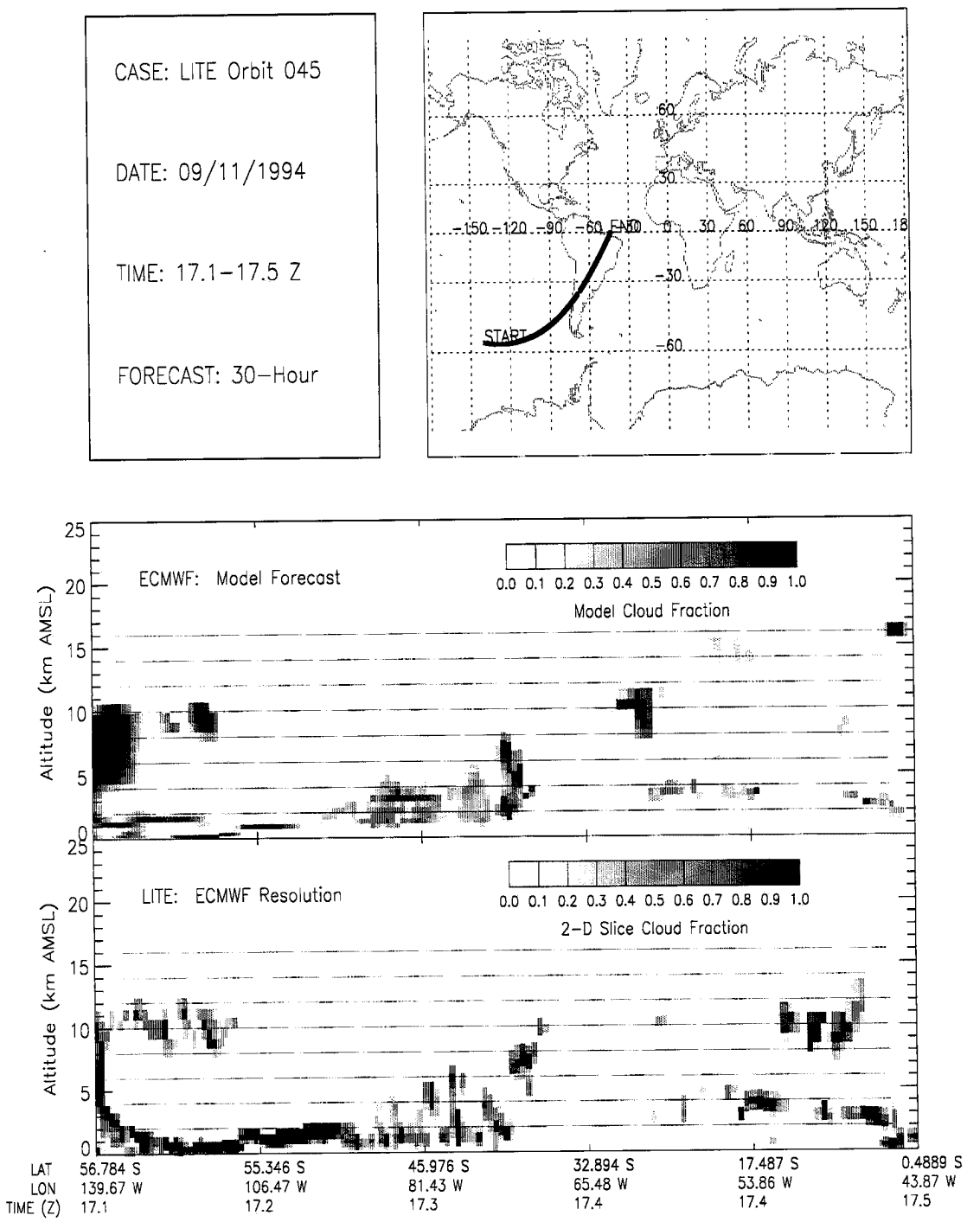

Figure B.29: LITE Orbit 045 Cloud Cover Comparison.

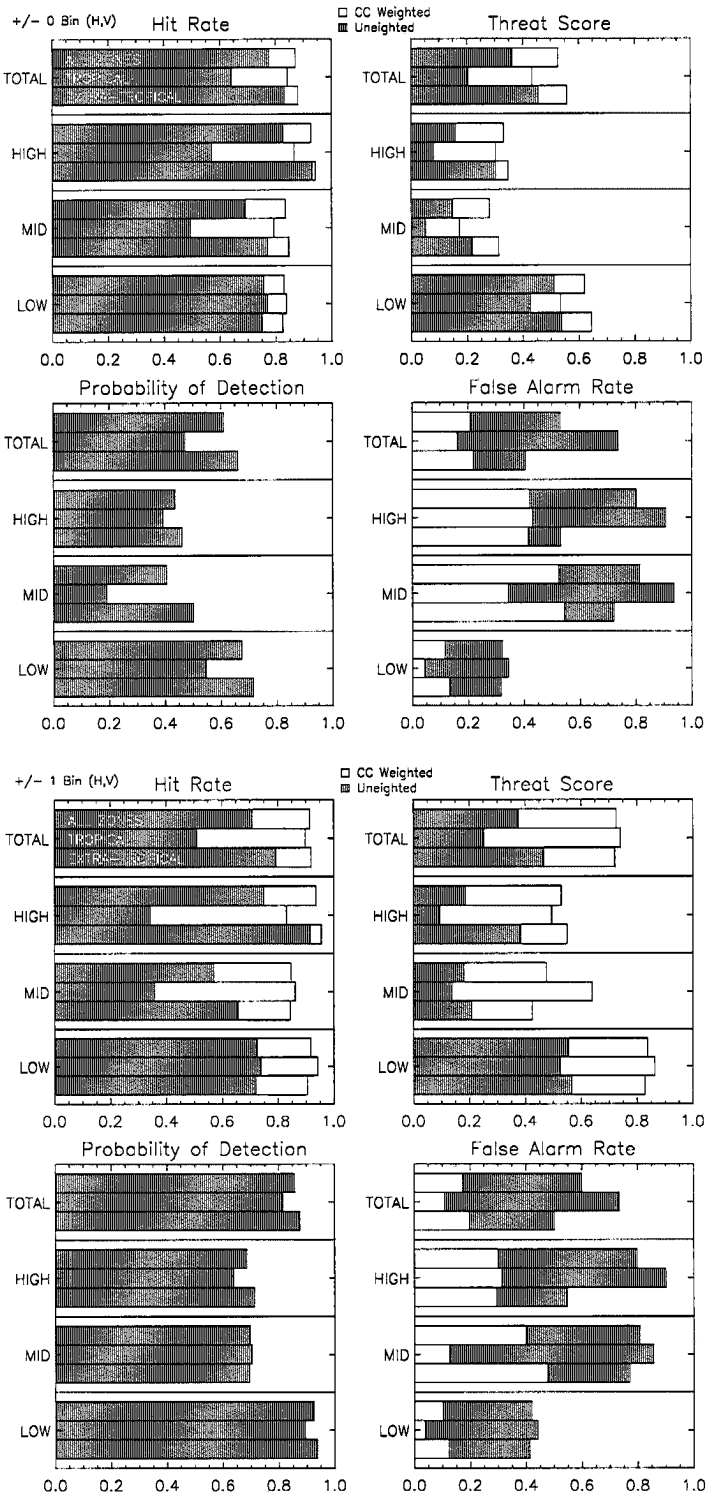

Figure B.30: LITE Orbit 045 Cloud Cover Statistics.

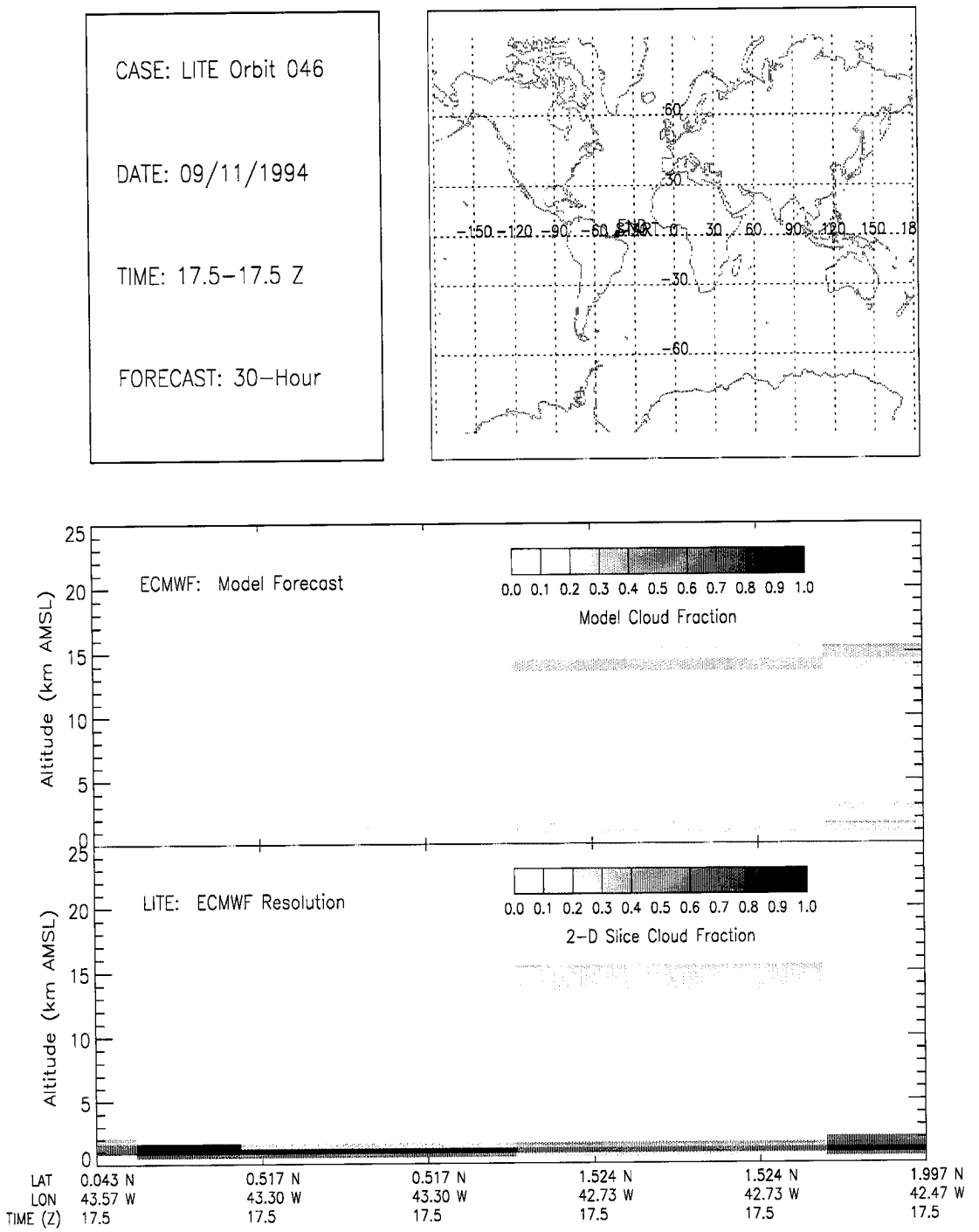

Figure B.31: LITE Orbit 046 Cloud Cover Comparison.

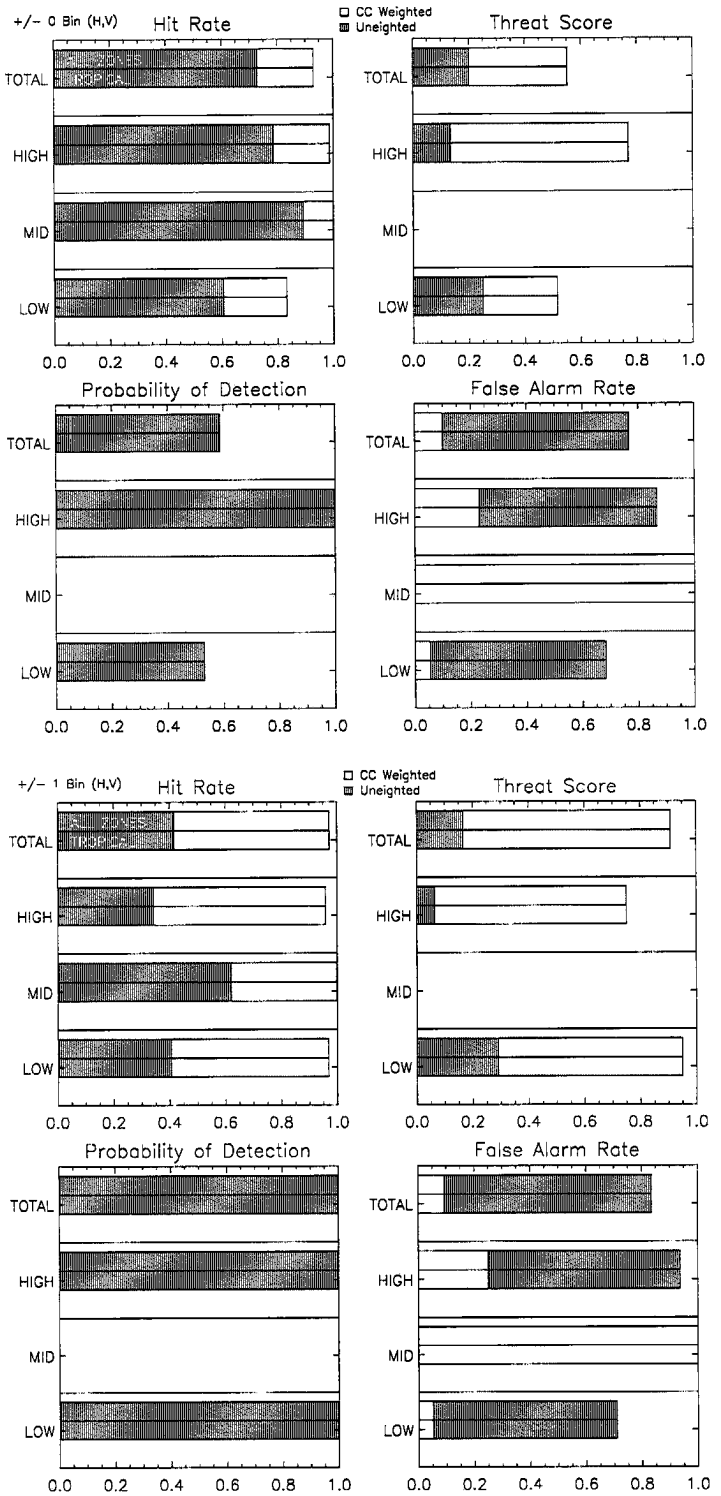

Figure B.32: LITE Orbit 046 Cloud Cover Statistics.

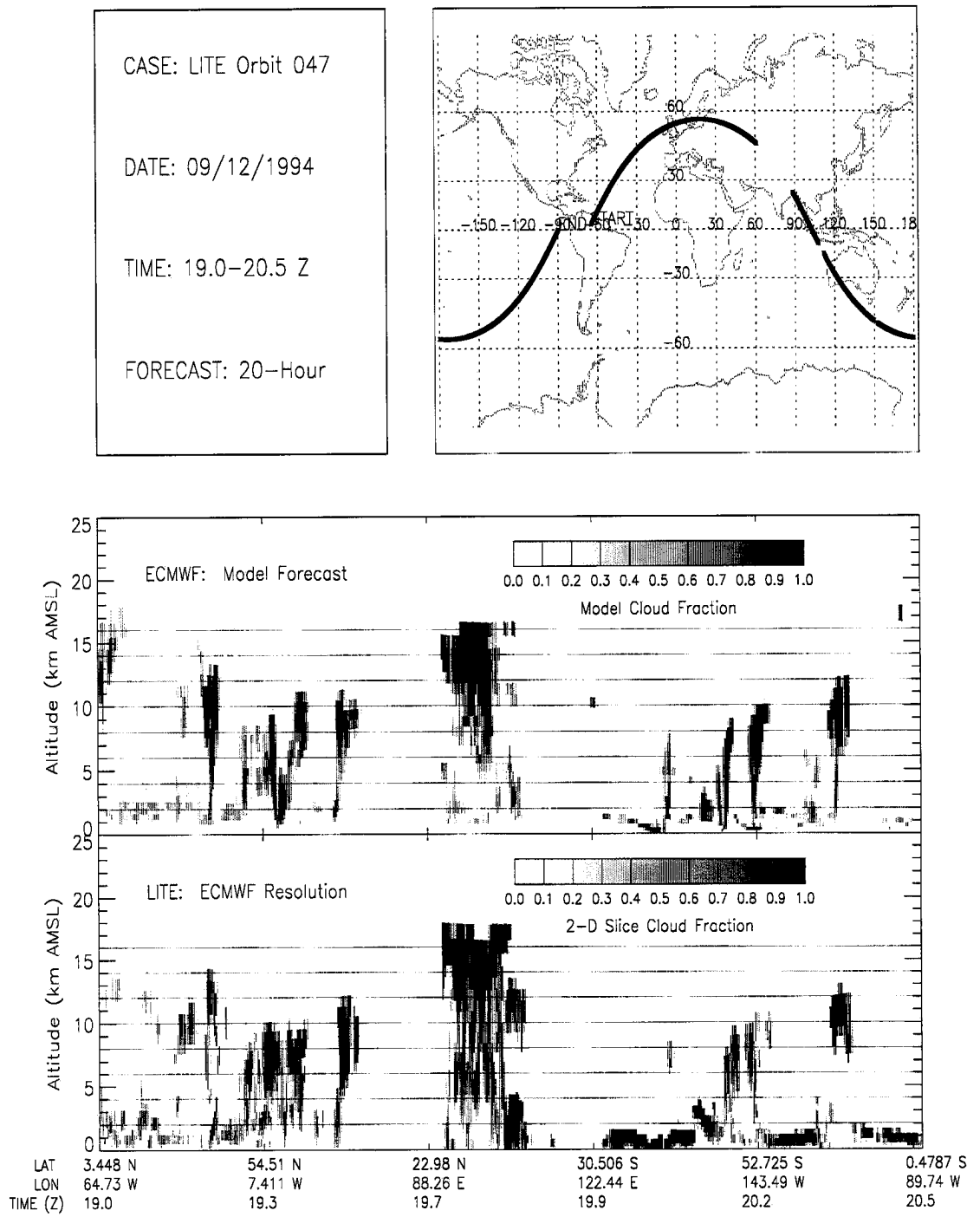

Figure B.33: LITE Orbit 047 Cloud Cover Comparison.

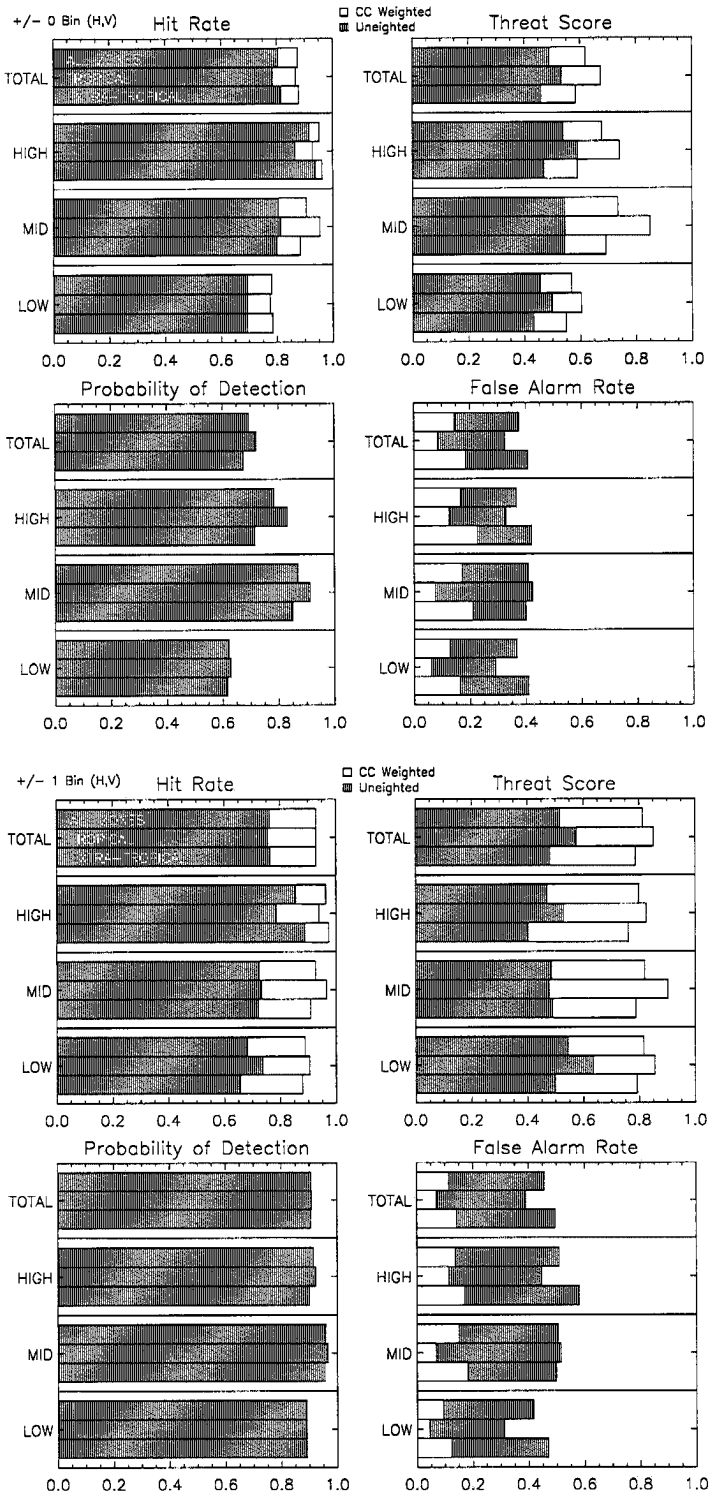

Figure B.34: LITE Orbit 047 Cloud Cover Statistics.

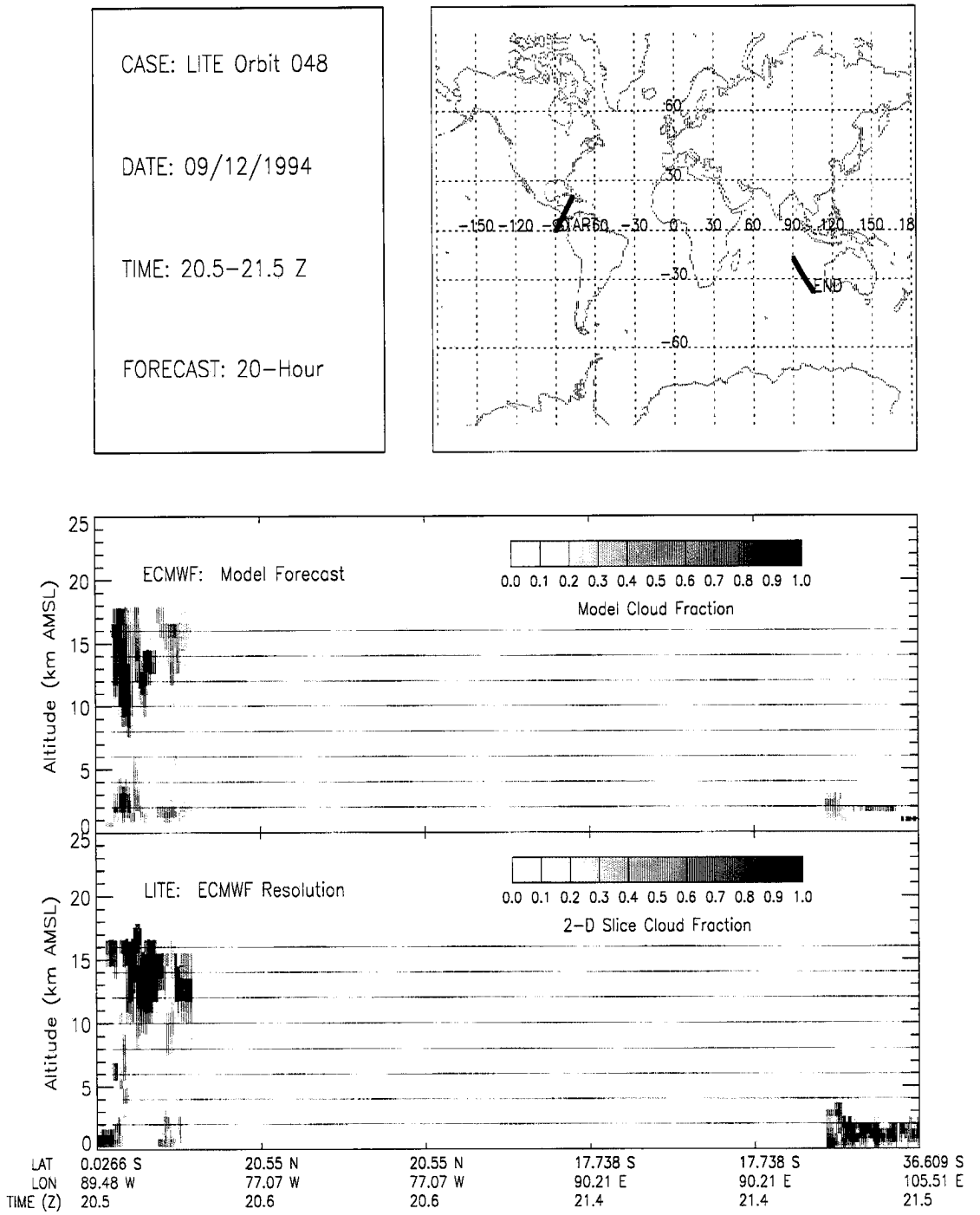

Figure B.35: LITE Orbit 048 Cloud Cover Comparison.

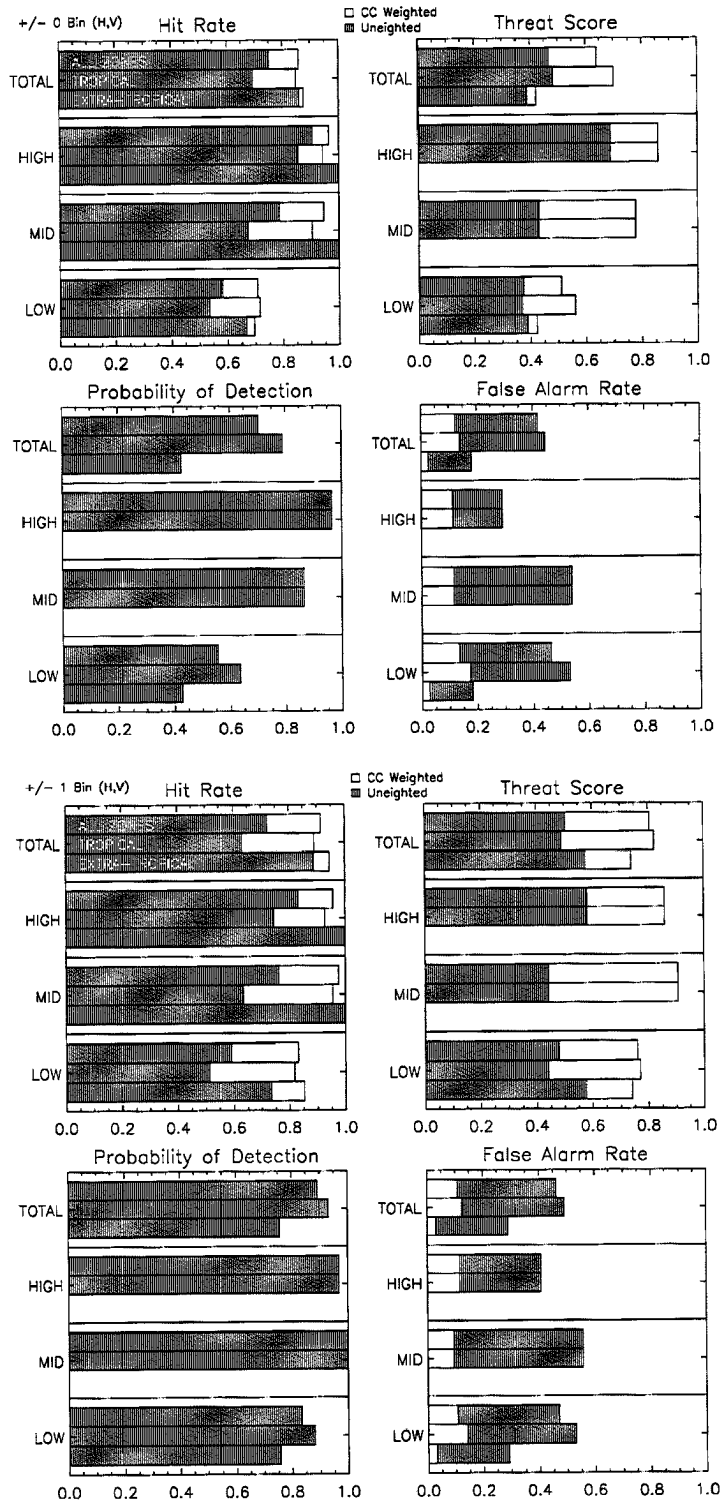

Figure B.36: LITE Orbit 048 Cloud Cover Statistics.

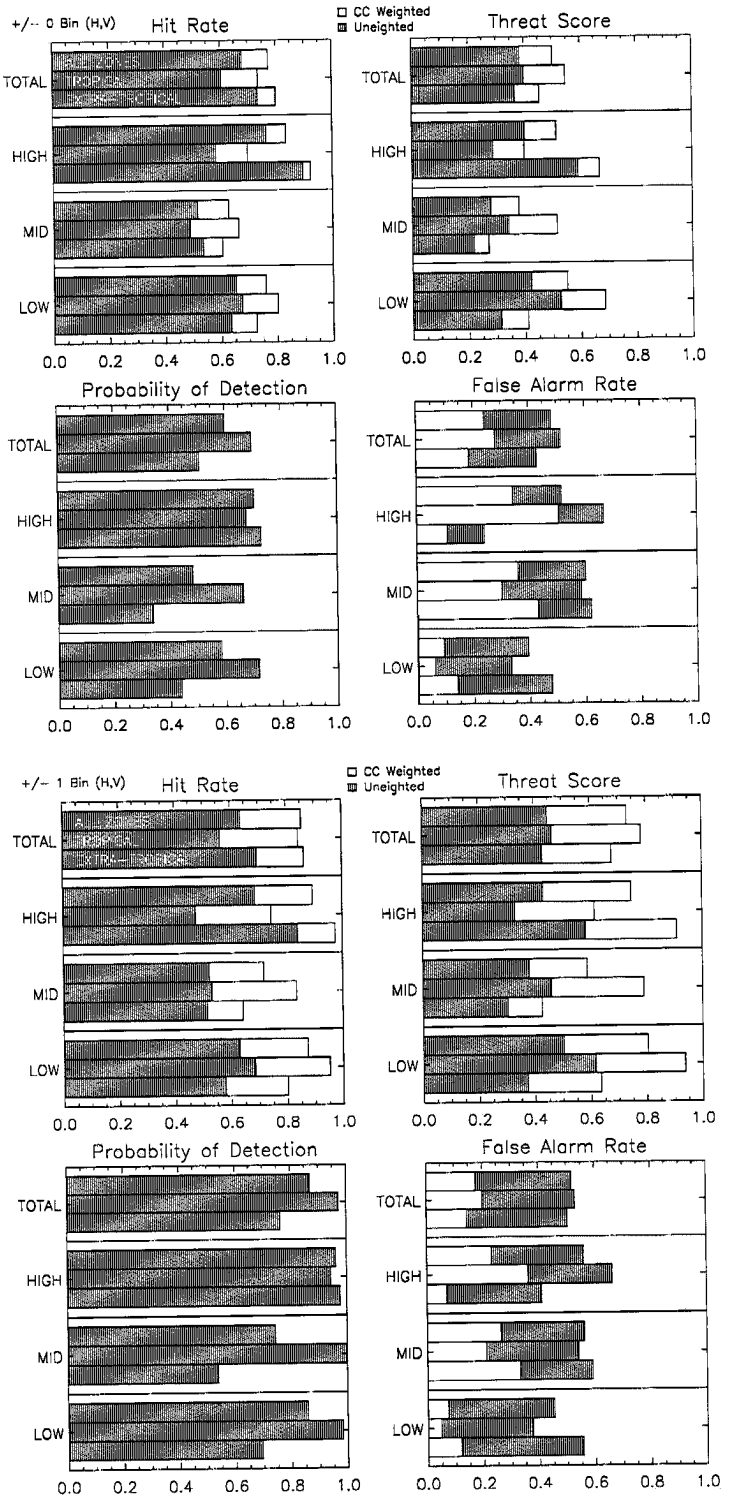

Figure B.38: LITE Orbit 050 Cloud Cover Statistics.

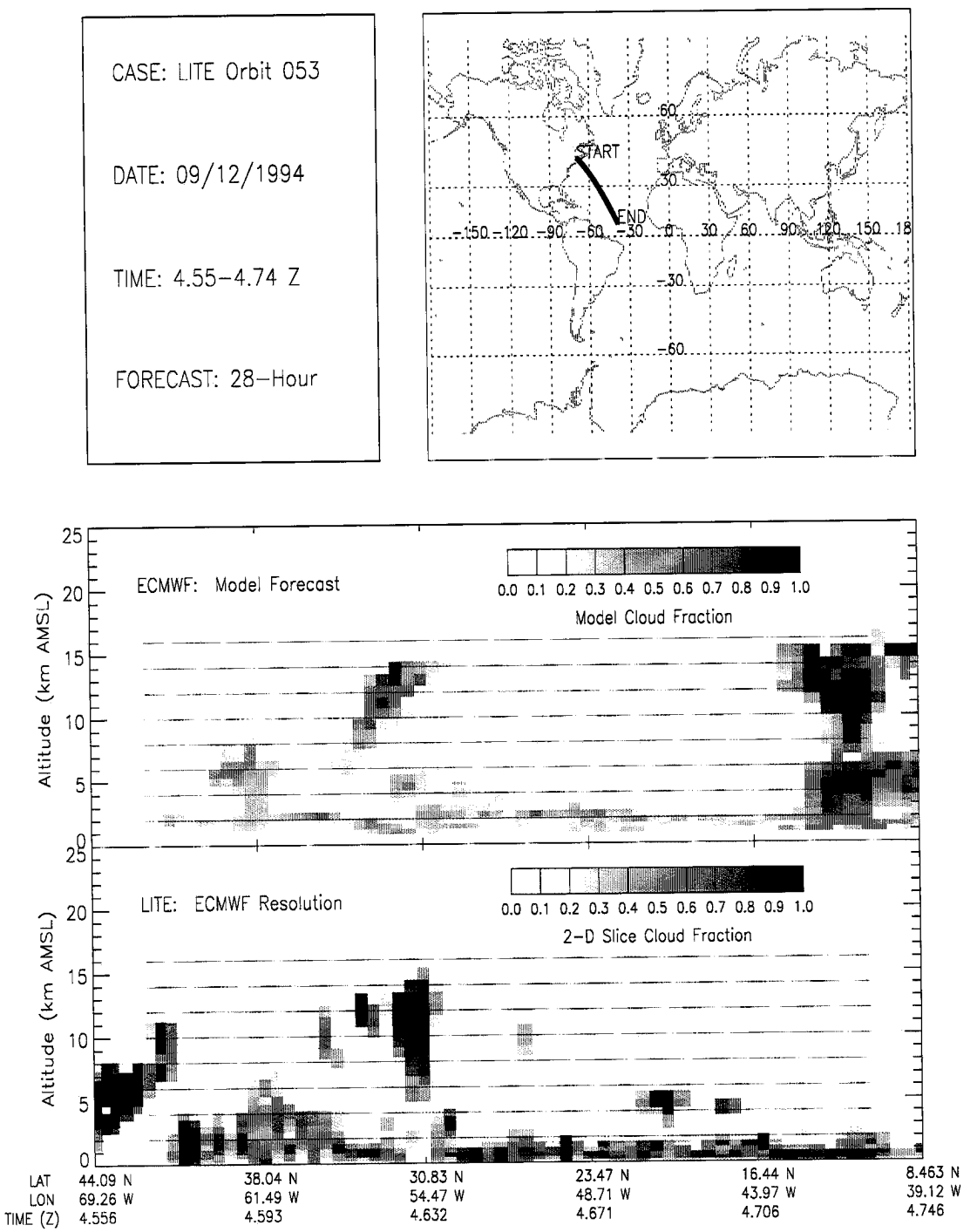

Figure B.39: LITE Orbit 053 Cloud Cover Comparison.

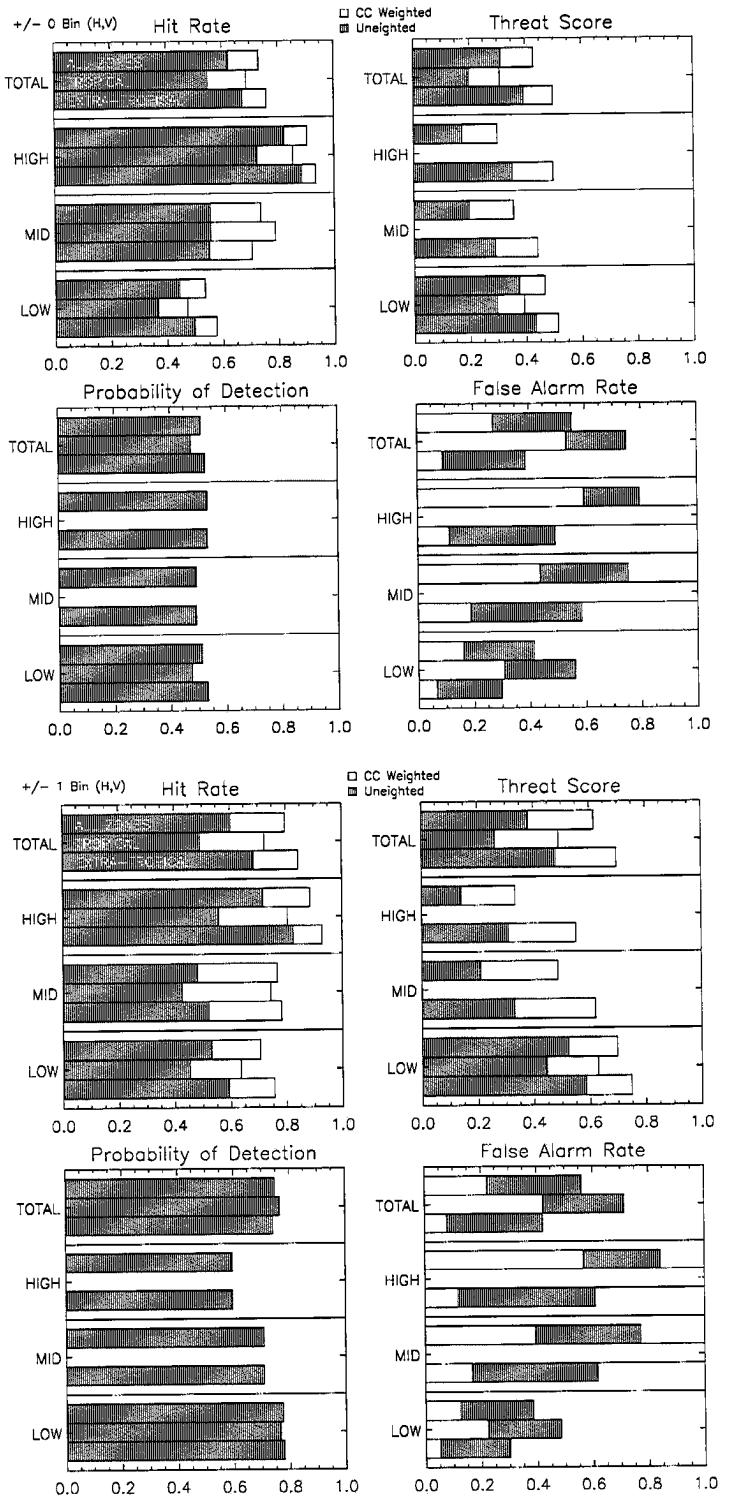

Figure B.40: LITE Orbit 053 Cloud Cover Statistics.

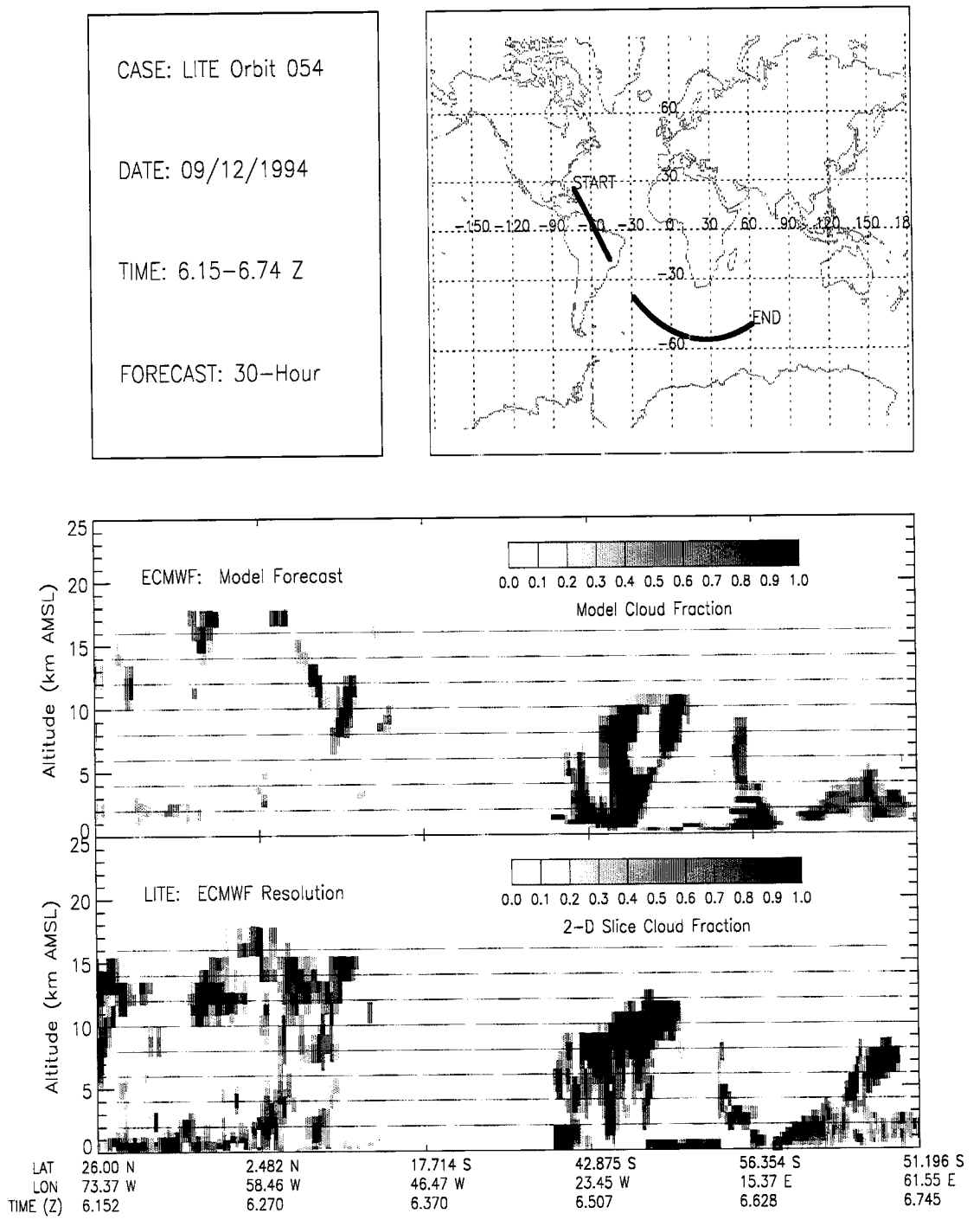

Figure B.41: LITE Orbit 054 Cloud Cover Comparison.

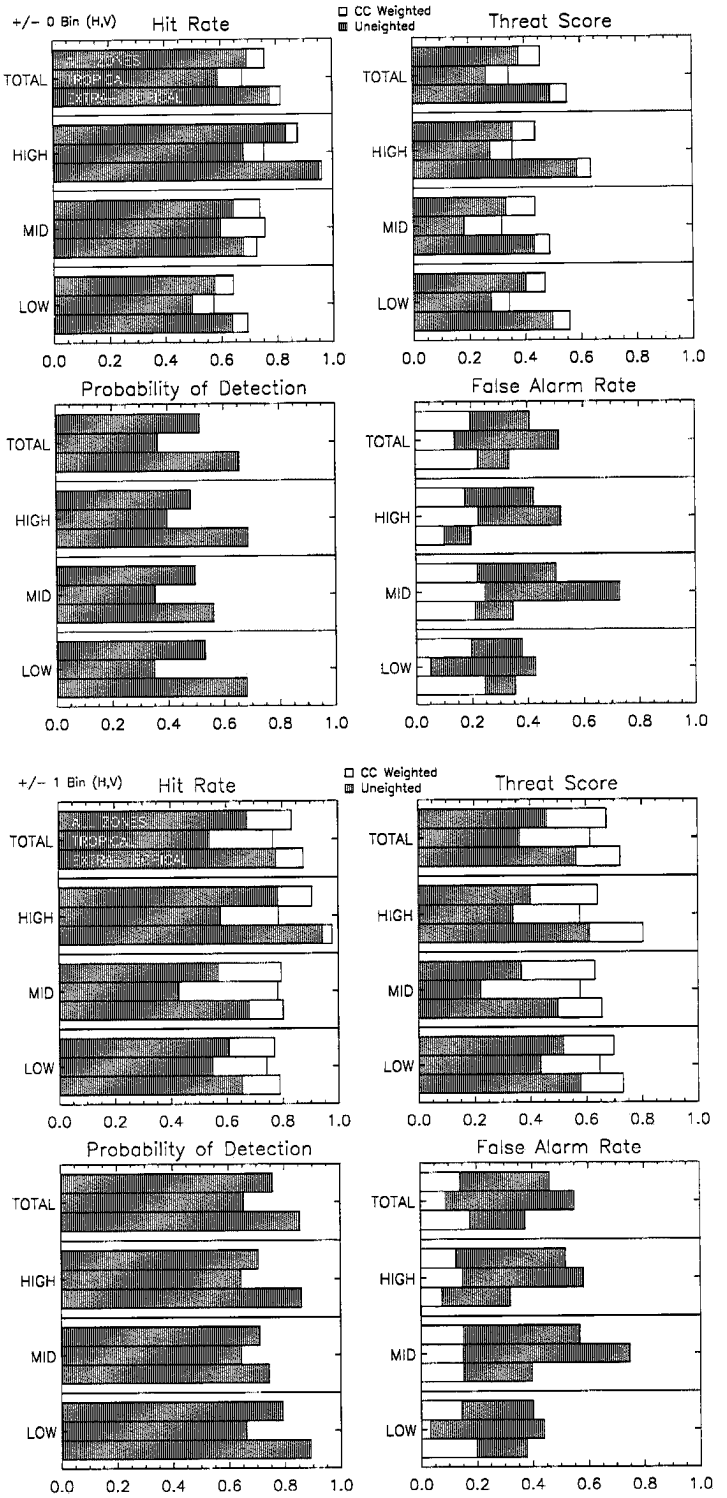

Figure B.42: LITE Orbit 054 Cloud Cover Statistics.

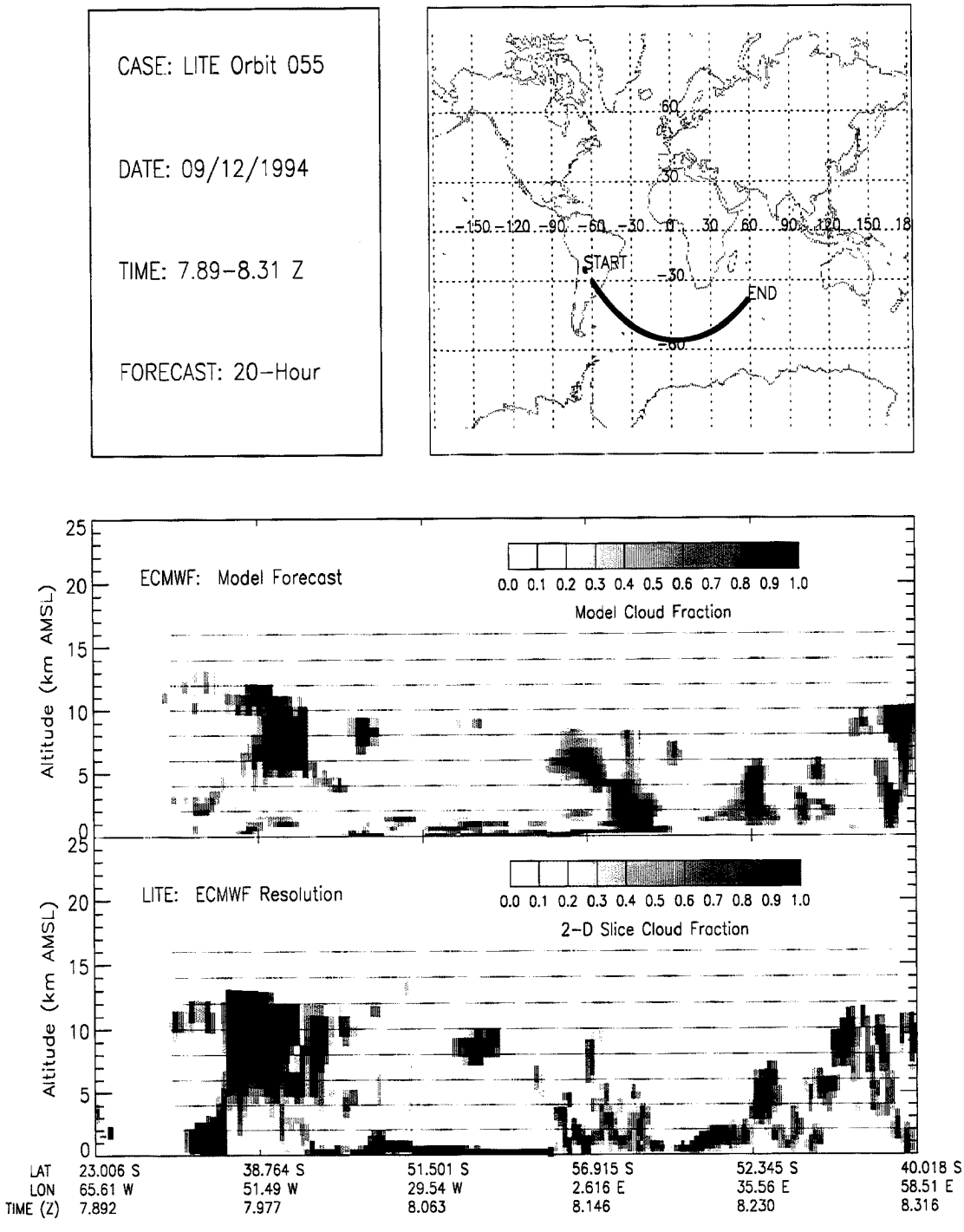

Figure B.43: LITE Orbit 055 Cloud Cover Comparison.

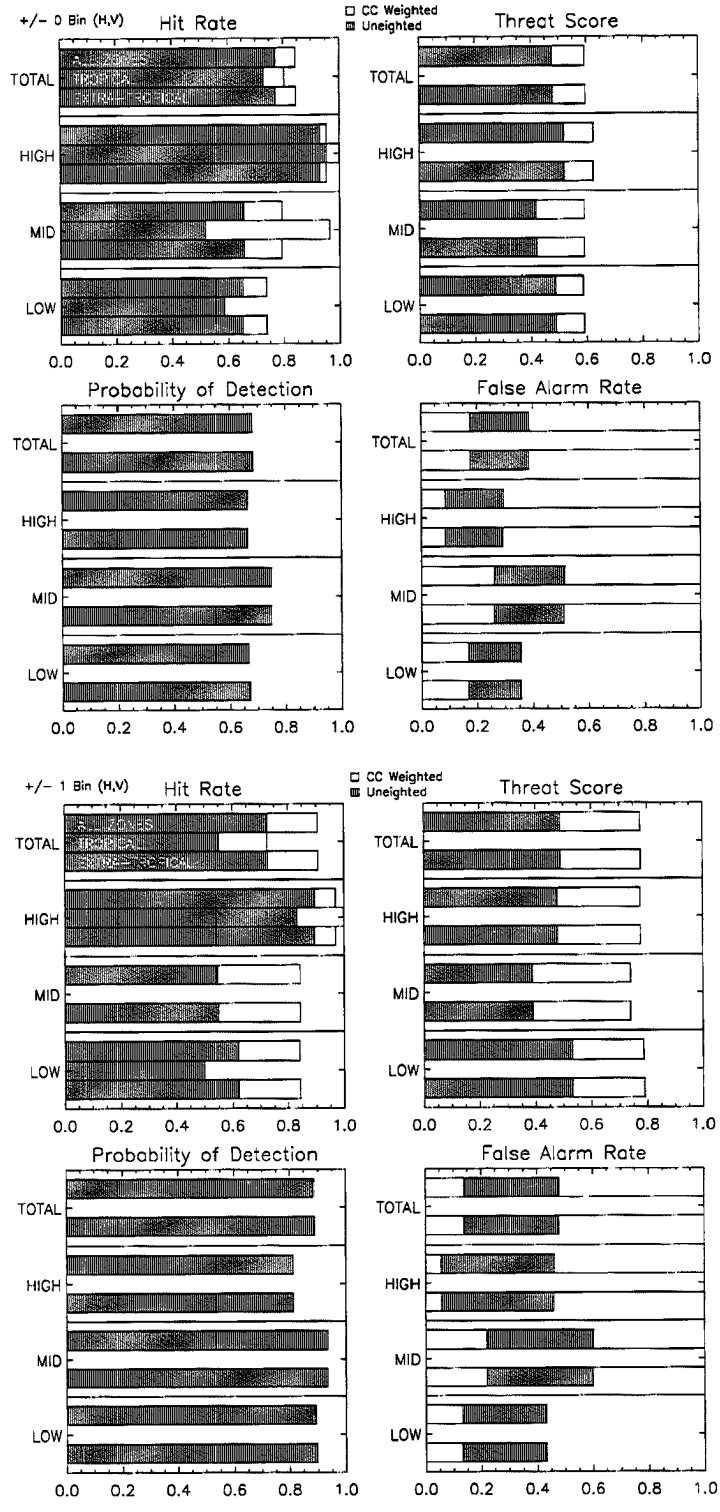

Figure B.44: LITE Orbit 055 Cloud Cover Statistics.

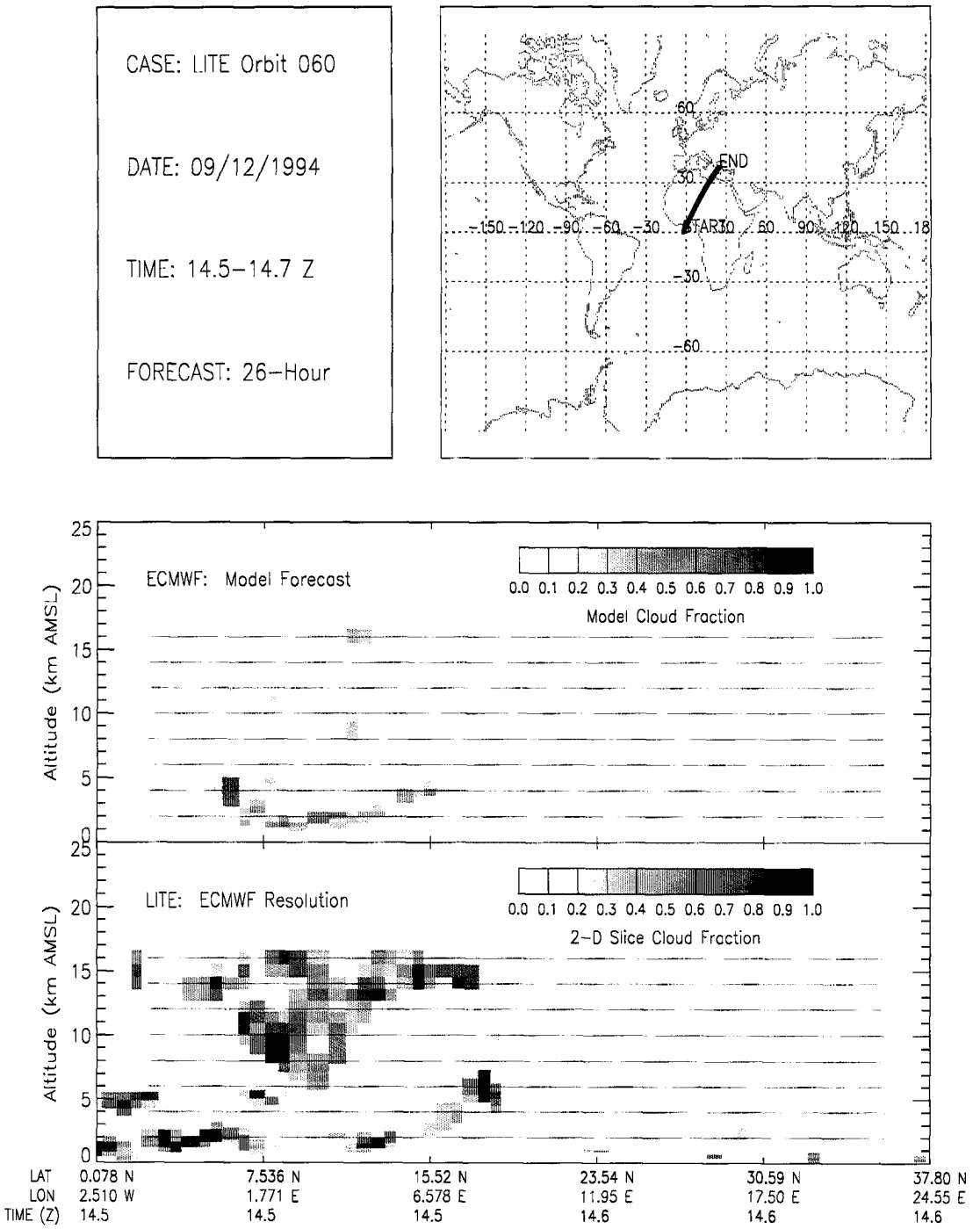

Figure B.45: LITE Orbit 060 Cloud Cover Comparison.

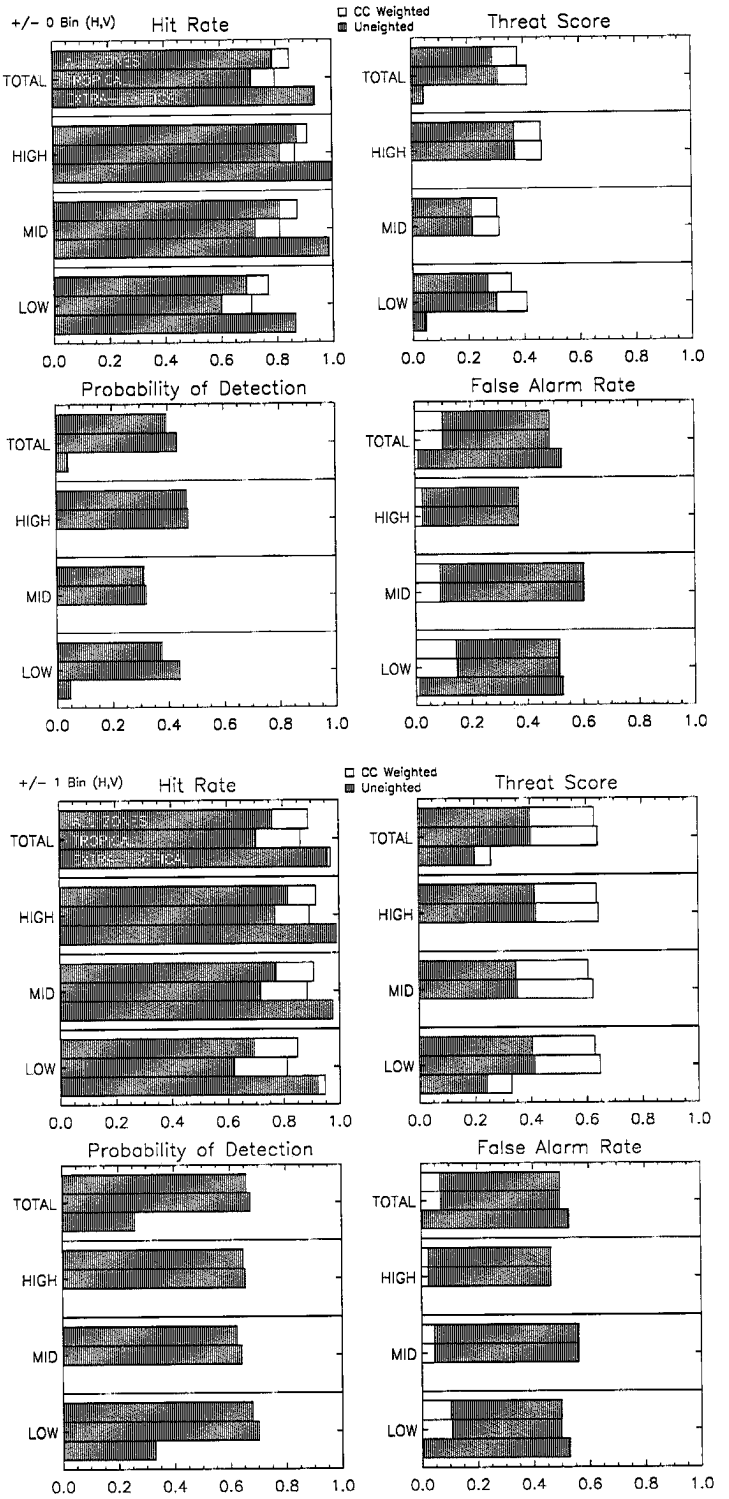

Figure B.46: LITE Orbit 060 Cloud Cover Statistics.

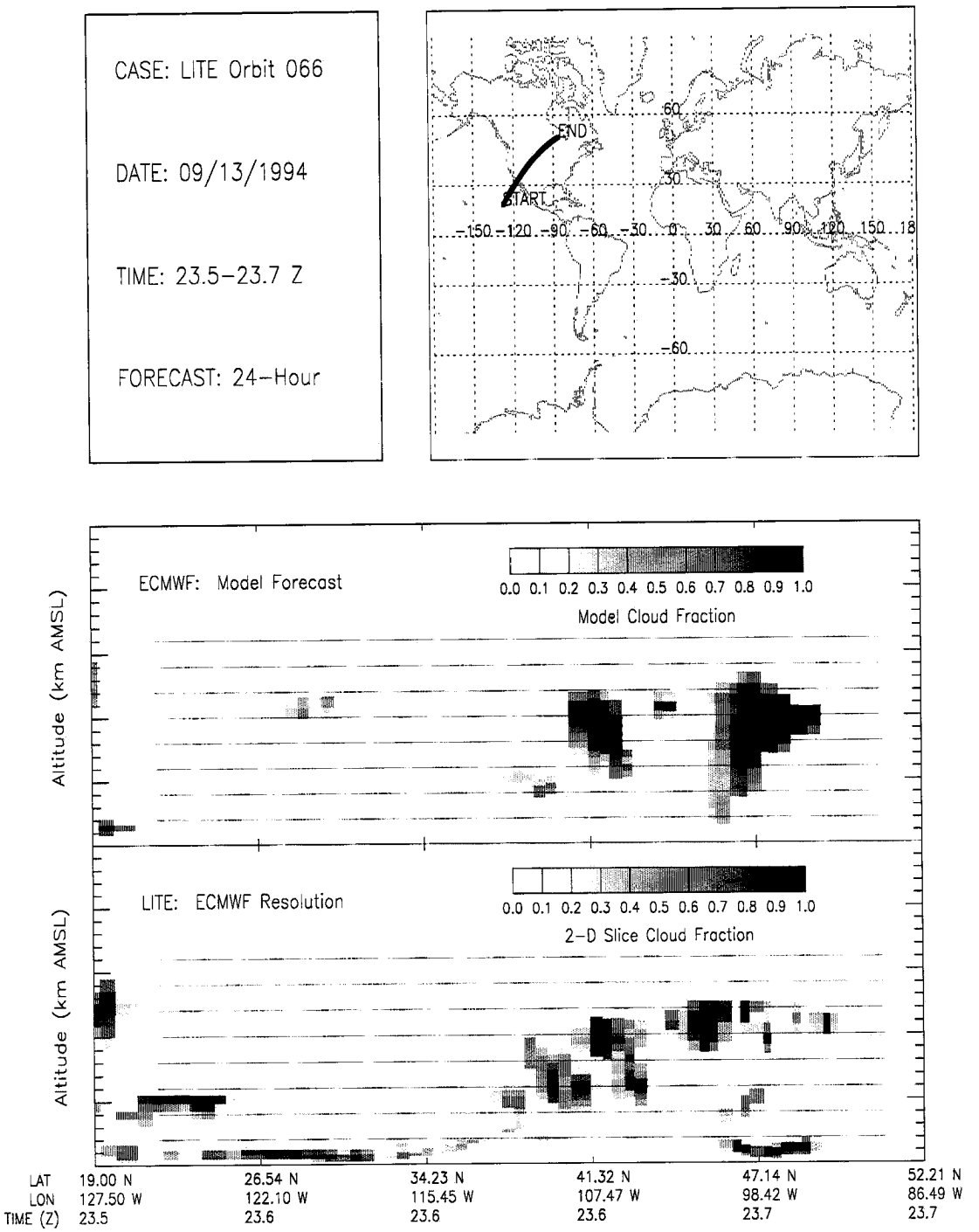

Figure B.47: LITE Orbit 066 Cloud Cover Comparison.

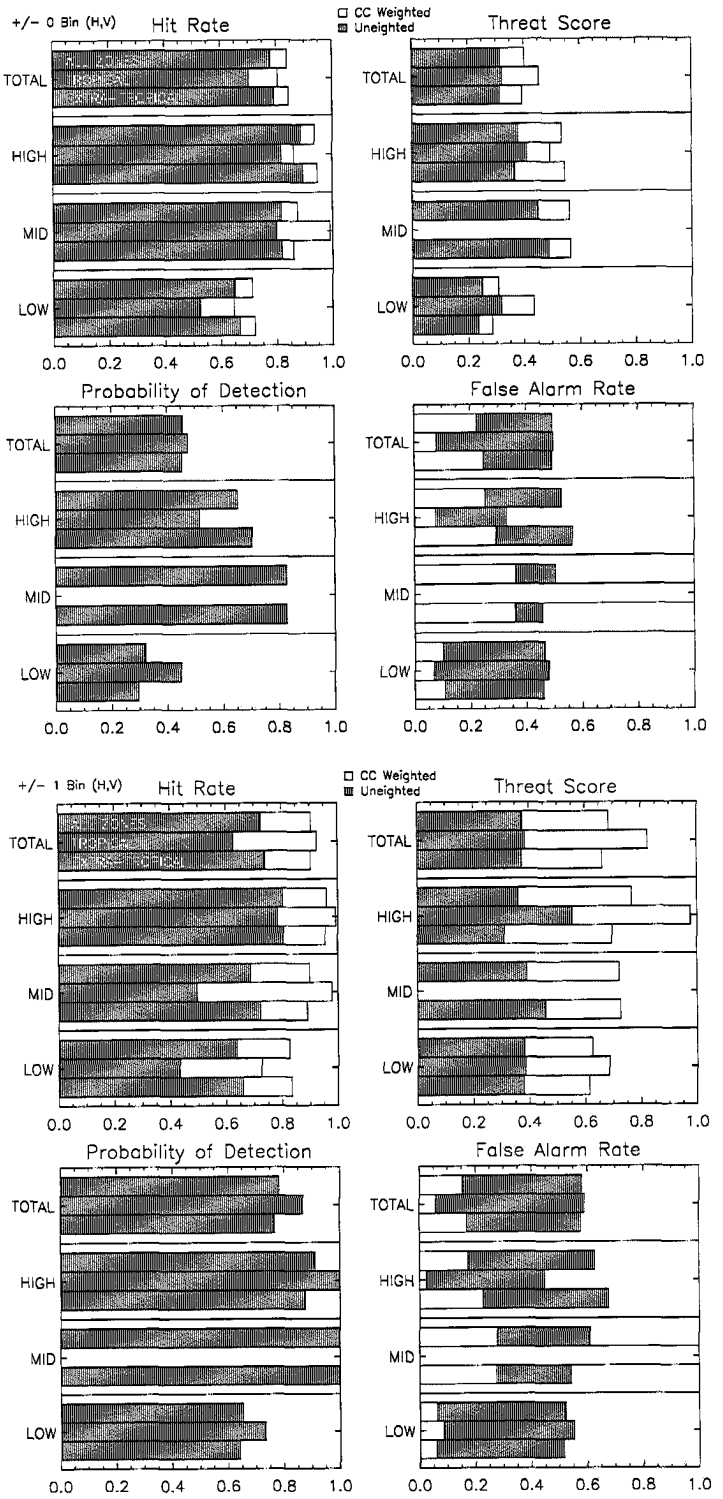

Figure B.48: LITE Orbit 066 Cloud Cover Statistics.

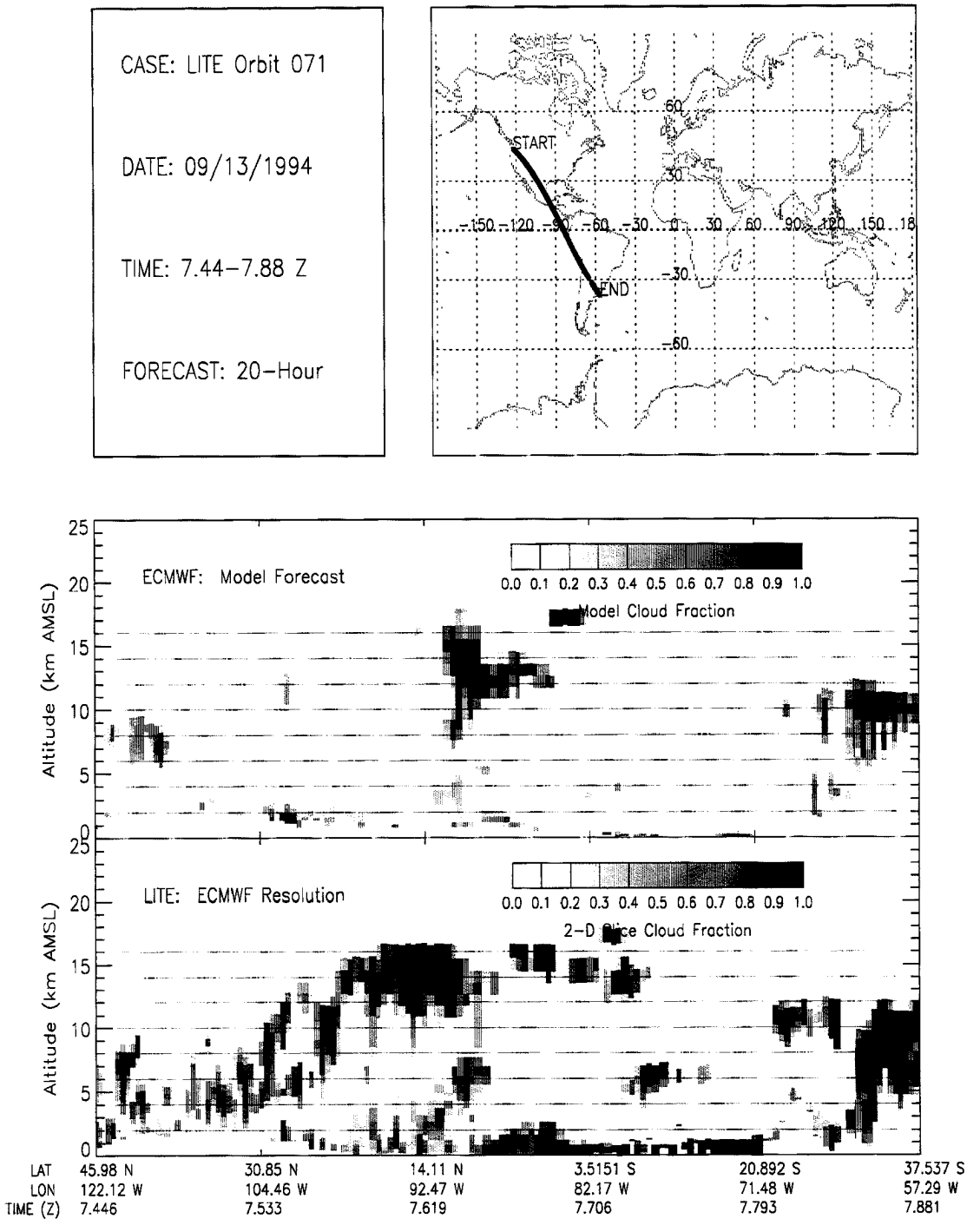

Figure B.49: LITE Orbit 071 Cloud Cover Comparison.

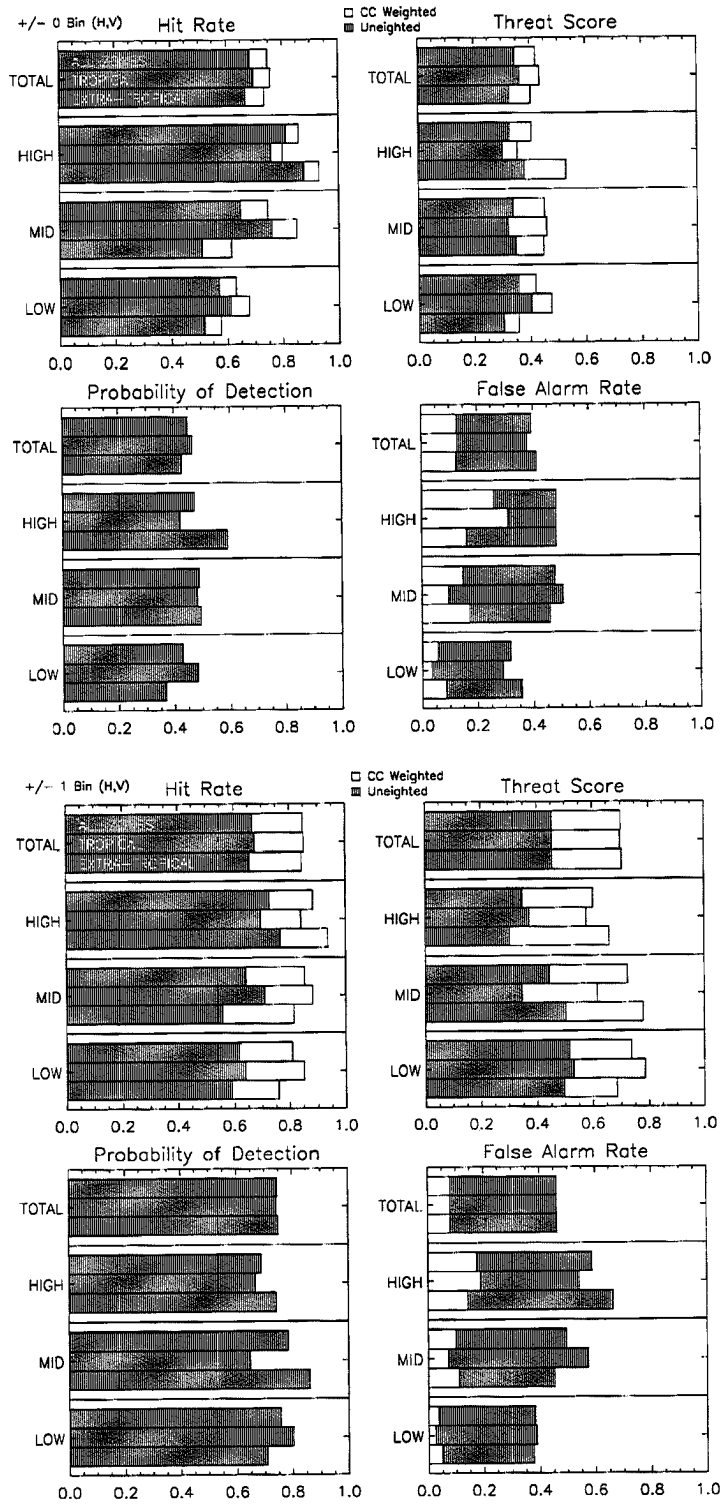

Figure B.50: LITE Orbit 071 Cloud Cover Statistics.

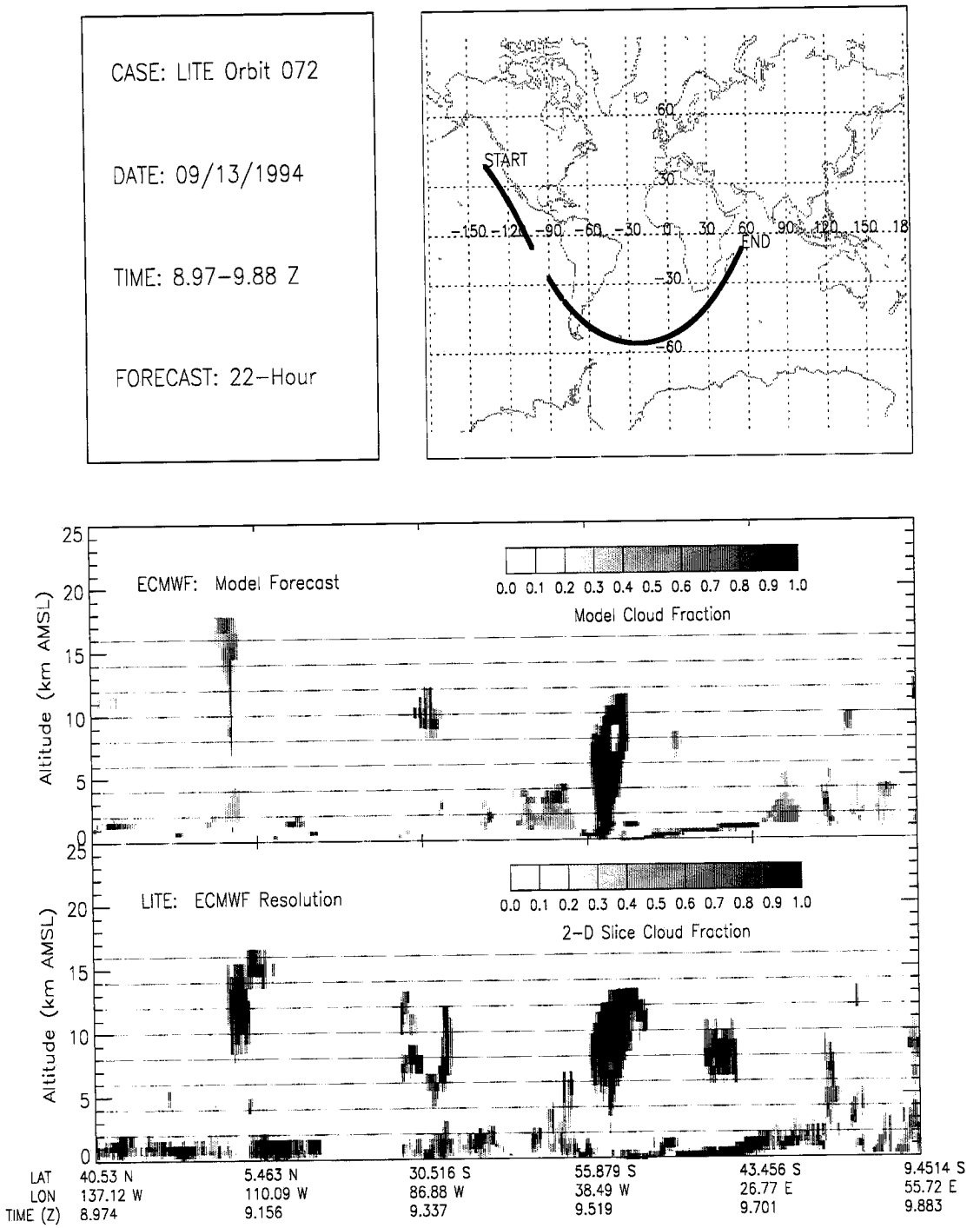

Figure B.51: LITE Orbit 072 Cloud Cover Comparison.

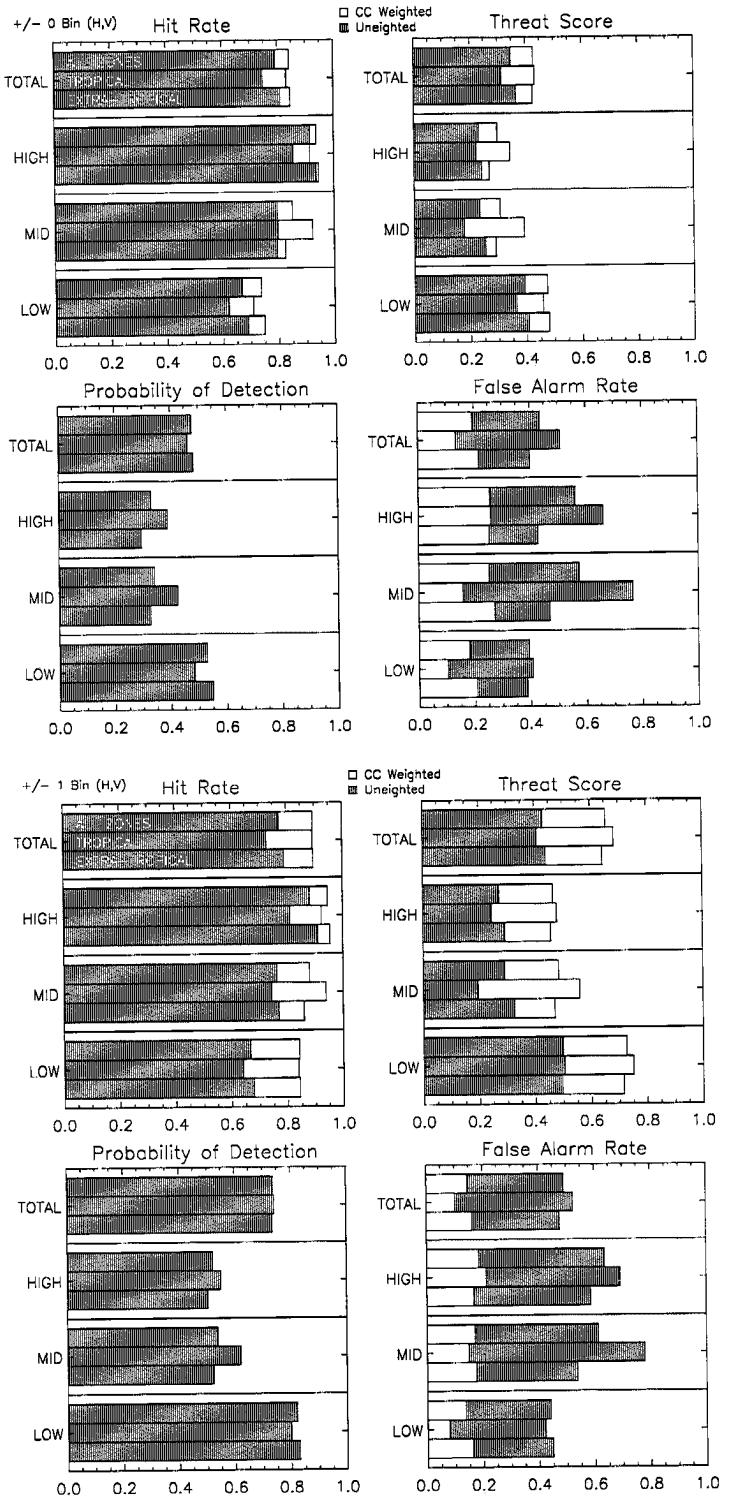

Figure B.52: LITE Orbit 072 Cloud Cover Statistics.

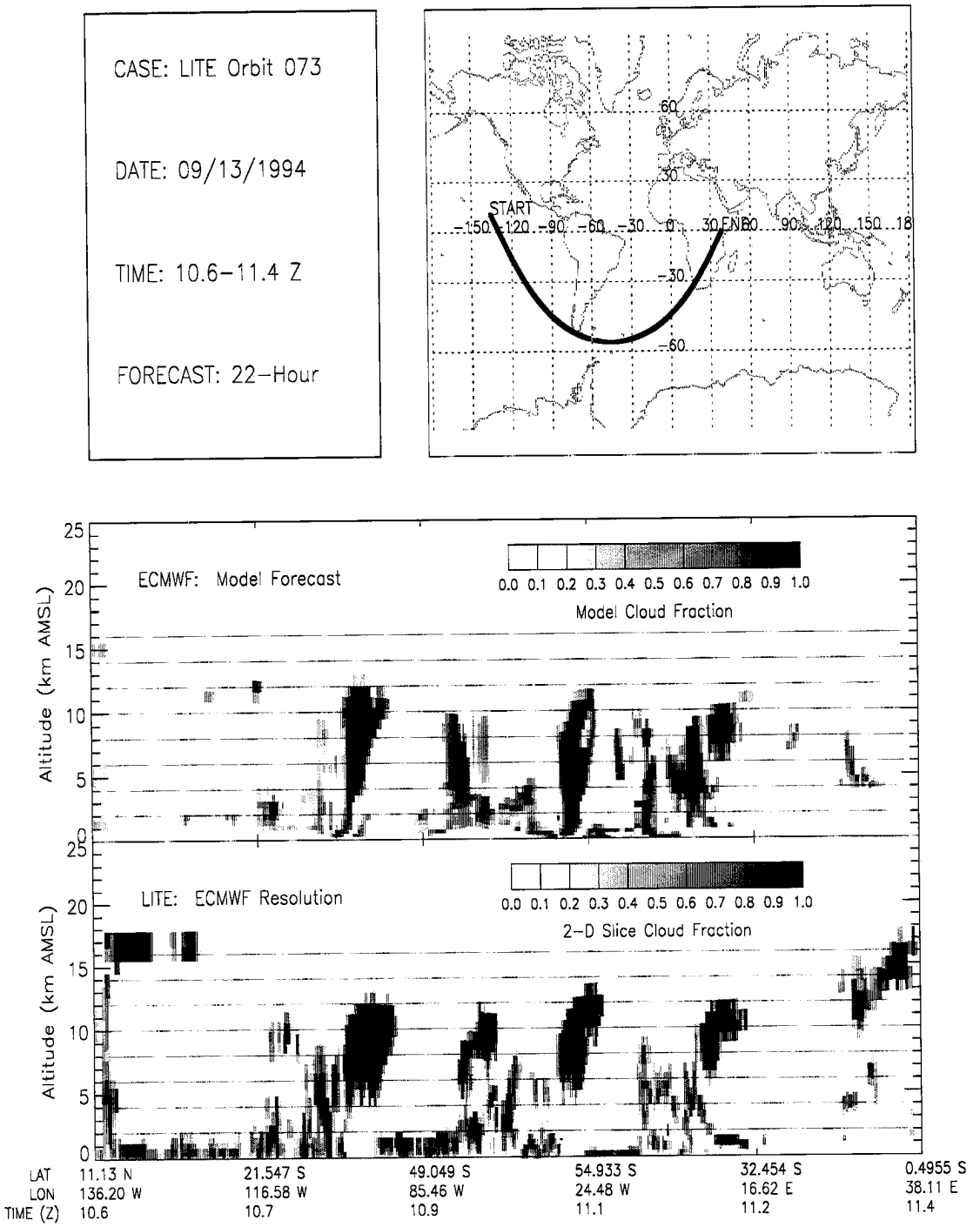

Figure B.53: LITE Orbit 073 Cloud Cover Comparison.

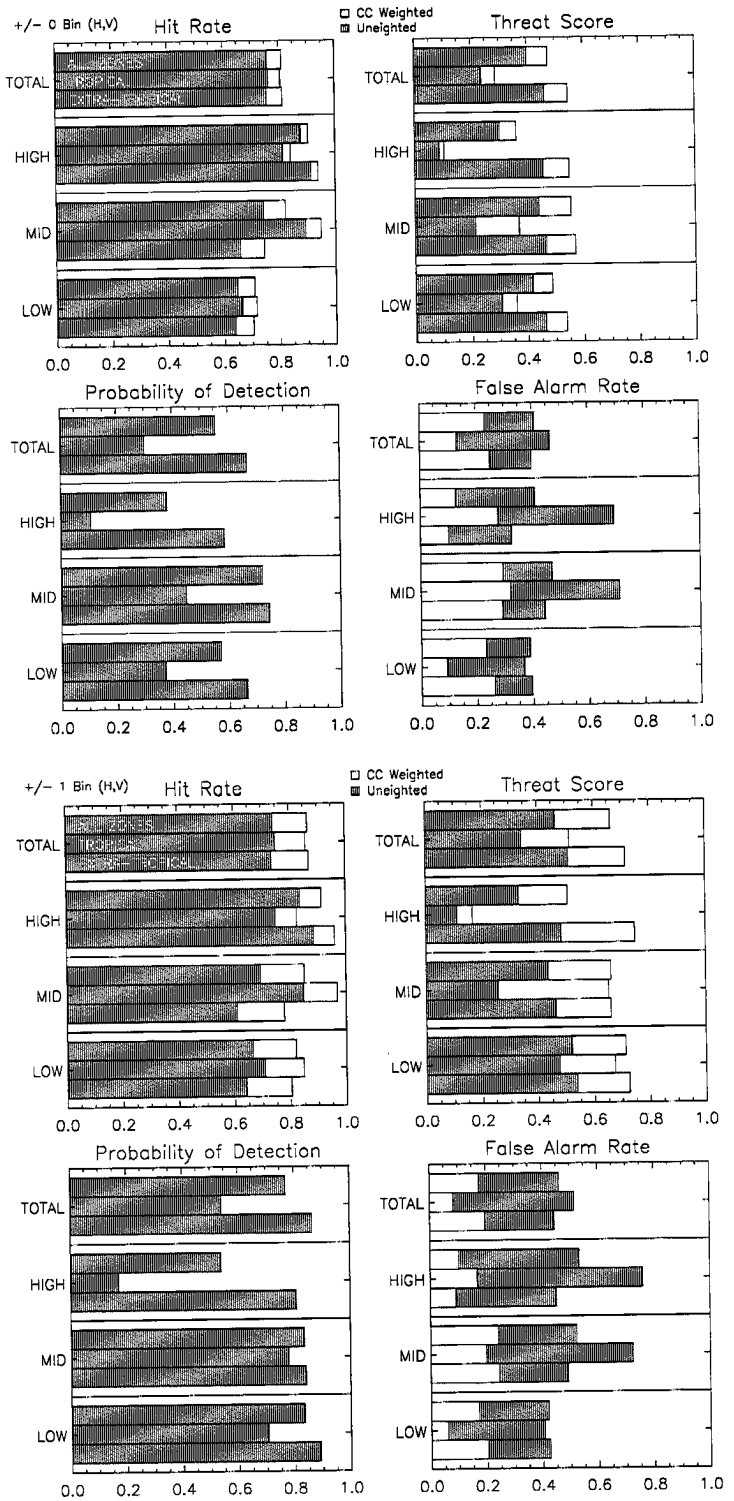

Figure B.54: LITE Orbit 073 Cloud Cover Statistics.

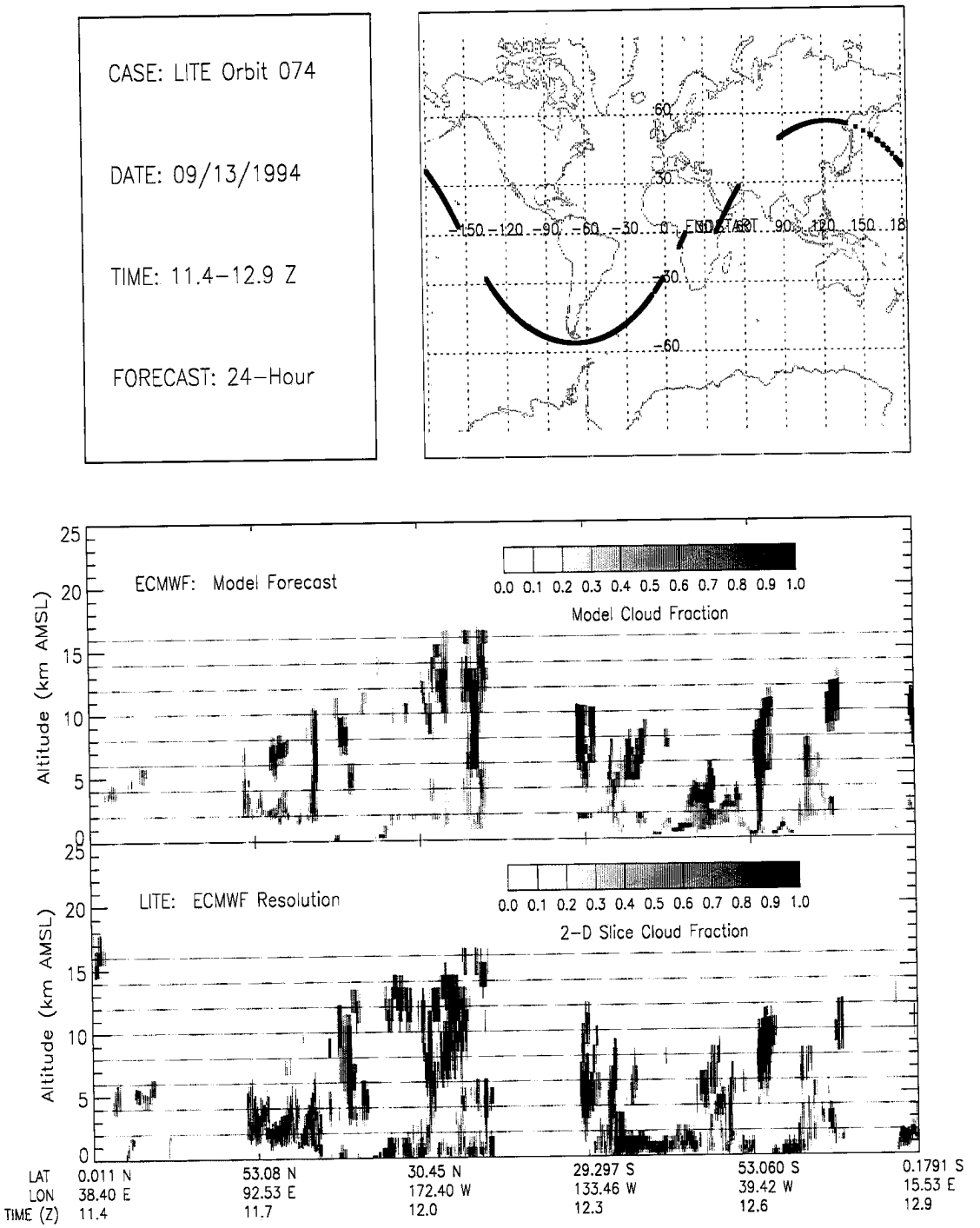

Figure B.55: LITE Orbit 074 Cloud Cover Comparison.

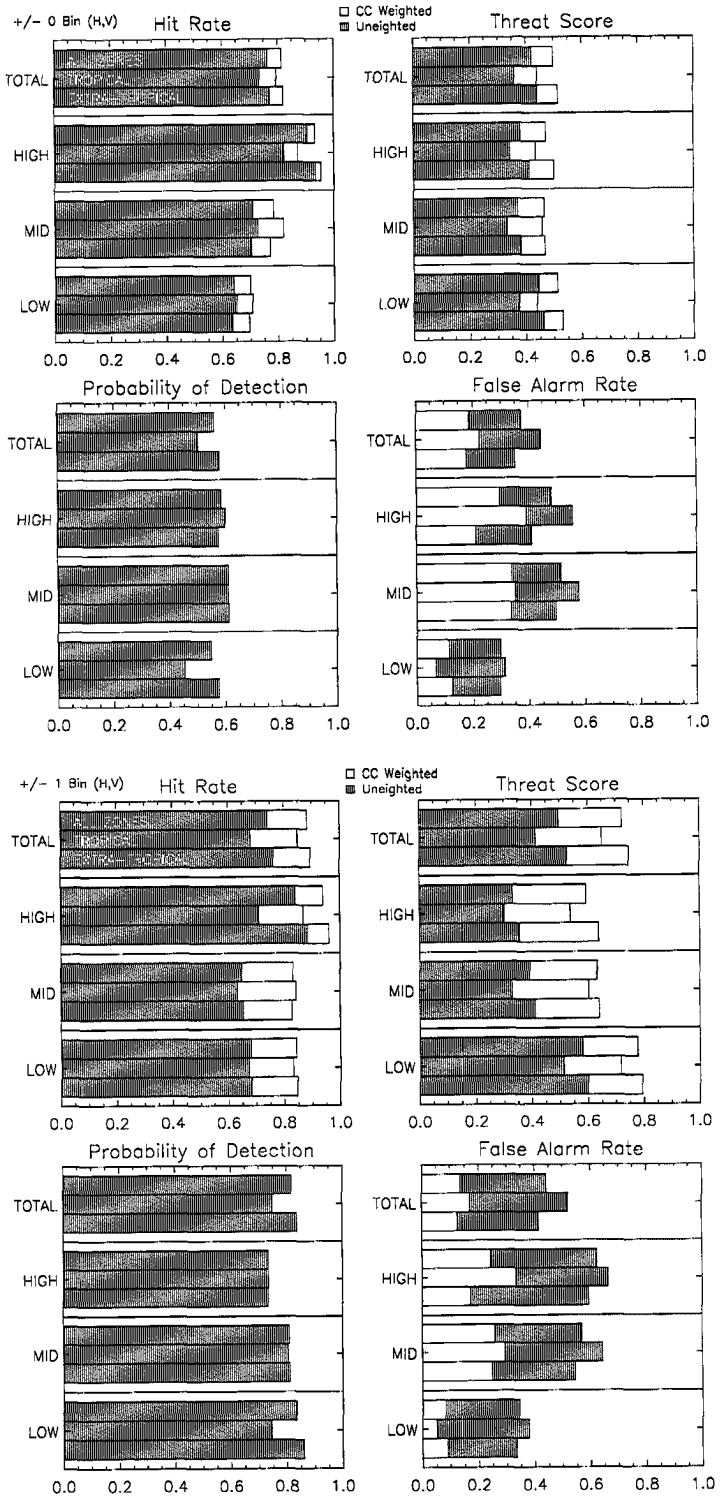

Figure B.56: LITE Orbit 074 Cloud Cover Statistics.

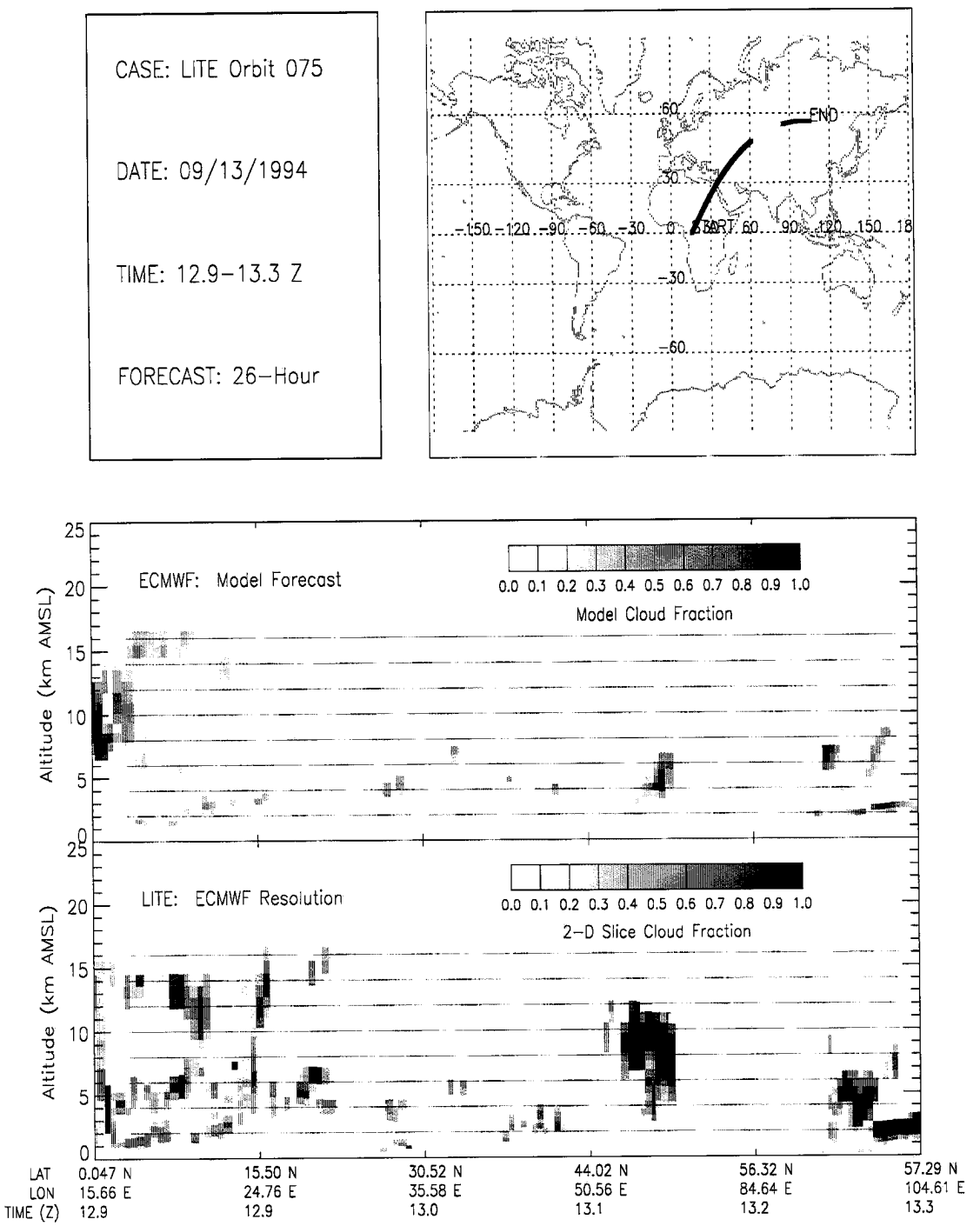

Figure B.57: LITE Orbit 075 Cloud Cover Comparison.

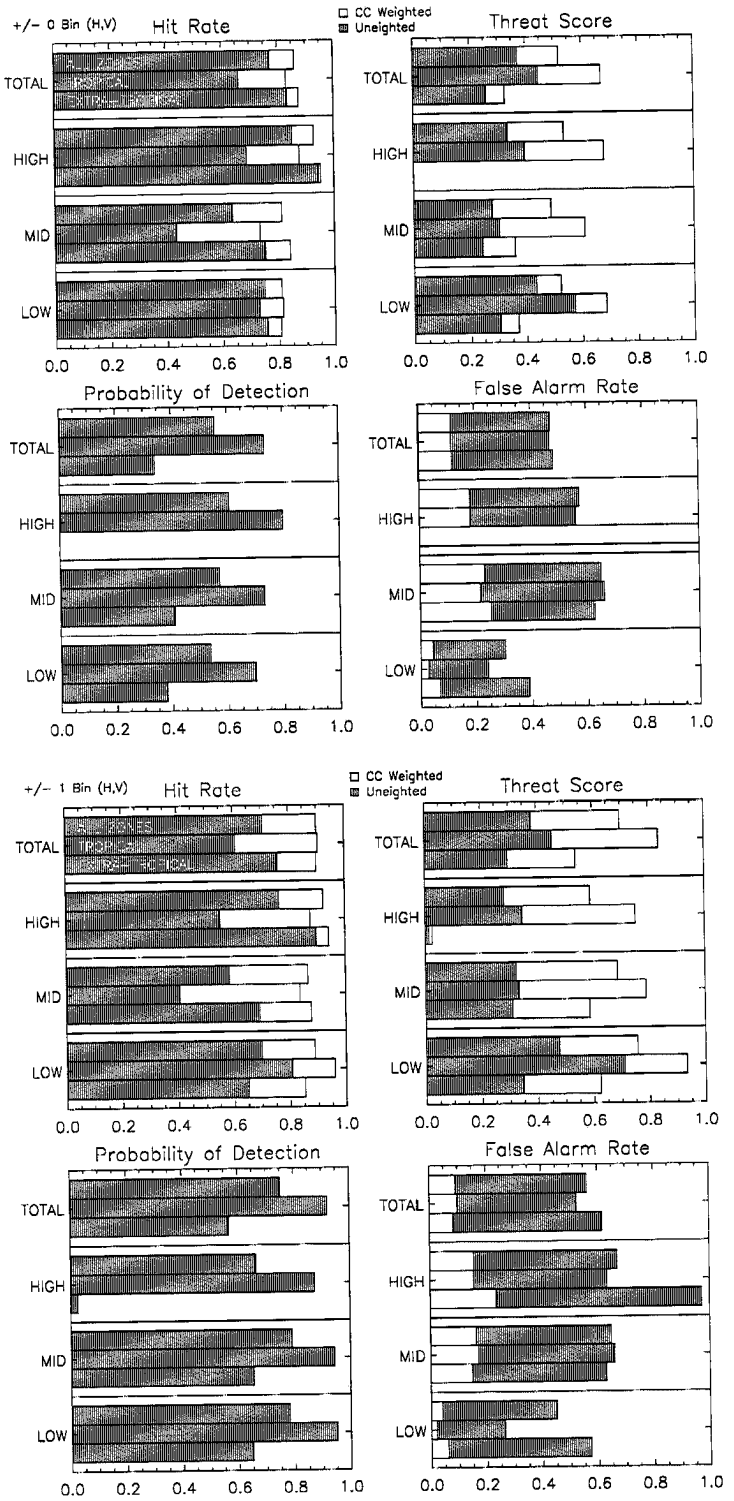

Figure B.58: LITE Orbit 075 Cloud Cover Statistics.

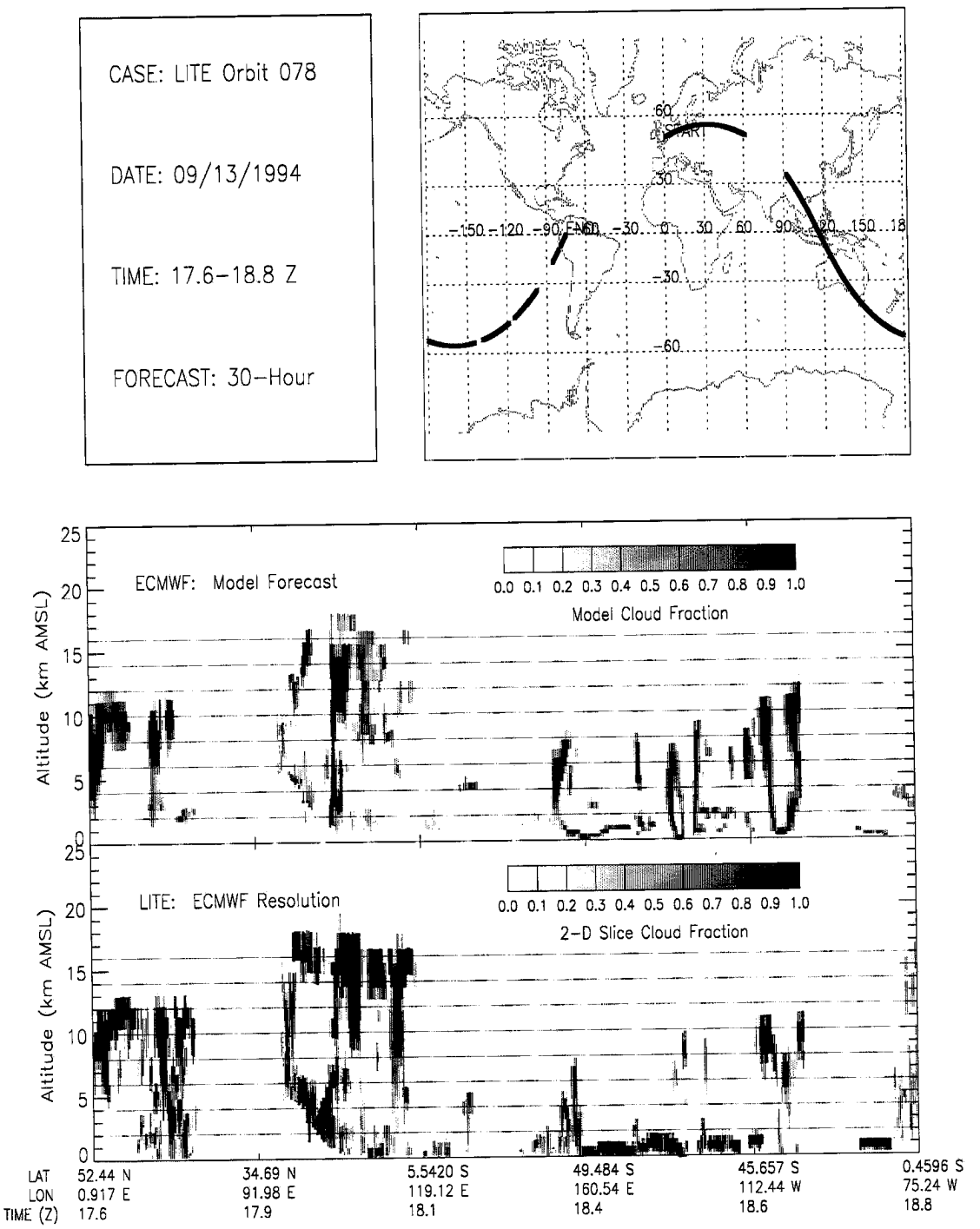

Figure B.59: LITE Orbit 078 Cloud Cover Comparison.

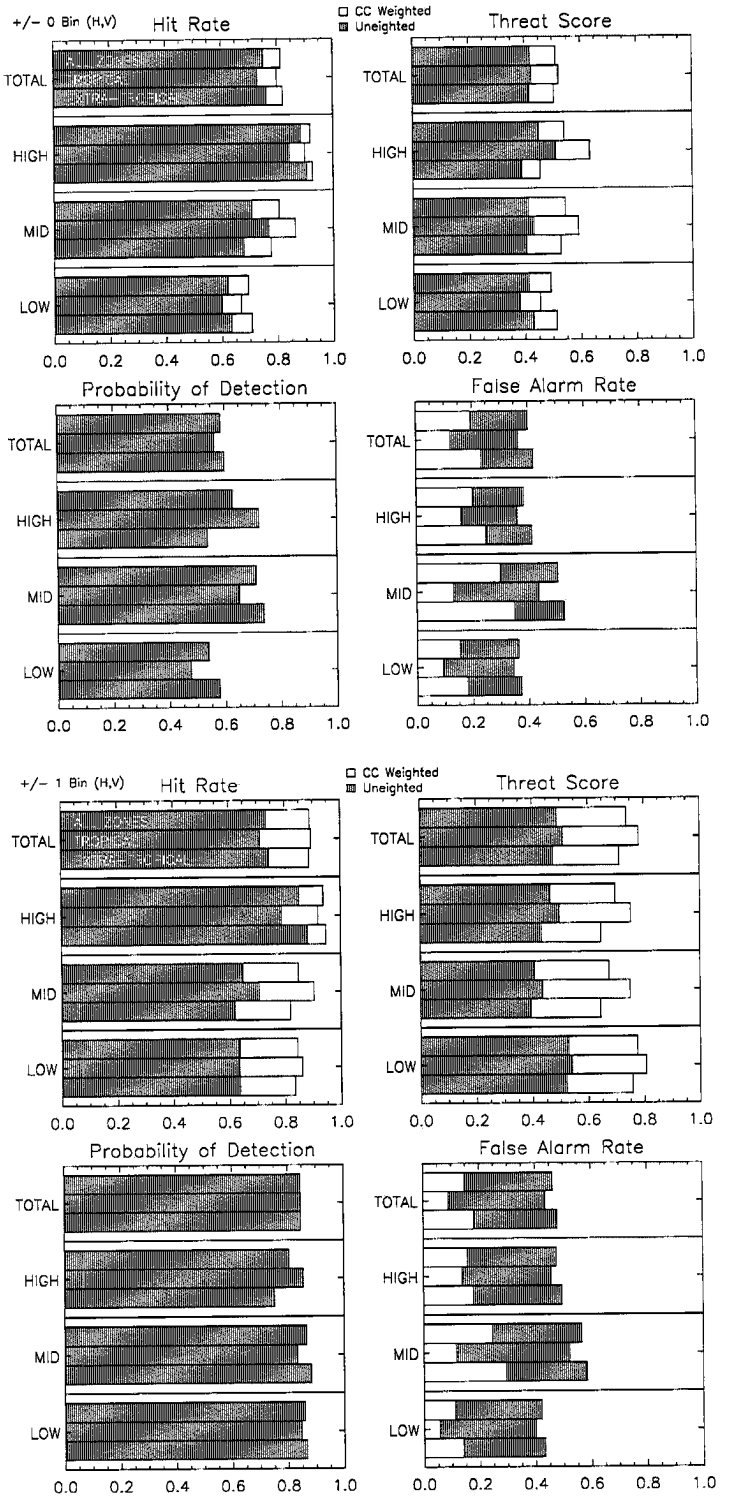

Figure B.60: LITE Orbit 078 Cloud Cover Statistics.

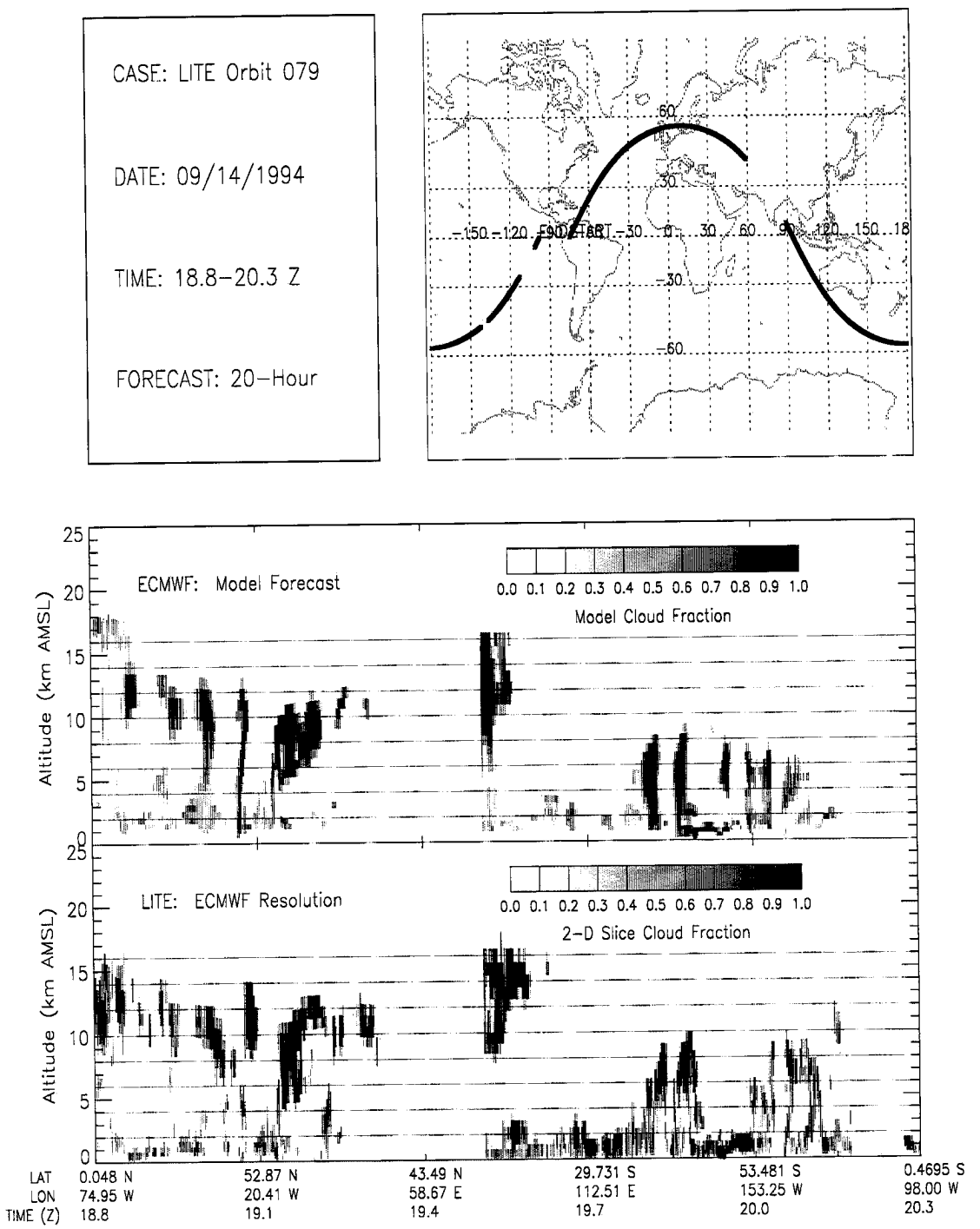

Figure B.61: LITE Orbit 079 Cloud Cover Comparison.

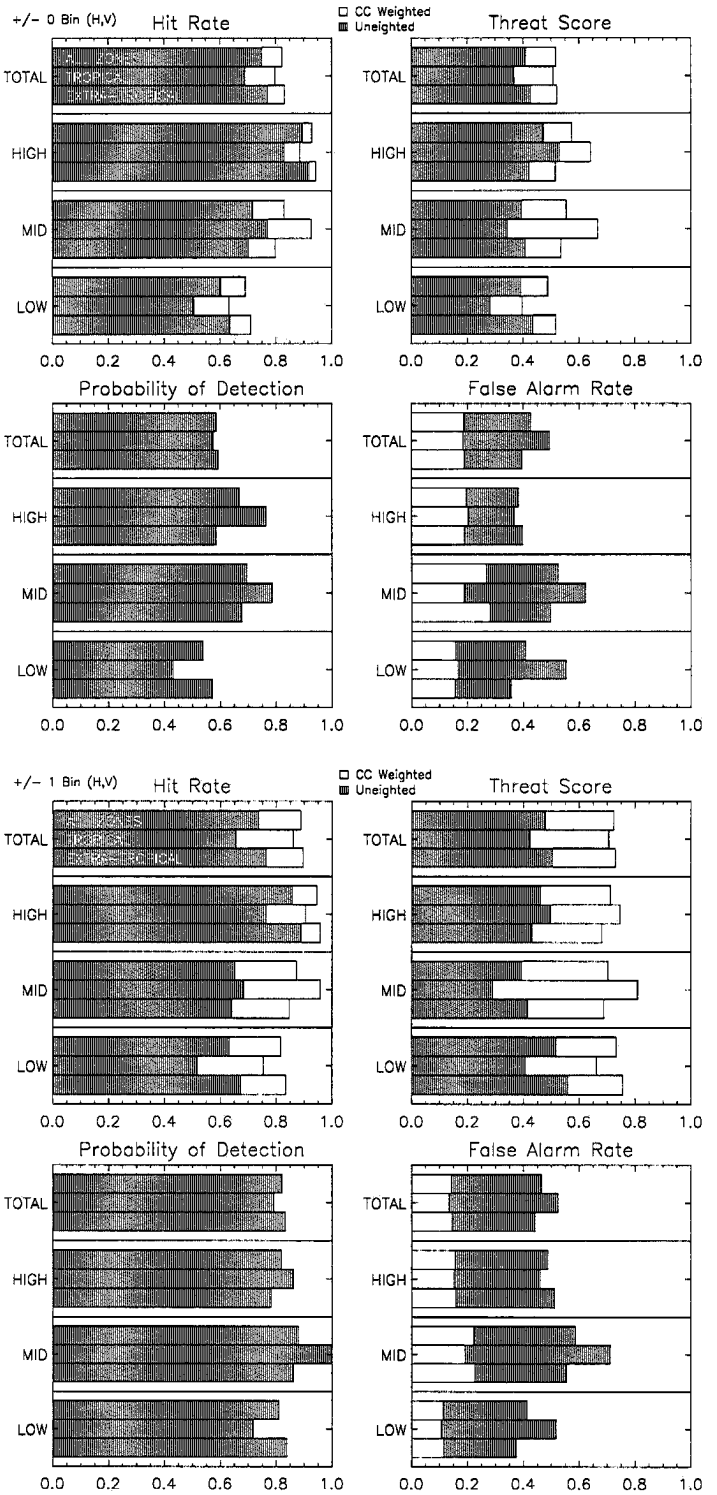

Figure B.62: LITE Orbit 079 Cloud Cover Statistics.

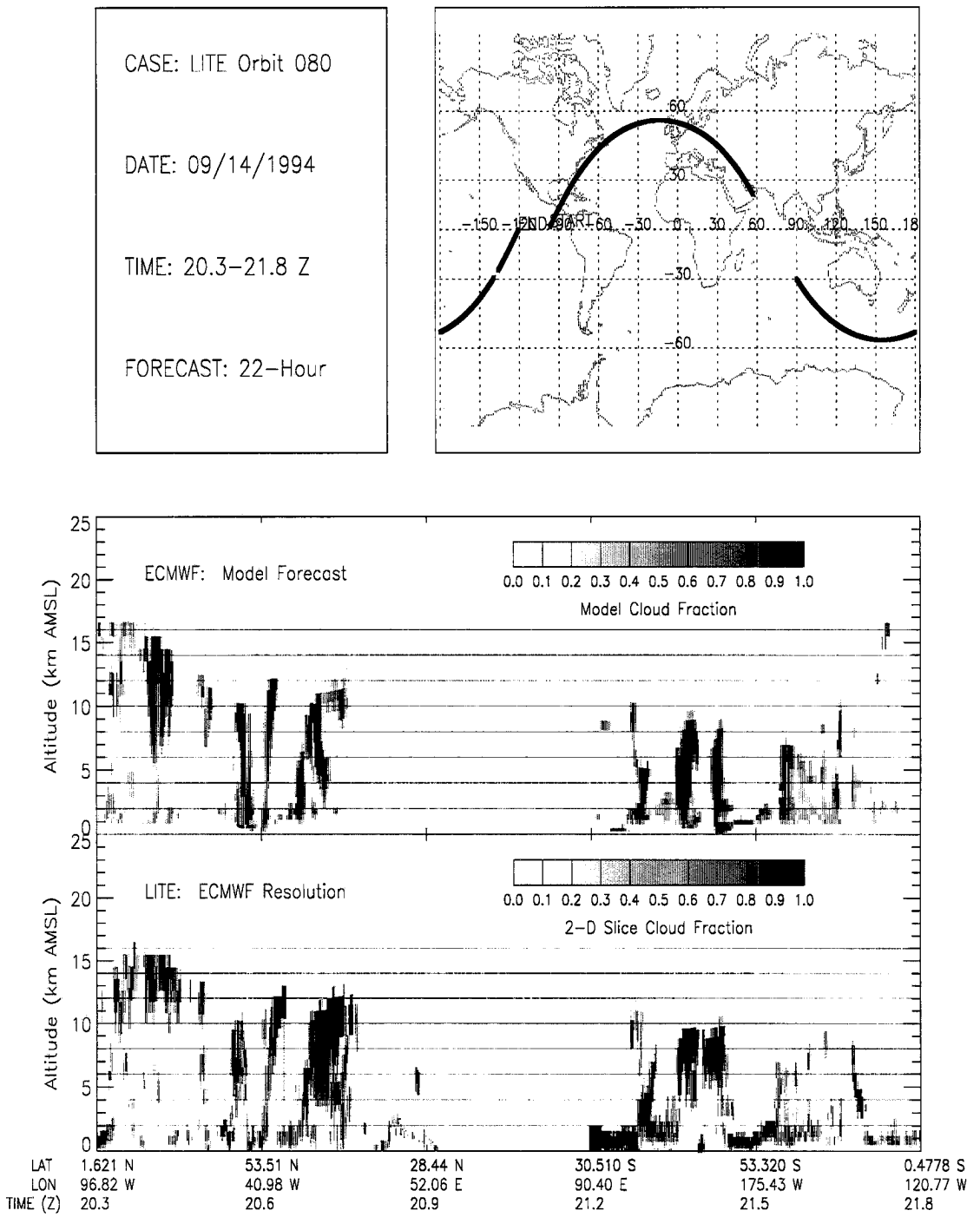

Figure B.63: LITE Orbit 080 Cloud Cover Comparison.

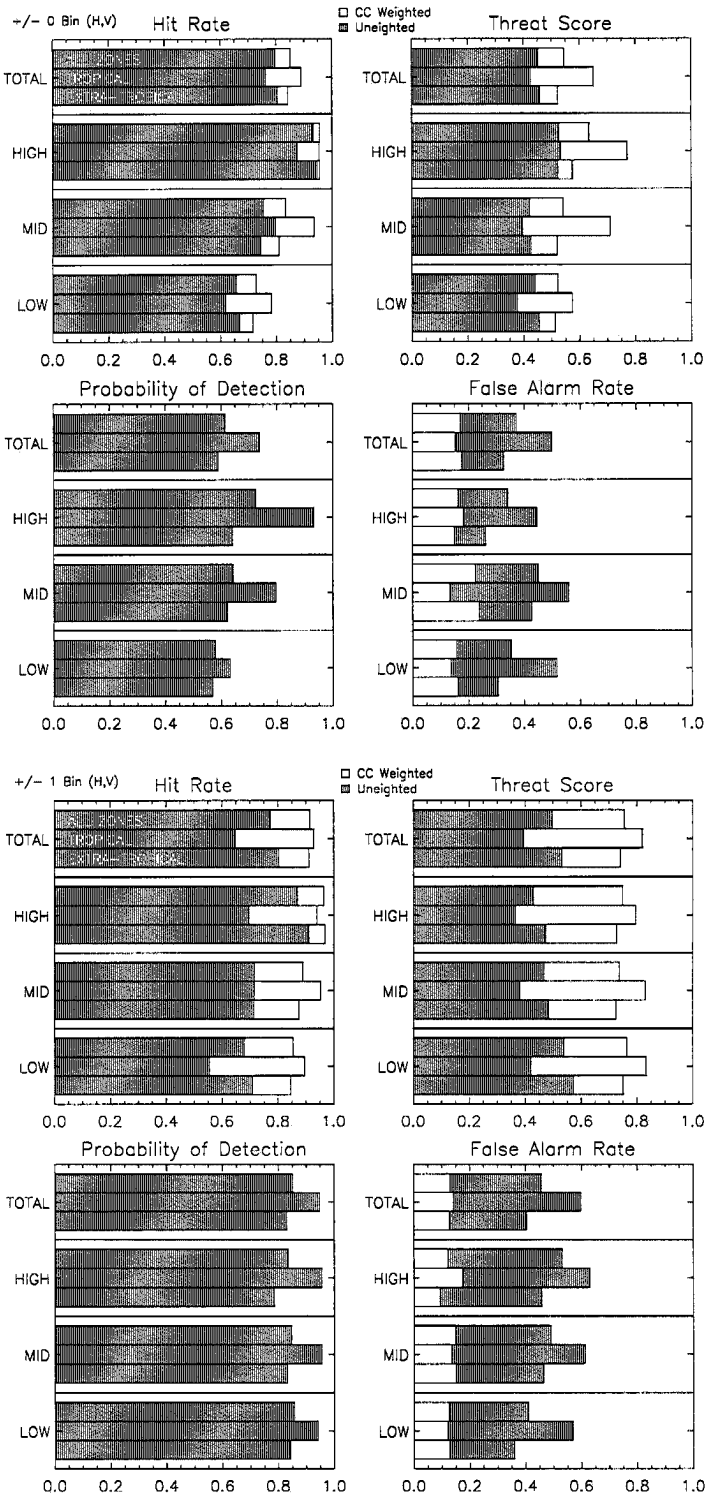

Figure B.64: LITE Orbit 080 Cloud Cover Statistics.

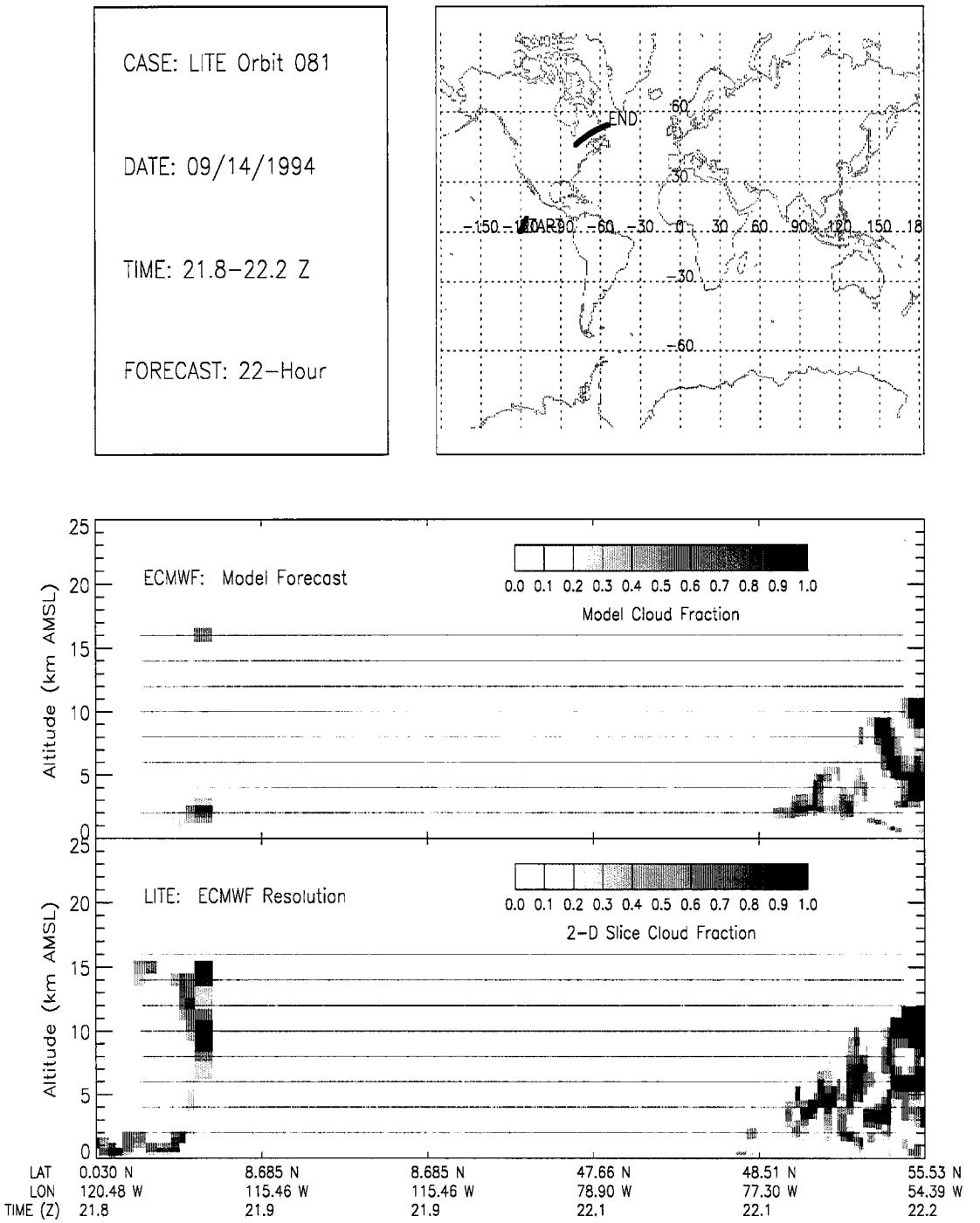

Figure B.65: LITE Orbit 081 Cloud Cover Comparison.

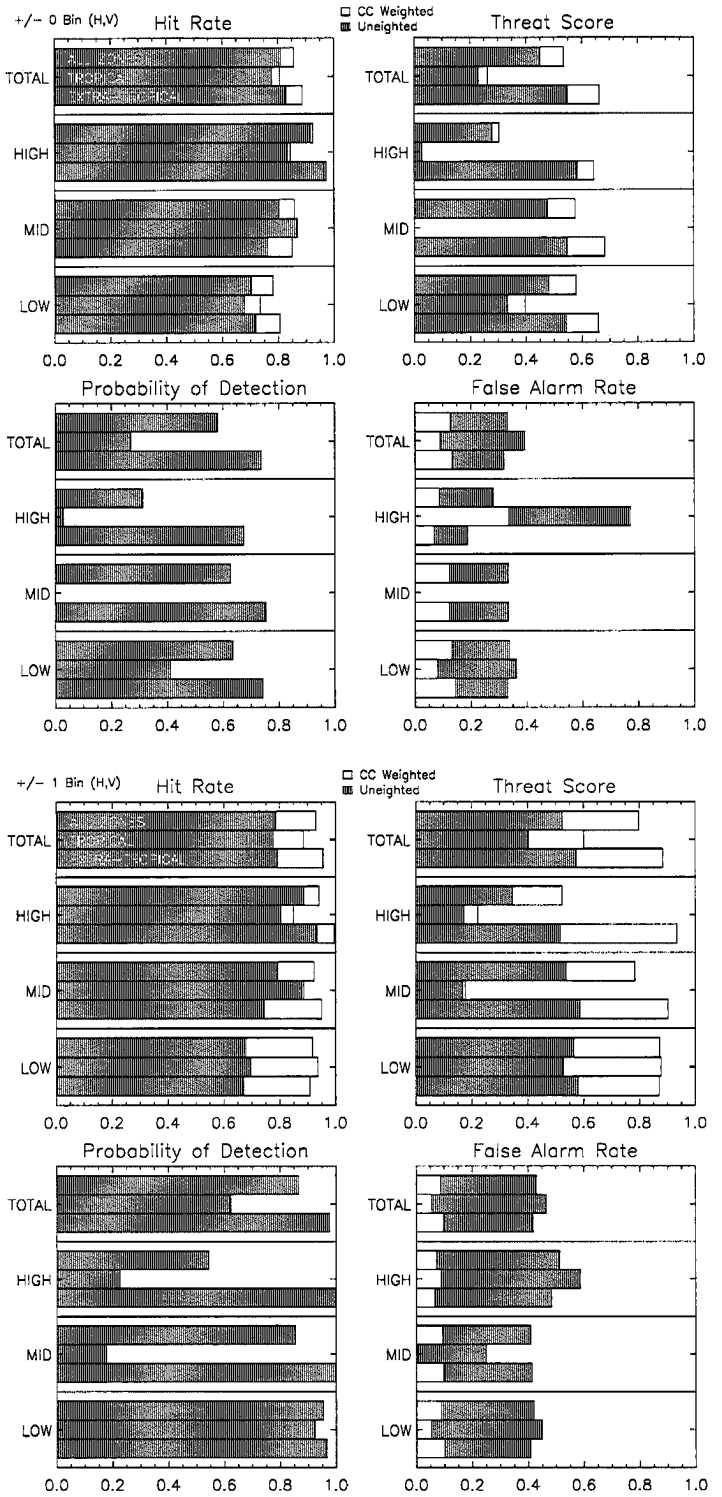

Figure B.66: LITE Orbit 081 Cloud Cover Statistics.

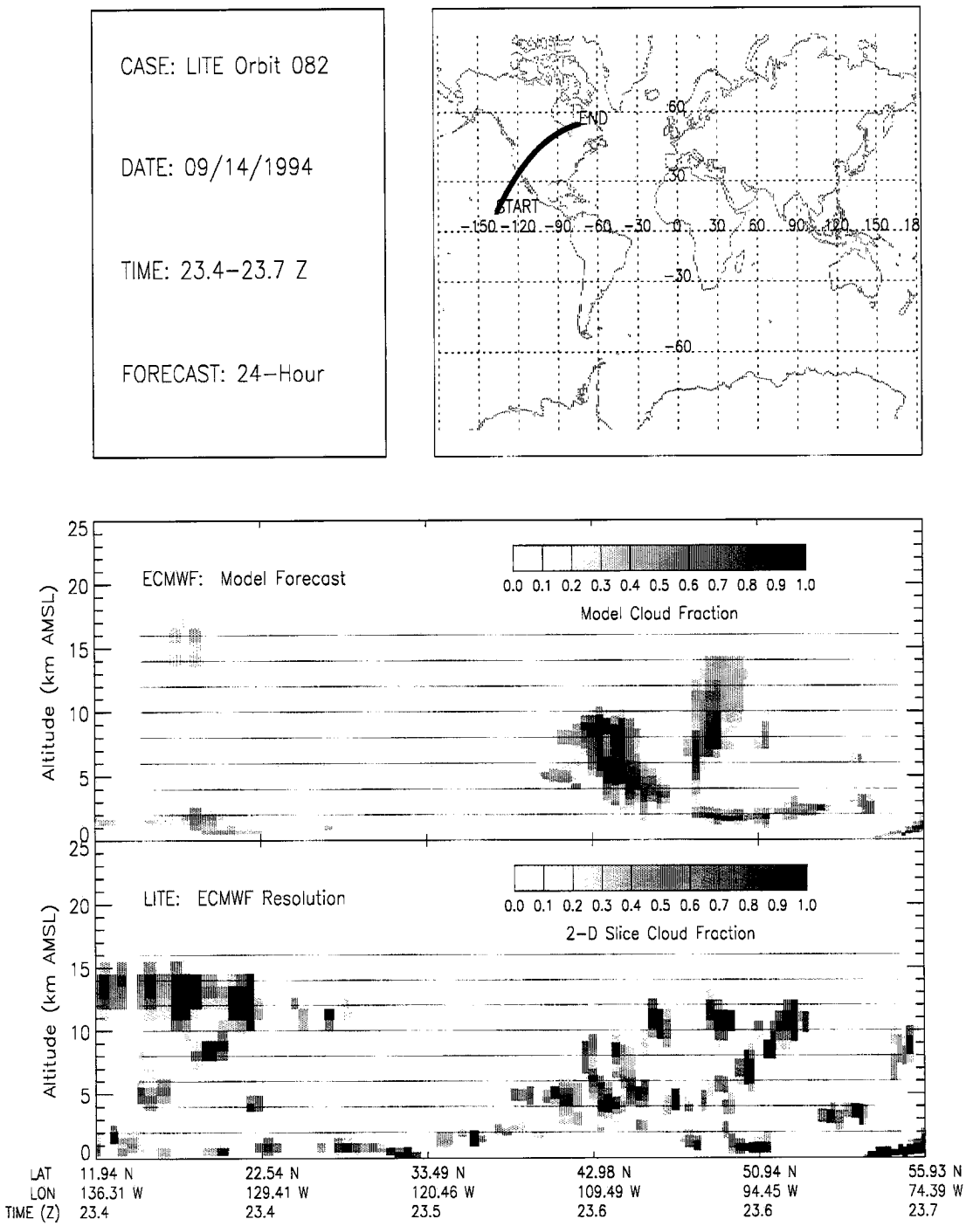

Figure B.67: LITE Orbit 082 Cloud Cover Comparison.

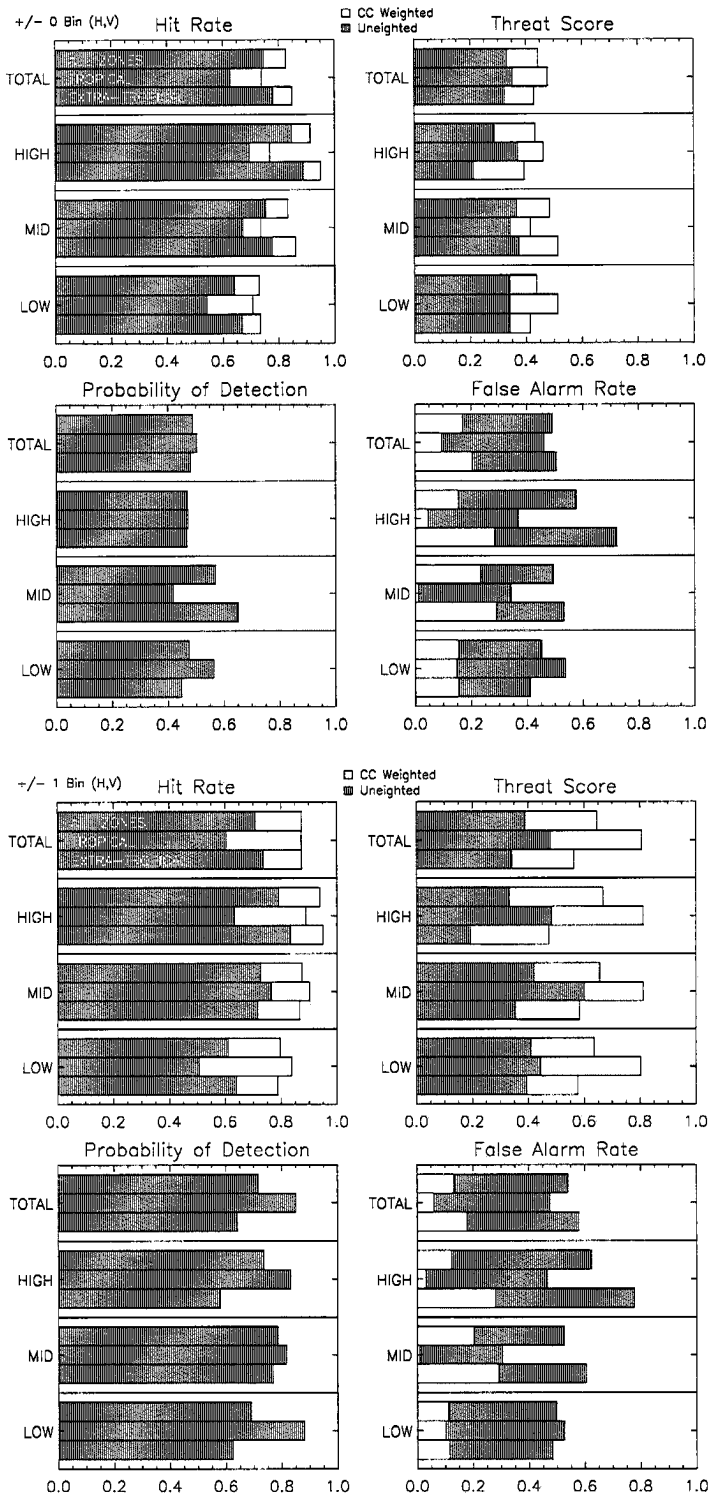

Figure B.68: LITE Orbit 082 Cloud Cover Statistics.

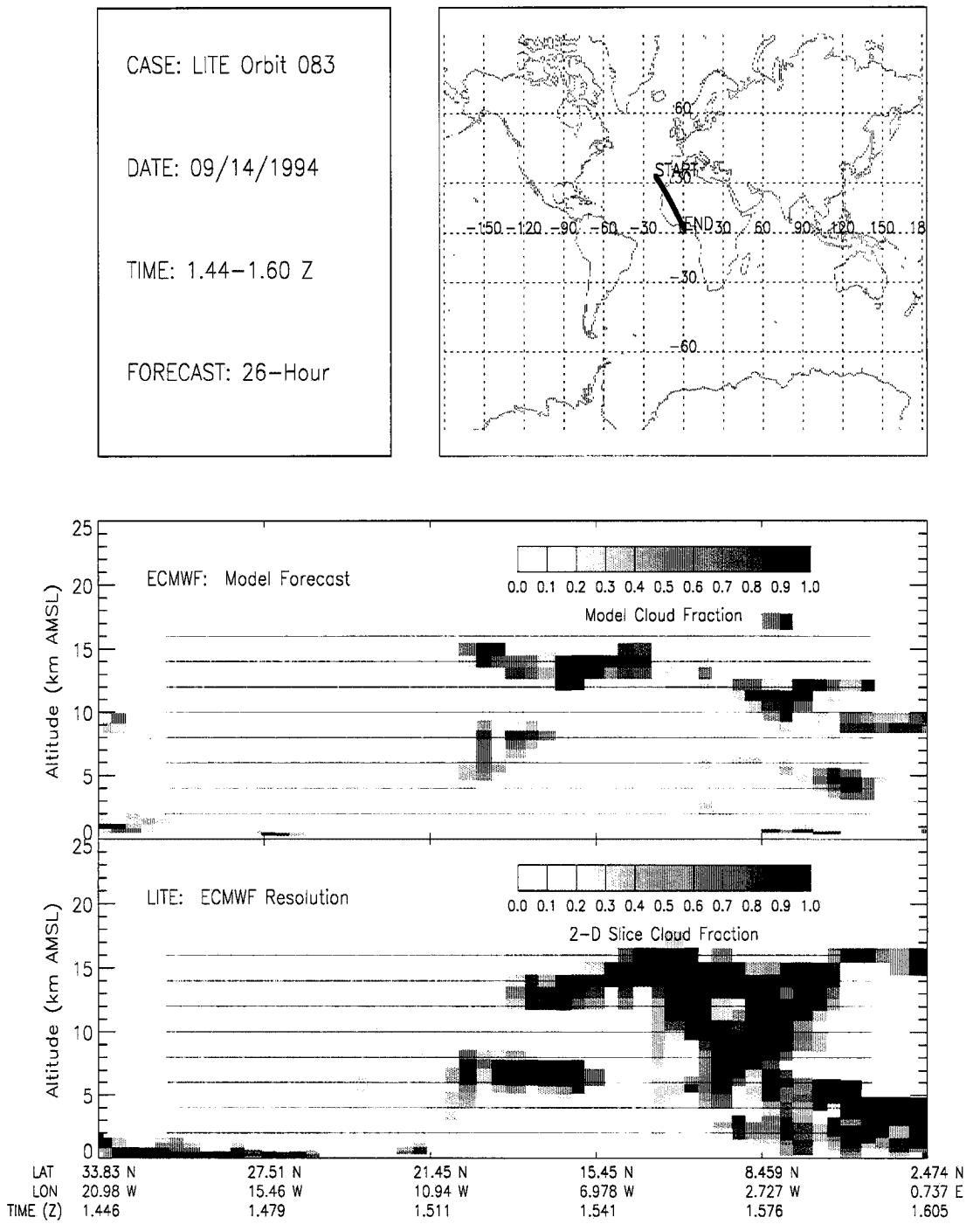

Figure B.69: LITE Orbit 083 Cloud Cover Comparison.

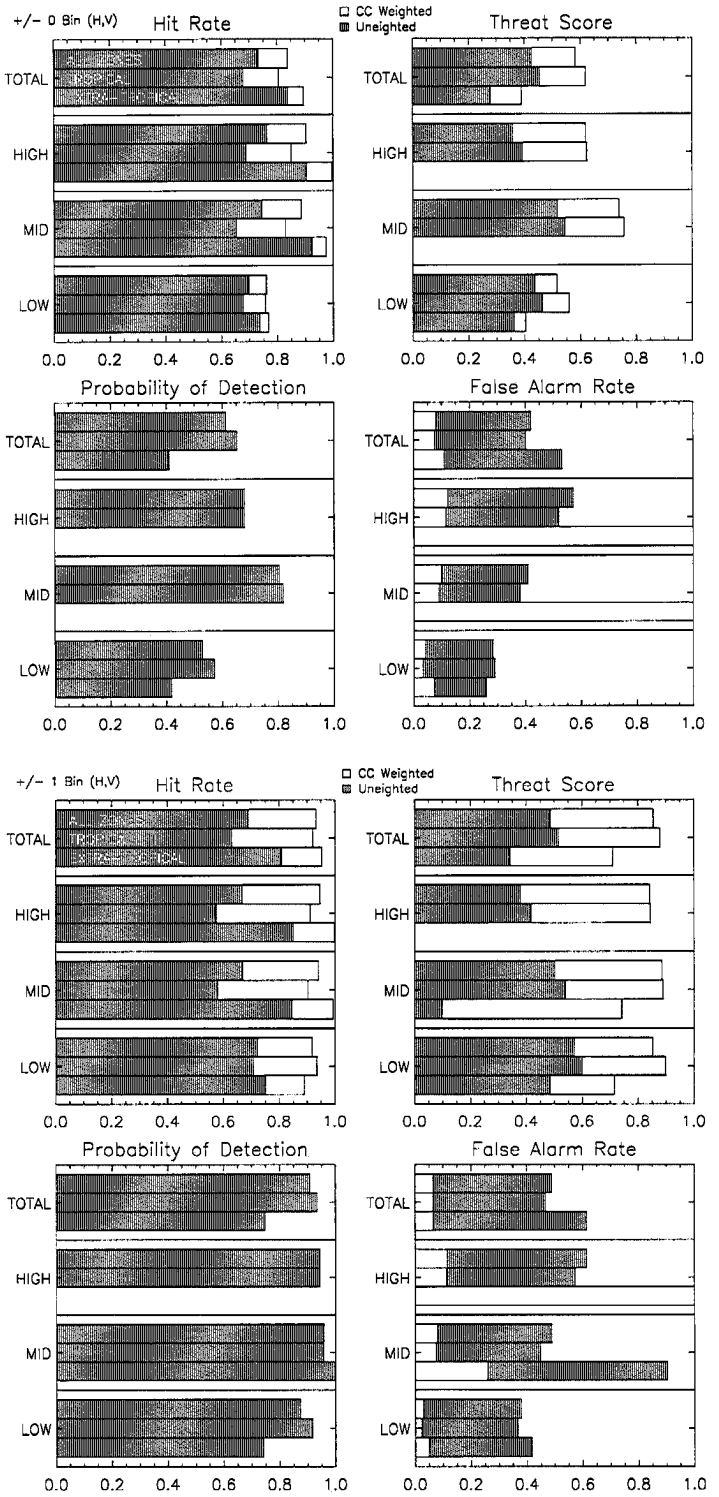

Figure B.70: LITE Orbit 083 Cloud Cover Statistics.

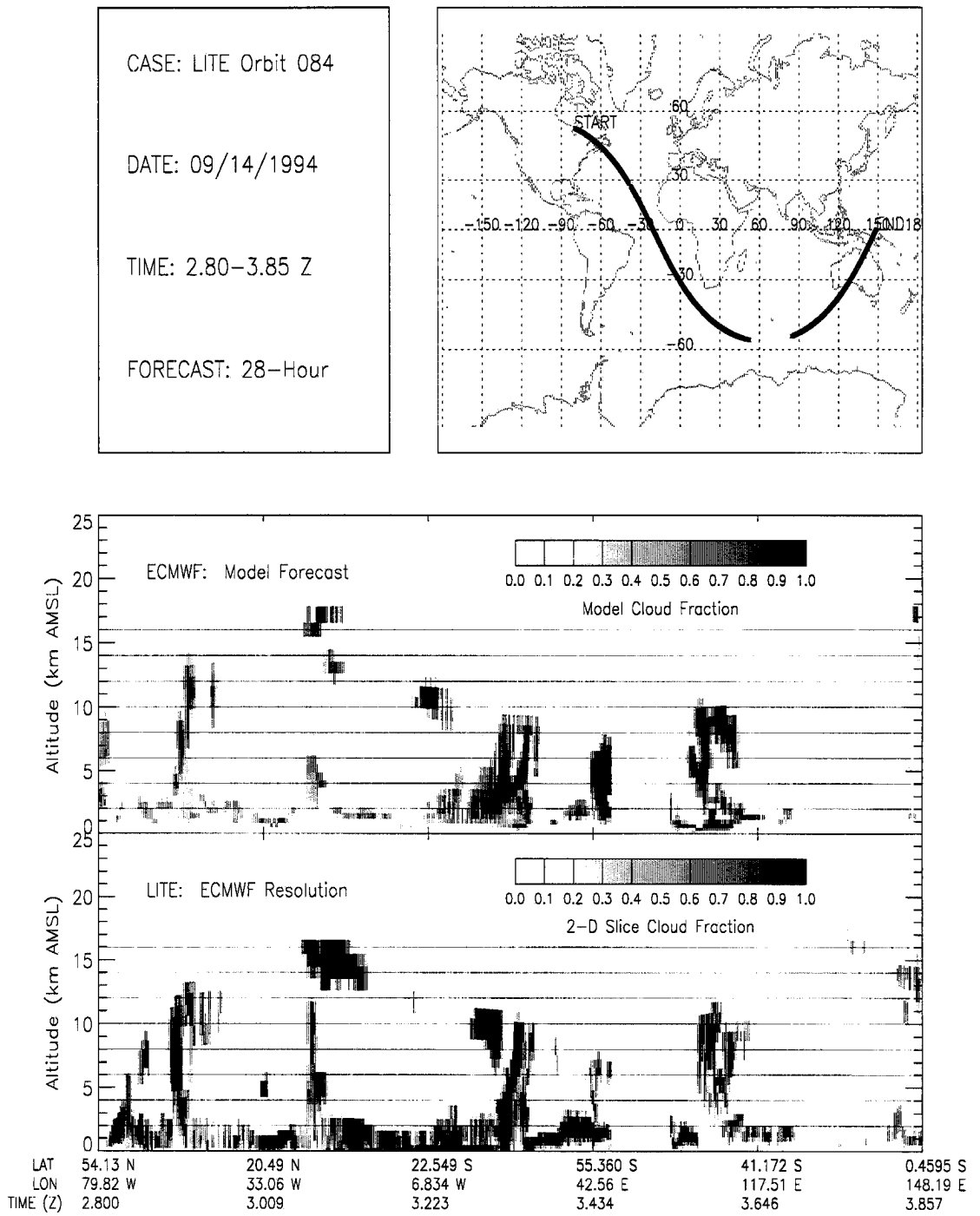

Figure B.71: LITE Orbit 084 Cloud Cover Comparison.

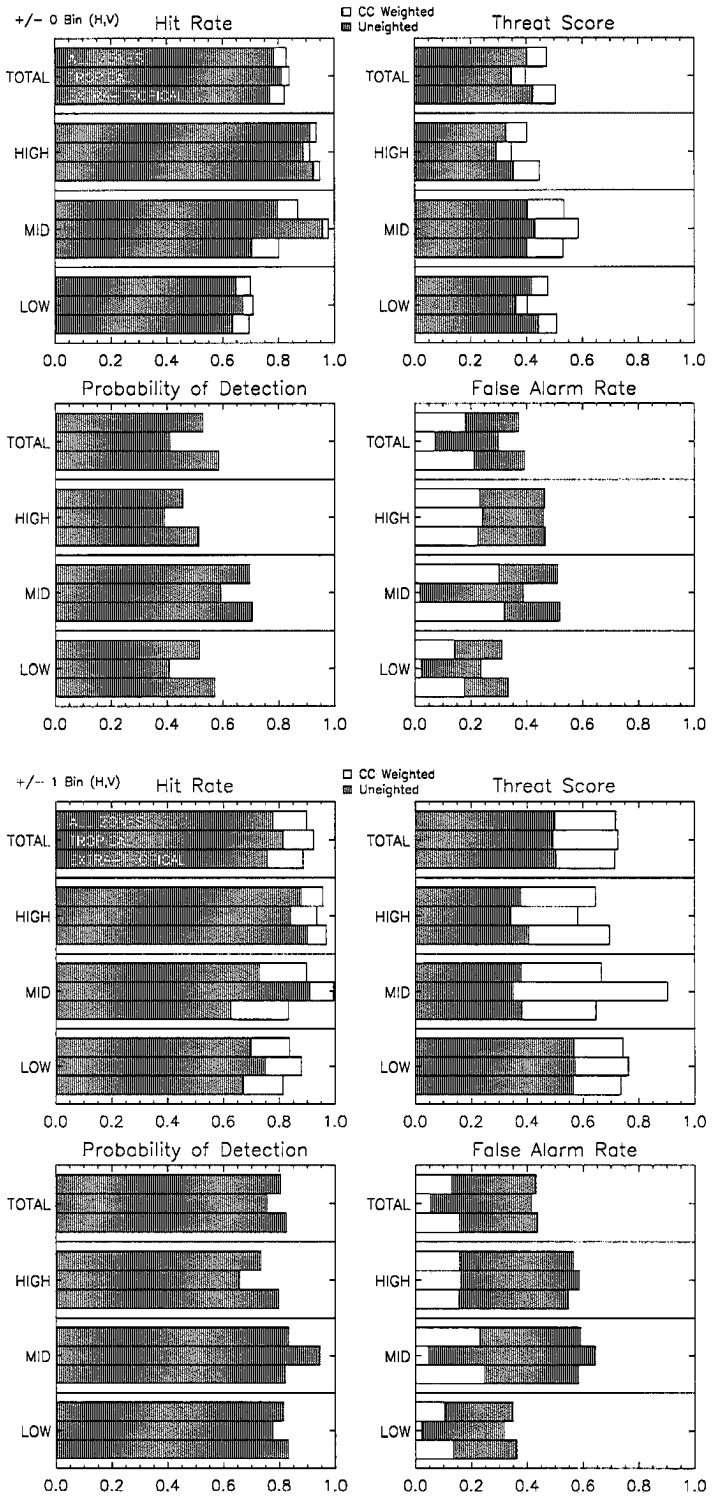

Figure B.72: LITE Orbit 084 Cloud Cover Statistics.

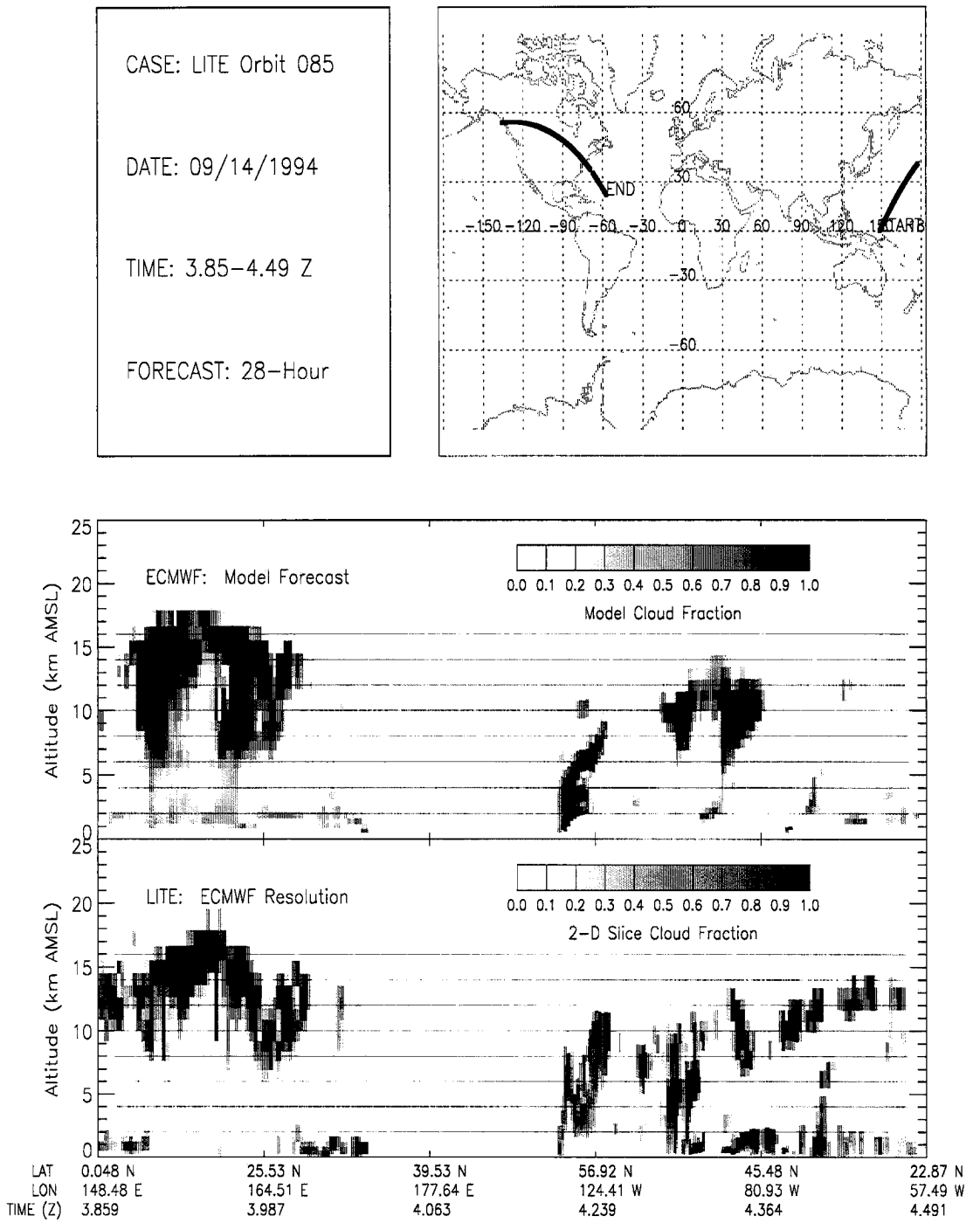

Figure B.73: LITE Orbit 085 Cloud Cover Comparison.

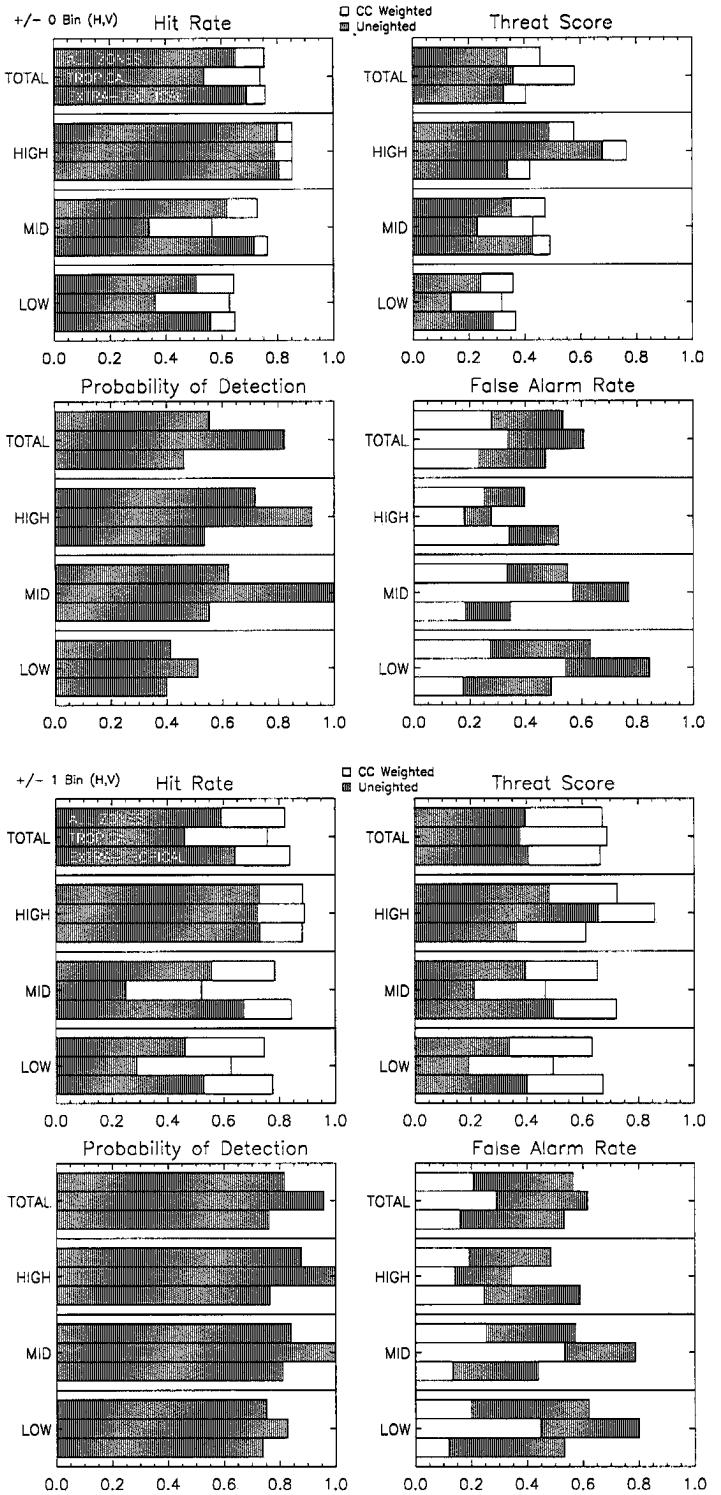

Figure B.74: LITE Orbit 085 Cloud Cover Statistics.

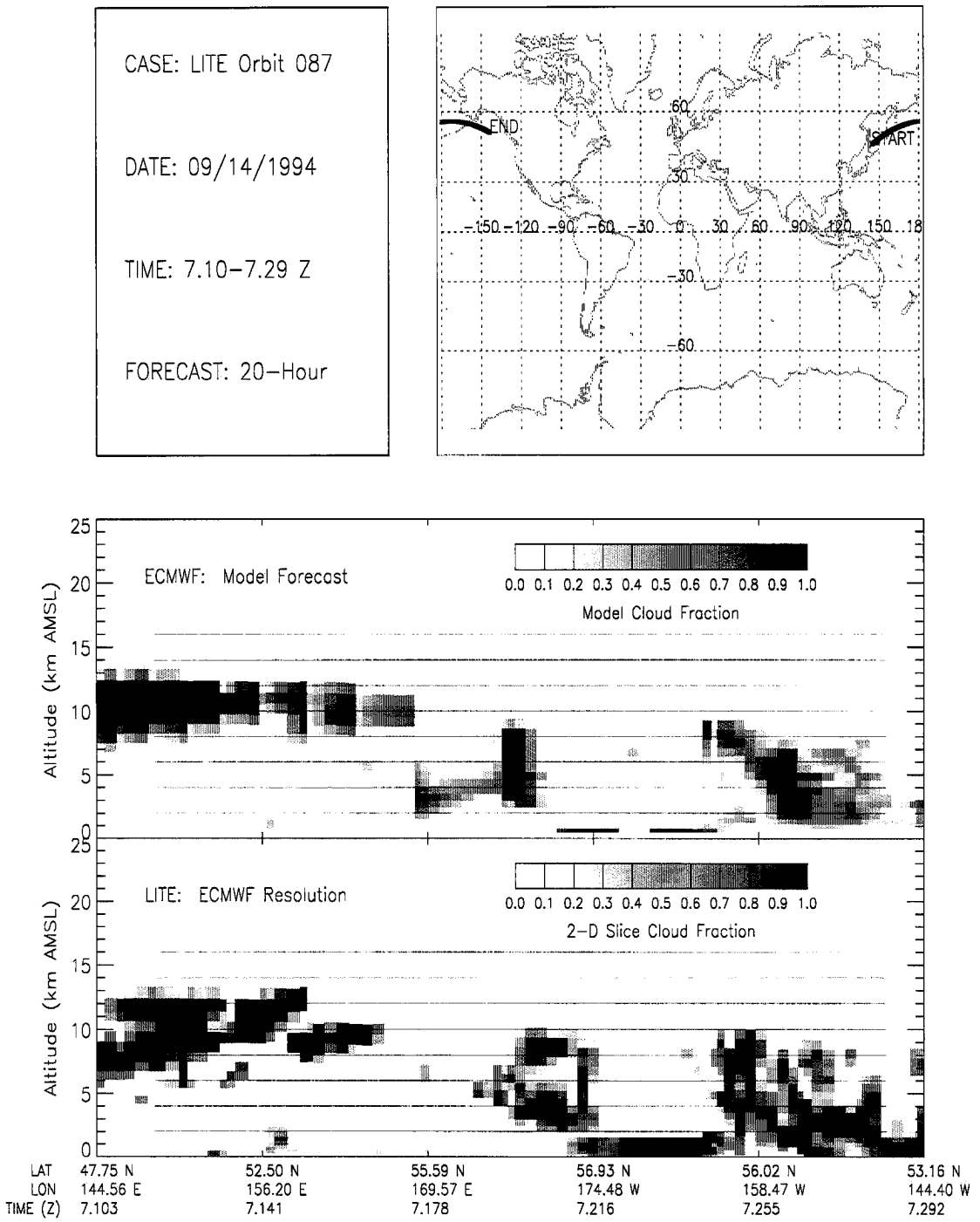

Figure B.75: LITE Orbit 087 Cloud Cover Comparison.

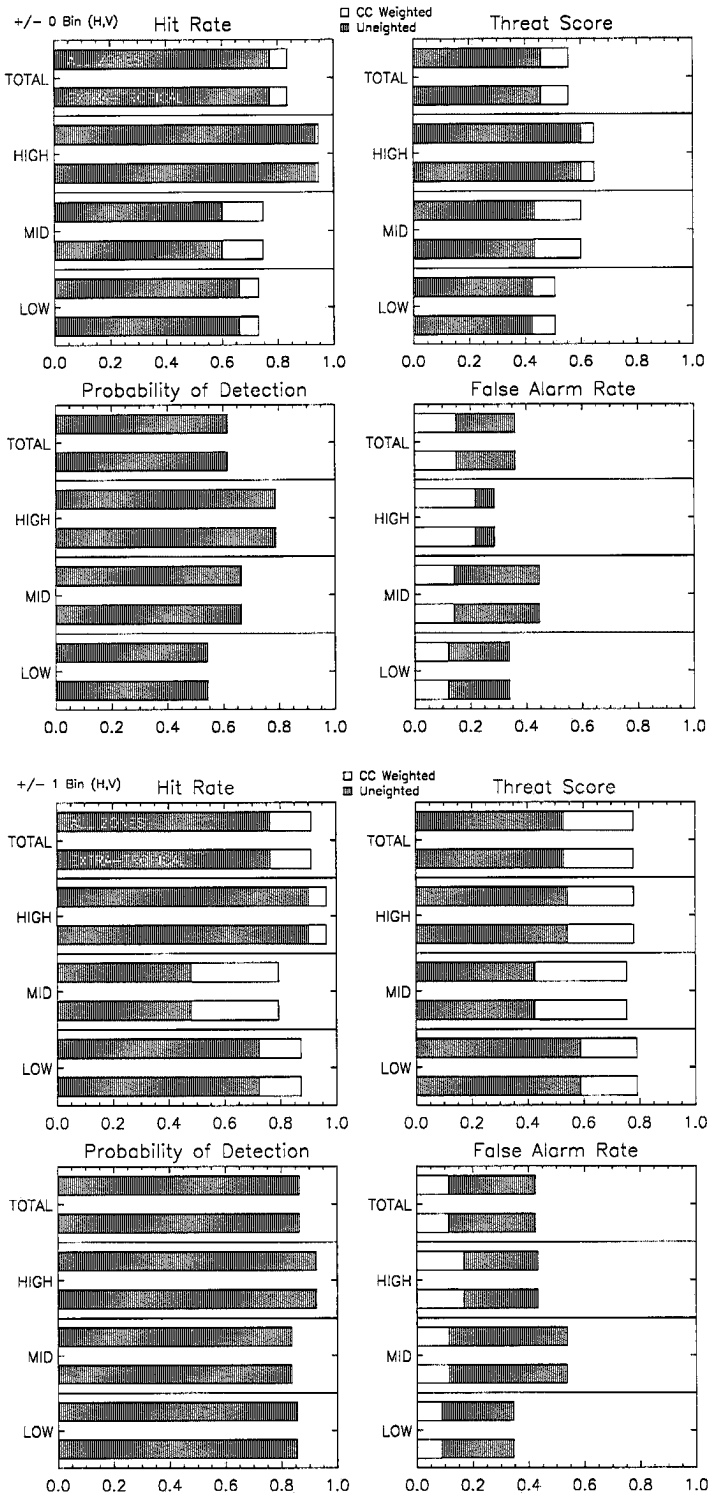

Figure B.76: LITE Orbit 087 Cloud Cover Statistics.

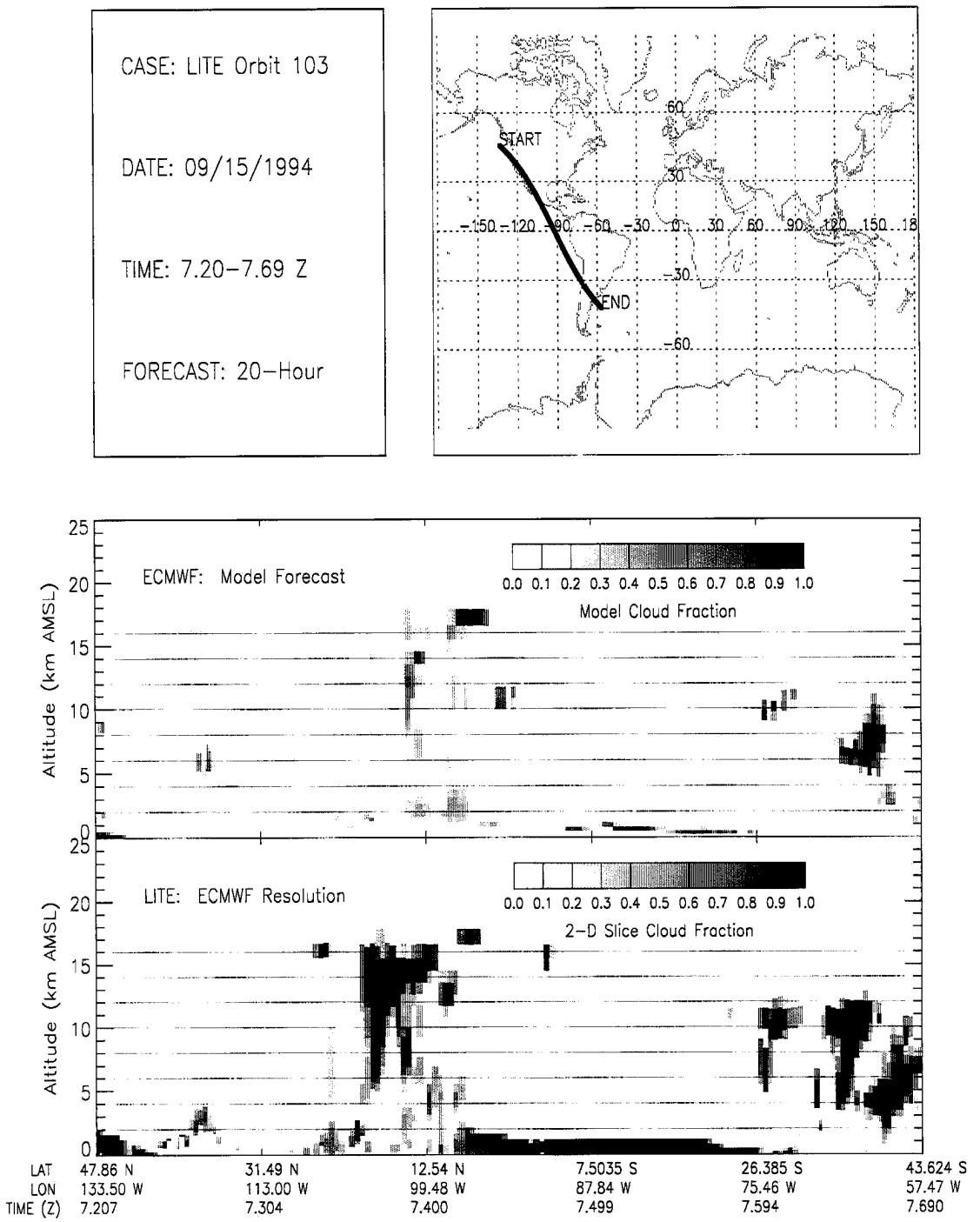

Figure B.77: LITE Orbit 103 Cloud Cover Comparison.

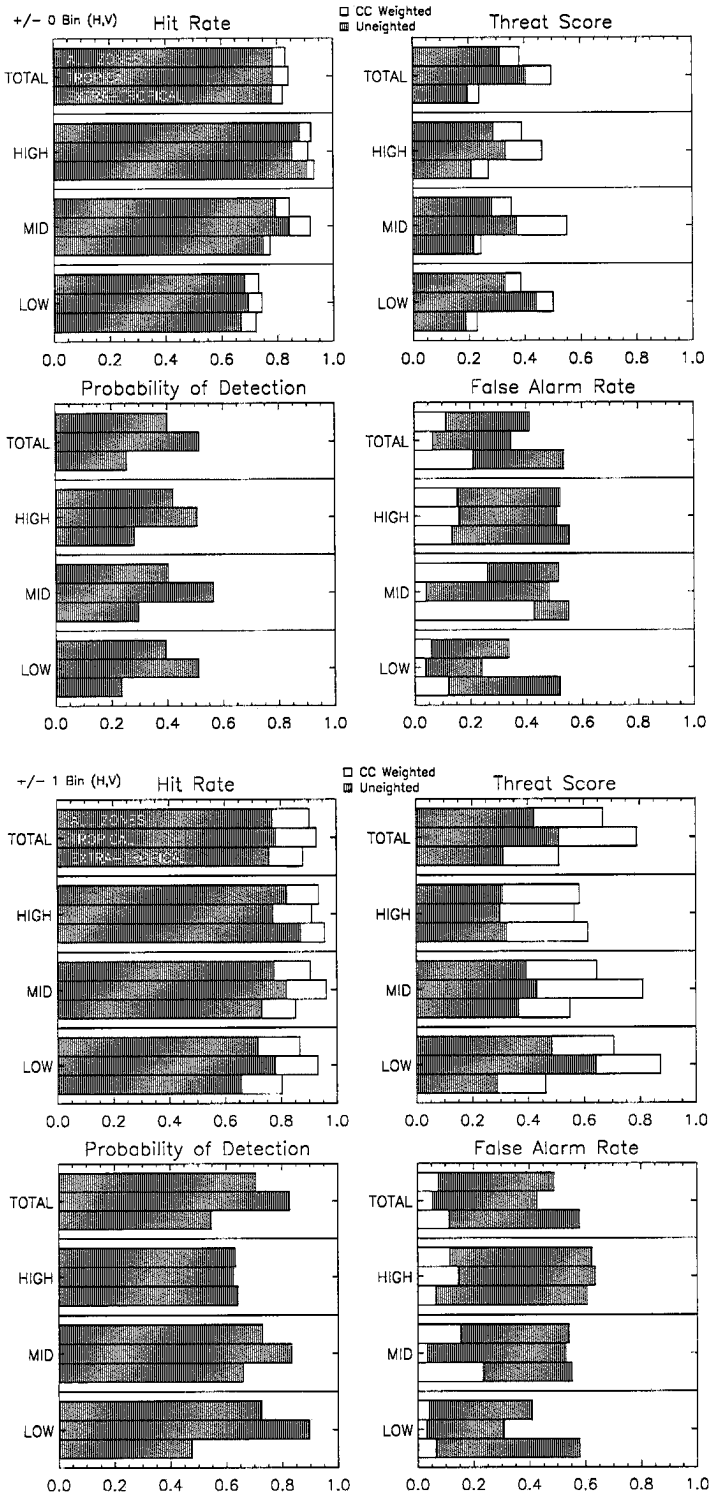

Figure B.78: LITE Orbit 103 Cloud Cover Statistics.

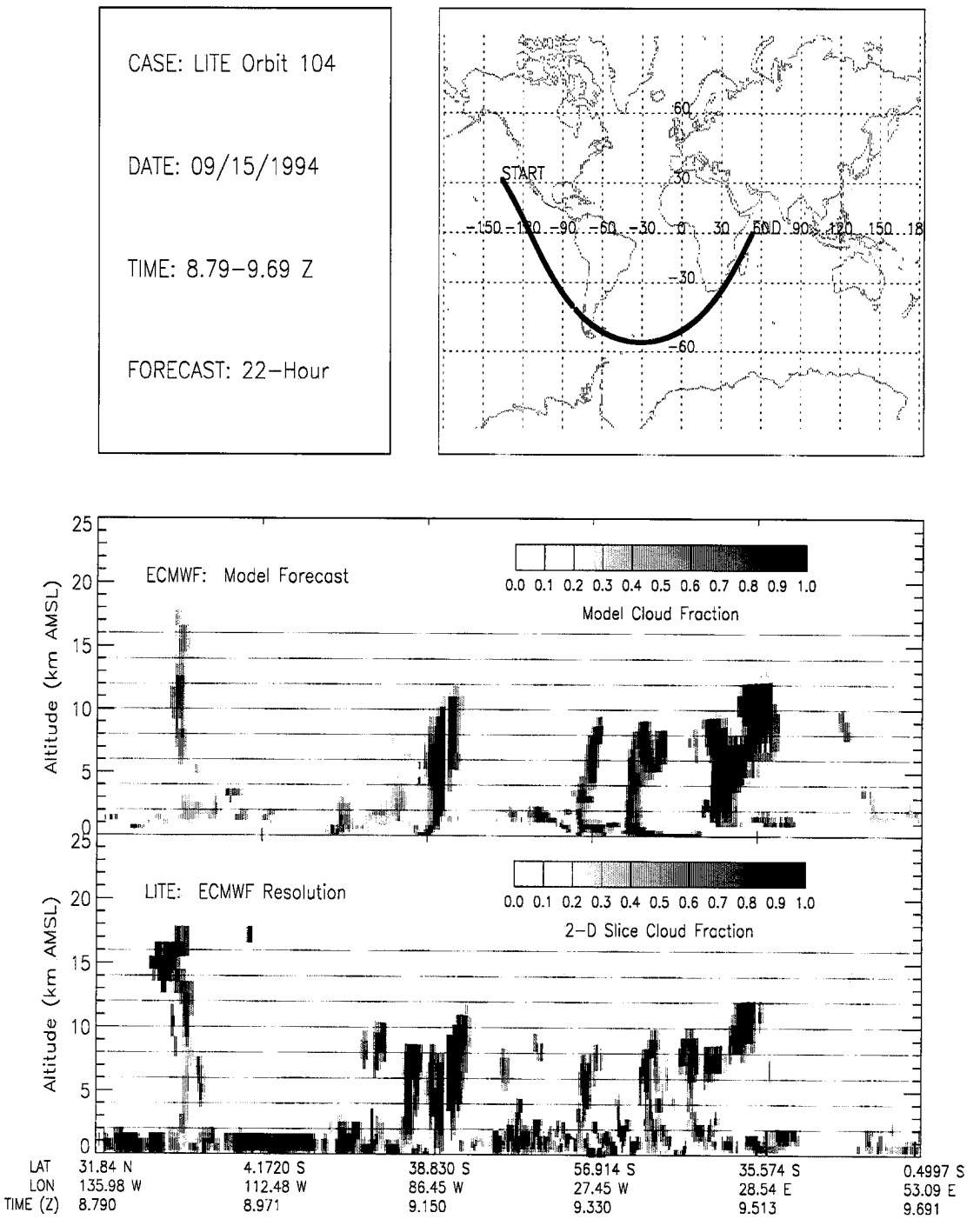

Figure B.79: LITE Orbit 104 Cloud Cover Comparison.

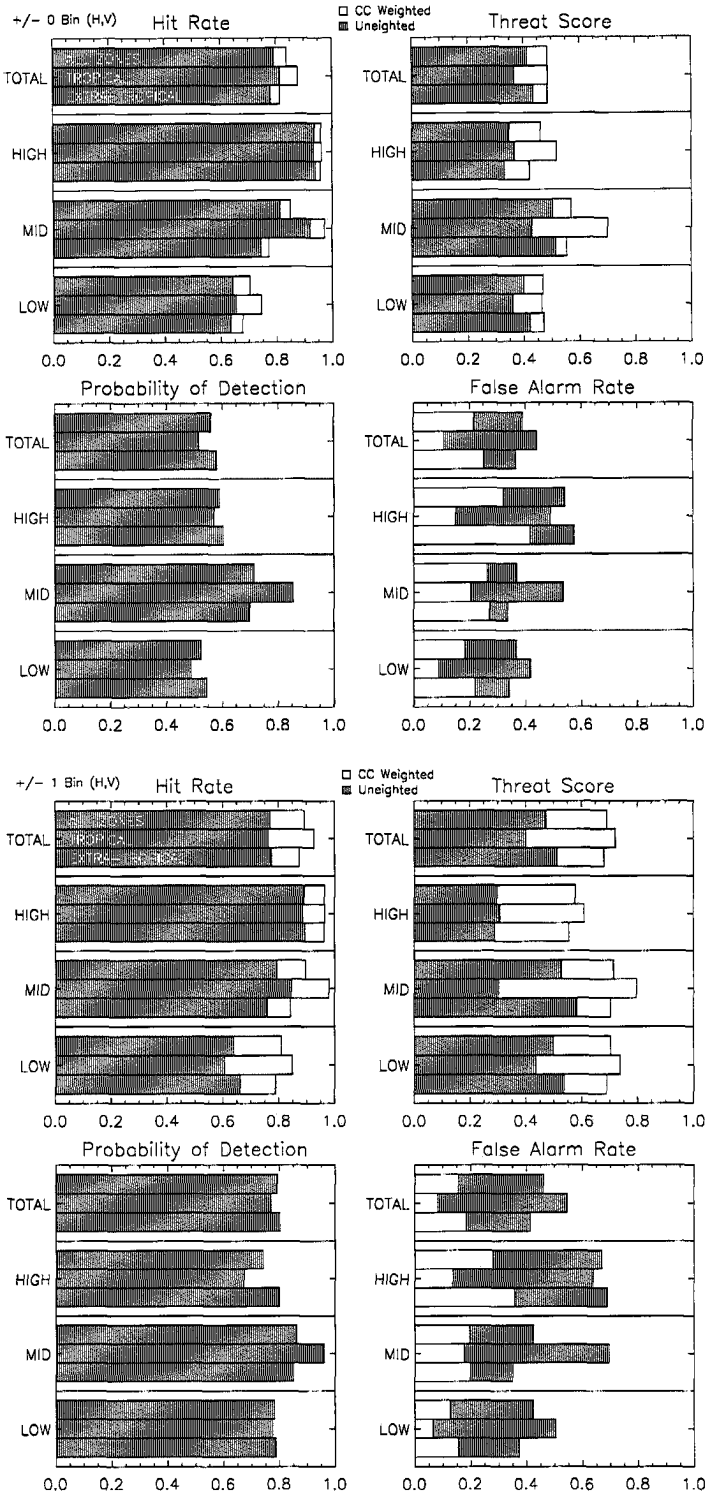

Figure B.80: LITE Orbit 104 Cloud Cover Statistics.

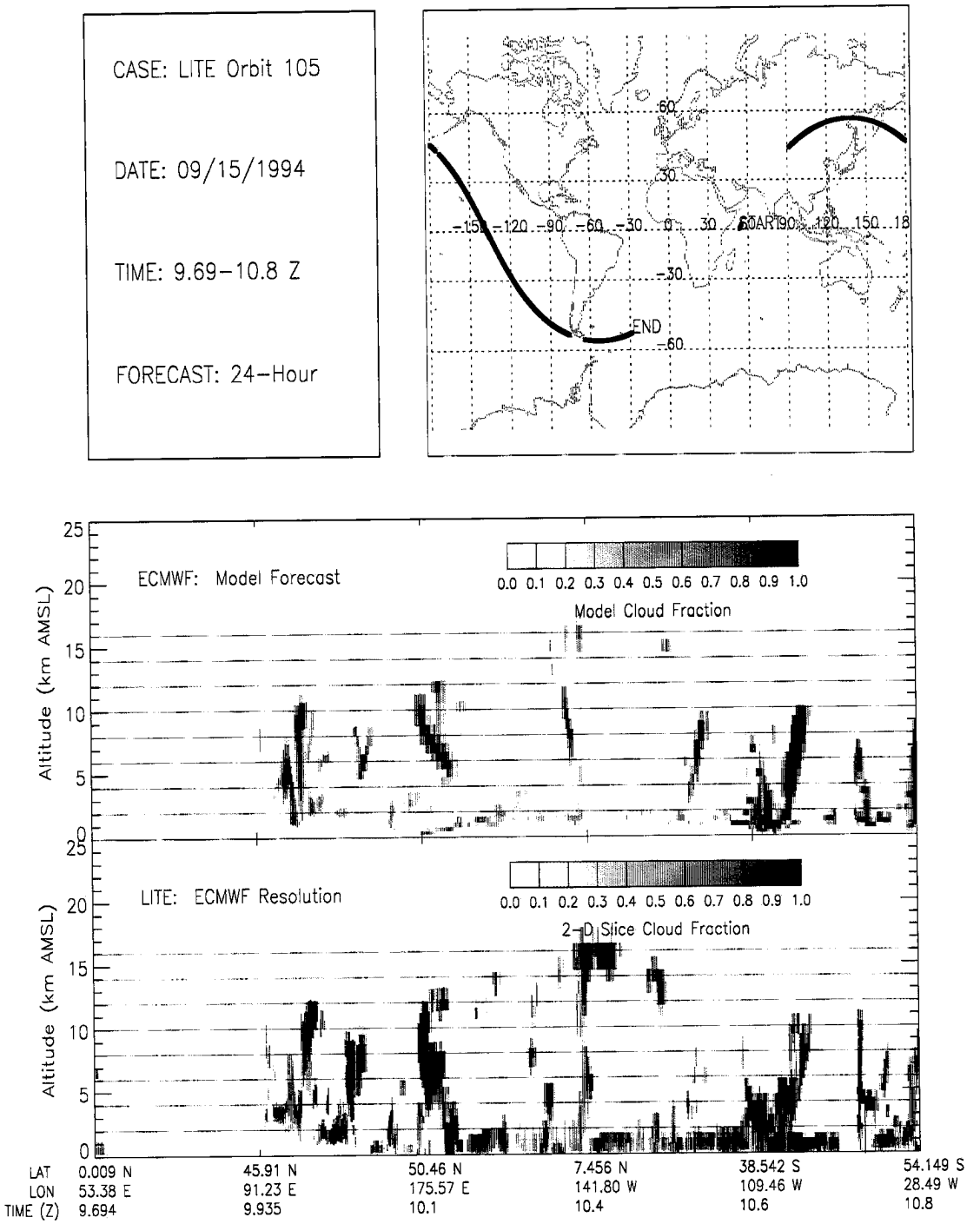

Figure B.81: LITE Orbit 105 Cloud Cover Comparison.

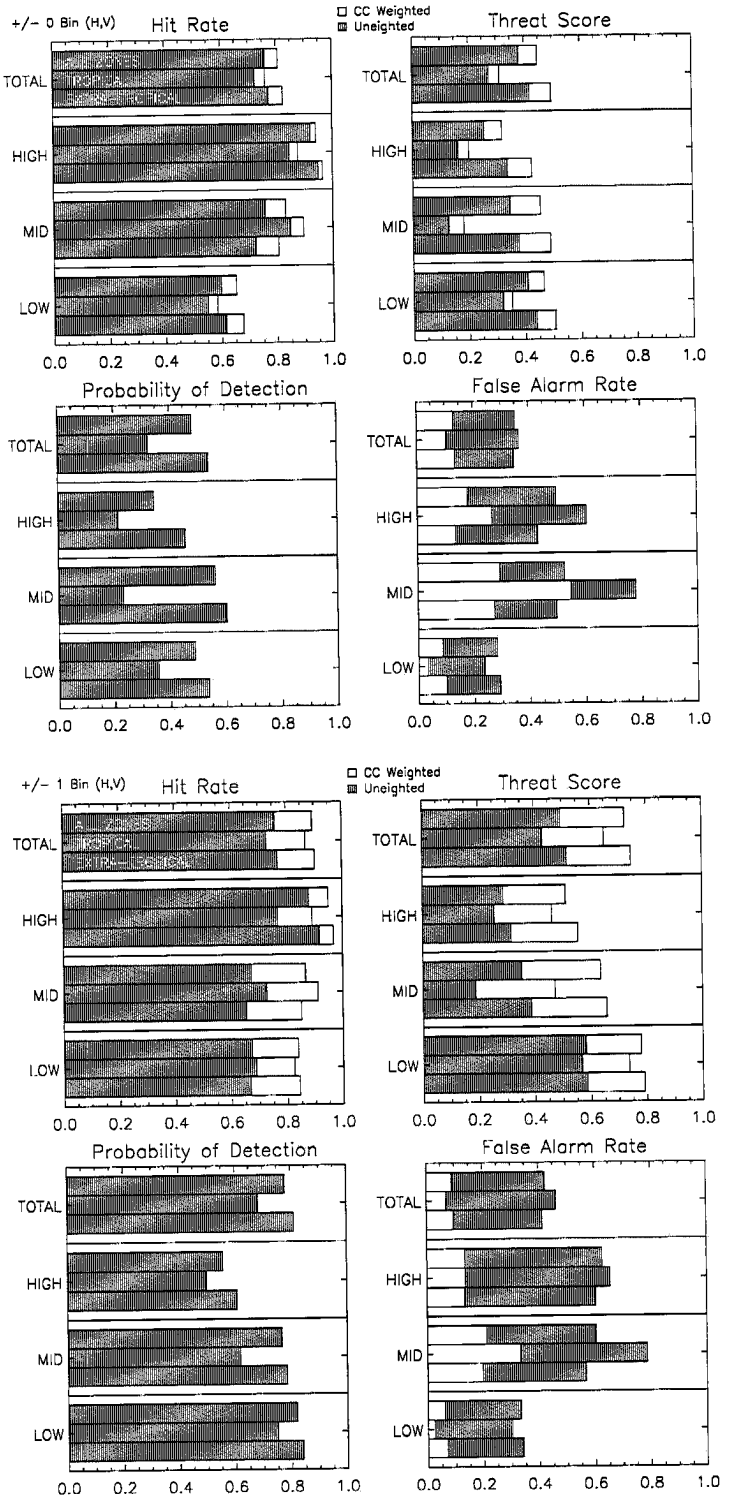

Figure B.82: LITE Orbit 105 Cloud Cover Statistics.

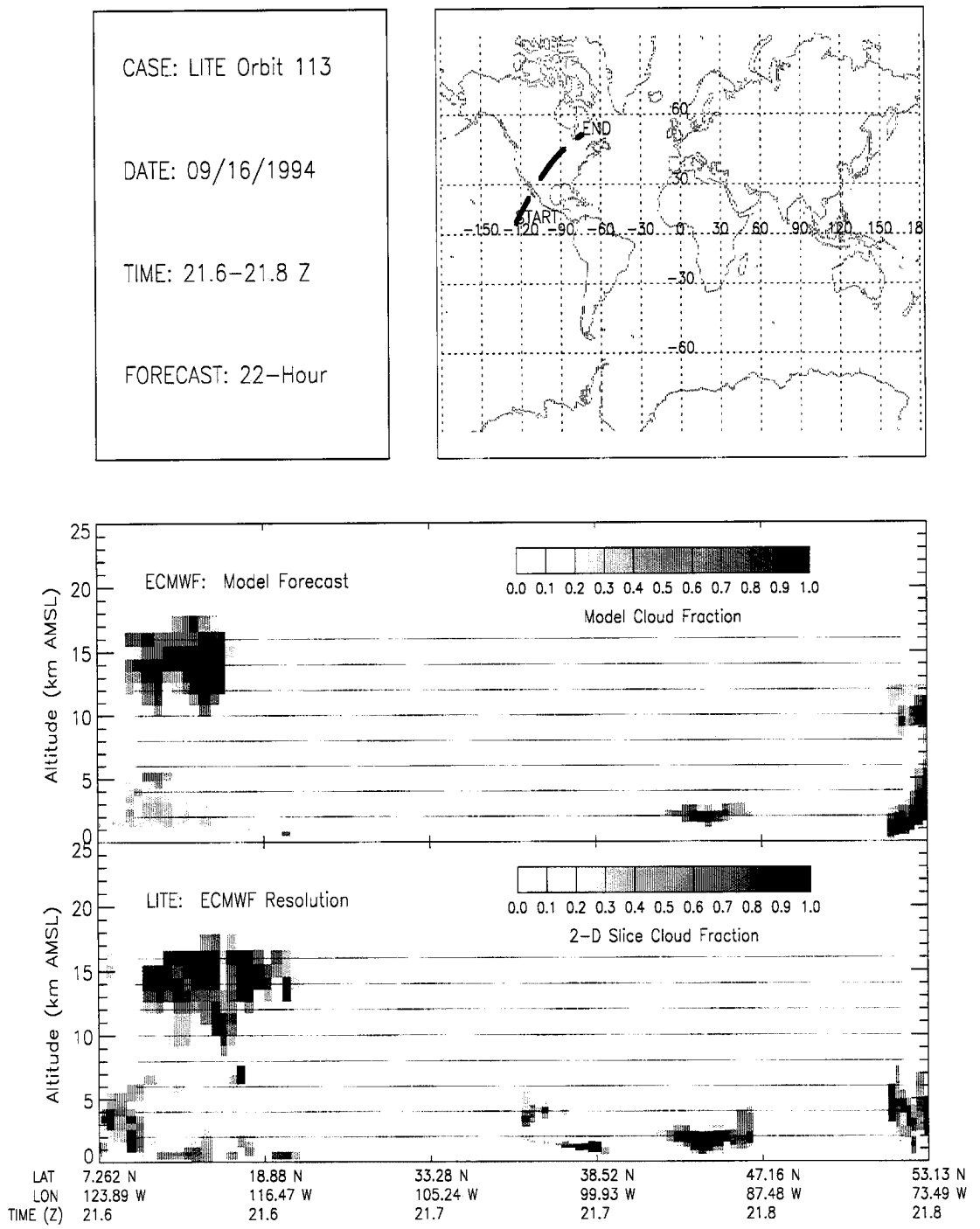

Figure B.83: LITE Orbit 113 Cloud Cover Comparison.

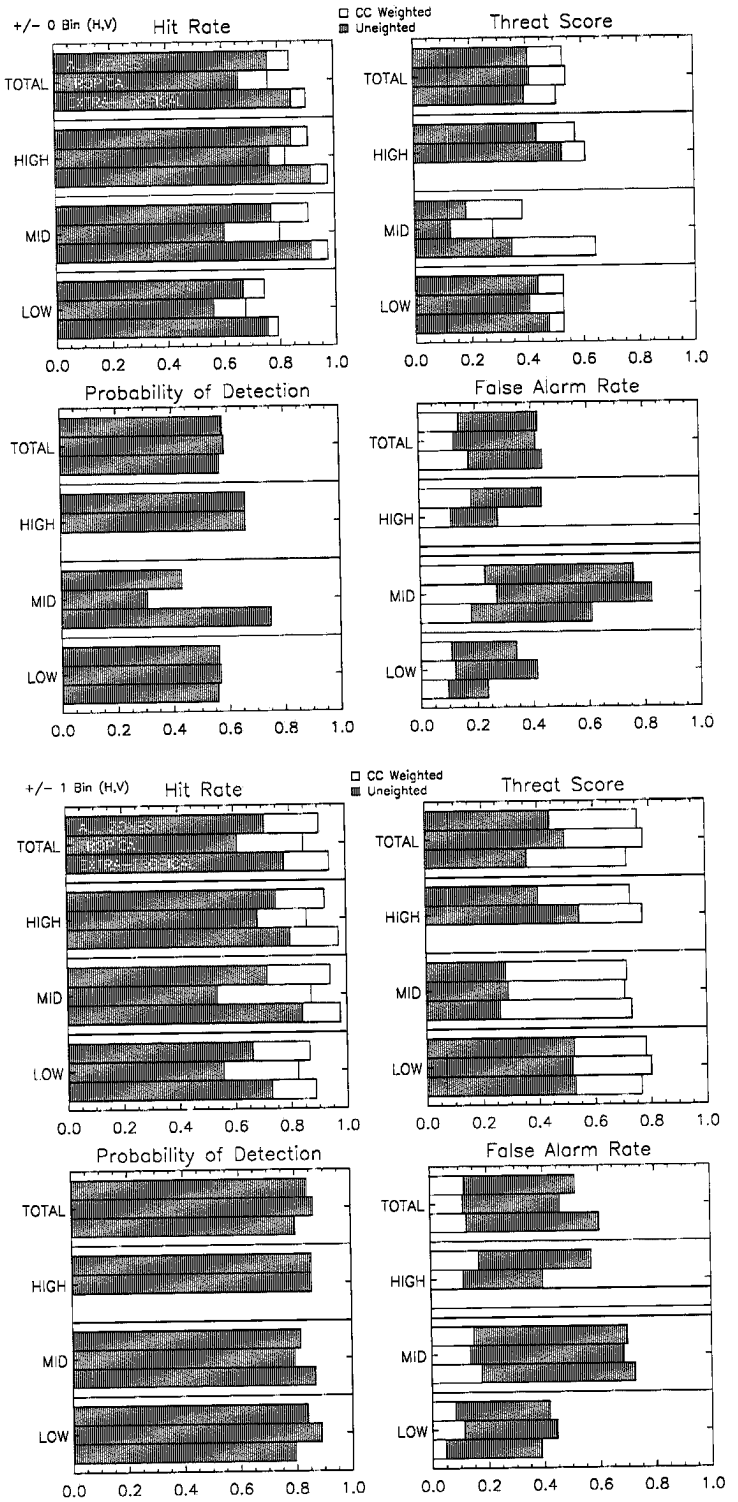

Figure B.84: LITE Orbit 113 Cloud Cover Statistics.

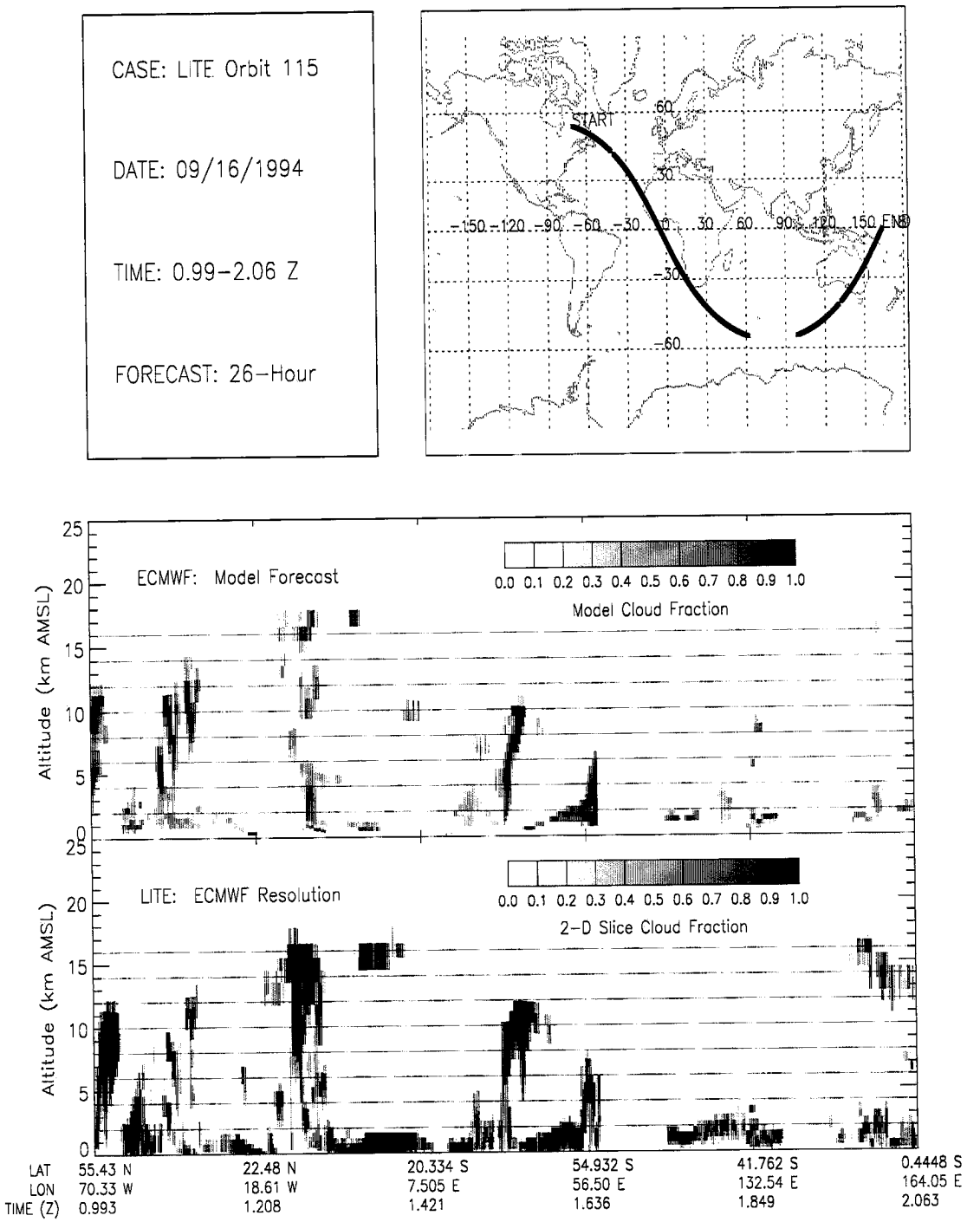

Figure B.85: LITE Orbit 115 Cloud Cover Comparison.

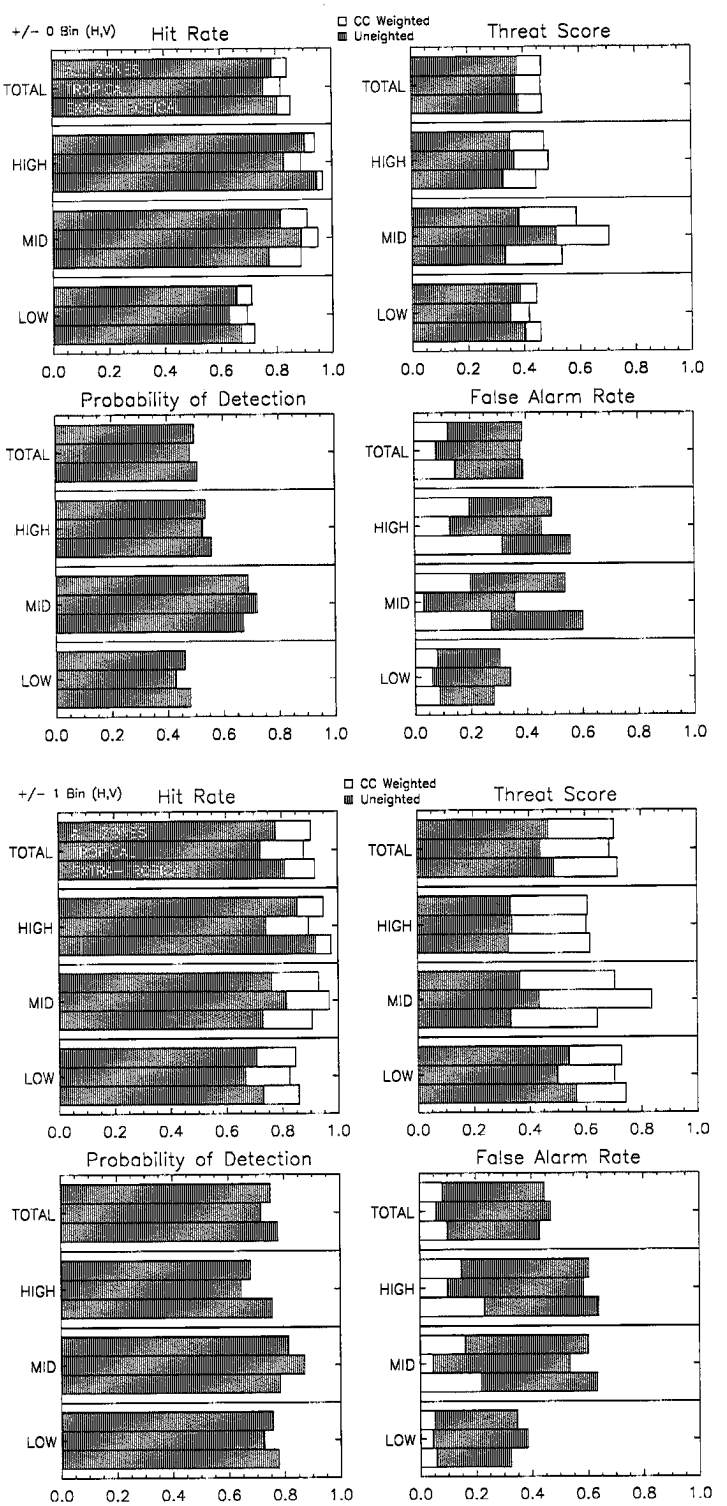

Figure B.86: LITE Orbit 115 Cloud Cover Statistics.

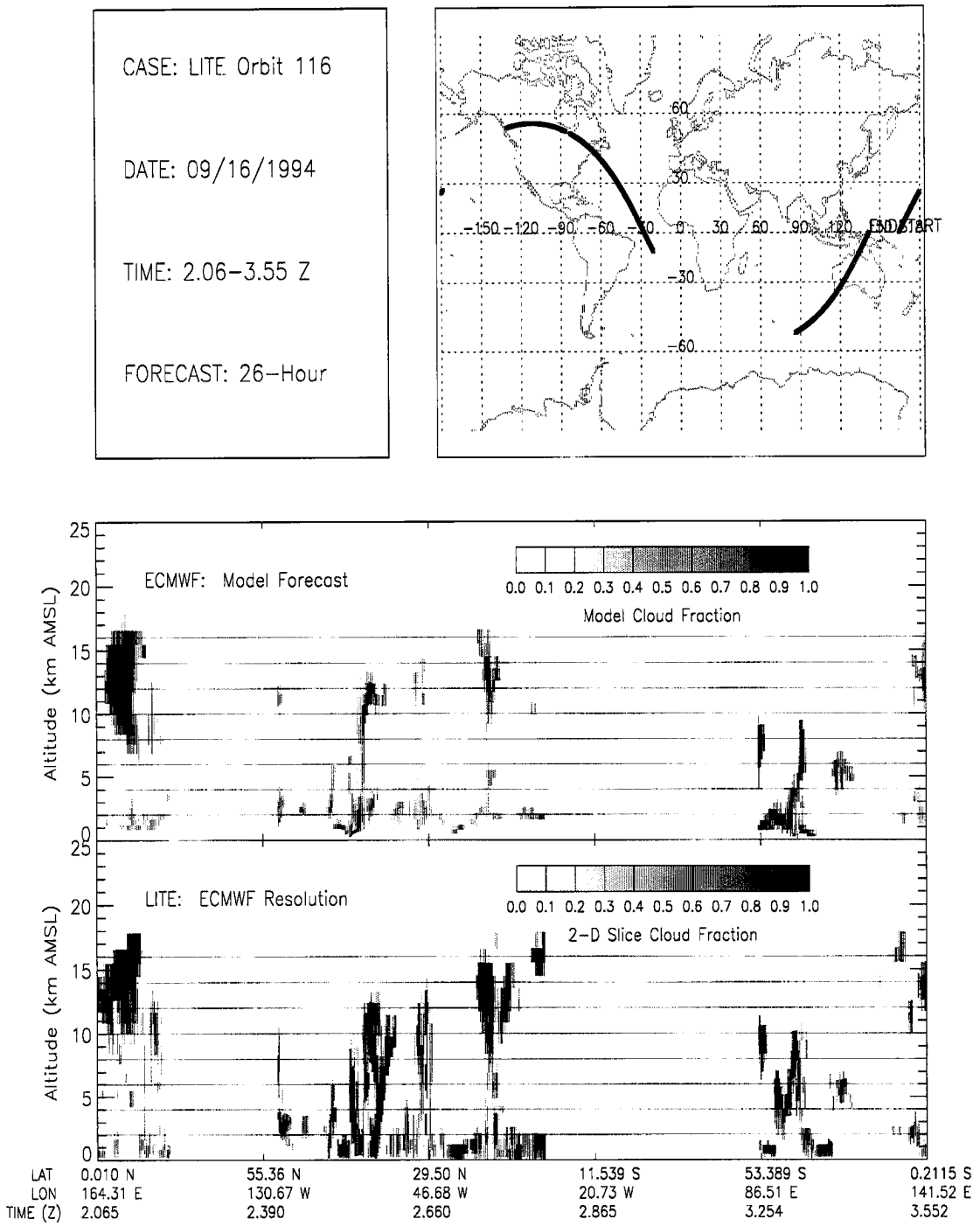

Figure B.87: LITE Orbit 116 Cloud Cover Comparison.

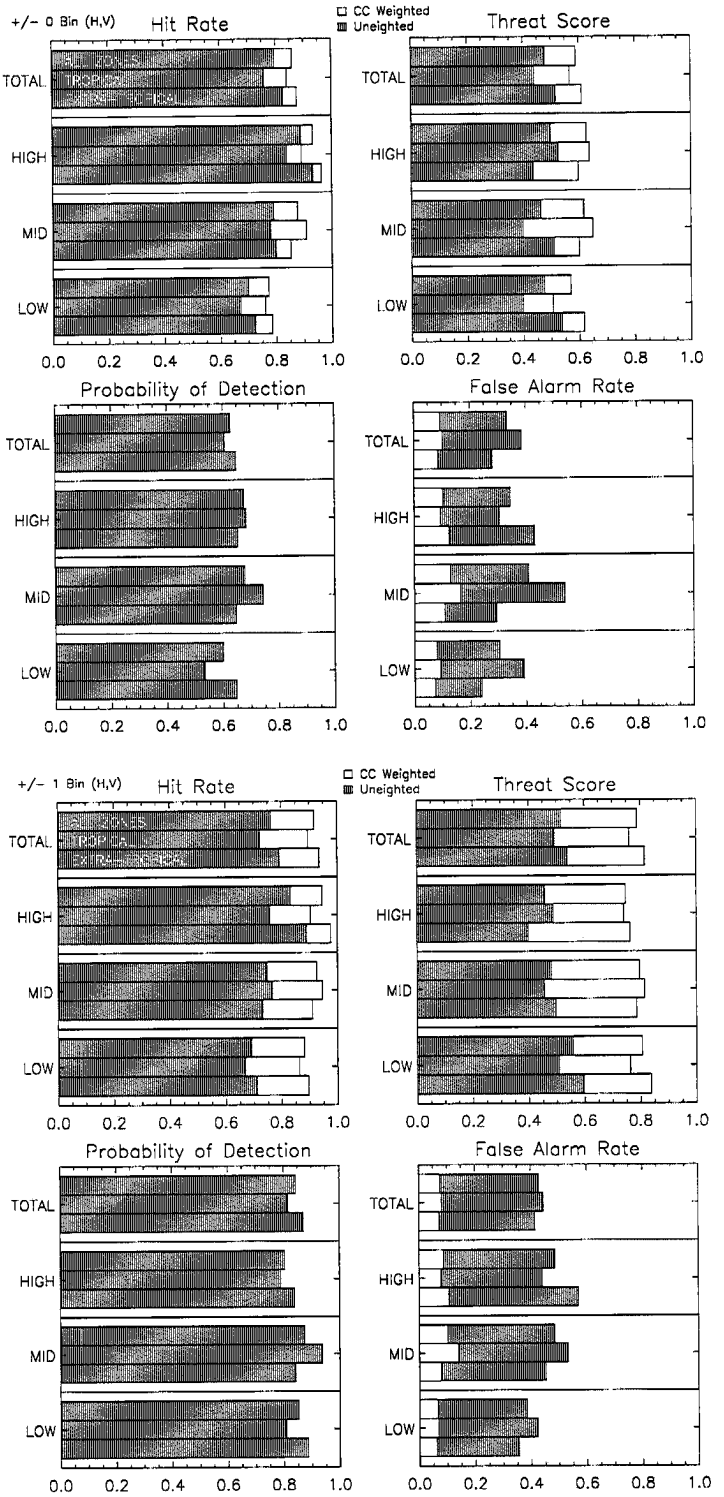

Figure B.88: LITE Orbit 116 Cloud Cover Statistics.

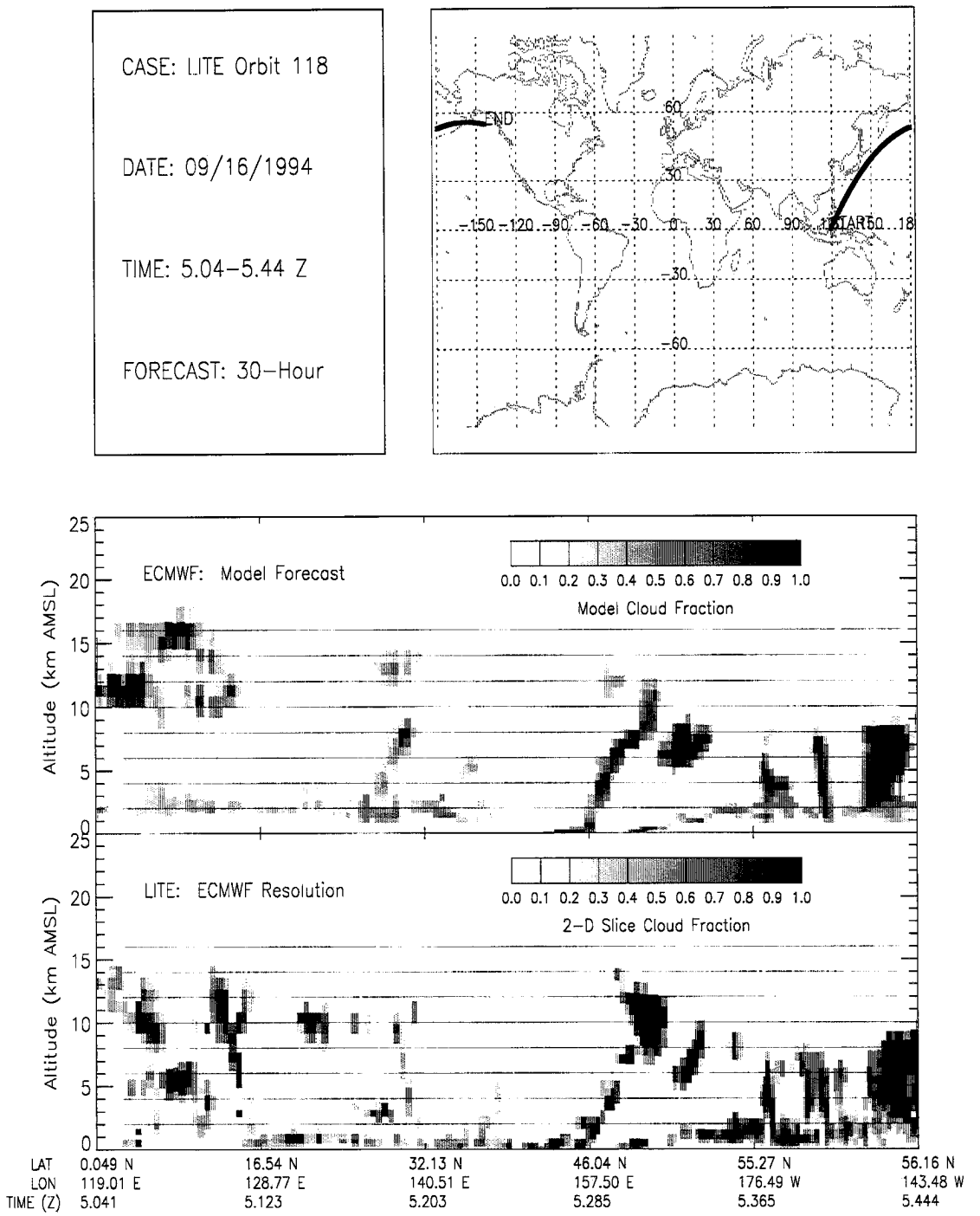

Figure B.89: LITE Orbit 118 Cloud Cover Comparison.

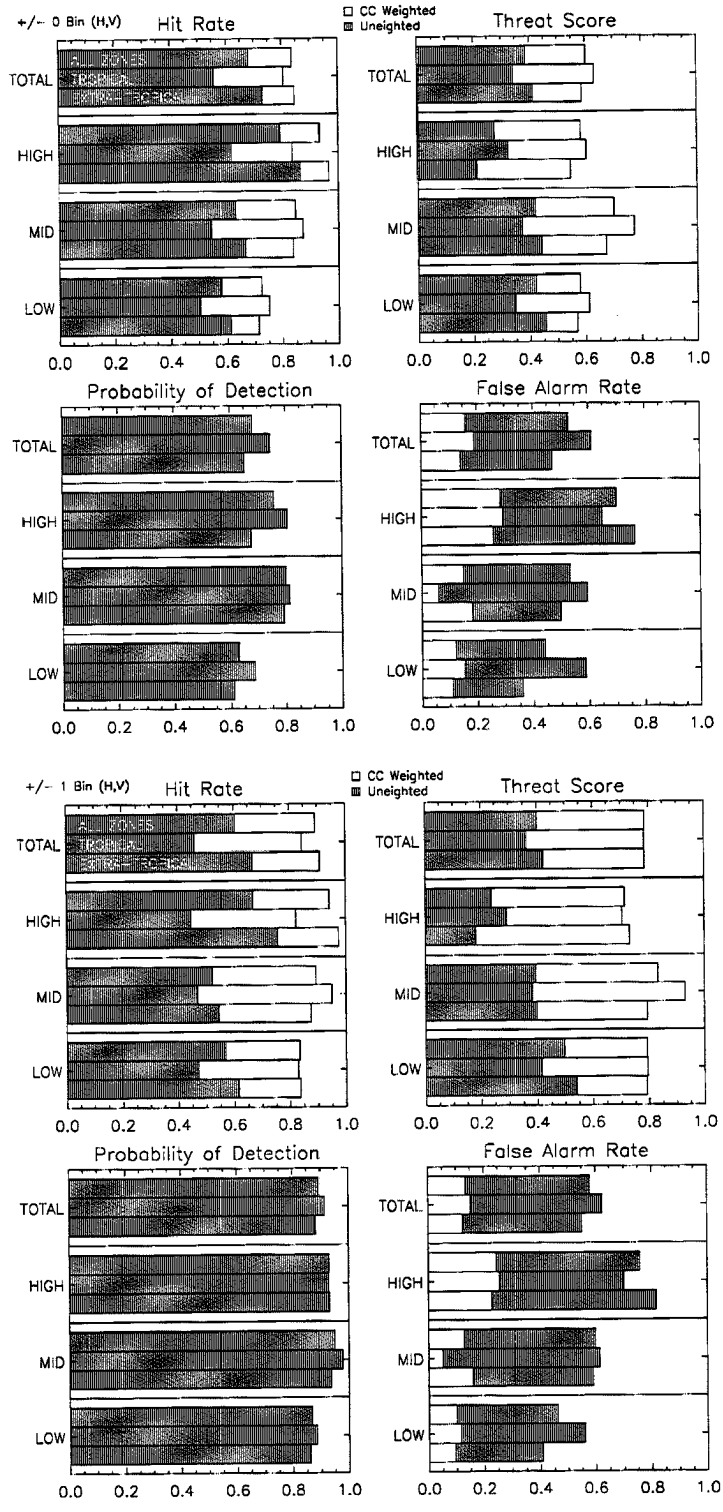

Figure B.90: LITE Orbit 118 Cloud Cover Statistics.

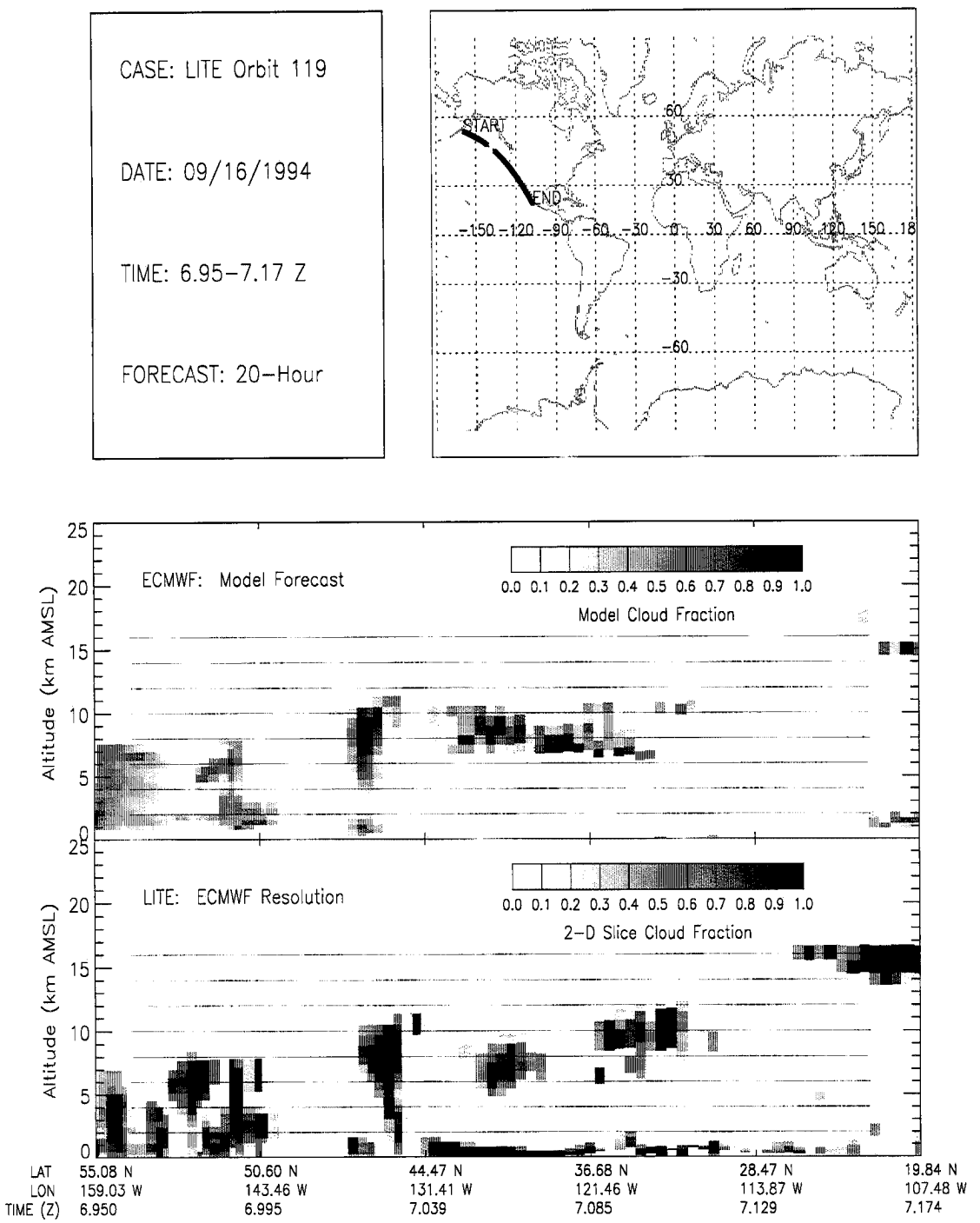

Figure B.91: LITE Orbit 119 Cloud Cover Comparison.

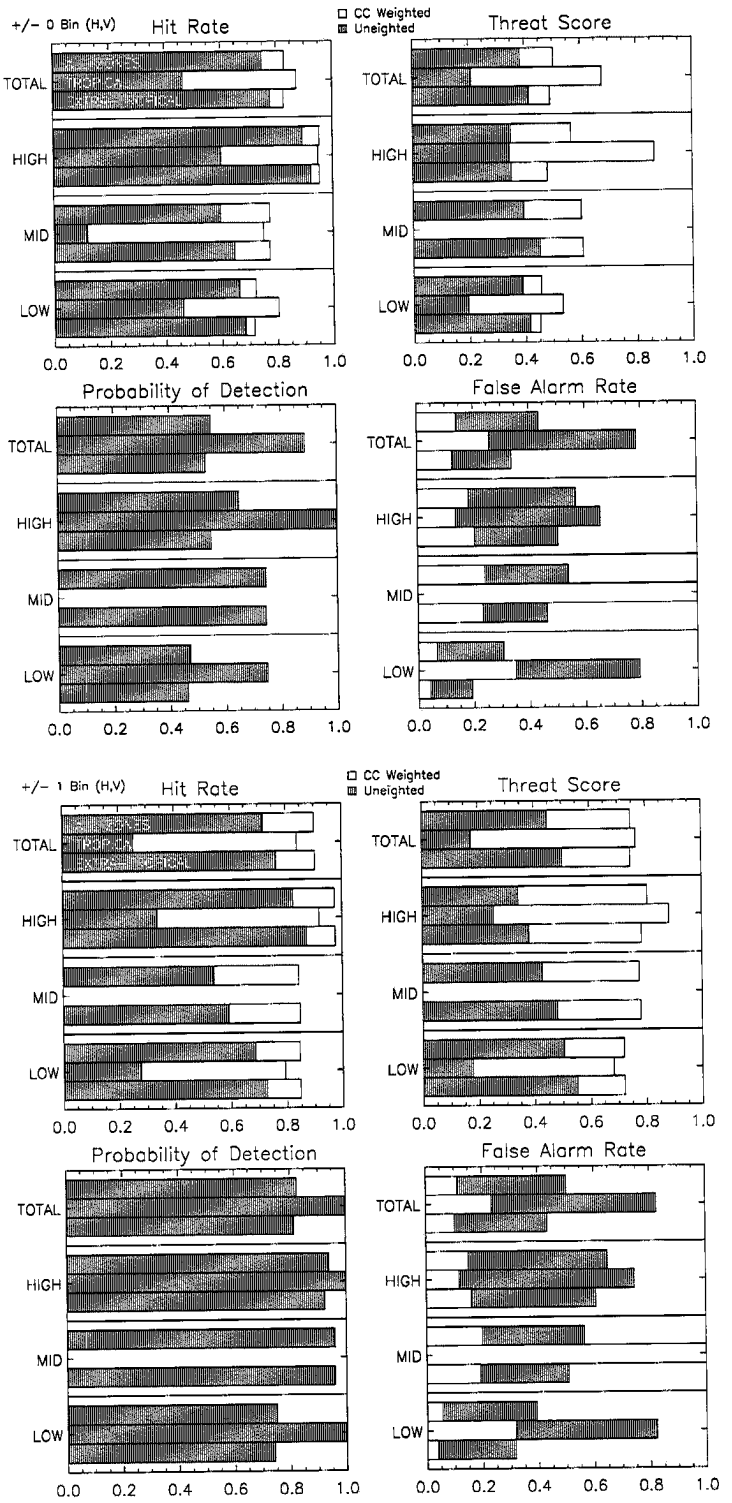

Figure B.92: LITE Orbit 119 Cloud Cover Statistics.

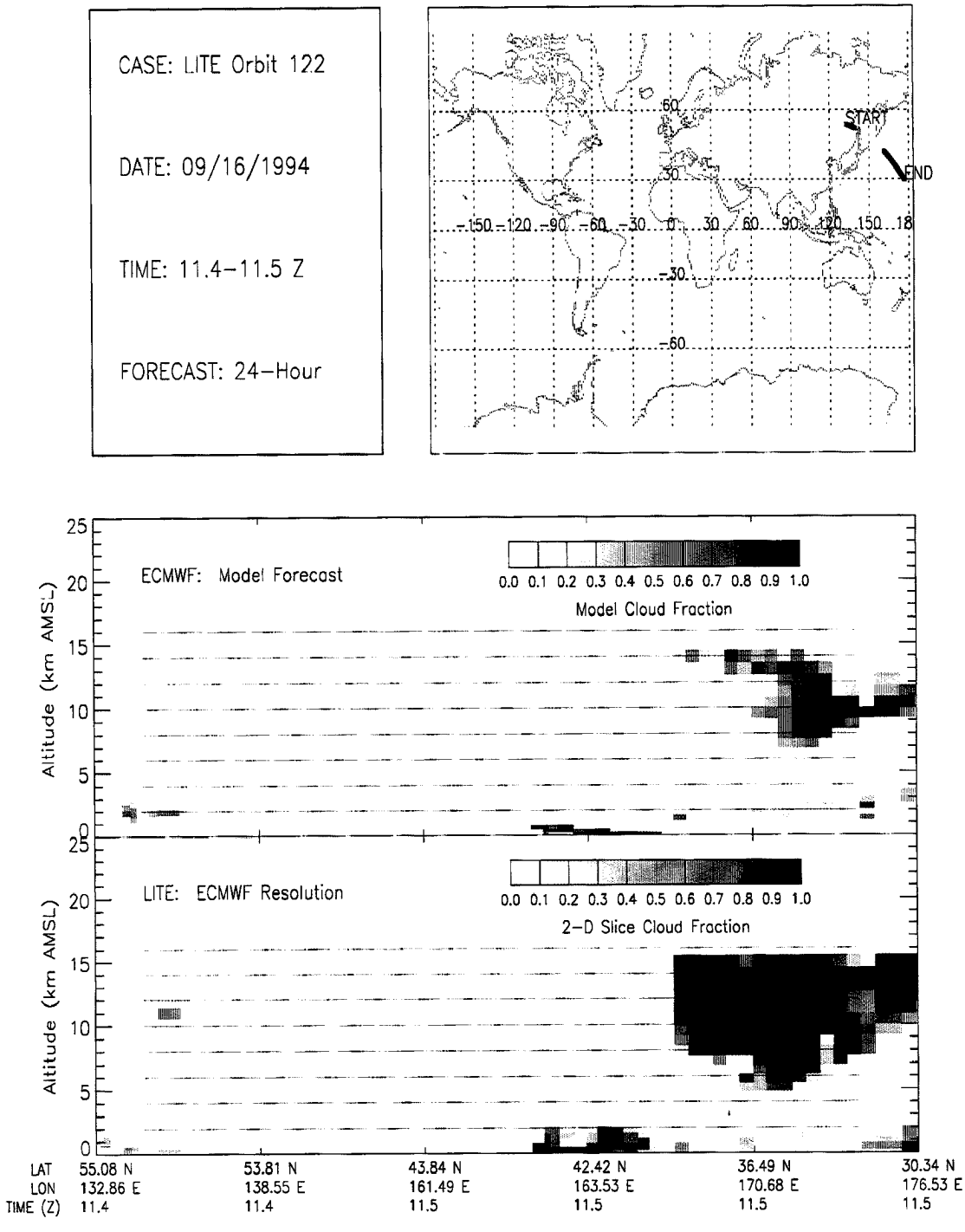

Figure B.93: LITE Orbit 122 Cloud Cover Comparison.

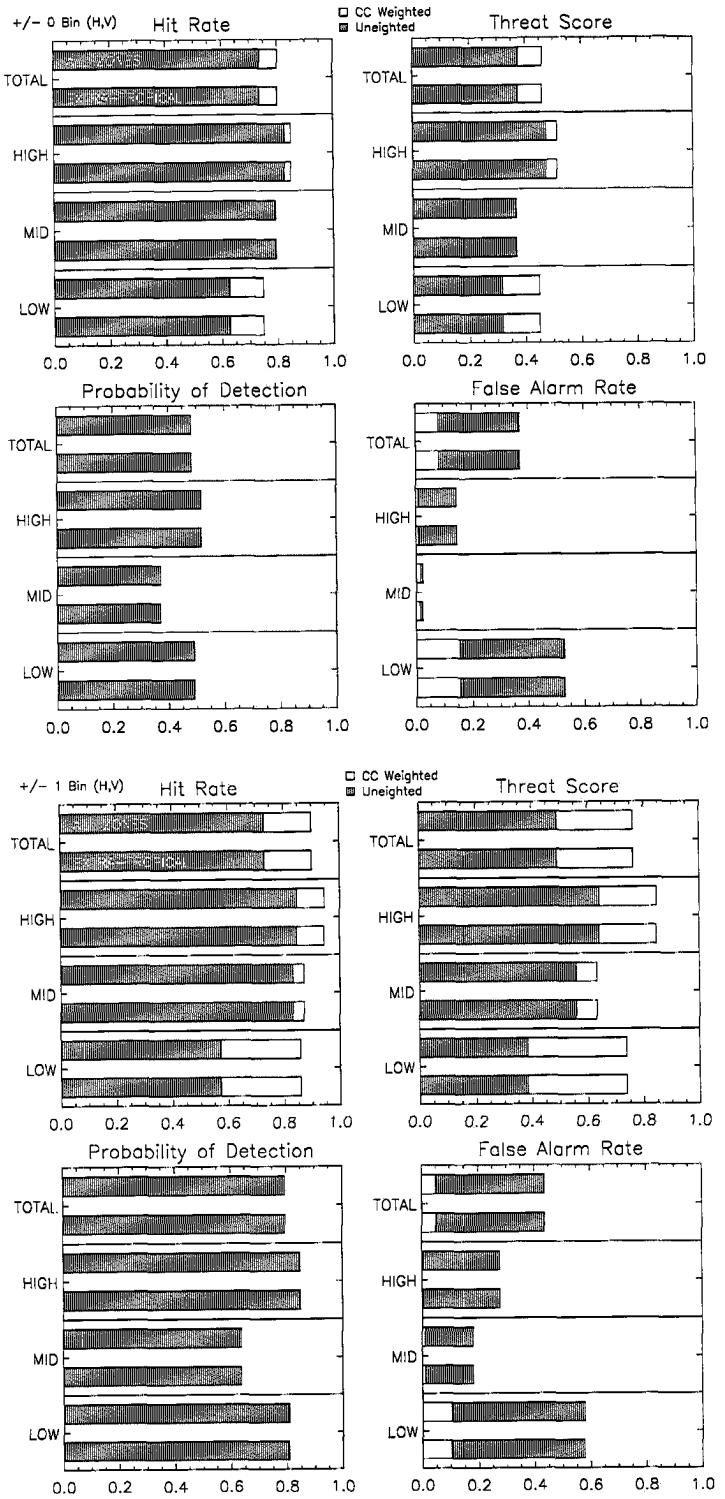

Figure B.94: LITE Orbit 122 Cloud Cover Statistics.

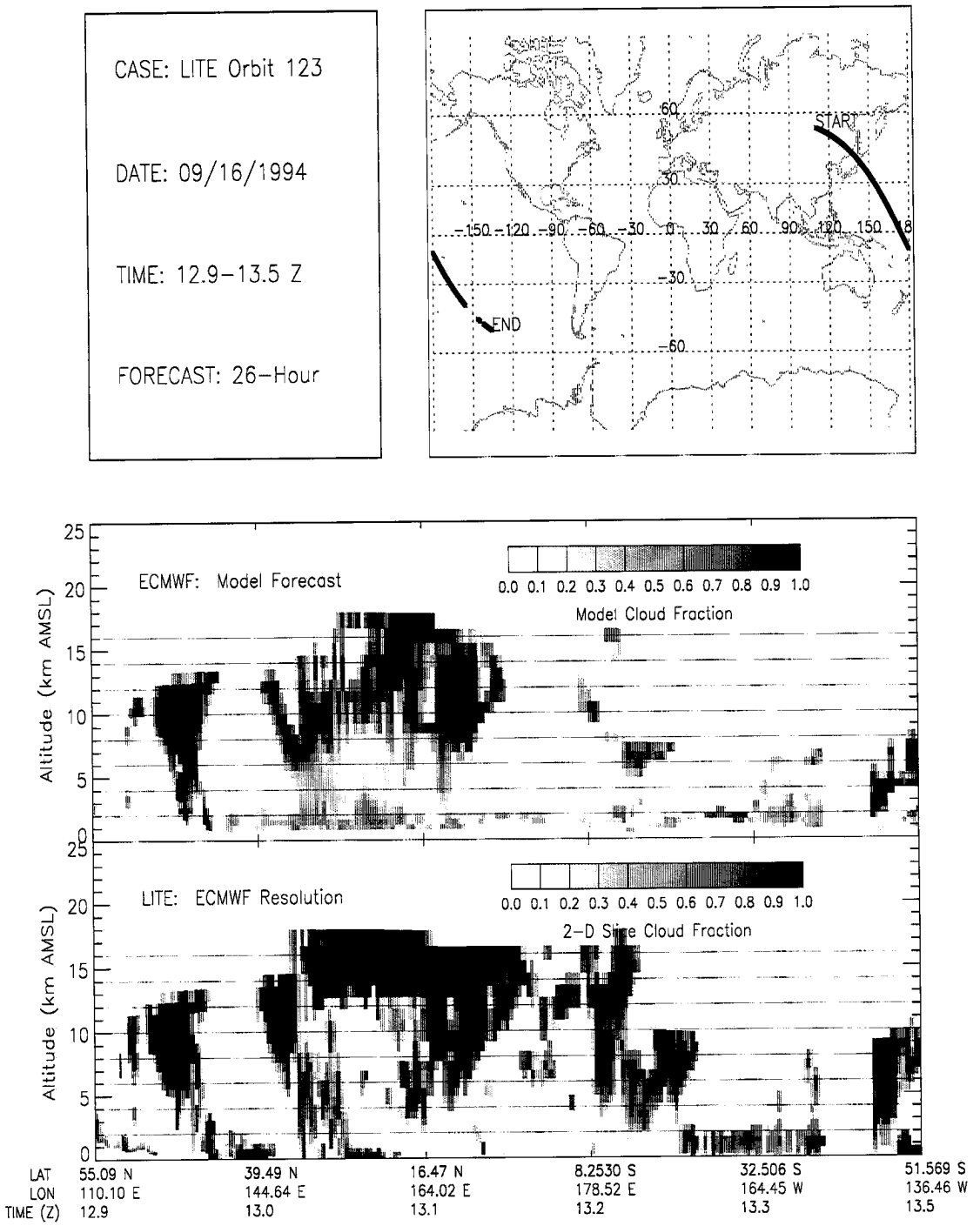

Figure B.95: LITE Orbit 123 Cloud Cover Comparison.

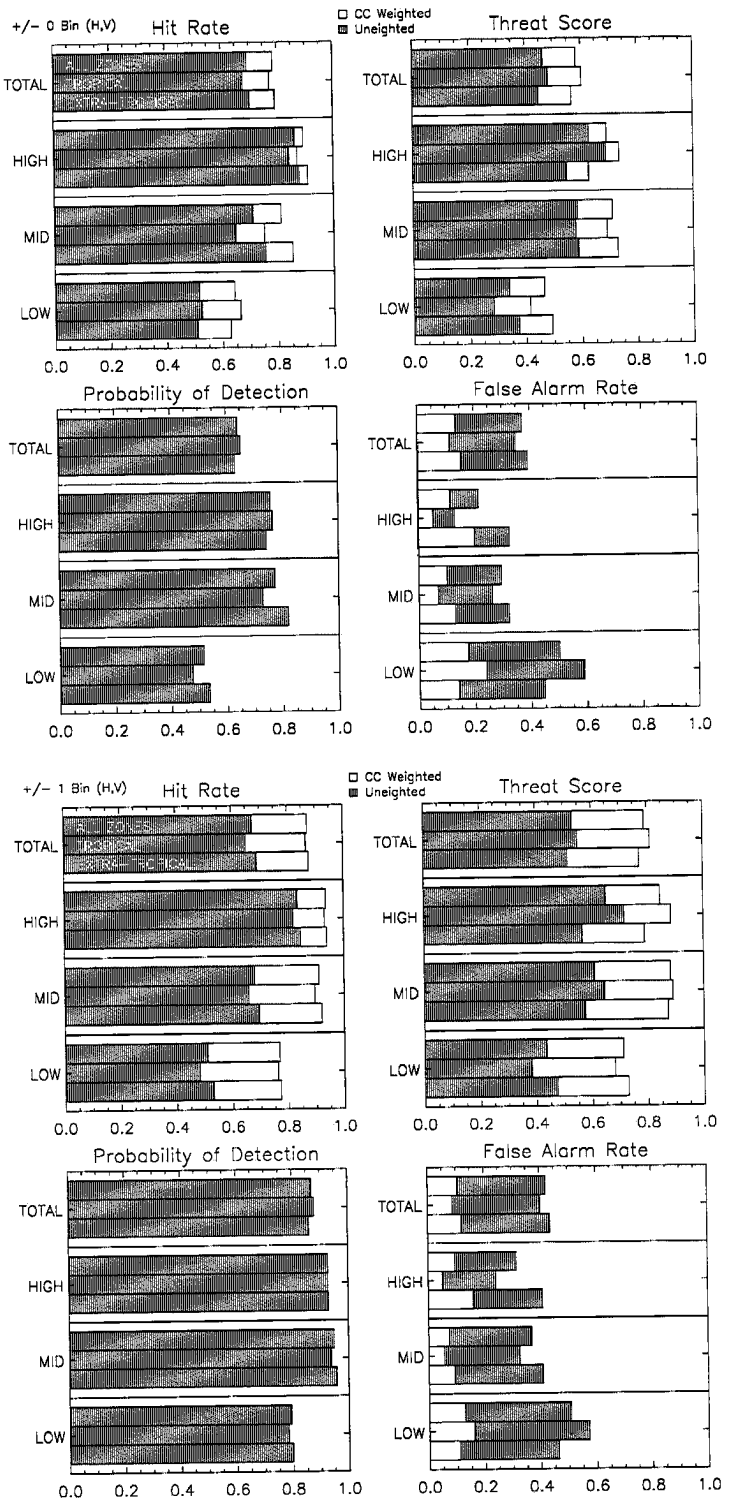

Figure B.96: LITE Orbit 123 Cloud Cover Statistics.

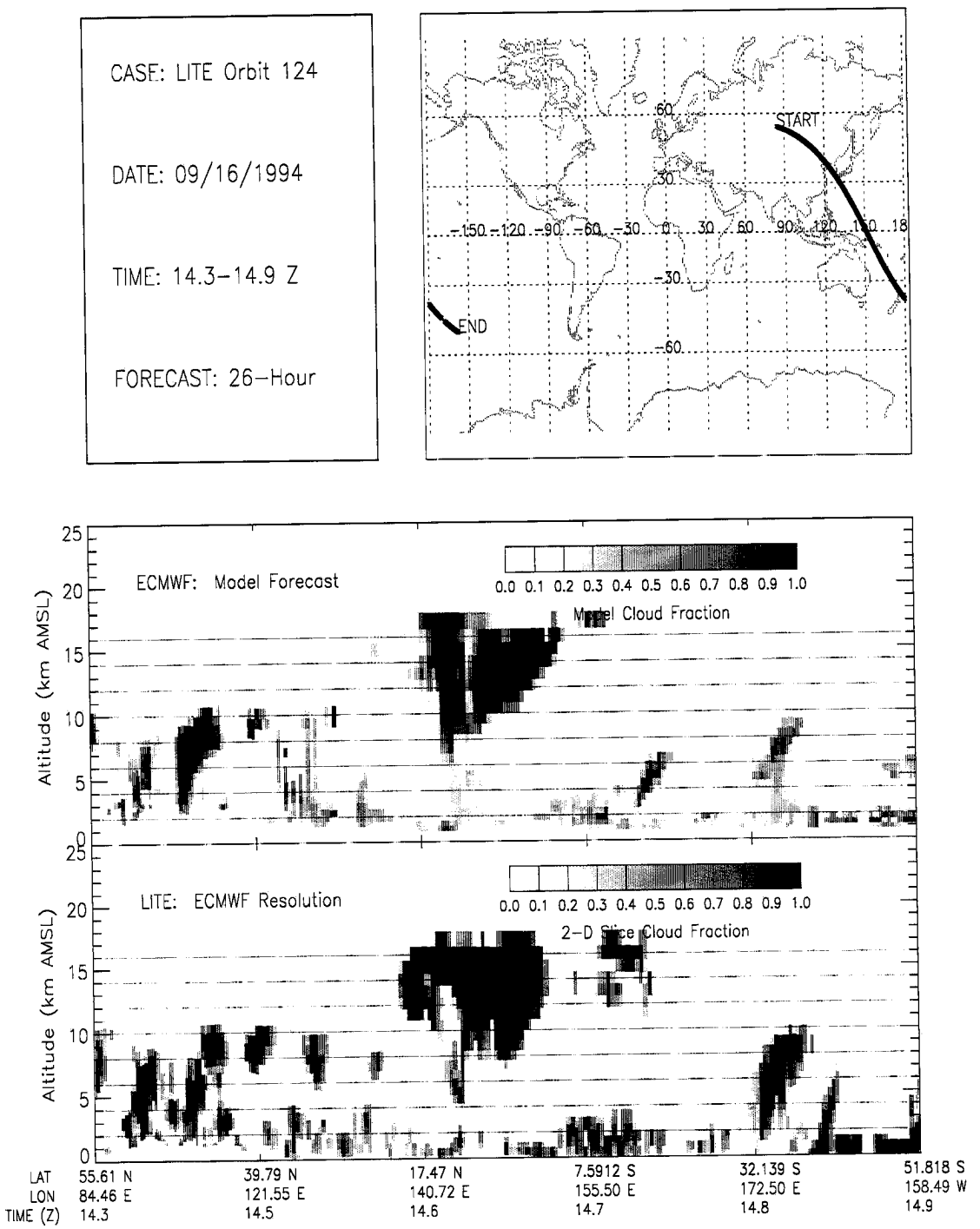

Figure B.97: LITE Orbit 124 Cloud Cover Comparison.

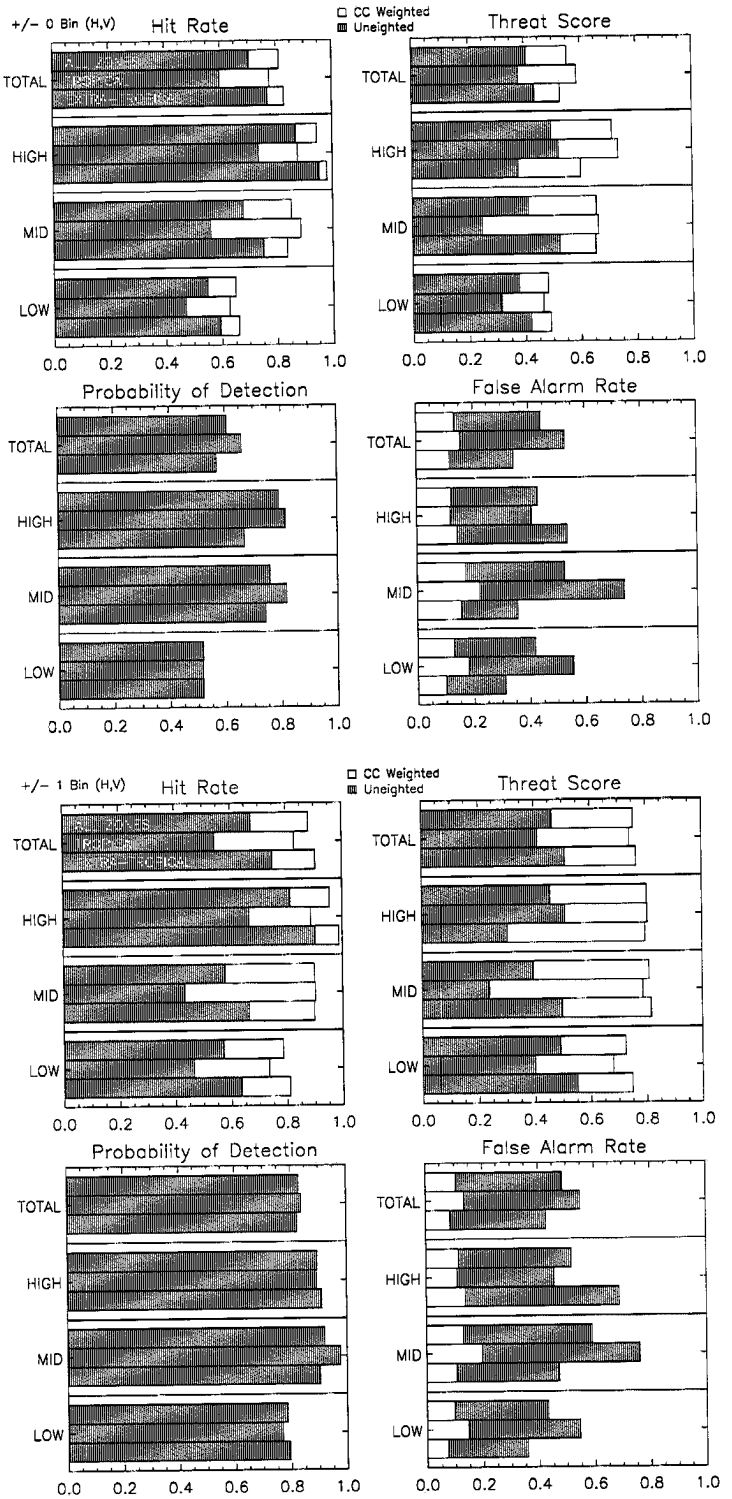

Figure B.98: LITE Orbit 124 Cloud Cover Statistics.

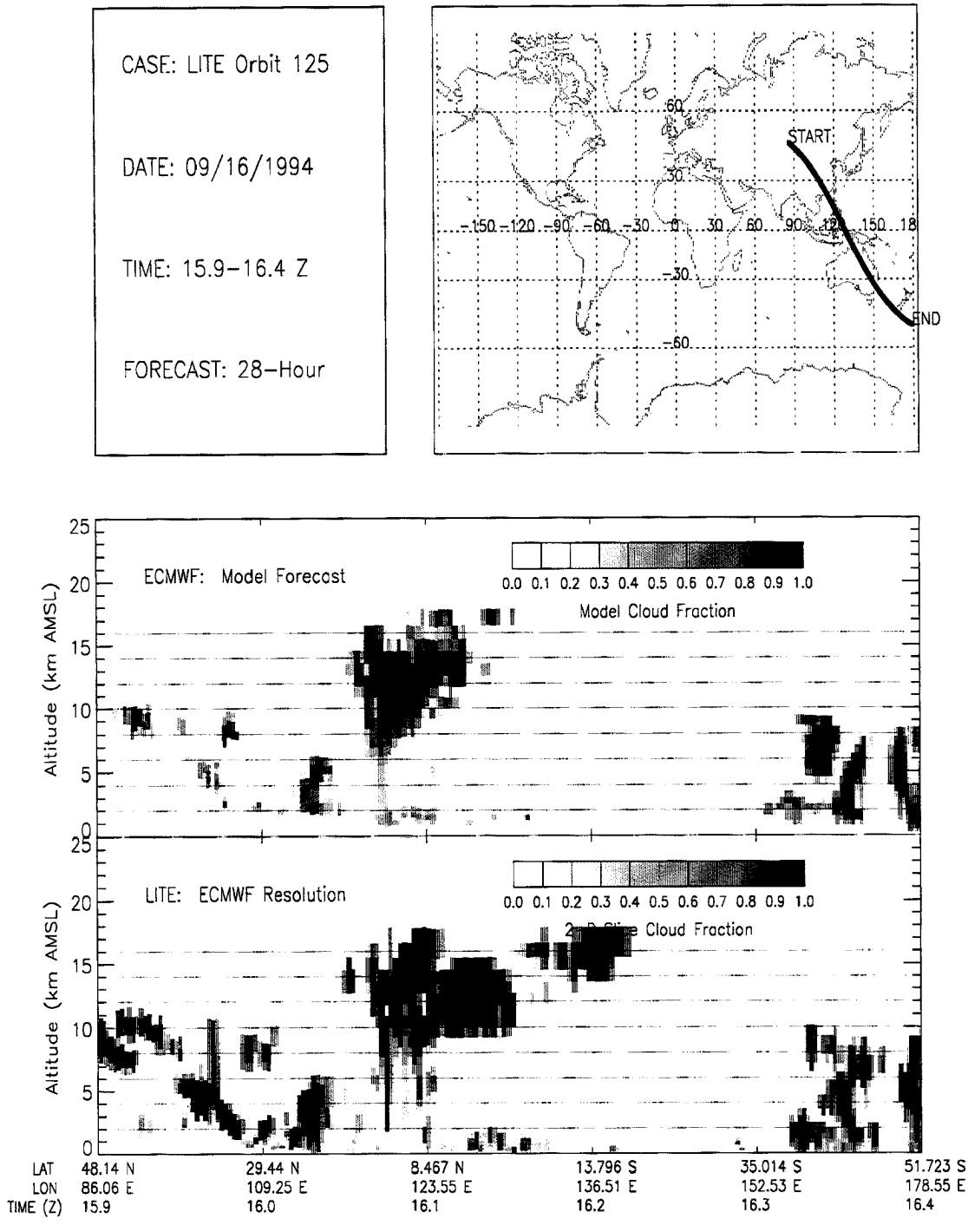

Figure B.99: LITE Orbit 125 Cloud Cover Comparison.

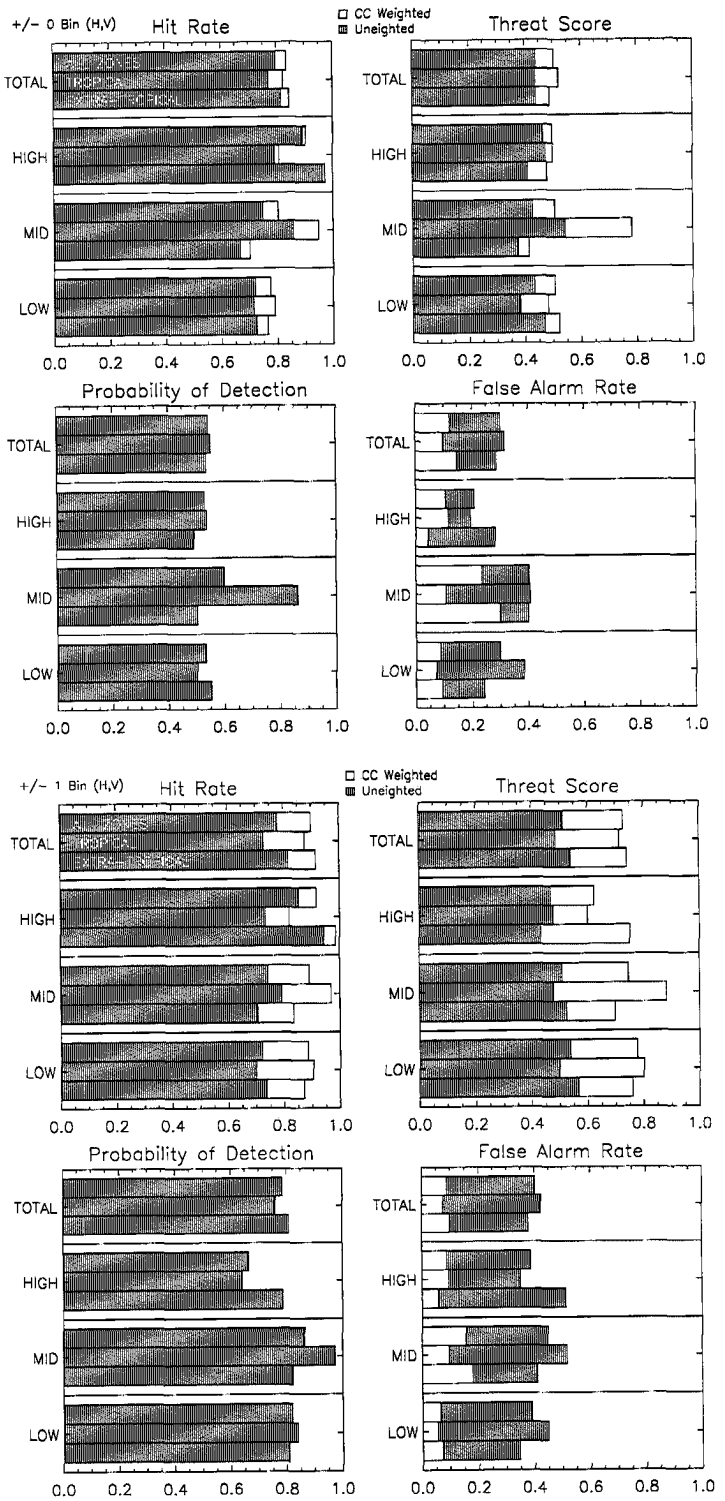

Figure B.100: LITE Orbit 125 Cloud Cover Statistics.

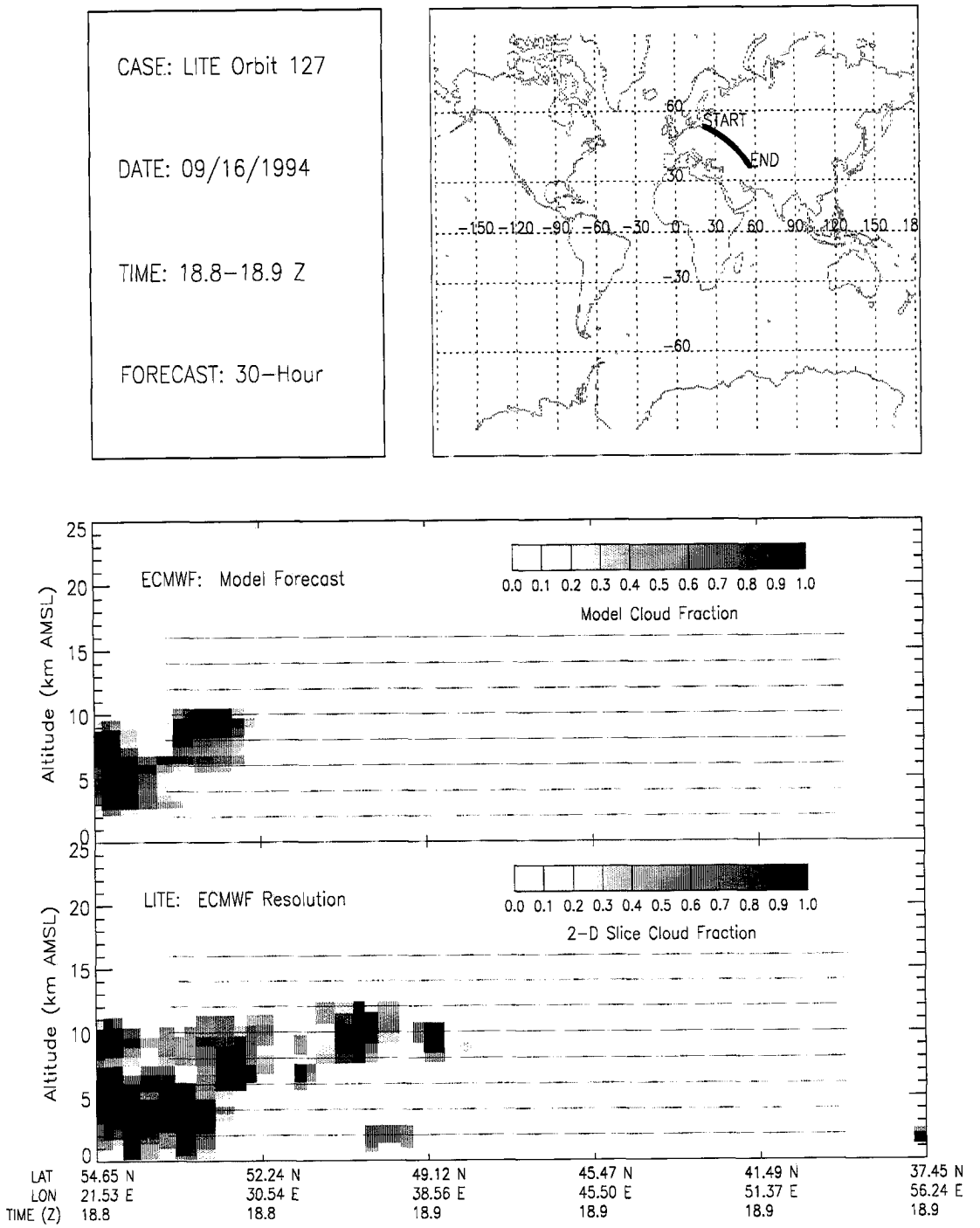

Figure B.101: LITE Orbit 127 Cloud Cover Comparison.

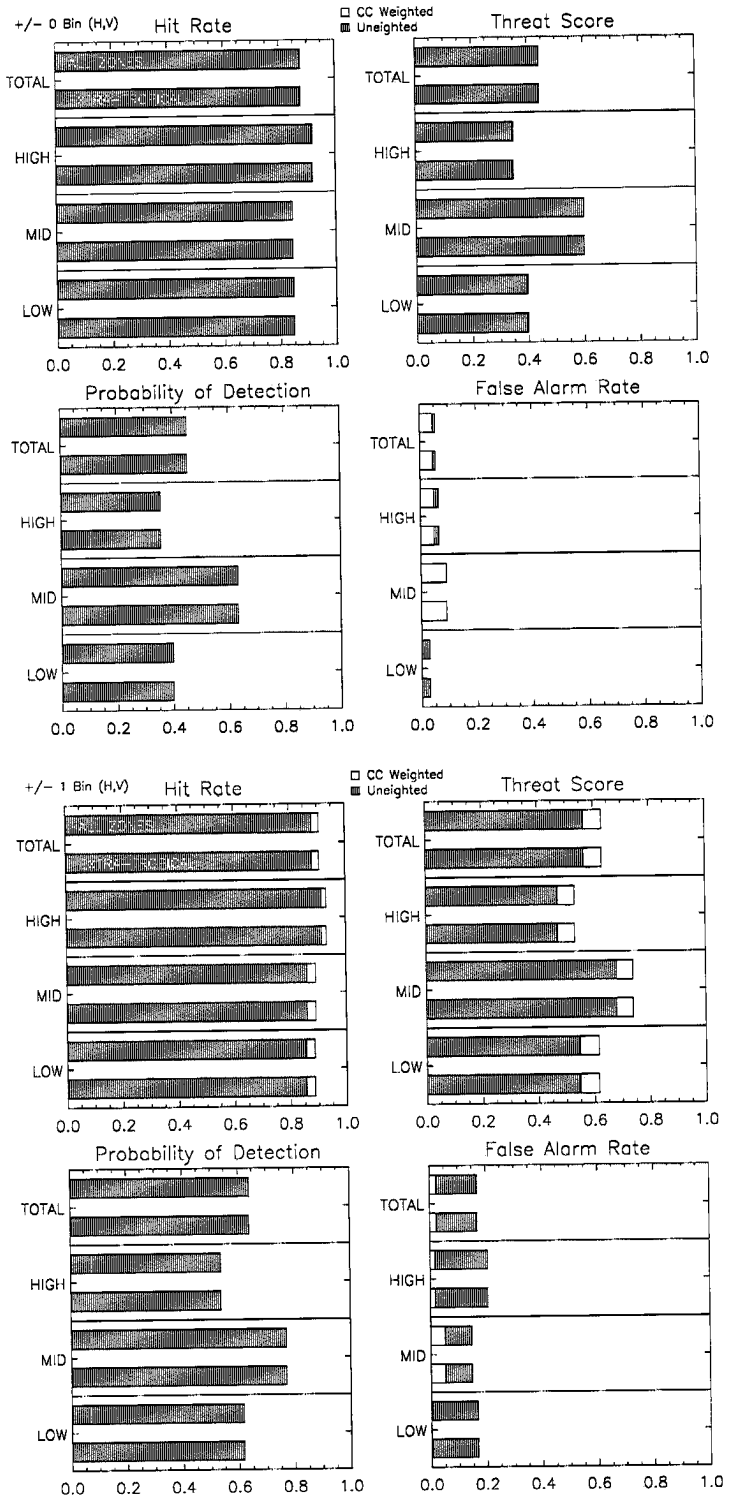

Figure B.102: LITE Orbit 127 Cloud Cover Statistics.

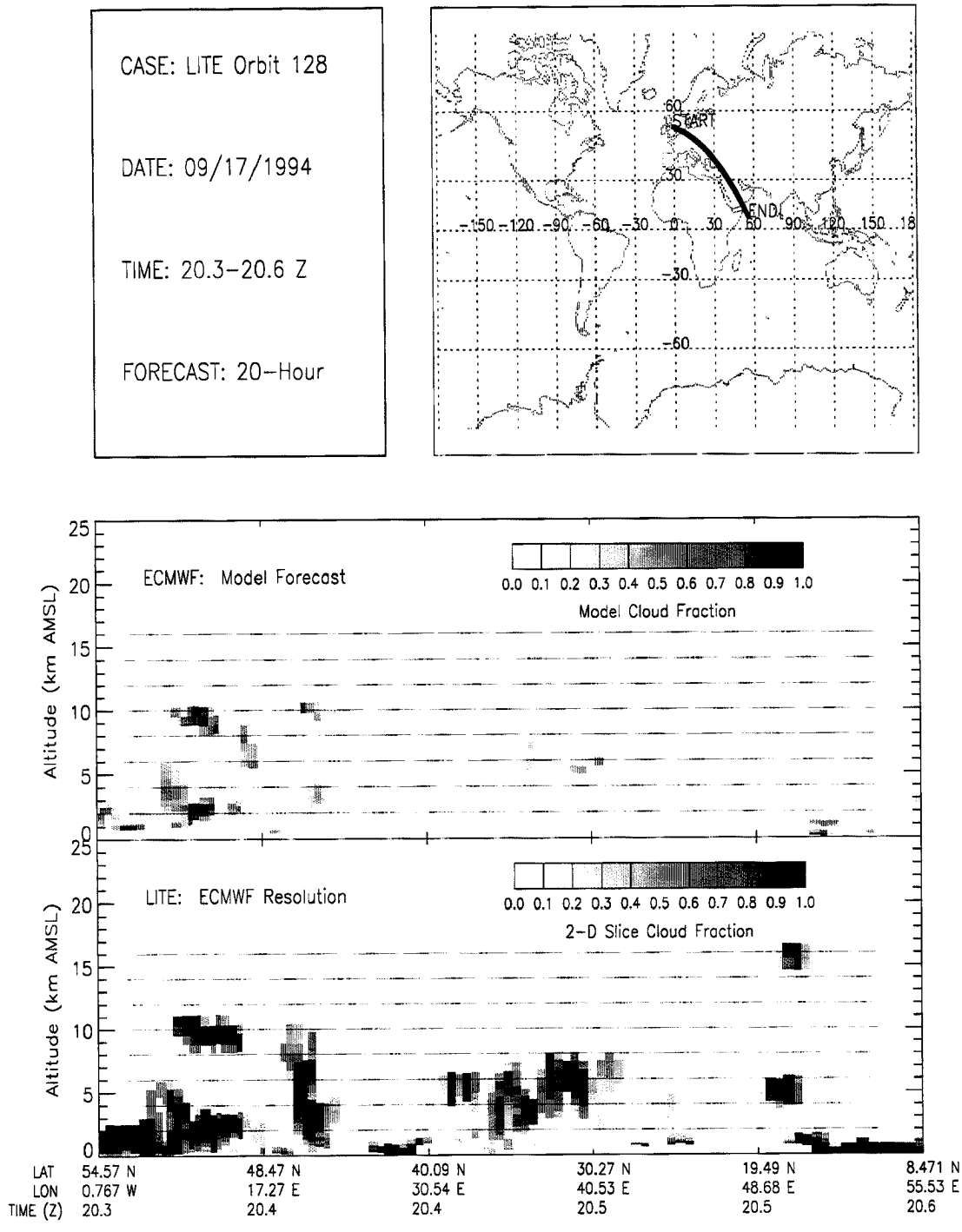

Figure B.103: LITE Orbit 128 Cloud Cover Comparison.

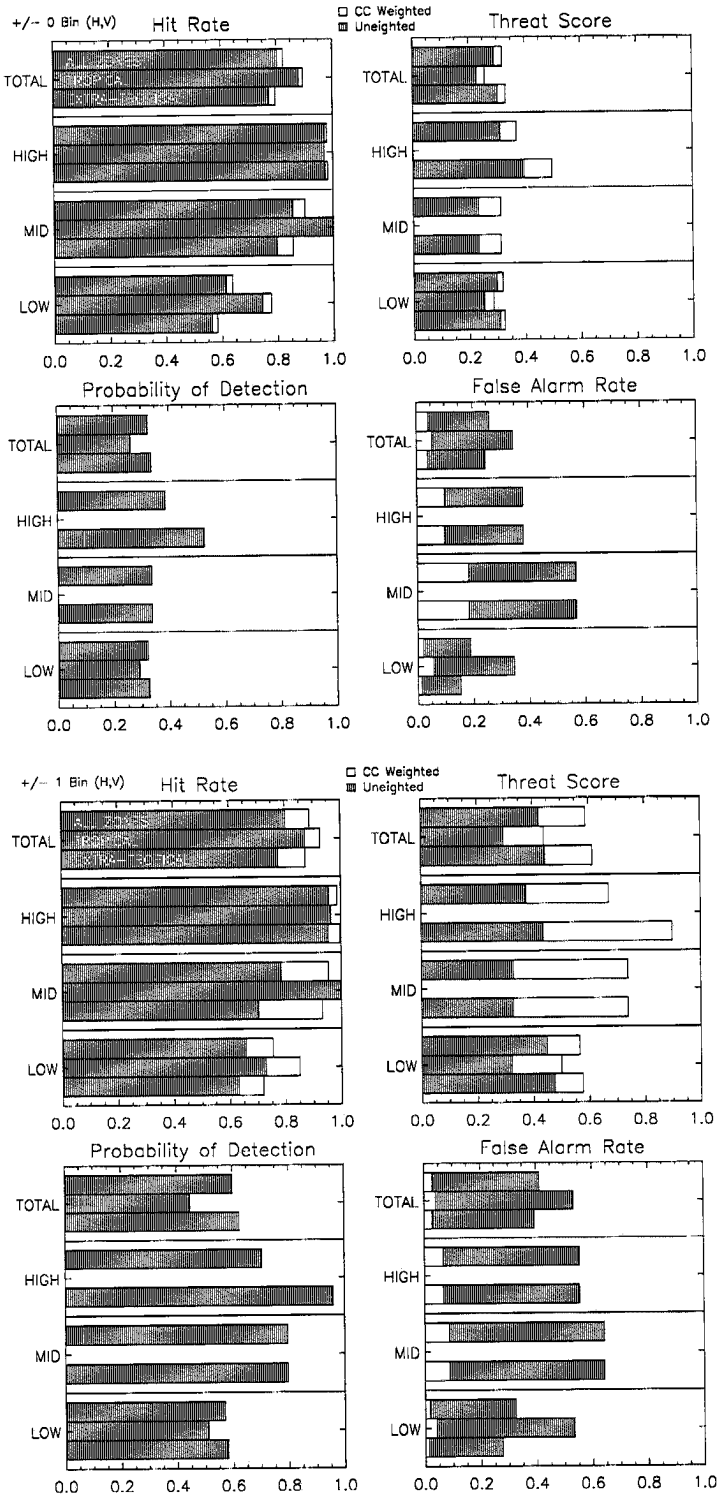

Figure B.104: LITE Orbit 128 Cloud Cover Statistics.

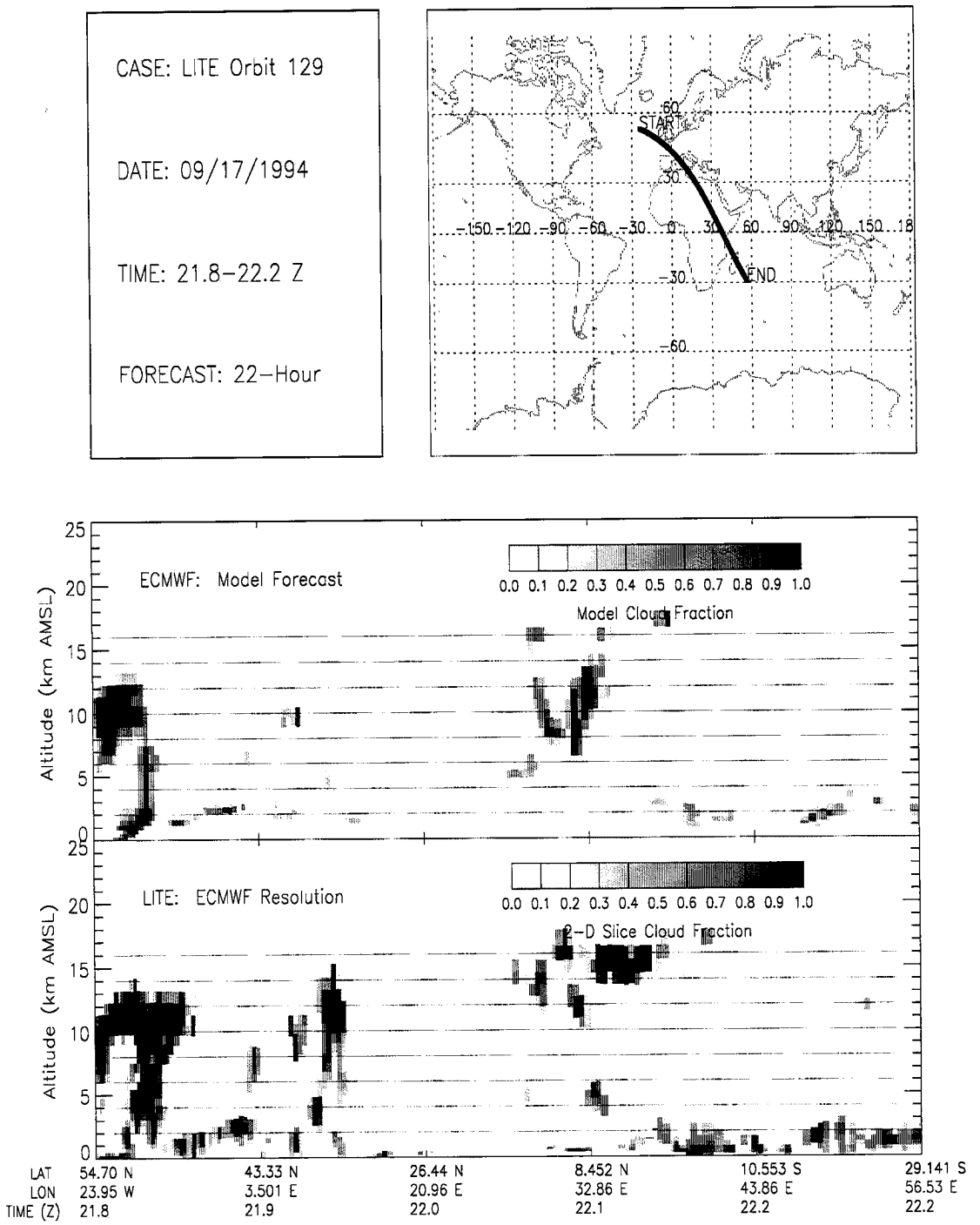

Figure B.105: LITE Orbit 129 Cloud Cover Comparison.

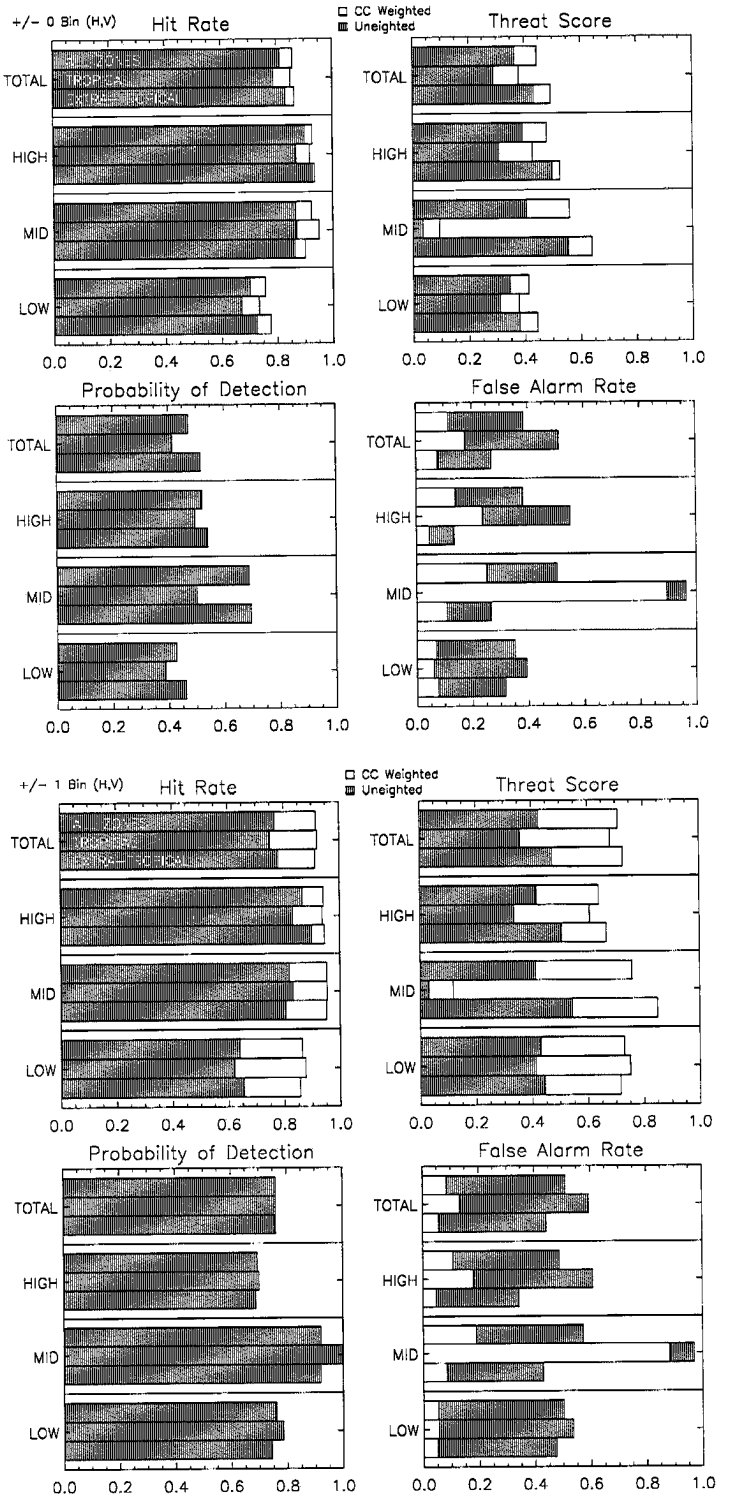

Figure B.106: LITE Orbit 129 Cloud Cover Statistics.

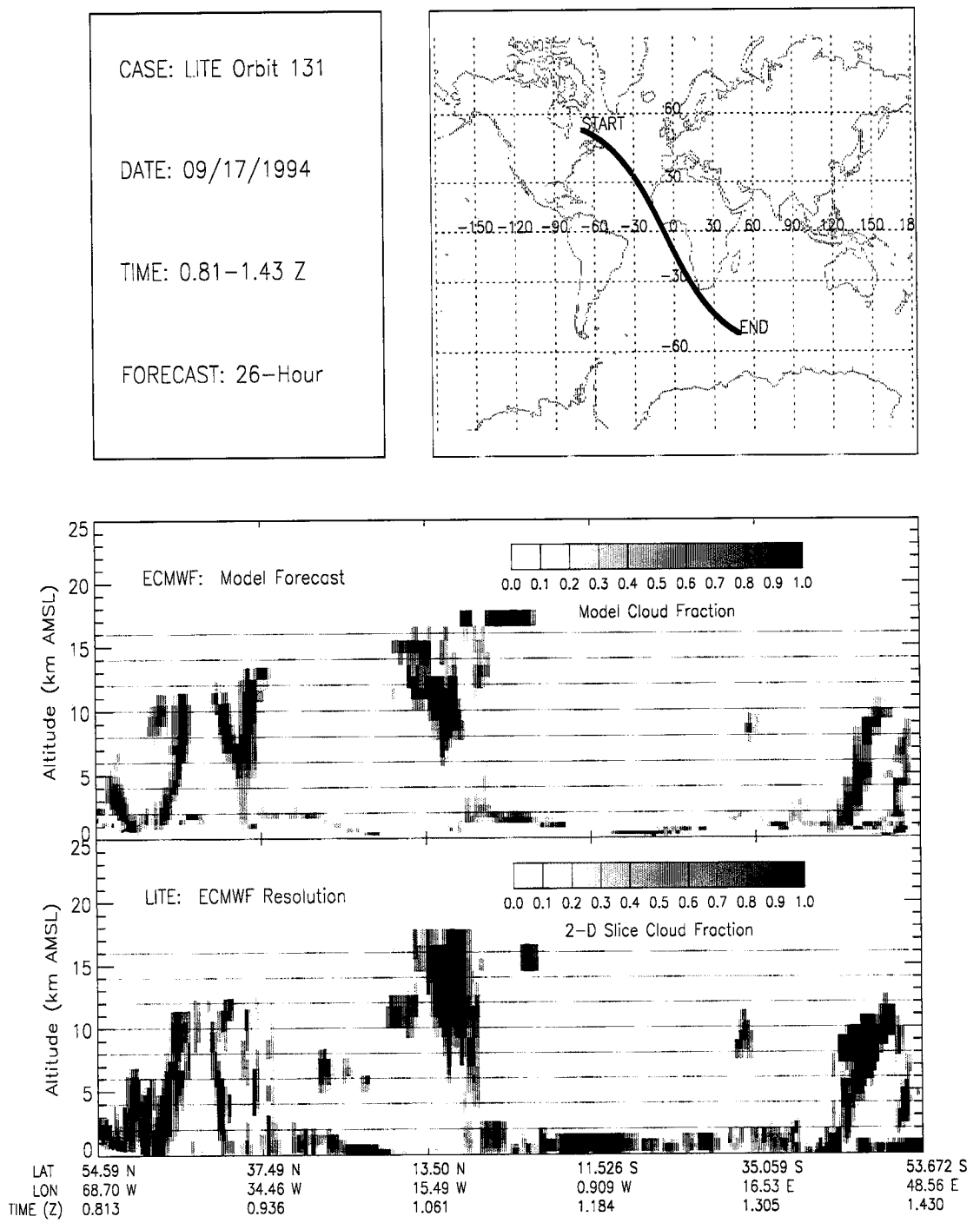

Figure B.107: LITE Orbit 131 Cloud Cover Comparison.

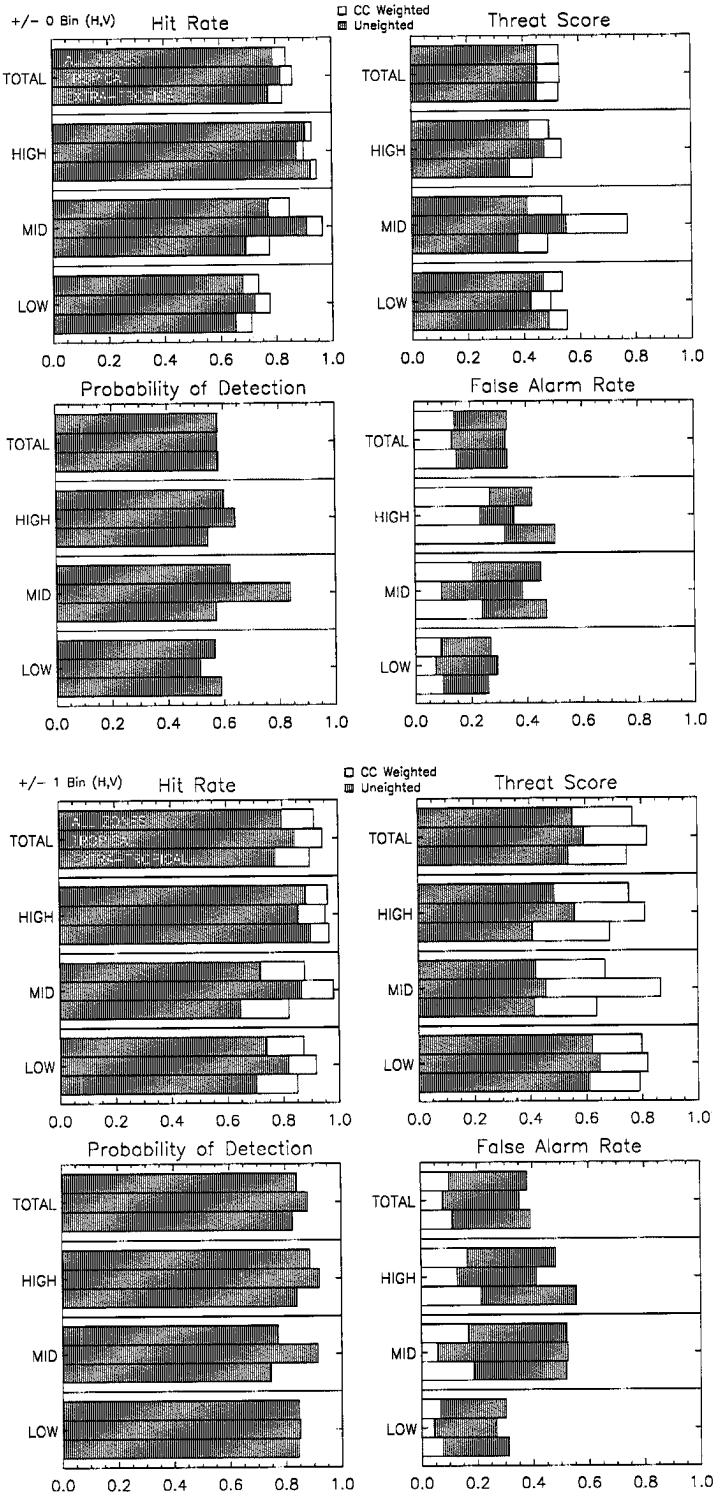

Figure B.108: LITE Orbit 131 Cloud Cover Statistics.

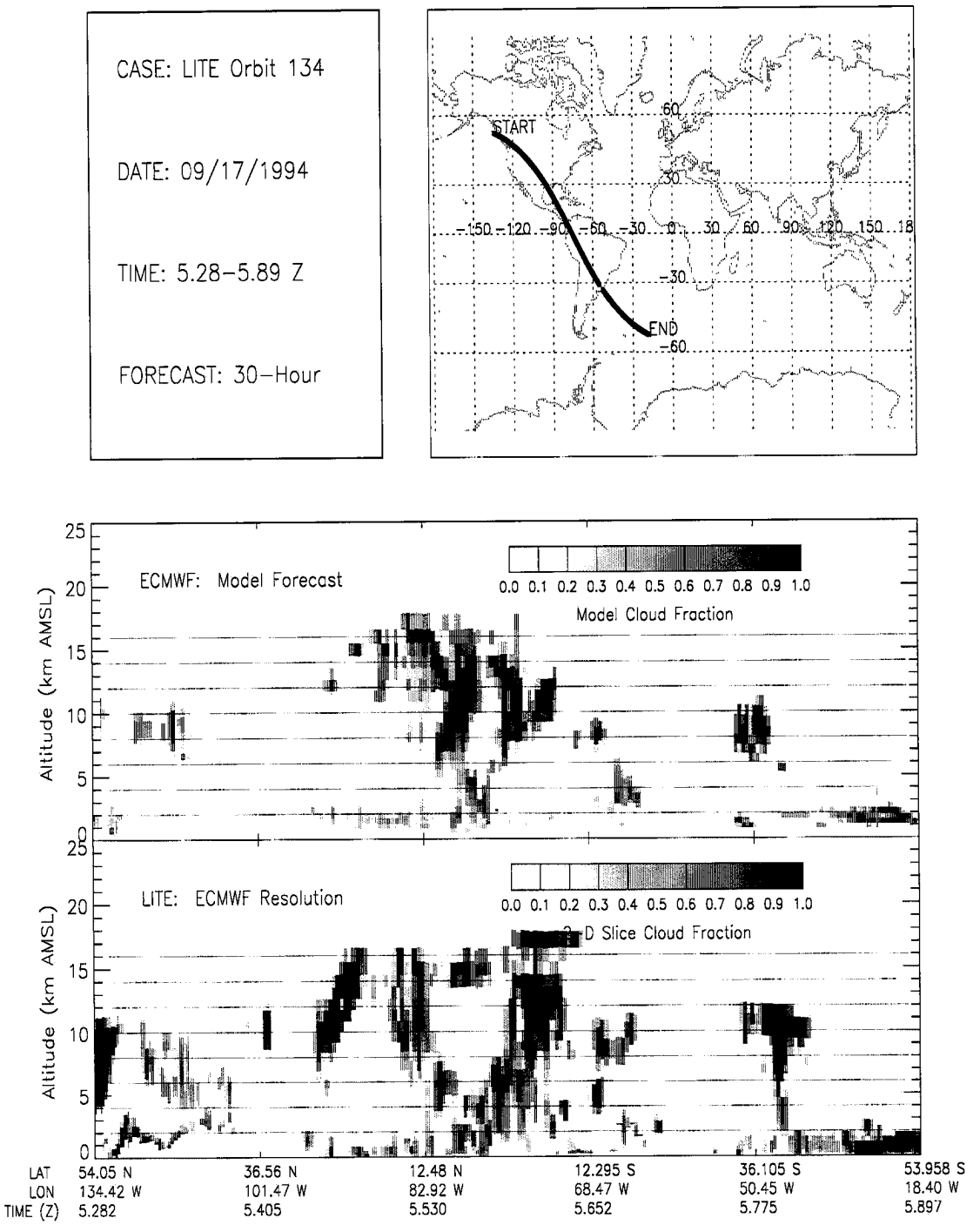

Figure B.109: LITE Orbit 134 Cloud Cover Comparison.

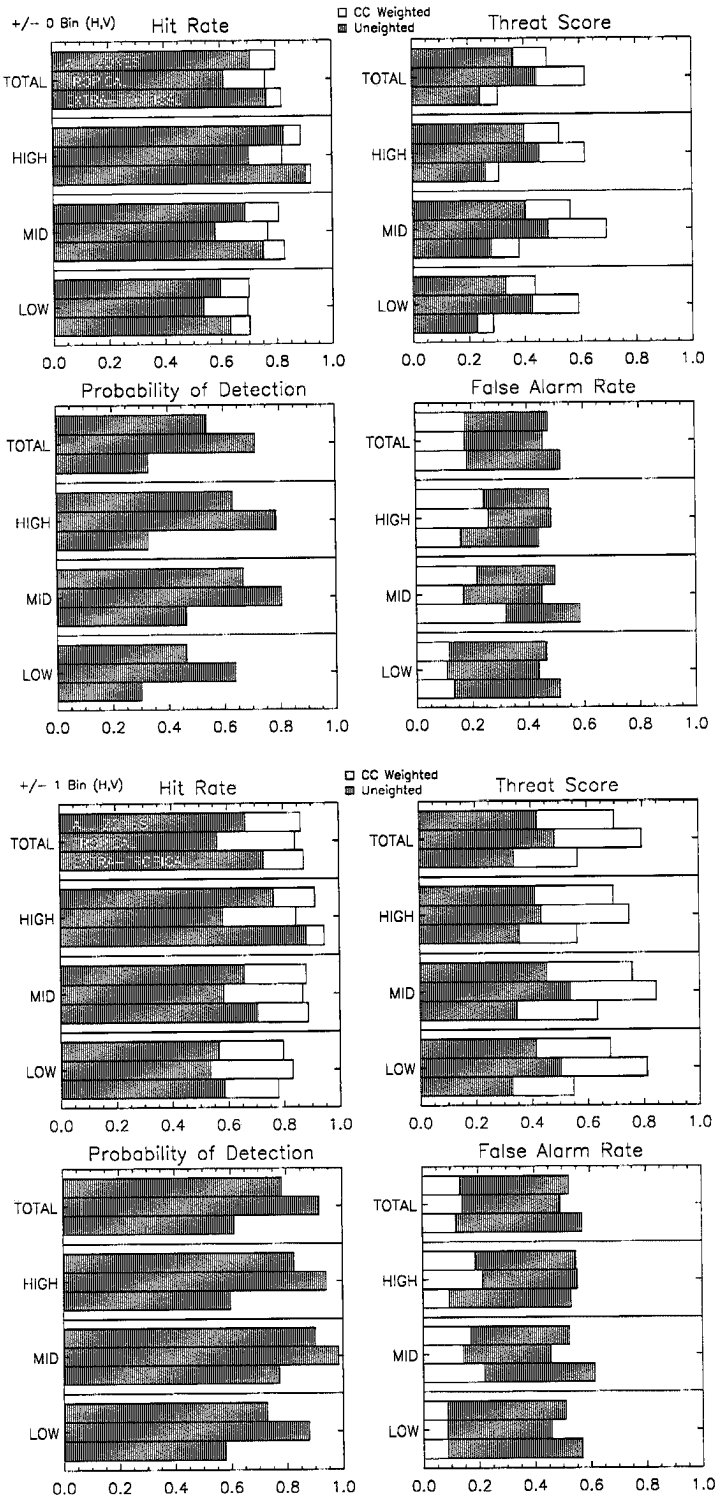

Figure B.110: LITE Orbit 134 Cloud Cover Statistics.

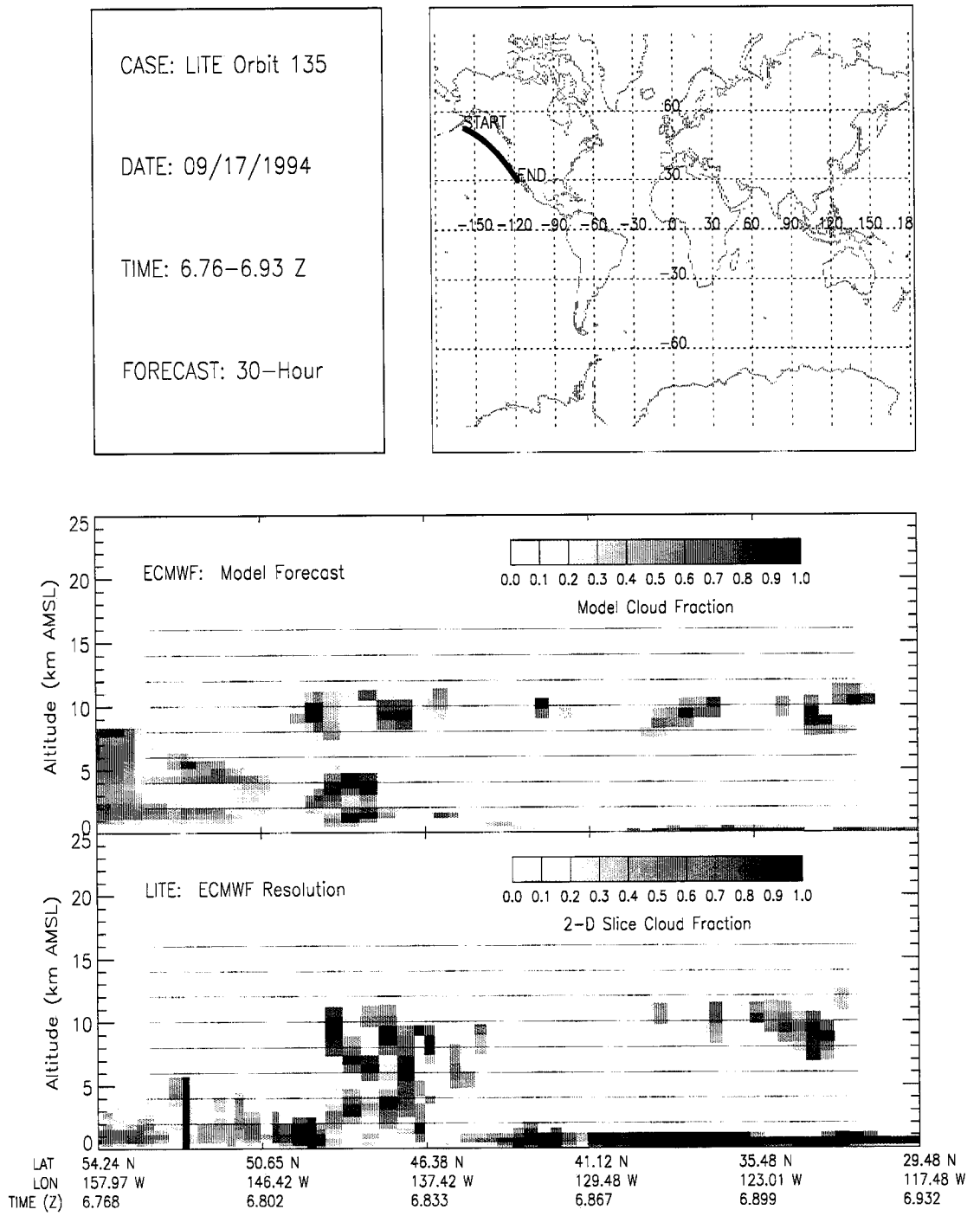

Figure B.111: LITE Orbit 135 Cloud Cover Comparison.

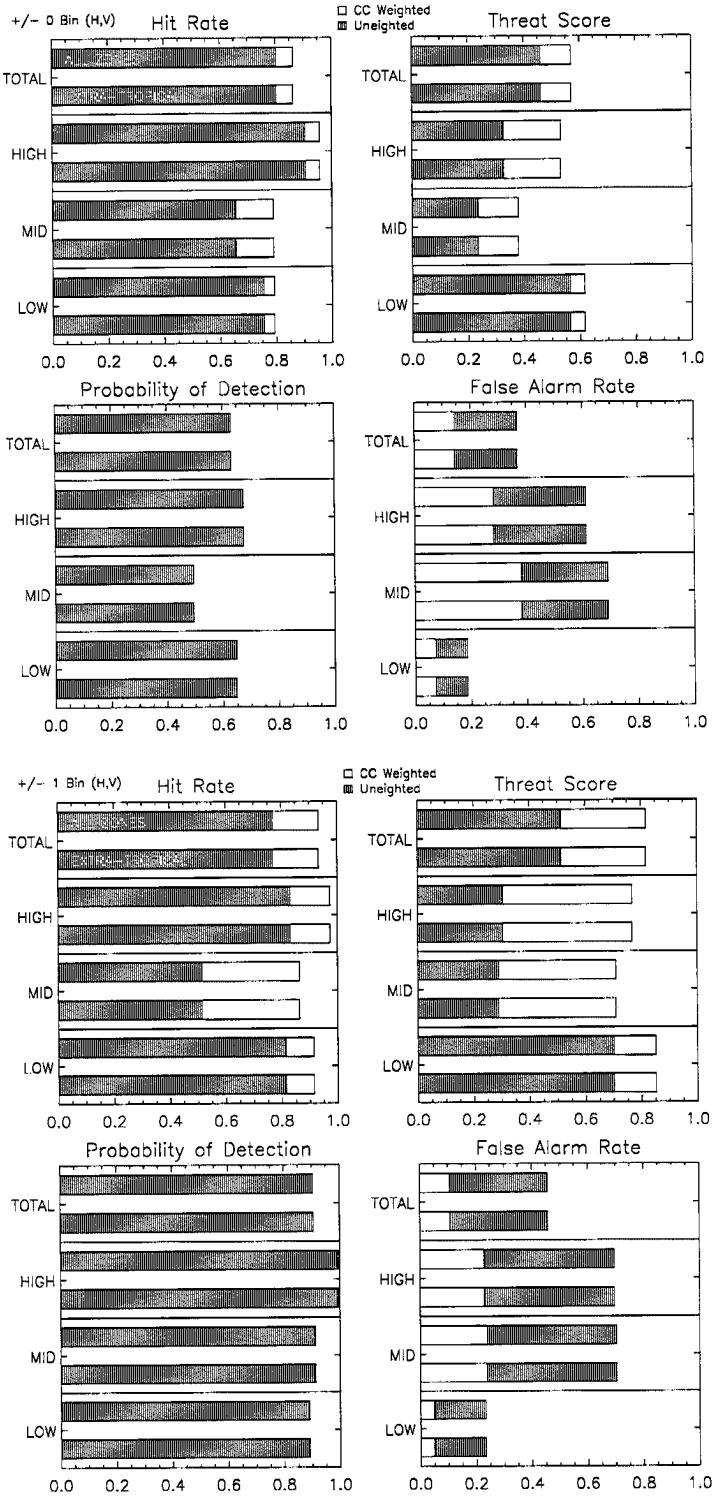

Figure B.112: LITE Orbit 135 Cloud Cover Statistics.

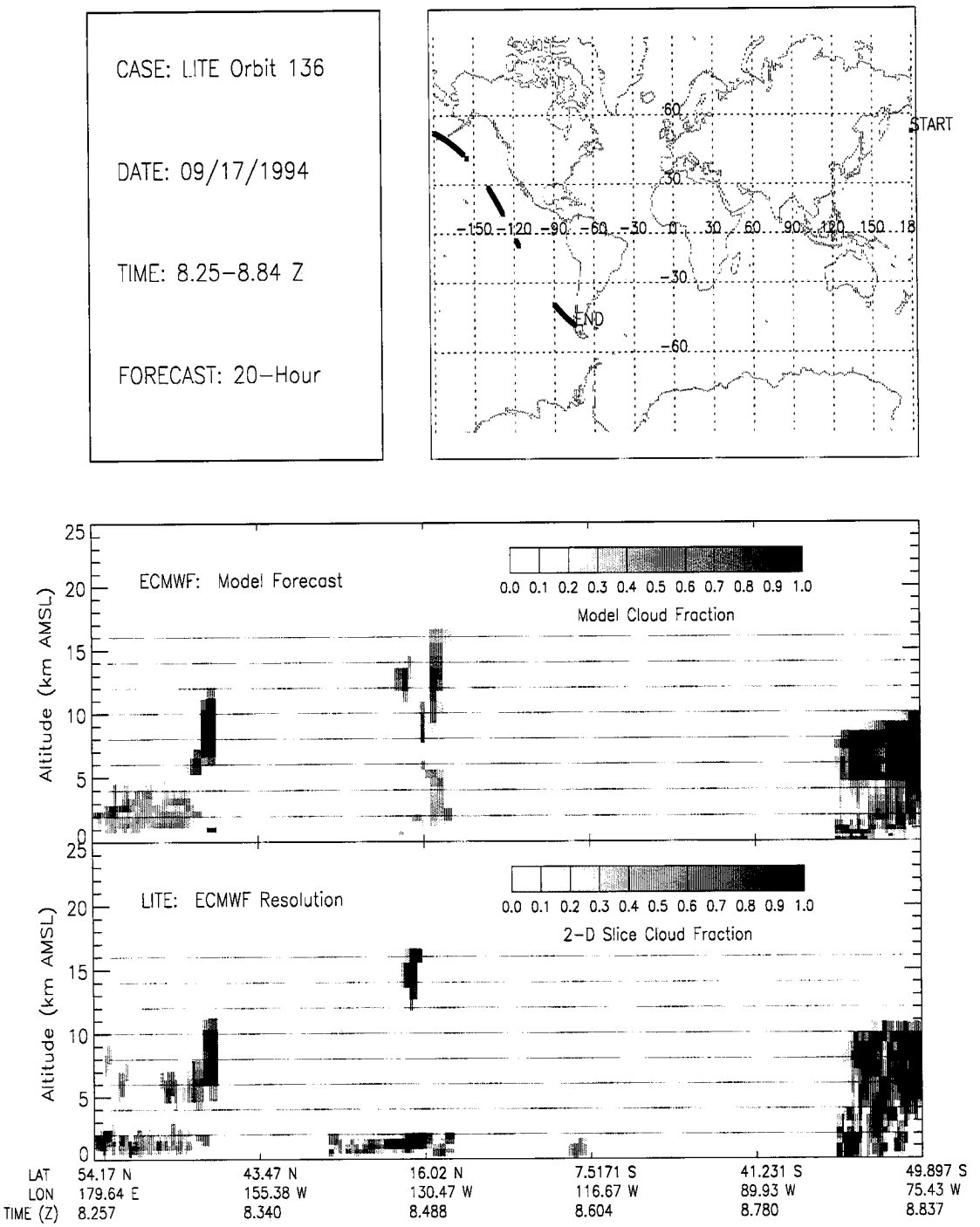

Figure B.113: LITE Orbit 136 Cloud Cover Comparison.

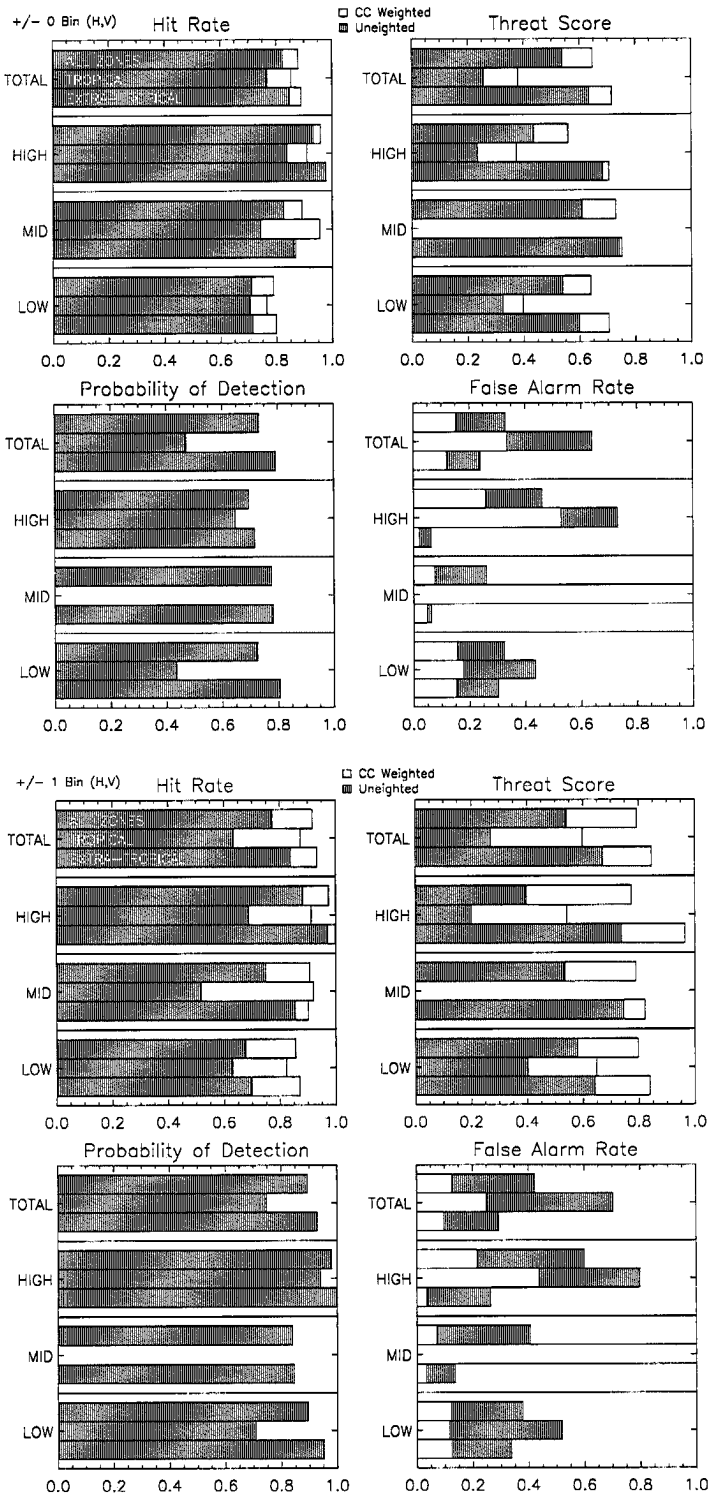

Figure B.114: LITE Orbit 136 Cloud Cover Statistics.

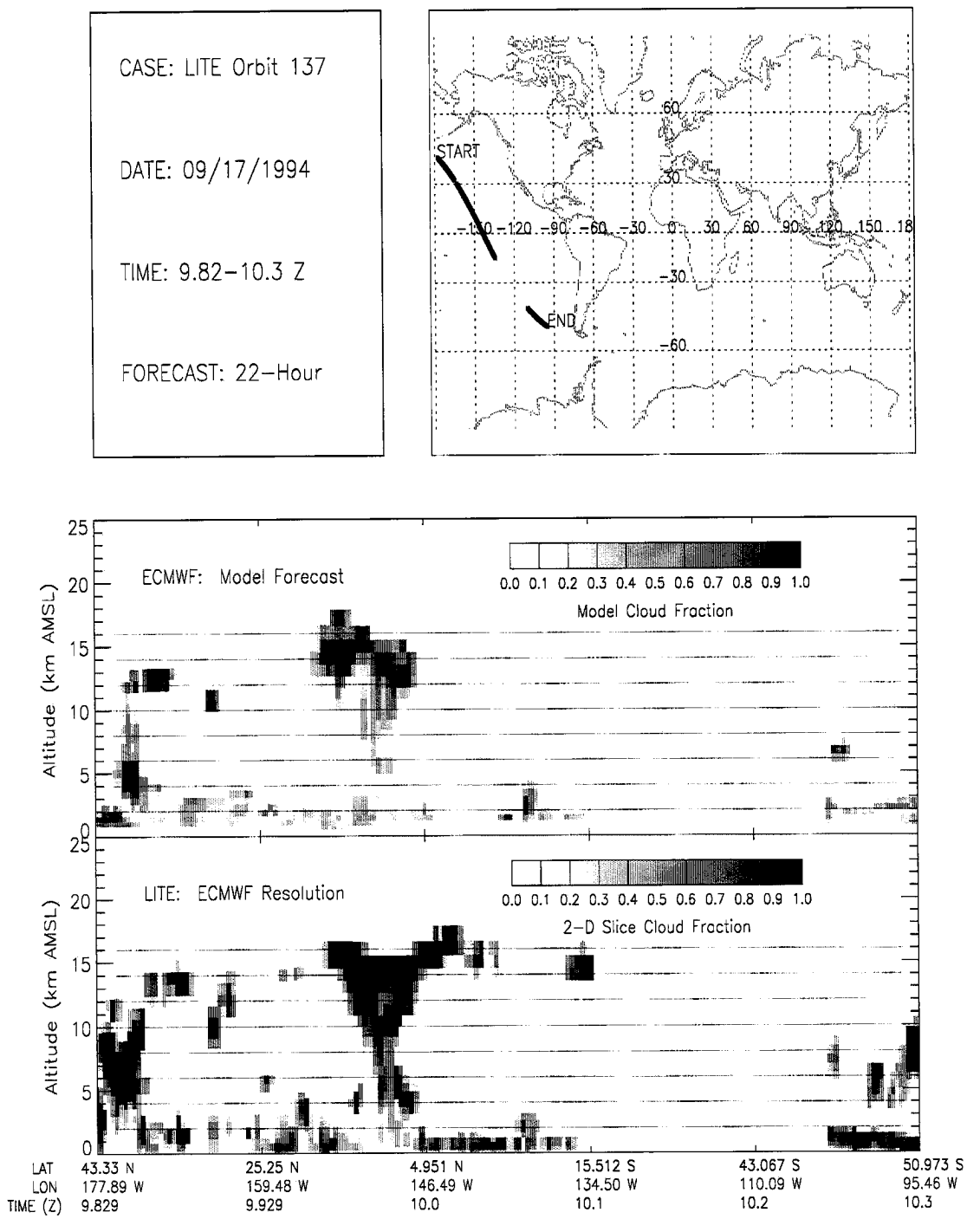

Figure B.115: LITE Orbit 137 Cloud Cover Comparison.

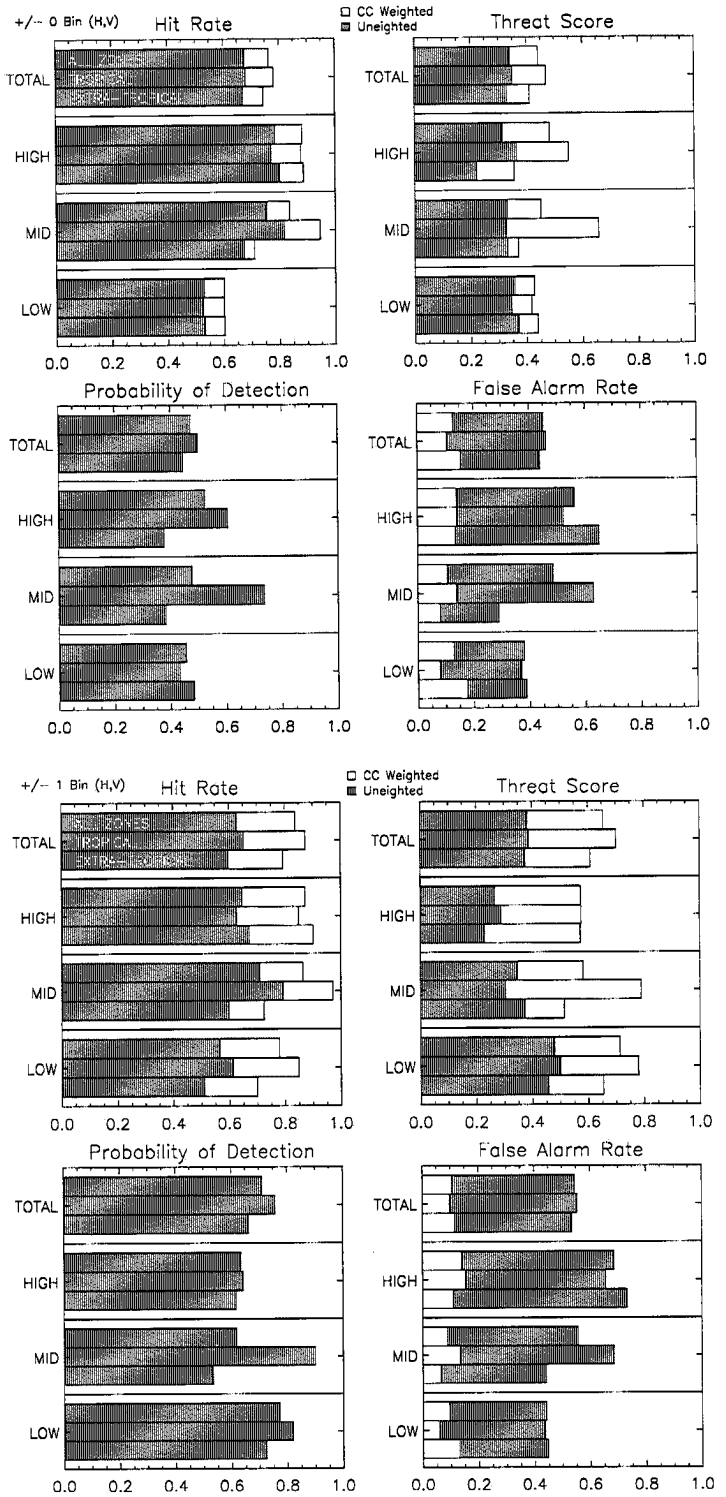

Figure B.116: LITE Orbit 137 Cloud Cover Statistics.

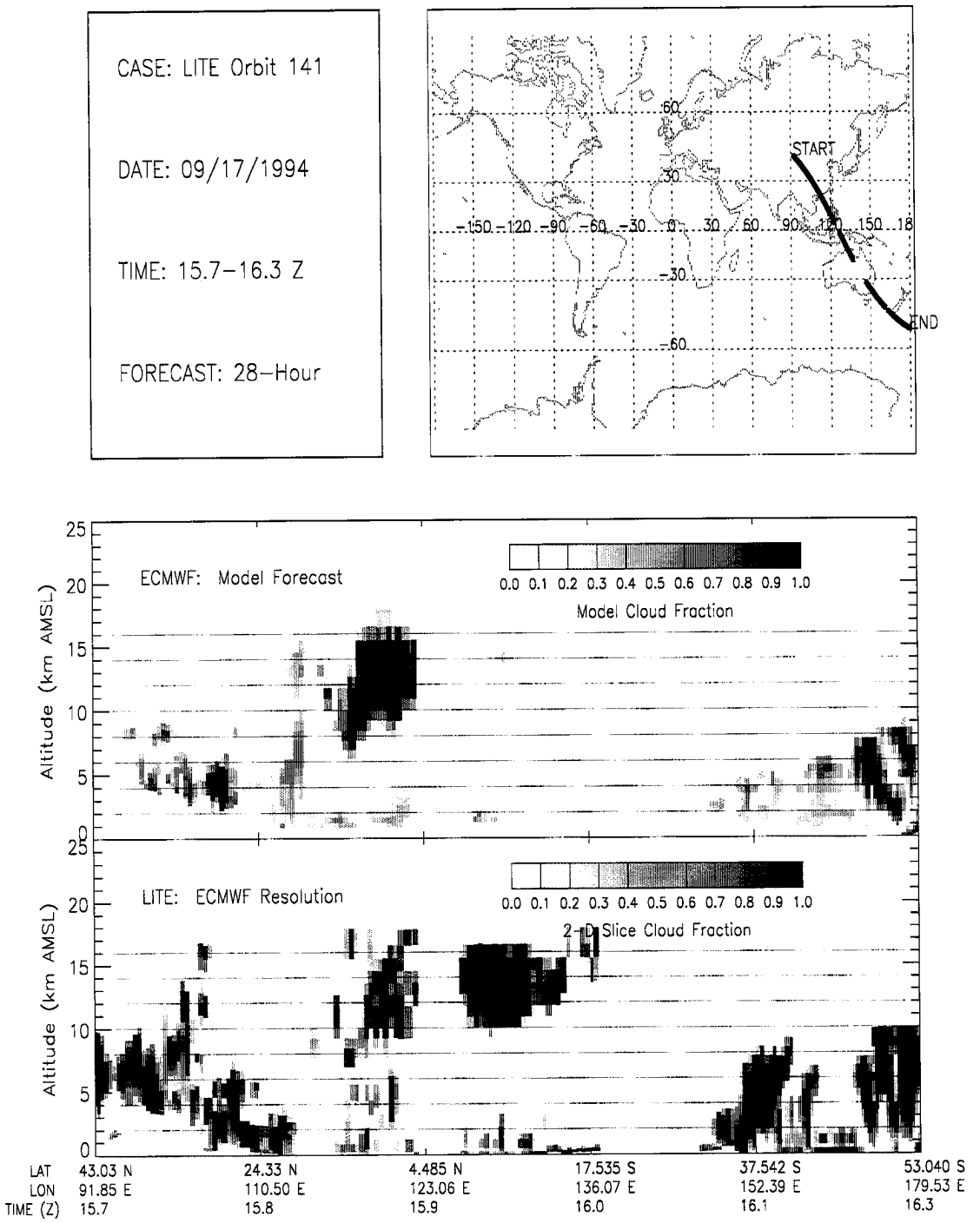

Figure B.117: LITE Orbit 141 Cloud Cover Comparison.

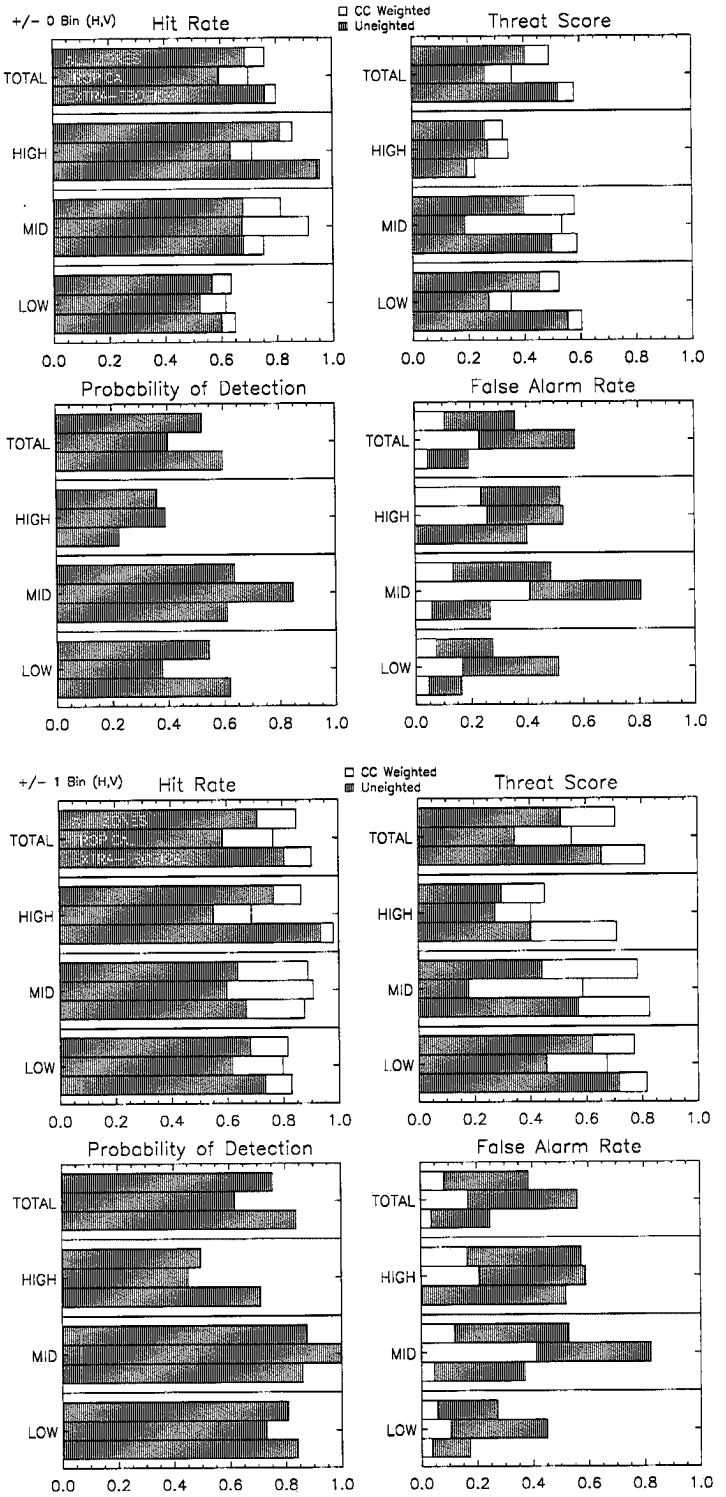

Figure B.118: LITE Orbit 141 Cloud Cover Statistics.

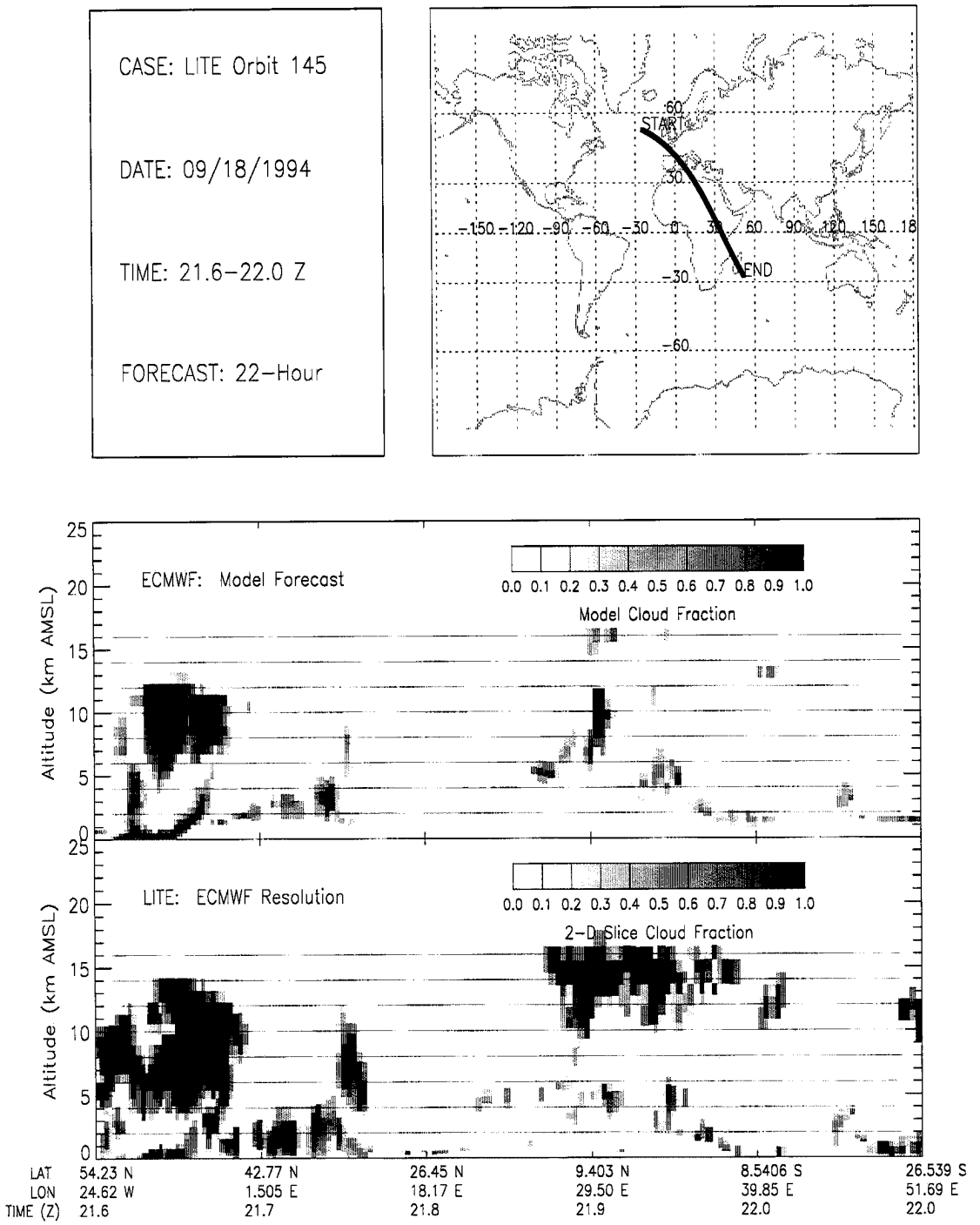

Figure B.119: LITE Orbit 145 Cloud Cover Comparison.

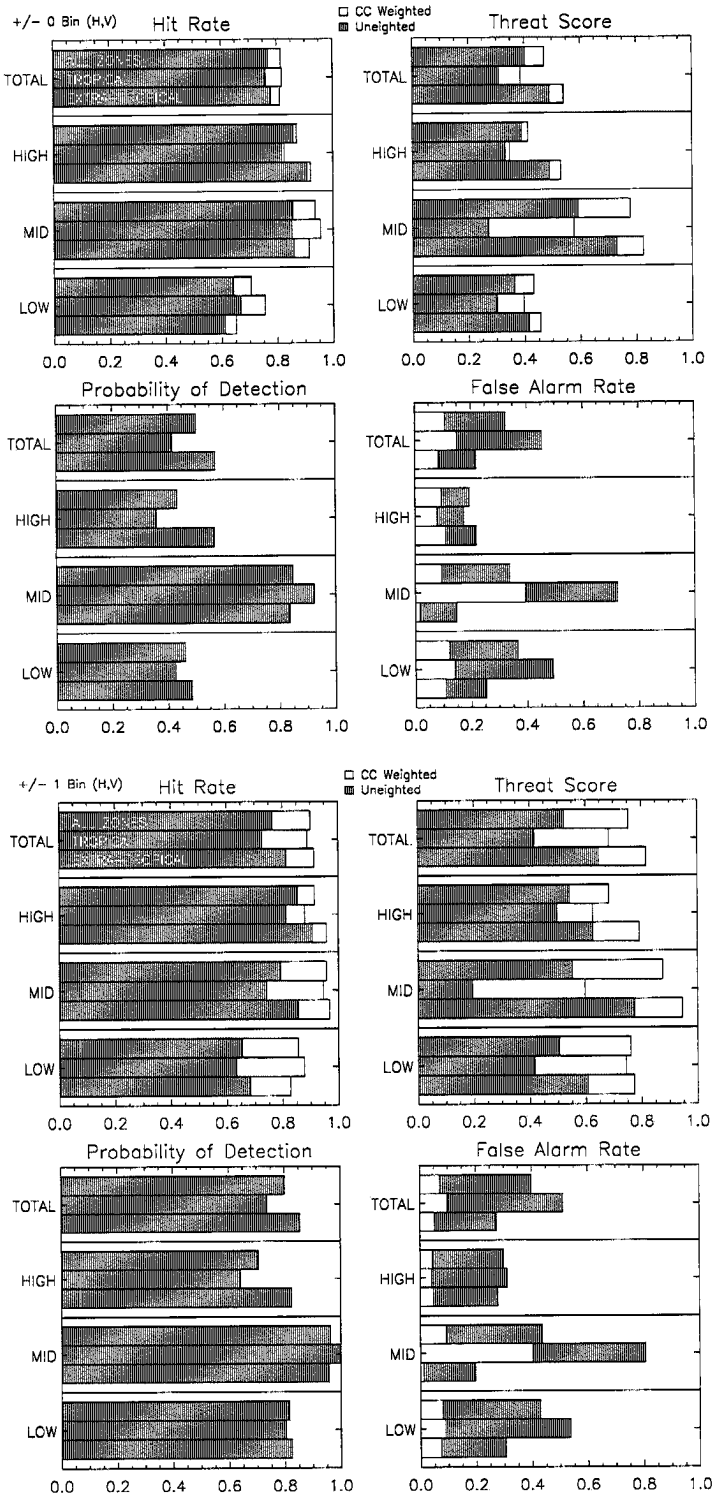

Figure B.120: LITE Orbit 145 Cloud Cover Statistics.

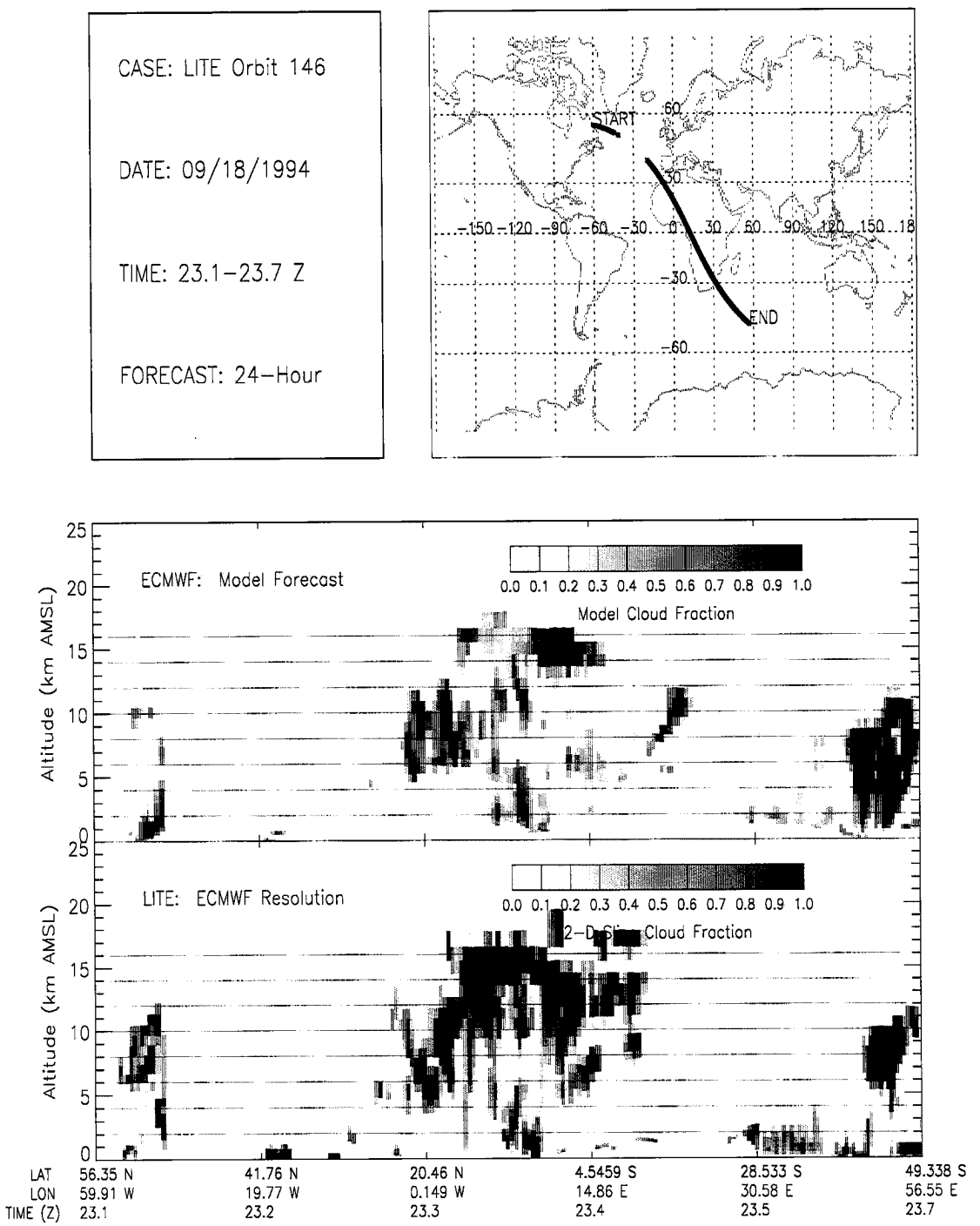

Figure B.121: LITE Orbit 146 Cloud Cover Comparison.

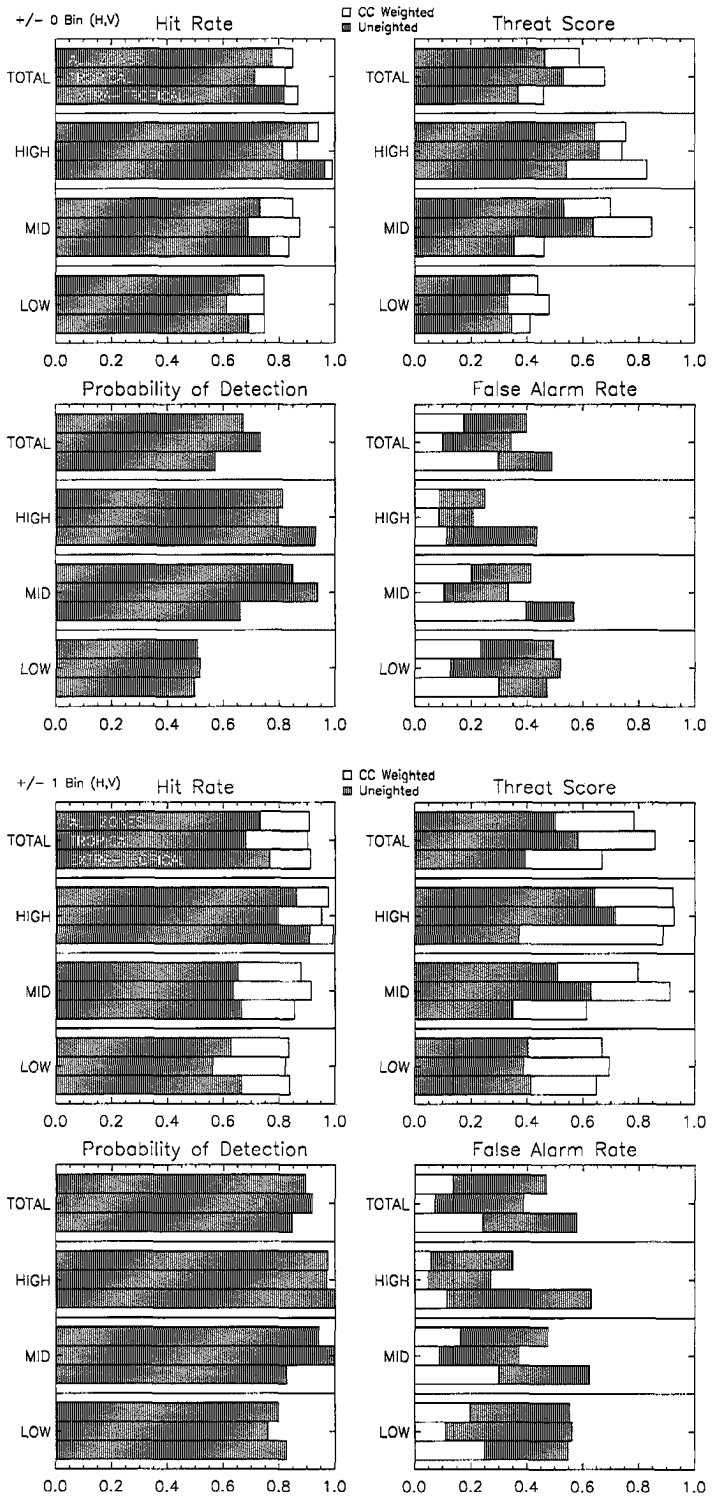

Figure B.122: LITE Orbit 146 Cloud Cover Statistics.

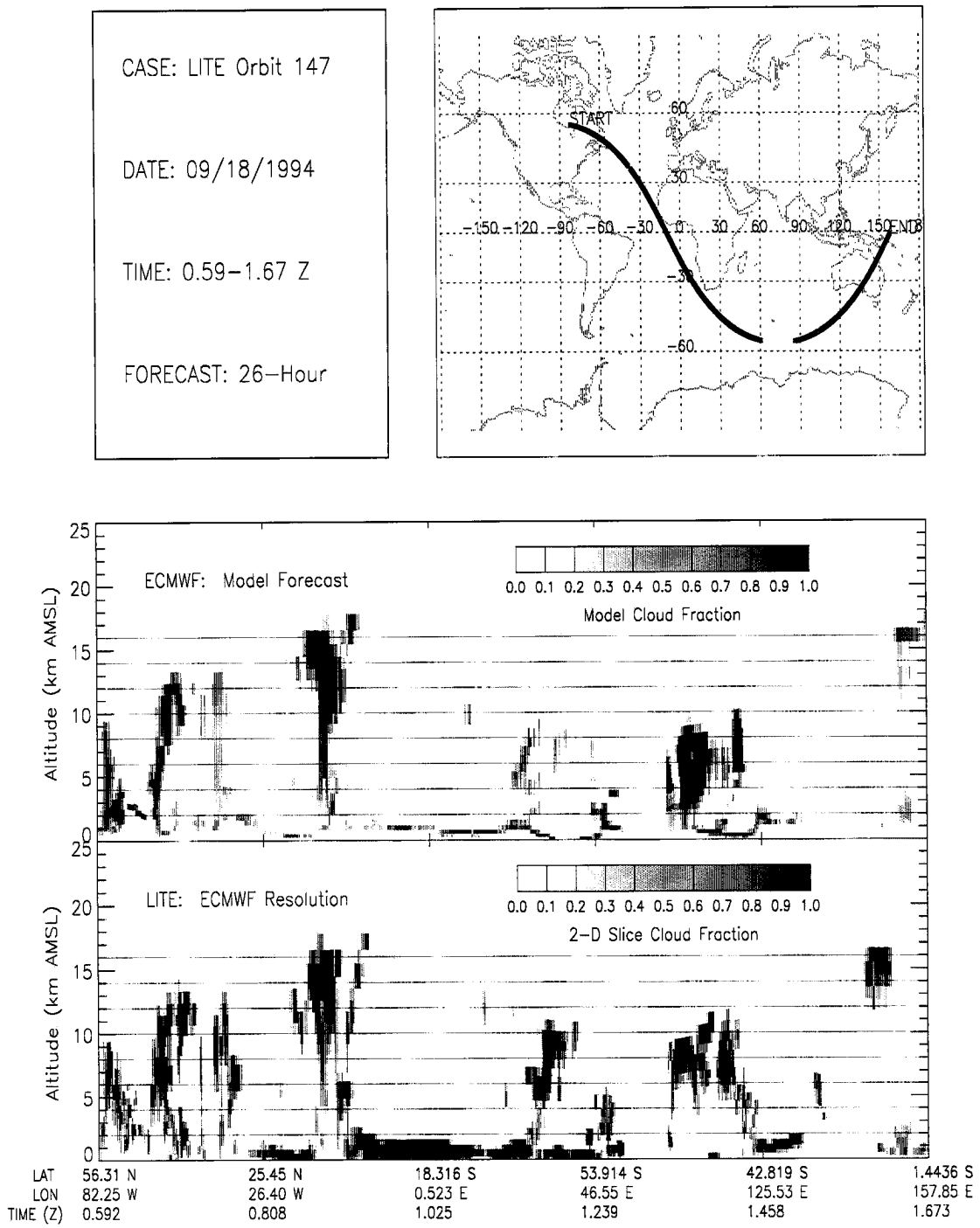

Figure B.123: LITE Orbit 147 Cloud Cover Comparison.

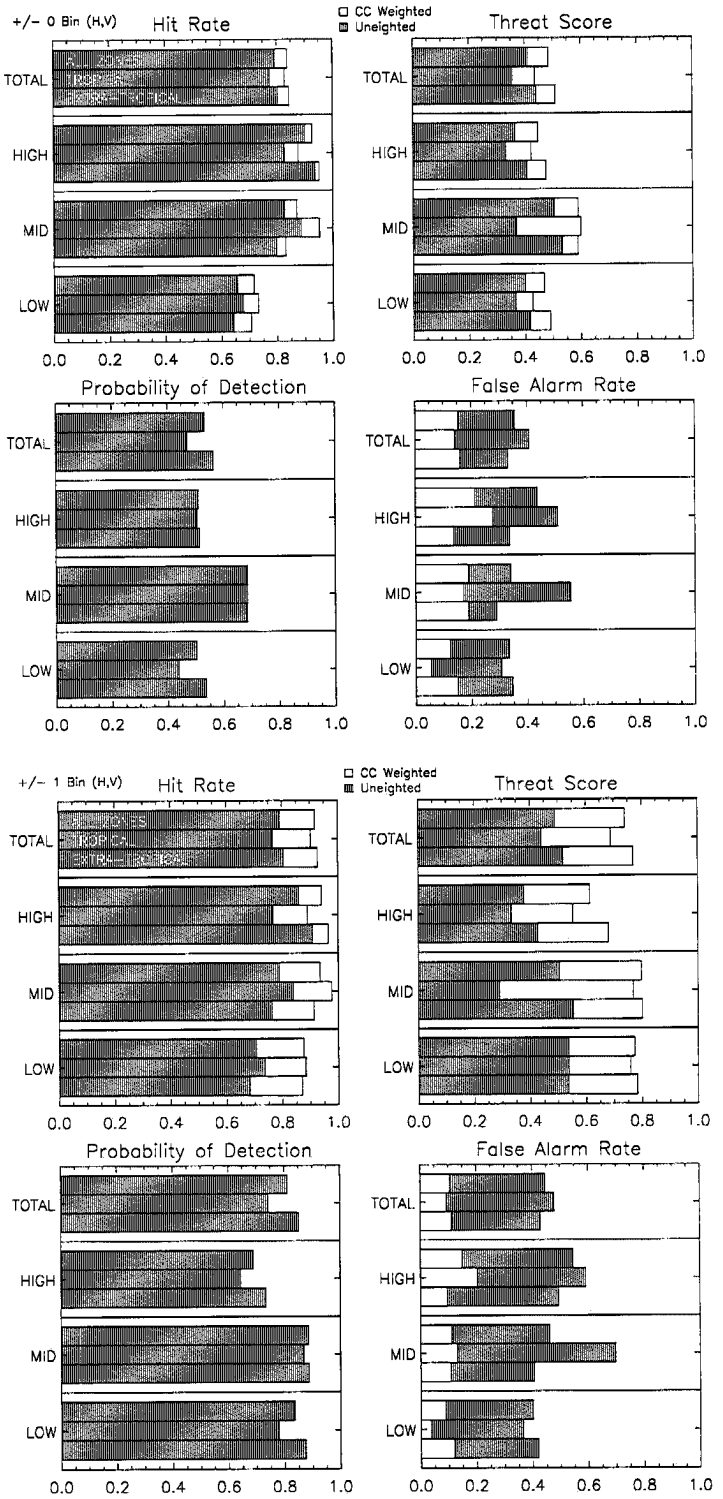

Figure B.124: LITE Orbit 147 Cloud Cover Statistics.

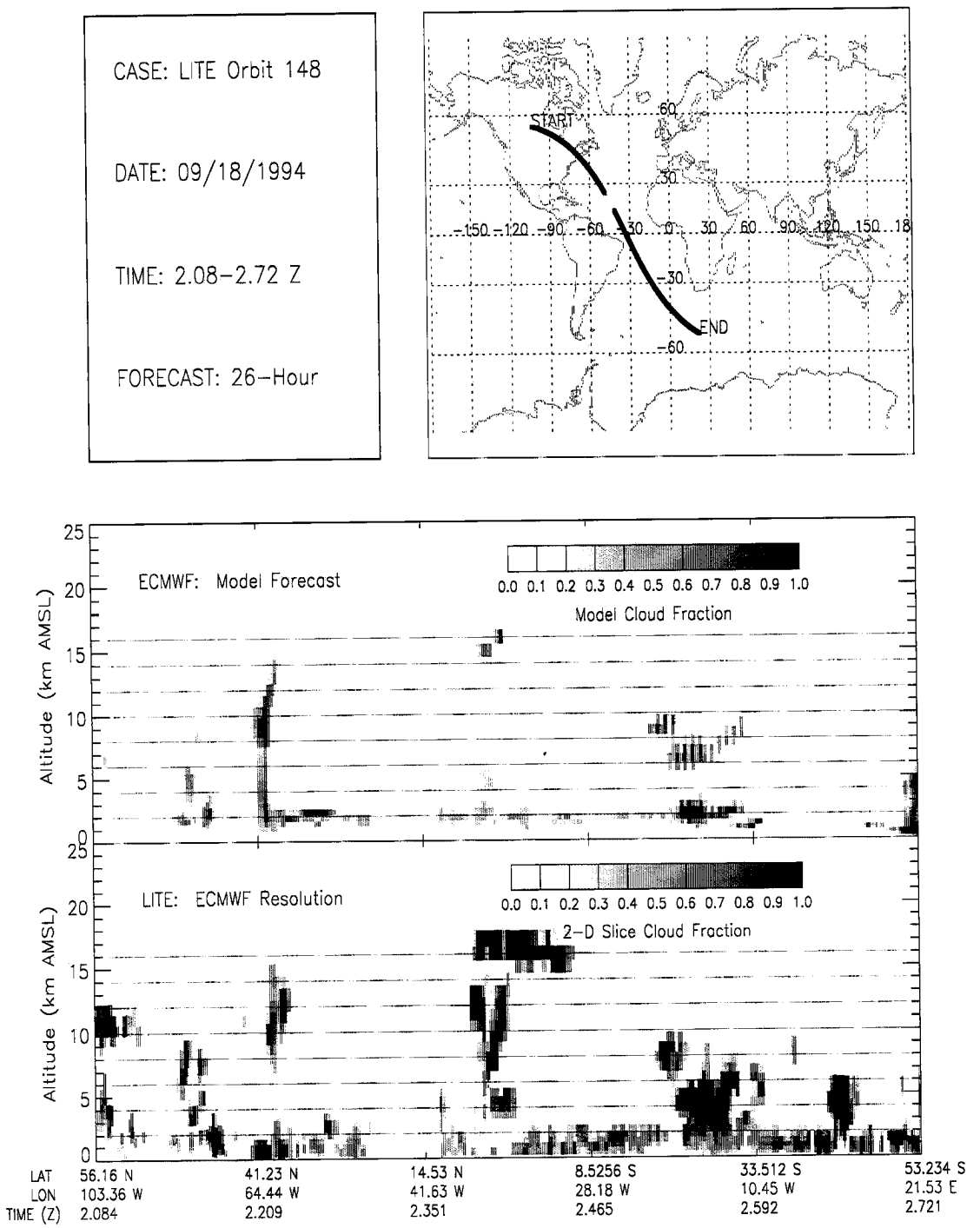

Figure B.125: LITE Orbit 148 Cloud Cover Comparison.

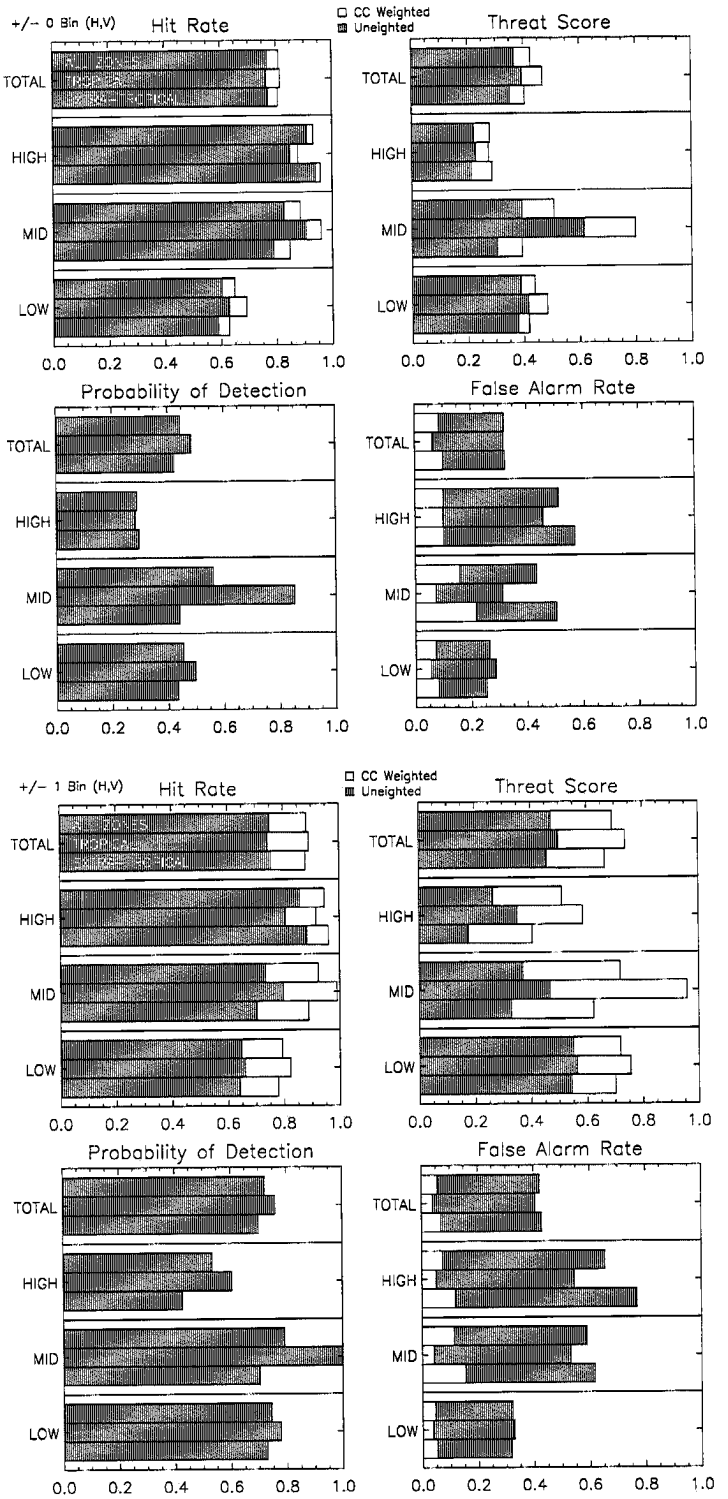

Figure B.126: LITE Orbit 148 Cloud Cover Statistics.

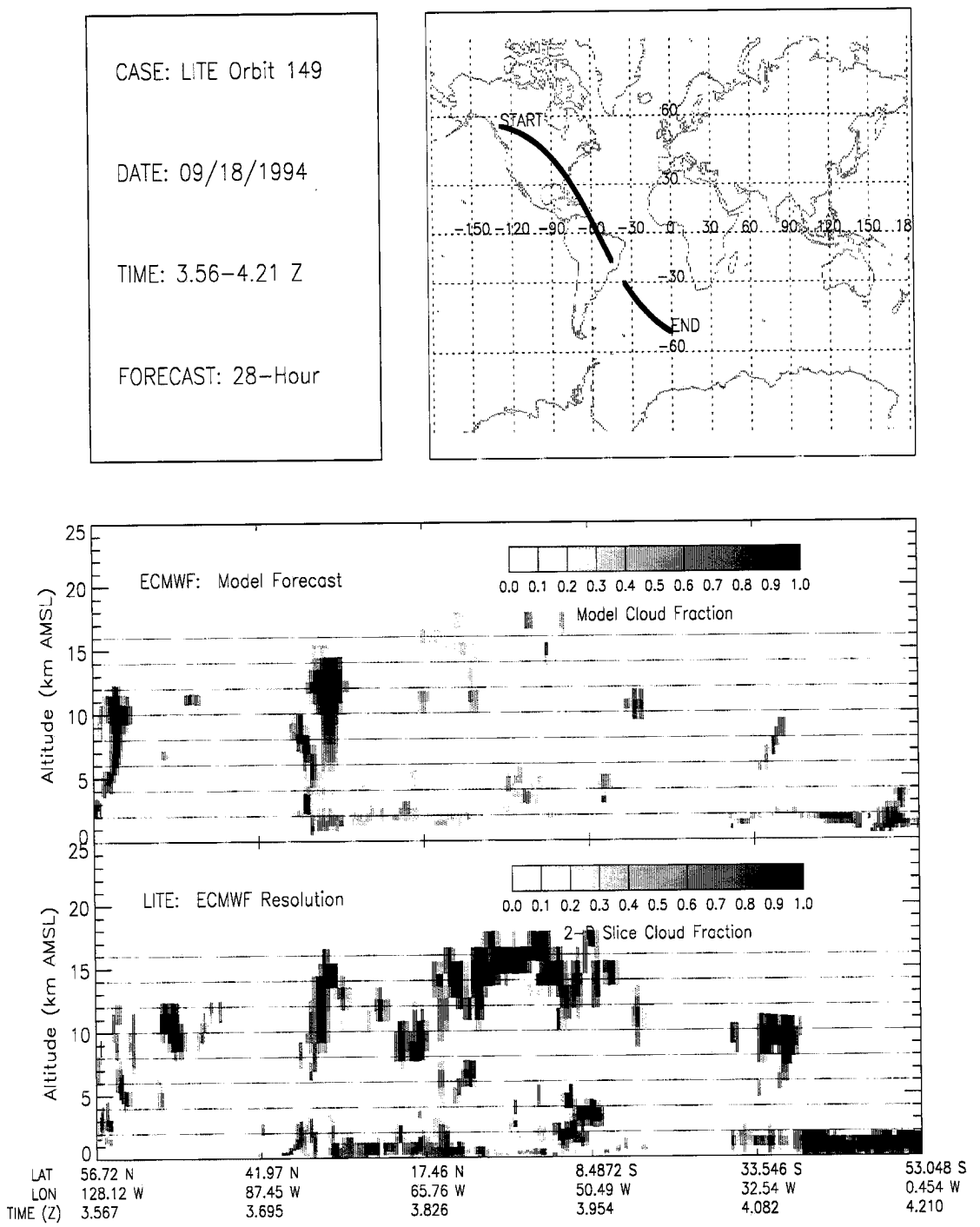

Figure B.127: LITE Orbit 149 Cloud Cover Comparison.

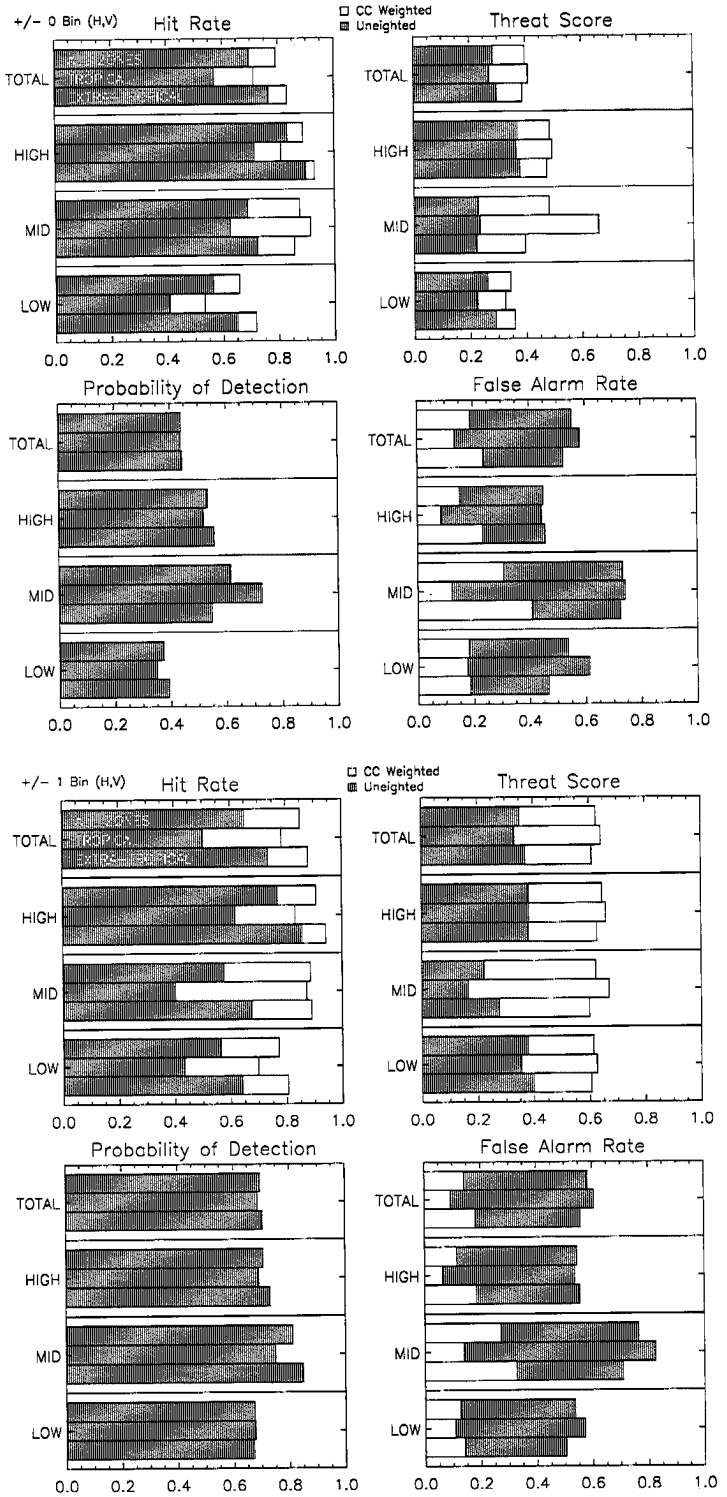

Figure B.128: LITE Orbit 149 Cloud Cover Statistics.

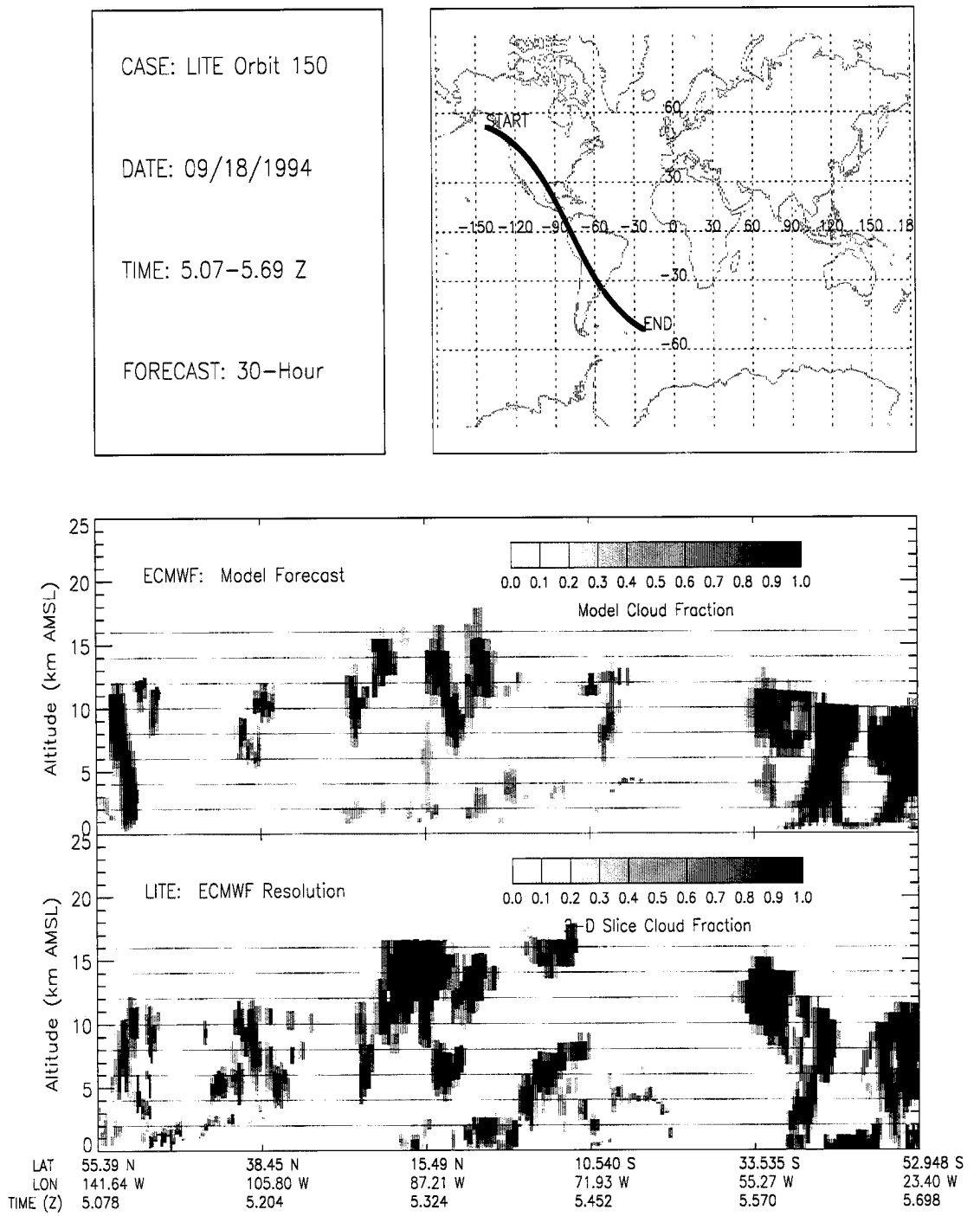

Figure B.129: LITE Orbit 150 Cloud Cover Comparison.

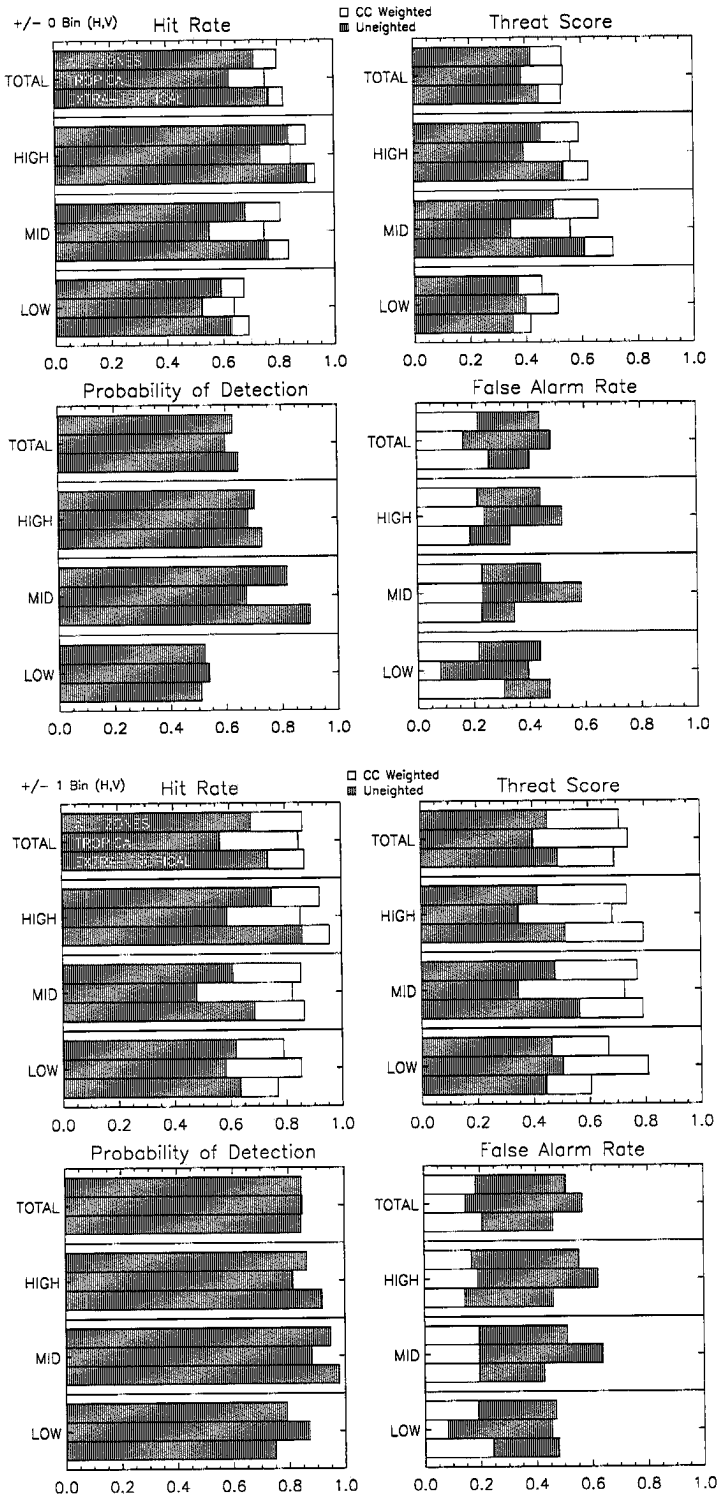

Figure B.130: LITE Orbit 150 Cloud Cover Statistics.

Appendix C

NOMENCLATURE AND ACRONYMS

- **ACR**: Airborne Cloud Radar
- **Adding Method**: Combining atmospheric layers having different optical properties
- **A priori Matrix (A)**: Retrieval matrix describing the retrieval dependence on the *a priori* estimate of $\vec{x}$
- **ARM**: Atmospheric Radiation Measurement program
- **Asymmetry Parameter (g)**: Expected value of the scattering phase function
- **ARM-SWIOP**: ARM Shortwave IOP
- **ARESE**: ARM Enhanced Shortwave Experiment
- **ATBD**: Algorithm Theoretical Basis Document
- **AVHRR**: Advanced Very High Resolution Radiometer
- **Azimuthal Asymmetry**: Describing the variation of a radiation field with respect to azimuth
- **Blackbody**: Hypothetical body that absorbs and emits perfectly ($\epsilon = 1.0$) at all wavelengths.
- **Brightness Temperature ($\mathbf{T}_B$)**: Observed temperature of an emissive scene described in terms of the equivalent temperature of a blackbody emitter
- **Broadband**: Describing a spectrally integrated quantity (either across the entire spectrum or as specified across an arbitrary spectral bandwidth)

- **BTD**: Brightness Temperature Difference (either between two channels for a single scene, or the same channel at two different times)
- **CART**: Cloud and Radiation Test-bed (ARM)
- **CAVEX**: CloudSat Antecedent Validation Experiment
- **CDL**: Cloud Detection Lidar
- **CERES**: Clouds and the Earth's Radiant Energy System
- **CFAD**: Cumulative Frequency in Altitude Diagram
- **CIRA**: Cooperative Institute for Research of the Atmosphere
- **CK**: Correlated-K distribution (technique for handling gaseous absorption across a spectral band interval)
- **CLEX**: Complex Layered cloud Experiment
- **CloudSat**: Satellite carrying first civilian W-band cloud radar in space. To be launched in 2003.
- **CONUS**: Referring to a sector of satellite imagery covering the CONtinental United States
- **CPR**: Cloud Profiling Radar (millimetric)
- **CRF**: Cloud Radiative Forcing (defined for the shortwave and longwave as the difference between clearsky and all-sky TOA broadband fluxes)
- **CSU**: Colorado State University
- **DAAC**: Distributed Active Archive Center
- **DAO**: Data Assimilation Office
- **DDH**: Diagnostiques des Domaines Horizontaux (Diagnostics for horizontal domains, which can be points or areas)

- **DMSP**: Defense Meteorological Satellite Program
- **DoD**: Department of Defense
- **DoE**: Department of Energy
- **Doubling Method**: Combining atmospheric layers having identical optical properties
- **Effective Radius**: Ratio of the third moment (volume) to the second (area) moment of the cloud droplet size distribution (a proxy for the effective particle size of the distribution)
- **Emissivity** (ϵ): Spectral quantity describing the level to which a material behaves as a blackbody (0-1)
- **ECMWF**: European Centre for Medium-range Weather Forecasts
- **EOS**: Earth Observing System
- **ERBE**: Earth Radiation Budget Experiment
- **ERBS**: Earth Radiation Budget Satellite
- **ESSP**: Earth System Science Pathfinder project
- **Estimation Problem**: Technique of determining the optimal solution yielding best agreement between observations and model
- **Extinction**: Describing the removal of energy along a path due to the processes of absorption or scattering.
- **Extinction Coefficient** (σ_{ext}): A measure of extinction strength per unit distance
- **FIRE**: First ISCCP Regional Experiment
- **Forward Model**: Numerical representation of the physical environment
- **GCM**: General Circulation Model

- **GEO**: Referring to geostationary satellite orbits
- **GEOS**: Goddard Earth Observing System
- **GOES**: Geostationary Observational Environmental Satellite
- **GSFC**: Goddard Space Flight Center (NASA)
- **IDL**: Interactive Data Language
- **IFS**: Integrated Forecasting System
- **IOP**: Intensive Observing Period
- **Interaction Principle**: Describing the boundary incident and exitant radiance fields accounting for multiple scattering
- **Inversion Problem**: Generation of virtual measurements of a system using an appropriate forward (radiative transfer) model
- **IR**: Referring to the infrared (roughly 3.0- to 14-μm) portion of the optical spectrum
- **ISCCP**: International Satellite Cloud Climatology Project
- **ITCZ**: Inter-Tropical Convergence Zone
- **Kernel Matrix (K)**: Describing the sensitivity of the forward model to perturbations of the parameters being retrieved
- **IWC**: Ice Water Content (kg/m^3)
- **IWP**: Ice Water Path (kg/m^2) (the ice water content integrated through the depth of the cloud)
- **JPL**: Jet Propulsion Laboratory (NASA)
- **LaRC**: NASA Langley Research Center
- **LANL**: Los Alamos National Laboratory

- **LEO**: Referring to Low-Earth-Orbit satellite orbits
- **LaRC**: Langley Research Center (NASA)
- **Lidar**: Light detection and ranging
- **LITE**: Lidar In-space Technology Experiment
- **LWC**: Liquid Water Content (kg/m^3)
- **LWP**: Liquid Water Path (kg/m^2) (the liquid water content integrated through the depth of the cloud)
- **MAS**: MODIS Airborne Simulator
- **MCC**: Mesoscale Convective Complex
- **MCSE**: Monterey Coastal Stratus Experiment
- **MDS**: Minimum Detectable Signal
- **MODIS**: Moderate-Resolution Imaging Spectroradiometer
- **Monochromatic**: At a single wavelength.
- **Monte Carlo**: A stochastic solution to the radiative transfer equation involving the physical tracing of photons through a medium
- **MS**: Multiple Scattering
- **NASA**: National Aeronautics and Space Administration
- **NESDIS**: National Environmental Satellite Data, and Information Service (NOAA)
- **NIR**: Near Infrared, defined here as 0.7- to 4.0-μm
- **NOAA**: National Oceanic and Atmospheric Administration
- **NWP**: Numerical Weather Prediction
- **Optical Depth (τ)**: Integrated extinction along a vertical path

- **Optical Thickness**: Integrated extinction along an arbitrary path
- **OSE**: Office of Earth Science
- **PACRIM**: The Pacific Rim Experiment (CLEX-2)
- **PBL**: Planetary Boundary Layer (interface between the Earth's surface and the free atmosphere)
- **PDF**: Probability Density Function
- **PICASSO-CENA**: Pathfinder Instruments for Cloud and Aerosol Spacebourne Observations/Climatologie Etendue des Nuages et des Aerosols
- **Phase**: Referring to water at various states of molecular excitement (ice, liquid, or vapor) dependent upon temperature and pressure according to the Clausius Clapeyron equation
- **Phase Function ($\mathbf{P}(\Theta)$)**: Describing the scattering behavior of radiation incident upon a cloud droplet distribution.
- **Plane Parallel**: Describing a medium represented as an infinite slab whose optical properties are horizontally-homogeneous.
- **Radar**: Radio Detection and Ranging
- **Radiometry**: Radiation+Geometry, the art of measuring radiation in terms of directional intensity and flux normal to a plane
- **Rayleigh Scatter**: Describing scatter of solar radiation by the molecular atmosphere (primarily applicable to $\lambda < 1.0\mu$m)
- **Ray-tracing**: The method of ascertaining scattering properties of complex particle morphologies via Monte Carlo methods
- **RTE**: Radiative Transfer Equation
- **SAR**: Synthetic Aperture Radar

- **Scattering Angle (Θ)**: Angle formed between the incident and scattered directions of a photon trajectory.
- **SERCAA**: Support of Environmental Requirements for Cloud Analysis and Archive (cirrus detection algorithm)
- **SGP**: Southern Great Plains (ARM)
- **Single Scatter Albedo ($\omega_\circ$)**: Probability of extinction due to scattering
- **SLADRT**: Shortwave/Longwave Adding/Doubling Radiative Transfer code
- **SNL**: Sandia National Laboratory
- **SNR**: Signal to Noise Ratio
- **Spatial**: Referring to the domain of physical space
- **Spectral**: Referring to a wavelength-dependent quantity
- **Solid Angle (Ω)**: Measured in steradians, corresponding to the surface area of an opening on the unit sphere
- **Solar Zenith Angle ($\mu_\circ$)**: Angle formed between solar direct beam and the local vertical
- **SSFR**: Solar Spectral Flux Radiometer
- **SSP**: Scanning Spectral Polarimeter
- **Streams**: Defining specific ray directions in discrete-ordinate radiation transfer
- **SUCCESS**: Subsonic Aircraft and Cloud Effects Special Study
- **TDDR**: Total/Direct/Diffuse Radiometer
- **Temporal**: Referring to the time domain
- **TOA**: Top Of Atmosphere

- **TRMM**: Tropical Rainfall Measuring Mission
- **TWP**: Tropical Western Pacific
- **UAV**: Unmanned Aerospace Vehicle (ARM)
- **UMass**: University of Massachusetts
- **VAS**: VISSR Atmospheric Sounder
- **Virtual Measurement**: Output of the forward model for a specified input state vector
- **Virtual Source**: A source of radiation owing to scattering into the the direction of interest
- **VIS**: Referring to the visible portion of the spectrum (0.4- to 0.7-μm)
- **VISSR**: Visible and Infrared Spin-Scan Radiometer
- **Wavelength (λ)**: Periodic distance of an electromagnetic wave
- **Wavenumber (ν)**: Number of periods of an electromagnetic wave found within a specified distance (conventionally, 1 centimeter)
- **WCRP**: World Climate Research Program
- **Window**: Referring to a spectral bandwidth where the atmospheric constituents are relatively transparent to radiation
- **WMO**: World Meteorological Organization